JANUARY 2018

AJNR

VOLUME 39 • PP 1–205

AJNR

AMERICAN JOURNAL OF NEURORADIOLOGY

JANUARY 2018
VOLUME 39
NUMBER 1
WWW.AJNR.ORG

THE JOURNAL OF DIAGNOSTIC AND INTERVENTIONAL NEURORADIOLOGY

Health care economics study guide
Fenestration of synovial cysts
MR elastography of glioma stiffness

Official Journal ASNR • ASFNR • ASHNR • ASPNR • ASSR

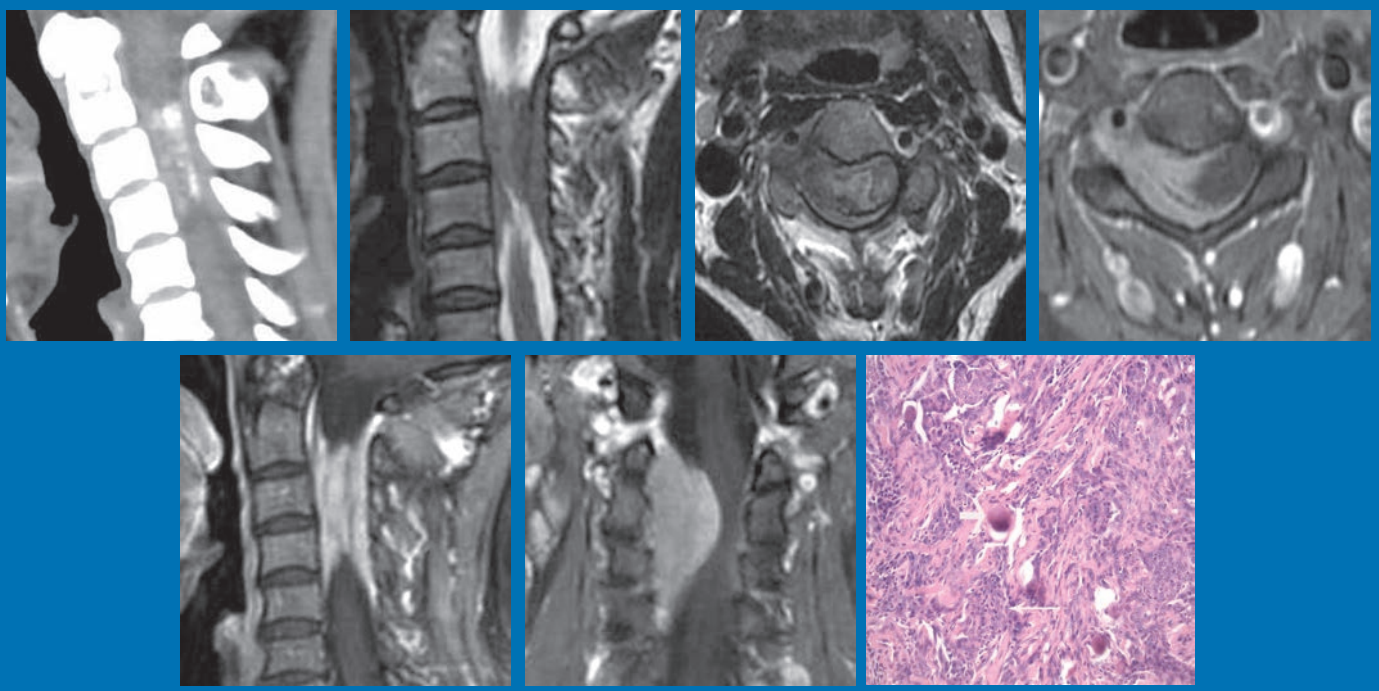

A 360-Degree Approach to Neuroendovascular Therapy

Aneurysm Therapy Solutions

LVIS® | LVIS® Jr.
Intraluminal Support Device

Braided Coil Assist Stents with High Neck Coverage, Excellent Opening, and Improved Radial Force*

**Humanitarian Device: Authorized by Federal Law for use with bare platinum embolic coils for the treatment of unruptured, wide neck (neck ≥ 4 mm or dome to neck ratio < 2), intracranial, saccular aneurysms arising from a parent vessel with a diameter ≥ 2.5 mm and ≤ 4.5 mm. The effectiveness of this device for this use has not been demonstrated.*

Access Product Solutions

Headway® DUO
Microcatheter

Innovative Catheter Technology and Construction in a Complete Range of Sizes and Softness

For more information or a product demonstration, contact your local MicroVention representative:

MicroVention® TERUMO

MicroVention, Inc.
Worldwide Headquarters PH +1.714.247.8000
35 Enterprise
Aliso Viejo, CA 92656 USA
MicroVention UK Limited PH +44 (0) 191 258 6777
MicroVention Europe, S.A.R.L. PH +33 (1) 39 21 77 46
MicroVention Deutschland GmbH PH +49 211 210 798-0
microvention.com

MICROVENTION, Scepter C, Scepter XC, Sofia, LVIS and Headway are registered trademarks of MicroVention, Inc. • Refer to Instructions for Use, contraindications and warnings for additional information. Federal (USA) law restricts this device for sale by or on the order of a physician. ©2017 MicroVention, Inc. Aug. 2017

stryker

Bending expectations of conformability and stability.

Enhanced conformability – The hybrid cell structure is designed to enhance stent opening and conformability in bifurcations and tight curves.

Ease of use – All sizes of the Neuroform Atlas Stent are deliverable through Excelsior® SL-10® and Excelsior XT-17™ Microcatheters.

Higher deployment accuracy – The Neuroform Atlas Stent is designed to have very low foreshortening, which enables very high deployment accuracy.

Neuroform Atlas™
STENT SYSTEM

The Neuroform Atlas Stent System is authorized under a Humanitarian Device Exemption (HDE). IRB approval is required prior to use.

Copyright © 2017 Stryker

Magic®

balt

FLOW-DEPENDENT MICROCATHETER SERIES

Now available through Balt USA

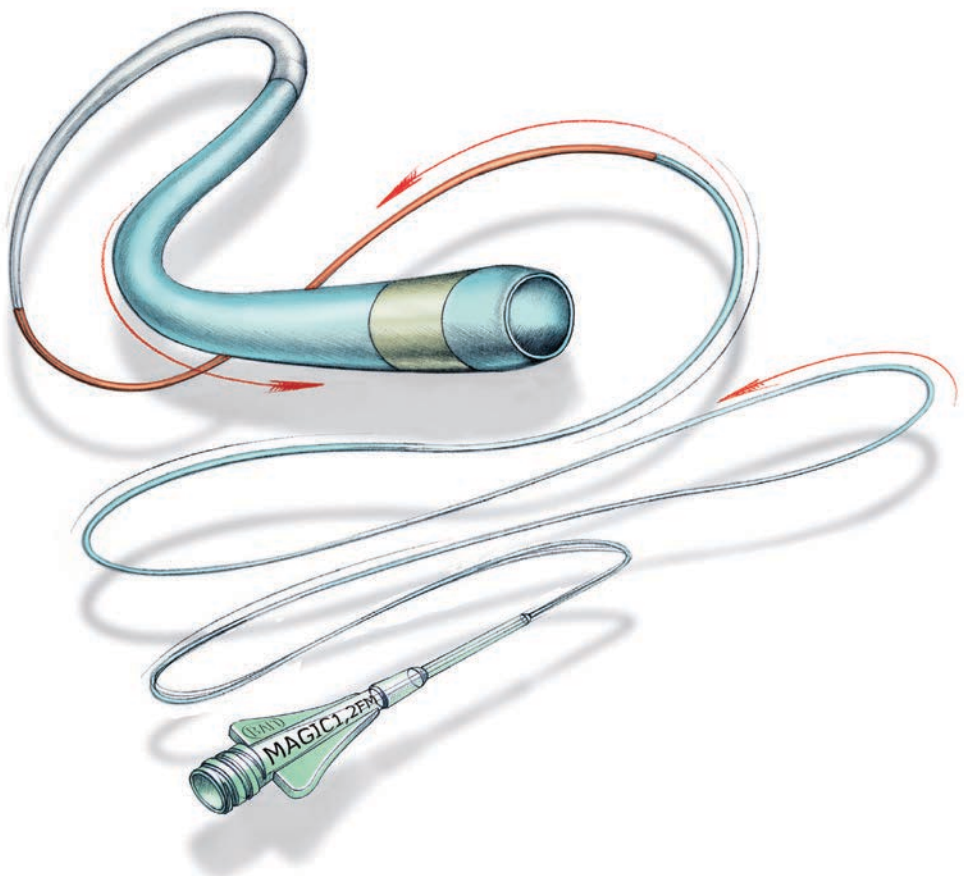

ordermagics@balt-usa.com

MAGIC catheters are designed for general intravascular use. They may be used for the controlled, selective regional infusion of therapeutic agents or embolic materials into vessels.[1]

Federal (USA) law restricts this device to sale, distribution by or on the order of a physician. Indications, contraindications, warnings and instructions for use can be found in the product labeling supplied with each device.

1. Magic Catheters IFU – Ind 19

balt
inspiring innovation

BALT USA
18 Technology Drive #169, Irvine, CA 92618
P 949.788.1443 **F** 949.788.1444

© 2017 BALT USA MKTG-068 Rev. B

One size really fits all?

TIGERTRIEVER

Adjustable clot retrieval

RAPIDMEDICAL

ASNR 56th Annual Meeting & The Foundation of the ASNR Symposium 2018

June 2 - 7, 2018 | Vancouver, B.C., CANADA

The Vancouver Convention Centre East
© 2013 Vancouver Convention Centre

Welcome and Greetings

Please join us in Vancouver, CANADA for the **56th Annual Meeting of the American Society of Neuroradiology** on June 2–7, 2018 at the Vancouver Convention Centre East. Surrounded by the coastal mountains and located on the waterfront, you can enjoy these spectacular views in the heart of downtown Vancouver. With its undeniable charm and friendly atmosphere, Vancouver is known around the world as both a popular tourist attraction and one of the best places to live.

ASNR enthusiastically presents **Neuroradiology: Adding Value and Improving Healthcare** at the Symposium of the Foundation of the ASNR, as well as the common thread throughout the Annual Meeting. Implementing a value-based strategy in imaging has grasped the attention of nearly every healthcare provider; in particular with Radiologists understanding that the future will demand their imaging practices deliver better value. Value in healthcare is typically defined as those imaging strategies that yield improved outcomes, lower costs, or both. As payment transitions from a fee-for-service to a value-based system, thus creating a fundamentally different marketplace dynamic, measuring good outcomes are at the center of this changeover. At this time of uncertainty what little remains clear is that without a well-defined knowledge of their outcomes, no medical specialty will be able to succeed in the future value-based system. The Symposium will feature how Neuroradiology, in its many subspecialty areas, adds value to clinical care pathways by directing healthcare practice towards better outcomes. The annual meeting programming will continue on this theme emphasizing imaging that improves health outcomes, while considering costs, thus adding value. Our discussions will incorporate many innovative approaches to how neuroimaging currently does and will continue to improve overall healthcare performance.

As the Program Chair for ASNR 2018, it is my pleasure and honor to welcome you to Vancouver, CANADA for our annual meeting! Vancouver is known for being a very walkable city with a compact downtown core hosting many places to enjoy. So pack your comfortable walking shoes and let's tour together with our colleagues and friends!

Pina Sanelli

Pina C. Sanelli, MD, MPH, FACR
ASNR 2018 Program Chair/President-Elect

NEURORADIOLOGY
Adding Value & Improving Healthcare

ASNR 2018 ▪ VANCOUVER

ASFNR ASHNR ASPNR ASSR SNIS

THE FOUNDATION OF THE ASNR

Pina C. Sanelli, MD, MPH, FACR
ASNR 2018 Program Chair/President-Elect

Programming developed in cooperation with the…

American Society of Functional Neuroradiology (ASFNR)
Max Wintermark, MD

American Society of Head and Neck Radiology (ASHNR)
Deborah R. Shatzkes, MD

American Society of Pediatric Neuroradiology (ASPNR)
Ashok Panigrahy, MD

American Society of Spine Radiology (ASSR)
John D. Barr, MD, FACR, FSIR, FAHA

Society of NeuroInterventional Surgery (SNIS)
Mahesh V. Jayaraman, MD

ASNR Health Policy (HPC) Committee
William D. Donovan, MD, MPH, FACR,
Gregory N. Nicola, MD, FACR

ASNR Computer Sciences & Informatics (CSI) Committee
John L. Go, MD, FACR

ASNR Research Scientist Programming Committee
Dikoma C. Shungu, PhD, Timothy P.L. Roberts, PhD

The International Hydrocephalus Imaging Working Group (IHIWG) / CSF Flow Group
Ari M Blitz, MD, Harold L. Rekate, MD and Bryn A. Martin, PhD

Meeting Registration Opening SOON!
Please visit 2018.asnr.org for more information

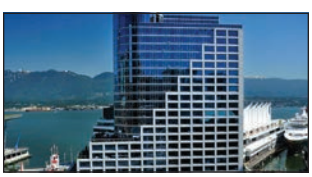

Fairmont Waterfront
© Copyright 2017 FRHI

Pan Pacific Vancouver
© 2017 Pan Pacific Hotels and Resorts

ASNR 56th Annual Meeting
c/o American Society of Neuroradiology
800 Enterprise Drive, Suite 205
Oak Brook, Illinois 60523-4216
Phone: 630-574-0220 + Fax: 630 574-0661
2018.asnr.org

AJNR

CALL FOR AJNR EDITORIAL FELLOWSHIP CANDIDATES

ASNR and AJNR are pleased once again to join efforts with other imaging-related journals that have training programs on editorial aspects of publishing for trainees or junior staff (3–5 years after training), including Radiology (Olmsted fellowship), AJR (Figley and Rogers fellowships), JACR (Bruce J. Hillman fellowship), and Radiologia.

2018 Candidate Information and Requirements

GOALS

- Increase interest in "editorial" and publication-related activities in younger individuals.
- Increase understanding and participation in the AJNR review process.
- Incorporate into AJNR's Editorial Board younger individuals who have previous experience in the review and publication process.
- Fill a specific need in neuroradiology not offered by other similar fellowships.
- Increase the relationship between "new" generation of neuroradiologists and more established individuals.
- Increase visibility of AJNR among younger neuroradiologists.

ACTIVITIES OF THE FELLOWSHIP

- Serve as Editorial Fellow for one year. This individual will be listed on the masthead as such.
- Review at least one manuscript per month for 12 months. Evaluate all review articles submitted to AJNR.
- Learn how electronic manuscript review systems work.
- Be involved in the final decision of selected manuscripts together with the Editor-in-Chief.
- Participate in all monthly Senior Editor telephone conference calls.
- Participate in all meetings of the Editors and Publications Committee during the annual meetings of ASNR and RSNA as per candidate's availability. The Foundation of the ASNR will provide $2000 funding for this activity.
- Evaluate progress and adjust program to specific needs in annual meeting or telephone conference with the Editor-in-Chief.
- Embark on an editorial scientific or bibliometric project that will lead to the submission of an article to AJNR or another appropriate journal as determined by the Editor-in-Chief. This project will be presented by the Editorial Fellow at the ASNR annual meeting.
- Serve as liaison between AJNR and ASNR's Young Professionals Network and the 3 YPs appointed to AJNR as special consultants. Participate in meetings and telephone calls with this group. Design one electronic survey/year, polling the group regarding readership attitudes and wishes.
- Recruit trainees as reviewers as determined by the Editor-in-Chief.
- Organize and host a Fellows' Journal Club podcast.
- Serve as Guest Editor for an issue of AJNR's News Digest with a timely topic.

QUALIFICATIONS

- Be a fellow in neuroradiology from North America, including Canada (this may be extended to include other countries).
- Be a junior faculty neuroradiology member (< 3 years) in either an academic or private environment.
- Be an "in-training" or member of ASNR in any other category.

APPLICATION

- Include a short letter of intent with statement of goals and desired research project. CV must be included.
- Include a letter of recommendation from the Division Chief or fellowship program director. A statement of protected time to perform the functions outlined is desirable.
- Applications will be evaluated by AJNR's Senior Editors and the Chair of the Publications Committee prior to the ASNR meeting. The name of the selected individual will be announced at the meeting.
- Applications should be received by March 1, 2018 and sent to Ms. Karen Halm, AJNR Managing Editor, electronically at khalm@asnr.org.

We're Inside Every Great Neuroradiologist!

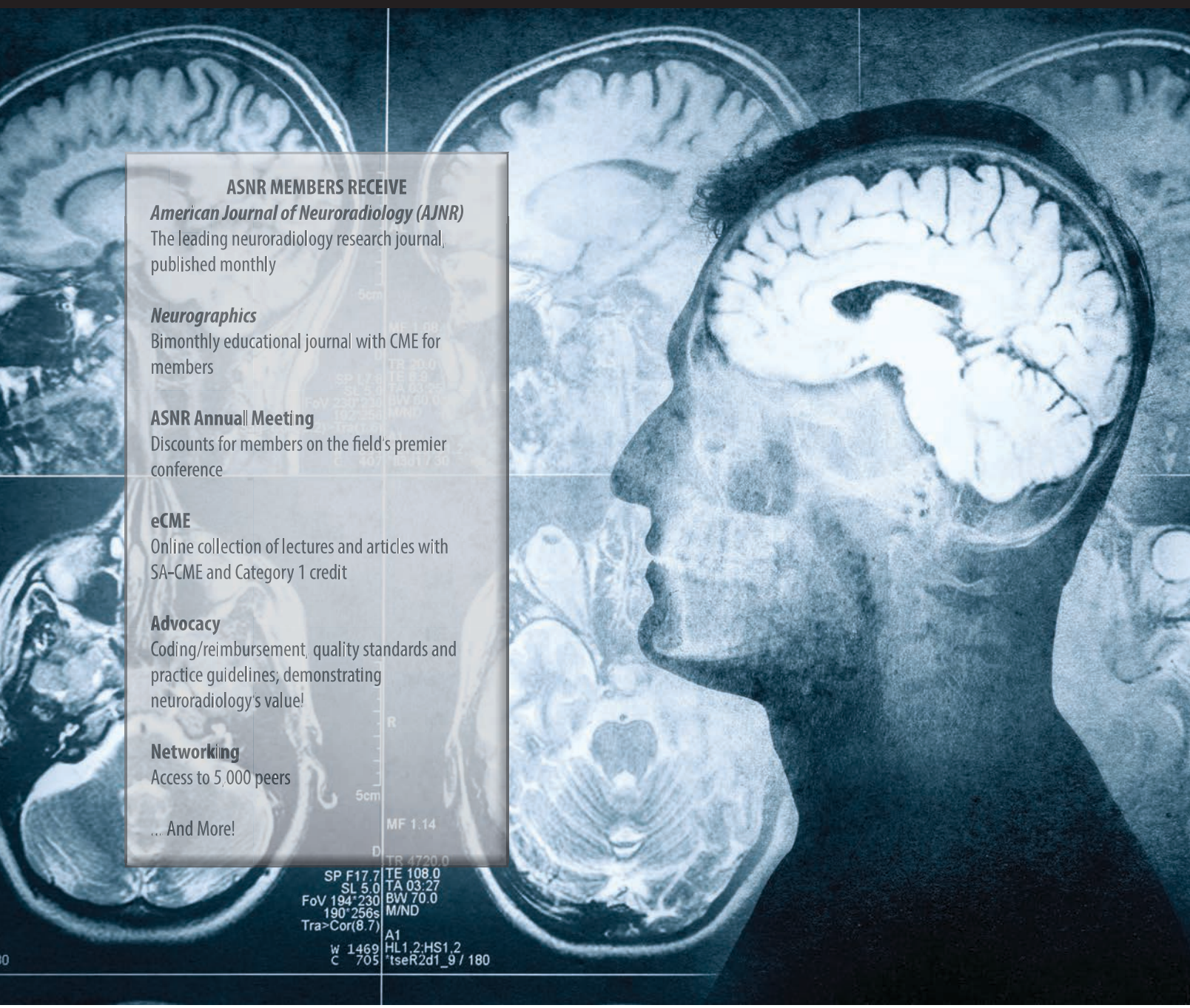

Join the leaders in neuroradiology today!
Learn more at www.asnr.org/join

ASNR
American Society of Neuroradiology

800 Enterprise Dr., Suite 205, Oak Brook, IL 60523 • (630)574-0220 • membership@asnr.org • www.asnr.org

ASHNR
American Society of
Head & Neck Radiology

52nd Annual Meeting | **American Society of**

Head & Neck Radiology

The Westin Savannah Harbor Golf Resort & Spa
Savannah, GA

September 26 - 30, 2018

Please contact Educational Symposia at 813-806-1000 or ASHNR@edusymp.com or visit www.ASHNR.org for additional information.

Simplify
the MOC Process

Manage
your CME Credits Online

CMEgateway.org

Available to Members of Participating Societies

- American Board of Radiology (ABR)
- American College of Radiology (ACR)
- American Roentgen Ray Society (ARRS)
- American Society of Neuroradiology (ASNR)
- Commnission on Accreditation of Medical Physics Educational Programs, Inc. (CAMPEP)
- Radiological Society of North America (RSNA)
- Society of Interventional Radiology (SIR)
- SNM
- The Society for Pediatric Radiology (SPR)

It's Easy and Free!

Log on to CME Gateway to:

- View or print reports of your CME credits from multiple societies from a single access point.
- Print an aggregated report or certificate from each participating organization.
- Link to SAMs and other tools to help with maintenance of certification.

American Board of Radiology (ABR) participation!

By activating ABR in your organizational profile, your MOC–fulfilling CME and SAM credits can be transferred to your own personalized database on the ABR Web site.

Sign Up Today!

go to CMEgateway.org

SAVE THE DATE 2018

12th Annual Meeting of the

American Society of

Functional Neuroradiology

October 15-17, 2018

Hotel del Coronado, San Diego, CA

October 14, 2018

Optional Hands-on BOLD fMRI Workshop

For More Information, Visit **www.asfnr.org**

Neuroform Atlas™ Stent System

See package insert for complete indications, contraindications, warnings and instructions for use.

Humanitarian Device. Authorized by Federal law for use with neurovascular embolic coils in patients who are ≥ 18 years of age for the treatment of wide neck, intracranial, saccular aneurysms arising from a parent vessel with a diameter of ≥ 2 mm and ≤ 4.5 mm that are not amenable to treatment with surgical clipping. Wide neck aneurysms are defined as having a neck ≥ 4 mm or a dome-to-neck ratio < 2. The effectiveness of this device for this use has not been demonstrated.

INDICATIONS FOR USE

The Neuroform Atlas™ Stent System is indicated for use with neurovascular embolic coils in patients who are ≥ 18 years of age for the treatment of wide neck, intracranial, saccular aneurysms arising from a parent vessel with a diameter of ≥ 2 mm and ≤ 4.5 mm that are not amenable to treatment with surgical clipping. Wide neck aneurysms are defined as having a neck ≥ 4 mm or a dome-to-neck ratio of < 2.

CONTRAINDICATIONS

Patients in whom antiplatelet and/or anticoagulation therapy is contraindicated.

POTENTIAL ADVERSE EVENTS

The potential adverse events listed below, as well as others, may be associated with the use of the Neuroform Atlas™ Stent System or with the procedure:

Allergic reaction to nitinol metal and medications, Aneurysm perforation or rupture, Coil herniation through stent into parent vessel, Death, Embolus, Headache, Hemorrhage, In-stent stenosis, Infection, Ischemia, Neurological deficit/intracranial sequelae, Pseudoaneurysm, Stent fracture, Stent migration/embolization, Stent misplacement, Stent thrombosis, Stroke, Transient ischemic attack, Vasospasm, Vessel occlusion or closure, Vessel perforation/rupture, Vessel dissection, Vessel trauma or damage, Vessel thrombosis, Visual impairment, and other procedural complications including but not limited to anesthetic and contrast media risks, hypotension, hypertension, access site complications.

WARNINGS

- Contents supplied STERILE using an ethylene oxide (EO) process. Do not use if sterile barrier is damaged. If damage is found, call your Stryker Neurovascular representative.
- For single use only. Do not reuse, reprocess or resterilize. Reuse, reprocessing or resterilization may compromise the structural integrity of the device and/or lead to device failure which, in turn, may result in patient injury, illness or death. Reuse, reprocessing or resterilization may also create a risk of contamination of the device and/or cause patient infection or cross-infection, including, but not limited to, the transmission of infectious disease(s) from one patient to another. Contamination of the device may lead to injury, illness or death of the patient.
- After use, dispose of product and packaging in accordance with hospital, administrative and/or local government policy.
- This device should only be used by physicians who have received appropriate training in interventional neuroradiology or interventional radiology and preclinical training on the use of this device as established by Stryker Neurovascular.
- Select a stent size (length) to maintain a minimum of 4 mm on each side of the aneurysm neck along the parent vessel. An incorrectly sized stent may result in damage to the vessel or stent migration. Therefore, the stent is not designed to treat an aneurysm with a neck greater than 22 mm in length.
- If excessive resistance is encountered during the use of the Neuroform Atlas™ Stent System or any of its components at any time during the procedure, discontinue use of the stent system. Continuing to move the stent system against resistance may result in damage to the vessel or a system component.
- Persons allergic to nickel titanium (Nitinol) may suffer an allergic response to this stent implant.
- Purge the system carefully to avoid the accidental introduction of air into the stent system.
- Confirm there are no air bubbles trapped anywhere in the stent system.

CAUTIONS / PRECAUTIONS

- Federal Law (USA) restricts this device to sale by or on the order of a physician.
- Use the Neuroform Atlas Stent System prior to the "Use By" date printed on the package
- Carefully inspect the sterile package and Neuroform Atlas Stent System prior to use to verify that neither has been damaged during shipment. Do not use kinked or damaged components; contact your Stryker Neurovascular representative.
- The stent delivery microcatheter and the Neuroform Atlas Stent delivery wire should not be used to recapture the stent.
- Exercise caution when crossing the deployed stent with adjunctive devices.
- After deployment, the stent may foreshorten from up to 6.3%.
- The max OD of the coiling microcatheter should not exceed the max OD of the stent delivery microcatheter.
- Standard interventional devices with distal tips > 1.8 F may not be able to pass through the interstices of the stent.
- Safety of the Neuroform Atlas Stent System in patients below the age of 18 has not been established.
- In cases where multiple aneurysms are to be treated, start at the most distal aneurysm first.

MAGNETIC RESONANCE IMAGING (MRI)

Safety Information Magnetic Resonance Conditional

Non-clinical testing and analysis have demonstrated that the Neuroform Atlas Stent is MR Conditional alone, or when overlapped with a second stent, and adjacent to a Stryker Neurovascular coil mass. A patient with the Neuroform Atlas Stent can be safely scanned immediately after placement of this implant, under the following conditions:

- Static magnetic field of 1.5 and 3.0 Tesla
- Maximum spatial gradient field up to 2500 Gauss/cm (25 Tesla/m)
- Maximum MR system reported whole body averaged specific absorption rate of 2 W/kg (Normal Operating Mode) and head averaged specific absorption rate of 3.2 W/kg.

Under the scan conditions defined above, the Neuroform Atlas Stent is expected to produce a maximum temperature rise of 4°C after 15 minutes of continuous scanning. The Neuroform Atlas Stent should not migrate in this MRI environment.

In non-clinical testing, the image artifact caused by the device extends approximately 2 mm from the Neuroform Atlas Stent when imaged with a spin echo pulse sequence and 3 Tesla MRI System. The artifact may obscure the device lumen. It may be necessary to optimize MR imaging parameters for the presence of this implant.

Excelsior® XT-17™ Microcatheter

See package insert for complete indications, contraindications, warnings and instructions for use.

INTENDED USE / INDICATIONS FOR USE

Stryker Neurovascular's Excelsior XT-17 Microcatheters are intended to assist in the delivery of diagnostic agents, such as contrast media, and therapeutic agents, such as occlusion coils, into the peripheral, coronary and neuro vasculature.

CONTRAINDICATIONS

None known.

POTENTIAL ADVERSE EVENTS

Potential adverse events associated with the use of microcatheters or with the endovascular procedures include, but are not limited to: access site complications, allergic reaction, aneurysm perforation, aneurysm rupture, death, embolism (air, foreign body, plaque, thrombus), hematoma, hemorrhage, infection, ischemia, neurological deficits, pseudoaneurysm, stroke, transient ischemic attack, vasospasm, vessel dissection, vessel occlusion, vessel perforation, vessel rupture, vessel thrombosis

WARNINGS

- The accessories are not intended for use inside the human body.
- Limited testing has been performed with solutions such as contrast media, saline and suspended embolic particles. The use of these microcatheters for delivery of solutions other than the types that have been tested for compatibility is not recommended. Do not use with glue or glue mixtures.
- Carefully inspect all devices prior to use. Verify shape, size and condition are suitable for the specific procedure.
- Exchange microcatheters frequently during lengthy procedures that require extensive guidewire manipulation or multiple guidewire exchanges.
- Never advance or withdraw an intravascular device against resistance until the cause of the resistance is determined by fluoroscopy. Movement of the microcatheter or guidewire against resistance could dislodge a clot, perforate a vessel wall, or damage microcatheter and guidewire. In severe cases, tip separation of the microcatheter or guidewire may occur.
- Contents supplied STERILE using an ethylene oxide (EO) process. Do not use if sterile barrier is damaged. If damage is found, call your Stryker Neurovascular representative.
- For single use only. Do not reuse, reprocess or resterilize. Reuse, reprocessing or resterilization may compromise the structural integrity of the device and/or lead to device failure which, in turn, may result in patient injury, illness or death. Reuse, reprocessing or resterilization may also create a risk of contamination of the device and/or cause patient infection or cross-infection, including, but not limited to, the transmission of infectious disease(s) from one patient to another. Contamination of the device may lead to injury, illness or death of the patient.
- After use, dispose of product and packaging in accordance with hospital, administrative and/or local government policy.
- These devices are intended for use only by physicians trained in performing endovascular procedures.
- Inspect product before use for any bends, kinks or damage. Do not use a microcatheter that has been damaged. Damaged microcatheters may rupture causing vessel trauma or tip detachment during steering maneuvers.
- The shaping mandrel is not intended for use inside the human body.
- Discontinue use of microcatheter for infusion if increased resistance is noted. Resistance indicates possible blockage. Remove and replace blocked microcatheter immediately. DO NOT attempt to clear blockage by over-pressurization. Doing so may cause the microcatheter to rupture, resulting in vascular damage or patient injury.
- Do not exceed 2,070 kPa (300 psi) infusion pressure. Excessive pressure could dislodge a clot, causing thromboemboli, or could result in a ruptured microcatheter or severed tip, causing vessel injury.

CAUTIONS / PRECAUTIONS

- To reduce the probability of coating damage in tortuous vasculature, use a guide catheter with a minimum internal diameter as specified in Table 1 above, and is recommended for use with Stryker Neurovascular hydrophilically coated microcatheters.
- To control the proper introduction, movement, positioning and removal of the microcatheter within the vascular system, users should employ standard clinical angiographic and fluoroscopic practices and techniques throughout the interventional procedure.
- Exercise care in handling of the microcatheter during a procedure to reduce the possibility of accidental breakage, bending or kinking.
- Use the product prior to the "Use By" date printed on the label.
- Limited testing indicates that Excelsior XT-17 Microcatheter is compatible with Dimethyl Sulfoxide (DMSO). The compatibility of Excelsior XT-17 Microcatheter with individual agents suspended in DMSO has not been established.
- Federal Law (USA) restricts this device to sale by or on the order of a physician.
- Wet dispenser coil or packaging tray and hydrophilically coated outer shaft of microcatheters prior to removal from packaging tray. Once the microcatheter has been wetted, do not allow to dry.
- The packaging mandrel is not intended for reuse. The packaging mandrel is not intended for use inside the human body.
- Check that all fittings are secure so that air is not introduced into guide catheter or microcatheter during continuous flush.
- In order to achieve optimal performance of Stryker Neurovascular Microcatheters and to maintain the lubricity of the Hydrolene® Coating surface, it is critical that a continuous flow of appropriate flush solution be maintained between the Stryker Neurovascular Microcatheter and guide catheter, and the microcatheter and any intraluminal device. In addition, flushing aids in preventing contrast crystal formation and/or clotting on both the intraluminal device and inside the guide catheter and/or the microcatheter lumen.
- Do not position microcatheter closer than 2.54 cm (1 in) from the steam source. Damage to the microcatheter may result.
- Excessive tightening of a hemostatic valve onto the microcatheter shaft may result in damage to the microcatheter. Removing the peel away introducer without a guidewire inserted in the microcatheter lumen might result in damage to the microcatheter shaft.
- To facilitate microcatheter handling, the proximal portion of the microcatheter does not have the hydrophilic surface. Greater resistance may be encountered when this section of the microcatheter is advanced into the RHV.

Excelsior® SL-10® Microcatheter

See package insert for complete indications, contraindications, warnings and instructions for use.

INTENDED USE / INDICATIONS FOR USE

Stryker Neurovascular Excelsior SL-10 Microcatheter is intended to assist in the delivery of diagnostic agents, such as contrast media, and therapeutic agents, such as occlusion coils, into the peripheral, coronary, and neurovasculature.

CONTRAINDICATIONS

None known.

POTENTIAL ADVERSE EVENTS

Potential adverse events associated with the use of microcatheters or with the endovascular procedures include, but are not limited to: access site complications, allergic reaction, aneurysm perforation, aneurysm rupture, death, embolism (air, foreign body, plaque, thrombus), hematoma, hemorrhage, infection, ischemia, neurological deficits, pseudoaneurysm, stroke, transient ischemic attack, vessel dissection, vessel occlusion, vessel perforation, vessel rupture, vessel thrombosis.

WARNINGS

- Contents supplied STERILE using an ethylene oxide (EO) process. Do not use if sterile barrier is damaged. If damage is found, call your Stryker Neurovascular representative.
- For single patient use only. Do not reuse, reprocess or resterilize. Reuse, reprocessing or resterilization may compromise the structural integrity of the device and/or lead to device failure which, in turn, may result in patient injury, illness or death. Reuse, reprocessing or resterilization may also create a risk of contamination of the device and/or cause patient infection or cross-infection, including, but not limited to, the transmission of infectious disease(s) from one patient to another. Contamination of the device may lead to injury, illness or death of the patient.
- After use, dispose of product and packaging in accordance with hospital, administrative and/or local government policy.
- **These devices are intended for use only by physicians trained in performing endovascular procedures.**
- Limited testing has been performed with solutions such as contrast media, saline and suspended embolic particles. The use of these catheters for delivery of solutions other than the types that have been tested for compatibility is not recommended. Do not use with glue or glue mixtures.
- The accessories are not intended for use inside the human body.
- Carefully inspect all devices prior to use. Verify shape, size and condition are suitable for the specific procedure.
- Exchange microcatheters frequently during lengthy procedures that require extensive guidewire manipulation or multiple guidewire exchanges.
- Never advance or withdraw an intravascular device against resistance until the cause of the resistance is determined by fluoroscopy. Movement of the microcatheter or guidewire against resistance could dislodge a clot, perforate a vessel wall, or damage microcatheter and guidewire. In severe cases, tip separation of the microcatheter or guidewire may occur.
- Inspect product before use for any bends, kinks or damage. Do not use a microcatheter that has been damaged. Damaged microcatheters may rupture causing vessel trauma or tip detachment during steering maneuvers.
- Shaping mandrel is not intended for use inside the human body.
- Discontinue use of microcatheter for infusion if increased resistance is noted. Resistance indicates possible blockage. Remove and replace blocked microcatheter immediately. DO NOT attempt to clear blockage by over-pressurization. Doing so may cause the microcatheter to rupture, resulting in vascular damage or patient injury.
- Do not exceed 2,070 kPa (300 psi) infusion pressure. Excessive pressure could dislodge a clot, causing thromboemboli, or could result in a ruptured microcatheter or severed tip, causing vessel injury.

CAUTIONS / PRECAUTIONS

- Federal Law (USA) restricts this device to sale by or on the order of a physician.
- To facilitate microcatheter handling, the proximal portion of the microcatheter does not have the hydrophilic surface. Greater resistance may be encountered when this section of the microcatheter is advanced into the RHV.
- Exercise care in handling of the microcatheter during a procedure to reduce the possibility of accidental breakage, bending or kinking.
- To reduce the probability of coating damage in tortuous vasculature, use a guide catheter with a minimum internal diameter that is ≥ 1.00 mm (0.038 in) and is recommended for use with Stryker Neurovascular hydrophilically coated microcatheters.
- To control the proper introduction, movement, positioning and removal of the microcatheter within the vascular system, users should employ standard clinical angiographic and fluoroscopic practices and techniques throughout the interventional procedure.
- Flush dispenser coil of hydrophilically coated microcatheters prior to removal from dispenser coil. Once the microcatheter has been wetted, do not allow to dry. Do not reinsert the microcatheter into dispenser coil.
- Do not position microcatheter closer than 2.54 cm (1 in) from the steam source. Damage to the microcatheter may result.
- Check that all fittings are secure so that air is not introduced into guide catheter or microcatheter during continuous flush.
- In order to achieve optimal performance of Stryker Neurovascular Microcatheters and to maintain the lubricity of the Hydrolene® Coating surface, it is critical that a continuous flow of appropriate flush solution be maintained between the Stryker Neurovascular Microcatheter and guide catheter, and the microcatheter and any intraluminal device. In addition, flushing aids in preventing contrast crystal formation and/or clotting on both the intraluminal device and inside the guide catheter and/or the microcatheter lumen.
- Excessive tightening of a hemostatic valve onto the microcatheter shaft may result in damage to the microcatheter.

Stryker Neurovascular
47900 Bayside Parkway
Fremont, CA 94538

strykerneurovascular.com

Date of Release: NOV/2017

EX_EN_US

Copyright © 2017 Stryker

Target® Detachable Coil

See package insert for complete indications, contraindications, warnings and instructions for use.

INTENDED USE / INDICATIONS FOR USE

Target Detachable Coils are intended to endovascularly obstruct or occlude blood flow in vascular abnormalities of the neurovascular and peripheral vessels.

Target Detachable Coils are indicated for endovascular embolization of:

- Intracranial aneurysms
- Other neurovascular abnormalities such as arteriovenous malformations and arteriovenous fistulae
- Arterial and venous embolizations in the peripheral vasculature

CONTRAINDICATIONS

None known.

POTENTIAL ADVERSE EVENTS

Potential complications include, but are not limited to: allergic reaction, aneurysm perforation and rupture, arrhythmia, death, edema, embolus, headache, hemorrhage, infection, ischemia, neurological/intracranial sequelae, post-embolization syndrome (fever, increased white blood cell count, discomfort), TIA/stroke, vasospasm, vessel occlusion or closure, vessel perforation, dissection, trauma or damage, vessel rupture, vessel thrombosis. Other procedural complications including but not limited to: anesthetic and contrast media risks, hypotension, hypertension, access site complications.

WARNINGS

- Contents supplied STERILE using an ethylene oxide (EO) process. Do not use if sterile barrier is damaged. If damage is found, call your Stryker Neurovascular representative.
- For single use only. Do not reuse, reprocess or resterilize. Reuse, reprocessing or resterilization may compromise the structural integrity of the device and/or lead to device failure which, in turn, may result in patient injury, illness or death. Reuse, reprocessing or resterilization may also create a risk of contamination of the device and/or cause patient infection or cross-infection, including, but not limited to, the transmission of infectious disease(s) from one patient to another. Contamination of the device may lead to injury, illness or death of the patient.
- After use, dispose of product and packaging in accordance with hospital, administrative and/or local government policy.
- **This device should only be used by physicians who have received appropriate training in interventional neuroradiology or interventional radiology and preclinical training on the use of this device as established by Stryker Neurovascular.**
- Patients with hypersensitivity to 316LVM stainless steel may suffer an allergic reaction to this implant.
- MR temperature testing was not conducted in arteriovenous malformations or fistulae models.
- The safety and performance characteristics of the Target Detachable Coil System (Target Detachable Coils, InZone Detachment Systems, delivery systems and accessories) have not been demonstrated with other manufacturer's devices (whether coils, coil delivery devices, coil detachment systems, catheters, guidewires, and/or other accessories). Due to the potential incompatibility of non Stryker Neurovascular devices with the Target Detachable Coil System, the use of other manufacturer's device(s) with the Target Detachable Coil System is not recommended.
- To reduce risk of coil migration, the diameter of the first and second coil should never be less than the width of the ostium.
- In order to achieve optimal performance of the Target Detachable Coil System and to reduce the risk of thromboembolic complications, it is critical that a continuous infusion of appropriate flush solution be maintained between a) the femoral sheath and guiding catheter, b) the 2-tip microcatheter and guiding catheter, and c) the 2-tip microcatheter and Stryker Neurovascular guidewire and delivery wire. Continuous flush also reduces the potential for thrombus formation on, and crystallization of infusate around, the detachment zone of the Target Detachable Coil.
- Do not use the product after the "Use By" date specified on the package.
- Reuse of the packaging hoop or use with any coil other than the original coil may result in contamination of, or damage to, the coil.

Damaged delivery wires may cause detachment failures, vessel injury or unpredictable distal tip response during coil deployment. If a delivery wire is damaged at any point during the procedure, do not attempt to straighten or otherwise repair it. Do not proceed with deployment or detachment. Remove the entire coil and replace with undamaged product.

- Utilization of damaged coils may affect coil delivery to, and stability inside, the vessel or aneurysm, possibly resulting in coil migration and/or stretching.
- The fluoro-saver marker is designed for use with a Rotating Hemostatic Valve (RHV). If used without an RHV, the distal end of the coil may be beyond the alignment marker when the fluoro-saver marker reaches the microcatheter hub.
- If the fluoro-saver marker is not visible, do not advance the coil without fluoroscopy.
- Do not rotate delivery wire during or after delivery of the coil. Rotating the Target Detachable Coil delivery wire may result in a stretched coil or premature detachment of the coil from the delivery wire, which could result in coil migration.
- Verify there is no coil loop protrusion into the parent vessel after coil placement and prior to coil detachment. Coil loop protrusion after coil placement may result in thromboembolic events if the coil is detached.
- Verify there is no movement of the coil after coil placement and prior to coil detachment. Movement of the coil after coil placement may indicate that the coil could migrate once it is detached.
- Failure to properly close the RHV compression fitting over the delivery wire before attaching the InZone® Detachment System could result in coil movement, aneurysm rupture or vessel perforation.
- Verify repeatedly that the distal shaft of the catheter is not under stress before detaching the Target Detachable Coil. Axial compression or tension forces could be stored in the 2-tip microcatheter causing the tip to move during coil delivery. Microcatheter tip movement could cause the aneurysm or vessel to rupture.
- Advancing the delivery wire beyond the microcatheter tip once the coil has been detached involves risk of aneurysm or vessel perforation.
- The long term effect of this product on extravascular tissues has not been established so care should be taken to retain this device in the intravascular space.

CAUTIONS / PRECAUTIONS

- Federal Law (USA) restricts this device to sale by or on the order of a physician.
- Besides the number of InZone Detachment System units needed to complete the case, there must be an extra InZone Detachment System unit as back up.
- Removing the delivery wire without grasping the introducer sheath and delivery wire together may result in the detachable coil sliding out of the introducer sheath.
- Failure to remove the introducer sheath after inserting the delivery wire into the RHV of the microcatheter will interrupt normal infusion of flush solution and allow back flow of blood into the microcatheter.
- Some low level overhead light near or adjacent to the patient is required to visualize the fluoro-saver marker; monitor light alone will not allow sufficient visualization of the fluoro-saver marker.
- Advance and retract the Target Detachable Coil carefully and smoothly without excessive force. If unusual friction is noticed, slowly withdraw the Target Detachable Coil and examine for damage. If damage is present, remove and use a new Target Detachable Coil. If friction or resistance is still noted, carefully remove the Target Detachable Coil and microcatheter and examine the microcatheter for damage.
- If it is necessary to reposition the Target Detachable Coil, verify under fluoroscopy that the coil moves with a one-to-one motion. If the coil does not move with a one-to-one motion or movement is difficult, the coil may have stretched and could possibly migrate or break. Gently remove both the coil and microcatheter and replace with new devices.
- Increased detachment times may occur when:
  - Other embolic agents are present.
  - Delivery wire and microcatheter markers are not properly aligned.
  - Thrombus is present on the coil detachment zone.
- Do not use detachment systems other than the InZone Detachment System.

Stryker Neurovascular
47900 Bayside Parkway
Fremont, CA 94538

strykerneurovascular.com

Date of Release: NOV/2017

EX_EN_US

Copyright © 2017 Stryker

MicroVention®
TERUMO

Access Product Solutions

Sofia® Plus

Distal Access Catheter

Soft Torqueable Catheter Optimized for Intracranial Access with Excellent Navigation and Trackability

Neurovascular Malformation Solutions

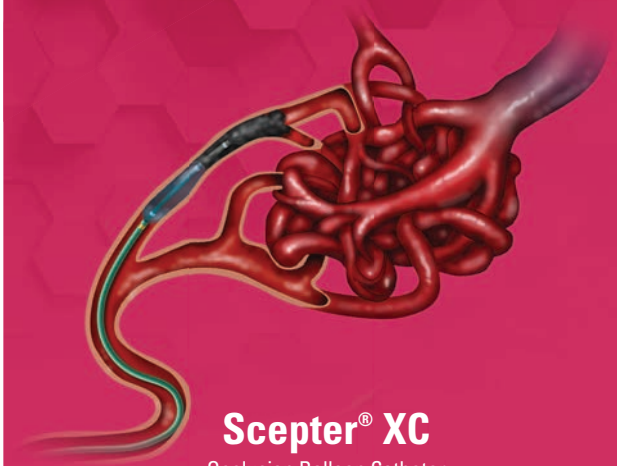

Scepter® XC

Occlusion Balloon Catheter

Clinical Applications in Four Key Areas: Balloon Remodeling, Stent Delivery, Liquid Embolic Injection, and Balloon-Test Occlusion

INDICATIONS FOR USE:

The SOFIA® Catheter is indicated for general intravascular use, including the neuro and peripheral vasculature. The SOFIA® Catheter can be used to facilitate introduction of diagnostic or therapeutic agents. The SOFIA® Catheter is not intended for use in coronary arteries.

The Scepter C® and Scepter XC® Occlusion Balloon Catheters are intended for use in the peripheral and neuro vasculature where temporary occlusion is desired. The balloon catheters provide temporary vascular occlusion which is useful in selectively stopping or controlling blood flow. The balloon catheters also offer balloon assisted embolization of intracranial aneurysms. For use in the peripheral vasculature for the infusion of diagnostic agents, such as contrast media, and therapeutic agents such as embolization materials. For neurovascular use for the infusion of diagnostic agents such as contrast media, and therapeutic agents, such as embolization materials, that have been approved or cleared for use in the neurovasculature and are compatible with the inner diameter of the Scepter C/XC Balloon Catheter.

The LVIS® Device is intended for use with bare platinum embolic coils for the treatment of unruptured, wide neck (neck ≥ 4 mm or dome to neck ratio < 2), intracranial, saccular aneurysms arising from a parent vessel with a diameter ≥ 2.5 mm and ≤ 4.5 mm.

The Headway® Duo Microcatheter is intended for general intravascular use, including the peripheral and coronary vasculature for the infusion of diagnostic agents, such as contrast media, and therapeutic agents, such as embolization materials. The Headway® Duo Microcatheter is intended for neurovascular use, for the infusion of diagnostic agents, such as contrast media, and therapeutic agents that have been cleared or approved for use in the neurovasculature and are compatible with the inner diameter of the Headway® Duo Microcatheter.

stryker

Smooth and stable.

Target Detachable Coils deliver consistently smooth deployment and exceptional microcatheter stability. Designed to work seamlessly together for framing, filling and finishing. Target Coils deliver the high performance you demand.

For more information, please visit www.strykerneurovascular.com/Target or contact your local Stryker sales representative.

Target®

DETACHABLE COILS

Copyright © 2017 Stryker
NV00018669 v2.0

Not for sale within the territory of the United States

VISIBLE ADAPTABILITY

DERIVO® Embolisation Device

- Very good visibility
- Excellent navigation and precise positioning
- BlueXide® surface
- Low level artefacts on MRI

www.acandis.com

acandis®

ENGINEERING STROKE SOLUTIONS

AJNR

AMERICAN JOURNAL OF NEURORADIOLOGY

JANUARY 2018
VOLUME 39
NUMBER 1
WWW.AJNR.ORG

Publication Preview at www.ajnr.org features articles released in advance of print. Visit www.ajnrblog.org to comment on AJNR content and chat with colleagues and AJNR's News Digest at http://ajnrdigest.org to read the stories behind the latest research in neuroimaging.

AJNR (Am J Neuroradiol ISSN 0195–6108) is a journal published monthly, owned and published by the American Society of Neuroradiology (ASNR), 800 Enterprise Drive, Suite 205, Oak Brook, IL 60523. Annual dues for the ASNR include $170.00 for journal subscription. The journal is printed by Cadmus Journal Services, 5457 Twin Knolls Road, Suite 200, Columbia, MD 21045; Periodicals postage paid at Oak Brook, IL and additional mailing offices. Printed in the U.S.A. POSTMASTER: Please send address changes to American Journal of Neuroradiology, P.O. Box 3000, Denville, NJ 07834, U.S.A. Subscription rates: nonmember $400 ($470 foreign) print and online, $320 online only; institutions $460 ($530 foreign) print and basic online, $915 ($980 foreign) print and extended online, $380 online only (basic), extended online $825; single copies are $35 each ($40 foreign). Indexed by PubMed/Medline, BIOSIS Previews, Current Contents (Clinical Medicine and Life Sciences), EMBASE, Google Scholar, HighWire Press, Q-Sensei, RefSeek, Science Citation Index, and SCI Expanded. Copyright © American Society of Neuroradiology.

ONLINE FEATURES

LETTERS

BOOK REVIEWS *R.M. Quencer, Section Editor*

Please visit www.ajnrblog.org to read and comment on Book Reviews.

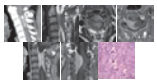

En plaque epidural psammomatous meningioma. Sagittal CT image (top left) shows dural calcification at C2–4. MR images show homogeneously enhancing mass surrounding the dura and cord with mass effect. Photomicrograph (bottom right) shows the presence of psammoma bodies.

Indicates Editor's Choices selection

Indicates Fellows' Journal Club selection

Indicates open access to non-subscribers at www.ajnr.org

Indicates article with supplemental on-line table

Indicates article with supplemental on-line photo

Indicates article with supplemental on-line video

EBM Evidence-Based Medicine Level 1

EBM Evidence-Based Medicine Level 2

AJNR

AMERICAN JOURNAL OF NEURORADIOLOGY

Publication Preview at www.ajnr.org features articles released in advance of print. Visit www.ajnrblog.org to comment on AJNR content and chat with colleagues and AJNR's News Digest at http://ajnrdigest.org to read the stories behind the latest research in neuroimaging.

JANUARY 2018 • VOLUME 39 • NUMBER 1 • WWW.AJNR.ORG

Official Journal:
American Society of Neuroradiology
American Society of Functional Neuroradiology
American Society of Head and Neck Radiology
American Society of Pediatric Neuroradiology
American Society of Spine Radiology

EDITOR-IN-CHIEF

Jeffrey S. Ross, MD
Professor of Radiology, Department of Radiology, Mayo Clinic College of Medicine, Phoenix, AZ

SENIOR EDITORS

Harry J. Cloft, MD, PhD
Professor of Radiology and Neurosurgery, Department of Radiology, Mayo Clinic College of Medicine, Rochester, MN

Thierry A.G.M. Huisman, MD
Professor of Radiology, Pediatrics, Neurology, and Neurosurgery, Chairman, Department of Imaging and Imaging Science, Johns Hopkins Bayview, Director, Pediatric Radiology and Pediatric Neuroradiology, Johns Hopkins Hospital, Baltimore, MD

Yvonne W. Lui, MD
Associate Professor of Radiology, Chief of Neuroradiology, New York University School of Medicine, New York, NY

C.D. Phillips, MD, FACR
Professor of Radiology, Weill Cornell Medical College, Director of Head and Neck Imaging, New York-Presbyterian Hospital, New York, NY

Pamela W. Schaefer, MD
Clinical Director of MRI and Associate Director of Neuroradiology, Massachusetts General Hospital, Boston, Massachusetts, Associate Professor, Radiology, Harvard Medical School, Cambridge, MA

Charles M. Strother, MD
Professor of Radiology, Emeritus, University of Wisconsin, Madison, WI

STATISTICAL SENIOR EDITOR

Bryan A. Comstock, MS
Senior Biostatistician, Department of Biostatistics, University of Washington, Seattle, WA

EDITORIAL BOARD
Ashley H. Aiken, *Atlanta, GA*
Lea M. Alhilali, *Phoenix, AZ*
John D. Barr, *Dallas, TX*
Ari Blitz, *Baltimore, MD*
Barton F. Branstetter IV, *Pittsburgh, PA*
Jonathan L. Brisman, *Lake Success, NY*
Julie Bykowski, *San Diego, CA*
Keith Cauley, *Danville, PA*
Asim F. Choudhri, *Memphis, TN*
Alessandro Cianfoni, *Lugano, Switzerland*
J. Matthew Debnam, *Houston, TX*
Seena Dehkharghani, *New York, NY*
Colin Derdeyn, *Iowa City, IA*
Rahul S. Desikan, *San Francisco, CA*
Yonghong Ding, *Rochester, MN*
Clifford J. Eskey, *Hanover, NH*
Saeed Fakhran, *Phoenix, AZ*
Massimo Filippi, *Milan, Italy*
Allan J. Fox, *Toronto, Ontario, Canada*
Wende N. Gibbs, *Los Angeles, CA*
Christine M. Glastonbury, *San Francisco, CA*
John L. Go, *Los Angeles, CA*
Allison Grayev, *Madison, WI*
Brent Griffith, *Detroit, MI*
Wan-Yuo Guo, *Taipei, Taiwan*
Ajay Gupta, *New York, NY*
Rakesh K. Gupta, *Lucknow, India*
Lotfi Hacein-Bey, *Sacramento, CA*
Christopher P. Hess, *San Francisco, CA*
Andrei Holodny, *New York, NY*
Benjamin Huang, *Chapel Hill, NC*
George J. Hunter, *Boston, MA*
Mahesh V. Jayaraman, *Providence, RI*
Valerie Jewells, *Chapel Hill, NC*
Christof Karmonik, *Houston, TX*
Timothy J. Kaufmann, *Rochester, MN*
Hillary R. Kelly, *Boston, MA*
Toshibumi Kinoshita, *Akita, Japan*
Kennith F. Layton, *Dallas, TX*
Michael M. Lell, *Nürnberg, Germany*
Michael Lev, *Boston, MA*
Karl-Olof Lovblad, *Geneva, Switzerland*
Franklin A. Marden, *Chicago, IL*
M. Gisele Matheus, *Charleston, SC*
Joseph C. McGowan, *Merion Station, PA*
Stephan Meckel, *Freiburg, Germany*
Christopher J. Moran, *St. Louis, MO*
Takahisa Mori, *Kamakura City, Japan*
Suresh Mukherji, *Ann Arbor, MI*
Amanda Murphy, *Toronto, Ontario, Canada*
Alexander J. Nemeth, *Chicago, IL*
Sasan Partovi, *Cleveland, OH*
Laurent Pierot, *Reims, France*
Jay J. Pillai, *Baltimore, MD*
Whitney B. Pope, *Los Angeles, CA*
M. Judith Donovan Post, *Miami, FL*
Tina Young Poussaint, *Boston, MA*
Joana Ramalho, *Lisbon, Portugal*
Otto Rapalino, *Boston, MA*
Álex Rovira-Cañellas, *Barcelona, Spain*
Paul M. Ruggieri, *Cleveland, OH*
Zoran Rumboldt, *Rovinj-Rovigno, Croatia*
Amit M. Saindane, *Atlanta, GA*
Erin Simon Schwartz, *Philadelphia, PA*
Lubdha M. Shah, *Salt Lake City, UT*
Aseem Sharma, *St. Louis, MO*
J. Keith Smith, *Chapel Hill, NC*
Maria Vittoria Spampinato, *Charleston, SC*
Gordon K. Sze, *New Haven, CT*
Krishnamoorthy Thamburaj, *Hershey, PA*
Cheng Hong Toh, *Taipei, Taiwan*
Thomas A. Tomsick, *Cincinnati, OH*
Aquilla S. Turk, *Charleston, SC*
Willem Jan van Rooij, *Tilburg, Netherlands*
Arastoo Vossough, *Philadelphia, PA*
Elysa Widjaja, *Toronto, Ontario, Canada*
Max Wintermark, *Stanford, CA*
Ronald L. Wolf, *Philadelphia, PA*
Kei Yamada, *Kyoto, Japan*
Carlos Zamora, *Chapel Hill, NC*

EDITORIAL FELLOW
Vahe Zohrabian, *New Haven, CT*

SPECIAL CONSULTANTS TO THE EDITOR
AJNR Blog Editor
Neil Lall, *Denver, CO*
Case of the Month Editor
Nicholas Stence, *Aurora, CO*
Case of the Week Editors
Juan Pablo Cruz, *Santiago, Chile*
Sapna Rawal, *Toronto, Ontario, Canada*
Classic Case Editor
Sandy Cheng-Yu Chen, *Taipei, Taiwan*
Facebook Editor
Peter Yi Shen, *Sacramento, CA*
Health Care and Socioeconomics Editor
Pina C. Sanelli, *New York, NY*
Physics Editor
Greg Zaharchuk, *Stanford, CA*
Podcast Editor
Wende N. Gibbs, *Los Angeles, CA*
Twitter Editor
Jennifer McCarty, *Atlanta, Georgia*

YOUNG PROFESSIONALS ADVISORY COMMITTEE
Asim K. Bag, *Birmingham, AL*
Anna E. Nidecker, *Sacramento, CA*
Peter Yi Shen, *Sacramento, CA*

Founding Editor
Juan M. Taveras
Editors Emeriti
Mauricio Castillo, Robert I. Grossman, Michael S. Huckman, Robert M. Quencer

Managing Editor
Karen Halm
Assistant Managing Editor
Laura Wilhelm
Digital Publications and Social Media Coordinator
Kylie Mason
Executive Director, ASNR
Mary Beth Hepp

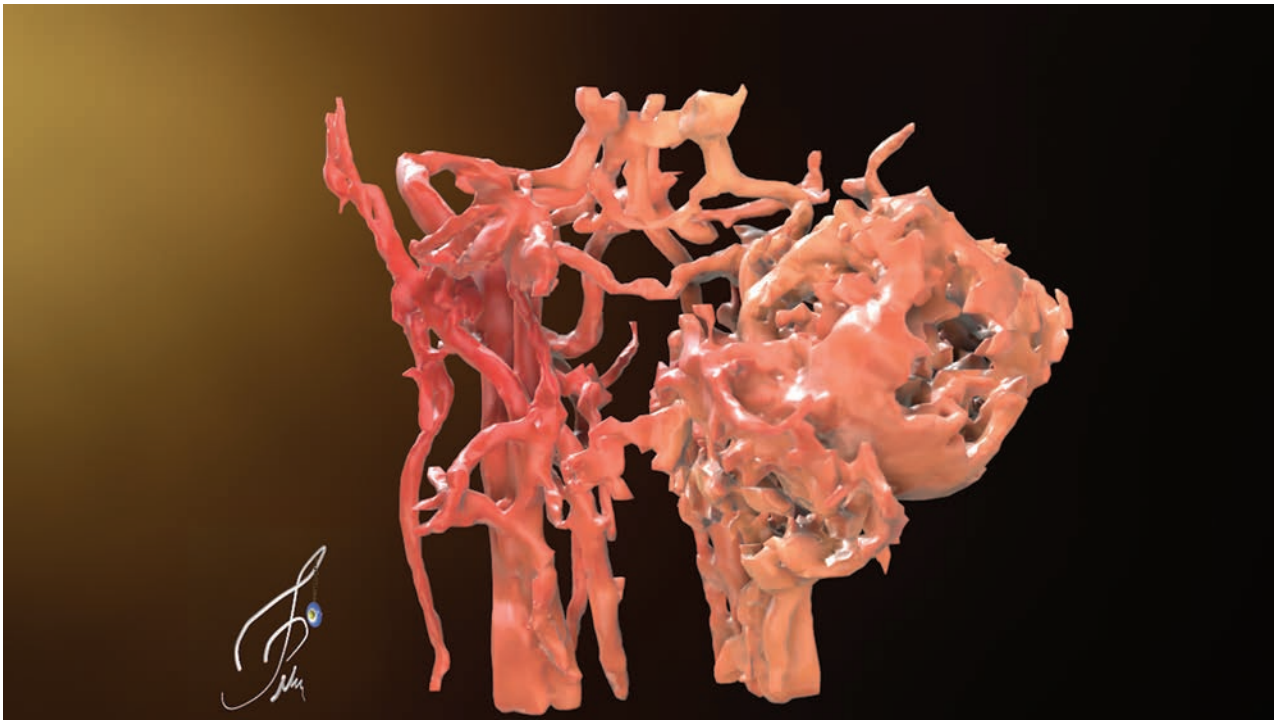

Title: Glomus Tumor of the Carotid Artery with Light Effects. This model was created from axial serial radiologic sections received from a patient with glomus tumor of the carotid artery by using medical reconstruction software (Mimics Research, Materialize HQ, Leuveen, Belgium) and then it was transferred to animation software (Cinema 4D, Maxon Computer, Friedrichsdorf, Germany) in object format for the addition of texture, lighting, and visual effects and stored as a high-resolution file.

Tuncay Peker, MD, Gazi University Faculty of Medicine, Department of Anatomy, Ankara, Turkey

Health Care Economics: A Study Guide for Neuroradiology Fellows, Part 1

S.L. Weiner, R. Tu, R. Javan, and M.R. Taheri

ABSTRACT

SUMMARY: Few resources are available in the medical literature for a comprehensive review of current health care economics as it relates to radiologists, specifically framed by topics defined by the Accreditation Council for Graduate Medical Education in the evaluation of neuroradiology fellows. Therefore, we present a comprehensive review article as a study guide for fellows to learn from and gain competence in the Accreditation Council for Graduate Medical Education neuroradiology milestones on health care economics.

ABBREVIATIONS: ACGME = Accreditation Council for Graduate Medical Education; ASNR = American Society of Neuroradiology; CMS = Centers for Medicare and Medicaid Services; CPT = Current Procedural Terminology; ICD = International Statistical Classification of Diseases and Related Health Problems; MACRA = Medicare Access and Children's Health Insurance Program Reauthorization Act; MPPR = Multiple Procedure Payment Reduction; PC = professional component; RUC = American Medical Association Specialty Society Relative Value Scale Update Committee; RVS = Resource-Based Relative Value Scale; RVU = relative value unit; TDABC = Time-Driven Activity-Based Costing; TC = technical component

Understanding and pragmatically applying the economic principles found in existing resources may be challenging for fellows, given the relatively fragmented dissemination of the principles in the literature. Therefore, we present a comprehensive review article as a study guide for fellows to learn from and gain competence in the ACGME neuroradiology milestones on health care economics. In addition, it is the authors' hope that this work might serve as a foundation for diagnostic radiology residents, other imaging subspecialty fellows, and practicing radiologists, facilitating implementation in real-world radiology practice. This review article primarily relates to Medicare and its unique role in the physician reimbursement process. The role of private payers is beyond the scope of this effort and will not be explored to any meaningful degree. Finally, this work will be presented as a 2-part review article, with Part 1 covering ACGME milestones 1–3 and Part 2 covering milestones 4–5.

MATERIALS AND METHODS

A search using the PubMed Medical Subject Heading terms "diagnostic imaging/economics" and "radiology/economics" performed in late 2016 resulted in a nonexhaustive compilation of approximately 50 review articles on current health care economics, nearly all of which were published within the past 5–6 years, many within the past 1–2 years. From these, approximately 20 reference articles were used to synthesize a relatively comprehensive compendium of useful reference information on the topic, with the ACGME neuroradiology milestones on health care economics and systems-based practice serving as a framework.

ACGME Neuroradiology Milestones on Health Care Economics and Systems-Based Practice: Defining the Levels

The ACGME neuroradiology milestones on health care economics and systems-based practice are made up of 5 levels per the most recent iteration of The Neuroradiology Milestone Project from July 2015.[1] In general, this project is part of a larger effort by the ACGME to assess the competence of residents and fellows in their respective specialties or subspecialties as they matriculate through their training program toward unsupervised practice. It provides a framework for assessing the development of trainees in several key elements of specialty/subspecialty competency across 6 core domains: medical knowledge, patient care, professionalism, interpersonal communication, practice-based learning, and system-based practice. More specifically, as a neuroradiology fellow progresses through his or her training program, the milestones serve as a benchmark for measuring competence in key elements related to the subspecialty of neuroradiology, one of which is health care economics. The 5 levels of each key element are presented as a developmental framework, moving from less advanced

From the Neuroradiology Section, Department of Radiology, George Washington University Hospital, Washington, DC.

Paper previously presented, in part, as a digital exhibit at: Annual Meeting of the American Society of Neuroradiology, April 22–27, 2017; Long Beach, California.

Please address correspondence to M. Reza Taheri, MD, PhD, 900 23rd St, NW, G2092, George Washington University, Washington, DC 20037; e-mail: rtaheri@mfa.gwu.edu

Indicates open access to non-subscribers at www.ajnr.org

http://dx.doi.org/10.3174/ajnr.A5381

Table 1: Neuroradiology Milestones—ACGME Report Worksheet[a]

Health Care Economics—Systems-Based Practice 1				
Level 1	**Level 2**	**Level 3**	**Level 4**	**Level 5**
Describes the technical and professional components of imaging costs in the subspecialty division	Participates in departmental cost-savings initiatives	Describes billing and coding of subspecialty-specific exams and recognizes and corrects incorrect coding; creates reports that contain the elements necessary to support exam coding	Describes Medicare reimbursement for radiology studies and available bonus payments for physicians	Describes the roles of the ACR and AMA in the valuation and revaluation of CPT codes

Note:—ACR indicates American College of Radiology; AMA, American Medical Association.

[a] Reprinted from The Neuroradiology Milestone Project, The Accreditation Council for Graduate Medical Education and the American Board of Radiology.[1]

(level 1) to more advanced (level 5). As the fellow progresses from entry into the training program to graduation, the goal is to move from novice to expert in the subspecialty, with level 4 (or above) being the target for graduation.

The 5 levels for measuring a neuroradiology fellow's competence in health care economics are outlined in Table 1 and are presented in order as major section headings (levels) in this article.

Historical Background

Under the Social Security Act of 1965 (P.L. 89–97, Approved July 30, 1965 [79 Stat. 286]; please refer to https://www.ssa.gov/OP_Home/comp2/F089-097.html), physicians were reimbursed for both their professional work and any practice expenses directly related to that work on an as-billed fee-for-service basis. Modest oversight was provided to facilitate billing that was "usual, customary, and reasonable," though there were no established national guidelines to ensure uniformity, which resulted in a wide range of reimbursements. This indiscriminate scheme persisted until 1982 when the Tax Equity and Fiscal Responsibility Act was passed into law. It established the diagnosis-related group, which was a payment system in which hospitals were paid an established (fixed) prospective fee for the cost of inpatient care based on specific patient diagnoses.[2,3] In 1983, Congress amended the Social Security Act to include a national diagnosis-related group–based hospital payment system for all patients on Medicare. Although Medicare costs stabilized via shorter hospital stays, radiologists' reimbursements leveled off or diminished; this change accelerated a trend at that time in which increasing numbers of radiologists were detaching themselves from hospital employment (and therefore the diagnosis-related group payment model). These radiologists began to set up professional corporations that contracted with hospitals and maintained separate billing arrangements. Although already prevalent, this program accelerated the separation of billing components; the professional fees are charged by the radiologists for the interpretation of inpatient imaging studies, and the technical fees are charged by the hospitals for the performance of the studies.[2]

However, in a setting of rising health care costs in the 1980s and burgeoning capitation of physician reimbursement, there was a call by Congress for greater scrutiny of the way government revenue was being distributed for medical services, which resulted in the creation of the Resource-Based Relative Value Scale (RVS), a constantly evolving entity that remains in use today.[2] Congress commissioned William Hsaio, PhD, of the Harvard School of Public Health to establish the RVS; he was, at the time, a national spokesperson on the concept. It estimated the discrete amount of work involved in providing specific medical services and ranked those services on the basis of the time needed to complete the work, the intensity of the work, and practice expense. Intensity was defined by technical/physical skill, mental effort/judgment, and stress, the latter being a gauge for the possibility of untoward legal action. The radiology community played an important role in the early adoption of the RVS system, having an RVS of its own as far back as 1963 at the request of the Department of Defense; this RVS became incorporated into the RVS used by all specialties. Broad adoption of the RVS was largely due to this early effort of the radiology community, which predated Dr Hsaio's effort, in concert with other specialties, resulting in its use by the greater medical community.[2] A timeline is presented in the Figure, which highlights additional historical details.

Level 1: Technical and Professional Components

Defining the Terms. Radiology services comprise 2 distinct billable elements, the technical component (TC) and the professional component (PC).[4] The TC is that portion of the global fee that reflects the cost of operating and maintaining the medical equipment, the cost of medical supplies, the cost of renting or purchasing the real estate that houses the equipment, the cost associated with having radiologic technologists who perform the examinations, and so forth. The PC refers to the cost associated with the radiologist's interpretation of the examination, which includes the written radiology report, which is the sum of the physician work, practice expense, and professional liability insurance inherent in the production of the report. In short, the technical fee reflects the cost of performing the study and the professional fee reflects the cost of interpreting the study, which vary on the basis of geographic location (Table 2).

Relative Value Unit. Many physicians, including radiologists, use relative value units (RVUs) as defined by Medicare as a measure of value in the Centers for Medicare and Medicaid Services (CMS) reimbursement formula for radiologist services. RVUs are typically the method used to allocate radiologist reimbursement, being based on the complexity, skill, and time required to perform a clinical treatment plan or procedure, which are elements related to the PC. In general, the TC amounts to a higher percentage of the global cost of a radiologic examination, due to the considerably larger overhead needed to maintain its various operational elements. For example, the current National Physician Fee Schedule Relative Value File breaks down a "brain MR imaging without contrast" in the Washington, DC area in the following manner: It

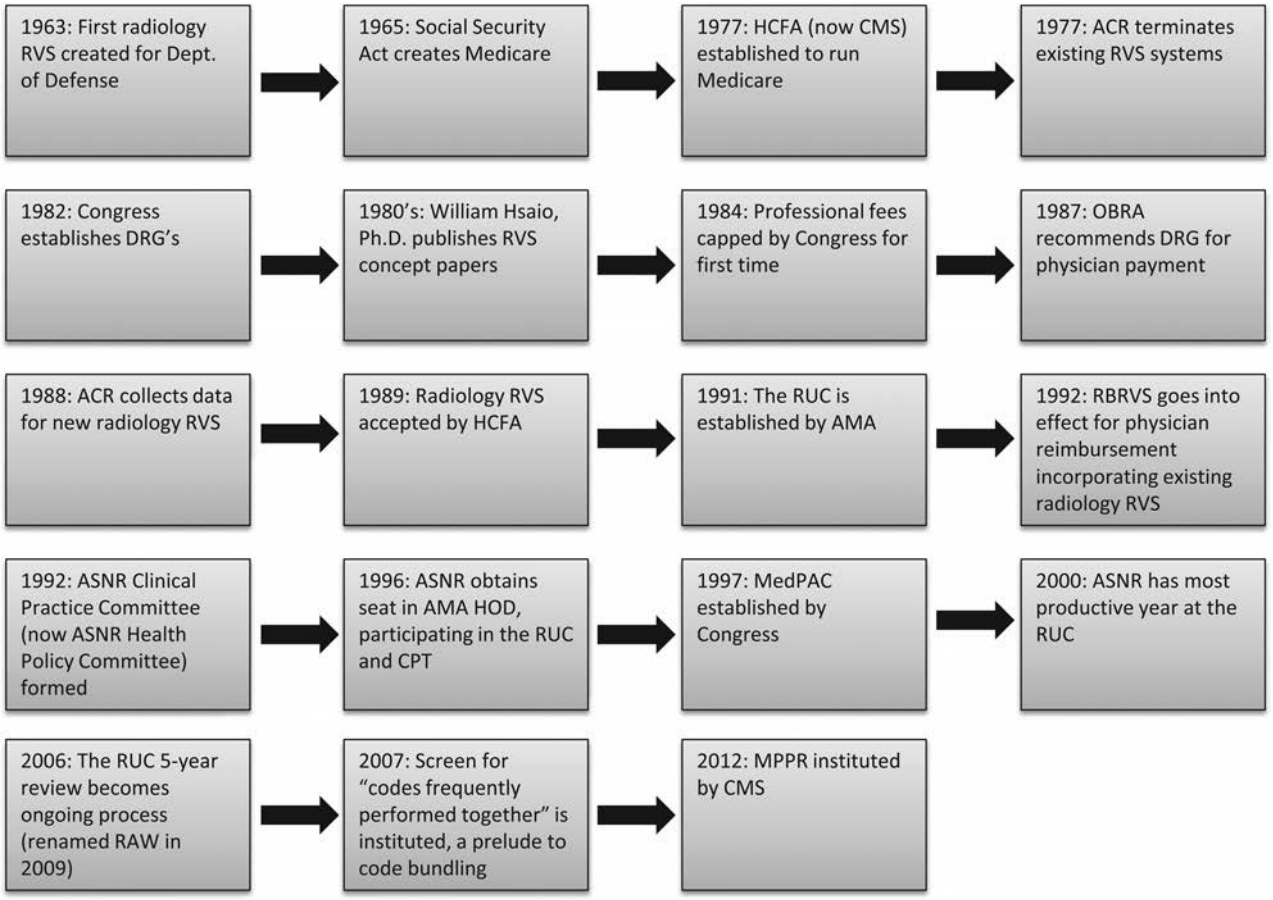

FIGURE. Timeline of the RVS. ACR indicates American College of Radiology; AMA, American Medical Association; HCFA, Health Care Financing Administration; HOD, House of Delegates; MedPAC, Medicare Payment Advisory Committee; OBRA, Omnibus Budget Reconciliation Act; RAW, Relativity Assessment Workgroup; DRG, diagnosis-related group; RBRVS, Resource-Based Relative Value Scale. Adapted with permission from Donovan.[2]

Table 2: Centers for Medicare and Medicaid Services

2017 CMS Component Fees for MRI Brain without Dye (HCPCS Code 70551)[5,6]			
	TC	PC	Global Fee
Arkansas	$137.58	$ 71.88	$209.46
District of Columbia	$190.74	$83.10	$ 273.84
Minnesota	$160.56	$74.15	$ 234.71

Note:—HCPCS indicates Healthcare Common Procedure Coding System.

is assigned 6.52 RVUs for the global payment, 4.41 RVUs for the technical component, and 2.11 RVUs for the professional component (1.48 RVUs for physician work).[6]

Basics of Current Procedural Terminology. Accurate and consistent physician reimbursement mandates a standardized language for medical procedures. In recognition of this need, the American Medical Association developed the Current Procedural Terminology (CPT; https://www.ama-assn.org/practice-management/cpt-current-procedural-terminology) nomenclature in 1965 as a description of medical services and procedures.[7] Initially, this manual focused on surgery, so radiology, much less neuroradiology, had little representation in the form of billable coding. In 1970 when the second edition was published, each code was expanded to 5 digits with the 70000–79999 code series applying to radiology. By the mid-to-late 1970s, the third and fourth editions were released, which contained increasingly detailed codes in keeping with the ever-growing complexity of the health care system. This procedural coding system has continued to evolve across the years, merging with other coding systems and via the Health Insurance Portability and Accountability Act of 1996, was updated to support standards for electronic transactions. These changes culminated in the establishment of the CPT-5 project, which resulted in nomenclature that facilitated new tracking procedures and specific reporting measures that could be used in performance-based payment. This expansion paved the way for the Centers for Medicare and Medicaid Services opting to formally incorporate CPT codes in Medicare claims processing. Finally, in 2000, CPT became the national coding standard for reporting medical services and procedures.[7]

The codes found in the CPT codebook are divided into 3 categories (Table 3). Category I codes are common to everyday clinical practice and are referred to the American Medical Association Specialty Society Relative Value Scale Update Committee for valuation.[8] They require US Food and Drug Administration approval for any related drugs or devices, must have demonstrated clinical efficacy validated by peer-reviewed literature, and must be the standard of care practiced by multiple physicians in the United States. Category II codes are used to report quality performance initiatives and are designed to facilitate data collection,

tracking of performance measures, and compliance with state and federal law, with minimal medical record review. They are not used for coding services or procedures that are billed. As Physician Quality Reporting System measures grow, the number of category II codes continues to increase (Physician Quality Reporting System will be more fully discussed later in this article). Category III codes were initially created in 2001 to track new or experimental procedures and technologies that aid the FDA in the approval process. They are temporary by definition, being approved for a 5-year period with the option of extending this period once, and are not assigned a work value. Therefore, payment for category III codes is discretionary. Considering the scientific evidence, a category III code can be converted to a category I code before the expiration of the initial or renewal term. If the procedure proves ineffective at the end of the term, the code can die. Category I and III codes have different rigors; having a code does not ensure coverage and payment.

Two key committees are responsible for proposing new CPT codes and changes to the code set: the CPT Editorial Panel and the CPT Advisory Committee. The CPT Editorial Panel oversees the development of new and revised codes and governs the maintenance of code sets.[7] The panel comprises physicians and other relevant stakeholders, including CMS representatives. The CPT Advisory Committee is made up of societal representatives from the American Medical Association House of Delegates and is the apparatus through which the American Society of Neuroradiology (ASNR) and other medical societies are represented. The Advisory Committee assists the CPT Editorial Panel by proposing code set changes and providing insight into coding proposals submitted by other interested stakeholders, whether they are other medical societies, industry vendors, insurance carriers, and so forth. These panels will be discussed later in this article.

Controversies

Multiple Procedure Payment Reduction. Multiple procedure payment reduction (MPPR) is a very controversial element of radiology reimbursements.[4] This cost-saving scheme was first proposed by CMS in 2006 across multiple code families, including those related to radiologic imaging; it applies to advanced imaging examinations defined as sonography, CT, CT angiography, MR imaging, and MR angiography. In this practice, Medicare will fully reimburse for the most expensive examination when multiple imaging examinations are performed on a single patient by the same physician or group during a single health care encounter (single patient session), but it will reduce reimbursements for subsequent imaging examinations performed during that encounter.

This practice was implemented in a graded manner during several years,[4] with a 25% reduction in 2006 to the TC of advanced imaging examinations of adjacent anatomy performed by the same physician, on the same patient, on the same day. In 2010, this reduction increased to 50% through the Affordable Care Act. MPPR was subsequently modified in 2011 by the CMS to include nonadjacent anatomy across different imaging modalities (regardless of the relevant code family). In other words, the imaging MPPR was modified to apply to multiple imaging services furnished within the same family of codes or across code families, currently applying to CT and CTA, MR imaging and MRA, and sonography services furnished to the same patient in the same session, regardless of the imaging technique, and not limited to contiguous body areas. Additional regulations were imposed in 2012, expanding the MPPR by cutting the PC by 25%. In 2013, the MPPR was further broadened by the CMS to apply to physicians in the same group practice (same Group National Provider Identifier) caring for the same patient on the same day. It is estimated that the total losses in both TC and PC imaging fee reimbursement due to the implementation of the MPPR policy were approximately $1.2 billion from 2006 to 2013.[4]

According to the CMS, the primary rationale for these cuts to reimbursement related to redundant work within both the TC and PC, when patients undergo multiple imaging examinations during a single day.[4] The justification for reducing the TC reimbursements related to activities that are not repeated during multiple examinations on the same patient during the same encounter, such as preparing and cleaning the examination room, educating the patient, obtaining informed consent, placing an IV line, and so forth. However, applying MPPR to a radiologist's interpretation (PC) of multiple imaging examinations is particularly controversial, because the radiologist is responsible for all subsequent images when multiple examinations are performed and these follow-up examinations are often as time-intensive as the initial examination. See Table 4 for an example of how MPPR can reduce technical and professional component reimbursement.

Code Bundling. With the development of new bundled CPT codes, further reductions in radiology reimbursement have been seen. The American Medical Association Specialty Society Relative Value Scale Update Committee (RUC) has pinpointed "potentially misvalued" services, which are defined as services performed and billed together with varying degrees of overlap or redundancy in time and effort. On the basis of methods provided by the CMS and the RUC, codes have been identified that have a history of being billed together 95%, 90%, and 75% of the time (and more

Table 3: Three categories of codes found in the CPT codebook

CPT Category	Description
I	FDA approved and common in clinical practice Based on peer-reviewed literature Referred to RUC for valuation
II	Used to report quality performance initiatives Decreased need for records review No reimbursement
III	Track new/experimental procedures Literature suggests possible future use Temporary, by definition

Table 4: How MPPR can reduce technical and professional component reimbursement

	Procedure 1	Procedure 2	Total Payment	MPPR Applied
TC	$500	$400	$900	$700 ($500 + [$0.50 × $400])
PC	$100	$80	$180	$160 ($100 + [$0.75 × $80])
Global	$600	$480	$1080	$860

recently 50% of the time), which often result in the creation of new revalued "bundled" codes. This practice, in turn, initiates a controversial cascade of payment reductions for the TC, PC, and hospital, with often little advanced notice between notification and implementation (approximately 3 months).[4]

The ASNR has played a proactive role in neuroradiology-related code valuation and revaluation recommendations brought before the RUC.[7] One prototypical procedure usually performed by neuroradiologists flagged by the "codes performed together screen" was myelography and the near-universal association among injection, supervisory, and interpretation codes. The ASNR, along with the American College of Radiology, revised the code set and presented both the new bundled code sets and the original free-standing codes to the RUC for valuation. Four new bundled codes were introduced in CPT 2015 for myelography with the same physician performing and supervising the procedure and interpreting the images. If separate providers perform the procedure and interpret the images, then the nonbundled codes are used.

Another example from 2010 involved carotid/cerebral angiography, for which a plethora of related procedure codes were flagged by the screen describing catheterization and injection as well as radiologic supervision and interpretation. As a result, after input from multiple stakeholders including the ASNR, a new series of codes were proposed and subsequently approved by the CPT Editorial Panel in 2012, which were then forwarded to the RUC for valuation. This revision, nonetheless, resulted in a substantial decrease in RVUs beginning in January 2013, which, in turn, caused physician reimbursement to plummet. A single-vessel selective diagnostic angiogram of an internal carotid artery that had a CMS valuation of 7.6 RVUs in 2012 would be replaced with a single bundled code for the procedure and interpretation valued at 6.5 RVUs in 2013, a reduction of 15%. A standard 4-vessel angiogram valued at 18.22 RVUs decreased to 14.25 RVUs, a reduction of 22%.

Bundling of codes has probably had the greatest impact in mammography. As a result, an entire group of breast interventions has been condensed into 14 new bundled codes, resulting in measurable reductions to the TC and PC across this group of interventions. Stereotactic breast biopsy alone has undergone reductions of up to 45% for the PC and up to 3% for the TC.[4] This reduction has untoward consequences when attempting to recruit trainees into breast imaging fellowships and radiologists into breast imaging careers/positions, not to mention its impact on retaining patients within a given radiologist's health care system.

In addition to myelography and carotid/cerebral angiography noted above, areas of neuroradiology most affected by code bundling include vertebroplasty/vertebral augmentation, scoliosis plain film series, and fetal MR imaging, to name a few. As CPT code families continue to be screened by the Relativity Assessment Workgroup (discussed later in this article) or CMS, the ASNR continues to represent the interests of neuroradiology. In cooperation with the CPT Editorial Panel, the ASNR has been instrumental in crafting new coding proposals for these procedures (and others) in their ongoing advocacy for the subspecialty.

Bundled Payments for Care Improvement Initiative. The Bundled Payments for Care Improvement Initiative offers providers a single combined reimbursement for a single illness or "episode of care" in an Accountable Care Organization, which seeks to incentivize higher value care and more effective coordination of providers across multiple settings via alternative payment models.[9] By offering a bundled payment, the assumption is that providers will develop their own internal controls and become jointly accountable for each episode of care; these results will cause providers to assume greater risk as costs burgeon compared with the aging fee-for-service model. This form of payment bundling is separate and distinct from the CPT code bundling discussed above, which refers to the redefining of multiple CPT codes for services often reported together in a single CPT code for a given combination of services. Both CPT code bundling and payment (or procedure) bundling have a similar effect, to reduce overall payment for a given combination of services.

The Bundled Payments for Care Improvement initiative seeks to align incentives for providers across a broad spectrum of medical and paramedical services provided by physicians, hospitals, nonphysician providers, and other health care facilities under 4 basic models: 1) acute care inpatient hospitalization with a standard discount related to Medicare Part A inpatient payments, 2 and 3) retrospective bundling of payments in which expenditures are reconciled against a target price for each episode of care, and 4) a prospective bundled payment scheme in which a lump sum payment is made to providers for the entire episode of care.[9] Each of these models has a different impact on providers, from maintaining status quo payment under the current fee-for-service system for model 1 to varying degrees of payment bundling, with model 4 ("prospective bundling") being the most ambitious with its single prospectively determined reimbursement made to the hospital to cover all services that occur during a single episode of care.

Level 2: Cost-Savings Initiatives

Time-Driven Activity-Based Costing. Time-Driven Activity-Based Costing (TDABC) is a strategic accounting and profitability tool used by many businesses, which can be applied by health care providers to monitor the cost of a patient's treatment pathway.[10] Combining this tool with the patient's outcome data provides a means to more objectively measure the value of care. It reveals to clinicians the underlying factors that drive costs and functions across a broad spectrum of medical settings and organizations. Clinicians are then able to identify variation in costs among similar providers across different pathways for the same medical services. For example, when one compares the average cost of primary total knee arthroplasty for an organization, the 90th percentile of total cost is nearly twice the average for an organization at the 10th percentile of total cost using the TDABC approach.[10] TDABC only applies to a practice or departmental effort to control its own costs and is independent of coding, billing, and reimbursement.

Current costing mechanisms lack standardization, given a patient's treatment plan, which often involves several departments, none of which use a standard treatment pathway for patients with similar illnesses. They often focus on only measuring and controlling costs for a small subset, such as a department or for individual procedures; this focus is not effective for reducing long-term

costs, given the pedantic micromanaging of line-item expenses with implementation of arbitrary limits on department spending, which can greatly reduce the value and quality of services provided.[10] These accounting problems are further exacerbated by the reimbursement systems and accounting practices currently in place at many health care organizations.

As mentioned above, many providers use RVUs to allocate clinical departmental costs to various procedures and treatments; this use tends to introduce substantial distortions into cost measurement. This allocation is problematic when attempting cost stratification, given the highly subjective judgments and aggregate data on which RVUs are based and the difficulty of validating them in actual clinical practice. Only reimbursed procedures and processes have RVUs assigned to them, not unreimbursed ones; therefore, they do not reflect the use of different staff and personnel with widely different compensation, thereby confusing procedure complexity with the resource time required to perform the procedure.

There are several foundational principles for measuring costs in health care, and TDABC provides a means for enabling each of them.[10] First, the cost of using a resource, whether personnel or equipment, depends only on the time the resource is in use and the price rate for that resource, even with varying reimbursement for different services. The cost of a clinician is the same if the time required for the procedure is the same, whether performing a high-RVU procedure or a low-RVU procedure. Second, the unit of analysis for measuring costs and outcomes should be the patient's medical condition. Third, costs should be measured over the entire treatment cycle for a given medical condition, including diagnosis, tests, education/counseling, interventions, and managing ongoing care. Fourth, if a resource is not used, it should be considered unused and not assigned to the services provided.

TDABC, a well-established method of cost measurement across multiple industries,[10] calculates the cost of resources used to perform a procedure or treat a patient across the care cycle by estimating the cost (rate) of each used resource and the time it is consumed over the full cycle of the patient's care for a particular medical condition. This is facilitated by creating a process map of the care cycle or procedure and identifying all clinical and administrative resources used to treat the specific medical condition. Various methods can be used to elicit information for the aforementioned process maps within an organization, including interviewing involved personnel about the care processes, direct observation via shadowing, data capture from the electronic medical record, and review of administrative data. When the project team can accurately measure the quantities of personnel, equipment time, and all material consumables used during the complete treatment cycle, the process map is considered complete. Next, the project team uses the payroll data of the institution to calculate the cost rate per minute of time of each resource, whether personnel, equipment, or space, and then multiplies the cost rate of each resource by the amount of time the patient spent in each resource, followed by summing of all resource cost rates to compute the total cost of the patient care cycle.

The results of a comprehensive TDABC analysis will provide hospitals and departments with valuable opportunities to intervene at multiple levels in the process; with analytic comparisons both before and after interventions, organizations will be provided the necessary information to identify and implement real and sustained reductions in costs.

Avoid Penalties: Preemptive Participation in Medicare Access and Children's Health Insurance Program Reauthorization Act. The US Department of Health and Human Services has put forth an ambitious plan for health care in the United States, focusing on "better care, smarter spending, and healthier people," seeking to tie 90% of the Medicare payment to the quality of care by 2018, which stands in contradistinction to the current fee-for-service system.[11] These principles underpin the bipartisan Medicare Access and Children's Health Insurance Program Reauthorization Act (MACRA) of 2015. MACRA seeks to achieve these goals by incentivizing quality over quantity and rewarding more efficient clinical decision-making, seeking to actuate patient-centered health care delivery that is meaningful, flexible, cost-effective, and practically feasible to improve health outcomes and the overall care experience. MACRA will be discussed in greater detail later in this article.

Another way to take part in cost saving in a practice or department is to preemptively begin laying the groundwork necessary to participate in the Merit-Based Incentive Payment System and various Advanced Alternative Payment Models, which are described in MACRA. A more complete discussion of these models will appear later in this article, but being ready to participate in these models now could result in measurable cost savings for the clinician and the practice/department. In 2019, MACRA will begin to impact physicians' Medicare Part B reimbursements. For example, under the Merit-Based Incentive Payment System clinicians will experience either negative, neutral, or positive adjustments to their traditional fee-for-service payments based on a range of performance measures.[11]

Practical Departmental Measures. Devising an evolving plan to address ongoing departmental cost-saving initiatives is not too difficult if one is willing to be proactive and use a little imagination. One way to take part is to actively identify departmental waste and approve a standing policy to correct it. For example, when one performs a procedure such as a lumbar puncture, it is more cost-efficient to use the vial of lidocaine already provided in the lumbar puncture kit as opposed to drawing from a separate larger external vial that may make the process slightly easier. A 20-mL bottle of lidocaine HCl 1% (10 mg/mL) can range anywhere from approximately $2.00 to $3.00 per bottle, depending on the manufacturer/distributor. Another cost-saving solution might be to obtain bicarbonate separately (if commonly used in the department/practice) and manually mix it with the lidocaine rather than ordering a lidocaine-bicarbonate preparation from the hospital pharmacist. This general idea can be applied across the board for all departmental procedures—that is, using items within the provided kits and exercising greater discretion as to when to use additional items that basically have the same functionality.

Level 3: Coding and Billing for Subspecialty-Specific Examinations and Reports

Report Elements That Support Examination Coding/Billing. Several key elements in the structured radiology report are necessary not only to meet published American College of Radiology Prac-

Table 5: Required content and noncontent attributes

Content Items	Noncontent Items
History (with relevant information)	Clarity/certainty
Technique (list procedures/materials)	Language (anatomic/pathologic/radiologic)
Exam quality (degradation factors)	Standardized format
Description	
Comparison	
Diagnosis	
Differential (when appropriate)	
Address clinical question	
Recommendations (when appropriate)	
Conclusions	

Table 6: Examples of the differences between ICD-9 and ICD-10 codes

Example	ICD-9	ICD-10
Neuroradiology	852.21 Subdural hemorrhage without coma	S06.5X0A Traumatic subdural hemorrhage without loss of consciousness, initial encounter
Musculoskeletal	813.45 Torus fracture of radius (alone)	S52.521A Torus fracture of lower end of right radius, initial encounter for closed fracture

tice Parameters, recommendations and standards that were evaluated using the Appraisal of Guidelines for Research and Evaluation tool, but also to support successful examination coding and billing.[12-14] The Appraisal of Guidelines for Research and Evaluation tool assesses the quality of guidelines (including the methodologic rigor and transparency with which a guideline is developed), provides a methodologic strategy for the development of guidelines, and outlines what and how information ought to be reported in guidelines.[15] There are both content and noncontent attributes that should be appropriately reflected in a typical radiology report. Required content and noncontent attributes are included in Table 5.[12]

Additionally, some items need to be included in the written radiology report to make it International Statistical Classification of Diseases and Related Health Problems-10 compliant (ICD-10; https://www.cms.gov/Medicare/Coding/ICD10/). ICD-10 is the 10th revision of the International Classification of Diseases (ICD), a medical classification list by the World Health Organization containing codes for various diseases, as well as signs and symptoms.[16] With ICD-10 codes, the amount of information required from the referring physician has increased dramatically compared with ICD-9 (the older ninth revision). Imaging facilities need to acquire a more complete history for a patient when scheduling an examination for precertification, dictation, and subsequent billing of a procedure. Important elements include a more specific clinical diagnosis and disease acuity, detailed anatomic site, secondary or tertiary diagnoses, laterality (eg, right-arm numbness), specifying initial-versus-subsequent encounters, and detailed procedure descriptions (when applicable). It is important to include as much clinical information as possible to help ensure compliance and avoid the pitfalls of being too brief. For example, it is insufficient to state "concern for infarct" in the indications section of the report. A more appropriate phrase might be "worsening right arm and hand weakness over the last hour, concern for acute infarct."

See Table 6 for examples that highlight the differences between ICD-9 and ICD-10 codes.[17,18]

Examples of Neuroradiology-Specific CPT Codes with RVU Values. The following are examples of neuroradiology-specific CPT codes with their respective CMS RVU values[6] to further highlight the individual components of each code and the relative weights of the technical and professional components of the global fee. Remember ICD codes relate to the classification of disease (patient clinical presentation), whereas CPT codes relate to the coding of diagnostic procedures, such as MR imaging (below).

CPT Code 70551: "MR Imaging Brain without Contrast." In the Washington, DC area, CPT code 70551 is assigned 6.52 RVUs for the global payment, 4.41 RVUs for the technical component, and 2.11 RVUs for the professional component (1.48 RVUs for physician work) from the Medicare code key.

CPT Code 72148: "MR Imaging Lumbar Spine without Contrast." In the Washington, DC area, CPT code 72148 is assigned 6.32 RVUs for the global payment, 4.19 RVUs for the technical component, and 2.13 RVUs for the professional component (1.48 RVUs for physician work) from the Medicare code key.

CONCLUSIONS

The tapestry of health care economics as it applies practically to radiologists is complex, with relatively fragmented dissemination in the current medical literature. Therefore, we have presented a tailored discussion in the form of a study guide for fellows to learn from and gain competence in the ACGME neuroradiology milestones on health care economics. While this article is targeted to neuroradiology fellows, it can be useful for others in the radiologic sciences and medicine as a whole. While not meant to be exhaustive, our aim is that this review article might serve as a foundation on which radiology residents, imaging subspecialty fellows, practicing radiologists, and other medical and allied health care professionals can build upon, facilitating their implementation in real-world radiology/clinical practice.

Because health care economics is a constantly evolving entity, the following Web sites are provided as resources to follow some of the latest changes in the health care economics landscape:

CPT information: https://www.ama-assn.org/practice-management/cpt-current-procedural-terminology; and https://www.ama-assn.org/practice-management/explore-recent-cpt-code-changes-actions

MACRA Merit-Based Incentive Payment System information: https://www.acr.org/Quality-Safety/Resources/MACRA-Resources

Medicare information: https://www.cms.gov/Medicare/Medicare.html

RUC information: https://www.ama-assn.org/about-us/ruc.

REFERENCES

1. The Accreditation Council for Graduate Medical Education and The American Board of Radiology. The Neuroradiology Milestone Project. Updated 2015. https://www.acgme.org/Portals/0/PDFs/Milestones/NeuroradiologyMilestones.pdf. Accessed April 30, 2017
2. Donovan WD. **The resource-based relative value scale and neuroradiology: ASNR's history at the RUC.** *Neuroimaging Clin N Am* 2012;22:421–36 CrossRef Medline
3. Rimler SB, Gale BD, Reede DL. **Diagnosis-related groups and hospital inpatient federal reimbursement.** *Radiographics* 2015;35:1825–34 CrossRef Medline
4. Baadh A, Peterkin Y, Wegener M, et al. **The relative value unit: history, current use, and controversies.** *Curr Probl Diagn Radiol* 2016;45:128–32 CrossRef Medline
5. Centers for Medicare and Medicaid Services. PFS relative value files. Updated 2016. https://www.cms.gov/medicare/medicare-fee-for-service-payment/physicianfeesched/pfs-relative-value-files.html. Accessed May 16, 2017
6. Centers for Medicare and Medicaid Services. Physician fee schedule search. Updated 2016. https://www.cms.gov/apps/physician-fee-schedule/search/search-criteria.aspx. Accessed May 16, 2017
7. Leslie Mazwi TM, Bello JA, Tu R, et al. **Current procedural terminology: history, structure, and relationship to valuation for the neuroradiologist.** *AJNR Am J Neuroradiol* 2016;37:1972–76 CrossRef Medline
8. Petrey WB, Allen B Jr, Thorwarth WT Jr, et al. **Radiology coding, reimbursement, and economics: a practical playbook for housestaff.** *J Am Coll Radiol* 2009;6:643–48 CrossRef Medline
9. Hirsch JA, Leslie-Mazwi TM, Barr RM, et al. **The bundled payments for care improvement initiative.** *J Neurointerv Surg* 2016;8:547–48 CrossRef Medline
10. Oklu R, Haas D, Kaplan RS, et al. **Time-driven activity-based costing in IR.** *J Vasc Interv Radiol* 2015;26:1827–31 CrossRef Medline
11. Rosenkrantz AB, Nicola GN, Allen B Jr, et al. **MACRA, alternative payment models, and the physician-focused payment model: implications for radiology.** *J Am Coll Radiol* 2017;14:744–51 CrossRef Medline
12. Pool F, Goergen S. **Quality of the written radiology report: a review of the literature.** *J Am Coll Radiol* 2010;7:634–43 CrossRef Medline
13. Fleming M, MacFarlane D, Torres WE, et al. **Magnitude of impact, overall and on subspecialties, of transitioning in radiology from ICD-9 to ICD-10 codes.** *J Am Coll Radiol* 2015;12:1155–61 CrossRef Medline
14. American Medical Association. Fact sheet: The differences between ICD-9 and ICD-10. https://www.unitypoint.org/waterloo/filesimages/for%20providers/icd9-icd10-differences.pdf. Accessed May 16, 2017.
15. The AGREE Next Steps Consortium. Appraisal of guidelines for research and evaluation II instrument. Updated 2013. http://www.agreetrust.org/wp-content/uploads/2013/10/AGREE-II-Users-Manual-and-23-item-Instrument_2009_UPDATE_2013.pdf. Accessed June 14, 2017
16. World Health Organization. Classification of diseases (ICD). Updated 2016. http://www.who.int/classifications/icd/en/. Accessed June 14, 2017
17. Centers for Medicare and Medicaid Services. ICD-9-CM diagnosis and procedure codes: Abbreviated and full code titles. Updated 2014. https://www.cms.gov/medicare/coding/ICD9providerdiagnosticcodes/codes.html. Accessed May 16, 2017
18. Centers for Medicare and Medicaid Services. 2017 ICD-10-CM and GEMs. Updated 2016. https://www.cms.gov/Medicare/Coding/ICD10/2017-ICD-10-CM-and-GEMs.html. Accessed May 16, 2017

Health Care Economics: A Study Guide for Neuroradiology Fellows, Part 2

S.L. Weiner, R. Tu, R. Javan, and M.R. Taheri

ABSTRACT

SUMMARY: In this second article, we continue the review of current health care economics as it relates to radiologists, specifically framed by topics defined by the Accreditation Council for Graduate Medical Education in the evaluation of neuroradiology fellows. The discussion in this article is focused on topics pertaining to levels 4 and 5, which are the more advanced levels of competency defined by the Accreditation Council for Graduate Medical Education Neuroradiology Milestones on Health Care Economics and System Based Practice.

ABBREVIATIONS: ACGME = Accreditation Council for Graduate Medical Education; ACR = American College of Radiology; AMA = American Medical Association; APM = Advanced Alternative Payment Model; ASNR = American Society of Neuroradiology; CMS = Centers for Medicare and Medicaid Services; CPT = Current Procedural Terminology; GPCI = geographic practice cost index; MACRA = Medicare Access and Children's Health Insurance Program Reauthorization Act; MedPAC = Medicare Payment Advisory Commission; MIPS = Merit-Based Incentive Payment System; PE = practice expense; PLI = professional liability insurance; PQRS = Physician Quality Reporting System; PW = physician's work; QCDR = Qualified Clinical Data Registries; RUC = American Medical Association Specialty Society Relative Value Scale Update Committee; RVU = relative value unit

Few resources are available in the medical literature for a comprehensive review of current health care economics as it relates to radiologists, specifically framed by topics defined by the Accreditation Council for Graduate Medical Education (ACGME) in the evaluation of neuroradiology fellows. Understanding and pragmatically applying the economic principles found in existing resources may be challenging for fellows, given the relatively fragmented dissemination of the principles in the literature. Therefore, we present a tailored discussion fashioned as a study guide for fellows to learn from and to gain competence in the ACGME neuroradiology milestones on health care economics. In addition, it is the authors' hope that this work might serve as a basic foundation for diagnostic radiology residents, other imaging subspecialty fellows, and practicing radiologists, facilitating their implementation in real-world radiology practice. This review article primarily relates to Medicare and its unique role in the physician reimbursement process. The role of private payers is beyond the scope of this effort and will not be explored to any meaningful degree. Finally, this work will be presented as a 2-part review article, with Part 1 covering ACGME milestones 1–3 and Part 2 covering milestones 4 and 5.

MATERIALS AND METHODS

A search using the PubMed Medical Subject Heading terms "diagnostic imaging/economics" and "radiology/economics" performed in late 2016 resulted in a nonexhaustive compilation of approximately 50 review articles on the topic of current health care economics, nearly all of which were published within the past 5–6 years, many within the past 1–2 years. From these, approximately 20 reference articles were used to synthesize a relatively comprehensive compendium of useful information on the topic, with the ACGME neuroradiology milestones on health care economics and systems-based practice serving as a framework.

ACGME Neuroradiology Milestones on Health Care Economics and Systems-Based Practice: Redefining the Levels

Please refer to Part 1 of this Review for the general background and explanation of the ACGME neuroradiology milestones.

The 5 levels for measuring a neuroradiology fellow's competence in health care economics are outlined in Table 1 of Part 1 of this review and are presented in order as major section headings (levels) within this article.

From the Neuroradiology Section, Department of Radiology, George Washington University Hospital, Washington, DC.

Paper previously presented, in part, as a digital exhibit at: Annual Meeting of the American Society of Neuroradiology, April 22–27, 2017; Long Beach, California.

Please address correspondence to M. Reza Taheri, MD, PhD, 900 23rd Street, NW, G2092, George Washington University, Washington, DC 20037; e-mail: rtaheri@mfa.gwu.edu

Indicates open access to non-subscribers at www.ajnr.org

http://dx.doi.org/10.3174/ajnr.A5382

Table 1: Physician payment calculation for a brain MR imaging without dye in the Washington, DC area

Payment Calculation
Total RVU = (1.48 × 1.048) + (4.95 × 1.205) + (0.09 × 1.271)
Total RVU = 1.55 + 5.96 + 0.11 = 7.62
Payment = 7.62 × $35.8887
Total = $273.47

Level 4: Medicare Reimbursements and Bonus Payments for Radiology Studies

Formula for Calculating a Dollar Value in a Physician Fee Schedule. Each Current Procedural Terminology (CPT) code has a corresponding relative value unit (RVU), which determines the physician's payment and the global payment. The physician payment formula for each CPT code contains 3 RVU components: 1 for physician's work (PW), 1 for practice Centers for Medicare and Medicaid Services (CMS) expense (PE), and 1 for professional liability insurance (PLI) expense.[2,3] Average CMS costs (total physician reimbursements across all codes) broken down proportionately into PW, PE, and PLI have been previously estimated at 52%, 44%, and 4%, respectively.[2] Each of these 3 RVU components is adjusted by a geographic practice cost index (GPCI), which accounts for variations in the cost of living, wages, malpractice premiums, and overhead costs in specific geographic locations. The GPCI is a weight and relativity methodology to neutralize the variation in PLI cost across regions so that in general, one area may gain RVUs at the cost of another. The data are reported by zip code; therefore, the GPCI may be different within a given state and even a given county. Most interesting, Puerto Rico and the Pacific territories follow CMS guidelines as well, and there is consideration for revision of GPCI methodology for these regions to increase their GPCI. Finally, as a reflection of the Protecting Access to Medicare Act legislation in 2014, the physicians in California will benefit from greater GPCI payments in aggregate.[4]

PW RVU represents the RVUs for the physician's time, skill, training, and intensity of work going into the production of a professional service. PE represents the RVUs of the physician's practice expenses going toward the service in question, including equipment, rent, supplies, and nonphysician staff costs. PLI represents the RVUs for the PLI premium or risk assigned to the service. Each of these 3 relative cost factors is adjusted for its own GPCI in the formula. In other words, there is 1 GPCI for PW, 1 for PE, and 1 for PLI. Finally, the total RVUs are multiplied by a conversion factor to determine a total payment amount. The conversion factor, which is updated annually, is currently $35.8887 for 2017 per the "Final Policy, Payment, and Quality Provisions in the Medicare Physician Fee Schedule for Calendar Year (CY) 2017" (https://www.cms.gov/Newsroom/MediaReleaseDatabase/Fact-sheets/2016-Fact-sheets-items/2016-11-02.html) on the CMS.gov Web site.

Therefore, based on the discussion above, the physician payment formula is as follows:

$$\text{Total Physician RVU} = (\text{PW RVU} \times \text{GPCI}_{\text{PW}}) + (\text{PE RVU} \times \text{GPCI}_{\text{PE}}) + (\text{PLI RVU} \times \text{GPCI}_{\text{PLI}}),$$

$$\text{Payment} = \text{Total RVU} \times \text{CF}.$$

A sample physician payment calculation using the payment formula above for a brain MR imaging without dye in the Washington, DC area is found in Table 1).[5,6]

Physician Quality Reporting System. In the early 2000s, a pay-for-performance plan was developed that used a fee-for-service model, which provided incentives for quality and efficiency improvement, known as the Physician Quality Reporting System (PQRS). CMS first introduced the PQRS in 2007 as a metric to quantify performance per a value-based reimbursement model, and it was later incorporated into the Affordable Care Act in 2010.[7] The PQRS was initiated as a voluntary program with bonus payments paid for reporting specified quality measures equaling up to 2% of a physician's Medicare reimbursement. Participatory incentives were 0.5% of all Medicare payments in 2014. Penalties for noncompliance were then instituted in 2015, ranging from 2% to 4% for groups opting not to participate, with incentive payments being phased out that same year. Compounding that issue, the number of quality measures required to avoid a penalty increased from 3 in 2014 to 9 in 2015.[8,9]

Examples of PQRS measures for neuroradiology include the following: radiology reports that include specific items for acute stroke imaging, including whether hemorrhage, mass, or acute infarction are present; specifying the diameter of the proximal internal carotid artery compared with the diameter of the distal internal carotid artery; and patients with cerebrovascular accident undergoing endovascular therapy who have a window to canalization time of <2 hours divided by all patients with cerebrovascular accident undergoing endovascular stroke treatment. Other examples of radiology-specific PQRS measures include the following: reporting fluoroscopy exposure time; comparison with prior imaging studies for all patients having bone scintigraphy; appropriate imaging follow-up of incidental abdominal lesions; imaging follow-up for incidental thyroid nodules; and a reminder system for women 40 years of age and older undergoing screening mammography, providing a target due date for the next mammogram. Another metric, which has a negative impact, reports the use of "probably benign" findings in screening mammography when findings of appropriate assessments are negative, benign, or incomplete. Finally, a metric exists for biopsy follow-up for new patients to ensure that the results of the biopsy have been reviewed and communicated to the patient and the referring physicians.[7,10]

There are, however, several problems with pay-for-performance plans such as the PQRS.[7] First, they offer no good tools to evaluate performance. In addition, the metrics used to assess performance are not reflective of health outcomes. Moreover, the measurement criteria are applied without a control to establish that any improvement can be attributed to the pay-for-performance plan. Finally, this kind of scheme can negatively transition from value-based reimbursement to "metric-based medicine," inadvertently bypassing the physician-patient relationship and the patient's satisfaction, in our eagerness to add value and avoid penalties. Truly implementing such pay-for-performance plans without improving health outcomes is both irrelevant and dangerous. Collecting data on measures that improve health outcomes and linking those measures to reimbursement will be an important step toward value-based health care.

Medicare Payment Advisory Commission. The Medicare Payment Advisory Commission (MedPAC) was established in 1997 by the Balanced Budget Amendment to serve as an advisory body to Congress in the areas of quality of care, access to care, and Medicare spending.[11] MedPAC continues to convene publicly to discuss items of policy and codify its recommendations to Congress. During the committee meetings, commissioners examine the findings of staff research, proposals by policy experts, and observations from other stakeholders. Committee members and staff will also hear suggestions and recommendations on issues related to Medicare through frequent meetings with stakeholders in the program, including congressional committee staff and CMS, health care providers and researchers, and beneficiary proponents. The recommendations of the Commission are published twice per year, in March and June.

Within chapter 4 of the March 2016 report of MedPAC to Congress (http://www.medpac.gov/search-results/page/6?indexCatalogue=searchresultsindex&searchQuery=March+2016+report&wordsMode=0), the Commission expressed persistent concerns regarding the fee schedule and nature of fee-for-service payments, which result in the undervaluation of primary care and the overvaluation of specialist practitioners, a recurring theme in MedPAC reports for many years. First, the Commission expressed concern that the resource-based relative value scale, which forms the basis for physician fee schedules, included mispriced services that resulted in an income divergence between primary care physicians and specialists. Second, members stated that fee-for-service payments allowed certain specialties to more readily boost the quantity of services provided (resulting in increased Medicare reimbursements), while MedPAC argued that other specialists had a more limited ability to increase the quantity of services. Using data from the Medical Group Management Association Physician Compensation and Production Survey of 2014, (http://www.mgma.com/Libraries/Assets/Key-Findings-PhysComp_FINAL-with-copyright.pdf), MedPAC found that average compensation was substantially higher for some specialties compared with others, with compensation for nonsurgical procedures and radiology being more than twice the average for that of the primary care physicians. MedPAC argued that these disparities persisted when reimbursement was examined on an hourly basis, accounting for variation in work hours per week. They also persisted when compensation was simulated as if all services the physicians provided were paid under the CMS fee schedule, suggesting that an important source of compensation disparity among primary care and specialist physicians was the fee schedule itself, not specialty-specific variation in payers.

MedPAC seeks to validate the RVUs of fee schedules to correct inaccuracies and curtail overcompensation for physicians at the higher end of the compensation scale. In addition, MedPAC has made recommendations for a per-beneficiary payment system for primary care, replacing the expiring Primary Care Incentive Payment Program, in an attempt to shift Medicare spending to primary care from procedural services. Per-beneficiary payments would be funded by reducing fees for all services within the fee schedule other than Primary Care Incentive Payment Program–defined primary care services, in a budget-neutral model, helping to rebalance the fee schedule toward greater payment equity between primary care and specialist services.

Imaging 3.0. Imaging 3.0 is a compilation of strategies and practical measures developed and put forth by the American College of Radiology (ACR) to help move radiology practices forward successfully, charting a course through the unique challenges and opportunities of our evolving health care system. It seeks to optimize the patient encounter, referring physician collaboration, value proposition, physician administration relations, financial management, and leadership in the professional, social, and political realms. The Medicare Access and Children's Health Insurance Program Reauthorization Act (MACRA) is one way in which physicians in general and radiologists in particular can take part in the financial management aspects of Imaging 3.0, and it will be discussed in more detail next.

MACRA. The Medicare Access and Children's Health Insurance Program Reauthorization Act of 2015 represents the new overarching vision of the US Department of Health and Human Services regarding health care in the United States, focusing on "better care, smarter spending, and healthier people."[12] MACRA seeks to achieve these goals by changing how health care is delivered to bolster value and quality over quantity and through encouraging more efficient clinical decision-making.[13] In April 2016, CMS released a detailed regulatory framework for implementing MACRA via the Quality Payment Program. The Quality Payment Program essentially requires that Medicare Part B payments be distributed via either advanced alternative payment models or the Merit-Based Incentive Payment System (MIPS, Table 2).[13,14]

The MIPS is a modified fee-for-service payment model brought under the quality umbrella by consolidating current federal performance programs, such as the PQRS noted above, the value-based payment modifier, and the practical use of an approved electronic medical record system and merging them with the Clinical Practice Improvement Activities. Detailed feedback on this proposal has been proffered by the ACR, Society of Interventional Radiology, and American Society of Neuroradiology, to name a few. Because a large proportion of eligible clinicians, including radiologists, will initially fall into the MIPS domain under the proposed Quality Payment Program structure, the MIPS will be discussed first.

Eligible clinician payment adjustments will be determined by the following provisions set forth in the MIPS component of the Quality Payment Program, receiving a composite performance score that reflects a combined weighting across 4 categories: 1) quality (replacing PQRS), 2) patient care information advancement (reflecting use of technologies such as an electronic medical record), 3) Clinical Practice Improvement Activities, and 4) cost.[14] Payment adjustment under MIPS will be based on an initial performance period starting in 2017, and MACRA will begin to impact physicians' Medicare Part B reimbursements in 2019. The initial weightings for 2019 for the 4 categories discussed above will be 50% for quality, 25% for Advancing Care Information, 15% for Clinical Practice Improvement Activities, and 10% for resource use. MIPS-eligible clinicians' Medicare Part B reimbursements are slated for 2019 for an upward or downward adjustment of 4%, based on performance measured in 2017, given

Table 2: Quality Payment Program—basic breakdown of MACRA

	MIPS	AAPM
Definition	Merit-Based Incentive Payment System	Advanced Alternative Payment Model
Payment adjustment components	Quality (replaces PQRS) Advancing care information required (eg, use of EMR) Implementing CPIAs is required Measures of cost	Quality measures like MIPS Otherwise, varies on the basis of APM model (eg, BPCI, Next Generation Accountable Care Organization Model, and so forth)
Basic inclusion requirements	Fail to meet the 3 requirements to be in an AAPM (see cell to the right)	Use of approved EMR Base reimbursement on quality measures like MIPS Required to bear "more than nominal" financial risk
Benefits/penalties	Upward or downward adjustment of 4%, based on performance measured in 2017 Percentage adjustment increases each year, reaching a maximum of ±9% in 2022 Increase in fee schedule conversion factor used to calculate Medicare Part B payments of 0.25% per year	QPs not subject to budget-neutral payment/adjustment Automatic 5% bonus payment based on aggregate Medicare Part B payments during the first 6 years Beginning in 2026, 3-fold increase for QPs in their fee schedule conversion factor used to calculate Medicare Part B payment of 0.75% per year for QPs
Effective date (begins impacting physicians' Medicare Part B reimbursements)	2019	2019

Note:—AAPM indicates Advanced Alternate Payment Model; BPCI, Bundled Payments for Care Improvement Initiative; EMR, electronic medical record; CPIA, Clinical Practice Improvement Activities; QP, Qualifying Participant.

the CMS proposed 2-year interval between performance measurement and payment adjustment. This percentage adjustment increases each year, reaching a maximum of ±9% in 2022, resulting in a potential huge payment differential of 18%. Positive or negative adjustments under MIPS will be based on a composite performance score with budget neutrality across the entire physician fee schedule, resulting in a portion of poor performers' reimbursements being redistributed to high performers.[14]

MIPS performance measures for radiologists according to the ruling of the CMS mirror PQRS measures as noted above and include the following: fluoroscopy exposure time; improper use of "probably benign" classification in mammogram screening reports; comparison with prior imaging studies for all patients in whom bone scintigraphy is performed; measuring the degree of stenosis in carotid imaging reports; a reminder system for screening mammography; use of a standardized nomenclature for CT; keeping a running tally of potential high-dose radiation imaging studies, specifically CT and nuclear medicine cardiac studies; using a radiation dose index registry; access to prior CT images for patient follow-up and comparison; follow-up CT for incidental pulmonary nodules per recommended guidelines; imaging follow-up of incidental abdominal lesions; imaging follow-up of incidental thyroid nodules; and use of dose-minimizing techniques for adult CT.[12]

Regarding MIPS performance measures, it seems logical that appropriate provisions for special consideration under the MIPS path need to be in place for clinicians with infrequent face-to-face patient encounters, such as radiologists, by reweighing MIPS performance categories to account for the unique circumstances facing these providers.[15] The CMS previously proposed granting special consideration to physicians with no more than 25 patient-facing encounters in a billing cycle. This proposed criterion would result in a large fraction of radiologists being evaluated on the basis of measures not reflective of their practice and beyond their direct control. The ACR, the American Society of Neuroradiology (ASNR), and the Society of Interventional Radiology have recommended that the language "nonpatient facing" not be used to describe MIPS-eligible clinicians and have recommended alternative criteria and thresholds for when clinicians could receive special consideration. Second, it was proposed that the definition of "patient-facing encounters" be related solely to codes applying to office and outpatient visits at the exclusion of all codes for surgical procedures, given that radiologists commonly perform a diverse range of interventions (surgical procedures) such as thoracenteses, paracenteses, and biopsies, without seeing the patient in consultation before or after the procedure or maintaining a separate clinic to provide associated patient management.

The Health and Human Services Secretary is required by MACRA legislation to use Qualified Clinical Data Registries (QCDR) to ensure compliance with MIPS. QCDR is a CMS-approved construct that allows the tracking of patients and disease via the collection of medical/clinical data, thereby fostering enhancement in the quality of care provided to patients.[16] The National Radiology Data Registries of the American College of Radiology have successfully received QCDR status, along with many other specialty societies. QCDR allows members of these societies the option of using specialty-specific data to comply with MIPS in a system that complies with all 4 MIPS performance categories discussed above. Using QCDR, physicians are reporting data reflective of quality of service as selected by peers, which will result in more consistent feedback, likely in the form of benchmark reports issued by the specialty society registry. QCDR reporting is favored by MACRA for both the freedom it provides to specialties and the voluminous amount of data it generates for CMS. In addition, QCDR can be used in its current form as a means to comply with PQRS.

The Advanced Alternative Payment Model (AAPM or just APM) is, by definition, any new approach to reimbursement for medical care that incentivizes higher value and quality while being exempt from the MIPS reporting requirements. The legislation lays out 3 strict criteria that an advanced APM must fulfill for its participants to attain MIPS-exempt status and receive the full benefit of participating in an APM.[13] These CMS-designated

APMs must do the following: 1) require the use of approved electronic medical record technology, 2) base reimbursement on quality measures comparable/similar to those in the MIPS quality performance category, and 3) require the participating entity to bear "more than nominal" risk financially under the Centers for Medicare and Medicaid Innovation authority. In addition, any individual clinicians who receive a certain percentage of either their Medicare Part B payments or covered Medicare beneficiaries through an APM are deemed APM-qualifying participants. In 2019, these percentages start at 25% of payments or 20% of patients and will increase in subsequent years. Participants who fulfill a lower percentage (20% payments/10% patients) are deemed a partial qualifying participant. Participants in an APM who do not meet the 3 requirements for being an APM are deemed MIPS-eligible clinicians.

MACRA provides greater overall benefits for full qualifying participants in an APM because they are exempt from MIPS participation altogether.[12] For example, qualifying participants are not subject to the budget-neutral positive or negative payment adjustments to which MIPS-participating clinicians are subject. Instead, the APM entity earns an automatic 5% bonus payment based on aggregate Medicare Part B payments during the first 6 years of the program implementation (2019–2024), regardless of the actual achievement on the APM performance measures or actual realized savings. This 5% bonus payment only partially offsets losses that an APM may incur, given the required substantial (more than nominal) financial risk, losses that have been defined by regulators to be up to 4% of total APM Part A and Part B expenditures over expected expenditures. Subsequently, beginning in 2026, qualifying participants will benefit from a 3-fold increase in the annual update to the conversion factor used to calculate Medicare Part B payments, amounting to 0.75% per year for qualifying participants, compared with an increase of only 0.25% per year for MIPS-participating clinicians. These differences are expected to encourage a growing number of clinicians to participate in APMs as opposed to MIPS.

Level 5: Valuation/Revaluation of CPT Codes—ACR and American Medical Association Roles

CPT Development Process. The process for the development of new and revised CPT codes begins with any individual qualified health professional seeing the need for a new code or updates to an existing code, such as a radiologist in the case of radiology-relevant codes.[17] The qualified health professional then submits a coding request form to the American Medical Association (AMA), which then reviews the proposed changes. The AMA staff then submits a request to the AMA CPT Advisory Committee, who reviews the request and presents it to the AMA CPT Editorial Panel, which convenes 3 times per year. The CPT Panel reviews the request and either approves, postpones, or rejects the proposal to add or revise the code. Finally, if the code is approved for a category I, the CPT Panel refers the code addition or change to the American Medical Association Specialty Society Relative Value Scale Update Committee (RUC) for valuation.

CPT Editorial Panel and CPT Advisory Committee. The AMA CPT Editorial Panel provides CPT review with physician input and is the forum for the development of new and revised CPT codes and ironing out problems related to code set maintenance.[18] It comprises representatives from physicians, nonphysician health care providers, payers, the American Hospital Association, CMS, and some of the major insurance companies. The panel convenes thrice yearly to evaluate all code change proposals that are brought before the panel.

The AMA CPT Advisory Committee is the group that grants medical societies the opportunity to provide input into the CPT editorial process.[18] The committee is quite large and comprises representatives of all national medical specialty societies that have seats in the AMA House of Delegates. It also comprises organizations representing limited-license professionals and other allied health care practitioners, such as the Health Care Provider Advisory Committee. The responsibilities of the CPT advisors include serving as a resource to the CPT Editorial Panel, submitting code-change proposals, and evaluating proposals forwarded by other groups that relate to the scope of practice of their specialty, whether submitted by individuals, vendors, payers, or others. The CPT advisors also produce supporting clinical documentation for new procedures and services being considered for new codes. They also promote and educate their societal members on the benefits and practical utility of CPT. Similar to the RUC, these society advisors work in cooperation with a plethora of staff provided by their respective organizations.

American Medical Association/Specialty Society Resource-Based Relative Value Scale Update Committee. The American Medical Association/Specialty Society Resource-Based Relative Value Scale Update Committee, also known as the RUC, is an expert multispecialty consensus panel formed by 31 physicians from multiple medical specialties and societies, including radiology. The AMA Board of Trustees chooses the RUC chairperson and the AMA representative to the RUC.[19] Specialty societies nominate individual members of the RUC who then must be approved by the AMA. The group, which first met in May 1991, is tasked with ongoing review of the accuracy and relevance of the resource-based relative value scale and determining the rank-order placement of newly introduced procedures into the system.[2,11] The CMS accepts the recommendations from the RUC more than 90% of the time, and per CMS, those changes must be made in an environment of budget neutrality. Therefore, if the RUC makes a recommendation to increase the RVUs for a particular service, the RVUs of all other services must be proportionately decreased. This potentially inimical situation is tempered by the frequent need for cooperation between societies to advance codes together in a setting of shifting alliances. Voting members of the RUC are barred from advocating for code valuations presented by the societies they represent and must sit on the committee as impartial judges of valuation. Such checks and balances function to dampen any intersocietal conflict that might arise.

The RUC meets 3 times per year to hear recommendations from advisors from >100 medical specialty societies regarding their assessment of the relative value of procedures performed by its members. As noted above, radiology holds a seat on the committee, with other imaging-related societies in regular attendance including the ASNR, the Society of Interventional Radiology, and the Society of Nuclear Medicine. The ASNR, in particular, con-

tinues to be currently represented at RUC committee meetings by RUC and CPT advisors. The representatives of these societies have forged a close working relationship across the years, despite occasional turnover in personnel.

Relativity Assessment Workgroup. A vital process explicit in the charter of the RUC was the review of the entire Resource-Based Relative Value Scale every 5 years. After the third such review in 2007, the CMS requested an ongoing review process via the "Five-Year Review Committee," which was subsequently renamed the "Relativity Assessment Workgroup."[20] This workgroup was tasked with reviewing potentially misvalued codes based on several screening criteria, including CPT codes missing a verifiable data trail, codes demonstrating increasing use, change in the physician specialty reporting the code, or change in the site of service. Another screen used by the Relativity Assessment Workgroup is for "codes performed together," which is particularly relevant to radiology as mentioned in the code bundling section above. CPT codes, which are typically reported together on a single Medicare patient on the same day of service (eg, CT abdomen and CT pelvis) may have efficiencies that should be accounted for when determining overall relative value. As alluded to in the code bundling section above, this screen has expanded in significance and scope with time, initially triggered when codes were reported together 95% of the time and now triggered when reported together 50% of the time.

The effort of the Relativity Assessment Workgroup in devising its own screening processes for potentially misvalued codes has been well-received by CMS and has frequently targeted radiology, given the high technical component costs of advanced imaging. The various specialty societies are mandated to respond to the Relativity Assessment Workgroup or CMS screening inquiry and to devise a strategy for verifying appropriate valuation of both the technical and professional components of procedures. Once a code is identified in a screen as being potentially misvalued, specialty societies with a stake in establishing an RVU for the procedure are given the opportunity to submit evidence that the code values flagged by the screen are valued appropriately and should remain unaltered or that confounding factors would trigger downstream consequences if the code or code family is revalued. If the evidence fails to convince the Relativity Assessment Workgroup or CMS, there is either a revaluing of the service via survey or revision of the CPT nomenclature or code structure. More often, this is in the form of code bundling.

National Correct Coding Initiative. The National Correct Coding Initiative, which is the CMS counterpart to the Relativity Assessment Workgroup, also reviews codes for possible misuse.[21] It was the National Correct Coding Initiative that identified 2 procedures, plain-film myelography and contrast-enhanced spinal CT as discussed above, requesting clarification from the AMA. The CMS was concerned that these concurrent procedures were potentially unnecessary and duplicative. After receiving detailed clarification from the ASNR that these are distinct procedures, the National Correct Coding Initiative put forth a recommendation that modifier 59 (Distinct Procedural Service) be appended to the CPT codes if the CT examination is performed following myelography on the same day on the same patient. Basically, modifier 59 identifies and clarifies procedures that might be mistaken as duplicative.

The RUC Process. The CPT code valuation process begins with the AMA RUC notifying member societies of the new/revised code after receiving the proposed changes from the CPT Panel.[17] The sponsoring society (eg, the ASNR) and other interested societies conduct a survey regarding the new code and subsequently present the survey results and recommendations to the RUC. The RUC then either refers the recommended values to CMS for consideration or defers its decision to the next meeting, at which time they will resurvey or further examine the valuation after the ACR gathers additional information to support the code valuation.

Role of the ASNR. Largely due to the initial effort of neuroradiologist J. Arliss Pollock, MD, in the early 1990s, as well as the subsequent effort of other neuroradiologists, the ASNR has enjoyed an active role in the sphere of socioeconomic policy, including active participation in both the CPT and RUC processes across the years.[11] Examples include the introduction of numerous new procedures including intraoperative MR imaging in 2003; kyphoplasty, intracranial angioplasty and stent placement, and carotid stent placement in 2005; and functional MR imaging in 2006. Moving these new technologies through CPT validation and RUC review required the collaboration of ASNR advisors and staff on multiple levels, including the synthesis of relevant research studies demonstrating effectiveness; gathering information to assess actual PW involved for each procedure to formulate reasonable RVU values; and finally, the presentation of the data and proposals to the CPT Panel and the RUC.[11]

The CMS Process. CMS then reviews the valuation recommendations from the RUC and releases a new CMS Medicare Physician Fee Schedule with proposed values.[17] After these values are given a period of public comment, CMS publishes the Medicare Physician Fee Schedule with the final values for the subsequent calendar year. Last, there is a public comment period for the final values. See the Figure for an overview of the CPT code-development process.

Code Bundling Revisited: Unintended Consequences. Various medical societies are keenly aware of the downstream effects that CPT code revisions and code bundling have had on their respective communities, including radiologic societies. Code bundling results in both revisions in Medicare payments and renegotiation of private insurance contracts, and these revisions are not always favorable.[20] For example, a new bundled service may fail to fully capture how a service is performed in the radiologic community, given the lack of procedural component parts reflected in the parent codes. The less detailed bundled code may lead to unintended inequities and confusion as to the reported cost of performing the procedure. One case in point was a multiyear project to bundle conscious sedation and anesthesia services into a base procedure, such as an interventional radiology procedure in which the physician performing the procedure typically performs the sedation. The CMS and RUC concluded that if such conscious sedation is typical, then it should not be billed separately and should be bundled into the base code being billed by the physician performing the procedure; this conclusion makes it extremely

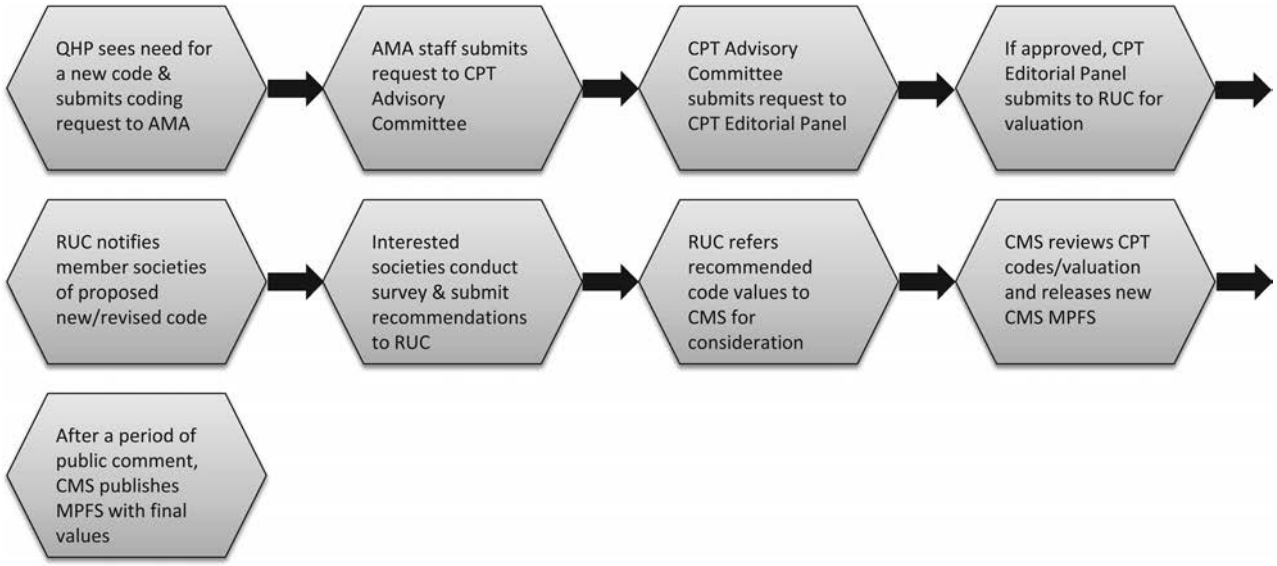

FIGURE. Overview of the CPT code development process. MPFS indicates Medicare Physician Fee Schedule; QHP, qualified healthcare professionals.

difficult to bill anesthesia services or conscious sedation in atypical circumstances or when an anesthesiologist is required. This led to confusion and payment inequities, which ultimately resulted in a new multiyear project of unbundling conscious sedation and anesthesia services from all previous base codes.

Ongoing Advocacy of the ACR on Behalf of Practicing Radiologists. The ACR has worked in support of the profession and patients through ongoing advocacy before Congress, federal agencies, state legislatures, and regulatory bodies.[22,23] It has obtained coverage for lung cancer screening CT for patients and providers; repealed the Sustainable Growth Rate Formula of Medicare; reduced the Multiple Procedure Payment Reduction by 80%, cutting it from 25% to 5%; retained women's annual mammography screening coverage beginning at age 40; supported funding for advanced radiologic science by supporting Congress-passed legislation to increase the National Institutes of Health budget for the National Institute for Biomedical Imaging and Bioengineering; and worked to establish coverage for CT colonography, to name a few items.

CONCLUSIONS

Health care economics as it applies practically to radiologists is complex, with relatively fragmented dissemination in the current medical literature. Therefore, we have presented a tailored discussion in the form of a study guide for fellows to learn and gain competence with respect to the ACGME neuroradiology milestones on health care economics. While this article is targeted to neuroradiology fellows, it can be useful for others in the radiologic sciences and medicine as a whole. While not meant to be exhaustive, our aim is for this review article to serve as a basic foundation on which diagnostic radiology residents, imaging subspecialty fellows, practicing radiologists, and other medical and allied health care professionals can build, facilitating their implementation in real-world radiology/clinical practice.

Because health care economics is a constantly evolving entity, the following Web sites are provided as resources to follow some of the latest changes in the health care economics landscape.

CPT information: https://www.ama-assn.org/practice-management/cpt-current-procedural-terminology; https://www.ama-assn.org/practice-management/explore-recent-cpt-code-changes-actions.

MACRA MIPS information: https://www.acr.org/Quality-Safety/Resources/MACRA-Resources.

Medicare information: https://www.cms.gov/Medicare/Medicare.html.

RUC information: https://www.ama-assn.org/about-us/ruc.

REFERENCES

1. The Accreditation Council for Graduate Medical Education and The American Board of Radiology. The neuroradiology milestone project. Updated 2015. https://www.acgme.org/Portals/0/PDFs/Milestones/NeuroradiologyMilestones.pdf. Accessed April 30, 2017
2. Baadh A, Peterkin Y, Wegener M, et al. **The relative value unit: history, current use, and controversies.** *Curr Probl Diagn Radiol* 2016;45:128–32 CrossRef Medline
3. Petrey WB, Allen B Jr, Thorwarth WT Jr, et al. **Radiology coding, reimbursement, and economics: a practical playbook for housestaff.** *J Am Coll Radiol* 2009;6:643–48 CrossRef Medline
4. Centers for Medicare and Medicaid Services. Proposed policy, payment, and quality provisions changes to the Medicare physician fee schedule for calendar year (CY) 2017. Updated 2016. http://www.cms.gov/Newsroom/MediaReleaseDatabase/Fact-sheets/2016-Fact-sheets-items/2016-07-07-2.html. Accessed June 14, 2017
5. Centers for Medicare and Medicaid Services. PFS relative value files. Updated 2016. https://www.cms.gov/medicare/medicare-fee-for-service-payment/physicianfeesched/pfs-relative-value-files.html. Accessed May 16, 2017
6. Centers for Medicare and Medicaid Services. Physician fee schedule search. Updated 2016. https://www.cms.gov/apps/physician-fee-schedule/search/search-criteria.aspx. Accessed May 16, 2017
7. Gupta D, Karst I, Mendelson EB. **Value-based reimbursement: impact of curtailing physician autonomy in medical decision making.** *AJR Am J Roentgenol* 2016;206:276–79 CrossRef Medline
8. Centers for Medicare and Medicaid Services. 2013 clinical quality measures. Updated 2015. https://www.cms.gov/Regulations-and-

Guidance/Legislation/EHRIncentivePrograms/cqm_through_2013.html. Accessed May 16, 2017
9. Centers for Medicare and Medicaid Services. 2014 clinical quality measures. Updated 2015. https://www.cms.gov/Regulations-and-Guidance/Legislation/EHRIncentivePrograms/2014_ClinicalQualityMeasures.html. Accessed May 16, 2017
10. American College of Radiology. Qualified clinical data registry (QCDR) PQRS measures supported 2016. Updated 2016. https://www.acr.org/~/media/ACR/Documents/PDF/QualitySafety/NRDR/QCDR/ACR%20QCDR%20Measures%20Supported%202016_PQRS.pdf. Accessed March 18, 2017
11. Donovan WD. **The resource-based relative value scale and neuroradiology: ASNR's history at the RUC.** *Neuroimaging Clin N Am* 2012;22:421–36 CrossRef Medline
12. Department of Health and Human Services. Center for Medicare & Medicaid Services. Federal Register 81:28161–6. 42 CFR Parts 414 and 495. Medicare program; Merit-Based Incentive Payment System (MIPS) and Alternative Payment Model (APM) incentive under the physician fee schedule, and criteria for physician focused payment models. Updated 2016. https://www.gpo.gov/fdsys/pkg/FR-2016-05-09/pdf/2016-10032.pdf. Accessed March 7, 2017
13. Rosenkrantz AB, Nicola GN, Allen B Jr, et al. **MACRA, alternative payment models, and the physician-focused payment model: implications for radiology.** *J Am Coll Radiol* 2017;14:744–51 CrossRef Medline
14. Rosenkrantz AB, Nicola GN, Allen B, et al. **MACRA, MIPS, and the new Medicare quality payment program: an update for radiologists.** *J Am Coll Radiol* 2017;14:316–23 CrossRef Medline
15. Rosenkrantz AB, Hirsch JA, Allen B, et al. **The proposed MACRA/MIPS threshold for patient-facing encounters: what it means for radiologists.** *J Am Coll Radiol* 2017;14:308–15 CrossRef Medline
16. Hirsch JA, Leslie-Mazwi TM, Patel AB, et al. **MACRA: background, opportunities and challenges for the neurointerventional specialist.** *J Neurointerv Surg* 2016;8:868–74 CrossRef Medline
17. American College of Radiology. CPT code development process flowchart. https://www.acr.org/~/media/ACR/Documents/PDF/Economics/CPT-Code-Development-Process-Flow81415.pdf. Accessed March 14, 2017
18. Hirsch JA, Leslie-Mazwi TM, Nicola GN, et al. **Current procedural terminology; a primer.** *J Neurointerv Surg* 2015;7:309–12 CrossRef Medline
19. The American Medical Association. Composition of the RVS update committee (RUC). https://www.ama-assn.org/about-us/composition-rvs-update-committee-ruc. Accessed June 14, 2017
20. Leslie Mazwi TM, Bello JA, Tu R, et al. **Current procedural terminology: history, structure, and relationship to valuation for the neuroradiologist.** *AJNR Am J Neuroradiol* 2016 Jul 14. [Epub ahead of print] CrossRef Medline
21. Chokshi FH, Tu RK, Nicola GN, et al. **Myelography CPT coding updates: effects of 4 new codes and unintended consequences.** *AJNR Am J Neuroradiol* 2016;37:997–99 CrossRef Medline
22. American College of Radiology. Recent ACR achievements on behalf of radiology. https://www.acr.org/Membership/Membership-Services/Member-Benefits/What-Does. Accessed March 14, 2017
23. American College of Radiology. Advocacy. https://www.acr.org/Advocacy. Accessed March 14, 2017

Influences for Gender Disparity in Academic Neuroradiology

M. Ahmadi, K. Khurshid, P.C. Sanelli, S. Jalal, T. Chahal, A. Norbash, S. Nicolaou, M. Castillo, and F. Khosa

ABSTRACT

BACKGROUND AND PURPOSE: There has been extensive interest in promoting gender equality within radiology, a predominately male field. In this study, our aim was to quantify gender representation in neuroradiology faculty rankings and determine any related factors that may contribute to any such disparity.

MATERIALS AND METHODS: We evaluated the academic and administrative faculty members of neuroradiology divisions for all on-line listed programs in the US and Canada. After excluding programs that did not fulfill our selection criteria, we generated a short list of 85 US and 8 Canadian programs. We found 465 faculty members who met the inclusion criteria for our study. We used Elsevier's SCOPUS for gathering the data pertaining to the publications, H-index, citations, and tenure of the productivity of each faculty member.

RESULTS: Gender disparity was insignificant when analyzing academic ranks. There are more men working in neuroimaging relative to women ($\chi^2 = 0.46$; $P = .79$). However, gender disparity was highly significant for leadership positions in neuroradiology ($\chi^2 = 6.76$; $P = .009$). The median H-index was higher among male faculty members (17.5) versus female faculty members (9). Female faculty members have odds of 0.84 compared with male faculty members of having a higher H-index, adjusting for publications, citations, academic ranks, leadership ranks, and interaction between gender and publications and gender and citations (9).

CONCLUSIONS: Neuroradiology faculty members follow the same male predominance seen in many other specialties of medicine. In this study, issues such as mentoring, role models, opportunities to engage in leadership/research activities, funding opportunities, and mindfulness regarding research productivity are explored.

Gender disparity among medical students, residents, physicians, and faculty members is widespread, and several reports show an underrepresentation of women in academic medicine.[1-6] It is interesting to note that in North America (US and Canada), female physicians have been shown to be equally likely as men to pursue a career in academic medicine.[5] Despite the similar amount of prospective interest in academics, the proportion of women who successfully advance to the rank of professor is significantly lower.[7,8] Women who occupy faculty positions are also more likely to leave academics for community or hospital practices.[9] This has been explained in part by a lack of adequate mentorship and the inability of women to be promoted at the same pace and on the same timeline as men. These factors contribute to the relative lack of female leaders in academic medicine.

Although there is gender parity for medical students and residents in the North America, when analyzing faculty members of medical institutions, female physicians only constitute 38% of faculty rosters.[1,3] When examining senior academic administration, the gender disparity increases even further. In the US, women account for only 21% of full professors, 16% of medical school deans, and 15% of department chairs.[1,3] The only academic rank in which women outnumber men in the US is the clinical instructor level.[1]

This is a concern because increased diversity allows for a more creative, productive, egalitarian, and innovative environment. A lack of gender parity within faculty rankings may specifically also adversely affect initiatives, collaborations, and research efforts where women's health is concerned. The described gender disparity also leads to a lack of female faculty members serving as mentors and role models. Medical students and those interested in

Received June 18, 2017; accepted after revision August 8.

From the Department of Emergency & Trauma Radiology (M.A., K.K., S.J., S.N., F.K.), Vancouver General Hospital, Vancouver, British Columbia, Canada; Faculty of Medicine (T.C.), University of British Columbia, Vancouver, British Columbia, Canada; Department of Radiology (P.C.S.), Northwell Health, Manhasset, New York; Department of Radiology (A.N.) University of California, San Diego, San Diego, California; and Department of Radiology (M.C.), University of North Carolina School of Medicine, Chapel Hill, North Carolina.

Please address correspondence to Faisal Khosa, MD, MBA, FFRRCSI, FRCPC, DABR, 3350–950 W 10th Avenue, Vancouver, BC, Canada V5Z 1M9; e-mail: fkhosa@gmail.com

http://dx.doi.org/10.3174/ajnr.A5443

pursuing medicine look to mentors for encouragement and inspiration.[10-12] The lack of strong corrective actions regarding gender disparities within academic medicine over the past decade suggests the need for active intervention.[1,3,10,11] An improved understanding of gender disparities in academic medicine would allow solutions to be formulated and implemented.

Previous research in anesthesia, gastroenterology, ophthalmology, otolaryngology, plastic surgery, and general surgery highlight gender disparities favoring men in relation to factors such as research productivity, income, leadership, and faculty promotion.[13-19] Not surprisingly, previous studies have also shown a similar male predominance in radiology.[20-22]

Radiology has men overrepresented in residency programs, academic departments, and private practice groups.[21] Prior reports show that in the US, women occupy 27% of the radiology residency positions.[23] When investigating contributory reasons, surveys of medical students have shown a lack of exposure early in their training, a lack of role models, and the apparent lack of patient contact as major deterrents for women considering radiology as a career choice.[24-26]

Prior reports have shown that women across the US are underrepresented in radiology senior faculty positions.[20,22] A study of female representation in radiology subspecialties such as neuroradiology has not been published in the literature. Our aim was to quantify the gender imbalance of neuroradiology faculty rankings and related or explanatory factors that may contribute to such a disparity. Our hope is our findings will help initiate additional research, and ultimately interventions, in both neuroradiology and the larger academic medical community.

MATERIALS AND METHODS

We tabulated the gender of academic and administrative faculty members in the neuroradiology divisions of all the programs across the US and Canada. First, we created a list of all diagnostic radiology programs in North America (Canada and US) by using the Web site of the Fellowship & Residency Electronic Interactive Database, or FREIDA, which provides a list of 227 Accreditation Council for Graduate Medical Education–accredited diagnostic radiology programs of the American Medical Association. For the diagnostic radiology programs in Canada, we referred to the Canadian Resident Matching Service Web site, which provided a total of 16 programs. Using these Web sites, we compiled the list of diagnostic radiology programs that included their faculty rosters on their individual Web sites. We excluded programs that did not include faculty rosters and those that had rosters but did not provide any information regarding administrative or faculty rank. We then filtered the remaining programs to specifically identify neuroradiology programs. After applying these selection criteria, we evaluated 85 US and 8 Canadian programs. Data collection started in July 2016 and included reviewing selected programs' Web sites for their faculty rosters and individual faculty. Inclusion criteria were full-time faculty members with the academic rank of professor, associate professor, or assistant professor with MD degrees and a listing on the affiliated university Web site. Faculty with departmental leadership roles such as chair, vice chair, program director, and associate and assistant program directors were included. Faculty not having stated academic ranks were excluded. Exclusion criteria were also applied to adjunct, emeritus, and retired faculty as well as faculty who did not have an MD degree or whose gender could not be ascertained. We used Elsevier's SCOPUS to determine the individual faculty member's publications, H-index, citations, and productivity. SCOPUS was chosen because it is a robust and reliable tool for measuring the H-index compared with Google Scholar and Web of Science.

RESULTS

We found 465 faculty members who met the inclusion criteria of our study. Among them, 76.9% (358/465) were men and 23.01% (107/465) were women. Most of them (87.3% [406/465]) were from the US, and 12.69% (59/465) were from Canada (Table 1). Faculty academic ranks were available for 447. Among them, 50.34% (225/447) were assistant professors, 27.74% (124/447) were associate professors, and 21.92% (98/447) were professors. Of the assistant professors, 75.11% (169/255) were men, whereas 24.89% (56/255) were women. Among associate professors, 76.61% (95/124) were men, whereas only 23.39% (29/124) were women. Last, among the professors, 78.57% (77/98) were men; however, 21.43% (21/98) were women. Of the 72 faculty serving in leadership positions, 84.7% (61/72) were men, and 15.28% (11/72) were women. Of those in the higher leadership ranks, 91.8% (56/61) were men, and only 8.2% (5/61) were women. In lower leadership ranks (eg, co-chair, deputy director), 63.6% were men (7/11), and 36.36% were women (4/11).

Data for citations, publication, and H-index did not follow a conventional or balanced distribution. For that reason, medians, ranges, and nonparametric tests were carried out. To calculate regression, all variables were first log-transformed.

In the bivariate analysis, the χ^2 test was used to evaluate the association of gender with academic and leadership rank.

There was a higher number of men (358 [76.9%]) among the neuroradiology faculty compared with women (107; [23.01%]). When considering gender incidence against leadership rank, the gender discrepancy was evidenced as highly significant ($\chi^2 = 6.76$; $P = .009$), with 87.5% of leadership ranks occupied by men compared with 12.5% of leadership ranks occupied with women. The median of time spent in academia among the male faculty was 20 years and was 17 years among the female faculty.

H-index was noted for 360 faculty members. After testing for association of gender with H-index using the Wilcoxon rank sum test, we found an insignificant difference (test statistics = 0.46; $P = .794$) when assessing the 2 genders. Upon applying the Kruskall-Wallis test, there was a significant difference between academic rank H-index (Fig 1) across all academic ranks ($\chi^2 = 113.32$; $P < .001$), with a median male H-index of 17.5 and a median female H-index of 9.

Data were tested for normality. Log-transformation was performed considering the continuous variables of H-index, citations, and the number of publications, which were initially skewed in distribution. At the univariate level, simple linear regression was applied. Each variable was regressed independently considering H-index, the assumptions were assessed, and their significance was reported. Gender relationships were our primary consideration of interest. Variables that both were investigated and were significant on univariate regression included gender,

Table 1: Description of baseline characteristics for neuroimaging faculty in North America

Variables	Men	Women	Total Available Numbers
Total population, no. (%)	358 (76.9)	107 (23.01)	465 (100)
Academic ranks, no. (%)			
Assistant professors	169 (75.11)	56 (24.89)	225 (100)
Associate professors	95 (76.61)	29 (23.39)	124 (100)
Professors	77 (78.57)	21 (21.43)	98 (100)
Leadership, no. (%)			
Heads, chiefs, chairs, and directors	56 (91.8)	5 (8.2)	61 (100)
Second in command: associate chiefs, vice chairs, deputy directors	7 (63.6)	4 (36.36)	11 (100)
Citations	USA	Canada	
Assistant professors	$n = 110$	$n = 29$	$n = 139$
Median	103.5	53	96
Range	0–4935	2–4507	0–4935
Associate professors	$n = 71$	$n = 23$	$n = 94$
Median	292	376	301.5
Range	0–15,039	4–7871	0–15,039
Professors	$n = 61$	$n = 19$	$n = 80$
Median	2065	1081	1745
Range	22–21,708	0–9548	0–21,708
Publications			
Assistant professors	$n = 128$	$n = 34$	$n = 162$
Median	12	12.5	12
Range	1–144	2–245	1–245
Associate professors	$n = 80$	$n = 24$	$n = 104$
Median	23	28.5	23.5
Range	2–349	2–177	2–349
Professors	$n = 70$	$n = 20$	$n = 90$
Median	81.5	55	72
Range	5–460	3–285	3–460

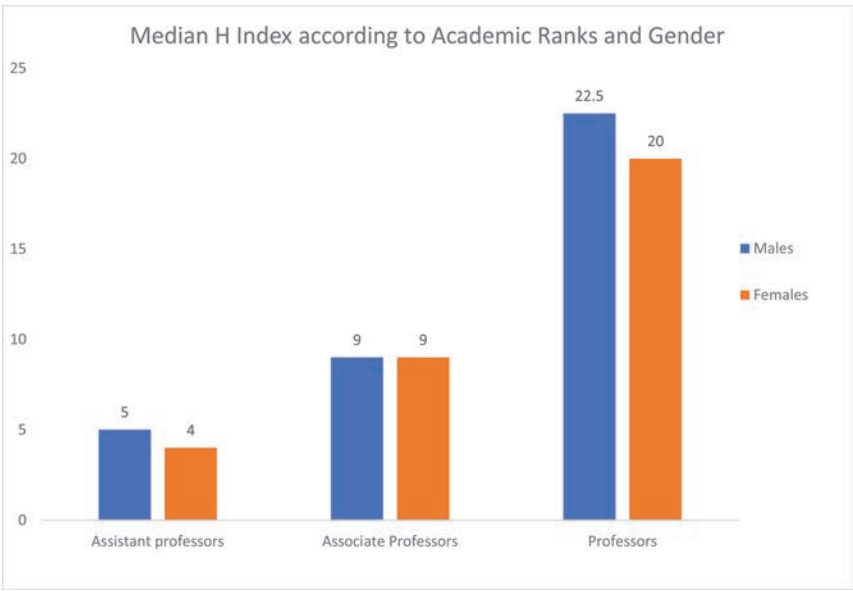

FIG 1. Distribution of median H-index according to academic ranks and gender.

publications, citations, years of active research, academic ranks, and leadership ranks. These variables were selected for inclusion into multivariable linear regression analyses. We checked for multicollinearity between independent variables, which were assessed by using a correlation coefficient. The Cramer V test was used for 1 nominal and 1 ordinal variable; the Spearman test was used for 1 continuous variable and 1 ordinal variable. A correlation of 0.8 was treated as the presence of multicollinearity. There was no multicollinearity seen. Main effects were identified by using a stepwise selection strategy and were based on the *P* value; we decided to either preserve a variable in the model or to drop it. As one example, years of research ($P = .30$) was dropped from the model. The multivariable analysis supported the inclusion of gender, citations, publications, academic rank, and leadership rank in the preliminary model. The final step was to check for interaction effect. Interaction terms were created between each of the main effects in the model; 2 examples include significant interaction between gender and citations and between gender and publications. Academic rank, publications, and citations were not confounders for the H-index.

The final model:

$$y(x) = \beta_0 + \beta_1(\text{Gender}) + \beta_2(\text{Publications}) + \beta_3(\text{Citations}) + \beta_{41}(\text{Academic Rank: Associate Professor}) + \beta_{42}(\text{Academic Rank: Professor}) + \beta_5(\text{Leadership Rank: Second in Command}) + \beta_{61}(\text{Gender} \times \text{Publications}) + \beta_{62}(\text{Gender} \times \text{Citations})$$

Female faculty had odds of 0.84 compared with male faculty, also having a higher H-index when adjusting for publications, citations, academic rank, leadership rank, and interaction between gender and publications and gender and citations. This prediction equation accounted for major variability in the model as adjusted with $R^2 = 0.92$; the *F* test was 57.11, and the *P* value was $\leq .001$. The remaining variability in the model may have been explained by variables such as full-time versus part-time employment, years of employment, and contract versus tenure positions. Examining these additional variables was beyond the scope of our paper, as we used data that were publicly available.

DISCUSSION

Neuroradiology faculty members are predominantly men, similar to the gender imbalance seen in diagnostic radiology and many other specialties in medicine as previously demonstrated.[13-19] Women fill only 25% of assistant professor positions, 23% of associate professor positions, and 21% of professor positions among neuroradiology faculty members analyzed in our study. It may be argued that women only comprise 27% of radiology residents according to 2014 Association of American Medical Colleges data, and a continuation of that fraction through the rising ranks suggests

Table 2: Association of academic hierarchy and leadership roles with gender of faculty

Association of Gender with Academic Rank				Association of Gender with Leadership Rank			
Men, no. (%)	Women, no. (%)	χ^2	*P* value	Men, no. (%)	Women, no. (%)	χ^2	*P* value
341 (76.29)	106 (23.71)	0.46	.79	63 (87.5)	9 (12.5)	6.76	.009

that the 20%–25% range in faculty rankings may be appropriate.[27] Gender disparity was highly significant for leadership positions ($\chi^2 = 6.76$; $P = .009$ [Table 2]).

The reasons for gender disparity in neuroradiology leadership positions are likely multifactorial and warrant examination. Previous studies exploring women in academic medicine have shown unique barriers faced by female physicians throughout their careers.[28] For example, female physicians have been shown to have fewer available same-sex mentors, receive fewer research opportunities, and also encounter greater difficulty in obtaining funding from the National Institutes of Health.[28] Some experts also believe that additional responsibilities such as child care and disproportionate home responsibilities outside of work are gender-specific barriers unique to women.[28] Hofler et al[29] examined these encumbrances and concluded that specialties that allow for more predictable work hours may lead to fewer gender disparities. Others refute these contentions and state that increasing numbers of women are choosing to make personal sacrifices at the expense of advancing their professional lives and careers.[30]

A recent study of women in leadership positions in emergency medicine residency programs by Cheng et al[31] demonstrated that of 133 university emergency medicine programs in the US, 7.5% have a female chair. Compared with other emergency medicine programs in the US overseen by male chairs, programs with female chairs had a higher percentage of female faculty (22% versus 31%). Studies have shown that having an identifiable mentor doubles a physician's chance of being promoted.[32] Mentorship, leadership, and promotion are connected, leading to the contention that female physicians with guidance, role models, and mentors are more likely to be promoted in academic centers.

In terms of satisfaction in regards to mentorship, previous studies have shown that male physicians report higher satisfaction with the mentoring experience than their female counterparts (53% versus 42.5%).[28] The lack of women in leadership positions within neuroradiology is a contributory cause for concern. Without active correction, this lack of female mentors will likely perpetuate the lack of women in academic leadership positions.

In exploring research productivity and citation counts, we assessed the H-index of faculty members to identify the presence of discrepancies between men and women. The H-index is based on the most cited papers of the author, other publications, and the number of citations they have received from other authors.[33] The H-index is widely used to evaluate and compare scholarly efforts and is particularly helpful when assessing impact because it represents not only quantity, but also quality of publications as judged by citability. This information is often used to help with promotion decisions and the allocation of funding resources and is therefore meaningful and important where academic rank promotion potential and leadership promotion are concerned.[33]

We studied the H-index for 360 of the total 465 faculty members, and we discovered that median H-index was higher among male faculty compared with female faculty (17.5 versus 9 [Table 3]). As one measure of potential future academic success, previous studies in *Academic Radiology* have suggested that an H-index of 10 may represent a reliable metric to determine the likelihood of receiving funding from the National Institutes of Health.[34] In our analysis, male faculty members had more citations and publications than women in all academic ranks (Table 1). Upon applying the Kruskall-Wallis test, there was a significant gender-related difference between academic ranks and H-index (Fig 1) across all academic ranks ($\chi^2 = 113.32$; $P \leq .0001$). As noted, female faculty members had fewer total citations compared with men (Table 1).

Table 3: Median H-index according to gender

H-Index	Men	Women
Overall		
Median	9	
Range	1–76	
$n = 360$	281	79
Median	17.5	9
Range	1–76	1–51

The demonstrated difference between academic ranks and H-index suggests the importance of research productivity. This finding also highlights concerns regarding barriers female physicians may face in academic faculty ranks. A recent study assessing radiology faculty demonstrated that men and women were similarly likely to be full professors; however, differences in promotion and research productivity were also present, suggesting that female radiologists may lack equal research opportunities.[35] Our findings suggest that to minimize gender disparities in leadership positions, female physicians will benefit from increased availability of mentors and opportunities for research and funding.

Limitations

One of our study limitations recognizes that we collected our information regarding faculty members from publicly accessible academic department Web sites. It is possible that the information on these Web sites may not have been up to date. One additional limitation is that our methodology represents a snapshot in time. This is important because a female faculty member may have served in a leadership role several years prior, which would not be present on current data, yet would be important for reporting their involvement. We were also unable to determine the H-index for 105 of the total 465 faculty members because of a lack of available information. In addition, we were not able to determine all sought statistics for each faculty member. For example, if we were able to secure career stage, age, and length of time the person has been in his or her current role, that would have allowed us to perform a more detailed analysis. Another variable that we were unable to reliably calculate but could help explain gender disparity in leadership roles is the shortened career duration of women in academic medicine, in many instances because of their choosing to recuse themselves from full-time academic positions as a result of shouldering a disproportionate share of home and child-

care responsibilities. Diamond et al[36] determined that women in their cohort had overall lower research productivity than men, but when they corrected for career duration, this difference was insignificant. Another consideration is that often authors publish under different names. This is important in several scenarios such as when a person, regardless of gender or sexual orientation, changes their name after marriage or divorce, takes their spouse's surname, or creates a hyphenated name; or in the case of a transgender person who may change his or her name. When these name changes are taken into consideration, it shows that the number of publications and H-index for female faculty may be erroneously underestimated. The inclusion or exclusion of middle initials can also contribute to miscalculations of attributable academic productivity.

CONCLUSIONS

Gender disparities exist in neuroradiology, especially where leadership positions are concerned. The gender discrepancies that are observed in this traditionally male-dominated field can be used to better inform the medical community regarding issues related to gender imbalances in academic medicine. We recommend that early mentorship, with ensuing increased directed opportunities and groomed career development of female faculty, could play a key role in helping diversify academic medicine. Many radiology societies have recognized the importance of mentorship and have created programs to help empower and promote women, including the American Association for Women Radiologists and the Women in Radiology branch of the Society of Interventional Radiology. In 2012, the American Society of Neuroradiology, American College of Radiology, and the American Association for Women Radiologists jointly funded the Women in Neuroradiology Leadership Award to support leadership training for female neuroradiologists. Ongoing studies are needed to examine trends over time relating and connecting factors such as mentorship, ranking promotion, academic productivity, and methods to help eliminate the underlying causes of the gender gap. We hope that our work will catalyze and substantiate further directed initiatives that will help female physicians achieve and occupy both senior faculty and leadership positions and help blaze pathways to durable success in leadership careers.

Disclosures: Alexander Norbash—*UNRELATED*: *Board Membership*: Boston Imaging Core Laboratories, *Comments*: co-founder; *Consultancy*: Stryker, IBM, GE Healthcare, *Comments*: scientific consultant. Savvas Nicolaou—*UNRELATED: Consultancy*: Siemens Healthcare, *Comments*: scientific consultant*. *Money paid to the institution.

REFERENCES

1. Association of American Medical Colleges. Women in Academic Medicine. https://www.aamc.org/members/gwims/statistics/. Accessed April 2, 2017
2. Nonnemaker L. **Women physicians in academic medicine: new insights from cohort studies.** *N Engl J Med* 2000;342:399–405 CrossRef Medline
3. Magrane D. **The changing representation of men and women in academic medicine.** *Association of American Medical Colleges: Analysis in Brief* 2005;5:1–2
4. Carr PL, Gunn CM, Kaplan SA, et al. **Inadequate progress for women in academic medicine: findings from the National Faculty Study.** *J Women's Health (Larchmt)* 2015;24:190–99 CrossRef Medline
5. Bickel J. **Women in academic medicine.** *J Am Med Womens Assoc (1972)* 2000;55:10–12, 19 Medline
6. Sidhu R, Rajashekhar P, Lavin VL, et al. **The gender imbalance in academic medicine: a study of female authorship in the United Kingdom.** *J R Soc Med* 2009;102:337–42 CrossRef Medline
7. Reck SJ, Stratman EJ, Vogel C, et al. **Assessment of residents' loss of interest in academic careers and identification of correctable factors.** *Arch Dermatol* 2006;142:855–58 CrossRef Medline
8. Bickel J, Brown AJ. **Generation X: implications for faculty recruitment and development in academic health centers.** *Acad Med* 2005; 80:205–10 CrossRef Medline
9. Alexander H, Lang J. **The long-term retention and attrition of U.S. medical school faculty.** *Association of American Medical Colleges: Analysis in Brief* 2008;8:1–3
10. Forman HP, Larson DB, Kaye AD, et al. **Masters of radiology panel discussion: women in radiology–how can we encourage more women to join the field and become leaders?** *AJR Am J Roentgenol* 2012;198:145–49 CrossRef Medline
11. Anzai Y, Meltzer CC, DeStigter KK, et al. **Entrepreneurial women in radiology: role models of success.** *J Am Coll Radiol* 2016;13:1378–82 CrossRef Medline
12. Levinson W, Kaufman K, Clark B, et al. **Mentors and role models for women in academic medicine.** *West J Med* 1991;154:423–26 Medline
13. Pashkova AA, Svider PF, Chang CY, et al. **Gender disparity among US anaesthesiologists: are women underrepresented in academic ranks and scholarly productivity?** *Acta Anaesthesiol Scand* 2013;57: 1058–64 CrossRef Medline
14. Singh A, Burke CA, Larive B, et al. **Do gender disparities persist in gastroenterology after 10 years of practice?** *Am J Gastroenterol* 2008; 103:1589–95 CrossRef Medline
15. Lopez SA, Svider PF, Misra P, et al. **Gender differences in promotion and scholarly impact: an analysis of 1460 academic ophthalmologists.** *J Surg Educ* 2014;71:851–59 CrossRef Medline
16. Eloy JA, Svider PF, Kovalerchik O, et al. **Gender differences in successful NIH grant funding in otolaryngology.** *Otolaryngol Head Neck Surg* 2013;149:77–83 CrossRef Medline
17. Paik AM, Mady LJ, Villanueva NL, et al. **Research productivity and gender disparities: a look at academic plastic surgery.** *J Surg Educ* 2014;71:593–600 CrossRef Medline
18. Mueller CM, Gaudilliere DK, Kin C, et al. **Gender disparities in scholarly productivity of US academic surgeons.** *J Surg Res* 2016; 203:28–33 CrossRef Medline
19. Wyrzykowski AD, Han E, Pettitt BJ, et al. **A profile of female academic surgeons: training, credentials, and academic success.** *Am Surg* 2006;72:1153–57; discussion 1158–59 Medline
20. Baker SR, Barry M, Chaudhry H, et al. **Women as radiologists: are there barriers to entry and advancement?** *J Am Coll Radiol* 2006;3: 131–34 CrossRef Medline
21. Zener R, Lee SY, Visscher KL, et al. **Women in radiology: exploring the gender disparity.** *J Am Coll Radiol* 2016;13:344–50.e1 CrossRef Medline
22. Vydareny KH, Waldrop SM, Jackson VP, et al. **Career advancement of men and women in academic radiology: is the playing field level?** *Acad Radiol* 2000;7:493–501 CrossRef Medline
23. Bluth EI, Bansal S, Macura KJ, et al. **Gender and the radiology workforce: results of the 2014 ACR workforce survey.** *J Am Coll Radiol* 2015;12:155–57 CrossRef Medline
24. Fielding JR, Major NM, Mullan BF, et al. **Choosing a specialty in medicine: female medical students and radiology.** *AJR Am J Roentgenol* 2007;188:897–900 CrossRef Medline
25. Roubidoux MA, Packer MM, et al. **Female medical students' interest in radiology careers.** *J Am Coll Radiol* 2009;6:246–53 CrossRef Medline
26. Potterton VK, Ruan S, Sunshine JH, et al. **Why don't female medical students choose diagnostic radiology? A review of the current literature.** *J Am Coll Radiol* 2004;1:583–90 CrossRef Medline
27. AAMC 2014 Physician Specialty Databook. https://www.aamc.org/

data/workforce/reports/439208/specialtydataandreports.html. Accessed April 1, 2017
28. Kaplan SH, Sullivan LM, Dukes KA, et al. **Sex differences in academic advancement. Results of a national study of pediatricians.** *N Engl J Med* 1996;335:1282–89 CrossRef Medline
29. Hofler L, Hacker M, Dodge L, et al. **Comparison of women in department leadership in obstetrics and gynecology with those in other specialties.** *Obstet Gynecol* 2016;127:442–47 CrossRef Medline
30. Burke CA, Sastri SV, Jacobsen G, et al. **Gender disparity in the practice of gastroenterology: the first 5 years of a career.** *Am J Gastroenterol* 2005;100:259–64 CrossRef Medline
31. Cheng D, Promes S, Clem K, et al. **Chairperson and faculty gender in academic emergency medicine departments.** *Acad Emerg Med* 2006; 13:904–06 CrossRef Medline
32. Beasley BW, Simon SD, Wright SM. **A time to be promoted. The prospective study of promotion in academia.** *J Gen Intern Med* 2006; 21:123–29 CrossRef Medline
33. Hirsch JE. **An index to quantify an individual's scientific research output.** *Proc Natl Acad Sci U S A* 2005;102:16569–72 CrossRef Medline
34. Rezek I, McDonald RJ, Kallmes DF. **Is the H-index predictive of greater NIH funding success among academic radiologists?** *Acad Radiol* 2011;18:1337–40 CrossRef Medline
35. Kapoor N, Blumenthal DM, Smith SE. **Gender differences in academic rank of radiologists in U.S. medical schools.** *Radiology* 2017; 283:140–47 CrossRef Medline
36. Diamond SJ, Thomas CR Jr, Desai S, et al. **Gender differences in publication productivity, academic rank, and career duration among U.S. academic gastroenterology faculty.** *Acad Med* 2016;91: 1158–63 CrossRef Medline

Deep Brain Nuclei T1 Shortening after Gadobenate Dimeglumine in Children: Influence of Radiation and Chemotherapy

S. Kinner, T.B. Schubert, R.J. Bruce, S.L. Rebsamen, C.A. Diamond, S.B. Reeder, and H.A. Rowley

ABSTRACT

BACKGROUND AND PURPOSE: Intrinsic T1-hyperintense signal has recently been reported in the deep gray nuclei on brain MR imaging after multiple doses of gadolinium-based contrast agents. Most reports have included adult patients and excluded those undergoing radiation or chemotherapy. We investigated whether T1 shortening is also observed in children and tried to determine whether radiochemotherapy is a risk factor for this phenomenon.

MATERIALS AND METHODS: In this single-center retrospective study, we reviewed clinical charts and images of all patients 18 years of age or younger with ≥4 gadobenate dimeglumine–enhanced MRIs for 6 years. Seventy-six children (mean age, 9.3 years; 60 unconfounded by treatment, 16 with radiochemotherapy) met the selection criteria (>4 MR imaging examinations; mean, 8). T1 signal intensity ratios for the dentate to pons and globus pallidus to thalamus were calculated and correlated with number of injections, time interval, and therapy.

RESULTS: Among the 60 children without radiochemotherapy, only 2 had elevated T1 signal intensity ratios ($n = 20$ and 16 injections). Twelve of the 16 children with radiochemotherapy showed elevated signal intensity ratios. Statistical analysis demonstrated a significant signal intensity ratio change for the number of injections ($P < .001$) and amount of gadolinium ($P = .008$), but not for the interscan time interval ($P = .35$). There was a significant difference in the average signal intensity ratio change between those with and without radiochemotherapy ($P < .001$). Chart review revealed no new neurologic deficits in any patients, related to their underlying conditions and prior surgeries.

CONCLUSIONS: Compared with published adult series, children show a similar pattern of T1 hyperintense signal changes of the dentate and globus pallidus after multiple gadobenate dimeglumine injections. The T1 signal changes in children may have a later onset but are accelerated by radiochemotherapy.

ABBREVIATION: RCTX = radiochemotherapy

During the past year, several reports have been published describing the hyperintense appearance of the deep brain nuclei of adult patients on unenhanced T1-weighted MR images. This increased signal intensity occurred in patients with normal renal function who underwent multiple gadolinium-enhanced MR imaging examinations.[1-13] This phenomenon has been evaluated using multiple different gadolinium-based contrast agents, including the linear agents gadodiamide,[1-4] gadobenate dimeglumine,[4,5] and gadopentetate dimeglumine[6-10] as well as the macrocyclic agents gadoterate meglumine[7,11] and gadobutrol.[8,10,12,13] Postmortem studies have demonstrated the presence of gadolinium in these deep nuclei within the brain, confirming that increased signal intensity is likely due to the deposition of gadolinium.[3,14,15] Recent animal studies have also shown this in rats.[16-18]

To date, most of the human studies have involved adult patients, with only 1 adult study including a small group of pediatric patients.[6] Three recent studies analyzed smaller groups of up to 21 children undergoing gadopentetate dimeglumine examinations.[19-21] In addition, 2 case reports described 3 pediatric patients with up to 35 contrast-enhanced MRIs, using gadopentetate dimeglumine.[22,23] Similar to the adult population, these patients had multiple courses of chemotherapy, radiation therapy, and external beam radiation for orbital rhabdomyosarcoma. In fact, earlier reports of an increased signal of the dentate nucleus in

Received May 17, 2017; accepted after revision August 22.

From the Departments of Radiology (S.K., T.B.S., R.J.B., S.L.R., S.B.R., H.A.R.), Pediatrics (C.A.D.), Medical Physics (S.B.R.), Emergency Medicine (S.B.R.), Biomedical Engineering (S.B.R.), and Medicine (S.B.R.), University of Wisconsin-Madison, Madison, Wisconsin; Department of Diagnostic and Interventional Radiology and Neuroradiology (S.K.), University Hospital Essen, Essen, Germany; and Clinic of Radiology and Nuclear Medicine (T.B.S.), Basel University Hospital, Basel, Switzerland.

Please address correspondence to Sonja Kinner, MD, Hufelandstr 55, University Hospital Essen, Essen, Germany; e-mail: Sonja.Kinner@uni-due.de

http://dx.doi.org/10.3174/ajnr.A5453

unenhanced T1-weighted images attributed the changes to brain irradiation.[24] This study included only patients 30 years of age and older and did not analyze the number of contrast-enhanced MRIs performed. Studies on unconfounded adult patients are rare.

A very recent publication evaluated whether increased signal intensities can also be found after multiple injections of the macrocyclic agent gadoterate meglumine in children.[25] As in all other pediatric patient studies, the authors explicitly excluded patients with a tumor in the cerebellum. Patients having had or undergoing chemotherapy were evaluated, but no subanalysis for differences was presented.

To date, pediatric studies are limited to investigations on the linear agent gadopentetate dimeglumine and the macrocyclic agent gadoterate meglumine. Therefore, the purpose of this retrospective study was 2-fold: 1) to investigate whether T1 shortening is also observed in children after multiple injections of gadobenate dimeglumine, and 2) to investigate whether brain radiation or chemotherapy or both impact this phenomenon.

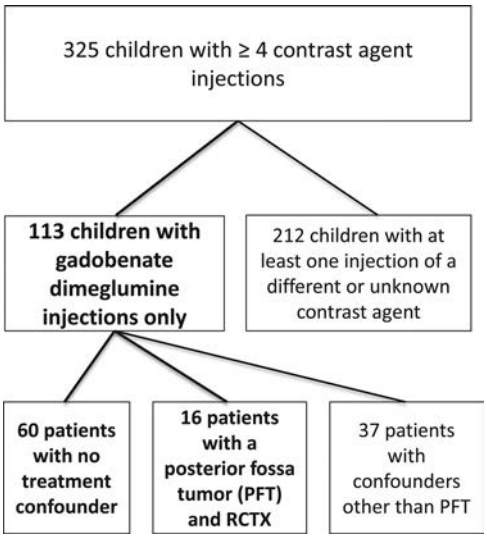

FIG 1. Flow chart showing the patient-selection criteria. PFT indicates posterior fossa tumor.

MATERIALS AND METHODS

Patients

In this institutional review board–approved (University Hospital Essen), single-center retrospective study, we performed a search of the image data base to extract all patients 18 years of age and younger with at least 4 contrast-enhanced MRIs archived on a PACS between August 2009 and September 2015. We reviewed all clinical charts and images to verify that all patients received only 1 gadolinium agent (gadobenate dimeglumine, used routinely from this time point onward). The remaining patients were screened for treatment variables and underlying diseases known to potentially present with increased T1 signal in deep brain nuclei (like Langerhans cell histiocytosis and neurofibromatosis). To create comparable groups, we chose to evaluate 2 groups: patients with no radiation and/or chemotherapy (RCTX) (group 1) and those with a posterior fossa tumor undergoing RCTX (group 2). Figure 1 represents a flow chart showing the patient selection. Patients with large, bilateral posterior fossa tumors involving or masking the dentate nucleus on both sides were excluded because these nuclei would be difficult or impossible to evaluate on preoperative imaging. In unilateral tumors, the dentate nucleus of the contralateral side was evaluated.

For all patients included in the study, age, sex, and diagnoses were documented. We also reviewed the electronic health records for any new or unexplained onset of movement disorders or cerebellar dysfunction. In the patients with posterior fossa tumors, whether they had surgery and which chemotherapy and radiation therapy they received were also assessed. If patients received radiation therapy, it was always a tumor-selective radiation therapy plan. In addition, the time interval between the first and last MR imaging was documented as well as the total cumulative amount of gadolinium injected across time.

MR Imaging Protocol

MR imaging of the brain was performed on clinical 1.5T (Optima MR450w or Signa HDxt; GE Healthcare, Milwaukee, Wisconsin) or 3T scanners (Discovery MR750 or MR750w; GE Healthcare) using 8-channel head coils. Imaging protocols included the following sequences before administration of gadobenate dimeglumine at a dosage of 0.1 mmol (0.2 mL) per kilogram of body weight: axial T1-weighted 3D inversion recovery–prepared fast-spoiled gradient-echo sequences (BRAVO: section thickness, 3 mm; TR, 8.5–9.3ms; TE, 3.2–3.7ms; flip angle, 13° [1.5T], 12° [3T]; TI, 450 ms) and/or sagittal T1-weighted 2D fluid-attenuated inversion recovery (section thickness, 3 mm; TR, 2212 ms [1.5T], 3050–3400 ms [3T]; TE, 8.4–8.8 ms [1.5T], 23.3–23.9 ms [3T]; flip angle, 90° [1.5T], 111° [3T]; TI, 750 ms [1.5T], 917–964 ms [3T]).

Image and Data Analysis

As a first step, visual analysis of the first and last MR imaging was performed, and a qualitative visual signal increase (present or not present) was documented. For objective image analysis, we analyzed images as previously described by Kanda et al[26]: De-identified images were imported and subsequently analyzed with open-source Digital Imaging and Communications in Medicine software OsiriX MD (Version 2.5.1 64-bit; http://www.osirix-viewer.com). Image analysis was performed by a radiologist with 10 years' experience in MR imaging and specific experience in neuroradiology and pediatric imaging. A freehand ROI was drawn on the unenhanced T1-weighted images in the bilateral dentate nuclei, the central pons, the middle cerebellar peduncle, and the left and right globus pallidus as well as the left and right thalamus, excluding the pulvinar thalami, which have been shown to exhibit T1 shortening as well in patients after multiple linear gadolinium-based contrast agent injections. To ensure accurate segmentation of the dentate nucleus, we performed correlation with T2- and T2*-weighted images when necessary. We also added the middle cerebellar peduncle as a correlation in addition to the pons, as described by Ramalho et al.[4] We therefore assessed not only the dentate-to-pons ratios but also the dentate-to-middle cerebellar peduncle ratios. Dentate-to-pons, dentate-to-middle cerebellar

Patient characteristics[a]

	Unconfounded Cases	Posterior Fossa Tumors	*P* Value
Total No. of patients	60	16	
Age (yr)	8.7 (6–14)	7.8 (4–10)	.095
Sex: female	30 (50.0%)	6 (37.5%)	.543
Contrast-enhanced MRIs	7 (5–9)	14.5 (11.2–16)	<.001
First-to-last MRI with contrast (yr)	3.1 (1.3–4.7)	3.4 (1.4–4.7)	.794
Accumulated dose of gadoterate dimeglumine (mL)	48.5 (31.1–87.2)	63.8 (49.8–130.5)	.161
Mean ratio change of dentate to pons	0.028 (0.007–0.049)	0.090 (0.049–0.132)	<.001
Mean ratio change of globus pallidus to thalamus	0.034 (0.013–0.055)	0.130 (0.091–0.168)	<.001

Note:—min indicates minimum; max, maximum.

[a] Data are presented as means with 95% confidence intervals in parentheses.

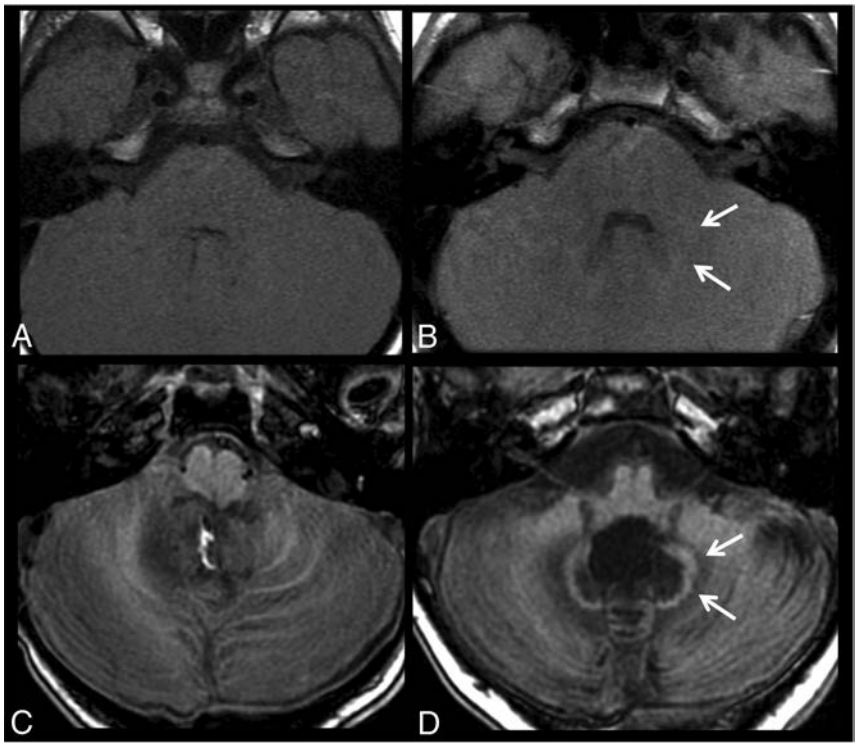

FIG 2. T1-weighted images acquired before (*A* and *C*) and after 20 gadobenate injections (*B* and *D*) in a patient with follow-up for optic glioma without radiation or chemotherapy (*A* and *B*) and a patient with medulloblastoma after an operation and radiochemotherapy (*C* and *D*). Subtle signal changes of the dentate (*arrows*) can be seen in the patient without any therapy, while the patient with RCTX shows distinct T1 signal changes of the dentate and perifocal edema.

peduncle, and globus pallidus-to-thalamus ratios were calculated from the first and last MR imaging dataset. The ratio change between the first and last imaging was calculated.

Statistical Analysis

Statistical analysis was performed with R statistical and computing software (http://www.r-project.org). Intraclass correlation coefficients (2,1) were used to assess the reliability of the ratio measurements between the means of the cerebellar peduncle and pons.

Mixed-effects linear regression was used to test the ratio between different factors (number of injections, time between first and last imaging, and amount of gadolinium injected) with subject as a random effect. Repeated-measures ANOVA was used to test whether the change in the ratio across time was significantly different between factor groups with subject as a random effect. Pearson correlation coefficients were calculated to assess the linear relationship between total gadolinium dosage and signal intensity ratio change for patients with and without therapy.

RESULTS

A total of 325 children with at least 4 contrast injections were identified. Of these, 76 children (mean age, 9.3 years) met the listed selection criteria (4–20 contrast-enhanced MRIs; mean, 8). Sixteen patients had posterior fossa tumors treated with radiation alone ($n = 2$), combined chemo- and radiation therapy ($n = 9$), and chemotherapy alone ($n = 5$), and 60 were unconfounded by such treatment. The characteristics of both patient groups can be found in the Table.

On visual inspection, 12 of the 16 patients with posterior fossa tumor and radiation or chemotherapy showed hyperintensities of the deep brain nuclei. These patients had undergone between 10 and 20 contrast injections, and the 4 patients without signal increase had <10 gadobenate dimeglumine injections. In the 60 patients without RCTX, only 2 patients were found to have a visual signal increase of the dentate nucleus or the globus pallidus between the first and last brain MR imaging. These patients had the highest contrast exposures, with 20 and 16 gadobenate dimeglumine injections.

Figure 2 shows a comparison of 2 patients after 20 injections, one with no treatment variables and 1 patient with medulloblastoma after radiochemotherapy. Figure 3 shows images before and after 10 gadobenate dimeglumine injections in a patient with no treatment variables and a second patient with a medulloblastoma, after surgery and radiochemotherapy.

Statistical analysis showed a statistically significant change in the signal ratio for the number of scans and contrast injections ($P < .001$) as well as the amount of gadolinium ($P = .008$), but not for the interscan time interval ($P = .353$). For each additional contrast-enhanced MR imaging, the signal ratio increased by 0.01 on average. There was a significant difference in the average change in ratio with time between those with RCTX versus those without ($P < .001$). A comparison of the ratio change for the

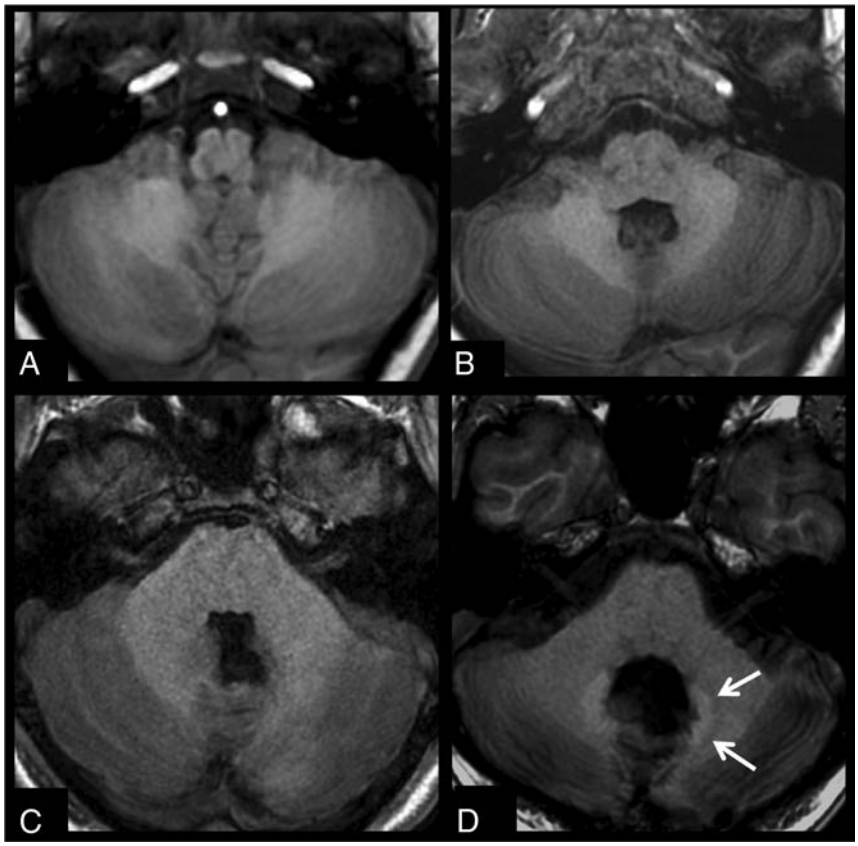

FIG 3. T1-weighted images acquired before (*A* and *C*) and after 10 gadobenate injections (*B* and *D*) in a patient being followed for a mass at the craniocervical junction with only surgical therapy (*A* and *B*) and a patient with medulloblastoma after an operation and radiochemotherapy (*C* and *D*). No signal change can be seen in the dentate for the patient without RCTX, while the patient with RCTX already shows signal changes after 10 injections.

dentate to pons and globus pallidus to thalamus showed no significant difference in average change in the ratio between measurements in the dentate and in the globus pallidus ($P = .199$), like that of children after focal radiation of the cerebellum ($P = .4$). Furthermore, no statistically significant difference was found for the use of the middle cerebellar peduncle or the pons as a control for the dentate ($P = .39$).

Figure 4 shows a distribution of the signal ratio change for the globus pallidus compared with thalamus in children with no treatment variables and children with radiochemotherapy.

Figure 5 shows the correlation of the total gadolinium dose administered and the signal ratio change for patients with and without therapy.

Directed neurologic chart review revealed no obvious new neurologic clinical deficits in the children with apparent T1 hyperintensities. We specifically searched for signs or symptoms referable to the extrapyramidal motor system such as tremor, bradykinesia, movement disorders, and motor dysfunction, which were not explained by the patient's known disease process.

DISCUSSION

In this retrospective study, we investigated whether pediatric patients show T1 shortening of deep brain nuclei after multiple doses of gadobenate dimeglumine and whether there is any difference between patients with and without radiation and/or chemotherapy.

This study has 4 messages we believe to be important:

First, children show a pattern of T1 signal changes of the dentate nucleus and globus pallidus after multiple injections of gadobenate dimeglumine, like that reported in adults. This has been shown for gadopentetate dimeglumine in a few recent small studies in children.[19-21] We were able to show it for gadobenate dimeglumine, another linear contrast agent, in a pediatric patient cohort for the first time. A first study in pediatric patients examining the effect of multiple doses of a macrocyclic contrast agent supports similar results in adults: Macrocyclic agents show no signal intensity increase after serial injections of a macrocyclic agent.[7,8,12,27] The study by Stojanov et al,[13] reporting a signal increase for a macrocyclic agent has been severely criticized because visual inspection of reported images did not seem to support the quantitative results of the study.

The second key finding is that patients without radiochemotherapy were much less likely to show T1 changes. In the absence of RCTX, only 2/60 showed these changes, and these occurred in the 2 patients with the most gadobenate dimeglumine injections ($n = 16$ and 20, respectively). This observation is consistent with findings in adults for gadobenate dimeglumine: Ramalho et al[4] investigated the influence of 2 linear contrast agents (gadodiamide and gadobenate dimeglumine) on the dentate nucleus and globus pallidus and showed a significant signal increase with gadodiamide-enhanced studies, but not with gadobenate dimeglumine. Their adult patient population comprised only patients without prior targeted or whole-brain radiation and those without multiple sclerosis and other diseases that might result in T1 shortening of deep brain nuclei and can thus be considered unconfounded like our 60-patient subgroup. However, the maximal number of MR images obtained in their patient population was 11 examinations. Because we saw an increase only after 16 examinations in unconfounded children, the number of injections might be too small in the study of Ramalho et al to find a visually discernible effect. Weberling et al,[5] however, investigated adult patients with melanoma with 5–15 injections of gadobenate dimeglumine (on average, 7.7 injections) and found an increase in signal intensity in the dentate nucleus. The results of Weberling et al in adults are therefore in line with ours in children: There seem to be a certain number of injections needed before signal intensity changes become visible. They, like Adin et al[6] and Radbruch et al,[7] did not find a correlation between radiation therapy and signal changes in adults, which is different from our results in children.

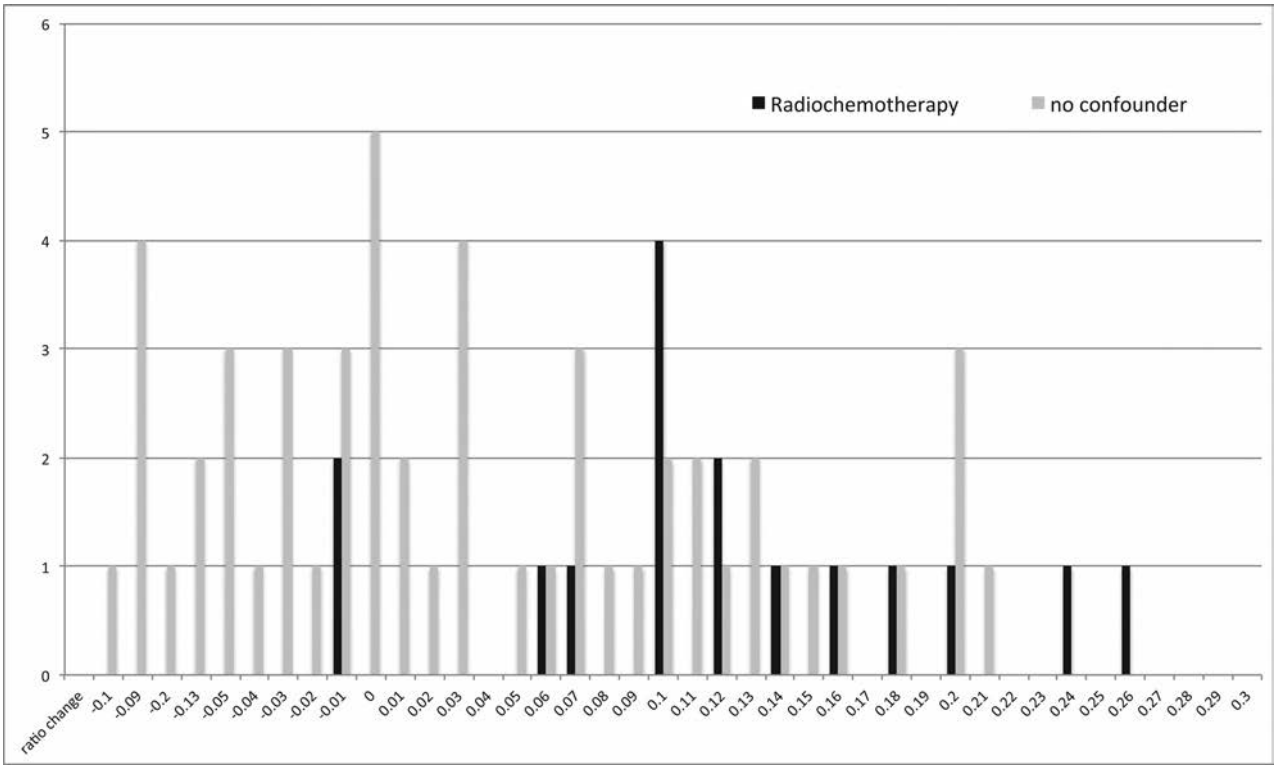

FIG 4. Distribution of the signal ratio change of the globus pallidus compared with the thalamus (globus pallidus to thalamus) in children with no treatment variables (*gray bars*) and children with radiochemotherapy (*black bars*) shows a shift/tendency to higher ratio changes in children with posterior fossa tumors under therapy.

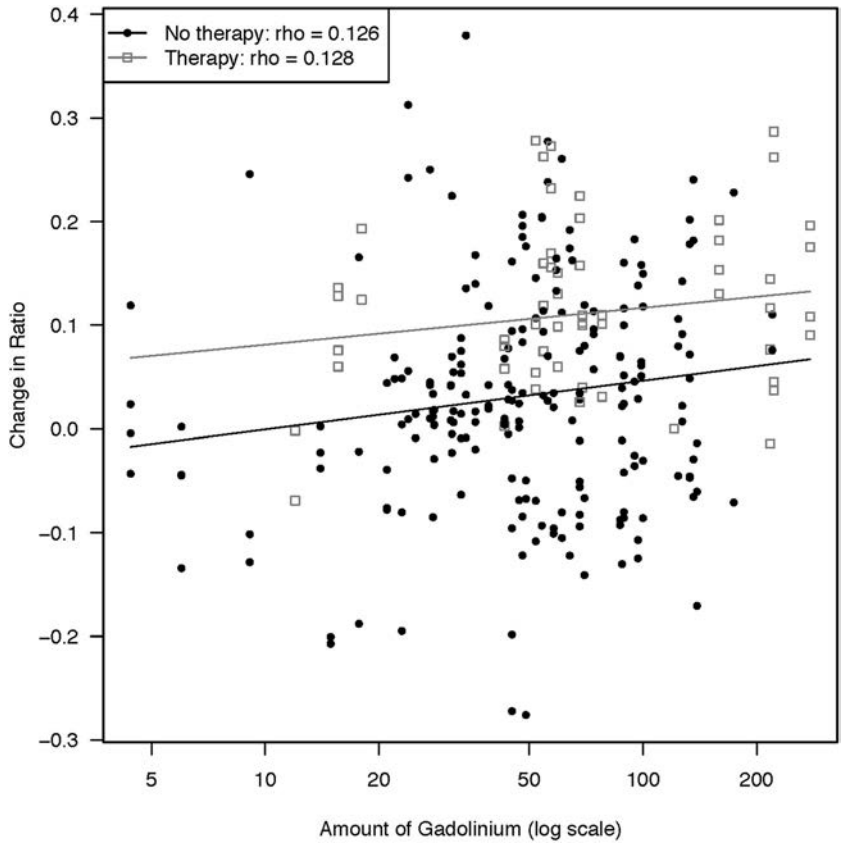

FIG 5. Scatterplot showing the correlation between cumulative gadolinium doses and signal ratio change for patients with and without therapy.

We also found that the time interval from gadolinium-based contrast agent injection until signal changes occur in children can be significantly reduced in the setting of radiochemotherapy, which impacts the blood-brain barrier. While Weberling et al[5] did not find a correlation for radiation therapy, they did not test for differences concerning chemotherapy. Because most of their adult patients had melanoma, it can be assumed that many patients received chemotherapy, even if not explicitly stated. This is important because we found that in patients receiving radiation therapy for posterior fossa tumors, the signal of the dentate changed like the signal of the globus pallidus, which leads to the presumption that radiation therapy itself locally does not lead to signal changes or acceleration of these changes, but rather the therapy (radiation therapy and/or chemotherapy) has an influence on the blood-brain barrier, which leads to uptake of gadolinium in any of the deep brain nuclei.

Montagne et al[28] showed, in a recent investigation, that blood-brain barrier breakdown is an early event in the aging human brain, starting from the hippocampus but also involving other brain

regions. The fact that children who did not undergo radiation or chemotherapy showed a later onset of signal increase might be also due to their still fully intact blood-brain barrier.

A key message that can be drawn from this study that is also in accordance with other studies is that the observed signal changes are apparently asymptomatic and are also independent of the time between injections. In all patients presented in prior studies, as in our patient group 2, presumed gadolinium deposition has not been linked to clinical deficits but does appear to be an imaging-observed adverse effect of therapy. Although neurologically asymptomatic, the appearance is dependent on the number of injections and the cumulative amount of gadolinium. Therefore, until more follow-up studies and prospective neurologic and neurocognitive surveillance are available, each injection of a gadolinium-based contrast agent should be carefully considered. Other contrast agents, like iron oxide particles, can be a possible alternate to gadolinium-based agents in brain imaging.[29,30]

During this analysis, we incidentally found that the red nucleus shows an intensity change like that of the dentate and globus pallidus. This finding might suggest the deposition of gadolinium in the red nucleus as well. New onset of tremor, gait disturbances, or other neurologic deficits have not been found in these children. Further analysis will show how signal changes in the dentate nucleus and globus pallidus might correlate with signal changes in other deep brain nuclei, especially the red nuclei, all of which are also known to take up iron as a normal physiologic finding, so changes might be difficult to analyze and attribute to a certain origin.

The linear gadolinium agent we studied here was originally chosen and continues to be used in our practice due to the combination of proved beneficial T1 enhancing effects and an excellent risk profile. Gadobenate has the highest relaxivity of any of the gadolinium agents marketed for central nervous system applications. It is been shown in multiple double-blind randomized crossover studies to show better tumor-enhancing performance metrics compared with any of the other agents.[31] It also has an excellent risk-benefit profile for nephrogenic systemic fibrosis, with thousands of renally impaired, high-risk patients given gadobenate due to diagnostic need in potentially life-threatening conditions, with no subsequent nephrogenic systemic fibrosis observed.[32] At the present time, we are therefore continuing to use this agent in our practice, while still recognizing the potential for apparently asymptomatic T1 shortening and presumably gadolinium deposition in the deep gray nuclei.

Our study clearly has limitations: First, we cannot prove that the contrast agent we used, gadobenate dimeglumine, is the reason for the later onset of signal changes in children compared with adults in the literature. Direct comparisons with adults from our data base are forthcoming. In addition, we cannot exclude gadolinium being deposited in the brain regions we used as comparators in children because we do not yet have postmortem studies in children. If this is the case, the postulated later onset in children might be due to different storage amounts. Furthermore, postmortem studies in children are especially needed.

Also, we cannot exclude the T1-weighted sequences we used having an influence on the detectability rate of signal changes. In a letter, Kanda et al[33] discussed different pulse sequences having different imaging appearances and different signal-to-noise ratios, which can have an influence on the image appearance and contrasts. We used conventional unenhanced T1-weighted gradient-echo sequences, which have been used in prior studies on this topic by different authors.[3,5,12] Another issue is that different magnetic field strengths were used in these patients. However, Adin et al[6] examined the influence of different field strengths in a subanalysis of their study and could show that no statistically significant difference was present.

CONCLUSIONS

Our study shows that children show a pattern of T1 signal changes of the dentate and globus pallidus after multiple injections of gadobenate dimeglumine like that in adults in published studies of this agent. The appearance in children may have a later onset and seems to be accelerated by radiation and chemotherapy.

Disclosures: Scott B. Reeder—*UNRELATED*: *Grant*: Bracco Diagnostics, *Comments*: provides an unrestricted grant for educational and research purposes*; *Other*: GE Healthcare, *Comments*: provides resources for research (but no money) to the University of Wisconsin*; *Grants/Grants Pending*: National Institutes of Health*; *Stock/Stock Options*: Elucent Medical, Cellectar Biosciences, Calimetrix, *Comments*: I hold shares/ownership in Elucent Medical and Collectar Biosciences and am a founder of Calimetrix.* Howard A. Rowley—*UNRELATED*: *Grant*: Bracco Diagnostics, *Comments*: fellowship funding support in a department (not in my section)*; *Consulting Fee or Honorarium*: Bracco Diagnostics, Guerbet, Bayer, GE Healthcare, *Comments*: These are all companies that make gadolinium contrast that have provided me with honoraria or consulting fees, directly or indirectly, in the past 3 years; *Support for Travel to Meetings for the Study or Other Purposes*: Bracco Diagnostics; *Consultancy*: GE Healthcare, *Comments*: consulting related to regulatory matters; *Payment for Lectures Including Service on Speakers Bureaus*: Bracco Diagnostics, *Comments*: accredited lectures on several topics, including MR physics, dementia, and other subject areas; *Patents (Planned, Pending or Issued)*: GE Healthcare, *Comments*: joint patent on an MRI pulse sequence, accepted by the Wisconsin patent office and pending issuance, not related to present work. **Money paid to the institution.*

REFERENCES

1. Errante Y, Cirimele V, Mallio CA, et al. **Progressive increase of T1 signal intensity of the dentate nucleus on unenhanced magnetic resonance images is associated with cumulative doses of intravenously administered gadodiamide in patients with normal renal function, suggesting dechelation**. *Invest Radiol* 2014;49:685–90 CrossRef Medline
2. Quattrocchi CC, Mallio CA, Errante Y, et al. **Gadodiamide and dentate nucleus T1 hyperintensity in patients with meningioma evaluated by multiple follow-up contrast-enhanced magnetic resonance examinations with no systemic interval therapy.** *Invest Radiol* 2015;50:470–72 CrossRef Medline
3. McDonald RJ, McDonald JS, Kallmes DF, et al. **Intracranial gadolinium deposition after contrast-enhanced MR imaging.** *Radiology* 2015;275:772–82 CrossRef Medline
4. Ramalho J, Castillo M, AlObaidy M, et al. **High signal intensity in globus pallidus and dentate nucleus on unenhanced T1-weighted MR images: evaluation of two linear gadolinium-based contrast agents.** *Radiology* 2015;276:836–44 CrossRef Medline
5. Weberling LD, Kieslich PJ, Kickingereder P, et al. **Increased signal intensity in the dentate nucleus on unenhanced T1-weighted images after gadobenate dimeglumine administration.** *Invest Radiol* 2015;50:743–48 CrossRef Medline
6. Adin ME, Kleinberg L, Vaidya D, et al. **Hyperintense dentate nuclei on T1-weighted MRI: relation to repeat gadolinium administration.** *AJNR Am J Neuroradiol* 2015;36:1859–65 CrossRef Medline
7. Radbruch A, Weberling LD, Kieslich PJ, et al. **Gadolinium retention in the dentate nucleus and globus pallidus is dependent on the class of contrast agent.** *Radiology* 2015;275:783–91 CrossRef Medline
8. Cao Y, Huang DQ, Shih G, et al. **Signal change in the dentate nucleus on T1-weighted MR images after multiple administrations of gado-**

pentetate dimeglumine versus gadobutrol. *AJR Am J Roentgenol* 2015;206:414–19 CrossRef Medline
9. Zhang Y, Cao Y, Shih GL, et al. **Extent of signal hyperintensity on unenhanced T1-weighted brain MR images after more than 35 administrations of linear gadolinium-based contrast agents.** *Radiology* 2017;282:516–25 CrossRef Medline
10. Schlemm L, Chien C, Bellmann-Strobl J, et al. **Gadopentetate but not gadobutrol accumulates in the dentate nucleus of multiple sclerosis patients.** *Mult Scler* 2017;23:963–72 CrossRef Medline
11. Eisele P, Alonso A, Szabo K, et al. **Lack of increased signal intensity in the dentate nucleus after repeated administration of a macrocyclic contrast agent in multiple sclerosis: an observational study.** *Medicine* 2016;95:e4624 CrossRef Medline
12. Radbruch A, Weberling LD, Kieslich PJ, et al. **High-signal intensity in the dentate nucleus and globus pallidus on unenhanced T1-weighted images: evaluation of the macrocyclic gadolinium-based contrast agent gadobutrol.** *Invest Radiol* 2015;50:805–10 CrossRef Medline
13. Stojanov D, Aracki-Trenkic A, Vojinovic S, et al. **Increasing signal intensity within the dentate nucleus and globus pallidus on unenhanced T1W magnetic resonance images in patients with relapsing-remitting multiple sclerosis: correlation with cumulative dose of a macrocyclic gadolinium-based contrast agent, gadobutrol.** *Eur Radiol* 2016;26:807–15 CrossRef Medline
14. Kanda T, Fukusato T, Matsuda M, et al. **Gadolinium-based contrast agent accumulates in the brain even in subjects without severe renal dysfunction: evaluation of autopsy brain specimens with inductively coupled plasma mass spectroscopy.** *Radiology* 2015;276:228–32 CrossRef Medline
15. Murata N, Gonzalez-Cuyar LF, Murata K, et al. **Macrocyclic and other non-group 1 gadolinium contrast agents deposit low levels of gadolinium in brain and bone tissue: preliminary results from 9 patients with normal renal function.** *Invest Radiol* 2016;51:447–53 CrossRef Medline
16. Robert P, Lehericy S, Grand S, et al. **T1-weighted hypersignal in the deep cerebellar nuclei after repeated administrations of gadolinium-based contrast agents in healthy rats: difference between linear and macrocyclic agents.** *Invest Radiol* 2015;50:473–80 CrossRef Medline
17. Frenzel T, Apte C, Jost G, et al. **Quantification and assessment of the chemical form of residual gadolinium in the brain after repeated administration of gadolinium-based contrast agents: comparative study in rats.** *Invest Radiol* 2017;52:396–404 CrossRef Medline
18. Jost G, Lenhard DC, Sieber MA, et al. **Signal increase on unenhanced T1-weighted images in the rat brain after repeated, extended doses of gadolinium-based contrast agents: comparison of linear and macrocyclic agents.** *Invest Radiol* 2016;51:83–89 CrossRef Medline
19. Hu HH, Pokorney A, Towbin RB, et al. **Increased signal intensities in the dentate nucleus and globus pallidus on unenhanced T1-weighted images: evidence in children undergoing multiple gadolinium MRI exams.** *Pediatr Radiol* 2016;46:1590–98 CrossRef Medline
20. Flood TF, Stence NV, Maloney JA, et al. **Pediatric brain: repeated exposure to linear gadolinium-based contrast material is associated with increased signal intensity at unenhanced T1-weighted MR imaging.** *Radiology* 2017;282:222–28 CrossRef Medline
21. Roberts DR, Chatterjee AR, Yazdani M, et al. **Pediatric patients demonstrate progressive T1-weighted hyperintensity in the dentate nucleus following multiple doses of gadolinium-based contrast agent.** *AJNR Am J Neuroradiol* 2016;37:2340–47 CrossRef Medline
22. Roberts DR, Holden KR. **Progressive increase of T1 signal intensity in the dentate nucleus and globus pallidus on unenhanced T1-weighted MR images in the pediatric brain exposed to multiple doses of gadolinium contrast.** *Brain Dev* 2016;38:331–36 CrossRef Medline
23. Miller JH, Hu HH, Pokorney A, et al. **MRI brain signal intensity changes of a child during the course of 35 gadolinium contrast examinations.** *Pediatrics* 2015;136:e1637-40 CrossRef Medline
24. Kasahara S, Miki Y, Kanagaki M, et al. **Hyperintense dentate nucleus on unenhanced T1-weighted MR images is associated with a history of brain irradiation.** *Radiology* 2011;258:222–28 CrossRef Medline
25. Radbruch A, Haase R, Kickingereder P, et al. **Pediatric brain: no increased signal intensity in the dentate nucleus on unenhanced T1-weighted MR images after consecutive exposure to a macrocyclic gadolinium-based contrast agent.** *Radiology* 2017;283:828–36 CrossRef Medline
26. Kanda T, Ishii K, Kawaguchi H, et al. **High signal intensity in the dentate nucleus and globus pallidus on unenhanced T1-weighted MR images: relationship with increasing cumulative dose of a gadolinium-based contrast material.** *Radiology* 2014;270:834–41 CrossRef Medline
27. Kanda T, Osawa M, Oba H, et al. **High signal intensity in dentate nucleus on unenhanced T1-weighted MR images: association with linear versus macrocyclic gadolinium chelate administration.** *Radiology* 2015;275:803–09 CrossRef Medline
28. Montagne A, Barnes SR, Sweeney MD, et al. **Blood-brain barrier breakdown in the aging human hippocampus.** *Neuron* 2015;85:296–302 CrossRef Medline
29. Corot C, Petry KG, Trivedi R, et al. **Macrophage imaging in central nervous system and in carotid atherosclerotic plaque using ultrasmall superparamagnetic iron oxide in magnetic resonance imaging.** *Invest Radiol* 2004;39:619–25 CrossRef Medline
30. Doyle KP, Quach LN, Arceuil HE, et al. **Ferumoxytol administration does not alter infarct volume or the inflammatory response to stroke in mice.** *Neurosci Lett* 2015;584:236–40 CrossRef Medline
31. Kanal E, Maravilla K, Rowley HA. **Gadolinium contrast agents for CNS imaging: current concepts and clinical evidence.** *AJNR Am J Neuroradiol* 2014;35:2215–26 CrossRef Medline
32. Bruce R, Wentland AL, Haemel AK, et al. **Incidence of nephrogenic systemic fibrosis using gadobenate dimeglumine in 1423 patients with renal insufficiency compared with gadodiamide.** *Invest Radiol* 2016;51:701–05 CrossRef Medline
33. Kanda T, Oba H, Toyoda K, et al. **Recent advances in understanding gadolinium retention in the brain.** *AJNR Am J Neuroradiol* 2016;37:E1–2 CrossRef Medline

MR Elastography Analysis of Glioma Stiffness and *IDH1*-Mutation Status

K.M. Pepin, K.P. McGee, A. Arani, D.S. Lake, K.J. Glaser, A. Manduca, I.F. Parney, R.L. Ehman, and J. Huston III

ABSTRACT

BACKGROUND AND PURPOSE: Our aim was to noninvasively evaluate gliomas with MR elastography to characterize the relationship of tumor stiffness with tumor grade and mutations in the *isocitrate dehydrogenase 1* (*IDH1*) gene.

MATERIALS AND METHODS: Tumor stiffness properties were prospectively quantified in 18 patients (mean age, 42 years; 6 women) with histologically proved gliomas using MR elastography from 2014 to 2016. Images were acquired on a 3T MR imaging unit with a vibration frequency of 60 Hz. Tumor stiffness was compared with unaffected contralateral white matter, across tumor grade, and by *IDH1*-mutation status. The performance of the use of tumor stiffness to predict tumor grade and *IDH1* mutation was evaluated with the Wilcoxon rank sum, 1-way ANOVA, and Tukey-Kramer tests.

RESULTS: Gliomas were softer than healthy brain parenchyma, 2.2 kPa compared with 3.3 kPa ($P < .001$), with grade IV tumors softer than grade II. Tumors with an *IDH1* mutation were significantly stiffer than those with wild type *IDH1*, 2.5 kPa versus 1.6 kPa, respectively ($P = .007$).

CONCLUSIONS: MR elastography demonstrated that not only were gliomas softer than normal brain but the degree of softening was directly correlated with tumor grade and *IDH1*-mutation status. Noninvasive determination of tumor grade and *IDH1* mutation may result in improved stratification of patients for different treatment options and the evaluation of novel therapeutics. This work reports on the emerging field of "mechanogenomics": the identification of genetic features such as *IDH1* mutation using intrinsic biomechanical information.

ABBREVIATIONS: GBM = glioblastoma; ECM = extracellular matrix; $|G^*|$ = magnitude of the complex shear modulus; *IDH1* = *isocitrate dehydrogenase 1*; MRE = MR elastography

While gliomas are rare compared with other cancers, they have a high mortality rate. Despite improvement in 5-year survival rates of many cancers, outcomes for brain tumors have remained relatively unchanged during the past 30 years, improving <2%.[1] Median survival is 12–15 months for glioblastomas (GBMs) and 2–5 years for lower grade gliomas. As our understanding of cancer biology, genetics, and treatment resistance mechanisms improves, the ability to stratify patients early with predictive biomarkers will be critical in the development of new therapies and the evaluation of treatment responses.[2] Gliomas are histopathologically typed and graded as outlined with the World Health Organization criteria, which provide important prognostic information as well as potential guidance on the clinical treatment of the tumor.[3] The World Health Organization classification was updated in 2016 to include molecular markers, which have important implications for patient outcome and may be critical information in the selection of a treatment strategy. Recent effort in the area of radiogenomics has explored the potential of using MR imaging phenotypes to noninvasively determine tumor genotypes, including the detection of 3 common genomic alterations in gliomas.[4] Mutations in the gene responsible for encoding a metabolic enzyme called *isocitrate dehydrogenase 1* (*IDH1*) frequently occur in low-grade gliomas, exhibiting different genetic and epigenetic etiology compared with *IDH1* wild type gliomas, and are considered a distinct disease entity with a poorer prognosis, independent of tumor grade.[5,6]

While only 6% of GBMs have mutations in *IDH1*, it is hypothesized that these tumors have evolved from lower grade gliomas, while low-grade gliomas that lack a mutation in *IDH1* could be

Received May 30, 2017; accepted after revision August 13.

From the Mayo Graduate School (K.M.P.) and Departments of Radiology (K.P.M., A.A., D.S.L., K.J.G., A.M., R.L.E., J.H.) and Neurosurgery (I.F.P.), Mayo Clinic College of Medicine, Rochester, Minnesota.

This work was supported, in part, by grants from the National Institutes of Health RO1 EB001981 and the Center for Individualizing Medicine, Imaging Biomarker Discovery Program, Mayo Clinic.

Please address correspondence to John Huston III, MD, Mayo Clinic College of Medicine, 200 First St SW, No. W4, Rochester, MN 55905; e-mail: jhuston@mayo.edu

Indicates open access to non-subscribers at www.ajnr.org

http://dx.doi.org/10.3174/ajnr.A5415

considered "preglioblastomas."[5,7] *IDH1* mutations may also be predictive of therapeutic outcome from specific treatments, such as increased radiosensitivity in vitro and differentiating patients who benefit from alkylating agent chemotherapy in combination with radiation therapy.[8,9] Recent effort has investigated noninvasive biomarkers to identify *IDH1*-mutant tumors in humans, including MR spectroscopy, using the association between mutations in *IDH1* and 2-hydroxygluterate in the tumor.[10] However, challenges related to long scan times, complex data processing, and low spectral resolution have limited clinical applications.[11]

Tumors are characterized by altered tissue- and cellular-level mechanics, and the stiffness of the extracellular matrix (ECM) in gliomas may be associated with a mutation in *IDH1*.[12,13] A recent study by Miroshnikova et al[13] demonstrated an overall correlation between tumor grade and *IDH1* mutational status with the ECM stiffness of human glioma brain biopsies. Using stiffness measurements from an atomic force microscope, they demonstrated increased ECM stiffness with tumor grade: The ECM from GBMs was stiffer than the ECM from lower grade gliomas. Additionally, the ECM of gliomas with a mutation in *IDH1* was softer than the ECM of wild type *IDH1* gliomas, regardless of histologic grade. These results demonstrate a microscopic mechanical correlation between ECM stiffness and tumor genotype. Additional work is needed to determine whether this finding correlates to macroscopic mechanical properties of gliomas.

MR elastography (MRE) is a technique used to noninvasively quantify the mechanical properties of tissue.[14-16] Previous studies have demonstrated the feasibility of using MRE to evaluate the viscoelastic properties of brain tumors, including gliomas, in which brain tumors were mainly softer than normal brain and benign variants; however, some tumors are stiffer than normal brain,[17] and GBMs were the softest brain tumors compared with meningiomas, vestibular schwannomas, and metastases.[18,19] Additional work demonstrated that the viscoelastic properties of GBMs were dependent on composition (eg, necrosis or cystic cavities) and that the mechanical properties were heterogeneous with both stiff and soft regions.[17,20] Recent work investigated the stiffness of 4 common brain tumors and stated that MRE may reflect the collagenous content of tumors.[19]

The purpose of this study was to noninvasively evaluate gliomas with MRE to characterize the relationship of tumor stiffness with tumor grade and mutations in the *IDH1* gene. We hypothesize that glioma stiffness will vary across tumor grade and that gliomas with an *IDH1* mutation will exhibit different mechanical properties than *IDH1* wild type gliomas.

MATERIALS AND METHODS

Patient Recruitment

This prospective study was approved by our institutional review board, and informed written consent was obtained from each subject. Inclusion criteria for the study consisted of subjects older than 18 years of age with biopsy-confirmed gliomas and a minimum tumor diameter of 2 cm. Subjects with contraindications to MR imaging (cardiac pacemaker, implanted metallic object, or claustrophobia) and lesions with extensive necrosis were excluded. Eighteen patients (mean age, 44 years; range, 25–68 for men, $n = 12$; and mean age, 40 years; range, 28–40 for women, $n = 6$) with a presumed or previous needle biopsy–diagnosed glioma scheduled for surgical resection were recruited for an MRE examination before tumor resection from April 2014 to December 2016. Diagnosis was confirmed following the operation by an experienced pathologist as part of clinical standard of care and included determination of tumor grade, histologic subtype, the presence of the 1p/19q codeletion, and *IDH1-R132H* mutations.

MR Image Acquisition

Preoperative imaging was performed with a 3T MR imaging scanner (Signa Excite; GE Healthcare, Milwaukee, Wisconsin). The MR imaging protocol for each subject included an anatomic T1-weighted inversion recovery echo-spoiled gradient-echo acquisition with the following parameters: TR/TE = 6.3/2.8 ms; TI = 400 ms; flip angle = 11°; 256 × 256 acquisition matrix; FOV = 27 cm; section thickness = 1.2 mm; 200 sagittal sections; bandwidth = 31.25 kHz; parallel imaging acceleration factor = 1.75. MRE imaging used a modified single-shot, flow-compensated, spin-echo EPI pulse sequence.[21,22]

MR Elastography Image Acquisition

Low-amplitude mechanical vibrations in the form of shear waves were introduced into the brain at a frequency of 60 Hz as previously described.[23] A custom-built soft, pillowlike passive driver was positioned beneath the subject's head in a standard 8-channel receive-only MR imaging head coil (Fig 1). A long flexible tube connected the passive driver to the active component located outside the scan room, which comprised a waveform generator, an amplifier, and an acoustic speaker. The resulting shear wave motion was imaged with the spin-echo EPI MRE pulse sequence by synchronizing motion-encoding gradients to the applied mechanical vibrations. The imaging parameters included the following: TR/TE = 3600/62 ms; 72 × 72 acquisition matrix reconstructed to 80 × 80; FOV = 24 cm; section thickness = 3 mm; 48 contiguous axial sections; bandwidth = 250 kHz; parallel imaging acceleration factor = 3; motion-encoding in the positive and negative x, y, and z directions; and 8 phase offsets sampled during 1 period of motion at 60 Hz. The MRE acquisition time was <7 minutes.

Image and Data Processing

Tissue viscoelastic shear properties were quantified from the measured displacement fields.[14,24,25] Assuming the tissue to be linear, isotropic, locally homogeneous, and viscoelastic, we quantified the complex shear modulus using previously described direct inversion methods (Fig 1).[22,26-28] Before direct inversion, several postprocessing steps were taken. First, the complex phase-difference images were calculated in the x, y, and z motion-encoding directions. Then, the curl of the input displacement field was calculated to reduce effects from the tissue boundaries and longitudinal wave propagation. A 2D low-pass filter was applied to reduce section-to-section phase discontinuities. A 3D direct inversion algorithm was used to calculate the complex shear modulus G^*.[22] Shear stiffness was reported as the magnitude of the complex shear modulus ($|G^*|$). A tumor ROI was manually drawn on each imaging section from T1-maps registered to the MRE space using information from all available imaging

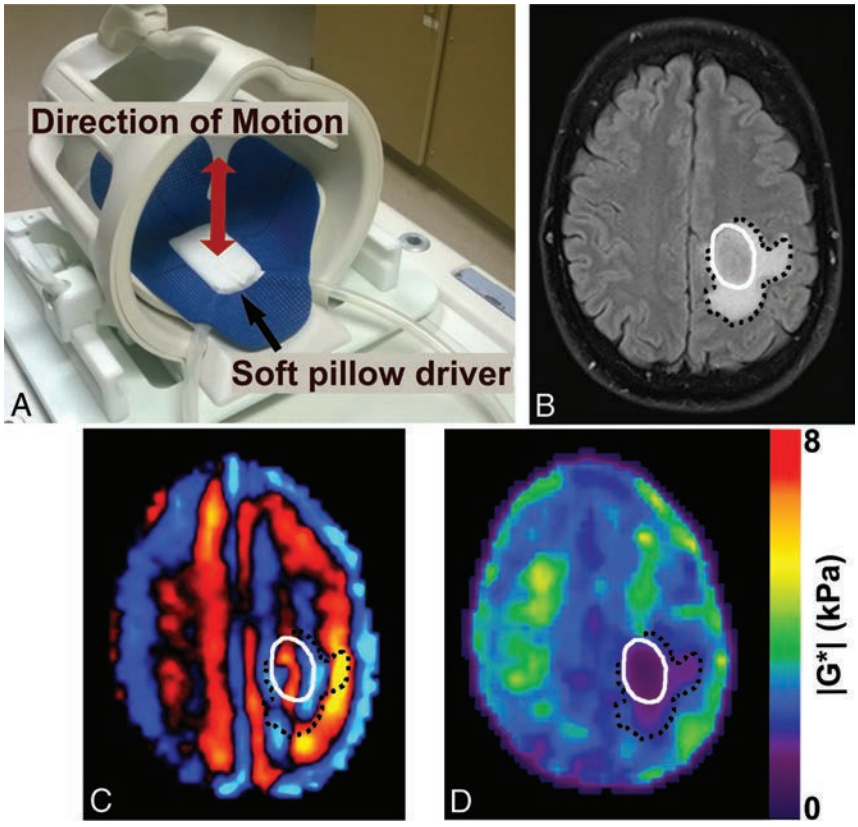

FIG 1. Brain MRE experimental setup and image processing. *A*, Brain MRE soft pillow driver placed within the 8-channel MR imaging head coil and positioned beneath the head to induce shear waves in the brain. *B*, Axial T2 FLAIR image of a glioblastoma, *IDH1* wild type (51-year-old man), with tumor denoted by a solid white line, and peritumoral edema, by a black dotted line. MRE shear wave image (*C*) and elastogram (*D*) or stiffness map display a soft tumor with a stiffness of 1.1 kPa in the tumor compared with 3.5 kPa in a size-matched region of unaffected white matter on the contralateral hemisphere.

sequences, including T1-, T2-, diffusion-, and contrast-enhanced T1-weighted images as previously described (research trainees, 1 year of experience under supervision of J.H., 26 years' experience).[22] Tumor stiffness was calculated as the median $|G^*|$ of all voxels contained in the ROI volume and was compared with a size-matched ROI in the unaffected white matter on the contralateral hemisphere to serve as a control. Group results are reported as mean ± SD (range).

Tumor volume was defined as the tumor ROI volume (cubic centimeter), calculated as the number of voxels contained in the ROI multiplied by the voxel volume. Contrast enhancement was assigned a label of nonenhancing, partially enhancing, or completely enhancing, determined from contrast-enhanced T1-weighted images obtained during a standard diagnostic MR imaging (J.H., 26 years' experience in neuroradiology).

Statistical Analysis

For each tumor ROI volume, the mean difference in tumor shear stiffness and unaffected contralateral normal white matter was analyzed with the Wilcoxon rank sum test. The mean differences in mean shear stiffness of *IDH1*+ and *IDH1*− tumors were analyzed with the Wilcoxon rank sum test. One-way ANOVA and Tukey-Kramer tests were used to compare the mean tumor shear stiffness between different tumor grades. A P value of $< .05$ was considered statistically significant. All calculations were performed with Matlab 2016a (MathWorks, Natick, Massachusetts) and R Core Team, 2015 (R Foundation for Statistical Computing, Vienna, Austria; http://www.r-project.org).

RESULTS

Patient Recruitment

MRE was performed on 18 patients. Following the operation, tumor grade was determined by clinical pathology and included 5 grade II, 7 grade III, and 6 grade IV tumors (Table). Twelve patients had tumors with a mutation in *IDH1-R132H*: 5/5 grade II, 5/7 grade III, and 2/6 grade IV tumors. Following the revision of the World Health Organization classification of gliomas in 2016, the 18 histopathology results were reclassified to reflect the new definitions.

Shear Stiffness and Tumor Grade

The mean shear stiffness of all gliomas was 2.2 ± 0.7 kPa (range, 1.1–3.8 kPa) compared with 3.3 ± 0.7 kPa (range, 1.2–4.1 kPa) in the contralateral unaffected white matter. In all except 2 cases, the tumor tissues were softer than normal brain tissue ($P < .001$). Tumor stiffness showed an inverse relationship with tumor grade: High-grade tumors were softer than lower grade tumors (Fig 2). For grades II, III, and IV, tumor stiffness was 2.7 ± 0.7 kPa (range, 2.1–3.8 kPa), 2.2 ± 0.6 kPa (range, 1.7–3.4 kPa), and 1.7 ± 0.5 kPa (range, 1.3–2.1 kPa), respectively. Grade IV GBMs were significantly softer than grade II gliomas ($P = .03$), but no statistically significant difference between grades II and III ($P = .19$) or between grades III and IV ($P = .23$) was observed. Additional correlations of tumor stiffness were investigated, including anatomic location, patient age, and tumor volume, but no significant trends were observed.

Shear Stiffness and IDH1 Mutations

Tumors with a mutation in *IDH1* ($n = 12$) were significantly stiffer than wild type *IDH1* ($n = 6$) tumors, with a shear stiffness of 2.5 ± 0.6 kPa (range, 1.5–3.8 kPa) and 1.6 ± 0.3 kPa (range, 1.1–1.9 kPa), respectively ($P = .007$, Fig 3). This observation was independent of tumor grade. There were 2 outliers, including a secondary GBM with a positive *IDH1* mutation and a shear stiffness of 1.5 kPa and a grade III infiltrating anaplastic glioma with a positive *IDH1* mutation and a shear modulus of 1.7 kPa. The MRE results from 2 grade III tumors are shown in Fig 4, to demonstrate the large stiffness heterogeneity between *IDH1* mutant and wild type tumors. While both were grade III gliomas, the mechanical properties were drastically different between the 2 tumors, with tumor stiffness equal to 3.3 kPa for the *IDH1* mutant tumor and 1.7 kPa for the *IDH1* wild type tumor.

Patient and tumor characteristics

No.	Sex	Age (yr)	Tumor Size (cm^3)	Location	Contrast Enhancement	*IDH1* Mutated?	1p/19q Codeleted?	Histologic and Genetic Classification	Grade
1	F	36	16.8	Left parietal	None	Yes	Yes	Oligodendroglioma, *IDH* mutant and 1p19q codeleted	II
2	M	39	60.6	Right temporal	None	Yes	No	Diffuse astrocytoma, *IDH* mutant	II
3	M	34	14.7	Left frontal	Partial	Yes	No	Diffuse astrocytoma, *IDH* mutant	II
4	M	31	54.7	Right frontal	None	Yes	Yes	Oligodendroglioma, *IDH* mutant and 1p19q codeleted	II
5	M	65	4.1	Left frontal	None	Yes	Yes	Oligodendroglioma	II
6	M	31	37.5	Left frontal	None	Yes	Yes	Oligodendroglioma, *IDH* mutant and 1p19q codeleted	III
7	F	35	66.9	Right frontal	None	Yes	No	Diffuse astrocytoma, *IDH* mutant	III
8	F	37	71.0	Left temporal	Partial	Yes	No	Diffuse astrocytoma, *IDH* mutant	III
9	M	51	59.9	Left temporal	None	Yes	Yes	Oligodendroglioma, *IDH* mutant and 1p19q codeleted	III
10	F	60	117.0	Right frontal	Partial	Yes	No	Diffuse astrocytoma, *IDH* mutant	III
11	F	44	75.6	Right frontal	None	No	No	Diffuse astrocytoma, *IDH* wild type	III
12	M	33	38.9	Left frontal	Partial	No	No	Diffuse astrocytoma, *IDH* wild type	III
13	F	28	5.5	Left frontal	Partial	Yes	–	Glioblastoma	IV
14	M	25	98.3	Right frontal	Partial	Yes	–	Glioblastoma	IV
15	M	51	27.6	Left postcentral gyrus	Complete	No	–	Glioblastoma	IV
16	M	46	9.5	Left temporal	None	No	–	Glioblastoma	IV
17	M	68	7.3	Left frontal	Complete	No	–	Glioblastoma	IV
18	M	55	37.1	Right thalamus	Complete	No	–	Glioblastoma	IV

Note:— – indicates not applicable.

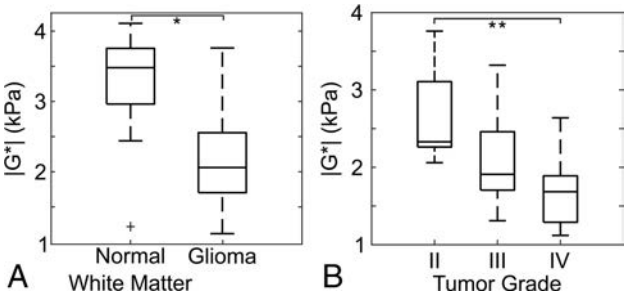

FIG 2. *A*, Gliomas are softer than normal brain tissue, compared with size-matched ROIs in the unaffected contralateral white matter (*asterisk* indicates $P < .001$). An outlier is indicated by a plus sign, and whiskers on the boxplot indicate the 25th and 75th percentiles. *B*, Glioma stiffness decreases with increasing tumor grade (*double asterisks* indicate $P < .05$).

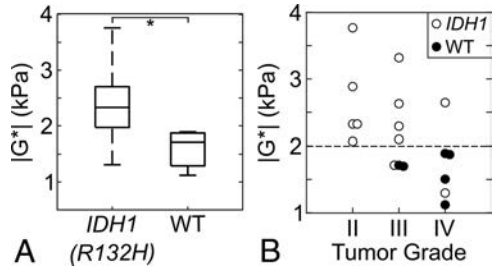

FIG 3. *A*, Comparison of the tumor stiffness (|G*|) between *IDH1–R132H* ($n = 12$) and wild type (WT) gliomas ($n = 6$). Gliomas with wild type *IDH1* were significantly softer than gliomas with a mutation in *IDH1–R132H* (*asterisk* indicates $P = .007$). The whiskers on the boxplot indicate the 25th and 75th percentiles. *B*, Tumor shear stiffness by tumor grade for all patients in this study including *IDH1–R132H* mutated tumors (*white circles*) and wild type *IDH1* (WT, *black circles*). The horizontal dotted line at 2.0 kPa separates the *IDH1*-mutated and wild type gliomas with a sensitivity and specificity of 83% and 100%. There is one secondary *IDH1*-mutated GBM with a low |G*| = 1.5 kPa, and it may be unique due to the secondary disease subtype.

DISCUSSION

This study demonstrates that gliomas are softer than normal brain and that the stiffness of gliomas decreases with increasing tumor grade, consistent with previous MRE results of brain tumors. One

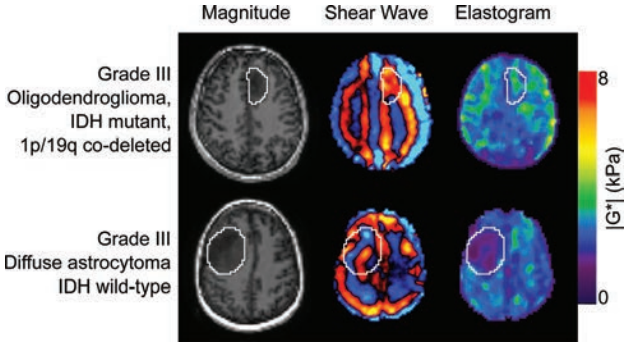

FIG 4. Stiffness heterogeneity of gliomas. Noncontrast, axial MRE magnitude images (*left column*), shear wave images (*middle column*), and elastograms (*right column*) for 2 patients with grade III gliomas. Images in the top row are from an oligodendroglioma with an *IDH1–R132H* mutation with |G*| = 3.3 kPa (a 31-year-old man), while the bottom row is from a diffuse astrocytoma with wild type *IDH1* with |G*| = 1.7 kPa (a 44-year-old woman).

study reported that primary brain tumors have a uniform loss of dissipative behavior and that the tumor mechanical properties are altered with increasing malignancy.[18] Similarly, another study investigated the mechanical properties of GBMs using MRE and found that most GBMs were softer than normal brain.[20] In these studies, low-grade gliomas were not included and no statistical analysis was reported for the relationship between tumor mechanical properties and tumor grade or *IDH1*-mutation status. A recent study demonstrated good correlation between glioma stiffness measurements and surgical assessment.[19] The results of this study are consistent with the quantitative stiffness values of gliomas reported in the literature.

The results presented in this work suggest that glioma stiffness may be a biomarker of *IDH1*-mutation status, with softer tumors being indicative of a wild type *IDH1*, irrespective of tumor grade. *IDH1* mutations in gliomas are associated with improved outcome.[5] The stiffness of the grade III gliomas with wild type *IDH1* was more comparable with the stiffness of grade IV tumors than of the *IDH1*-mutated grade III tumors. One outlier was an *IDH1*-mutated GBM with a relatively low stiffness (1.5 kPa compared

with a mean of 2.5 kPa for *IDH*-mutated gliomas). This tumor was a secondary GBM; 76% of secondary GBMs are *IDH1*-mutated compared with 6% of primary GBMs.[5,6] The considerable softness of this GBM may be from previous radiation therapy. Further investigation is needed to understand the heterogeneity in glioma stiffness between primary and secondary malignancies for all tumor grades and different histologic subtypes. These data provide the evidence to support the concept of "mechanogenomics"—the identification of genetic features such as *IDH1* mutation using intrinsic biomechanical information and MRE-derived shear stiffness—possibly being used as a biomarker to both identify and spatially resolve genetically induced alterations of tissue biomechanical properties.

This study found an inverse relationship between tumor stiffness, in which GBMs were softer than lower grade tumors and gliomas with wild type *IDH1* were softer than those with mutated *IDH1*, regardless of tumor grade. This is opposite of the relationship found in the recent study by Miroshnikova et al[13] of ECM stiffness in gliomas, in which the ECM of gliomas with an *IDH1* mutation was associated with a softer ECM, independent of histologic grade. Macroscopic tumor stiffness comprises >1 constituent part, and in that study, ECM stiffness was not correlated with the levels or distribution of type I collagen, vasculature, or cellularity. Additional factors that may affect macroscopic tumor stiffness include cellularity, increased vessel density, and interstitial fluid pressure.[29,30] Each of these factors may contribute to the overall tumor stiffness and potentially explain the opposite relationship of whole-tumor stiffness with tumor grade and *IDH1*-mutation status observed in this study. While the opposite trends were observed in this study, the same correlations were found in which stiffness was correlated with tumor grade and *IDH1* mutations, irrespective of tumor grade. Further work is needed to understand the relationship between the microscopic ECM stiffness and the macroscopic whole-tumor stiffness in gliomas.

The mechanisms behind these mechanogenomic differences are not well-understood and therefore require further investigation to determine the diagnostic accuracy of this technique and to investigate the relationship between tumor mechanical properties and progression-free survival and overall survival. Additionally, the role of other common somatic driver mutations, including the codeletion of the 1p and 19q chromosomal arms, methylguanine methyltransferase methylation status, and *TERT* promotor mutations need to be investigated. In the case of low-grade gliomas, there is an important need for a noninvasive technique capable of detecting malignant transformation to a higher grade. The serial assessment of tumor mechanical properties using MRE may help identify these events before imaging changes on standard anatomic MR imaging are seen. Previous results suggesting the completeness of nonenhancing tumor resection are an important prognostic factor in *IDH1*-mutant tumors, and a priori knowledge of *IDH1* status may help guide the extent of planned resection.[31] The potential of mechanogenomics with MRE to reliably and prospectively identify *IDH1* mutation preoperatively may have a large impact on surgical planning and postoperative patient management.

There are several limitations in this pilot study, including sample size and representation of lower grade tumors. The inclusion criteria for this study required a minimum tumor diameter of 2 cm. Improvement in the MRE acquisition and data processing could allow the quantification of mechanical properties in smaller tumors. Imaging plays an invaluable role in the treatment and monitoring of gliomas, but there is room for improvement. Common critiques of imaging techniques are low specificity and lack of histologic correlation. For instance, in the area of therapeutic response, the development of new targeted chemotherapy and radiation therapies may result in complicated imaging changes (either pseudoprogression or pseudoresponse), which are not adequately assessed with morphologic or anatomic imaging techniques. While our understanding of *IDH1* mutations and glioma biology has increased dramatically during the past few years, the optimal strategies for therapeutic interventions remain unclear. The ability to noninvasively detect this mutation may have important implications for stratifying patients for treatment and monitoring of response. Future work is needed to confirm these results and investigate additional tumor genotypes with prognostic and therapeutic significance for gliomas, including the 1p19q codeletion and methylguanine methyltransferase methylation status, as well as stiffness differences with histopathologic subtype.

CONCLUSIONS

Our study confirms that gliomas of all grades are softer than normal brain tissue and that tumor stiffness decreases with increasing tumor grade. In addition, gliomas with a mutation in *IDH1* are stiffer than wild type *IDH1* gliomas. The quantitative analysis of brain tumor mechanical properties may aid in the initial clinical assessment, surgical management, and postoperative monitoring of gliomas.

ACKNOWLEDGMENTS

The authors would like to thank Nikoo Fattahi, MD, Mona El Sheikh, MD, and Jann Sarkaria, MD, for their technical contributions. We would also like to thank Sonia Watson and Andrea Moran for their assistance in editing the manuscript.

Disclosures: Kiaran P. McGee—*UNRELATED*: *Royalties*: Resoundant; *Stock/Stock Options*: Resoundant. Kevin J. Glaser—*UNRELATED*: *Patents (Planned, Pending or Issued)*: MR Elastography Technology, *Comments*: Mayo Clinic and Kevin J. Glaser have patents covering MR elastography technology*; *Royalties*: MR Elastography Technology, *Comments*: Mayo Clinic and Kevin J. Glaser receive royalties from the licensing of MR elastography and technology; *Stock/Stock Options*: Resoundant, *Comments*: Kevin J. Glaser owns stock in Resoundant, a company owned by Mayo Clinic. Armando Manduca—*UNRELATED*: *Royalties*: Resoundant, *Comments*: Mayo Clinic and I receive some royalties for general activities in the field of MR elastography, though nothing specific to this work; *Stock/Stock Options*: Resoundant, *Comments*: I own some stock in Resoundant, a company that works in the general area of MR elastography. Richard L. Ehman—*RELATED*: *Grant*: National Institutes of Health EB001981*; *UNRELATED: Board Membership*: Resoundant, *Comments*: uncompensated*; *Grants/Grants Pending*: Resoundant*; *Patents (Planned, Pending or Issued)*: intellectual property related to MR elastography*; *Royalties*: Mayo Clinic; *Stock/Stock Options*: Resoundant*; *Travel/Accommodations/Meeting Expenses Unrelated to Activities Listed*: Radiological Society of North America, Resoundant, Bristol-Myers Squibb.* John Huston—*UNRELATED*: *Royalties*: Mayo Clinic, *Comments*: for MR elastography intellectual property; *Stock/Stock Options*: Resoundant. *Money paid to the institution.

REFERENCES

1. Australian Institute of Health and Welfare. *Cancer in Australia: An Overview 2014.* Cancer Series No. 90. Cat. No. CAN 88. Canberra: Australian Institute of Health and Welfare; 2014
2. Miles K. **Can imaging help improve the survival of cancer patients?** *Cancer Imaging* 2011;1:Spec No A:S86–92 CrossRef Medline

3. Louis DN, Perry A, Reifenberger G, et al. **The 2016 World Health Organization Classification of Tumors of the Central Nervous System: a summary.** *Acta Neuropathol* 2016;131:803–20 CrossRef Medline
4. Smits M, van den Bent MJ. **Imaging correlates of adult glioma genotypes.** *Radiology* 2017;284:316–31 CrossRef Medline
5. Yan H, Parsons DW, Jin G, et al. **IDH1 and IDH2 mutations in gliomas.** *N Engl J Med* 2009;360:765–73 CrossRef Medline
6. Labussiere M, Sanson M, Idbaih A, et al. **IDH1 gene mutations: a new paradigm in glioma prognosis and therapy?** *Oncologist* 2010;15:196–99 CrossRef Medline
7. Gorovets D, Kannan K, Shen R, et al. **IDH mutation and neuroglial developmental features define clinically distinct subclasses of lower grade diffuse astrocytic glioma.** *Clin Cancer Res* 2012;18:2490–501 CrossRef Medline
8. Li S, Chou AP, Chen W, et al. **Overexpression of isocitrate dehydrogenase mutant proteins renders glioma cells more sensitive to radiation.** *Neuro Oncol* 2013;15:57–68 CrossRef Medline
9. Cairncross JG, Wang M, Jenkins RB, et al. **Benefit from procarbazine, lomustine, and vincristine in oligodendroglial tumors is associated with mutation of IDH.** *J Clin Oncol* 2014;32:783–90 CrossRef Medline
10. Choi C, Ganji SK, DeBerardinis RJ, et al. **2-hydroxyglutarate detection by magnetic resonance spectroscopy in IDH-mutated patients with gliomas.** *Nat Med* 2012;18:624–29 CrossRef Medline
11. Lin G, Chung YL. **Current opportunities and challenges of magnetic resonance spectroscopy, positron emission tomography, and mass spectrometry imaging for mapping cancer metabolism in vivo.** *Biomed Res Int* 2014;2014:625095 CrossRef Medline
12. Kumar S, Weaver VM. **Mechanics, malignancy, and metastasis: the force journey of a tumor cell.** *Cancer Metastasis Rev* 2009;28:113–27 CrossRef Medline
13. Miroshnikova YA, Mouw JK, Barnes JM, et al. **Tissue mechanics promote IDH1-dependent HIF1α-tenascin C feedback to regulate glioblastoma aggression.** *Nat Cell Biol* 2016;18:1336–45 CrossRef Medline
14. Muthupillai R, Lomas DJ, Rossman PJ, et al. **Magnetic resonance elastography by direct visualization of propagating acoustic strain waves.** *Science* 1995;269:1854–57 CrossRef Medline
15. Muthupillai R, Lomas DJ, Rossman PJ, et al. **Visualizing propagating transverse mechanical waves in tissue-like media using magnetic resonance imaging.** In: Tortoli P, Masotti L, eds. *Acoustical Imaging.* Vol 22. Boston: Springer; 1996;279–83
16. Pepin KM, Ehman RL, McGee KP. **Magnetic resonance elastography (MRE) in cancer: technique, analysis, and applications.** *Prog Nucl Magn Reson Spectrosc* 2015;90–91:32–48 CrossRef Medline
17. Simon M, Guo J, Papazoglou S, et al. **Non-invasive characterization of intracranial tumors by magnetic resonance elastography.** *New J Phys* 2013;15:1–15 CrossRef
18. Reiss-Zimmermann M, Streitberger KJ, Sack I, et al. **High resolution imaging of viscoelastic properties of intracranial tumours by multi-frequency magnetic resonance elastography.** *Clin Neuroradiol* 2015;25:371–78 CrossRef Medline
19. Sakai N, Takehara Y, Yamashita S, et al. **Shear stiffness of 4 common intracranial tumors measured using MR elastography: comparison with intraoperative consistency grading.** *AJNR Am J Neuroradiol* 2016;37:1851–59 CrossRef Medline
20. Streitberger KJ, Reiss-Zimmermann M, Freimann FB, et al. **High-resolution mechanical imaging of glioblastoma by multifrequency magnetic resonance elastography.** *PLoS One* 2014;9:e110588 CrossRef Medline
21. Murphy MC, Huston J 3rd, Glaser KJ, et al. **Preoperative assessment of meningioma stiffness using magnetic resonance elastography.** *J Neurosurg* 2013;118:643–48 CrossRef Medline
22. Murphy MC, Huston J 3rd, Jack CR Jr, et al. **Measuring the characteristic topography of brain stiffness with magnetic resonance elastography.** *PLoS One* 2013;8:e81668 CrossRef Medline
23. Murphy MC, Huston J 3rd, Jack CR Jr, et al. **Decreased brain stiffness in Alzheimer's disease determined by magnetic resonance elastography.** *J Magn Reson Imaging* 2011;34:494–98 CrossRef Medline
24. Sinkus R, Tanter M, Xydeas T, et al. **Viscoelastic shear properties of in vivo breast lesions measured by MR elastography.** *Magn Reson Imaging* 2005;23:159–65 CrossRef Medline
25. Papazoglou S, Hamhaber U, Braun J, et al. **Algebraic Helmholtz inversion in planar magnetic resonance elastography.** *Phys Med Biol* 2008;53:3147–58 CrossRef Medline
26. Manduca A, Oliphant TE, Dresner MA, et al. **Magnetic resonance elastography: non-invasive mapping of tissue elasticity.** *Med Image Anal* 2001;5:237–54 CrossRef Medline
27. Clayton EH, Genin GM, Bayly PV. **Transmission, attenuation and reflection of shear waves in the human brain.** *J R Soc Interface* 2012;9:2899–910 CrossRef Medline
28. Sack I, Beierbach B, Hamhaber U, et al. **Non-invasive measurement of brain viscoelasticity using magnetic resonance elastography.** *NMR Biomed* 2008;21:265–71 CrossRef Medline
29. Jugé L, Doan BT, Seguin J, et al. **Colon tumor growth and antivascular treatment in mice: complementary assessment with MR elastography and diffusion-weighted MR imaging.** *Radiology* 2012;264:436–44 CrossRef Medline
30. Heldin CH, Rubin K, Pietras K, et al. **High interstitial fluid pressure—an obstacle in cancer therapy.** *Nat Rev Cancer* 2004;4:806–13 CrossRef Medline
31. Beiko J, Suki D, Hess KR, et al. **IDH1 mutant malignant astrocytomas are more amenable to surgical resection and have a survival benefit associated with maximal surgical resection.** *Neuro Oncol* 2014;16:81–91 CrossRef Medline

Prediction of *IDH1*-Mutation and 1p/19q-Codeletion Status Using Preoperative MR Imaging Phenotypes in Lower Grade Gliomas

Y.W. Park, K. Han, S.S. Ahn, S. Bae, Y.S. Choi, J.H. Chang, S.H. Kim, S.-G. Kang, and S.-K. Lee

ABSTRACT

BACKGROUND AND PURPOSE: WHO grade II gliomas are divided into three classes: *isocitrate dehydrogenase (IDH)*-wildtype, *IDH*-mutant and no 1p/19q codeletion, and *IDH*-mutant and 1p/19q-codeleted. Different molecular subtypes have been reported to have prognostic differences and different chemosensitivity. Our aim was to evaluate the predictive value of imaging phenotypes assessed with the Visually AcceSAble Rembrandt Images lexicon for molecular classification of lower grade gliomas.

MATERIALS AND METHODS: MR imaging scans of 175 patients with lower grade gliomas with known *IDH1* mutation and 1p/19q-codeletion status were included (78 grade II and 97 grade III) in the discovery set. MR imaging features were reviewed by using Visually AcceSAble Rembrandt Images (VASARI); their associations with molecular markers were assessed. The predictive power of imaging features for *IDH1*-wild type tumors was evaluated using the Least Absolute Shrinkage and Selection Operator. We tested the model in a validation set (40 subjects).

RESULTS: Various imaging features were significantly different according to *IDH1* mutation. Nonlobar location, larger proportion of enhancing tumors, multifocal/multicentric distribution, and poor definition of nonenhancing margins were independent predictors of an *IDH1* wild type according to the Least Absolute Shrinkage and Selection Operator. The areas under the curve for the prediction model were 0.859 and 0.778 in the discovery and validation sets, respectively. The *IDH1*-mutant, 1p/19q-codeleted group frequently had mixed/restricted diffusion characteristics and showed more pial invasion compared with the *IDH1*-mutant, no codeletion group.

CONCLUSIONS: Preoperative MR imaging phenotypes are different according to the molecular markers of lower grade gliomas, and they may be helpful in predicting the *IDH1*-mutation status.

ABBREVIATIONS: AUC = area under the receiver operating curve; *IDH1* = *isocitrate dehydrogenase 1*; LASSO = Least Absolute Shrinkage and Selection Operator; LGG = lower grade glioma; VASARI = Visually AcceSAble Rembrandt Images; WHO = World Health Organization

Recently, the *2016 World Health Organization Classification of Tumors of the Central Nervous System* was published. In the new classification, both genotype and phenotype are combined to define each diagnostic category of diffuse gliomas.[1] For the diagnosis of lower grade gliomas (LGGs), which are World Health Organization (WHO) grade II and III gliomas, the *isocitrate dehydrogenase* (*IDH*) mutation status, and 1p/19q-codeletion status are combined with the histologic phenotype, and the genotype takes precedence over the histologic phenotype in cases of discordance. Recent studies of genomic analysis found that diffuse gliomas may have distinct clinical behavior according to their molecular marker status.[2,3] The results of these studies have been reflected in the *2016 World Health Organization Classification of Tumors of the Central Nervous System*, which is based on the integrated diagnosis, combining phenotypic and genotypic classifications.[4]

The molecular subtypes of diffuse gliomas are divided into 3 classes: *IDH* wild type, *IDH* mutant and no 1p/19q codeletion, and *IDH* mutant and 1p/19 codeleted.[1] Different molecular subtypes have been reported to have prognostic differences and different chemosensitivity.[3,5] Thus, predicting the molecular subtype of LGGs preoperatively by MR imaging may aid in predicting the prognosis and planning the treatment strategy.

Received May 26, 2017; accepted after revision August 14.

From the Department of Radiology (Y.W.P.), Ewha Womans University College of Medicine, Seoul, Korea; and Departments of Radiology and Research Institute of Radiological Science (Y.W.P., K.H., S.-K.L., S.B., Y.S.C., S.S.A.), Neurosurgery (J.H.C., S.-G.K.), and Pathology (S.H.K.), Yonsei University College of Medicine, Seoul, Korea.

S.S. Ahn was supported by faculty research grants of the Yonsei University College of Medicine (6-2015-0079).

Please address correspondence to Sung Soo Ahn, MD, PhD, Department of Radiology and Research Institute of Radiological Science, Yonsei University College of Medicine, 50-1 Yonsei-ro, Seodaemun-gu, Seoul 120-752, Korea; e-mail: sungsoo@yuhs.ac

Indicates article with supplemental on-line tables.

Indicates article with supplemental on-line photos.

http://dx.doi.org/10.3174/ajnr.A5421

The recently developed lexicon, Visually AcceSAble Rembrandt Images (VASARI), is a tool for describing the baseline imaging features of human gliomas with MR imaging.[6] Using specific guidelines and controlled lexicon, the feature set is designed to comprehensively describe the tumor in consistent and reproducible terms. The imaging features recorded have been reported to be clinically meaningful, widely available, reproducible, and biologically relevant.[6-8]

The purpose of this study was to evaluate the predictive value of imaging phenotypes assessed with the VASARI lexicon for the molecular classification of LGGs preoperatively.

MATERIALS AND METHODS

Patient Population

The Severance Hospital institutional review board waived patient consent for this retrospective study. Between January 2007 and February 2017, three hundred sixty-six patients with pathologically diagnosed LGGs were included in this study. Inclusion criteria were as follows: 1) WHO grade II and III gliomas confirmed by histopathology; and 2) patients who underwent preoperative MR imaging. Exclusion criteria were the following: 1) an unknown *IDH1*-mutation status; 2) patients with a previous history of brain tumors; 3) patients with incomplete MR imaging sequences or suboptimal image quality for the VASARI lexicon review; and 4) patients younger than 18 years of age. The extent of tumor resection was classified as total, subtotal (<100% and ≥75% of gross total removal), or partial (<75% of gross tumor removal) resection or stereotactic biopsy only on the basis of the surgeon's intraoperative impressions in conjunction with postoperative MR imaging findings. The study population was chronologically divided into 2 sets. First, 175 consecutive patients diagnosed as having LGGs between January 2007 and May 2016 were included in the discovery set, and 40 consecutive patients diagnosed as having LGGs between June 2016 and February 2017 were included in the independent validation set. The flow chart of the study population is shown in On-line Fig 1. Patient characteristics of the discovery and validation sets are shown in On-line Table 1. The mean interval between the MR imaging examination and the operation was 10.73 ± 12.49 days.

Peptide nucleic acid–mediated clamping polymerase chain reaction and immunohistochemical analysis were performed to detect an *IDH1*-R132H mutation.[9] In the immunohistochemical analysis, the monoclonal antibody H09 was used, and the degree of *IDH1*-R132H staining was determined as positive in patients with any stained cells.[10] If immunohistochemical staining results were negative, we confirmed the *IDH1* status by peptide nucleic acid–mediated clamping polymerase chain reaction. Fluorescent in situ hybridization analysis was used to investigate the 1p/19q codeletion.[11]

MR Imaging Protocol

Preoperative MR imaging was performed with a 3T MR imaging scanner (Achieva; Philips Medical Systems, Best, Netherlands) with an 8-channel sensitivity-encoding head coil. The preoperative MR imaging protocol included T1-weighted (TR/TE, 1800–2000/10–15 ms; FOV, 240 mm; section thickness, 5 mm; matrix, 256 × 256), T2-weighted (TR/TE, 2800–3000/80–100 ms; FOV, 240 mm; section thickness, 5 mm; matrix, 256 × 256), and fluid-attenuated inversion recovery images (TR/TE, 9000–10,000/110–125 ms; FOV, 240 mm; section thickness, 5 mm; matrix, 256 × 256). 3D contrast-enhanced T1-weighted images (TR/TE, 6.3–8.3/3.1–4 ms; FOV, 240 mm; section thickness, 1 mm; and matrix, 192 × 192) were acquired after administering 0.1 mL/kg of gadolinium-based contrast material (gadobutrol, Gadovist; Bayer Schering Pharma, Berlin, Germany). Diffusion tensor imaging was performed with b-values of 600 and 0 s/mm^2, 32 directions, and the following parameters: TR/TE, 8413.4/77 ms; FOV, 220 mm; section thickness, 2 mm; and matrix, 112 × 112.

Imaging Analysis

Two neuroradiologists (S.S.A. and Y.W.P. with 10 and 5 years of experience, respectively), blinded to the molecular data, independently reviewed the MR imaging scans for tumor size, location, and tumor morphology using a standardized imaging feature set, VASARI. Discrepancies between the 2 radiologists were settled by consensus. The VASARI lexicon for MR imaging annotation consists of 26 imaging descriptors based on different MR imaging features. The exact description of all the features can be found at the Cancer Imaging Archive of the National Cancer Institute (https://wiki.cancerimagingarchive.net/display/Public/VASARI+Research+Project), which includes imaging features related to lesion location, morphology of the lesion substance, morphology of the lesion margin, alterations near the lesion, and remote alterations.

Statistical Analysis

The interrater agreement for the imaging features was assessed by using the Cohen κ coefficient test. The Student *t* and Pearson χ^2 tests were performed to evaluate the association between the imaging features and *IDH1*-mutation status in the discovery group, including the WHO grade II and III subgroups. Next, because the number of significant imaging features was relatively large compared with the number of patients when comparing the *IDH1*-wild type and *IDH1*-mutant groups, we used the regularization method to assess the predictive power of the imaging features based on the Least Absolute Shrinkage and Selection Operator (LASSO), which reduces the potential risk of overfitting or false discovery. We used 10-fold cross-validation to find the optimal regularization parameter for LASSO. We estimated the area under the receiver operating characteristic curve (AUC) to assess the predictive ability of variables by selecting significant variables based on LASSO. The 10-fold cross-validated AUC is the average of the predictive AUC of 10 validation datasets generated by the cross-validation process. Then, using the significant variables from the discovery set, we obtained the AUC in the validation set. The 5-fold cross-validated AUC was estimated to assess the predictive ability of variables by LASSO in the grade II and III subgroups.

The Student *t* and Pearson χ^2 tests were performed to evaluate the association between the imaging features and 1p/19q-codeletion status in the *IDH1*-mutant subgroup of the discovery group. LASSO was not performed to predict the 1p/19q-codeletion status in the *IDH1*-mutant subgroup because there were few significant parameters according to the 1p/19q-codeletion status. Statistical

analysis was performed by with R statistical and computing software (http://www.r-project.org). Statistical significance was set at $P < .05$.

RESULTS

Characteristics of the 175 enrolled patients in the discovery set according to the *IDH1*-mutation status and 1p19q-codeletion status are summarized in On-line Table 2.

Interrater Agreement

Interrater analysis showed significant agreement in all VASARI imaging features. Interrater agreement for all the imaging features was good to excellent (κ value = 0.715–1.000) (On-line Table 3).

Table 1: Prediction for an *IDH1*-mutation status in lower grade gliomas using the LASSO procedure

Imaging Parameters	Adjusted Odds Ratio for *IDH*-Wild Type
LGGs (WHO grade II/III gliomas)	
Nonlobar location	2.38
Proportion of enhancing tumor of >33%	1.66
Multifocal/multicentric distribution	2.93
Poor definition of nonenhancing margin	1.30
WHO grade II gliomas	
Side of tumor epicenter (central)	1.36
Multifocal/multicentric distribution	7.00
Pial invasion	1.48
Ependymal involvement	1.62
WHO grade III gliomas	
Nonlobar location	2.33
Proportion of enhancing tumor of >33%	1.25
Multifocal/multicentric distribution	2.27
Cortical involvement	0.99

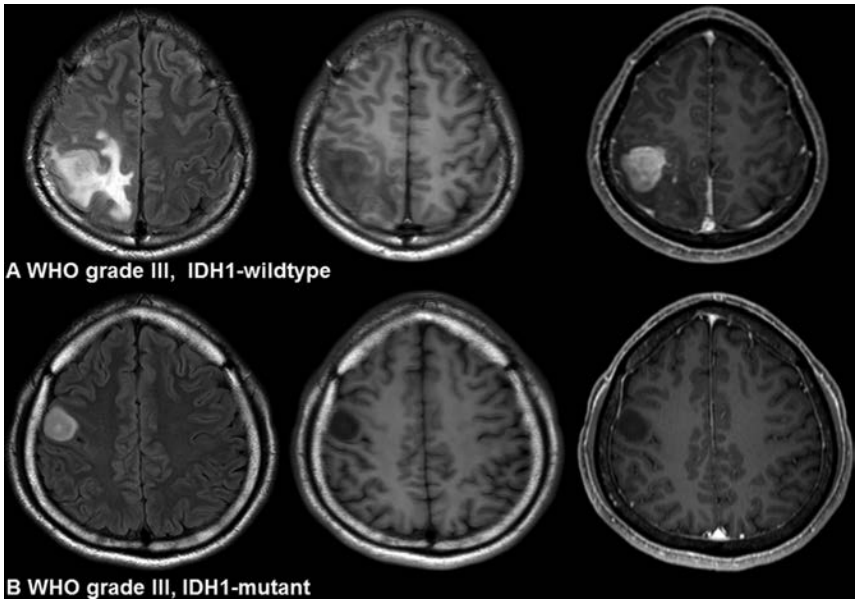

FIG 1. Imaging characteristics of *IDH1*-wild type and *IDH1*-mutant gliomas. *A*, A 24-year-old woman with an *IDH1*-wild type lower grade glioma (anaplastic astrocytoma, World Health Organization grade III). The imaging features are as follows: a lobar location, proportion of enhancing tumor of >33%, and poorly defined nonenhancing margin. *B*, A 42-year-old man with an *IDH1*-mutant lower grade glioma (anaplastic astrocytoma, WHO grade III). The imaging features are as follows: a lobar location with focal distribution, proportion of enhancing tumor of <33%, and well-defined nonenhancing margin.

Significant Imaging Features in Differentiating IDH-Mutant and IDH-Wild Type LGGs (WHO Grade II and III Gliomas)

Various imaging features were significantly different between the *IDH1*-wild type and *IDH1*-mutant groups according to the Student *t* test and χ^2 tests (On-line Table 4). The significantly different features included the major axis length, tumor location, side of the tumor epicenter, presence of enhancement, proportion of enhancing tumors, proportion of edema, proportion of necrosis, cysts, multifocal/multicentric distribution, infiltrative tumors, solid tumor enhancement, enhancing margin, nonenhancing margin, diffusion characteristics, pial invasion, ependymal extension, cortical involvement, and deep white matter invasion. Among them, 4 factors were independently associated with predicting the *IDH1* mutation by the LASSO procedure (On-line Fig 2), including the nonlobar tumor location, proportion of enhancing tumors of >33%, multifocal/multicentric distribution, and definition of the nonenhancing margin (Table 1). The *IDH1*-mutant group had a lobar tumor location and smaller proportion of enhancing tumors (Fig 1). However, the *IDH1*-wild type group had multifocal/multicentric distribution and poor definition of the nonenhancing margin. The AUC for the optimal model was 0.859 (95% confidence interval, 0.784–0.934). When the 4 parameters were used for diagnosis in the independent validation set, it reached an AUC of 0.778 (95% confidence interval, 0.619–0.893).

Significant Imaging Features in Differentiating IDH-Mutant and IDH-Wild Type Gliomas in WHO Grade II Gliomas

Various imaging features were significantly different between the *IDH1*-wild type and *IDH1*-mutant WHO grade II subgroups according to the Student *t* test and χ^2 test results (On-line Table 5). Among them, 4 factors were independently associated with predicting the *IDH1* mutation by the LASSO procedure. Significant differences were noted between the *IDH1*-wild type group and *IDH1*-mutant group, including the side of the tumor epicenter (central), multifocal/multicentric distribution, pial invasion, and ependymal involvement (Table 1). The AUC for the optimal model was 0.830 (95% CI, 0.753–0.907).

Significant Imaging Features in Differentiating IDH-Mutant and IDH-Wild Type Gliomas in WHO Grade III Gliomas

Various imaging features were significantly different between the *IDH1*-wild type and *IDH1*-mutant WHO grade III subgroups according to the Student *t* test and χ^2 test results (On-line Table 6). Among them, 4 factors were independently associated with predicting the *IDH1* mutation by the LASSO proce-

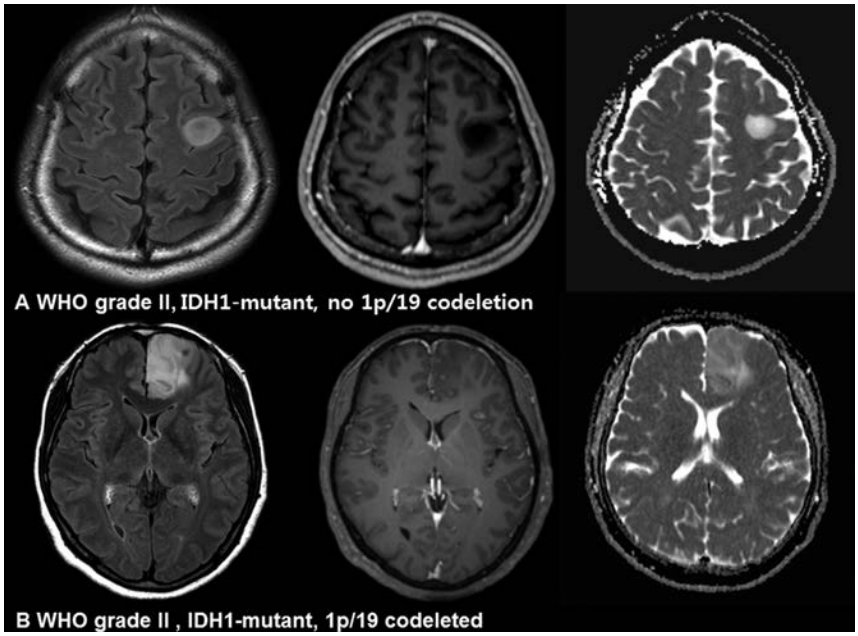

FIG 2. Imaging characteristics of *IDH1*-mutant, no 1p/19q-codeletion and *IDH1*-mutant, 1p/19q-codeleted gliomas. *A*, A 34-year-old man with an *IDH1*-mutant, no 1p/19q-codeletion glioma (diffuse astrocytoma, World Health Organization grade II). The nonenhancing T2 hyperintense mass shows increased diffusivity. *B*, A 49-year-old woman with an *IDH1*-mutant, 1p/19q-codeleted glioma (oligodendroglioma, WHO grade II). The infiltrative T2 hyperintense mass shows a mixed pattern of high and intermediate ADC values.

dure. Significant differences were noted between the *IDH1*-wild type group and *IDH1*-mutant group, including the nonlobar tumor location, proportion of enhancing tumors of >33%, multifocal/multicentric diffusion, and cortical involvement (Table 1). The AUC for the optimal model was 0.873 (95% CI, 0.794–0.952).

Significant Imaging Features in Differentiating the IDH-*Mutant, No 1p/19q-Codeletion and* IDH-*Mutant, 1p/19q-Codeleted Groups*

The frequency of pial invasion and diffusion characteristics was significantly different according to the 1p/19q-codeletion status in the *IDH1*-mutant subgroup ($P = .039$ and .020, respectively) (On-line Table 7). The *IDH1*-mutant, 1p/19q-codeleted group had significantly more pial invasion and a mixed pattern of high and intermediate ADC values or restricted diffusion characteristics than the *IDH*-mutant, no 1p/19q-codeletion group (Fig 2).

DISCUSSION

In our study, we comprehensively analyzed the MR imaging features of VASARI according to the molecular subtypes of LGGs. A noninvasive prediction of *IDH* mutation is important; a recent study suggested that in *IDH1*-mutant gliomas, maximal surgical resection, including enhancing and nonenhancing tumors, may contribute to a better prognosis.[12] In contrast, a survival benefit was noted in the complete resection of only enhancing tumors of *IDH1*-wild type gliomas, whereas no survival benefit was observed in further resection of the nonenhancing tumor portion. Although maximal resection of total tumor volume remains the optimal treatment, inference can be made about the contrast-enhancing portion of tumors and accessibility based on *IDH1*-mutation status in planning and performing an operation.[13] The overall survival, progression-free survival, and response to chemoradiotherapy are different according to the *IDH*-mutation status[3,14,15]; therefore, preoperative prediction of the molecular classification of LGGs is useful to guide the treatment decision and predict the prognosis. In addition, a selective inhibitor impaired the growth of *IDH1*-mutant glioma cells,[16] and the noninvasive prediction of *IDH1* mutation could assist in the development of treatment strategies such as targeted therapy.

Our proposed approach can be applied by visual assessment of conventional MR imaging, which is practical for implementation and economical. Overall, *IDH1*-mutant gliomas exhibited less invasive imaging features compared with *IDH*-wild type gliomas. All *IDH1*-mutant gliomas presented with a unilateral epicenter and focal distribution. With the 4 significant imaging features selected by the LASSO procedure, which are the nonlobar location, proportion of the enhancing tumor, multifocal/multicentric distribution, and definition of the nonenhancing margin, AUCs were 0.859 in the discovery set and 0.778 in the validation set in our study. In the WHO grade II and III subgroups, the significant imaging features according to the *IDH1*-mutation status mostly overlapped, except that pial invasion and ependymal extension were also significant factors in WHO grade II gliomas, and the tumor location, proportion of enhancement, and definition of the enhancing margin were significant factors in WHO grade III gliomas. A recent study showed that the proportion of necrosis and lesion size predicted the *IDH1*-mutation status, which correlates with our results.[17] In WHO grade III gliomas, *IDH*-mutant tumors are strongly associated with a frontal location,[18-20] whereas *IDH*-wild type tumors are frequently located outside the frontal lobe.[19,20] The predominant frontal lobe location of *IDH*-mutant gliomas may be because neuroglial progenitor cells in the forebrain subventricular zone are likely cells of origin for *IDH*-mutant gliomas.[21,22] In another study with WHO grade II gliomas, *IDH*-wild type tumors had greater tumor volume and an infiltrative pattern on MR images.[23] Moreover, in WHO grade II and III astrocytomas, *IDH*-mutant gliomas were predominantly located in a single lobe and had less contrast enhancement,[24] which are in accordance with our results. In glioblastomas, *IDH1*-wild type tumors showed a higher proportion of enhancing tumor,[25] and *IDH1*-mutant tumor had a less invasive phenotype and frontal lobe predominance,[25-27] which is like our findings in LGGs.

Conflicting results have been reported regarding the association between the *IDH* mutation and tumor borders.[24,28] These discordant results may be because in 1 study, the margins of the

nonenhancing and enhancing portions were not differentiated,[24] whereas in our study, *IDH1*-mutant tumors frequently showed a poorly defined enhancing margin and a well-defined nonenhancing margin, which correlated with the results of another study.[28] In many patients with *IDH1*-mutant tumors, there was no enhancement, and if enhancement was present, it was faint, thereby displaying a poorly defined enhancing margin. In terms of the nonenhancing margin, a recent study also showed that grade II and III astrocytomas with *IDH* mutation had sharp borders on T2-weighted imaging,[29] which is consistent with our results. In WHO grade II and III astrocytomas, *IDH1*-wild type tumors showed lower apparent diffusion coefficient values than *IDH1*-mutant tumors, concordant with our results.[28,30]

Increased cell proliferation or cellularity decreases ADC values in glioblastomas.[13,31] This feature may suggest that *IDH* mutations can decrease glioma proliferation, and it explains why an *IDH* mutation is a favorable prognostic marker in patients with gliomas.[2,32] Pial invasion and ependymal extension were also significant factors in WHO grade II gliomas in our study, according to the *IDH1*-mutation status. In the previous literature, there was no discussion of the imaging findings of pial invasion, possibly because these findings were not included in the analyses. The increased incidence of pial invasion in *IDH*-wild type gliomas may be due to the invasiveness of *IDH*-wild type gliomas, but further study is indicated to validate the finding. Recent studies have shown that glioblastomas with ependymal extension showed a significant decrease in overall survival.[33] This may be because tumors arising from neural stem cells in the subventricular zone have a higher potential for invasiveness, which may be correlated with ependymal involvement.[34]

LGGs with an *IDH* mutation and 1p/19q codeletion are associated with favorable outcomes and have sensitivity to chemotherapy with alkylating agents.[2,3,35-37] Several studies have analyzed the association between a 1p/19q codeletion and MR imaging features.[17,19,20,28,38-40] In our study, *IDH1*-mutant, 1p/19q-codeleted gliomas more frequently had a mixed pattern of high and intermediate ADC values or restricted diffusion characteristics and more pial invasion compared with *IDH1*-mutant, no codeletion gliomas. There has been controversy regarding the association between a 1p/19q codeletion and tumor borders.[19,20,28,39] Other studies have reported a low accuracy for predicting 1p/19q codeletion using conventional and advanced MR imaging.[28,40] The frequent mixed pattern of high and intermediate ADC values or restricted diffusion characteristics in *IDH1*-mutant, 1p/19q-codeleted gliomas may reflect the difference in oligodendroglial tumor biology compared with other gliomas.[41]

Several studies have shown discordant results about the association between the ADC and 1p/19q status,[28,40] which may be because the evaluation was performed in different study groups. Previous studies included patients with oligodendroglial tumors based on histopathology findings regardless of the *IDH*-mutation status; then, the authors classified them into groups with and without 1p/19q codeletion. Therefore, a small number of patients with *IDH*-wild type gliomas were included in those studies.[20,28,39] However, our study analyzed the association between imaging features and the 1p/19q codeletion in an *IDH1*-mutant subgroup, and the different inclusion criteria may have partially contributed to discordant results. Further study is needed to validate our results in a larger population with a homogeneous group.

For reproducible and reliable evaluation of imaging features, imaging analysis was performed on the basis of VASARI MR imaging features.[6] A controlled set of imaging features (ie, VASARI) has many benefits, including good-to-excellent interrater agreement. A controlled lexicon will facilitate more concrete knowledge regarding the relationship of imaging features with clinical and genotypic features and improve the communication of results among clinicians.[7] Several studies have used the VASARI lexicon to evaluate imaging features, and 1 study found that invasive imaging characteristics assessed with VASARI were associated with upregulation of the oncogene in glioblastomas.[25,26]

Our study has several significant limitations. First, it was based on a single-center, retrospectively collected dataset. Second, prognostic markers were not analyzed because patients with LGGs have relatively long overall survival, especially with WHO grade II gliomas. Further studies are necessary to correlate prognostic markers such as overall survival and progression-free survival with genotypic and imaging features. Third, there is the possibility of biopsy sampling error in cases of stereotactic biopsy or subtotal/partial resections, as previously reported.[31] Fourth, several imaging features noted as significant in the LASSO procedure in predicting *IDH*-wild type in WHO grade II gliomas showed a relatively low incidence, as seen in On-line Table 5; therefore, features may have limited value for clinical application. Considering the low incidence of *IDH* mutation in grade II gliomas, further studies with larger populations are necessary to find noninvasive imaging biomarkers with detailed imaging feature analysis in WHO grade II gliomas.

CONCLUSIONS

Preoperative MR imaging phenotypes are different according to the molecular markers in LGGs, and they may be helpful in predicting the *IDH1*-mutation status. The imaging phenotypes of nonlobar location, proportion of enhancing tumor, multifocal/multicentric distribution, and poor definition of nonenhancing margin assist in predicting *IDH1*-wild type LGGs.

Disclosures: Yae Won Park—*RELATED*: *Grant*: Yonsei University College of Medicine (6-2015-0079), *Comments*: faculty research grants of the Yonsei University College of Medicine (6-2015-0079)*. *Money paid to the institution.

REFERENCES

1. Louis DN, Perry A, Reifenberger G, et al. **The 2016 World Health Organization Classification of Tumors of the Central Nervous System: a summary.** *Acta Neuropathol* 2016;131:803–20 CrossRef Medline
2. Eckel-Passow JE, Lachance DH, Molinaro AM, et al. **Glioma groups based on 1p/19q, IDH, and TERT promoter mutations in tumors.** *N Engl J Med* 2015;372:2499–508 CrossRef Medline
3. Brat DJ, Verhaak RG, Aldape KD, et al; Cancer Genome Atlas Research Network. **Comprehensive, integrative genomic analysis of diffuse lower-grade gliomas.** *N Engl J Med* 2015;372:2481–98 CrossRef Medline
4. Louis DN, Perry A, Burger P, et al. **International Society of Neuropathology–Haarlem consensus guidelines for nervous system tumor classification and grading.** *Brain Pathol* 2014;24:429–35 CrossRef Medline
5. Kaloshi G, Benouaich-Amiel A, Diakite F, et al. **Temozolomide for**

low-grade gliomas: predictive impact of 1p/19q loss on response and outcome. *Neurology* 2007;68:1831–36 CrossRef Medline
6. Gutman DA, Cooper LA, Hwang SN, et al. **MR imaging predictors of molecular profile and survival: multi-institutional study of the TCGA glioblastoma data set.** *Radiology* 2013;267:560–69 CrossRef Medline
7. Mazurowski MA, Desjardins A, Malof JM. **Imaging descriptors improve the predictive power of survival models for glioblastoma patients.** *Neuro Oncol* 2013;15:1389–94 CrossRef Medline
8. Gutman DA, Dunn WD Jr, Grossmann P, et al. **Somatic mutations associated with MRI-derived volumetric features in glioblastoma.** *Neuroradiology* 2015;57:1227–37 CrossRef Medline
9. Yan H, Parsons DW, Jin G, et al. **IDH1 and IDH2 mutations in gliomas.** *N Engl J Med* 2009;360:765–73 CrossRef Medline
10. Takano S, Tian W, Matsuda M, et al. **Detection of IDH1 mutation in human gliomas: comparison of immunohistochemistry and sequencing.** *Brain Tumor Pathol* 2011;28:115–23 CrossRef Medline
11. Riemenschneider MJ, Jeuken JW, Wesseling P, et al. **Molecular diagnostics of gliomas: state of the art.** *Acta Neuropathol* 2010;120:567–84 CrossRef Medline
12. Beiko J, Suki D, Hess KR, et al. **IDH1-mutant malignant astrocytomas are more amenable to surgical resection and have a survival benefit associated with maximal surgical resection.** *Neuro Oncol* 2014;16:81–91 CrossRef Medline
13. Wang S, Kim S, Chawla S, et al. **Differentiation between glioblastomas and solitary brain metastases using diffusion tensor imaging.** *Neuroimage* 2009;44:653–60 CrossRef Medline
14. van den Bent MJ, Brandes AA, Taphoorn MJ, et al. **Adjuvant procarbazine, lomustine, and vincristine chemotherapy in newly diagnosed anaplastic oligodendroglioma: long-term follow-up of EORTC brain tumor group study 26951.** *J Clin Oncol* 2013;31:344–50 CrossRef Medline
15. Cairncross G, Wang M, Shaw E, et al. **Phase III trial of chemoradiotherapy for anaplastic oligodendroglioma: long-term results of RTOG 9402.** *J Clin Oncol* 2013;31:337–43 CrossRef Medline
16. Rohle D, Popovici-Muller J, Palaskas N, et al. **An inhibitor of-mutant IDH1 delays growth and promotes differentiation of glioma cells.** *Science* 2013;340:626–30 CrossRef Medline
17. Zhou H, Vallières M, Bai HX, et al. **MRI features predict survival and molecular markers in diffuse lower-grade gliomas.** *Neuro Oncol* 2017;19:862–870 CrossRef Medline
18. Zhang CB, Bao ZS, Wang HJ, et al. **Correlation of IDH1/2 mutation with clinicopathologic factors and prognosis in anaplastic gliomas: a report of 203 patients from China.** *J Cancer Res Clin Oncol* 2014;140:45–51 CrossRef Medline
19. Sonoda Y, Shibahara I, Kawaguchi T, et al. **Association between molecular alterations and tumor location and MRI characteristics in anaplastic gliomas.** *Brain Tumor Pathol* 2015;32:99–104 CrossRef Medline
20. Reyes-Botero G, Dehais C, Idbaih A, et al. **Contrast enhancement in 1p/19q-codeleted anaplastic oligodendrogliomas is associated with 9p loss, genomic instability, and angiogenic gene expression.** *Neuro Oncol* 2014;16:662–70 CrossRef Medline
21. Lai A, Kharbanda S, Pope WB, et al. **Evidence for sequenced molecular evolution of IDH1 mutant glioblastoma from a distinct cell of origin.** *J Clin Oncol* 2011;29:4482–90 CrossRef Medline
22. Persson AI, Petritsch C, Swartling FJ, et al. **Non-stem cell origin for oligodendroglioma.** *Cancer Cell* 2010;18:669–82 CrossRef Medline
23. Metellus P, Coulibaly B, Colin C, et al. **Absence of IDH mutation identifies a novel radiologic and molecular subtype of WHO grade II gliomas with dismal prognosis.** *Acta Neuropathol* 2010;120:719–29 CrossRef Medline
24. Qi S, Yu L, Li H, et al. **Isocitrate dehydrogenase mutation is associated with tumor location and magnetic resonance imaging characteristics in astrocytic neoplasms.** *Oncol Lett* 2014;7:1895–902 CrossRef Medline
25. Colen RR, Vangel M, Wang J, et al. **Imaging genomic mapping of an invasive MRI phenotype predicts patient outcome and metabolic dysfunction: a TCGA glioma phenotype research group project.** *BMC Med Genomics* 2014;7:30 CrossRef Medline
26. Gevaert O, Mitchell LA, Achrol AS, et al. **Glioblastoma multiforme: exploratory radiogenomic analysis by using quantitative image features.** *Radiology* 2014;273:168–74 CrossRef Medline
27. Price SJ, Allinson K, Liu H, et al. **Less invasive phenotype found in isocitrate dehydrogenase–mutated glioblastomas than in isocitrate dehydrogenase wild-type glioblastomas: a diffusion-tensor imaging study.** *Radiology* 2017;283:215–21 CrossRef Medline
28. Xiong J, Tan W, Wen J, et al. **Combination of diffusion tensor imaging and conventional MRI correlates with isocitrate dehydrogenase 1/2 mutations but not 1p/19q genotyping in oligodendroglial tumours.** *Eur Radiol* 2016;26:1705–15 CrossRef Medline
29. Xing Z, Yang X, She D, et al. **Noninvasive assessment of IDH mutational status in World Health Organization grade II and III astrocytomas using DWI and DSC-PWI combined with conventional MR imaging.** *AJNR Am J Neuroradiol* 2017;38:1138–44 CrossRef Medline
30. Tan W, Huang W, Yin B, et al. **Can diffusion tensor imaging noninvasively detect IDH1 gene mutations in astrogliomas? A retrospective study of 112 cases.** *AJNR Am J Neuroradiol* 2014;35:920–27 CrossRef Medline
31. Beppu T, Inoue T, Shibata Y, et al. **Fractional anisotropy value by diffusion tensor magnetic resonance imaging as a predictor of cell density and proliferation activity of glioblastomas.** *Surg Neurol* 2005;63:56–61; discussion 61 CrossRef Medline
32. Sanson M, Marie Y, Paris S, et al. **Isocitrate dehydrogenase 1 codon 132 mutation is an important prognostic biomarker in gliomas.** *J Clin Oncol* 2009;27:4150–54 CrossRef Medline
33. Colen RR, Vangel M, Wang J, et al; TCGA Glioma Phenotype Research Group. **Imaging genomic mapping of an invasive MRI phenotype predicts patient outcome and metabolic dysfunction: a TCGA glioma phenotype research group project.** *BMC Med Genomics* 2014;7:30 CrossRef Medline
34. Lim DA, Cha S, Mayo MC, et al. **Relationship of glioblastoma multiforme to neural stem cell regions predicts invasive and multifocal tumor phenotype.** *Neuro Oncol* 2007;9:424–29 CrossRef Medline
35. van den Bent MJ. **Practice changing mature results of RTOG study 9802: another positive PCV trial makes adjuvant chemotherapy part of standard of care in low-grade glioma.** *Neuro Oncol* 2014;16:1570–74 CrossRef Medline
36. Suzuki H, Aoki K, Chiba K, et al. **Mutational landscape and clonal architecture in grade II and III gliomas.** *Nat Genet* 2015;47:458–68 CrossRef Medline
37. Aldape K, Burger PC, Perry A. **Clinicopathologic aspects of 1p/19q loss and the diagnosis of oligodendroglioma.** *Arch Pathol Lab Med* 2007;131:242–51 Medline
38. Khayal IS, Vandenberg SR, Smith KJ, et al. **MRI apparent diffusion coefficient reflects histopathologic subtype, axonal disruption, and tumor fraction in diffuse-type grade II gliomas.** *Neuro Oncol* 2011;13:1192–201 CrossRef Medline
39. Jenkinson MD, du Plessis DG, Smith TS, et al. **Histological growth patterns and genotype in oligodendroglial tumours: correlation with MRI features.** *Brain* 2006;129:1884–91 CrossRef Medline
40. Fellah S, Caudal D, De Paula AM, et al. **Multimodal MR imaging (diffusion, perfusion, and spectroscopy): is it possible to distinguish oligodendroglial tumor grade and 1p/19q codeletion in the pretherapeutic diagnosis?** *AJNR Am J Neuroradiol* 2013;34:1326–33 CrossRef Medline
41. Jenkinson MD, du Plessis DG, Smith TS, et al. **Cellularity and apparent diffusion coefficient in oligodendroglial tumours characterized by genotype.** *J Neurooncol* 2010;96:385–92 CrossRef Medline

Improved Spatiotemporal Resolution of Dynamic Susceptibility Contrast Perfusion MRI in Brain Tumors Using Simultaneous Multi-Slice Echo-Planar Imaging

A. Chakhoyan, K. Leu, W.B. Pope, T.F. Cloughesy, and B.M. Ellingson

ABSTRACT

SUMMARY: DSC perfusion MR imaging in brain tumors requires a trade-off between spatial and temporal resolution, resulting in less spatial coverage to meet the temporal resolution requirements for accurate relative CBV estimation. DSC-MR imaging could potentially benefit from the advantages associated with simultaneous multi-slice imaging, including increased spatiotemporal resolution. In the current article, we demonstrate how simultaneous multi-slice EPI can be used to improve DSC-MR imaging spatiotemporal resolution in patients with glioblastoma.

ABBREVIATIONS: rCBV = relative CBV; SMS = simultaneous multi-slice

DSC perfusion MR imaging estimates of relative CBV (rCBV) have been shown to differentiate histologic tumor grade,[1,2] predict survival, and be useful for therapeutic monitoring in brain tumors[3]; however, DSC requires compromises in image resolution, slice coverage, and temporal resolution. The TR must be short enough to capture the rapid passage of the contrast bolus through the blood vasculature, but at the same time, there must be enough spatial coverage to encapsulate the entire tumor or brain. Simultaneous multi-slice (SMS) EPI[4] has drawn widespread attention due to the advent of highly accelerated images[5] through the application of composite radiofrequency pulses to simultaneously excite multiple slice planes.[6] The SMS technique excites multiple slices physically separated across the z-axis simultaneously so that each SMS "slab" has slices acquired interleaved within that section. SMS has been shown to not have appreciable loss in SNR compared with traditional methods,[4] and studies have shown that SMS is effective in reducing the acquisition time with higher spatiotemporal resolution.[5,7,8] In the current article, we demonstrate the clinical utility of using SMS-EPI to increase the spatiotemporal resolution of DSC-MR imaging in patients with glioblastoma.

MATERIALS AND METHODS

Patients

Thirteen patients with pathologically confirmed primary glioblastoma with recurrence based on either MR imaging, clinical deterioration, and/or histology were enrolled in this prospective study, which was approved by our local ethics institutional review board (University of California, Los Angeles). All patients underwent DSC-MR imaging with conventional single-shot EPI followed by SMS-EPI, 1–2 months later.

DSC-MR Imaging Acquisition

A preload bolus of 0.025 mmol/kg of Gd-DTPA (Magnevist; Bayer HealthCare Pharmaceuticals, Wayne, New Jersey) was administered to reduce leakage effects followed by 0.075 mmol/kg of Gd-DTPA at a rate of 5 mL/s. Two minutes of data were acquired, including a 30-second prebolus baseline and 90 seconds of data during and following contrast injection.

Conventional DSC-MR imaging was then acquired using a single-shot gradient-echo EPI at 3T (Prisma; Siemens, Erlangen, Germany) with TE = 35 ms, TR = 1.25–1.9 seconds, flip angle = 60°, FOV = 24 × 24 cm, matrix size = 128 × 128, generalized

Received April 30, 2017; accepted after revision August 24.

From the UCLA Brain Tumor Imaging Laboratory (A.C., K.L., B.M.E.), Center for Computer Vision and Imaging Biomarkers, University of California, Los Angeles, Los Angeles, California; Departments of Radiological Sciences (A.C., K.L., W.B.P., B.M.E.), Biomedical Physics (B.M.E.), Psychiatry and Biobehavioral Sciences (B.M.E.), UCLA Brain Research Institute (T.F.C., B.M.E.), and Neurology (T.F.C.), David Geffen School of Medicine, University of California, Los Angeles, Los Angeles, California; and Department of Bioengineering (K.L., B.M.E.), Henry Samueli School of Engineering and Applied Science, and UCLA Neuro-Oncology Program (T.F.C., B.M.E.), University of California, Los Angeles, Los Angeles, California.

This work was supported by the American Cancer Society Research Scholar Grant RSG-15-003-01-CCE (B.M.E.); the National Institutes of Health/National Cancer Institute R21CA167354 (B.M.E.); an American Brain Tumor Association Research Collaboration Grant supported by Humor to Fight the Tumor, ARC1700002 (B.M.E.); a National Brain Tumor Society research grant (B.M.E.); a National Institutes of Health/National Institute of General Medical Sciences training grant, GM08042 (K.L.); and the University of California, Los Angeles Medical Scientist Training Program (K.L.).

Please address correspondence to Benjamin M. Ellingson, PhD, Departments of Radiological Sciences and Psychiatry, David Geffen School of Medicine, University of California, Los Angeles, 924 Westwood Blvd, Suite 615, Los Angeles, CA 90024; e-mail: bellingson@mednet.ucla.edu; @ben_ellingson

Indicates open access to non-subscribers at www.ajnr.org

http://dx.doi.org/10.3174/ajnr.A5433

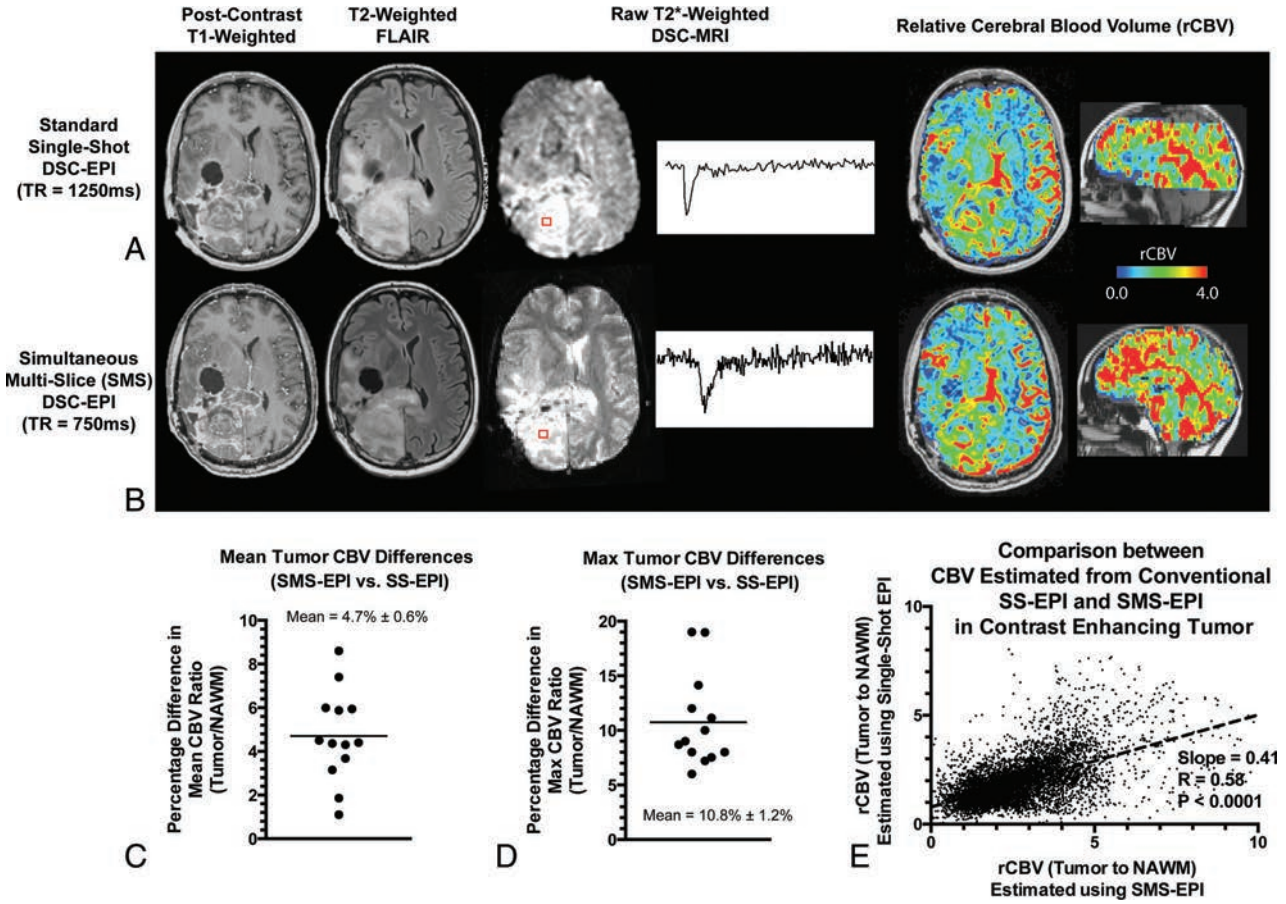

FIG 1. Postcontrast T1-weighted images, T2-weighted FLAIR images, and raw T2*-weighted DSC MR images with corresponding signal-time curves across time from tumor regions accompanied by resulting relative cerebral blood volume maps for conventional single-shot EPI (*A*) and simultaneous multi-slice EPI (*B*) (left to right). Percentage difference in mean tumor rCBV ratio (tumor to normal-appearing white matter) (*C*) and percentage difference in the maximum tumor rCBV ratio (tumor to normal-appearing white matter) (*D*) in 13 patients with recurrent glioblastoma. *E*, Voxelwise correlation of rCBV ratio between conventional single-shot EPI and SMS-EPI.

autocalibrating partially parallel acquisition = 2, slice thickness = 5 mm with no interslice gap, and 15- to 20-slice coverage. The voxel size was 1.875 × 1.875 × 5 mm, and the temporal resolution was 1.25–1.90 seconds.

Accelerated DSC-MR imaging was obtained with single-shot SMS-EPI with TE = 35ms, TR = 750 ms, flip angle = 60°, FOV = 21.6 × 24 cm, matrix size = 180 × 200, slice thickness = 4 mm with no interslice gap, controlled aliasing in parallel imaging results in higher acceleration factor = 2, and an SMS acceleration factor of 4 for a total of 30 slices through the whole brain. Voxel sizes were 1.2 × 1.2 × 4 mm with temporal resolution of 0.75 seconds.

Postprocessing of DSC-MR Imaging

Relative cerebral blood volume maps were generated with custom scripts including correction for bidirectional contrast agent exchange between the vascular and extravascular space.[9] All rCBV values were normalized to contralateral normal-appearing white matter.

ROI and Statistical Analyses

Contrast-enhancing tumor ROIs were defined in 3D using custom scripts from Analysis of Functional Neuro Images (AFNI; http://afni.nimh.nih.gov/afni), excluding hemorrhage, large vessels, and central necrosis, followed by manual editing to exclude nonlesional voxels.[9] Additionally, 2-cm-diameter spheric ROIs were placed on contralateral normal-appearing white matter for normalization of rCBV measurements. The percentage difference in the mean rCBV ratio, maximum tumor rCBV difference, and voxelwise correlations between single-shot EPI and SMS-EPI were estimated from the resulting data for all 13 patients. GraphPad Prism software, Version 6.0h (GraphPad Software, San Diego, California) was used for all statistical analyses.

RESULTS

Both raw DSC and calculated rCBV maps were of comparable quality; however, rCBV maps calculated with SMS-EPI were obtained for the entire brain and at slightly higher spatial resolution compared with rCBV maps obtained with conventional single-shot EPI (Fig 1*A*, -*B*). The mean tumor rCBV difference between these 2 techniques was 4.7% ± 0.6% (Fig 1*C*), and the maximum tumor rCBV difference was 10.8% ± 1.2% (Fig 1*D*). Voxelwise correlations in rCBV between the 2 techniques showed a significant association in all patients examined (Fig 1*E*), with rCBV ratios in the tumor with respect to normal-appearing white matter slightly higher when estimated using SMS-EPI.

CONCLUSIONS

SMS-EPI can increase the spatiotemporal resolution in DSC-MR imaging, resulting in larger brain coverage (12 versus 10 cm), higher in-plane spatial resolution (1.2 × 1.2 × 4 mm versus 1.875 × 1.875 × 5 mm), and faster temporal resolution (0.75 versus 1.25–1.90 seconds), with comparable results in quantification of tumor vascularity and clinical feasibility. While the potential impact on slice-to-slice perfusion quantitation is not currently known and results suggest that there may be little effect, a larger study is warranted. Together, these data demonstrate the potential clinical value of using SMS-EPI to estimate rCBV in patients with brain tumors with a high degree of reproducibility in terms of vascular biology quantification compared with historical test-retest studies.[10]

Disclosures: Whitney B. Pope—*RELATED*: *Consulting Fee or Honorarium*: Bracco; *UNRELATED*: *Grants/Grants Pending*: Guerbet.* Benjamin M. Ellingson—*RELATED*: *Grant*: Siemens; *UNRELATED*: *Board Membership*: MedQIA, Medicenna, Roche, Agios Pharmaceuticals, Bristol-Myers Squib; *Consultancy*: MedQIA, Medicenna, Roche, Agios Pharmaceuticals, Bristol-Myers Squib. *Money paid to the institution.

REFERENCES

1. Aronen HJ, Gazit IE, Louis DN, et al. **Cerebral blood volume maps of gliomas: comparison with tumor grade and histologic findings.** *Radiology* 1994;191:41–51 CrossRef Medline
2. Cha S, Knopp EA, Johnson G, et al. **Intracranial mass lesions: dynamic contrast-enhanced susceptibility-weighted echo-planar perfusion MR imaging.** *Radiology* 2002;223:11–29 CrossRef Medline
3. Law M, Yang S, Wang H, et al. **Glioma grading: sensitivity, specificity, and predictive values of perfusion MR imaging and proton MR spectroscopic imaging compared with conventional MR imaging.** *AJNR Am J Neuroradiol* 2003;24:1989–98 Medline
4. Barth M, Breuer F, Koopmans PJ, et al. **Simultaneous multislice (SMS) imaging techniques.** *Magn Reson Med* 2016;75:63–81 CrossRef Medline
5. Feinberg DA, Moeller S, Smith SM, et al. **Multiplexed echo planar imaging for sub-second whole brain FMRI and fast diffusion imaging.** *PLoS One* 2010;5:e15710 CrossRef Medline
6. Maudsley AA. **Multiple-line-scanning spin density imaging.** *J Magn Reson* 1980;41:112–26
7. Chen L, T Vu A, Xu J, et al. **Evaluation of highly accelerated simultaneous multi-slice EPI for fMRI.** *Neuroimage* 2015;104:452–59 CrossRef Medline
8. Feinberg DA, Setsompop K. **Ultra-fast MRI of the human brain with simultaneous multi-slice imaging.** *J Magn Reson* 2013;229:90–100 CrossRef Medline
9. Ellingson BM, Cloughesy TF, Lai A, et al. **Quantitative volumetric analysis of conventional MRI response in recurrent glioblastoma treated with bevacizumab.** *Neuro Oncol* 2011;13:401–09 CrossRef Medline
10. Henry ME, Kaufman MJ, Lange N, et al. **Test-retest reliability of DSC MRI CBV mapping in healthy volunteers.** *Neuroreport* 2001;12:1567–69 CrossRef Medline

Reproducibility of Deep Gray Matter Atrophy Rate Measurement in a Large Multicenter Dataset

A. Meijerman, H. Amiri, M.D. Steenwijk, M.A. Jonker, R.A. van Schijndel, K.S. Cover, and H. Vrenken, for the Alzheimer's Disease Neuroimaging Initiative

ABSTRACT

BACKGROUND AND PURPOSE: Precise in vivo measurement of deep GM volume change is a highly demanded prerequisite for an adequate evaluation of disease progression and new treatments. However, quantitative data on the reproducibility of deep GM structure volumetry are not yet available. In this paper we aim to investigate this reproducibility using a large multicenter dataset.

MATERIALS AND METHODS: We have assessed the reproducibility of 2 automated segmentation software packages (FreeSurfer and the FMRIB Integrated Registration and Segmentation Tool) by quantifying the volume changes of deep GM structures by using back-to-back MR imaging scans from the Alzheimer Disease Neuroimaging Initiative's multicenter dataset. Five hundred sixty-two subjects with scans at baseline and 1 year were included. Reproducibility was investigated in the bilateral caudate nucleus, putamen, amygdala, globus pallidus, and thalamus by carrying out descriptives as well as multilevel and variance component analysis.

RESULTS: Median absolute back-to-back differences varied between GM structures, ranging from 59.6–156.4 μL for volume change, and 1.26%–8.63% for percentage volume change. FreeSurfer had a better performance for the outcome of longitudinal volume change for the bilateral amygdala, putamen, left caudate nucleus ($P < .005$), and right thalamus ($P < .001$). For longitudinal percentage volume change, Freesurfer performed better for the left amygdala, bilateral caudate nucleus, and left putamen ($P < .001$). Smaller limits of agreement were found for FreeSurfer for both outcomes for all GM structures except the globus pallidus. Our results showed that back-to-back differences in 1-year percentage volume change were approximately 1.5–3.5 times larger than the mean measured 1-year volume change of those structures.

CONCLUSIONS: Longitudinal deep GM atrophy measures should be interpreted with caution. Furthermore, deep GM atrophy measurement techniques require substantially improved reproducibility, specifically when aiming for personalized medicine.

ABBREVIATIONS: AD = Alzheimer disease; ADNI = Alzheimer Disease Neuroimaging Initiative; BTB = back-to-back; FIRST = FMRIB Integrated Registration and Segmentation Tool; LoA = limit of agreement; MCI = mild cognitive impairment; SEM = standard error of measurement

Neurodegeneration occurs in Alzheimer disease (AD). The process is characterized by neuronal loss and axonal and synaptic degeneration.[1-4] Growing evidence reveals that this process happens within early phases of the disease and before making

Received June 16, 2017; accepted after revision August 28.

From the Departments of Radiology and Nuclear Medicine (A.M., H.A., M.D.S., R.A.v.S., K.S.C., H.V.) and Epidemiology and Biostatistics (A.M., M.A.J.), Vrije University Medical Center, Amsterdam, The Netherlands; and the Neuroscience Research Center, Institute of Neuropharmacology (H.A.), Kerman University of Medical Sciences, Kerman, Iran.

This work was supported by the Alzheimer Disease Neuroimaging Initiative (ADNI) (National Institutes of Health grant U01 AG024904) and Department of Defense ADNI (Department of Defense award number W81XWH-12-2-0012). ADNI is funded by the National Institute on Aging, the National Institute of Biomedical Imaging and Bioengineering, and through generous contributions from the following: AbbVie, Alzheimer's Association; Alzheimer's Drug Discovery Foundation; Araclon Biotech; BioClinica, Inc.; Biogen; Bristol-Myers Squibb Company; CereSpir, Inc.; Eisai Inc.; Elan Pharmaceuticals, Inc.; Eli Lilly and Company; EuroImmun; F. Hoffmann-La Roche Ltd and its affiliated company Genentech, Inc.; Fujirebio; GE Healthcare; IXICO Ltd.; Janssen Alzheimer Immunotherapy Research & Development, LLC.; Johnson & Johnson Pharmaceutical Research & Development LLC.; Lumosity; Lundbeck; Merck & Co., Inc.; Meso Scale Diagnostics, LLC.; NeuroRx Research; Neurotrack Technologies; Novartis Pharmaceuticals Corporation; Pfizer Inc.; Piramal Imaging; Servier; Takeda Pharmaceutical Company; and Transition Therapeutics. The Canadian Institutes of Health Research is providing funds to support ADNI clinical sites in Canada. Private sector contributions are facilitated by the Foundation for the National Institutes of Health (www.fnih.org). The grantee organization is the Northern California Institute for Research and Education, and the study is coordinated by the Alzheimer Disease Cooperative Study at the University of California, San Diego. ADNI data are disseminated by the Laboratory for Neuro Imaging at the University of Southern California.

A. Meijerman and H. Amiri contributed equally to this work.

Data used in preparation of this article were obtained from the Alzheimer's Disease Neuroimaging Initiative (ADNI) data base (adni.loni.usc.edu). As such, the investigators within the ADNI contributed to the design and implementation of ADNI and/or provided data, but did not participate in the analysis or writing of this report. A complete listing of ADNI investigators can be found at: http://adni.loni.usc.edu/wp-content/uploads/how_to_apply/ADNI_Acknowledgement_List.pdf.

Please address correspondence to Houshang Amiri, PhD, Vrije University Medical Center, De Boelelaan 1117, 1081 HV Amsterdam; e-mail: amiri.houshang@gmail.com

Indicates open access to non-subscribers at www.ajnr.org

http://dx.doi.org/10.3174/ajnr.A5459

a clinical diagnosis.[5,6] The development of neurodegeneration on a large scale during disease leads to loss of tissue volume (the so-called atrophy), which can be quantified by using structural MR imaging.

Atrophy has been found to be associated with impaired neurologic and neurocognitive performance.[7-10] More recently, research revealed that deep GM atrophy specifically plays an important role in the characterization, course, and progression of AD[11-17] and in other diseases like MS[18-20] and Parkinson disease.[21-23] Measurements of deep GM atrophy could therefore be of importance in the evaluation of neuroprotective treatment (eg, in investigating drug efficacy). Currently, a growing number of clinical trials are incorporating brain volume changes as an early biomarker.[24] To use atrophy as a reliable biomarker for the extent of neurodegeneration and axonal damage, the precision and reproducibility of volume change measurement techniques should be evaluated. Of note, having precise and reproducible methods would increase statistical power, which reduces sample sizes for detecting effects in clinical trials.

Among automated tissue segmentation software for deep GM structures, FreeSurfer (http://surfer.nmr.mgh.harvard.edu)[25] and the FMRIB Integrated Registration and Segmentation Tool (FIRST; part of FSL, http://fsl.fmrib.ox.ac.uk/fsl/fslwiki/FIRST)[26-29] are freely available and widely used. Whereas FreeSurfer has a longitudinal pipeline by which multiple time points can be analyzed, FIRST is a cross-sectional technique that analyses only a single time point. Despite the importance of the measurement of deep GM atrophy rate, little is known about reproducibility of the measurements over time in large multicenter datasets.

In this paper, to assess reproducibility, we used data from the Alzheimer Disease Neuroimaging Initiative (ADNI) study[30] acquired at 1.5T, including 2 back-to-back (BTB) 3D T1-weighted images at each time point.[31] We quantified reproducibility by using BTB differences of 1-year volume change and of percentage volume change for the bilateral amygdala, caudate nucleus, globus pallidus, putamen, and thalamus. To this end, we used 3 different statistical methods. First, we used descriptive statistics by which median absolute differences are reported. This method is frequently used, but its outcome measures cannot be compared statistically between methods. Therefore, we additionally used analytical statistics based on the difference in the regression coefficient. Lastly, we used the method of determination of the standard error of measurement, which very precisely maps reproducibility by modeling different components related to variability in BTB measures.

MATERIALS AND METHODS

ADNI Dataset

Data used in this study were taken from the ADNI1 study.[30] The primary goal of the ADNI has been to test whether serial MR imaging, PET, other biologic markers, and clinical and neuropsychologic assessments can be combined to measure the progression of mild cognitive impairment (MCI) and early AD.

A total of 800 included subjects from 55 sites in the US and Canada were enrolled between 2004 and 2010 and were followed up in a 2- to 3-year time interval. Written informed consent was obtained before each baseline visit. Inclusion criteria were age between 55–90 years, having a study partner able to provide an independent evaluation of functioning, and speaking either English or Spanish. All subjects were willing and able to undergo all test procedures including neuroimaging and agreed to longitudinal follow-up. Exclusion criteria were specific psychoactive medications. For control subjects, inclusion criteria were as follows: Mini-Mental State Examination scores between 24–30 (inclusive), a clinical dementia rating of 0, and no history of depression, MCI, and dementia. The age range was matched to that of MCI and AD subjects. For subjects with MCI, inclusion criteria were as follows: Mini-Mental State Examination scores between 24–30 (inclusive), a memory complaint, objective memory loss measured by education-adjusted scores on the Wechsler Memory Scale Logical Memory II, a clinical dementia rating of 0.5, absence of high levels of impairment in other cognitive domains, essentially preserved activities of daily living, and an absence of dementia. For subjects with mild AD, inclusion criteria were as follows: Mini-Mental State Examination scores between 20–26 (inclusive), clinical dementia rating of 0.5 or 1.0, and meets National Institute of Neurological and Communicative Disorders and Stroke/Alzheimer's Disease and Related Disorders Association criteria for probable AD. A standardized imaging protocol carried out over qualified sites included the acquisition of 2 sequential 3D T1-weighted MPRAGE scans (ie, BTB) at baseline and at the 1-year study time point.[32]

Subjects

Our study involved 562 subjects who had exactly 2 MPRAGE scans acquired at both the baseline and at 1 year, with 3D T1-weighted BTB images acquired at both time points at 1.5T. Three hundred twenty-two (57.3%) subjects were male and 240 (42.7%) were female. The median age at baseline was 75.3 years (interquartile range, 8.7). One hundred fourteen (30.4%) were diagnosed with probable AD, 277 (49.3%) with MCI, and 171 (20.3%) were healthy controls. Data were requested after written compliance to the ADNI data use agreement and data sharing policy and were obtained from the ADNI data image and data archive LONI (Laboratory of Neuro Imaging; http://adni.loni.usc.edu). All data were received anonymized by ADNI procedures and with assignment of a unique ADNI study number to subjects.

Volumetric Measurements

MR image acquisition included standard automated adjustments with no additional postprocessing such as intensity nonuniformity correction or gradient warp correction. DICOM images of subjects were converted to NIfTI format for further processing by using dicom2nifti (http://www.cabiatl.com/mricro/mricron/dcm2nii.html).

Automated deep GM segmentations were performed on the NCAgrid (a 64-bit Linux computer cluster with 512 cores) by using 2 freely available and frequently used software packages: FreeSurfer version 5.3.0[25] and FIRST implemented in FSL version 5.0.8.[26-29]

For FreeSurfer, images were segmented by using the longitudinal image processing stream, which analyzes 2 time points simultaneously to improve the estimation of volumes and volume

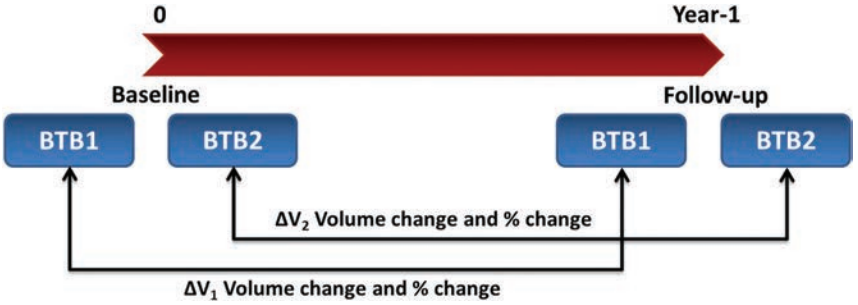

FIG 1. Scheme showing both BTB scans at each time point and calculation of the volume change and percentage volume change.

change. Within FIRST, the default parameters were used.[25] Segmentations were carried out for both BTB scans at baseline and at the 1-year study time point, leading to a total number of 134,880 segmentations.

Outcome Measures

The 2 derived main outcome measures in our study were the longitudinal volume change and percentage volume change. The volume change (ΔV, in μL) was calculated for each longitudinal scan pair (two BTB1 and two BTB2) as:

$$\Delta V_1 = V^{\text{Year 1(BTB1)}} - V^{\text{Baseline(BTB1)}}$$

and

$$\Delta V_2 = V^{\text{Year 1(BTB2)}} - V^{\text{Baseline(BTB2)}}$$

The percentage volume change for both ΔV_1 and ΔV_2 was calculated separately as:

$$100 \times (\Delta V \div V^{\text{Baseline}})$$

Fig 1 schematically shows study time points and the calculation of the volume change and percentage volume change by using BTB scans.

In both BTB scans (BTB1 and BTB2), at each time point, the brain is assumed to be identical; therefore $\Delta V_2 - \Delta V_1$ can be used as a measure of reproducibility for each outcome measure (ie, absolute and percentage volume change).

Statistical Analysis

Data distribution and missing data were carefully checked before all statistical analyses. Reproducibility according to BTB scans is reported by using 3 methods of analysis for both software packages. First, we used median absolute BTB differences. Second, we compared the absolute BTB differences based on differences in the regression coefficient (effect size). This involved the construction of separate linear multilevel models for each deep GM structure and each hemisphere. Data were natural log-transformed before analysis to avoid fitting the model to a skewed distribution of our data. In our multilevel models, a random intercept was chosen to correct for the dependency of observations clustering within each same subject. Variance around the intercept was assumed to be normally distributed. Statistics were reported as *P* values, back-transformed effect sizes, and their corresponding 95% confidence intervals.

Finally, as a third method, we assessed reproducibility by determining the limit of agreement (LoA), which is considered as a very sensitive method of analysis.[33-35] This was done by constructing separate linear multilevel models for each deep GM structure summing the variance components attributable to BTB scans to determine the level of random bias in both outcome variables. Because the method is based on variance, contrary to the first 2 methods, it uses the original (nonabsolute) values of each volume change analysis. Fixed factors in our multilevel model included hemisphere, software package (FreeSurfer or FIRST), sex, diagnostic group, and all possible interactions between these variables. Random factors in the model included hemispheres, software package, time point, all possible interactions between them, and the use of a random intercept on the subject level. Nesting of the factors was carried out according to the method described by Mulder and colleagues.[35] We used restricted maximum likelihood as the estimating procedure in all multilevel analyses and assumed an independent covariance matrix. The best fitting model to the data was then chosen based on the lowest Akaike information criterion. Interscan standard errors of measurement (SEMs) attributable to BTB scans for each software package were calculated by summing the random variance components of the multilevel models related to BTB (ie, the variance attributable to the interaction between the random chosen variables and time point; see Equation 1 below). The separate variance components required to sum SEM were assumed to be independent of each other. The variance component containing the highest interaction (ie, σ^2 [time point $\times$ hemisphere $\times$ software package) was considered to be completely part of the error variance in our calculations. Furthermore, all variance components containing a time point were allowed to vary within software package.

1) $$\text{SEM}^2 = \sigma^2(\text{time point}) + \sigma^2(\text{time point} \times \text{hemisphere}) + \sigma^2(\text{time point} \times \text{software package}) + \sigma^2(\text{error})$$

Then, LoA, as a measure of reproducibility, was derived and reported from the SEM for each software package by using Equation 2. The lower the LoA, the better the reproducibility.

2) $$\text{LoA} = \pm 1.96 \times \sqrt{2} \times \text{SEM}$$

The quality of all MR images was inspected visually. Regarding the quality of the segmentation, we identified severe outliers based on implausible results of the outcome measures. Implausible outliers in terms of longitudinal volume change or percentage longitudinal volume change were considered to be a consequence of a failure in segmentation. An implausible outlier was identified if the longitudinal BTB difference was more than 25% of its corresponding baseline volume. We created separate linear multilevel models with and without implausible large outliers to evaluate their impact on our SEM. These outliers were treated as missing data in our final analysis. In addition, we compared the number of outliers between FreeSurfer and FIRST in all deep GM structures. This was carried out by using the binominal

Table 1: Nonannualized atrophy rates for deep GM structures for each hemisphere per group

GM Structure	Software	Hemisphere	Atrophy Rate for Control Patients, %	Atrophy Rate for Patients with MCI, %	Atrophy Rate for Patients with AD, %
Caudate nucleus	FreeSurfer	Left	−0.33	−0.95	−1.63
	FIRST	Left	−0.84	−0.78	−1.72
	FreeSurfer	Right	−0.35	−0.78	−1.58
	FIRST	Right	−1.07	−0.66	−1.42
Putamen	FreeSurfer	Left	−0.04	−0.69	−2.50
	FIRST	Left	−0.44	−1.20	−2.16
	FreeSurfer	Right	−0.37	−0.73	−1.72
	FIRST	Right	−0.61	−1.11	−1.71
Amygdala	FreeSurfer	Left	−0.56	−2.70	−4.67
	FIRST	Left	−0.90	−1.59	−4.36
	FreeSurfer	Right	−0.70	−2.25	−3.95
	FIRST	Right	−0.38	−3.60	−3.57
Globus pallidus	FreeSurfer	Left	−0.45	0.25	0.58
	FIRST	Left	−0.10	−0.92	−1.43
	FreeSurfer	Right	−0.11	−0.38	−0.50
	FIRST	Right	−0.67	−0.90	−1.87
Thalamus	FreeSurfer	Left	−0.88	−1.69	−2.06
	FIRST	Left	−0.90	−0.85	−1.05
	FreeSurfer	Right	−0.78	−1.38	−2.29
	FIRST	Right	−0.62	−0.71	−0.94

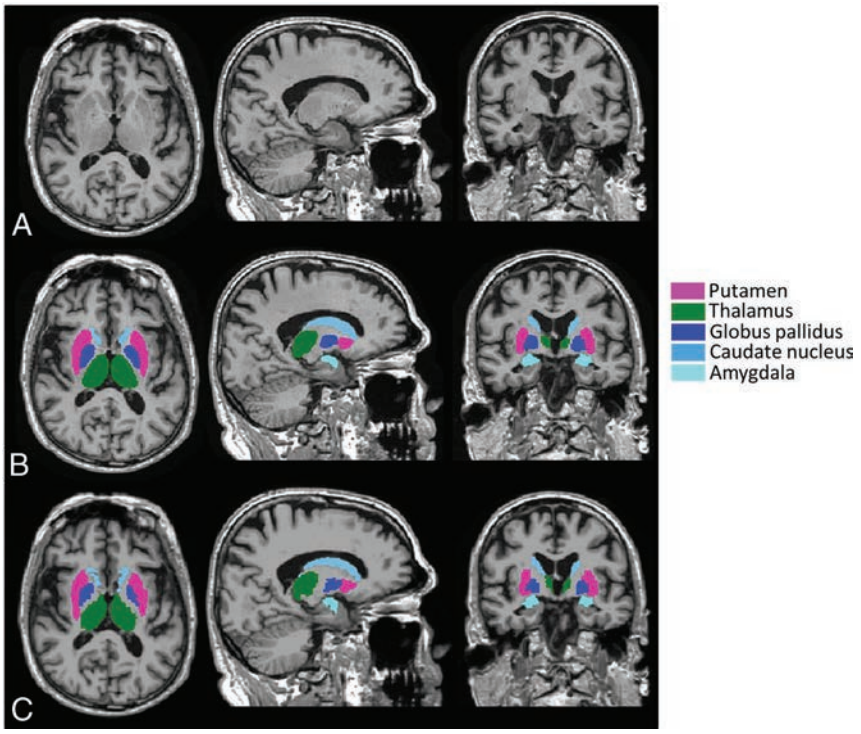

FIG 2. *A*, An example of a 3D T1-weighted image segmented with *B*, FIRST and *C*, FreeSurfer.

test, which tested an equal distribution of the number of outliers for both FreeSurfer and FIRST.

For illustrating agreement, Bland-Altman plots were created. A Bland-Altman plot represents the difference in BTB of an outcome measure versus its mean.[36,37] We created plots for both outcome measures of FreeSurfer and FIRST, with and without implausible outliers. In this paper, for this method, we present the results of analysis performed on data excluding implausible outliers.

All statistical analysis was carried out by using SPSS version 21 (IBM, Armonk, New York) except for the modeling of data to obtain SEM and derived LoAs, which was carried out by using SAS Studio version 3.4 (SAS Institute, Cary, North Carolina). The level of significance in our models was set to 0.05 (5%).

RESULTS

Median follow-up time ($\chi^2 = 1.566$; *df*, 2; $P = .45$) and age ($\chi^2 = 0.992$; *df*, 2; $P = .60$) did not differ between the 3 study groups. To enable a direct comparison of reproducibility metrics to the measured (percentage) volume change values, nonannualized median atrophy rates are presented in Table 1. As expected, atrophy rates were generally higher in patients with AD compared with patients with MCI and control patients, with the highest rates found for the amygdala. For 2 different male healthy control patients, FreeSurfer and FIRST segmentation failed. Therefore, for each software package, 561 subjects were included in the longitudinal data analysis. A typical example of FreeSurfer and FIRST segmentations is shown in Fig 2. BTB differences are illustrated by the example in Fig 3, which shows Bland-Altman plots of BTB difference in longitudinal volume change for the left caudate nucleus for both FreeSurfer and FIRST, excluding the improbable outliers.

Descriptive Statistics

Descriptive statistics for each hemisphere for each deep GM structure for measuring longitudinal volume change and longitudinal percentage volume change are presented in Tables 2 and 3, respectively. Based on these reported descriptive statistics (median absolute BTB differences with corresponding 90th percentile indicating spread), as expected, the smaller

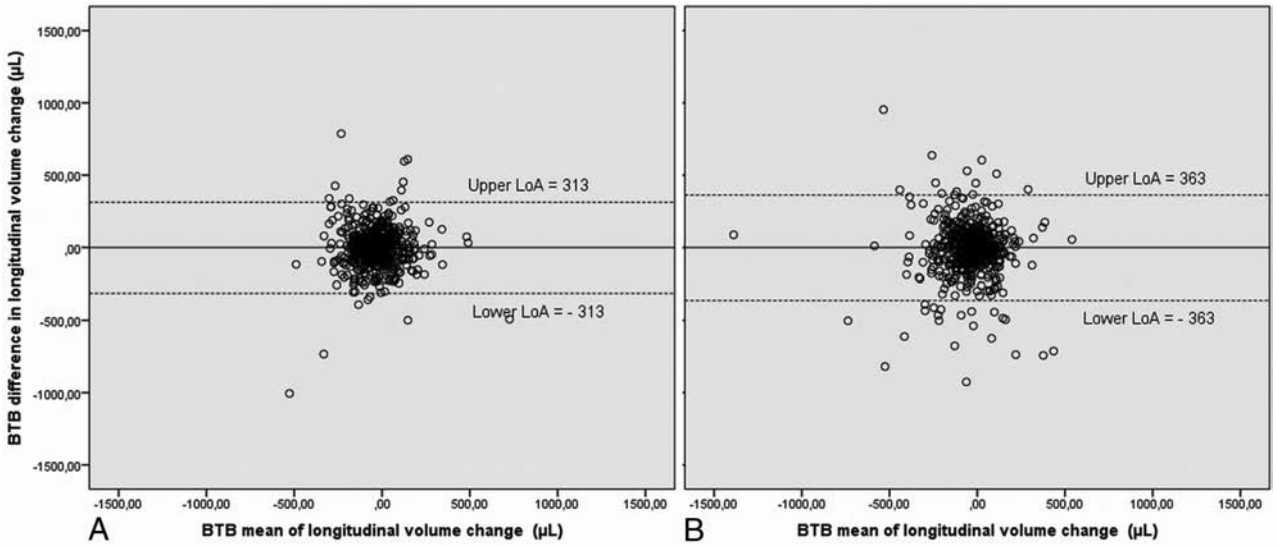

FIG 3. Bland-Altman plots for the left caudate nucleus, presented for the outcome measures of BTB difference in longitudinal volume change, to illustrate agreement for *A*, FreeSurfer and *B*, FIRST. Plots show the difference between the 2 measurements (ie, the "BTB difference") along the vertical axis versus the mean of the 2 measurements along the horizontal axis. LoAs for FreeSurfer are obviously smaller (ie, better reproducibility) than those of FIRST.

Table 2: Median absolute BTB difference in longitudinal volume change for each deep GM structure for both hemispheres. Effect size, corresponding 95% confidence CI, and *P* values based on linear multilevel modelling are also presented

GM Structure	Software	Hemisphere	Median Absolute Difference, µl	90th Percentile	*P* Value	Effect	95% CI Lower	95% CI Upper
Caudate nucleus	FreeSurfer	Left	71.80	219.88	.003	0.82	0.72	0.93
	FIRST	Left	85.84	442.31				
	FreeSurfer	Right	74.20	253.22	.09	0.90	0.79	1.02
	FIRST	Right	87.26	264.69				
Putamen	FreeSurfer	Left	117.00	315.58	<.001	0.73	0.64	0.84
	FIRST	Left	156.39	412.49				
	FreeSurfer	Right	114.30	326.22	.003	0.77	0.64	0.91
	FIRST	Right	142.44	406.71				
Amygdala	FreeSurfer	Left	63.50	173.60	<.001	0.76	0.66	0.87
	FIRST	Left	84.38	260.14				
	FreeSurfer	Right	77.00	196.54	<.001	0.73	0.64	0.83
	FIRST	Right	101.25	331.70				
Globus pallidus	FreeSurfer	Left	59.60	180.56	.75	1.03	0.87	1.22
	FIRST	Left	62.05	185.44				
	FreeSurfer	Right	60.00	164.38	.48	0.96	0.85	1.08
	FIRST	Right	60.06	200.23				
Thalamus	FreeSurfer	Left	100.90	315.08	.10	1.13	0.98	1.30
	FIRST	Left	91.76	262.30				
	FreeSurfer	Right	88.20	243.46	<.001	0.78	0.69	0.89
	FIRST	Right	114.81	308.71				

deep GM structures tended to have smaller BTB differences in longitudinal volume change and larger BTB differences in percentage volume change.

Effect Sizes

Effect sizes, based on the difference in the regression coefficient, corresponding *P* values, and 95% confidence intervals of comparison between segmentation by using FreeSurfer and FIRST are presented in Tables 2 and 3. The effect size in these Tables can be interpreted as the mean improvement of reproducibility in both longitudinal outcome variables when switching from FSL to FreeSurfer. For the outcome measure of the absolute BTB difference in longitudinal volume change, FreeSurfer performed significantly better than FIRST for the left and right amygdala (both $P < .001$), left caudate nucleus ($P = .003$), left ($P < .001$) and right ($P = .003$) putamen, and right thalamus ($P < .001$). Concerning the outcome measure of the absolute BTB difference in longitudinal percentage volume change, FreeSurfer performed significantly better than FIRST for the left amygdala ($P = .02$), left ($P = .002$) and right ($P = .004$) caudate nucleus, and left putamen ($P < .001$). For the right amygdala and putamen, results are not presented because of lack of validity caused by failures in model fit.

Outliers

For the right amygdala, number of outliers were significantly different in all groups, when comparing 2 segmentation software packages ($P < .002$). This difference was not significant for other structures. Table 4 shows the number of excluded cases (extreme

Table 3: Median absolute BTB difference in longitudinal percentage volume change for each deep GM structure for both hemispheres. Effect size, corresponding 95% CI and *P* values based on linear multilevel modelling are also presented

GM Structure	Software	Hemisphere	Median Absolute Difference, %	90th Percentile	*P* Value	Effect	95% CI Lower	95% CI Upper
Caudate nucleus	FreeSurfer	Left	2.04	6.04	.002	0.09	0.02	0.41
	FIRST	Left	2.71	13.37				
	FreeSurfer	Right	2.08	6.92	.004	0.16	0.05	0.55
	FIRST	Right	2.63	8.15				
Putamen[a]	FreeSurfer	Left	2.48	6.87	<.001	0.07	0.02	0.29
	FIRST	Left	3.43	9.51				
	FreeSurfer	Right	2.46	6.77	NA	NA	NA	NA
	FIRST	Right	3.32	9.48				
Amygdala[a]	FreeSurfer	Left	6.14	17.64	.02	0.07	0.01	0.69
	FIRST	Left	6.60	21.29				
	FreeSurfer	Right	6.24	16.52	NA	NA	NA	NA
	FIRST	Right	8.63	28.95				
Globus pallidus	FreeSurfer	Left	4.32	13.04	.49	1.63	0.40	6.63
	FIRST	Left	3.65	10.92				
	FreeSurfer	Right	4.30	12.22	.94	0.95	0.29	3.17
	FIRST	Right	3.54	11.75				
Thalamus	FreeSurfer	Left	1.52	4.61	.33	0.62	0.23	1.64
	FIRST	Left	1.26	3.53				
	FreeSurfer	Right	1.41	3.82	.05	0.33	0.11	1.01
	FIRST	Right	1.59	4.31				

Note:—NA indicates not available.

[a] For the right amygdala and putamen, results are not presented because of lack of validity caused by failures in the model fit.

Table 4: Number and proportion of excluded cases (extreme outliers) presented for each software for each deep GM structure

GM Structure	Software	Number of Outliers	% Within Segmentation	% Within Total Sample
Caudate nucleus	FreeSurfer	1	2.8	0.02
	FIRST	35	97.2	0.77
Putamen	FreeSurfer	0	0.0	0.00
	FIRST	37	100.0	0.82
Amygdala	FreeSurfer	33	17.8	0.73
	FIRST	152	82.2	3.38
Globus pallidus	FreeSurfer	21	39.6	0.46
	FIRST	32	60.4	0.71
Thalamus	FreeSurfer	0	0.0	0.00
	FIRST	29	100.0	0.64

outliers) for each deep GM structure and their proportion within each segmentation software used and the total sample size. The proportion of excluded cases was relatively small in the total sample of data; however it turned out to be more frequent when using FIRST compared with FreeSurfer.

Limits of Agreement

Based on our third method to evaluate reproducibility, values for the LoAs of FreeSurfer and FIRST derived from linear multilevel modeling are reported in Table 5. This analysis showed a visible trend for a better performance of FreeSurfer for both the measurement of longitudinal volume change and longitudinal percentage volume change, except for the globus pallidus, for which FIRST performed better. There was also a trend for an influence of the typical cross-sectional volume of a structure. Smaller deep GM structures showed smaller LoAs for longitudinal volume change measurement and larger LoAs for longitudinal percentage volume change.

DISCUSSION

Brain atrophy reflecting neurodegeneration and neuroaxonal damage is known to be an important characteristic of diseases like AD and MS. In the current study, we investigated the reproducibility of volume change and percentage volume change measurement of 5 deep GM structures in a large multicenter dataset. To this end, we used 2 frequently used segmentation software packages, FreeSurfer and FIRST.

It is worth mentioning that FreeSurfer does provide a longitudinal pipeline to analyze multiple time points whereas FIRST only offers a cross-sectional analysis. Strikingly, for both software packages, the reproducibility error was comparable with the measured atrophy rates. Our results showed that BTB differences in 1-year percentage volume change (ranging from 1.26% for left thalamus to 8.63% for right amygdala) were roughly 1.5–3.5 times larger than the average atrophy rates of these deep GM structures (approximately 0.9% and 2.5%, respectively).

We used 3 different statistical methods that complement each other. Although reporting median and 90th percentile absolute differences alone is an easy and robust way to interpret results, statistical comparison in outcome measurements between methods of segmentation is not possible. Therefore, we next performed additional analytical statistics based on the difference in the regression coefficient. Finally, we used the method of determination of SEM, which provides a very precise way to map reproducibility and allows modeling of different sources of variability. This method is also proposed to be applied in determining agreement to map measurement error, an important measurement property in medicine.[33,34,38] The sensitivity of this method is mainly attributable to the determination of specific variance components of a model, from which LoAs can be determined. In addition, the SEM method is a more suitable way for determining specific random variance in an outcome measure, which could provide additional information of the estimation of variance in a population. Using a large ADNI dataset makes such estimations more accurate. Another advantage of this method is that it is based on spread, contrary to the second regression-based method, and instead of

Table 5: SEMs and LoAs derived from variance component analysis out of a linear multilevel model for each deep GM structure

GM Structure	Software	SEM Longitudinal Volume Change, μl	LoA, μl	SEM % Longitudinal Volume Change	LoA, %
Caudate nucleus	FreeSurfer	112.89	312.92	2.90	8.05
	FIRST	125.83	348.79	3.76	10.42
Putamen	FreeSurfer	150.64	417.54	2.98	8.27
	FIRST	181.05	501.85	3.86	10.69
Amygdala	FreeSurfer	78.14	216.59	7.05	19.54
	FIRST	146.23	405.33	7.86	21.77
Globus pallidus	FreeSurfer	80.33	222.67	5.30	14.69
	FIRST	74.22	205.74	4.64	12.87
Thalamus	FreeSurfer	128.02	354.86	1.87	5.17
	FIRST	142.53	395.07	1.96	5.43

signed or absolute BTB differences, the clinical variables of interest (eg, volume change, percentage volume change) are modeled directly. This method for determining LoAs, however, is strongly affected by large outliers, and its procedure is much more costly and time-consuming.

Both methods of analytical statistics, namely determination of SEM with derived LoAs and the method based on difference in the regression coefficient, were carried out by using linear multilevel modeling. The general advantages of linear multilevel analysis are its flexibility in dealing with missing data, the ability to objectively include factors and covariates into 1 whole model, and a necessary applied correction for the dependency of data for measurements within the same subjects.[39,40]

For both software packages, the reproducibility error was substantial compared with the measured atrophy (see Table 1 for the measured atrophy). However, FreeSurfer had better reproducibility compared with FIRST within the whole longitudinal outcome spectrum (except for globus pallidus), though the differences were not very large. The reproducibility was dependent on the structure baseline volume and also on the desired outcome measure (ie, volume change or percentage volume change). For example, compared with larger structures, smaller GM structures had smaller reproducibility errors for volume change and larger reproducibility errors for percentage volume change. For the structures measured in our study, when measuring the longitudinal volume change, the larger GM structures (putamen and thalamus) had BTB differences roughly twice as large as smaller structures (amygdala, globus pallidus), whereas for the outcome of longitudinal percentage volume change, this was reversed: here, larger structures outperformed smaller structures by approximately a factor of 5. A study on cross-sectional volume measurement by using FreeSurfer,[41] reported generally larger relative scan–rescan errors for smaller structures. Such variability could cause poorer reproducibility of longitudinal volume change for smaller structures.

This poor reproducibility could be linked to the poor delineation of such brain structures by using automated software. To improve this, increase in the SNR and contrast-to-noise ratio (eg, by increasing the field strength or by further optimization of the acquisition) are recommended. In addition, multimodal segmentation, which includes other tissue information such as diffusion and susceptibility, could increase the accuracy and reproducibility of the segmentation and volume estimation.

Our study had some limitations. Because of the very large number of segmentations performed, visual inspection of segmentation results was impractical. However, we used an automated method to exclude gross segmentation errors by using the BTB information. The very few occurring implausible outliers in our outcome measures were assumed to be caused by incorrect segmentations of 1 or more scans of that subject. To identify such gross outliers without excluding true atrophies, we applied a very wide cutoff criterion of 25% in longitudinal volume change or in percentage volume change compared with the baseline. As expected, the LoAs were very large when including the improbable outliers.

CONCLUSIONS

We provided quantitative information for 5 deep GM structures by using the widely used segmentation algorithms FreeSurfer and FIRST by 3 different methods of analysis. In general, FreeSurfer performance was better than that of FIRST. However, our results showed that BTB differences in 1-year percentage volume change were roughly 1.5–3.5 times larger than the atrophy rates of those deep GM structures. This suggests that longitudinal deep GM atrophy measures should be interpreted with caution. Finally, to provide a reliable additional biomarker, deep GM atrophy measurement techniques require substantially improved reproducibility, specifically when aiming for personalized medicine.

Disclosures: Marianne Jonker—*UNRELATED*: *Consulting Fee or Honorarium:* Vrije University Medical Center, Department of Epidemiology and Biostatistics, *Comments*: as a common practice, our department is paid for doing consultancy*. Ronald van Schijndel—*OTHER RELATIONSHIPS*: Image Analysis Center (IAC), *Comments*: partly working for the IAC, which is a contract research organization of the Vrije University Medical Center. Keith Cover—*UNRELATED*: *Grants/Grants Pending*: European Community FP7 Project, *Comments*: funded by the Neugrid4you project (grant agreement 2835262) from 2011 to 2015; studied methods for measuring atrophy of the brain in MRI*. Hugo Vrenken—*UNRELATED*: *Grants/Grants Pending*: Novartis Pharma, *Comments*: brain atrophy in MS; Teva Europe, *Comments*: brain atrophy in MS; Merck Serono, *Comments*: brain atrophy and lesions in MS*. *Money paid to the institution.

REFERENCES

1. Burns JM, Morris JC. **Neuropathology of Alzheimer's disease, nondemented aging and MCI.** In: *Mild Cognitive Impairment and Early Alzheimer's Disease: Detection and Diagnosis.* Hoboken: John Wiley & Sons; 2008:17–34
2. Iqbal K, Liu F, Gong CX, et al. **Mechanisms of tau-induced neurodegeneration.** *Acta Neuropathol* 2009;118:53–69 CrossRef Medline
3. Overk CR, Masliah E. **Pathogenesis of synaptic degeneration in Alzheimer's disease and Lewy body disease.** *Biochem Pharmacol* 2014; 88:508–16 CrossRef Medline

4. Stelmashook EV, Isaev NK, Genrikhs EE, et al. **Role of zinc and copper ions in the pathogenetic mechanisms of Alzheimer's and Parkinson's diseases.** *Biochemistry (Mosc)* 2014;79:391–96 CrossRef Medline
5. Mufson EJ, Binder L, Counts SE, et al. **Mild cognitive impairment: pathology and mechanisms.** *Acta Neuropathol* 2012;123:13–30 CrossRef Medline
6. Stephan BC, Hunter S, Harris D, et al. **The neuropathological profile of mild cognitive impairment (MCI): a systematic review.** *Mol Psychiatry* 2012;17:1056–76 CrossRef Medline
7. Maghzi AH, Revirajan N, Julian LJ, et al. **Magnetic resonance imaging correlates of clinical outcomes in early multiple sclerosis.** *Mult Scler Relat Disord* 2014;3:720–27 CrossRef Medline
8. Rudick RA, Fisher E, Lee JC, et al. **Use of the brain parenchymal fraction to measure whole brain atrophy in relapsing-remitting MS. Multiple Sclerosis Collaborative Research Group.** *Neurology* 1999;53:1698–704 CrossRef Medline
9. Sluimer JD, van der Flier WM, Karas GB, et al. **Whole-brain atrophy rate and cognitive decline: longitudinal MR study of memory clinic patients.** *Radiology* 2008;248:590–98 CrossRef Medline
10. Vercellino M, Masera S, Lorenzatti M, et al. **Demyelination, inflammation, and neurodegeneration in multiple sclerosis deep gray matter.** *J Neuropathol Exp Neurol* 2009;68:489–502 CrossRef Medline
11. Jiji S, Smitha KA, Gupta AK, et al. **Segmentation and volumetric analysis of the caudate nucleus in Alzheimer's disease.** *Eur J Radiol* 2013;82:1525–30 CrossRef Medline
12. Leung KK, Bartlett JW, Barnes J, et al. **Cerebral atrophy in mild cognitive impairment and Alzheimer disease: rates and acceleration.** *Neurology* 2013;80:648–54 CrossRef Medline
13. Macfarlane MD, Looi JC, Walterfang M, et al. **Executive dysfunction correlates with caudate nucleus atrophy in patients with white matter changes on MRI: a subset of LADIS.** *Psychiatry Res* 2013;214:16–23 CrossRef Medline
14. Miller MI, Younes L, Ratnanather JT, et al. **Amygdalar atrophy in symptomatic Alzheimer's disease based on diffeomorphometry: the BIOCARD cohort.** *Neurobiol Aging* 2015;36 Suppl 1:S3–S10 CrossRef Medline
15. Skup M, Zhu H, Wang Y, et al. **Sex differences in grey matter atrophy patterns among AD and aMCI patients: results from ADNI.** *Neuroimage* 2011;56:890–906 CrossRef Medline
16. Štěpán-Buksakowska I, Szabó N, Hořínek D, et al. **Cortical and subcortical atrophy in Alzheimer disease: parallel atrophy of thalamus and hippocampus.** *Alzheimer Dis Assoc Disord* 2014;28:65–72 CrossRef Medline
17. Yi HA, Möller C, Dieleman N, et al. **Relation between subcortical grey matter atrophy and conversion from mild cognitive impairment to Alzheimer's disease.** *J Neurol Neurosurg Psychiatry* 2016;87:425–32 CrossRef Medline
18. Batista S, Zivadinov R, Hoogs M, et al. **Basal ganglia, thalamus and neocortical atrophy predicting slowed cognitive processing in multiple sclerosis.** *J Neurol* 2012;259:139–46 CrossRef Medline
19. Ramasamy DP, Benedict RH, Cox JL, et al. **Extent of cerebellum, subcortical and cortical atrophy in patients with MS: a case-control study.** *J Neurol Sci* 2009;282:47–54 CrossRef Medline
20. Shiee N, Bazin PL, Zackowski KM, et al. **Revisiting brain atrophy and its relationship to disability in multiple sclerosis.** *PLoS One* 2012;7:e37049 CrossRef Medline
21. Hanganu A, Bedetti C, Degroot C, et al. **Mild cognitive impairment is linked with faster rate of cortical thinning in patients with Parkinson's disease longitudinally.** *Brain* 2014;137:1120–29 CrossRef Medline
22. Mak E, Bergsland N, Dwyer MG, et al. **Subcortical atrophy is associated with cognitive impairment in mild Parkinson disease: a combined investigation of volumetric changes, cortical thickness, and vertex-based shape analysis.** *AJNR Am J Neuroradiol* 2014;35:2257–64 CrossRef Medline
23. Nemmi F, Sabatini U, Rascol O, et al. **Parkinson's disease and local atrophy in subcortical nuclei: insight from shape analysis.** *Neurobiol Aging* 2015;36:424–33 CrossRef Medline
24. Kishi T, Matsunaga S, Oya K, et al. **Protection against brain atrophy by anti-dementia medication in mild cognitive impairment and Alzheimer's disease: meta-analysis of longitudinal randomized placebo-controlled trials**. *Int J Neuropsychopharmacol* 2015;18:pyv070 CrossRef Medline
25. Patenaude B, Smith SM, Kennedy DN, et al. **A Bayesian model of shape and appearance for subcortical brain segmentation.** *Neuroimage* 2011;56:907–22 CrossRef Medline
26. Fischl B, Salat DH, Busa E, et al. **Whole brain segmentation: automated labeling of neuroanatomical structures in the human brain.** *Neuron* 2002;33:341–55 CrossRef Medline
27. Fischl B, van der Kouwe A, Destrieux C, et al. **Automatically parcellating the human cerebral cortex.** *Cereb Cortex* 2004;14:11–22 CrossRef Medline
28. Reuter M, Rosas HD, Fischl B. **Highly accurate inverse consistent registration: a robust approach.** *Neuroimage* 2010;53:1181–96 CrossRef Medline
29. Reuter M, Schmansky NJ, Rosas HD, et al. **Within-subject template estimation for unbiased longitudinal image analysis.** *Neuroimage* 2012;61:1402–18 CrossRef Medline
30. Mueller SG, Weiner MW, Thal LJ, et al. **Ways toward an early diagnosis in Alzheimer's disease: the Alzheimer's Disease Neuroimaging Initiative (ADNI).** *Alzheimers Dement* 2005;1:55–66 CrossRef Medline
31. Cover KS, van Schijndel RA, van Dijk BW, et al. **Assessing the reproducibility of the SienaX and Siena brain atrophy measures using the ADNI back-to-back MP-RAGE MRI scans.** *Psychiatry Res* 2011;193:182–90 CrossRef Medline
32. Jack CR Jr., Bernstein MA, Fox NC, et al. **The Alzheimer's Disease Neuroimaging Initiative (ADNI): MRI methods.** *J Magn Reson Imaging* 2008;27:685–91 CrossRef Medline
33. Carstensen B, Simpson J, Gurrin LC. **Statistical models for assessing agreement in method comparison studies with replicate measurements.** *Int J Biostat* 2008;4:Article 16 CrossRef
34. de Vet HCW, Terwee CB, Mokkink LB, et al. *Measurement in Medicine: A Practical Guide.* New York: Cambridge University Press; 2011
35. Mulder ER, de Jong RA, Knol DL, et al. **Hippocampal volume change measurement: quantitative assessment of the reproducibility of expert manual outlining and the automated methods FreeSurfer and FIRST.** *Neuroimage* 2014;92:169–81 CrossRef Medline
36. Bland JM, Altman DG. **Statistical methods for assessing agreement between two methods of clinical measurement.** *Lancet* 1986;1:307–10 CrossRef Medline
37. Euser AM, Dekker FW, le Cessie S. **A practical approach to Bland-Altman plots and variation coefficients for log transformed variables.** *J Clin Epidemiol* 2008;61:978–82 CrossRef Medline
38. Terwee CB, Bot SD, de Boer MR, et al. **Quality criteria were proposed for measurement properties of health status questionnaires.** *J Clin Epidemiol* 2007;60:34–42 CrossRef Medline
39. Twisk JWR. *Applied Multilevel Analysis: A Practical Guide for Medical Researchers.* New York: Cambridge University Press; 2006
40. Twisk JWR. *Applied Longitudinal Data Analysis for Epidemiology.* New York: Cambridge University Press; 2013
41. Jovicich J, Czanner S, Han X, et al. **MRI-derived measurements of human subcortical, ventricular and intracranial brain volumes: reliability effects of scan sessions, acquisition sequences, data analyses, scanner upgrade, scanner vendors and field strengths.** *Neuroimage* 2009;46:177–92 CrossRef Medline

Brain Structural Changes following HIV Infection: Meta-Analysis

E.E. O'Connor, Timothy A. Zeffiro, and Thomas A. Zeffiro

ABSTRACT

BACKGROUND: Numerous studies have used structural neuroimaging to measure HIV effects on brain macroarchitecture. While many have reported changes in total brain volume, gray matter volume, white matter volume, CSF volume, and basal ganglia volume following HIV infection, quantitative inconsistencies observed across studies are large.

PURPOSE: Our aim was to evaluate the consistency and temporal stability of serostatus effects on a range of structural neuroimaging measures.

DATA SOURCES: PubMed, reference lists, and corresponding authors.

STUDY SELECTION: The meta-analysis included 19 cross-sectional studies reporting HIV effects on cortical and subcortical volume from 1993 to 2016.

DATA ANALYSIS: Random-effects meta-analysis was used to estimate individual study standardized mean differences and study heterogeneity. Meta-regression was used to examine the effects of the study publication year.

DATA SYNTHESIS: Meta-analysis revealed standardized mean differences related to the serostatus of −0.65 ($P = .002$) for total brain volume, −0.28 for gray matter volume ($P = .008$), −0.24 ($P = .076$) for white matter volume, and 0.56 ($P = .001$) for CSF volume. Basal ganglia volume differences related to serostatus were not significant. Nevertheless, estimates of between-study heterogeneity suggested that much of the observed variance was between studies. Publication year was associated with recent reductions in many neurostructural effects.

LIMITATIONS: Many studies pooled participants with varying durations of treatment, disease, and comorbidities. Image-acquisition methods changed with time.

CONCLUSIONS: While published studies of HIV effects on brain structure had substantial variations that are likely to result from changes in HIV treatment practice during the study period, quantitative neurostructural measures can reliably detect the effects of HIV infection during treatment, serving as reliable biomarkers.

ABBREVIATIONS: ART = antiretroviral therapy; CSFv = CSF volume; GMv = gray matter volume; SMD = standardized mean difference; TBv = total brain volume; WMv = white matter volume

Since the onset of the AIDS epidemic, it has been known that HIV can have deleterious effects on both brain structure and function. In early studies using structural neuroimaging to measure brain macroarchitecture and microarchitecture, effects in HIV groups were due largely to opportunistic infections and HIV encephalitis.[1] The advent of combination antiretroviral therapy (ART), promoting immune system reconstitution, markedly decreased the incidence of CNS opportunistic infection and acute HIV encephalitis.[2] In the ensuing decades, HIV serostatus effects

Received March 29, 2017; accepted after revision August 13.

From the Department of Radiology (E.E.O.), University of Maryland Medical System, Baltimore, Maryland; and Neurometrika (Timothy A. Zeffiro, Thomas A. Zeffiro), Potomac, Maryland.

This work was partially supported by the Comprehensive NeuroAIDS Center grant (P30MH0921777).

Please address correspondence to Erin O'Connor, MD, University of Maryland Medical Center, Department of Radiology and Nuclear Medicine, 22 S Greene St, Baltimore, MD 21201; e-mail: erin.oconnor@umm.edu; @LanternLab

Indicates open access to non-subscribers at www.ajnr.org

Indicates article with supplemental on-line appendix and tables.
Indicates article with supplemental on-line photo.

http://dx.doi.org/10.3174/ajnr.A5432

on brain structure have been consistently reported, with clear effects on WM microstructure.[3] Nevertheless, peripheral viral suppression has not always prevented progressive cognitive and motor impairment, and the origin of these behavioral effects during treatment is still debated, with several ART-era studies demonstrating structural associations with cognitive deficits during treatment.[4-6]

Early brain structural studies in HIV-infected participants found decreases in brain parenchyma,[7] white matter,[8] and basal ganglia[7,9] volume. During the ART era, observations of cortical,[10] subcortical, gray matter,[9] and white matter[10] atrophy have continued, with decreases in cortical gray matter and brain parenchymal volume observed even in the first year of HIV infection.[11] While many studies have reported reduced total brain volume (TBv), total gray matter volume (GMv), white matter volume (WMv), basal ganglia volume, or increased CSF volume (CSFv) following HIV infection, quantitative inconsistencies observed across studies are large. The source of these inconsistencies is unclear, with possible mechanisms including image-acquisition methods, infection duration, ART treatment effects, sample demographics, and comorbidities commonly seen in seropositive patients.

To determine whether structural neuroimaging reveals consistent serostatus effects, we examined structural MR imaging studies in HIV-infected subjects, using meta-analytic techniques to explore the consistency of quantitative differences detected in structural neuroimaging studies from 1993 to 2016. Measures examined included TBv, GMv, WMv, CSFv, and subcortical GMv. We also investigated whether the observed HIV effects on brain structure are stable with time or have changed. Given that ART effectively suppresses peripheral viral load and allows immune system reconstitution, concurrent cessation of brain injury seems likely. We, therefore, expected that the structural effects of HIV infection would diminish in more recent HIV neurostructural studies that included large percentages of HIV-infected participants receiving ART.

MATERIALS AND METHODS

Meta-Analysis of HIV Effects on Brain Structure

To summarize the literature on HIV effects on brain structure, we followed Preferred Reporting Items for Systematic Reviews and Meta-Analyses (PRISMA)[12] standards. Six PubMed computerized searches were performed on September 25, 2016, with the following terms: "HIV" and "structural and MR imaging brain" yielded 77 records; "HIV" and "MR imaging" and "basal ganglia atrophy" yielded 42 records; "HIV" and "MR imaging" and "caudate atrophy" yielded 24 records; "HIV" and "MR imaging" and "gray matter atrophy" yielded 38 records; "HIV" and "MR imaging" and "gray matter" yielded 102 records; and "HIV" and "MR imaging" and "brain volume" yielded 112 records. Of these 395 records, 151 were duplicates, leaving a total of 244 records to be examined. An additional 13 records were added from the reference lists of articles, resulting in 257 articles to be screened. Of the 257 articles screened on the first pass by reading the abstract, 182 were excluded if they were the following: 1) animal studies, 2) review articles, 3) not written in English, 4) case reports, or 5) without seronegative controls, leaving 75 full-text articles to be assessed for eligibility. Thirty-eight of 75 full-text articles assessed for eligibility were excluded for the following reasons: 1) They were review articles, 2) they did not have seronegative controls, 3) they did not study quantitative HIV effects on brain volume, or 4) they studied the association of serostatus and brain volume with neuropsychological performance, and 5) they did not provide a means of contacting the authors. Of the 38 eligible full-text articles, 19 studies completed between 1993 and 2016 were included in the meta-analysis, with 9 studies reporting TBv,[7,11,13-19] 10 reporting GMv,[8,10,11,13,16-18,20-22] 10 reporting WMv,[8,10,11,13,16-18,20-22] 12 reporting CSFv,[7,8,10,13,14,17,18,20-24] 8 reporting caudate volume,[4,7,11,18-20,25,26] 7 reporting putaminal volume,[4,7,11,18,19,25,26] and 6 reporting globus pallidus volume.[7,10,11,18,19,25] If the requisite numbers could not be located in the text or accompanying tables, ≥1 attempt was made to contact the corresponding authors of 20 studies for more information. Five authors responded and provided the requisite additional information. The remaining 19 studies, listed in the On-line Appendix, were excluded because the data were no longer available, the data could not be shared, or the authors did not respond to inquiries (Fig 1).

Statistical Analysis

Mean structural values and their SDs for TBv, GMv, WMv, CSFv, caudate volume, putaminal volume, and pallidum volume were taken from the article tables and converted into consistent units.

We used R statistical and computing software, Version 3.4.1 (http://www.r-project.org) and the meta-analysis package meta[27] to estimate the standardized mean difference (SMD) in TBv, GMv, WMv, and CSFv and caudate, putaminal, and pallidum volumes for each study; then, we calculated a weighted average of these estimates across studies. The metacont function from meta uses the same estimator as RevMan5 (http://community.cochrane.org/tools/review-production-tools/revman-5/revman-5-download). This is a version of the standardized mean difference called Hedges *g*, based on the pooled sample variance. Random-effects models were used to test for serostatus group effects. The I^2 statistic, representing the proportion of between-study variation due to heterogeneity, was used to estimate study inconsistency.[28] τ^2 was computed as an estimate of between-study variance, with values of >1 suggesting substantial heterogeneity. Forest plots were used to visualize variations in standardized mean differences across studies. Radial plots were used to visualize study heterogeneity, with less precise effect estimates lying near the origin and more precise estimates occurring farther away. Study bias was explored by examining funnel plots of sample size versus effect size. Meta-regression was used to examine imaging protocol and publication year effects.

RESULTS

Serostatus Effects

Random-effects meta-analysis of TBv revealed a reduction (SMD = −0.58) related to serostatus (test of SMD = 0: $z = -3.1$, $P = .0018$), with study heterogeneity Q = 26.1 ($df = 8$), $P = .001$; and τ^2 (variation in SMD attributable to heterogeneity) = 69%. The τ^2 of between-study variance was 0.23. Five of the 9 studies had confidence intervals that included zero (Fig 2*A*).

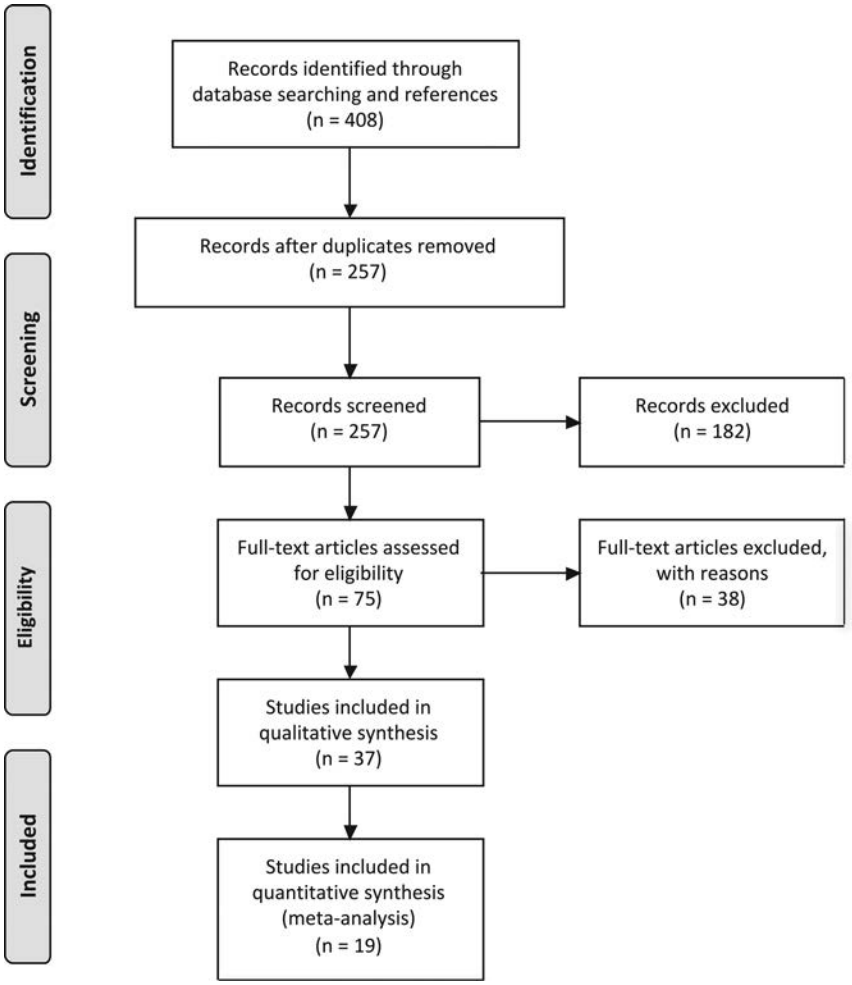

FIG 1. Meta-analysis flow diagram for study selection.

Next, we examined the serostatus effects on individual tissue compartments. Analysis of GMv revealed a reduction (SMD = −0.28) related to serostatus (test of SMD = 0: $z = -2.65$, $P = .0081$), with study heterogeneity $Q = 14.8$ ($df = 9$), $P = .096$, $I^2 = 39\%$, and $\tau^2 = 0.04$. Seven of the 10 studies had confidence intervals that included zero (Fig 3*A*). Analysis of WMv revealed a nonsignificant reduction (SMD = −0.24) related to serostatus (test of SMD = 0: $z = -1.78$, $P = .076$), with study heterogeneity $Q = 24.3$ ($df = 9$), $P = .004$, $I^2 = 63\%$, and $\tau^2 = 0.11$. Nine of the 10 studies had confidence intervals that included zero (Fig 4*A*). Analysis of CSFv revealed an increase (SMD = 0.56) related to serostatus (test of SMD = 0: $z = 3.29$, $P = .001$), with study heterogeneity $Q = 61$ ($df = 11$), $P < .001$, $I^2 = 82\%$, and $\tau^2 = 0.26$ (Fig 5*A*).

Although the included studies had a large range of group sample sizes, ranging from 5 to 85, it is possible that the known tendency for small-sample neuroimaging studies to go unpublished might have contributed to publication bias effects. Panel *C* of Figs 2–5 shows funnel plots of the estimated treatment effects against a measure of their precision, here the standard error. All show asymmetry consistent with small-study effects. If small-study effects were absent, the treatment effects of all studies should be distributed symmetrically around the average treatment effect. In addition, linear regression tests of funnel plot asymmetry were statistically significant for TBv ($P = .001$), GMv ($P = .008$), WMv ($P = .025$), and CSFv ($P = .014$). These results could reflect reporting bias because it is unlikely that small neurostructural studies that have failed to detect serostatus effects would find a place in most neuroimaging journals. Thus, the observed average effect sizes for each tissue compartment may reflect overestimates of their true values. Future studies may mitigate these effects owing to the increasing willingness of investigators to participate in more open data sharing, allowing aggregation and re-analysis of data that might not have shown serostatus effects in their original samples.

Next, we examined the serostatus effects on basal ganglia structures. Analysis of caudate volume revealed a nonsignificant reduction (SMD = −0.23) related to serostatus (test of SMD = 0: $z = -1.27$, $P = .20$) (Fig 6*A*). Analysis of putaminal volume revealed a nonsignificant reduction (SMD = −0.22) related to serostatus (test of SMD = 0: $z = -1.00$, $P = .32$) (Fig 6*B*). Analysis of pallidal volume revealed a nonsignificant reduction (SMD = −0.024) related to serostatus (test of SMD = 0: $z = -0.09$, $P = .92$) (Fig 6*C*).

Covariate Effects

Temporal changes in serostatus effects were investigated using random-effects meta-regression, examining changes in SMDs for each measure with time. TBv SMDs became smaller with publication year, reflecting less volume loss in the seropositive group ($P = .003$). WMv SMDs also became smaller, with less seropositive volume loss ($P = .028$), and CSFv SMDs became smaller with time, reflecting less CSFv increase related to seropositivity ($P < .001$). GMv SMDs also became smaller with time, but this effect was not statistically significant ($P = .086$) (Fig 7). Possible small-sample effects are shown in the On-line Figure.

Summaries of image acquisition protocols revealed that earlier studies tended to use 1.5T MR imaging systems and large voxels, while more recent studies used 3T MR imaging systems and smaller voxel volumes (On-line Table 1). Field strength and voxel volume are expected to have opposing effects on image SNR; thus, their effects may cancel each other out. Meta-regression revealed that there were no effects of field strength and voxel size on SMD. Because these 2 variables were confounded with publication year, it was not possible to examine their individual contributions statistically.

Summaries of participant clinical characteristics revealed that the more recent studies had a higher proportion of participants receiving ART, the treatment with the highest known efficacy

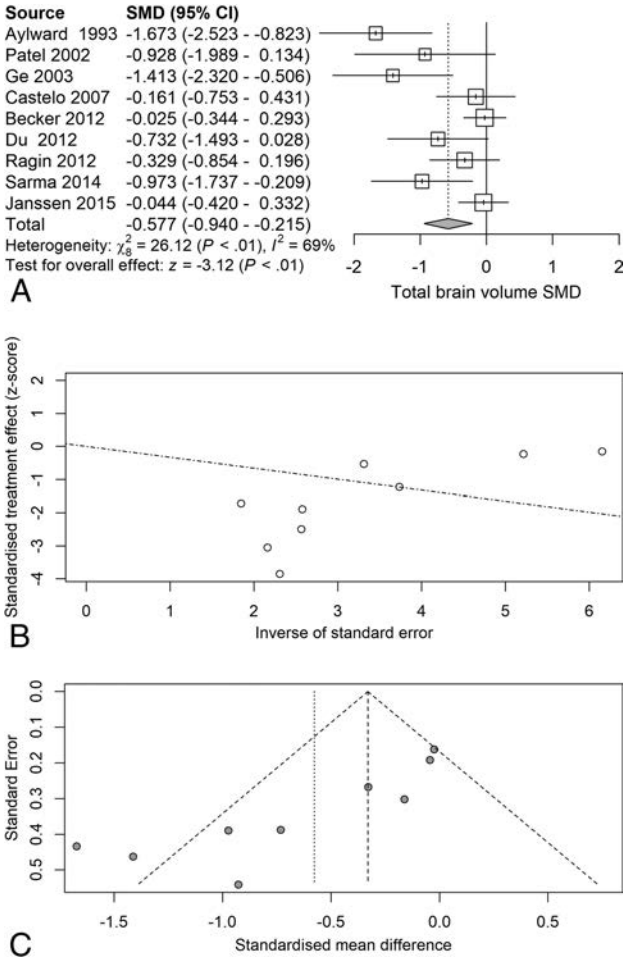

FIG 2. Total brain volume standardized mean differences across studies comparing seropositive with seronegative participants. *A*, Forest plot. *B*, Funnel plot. *C*, Radial plot.

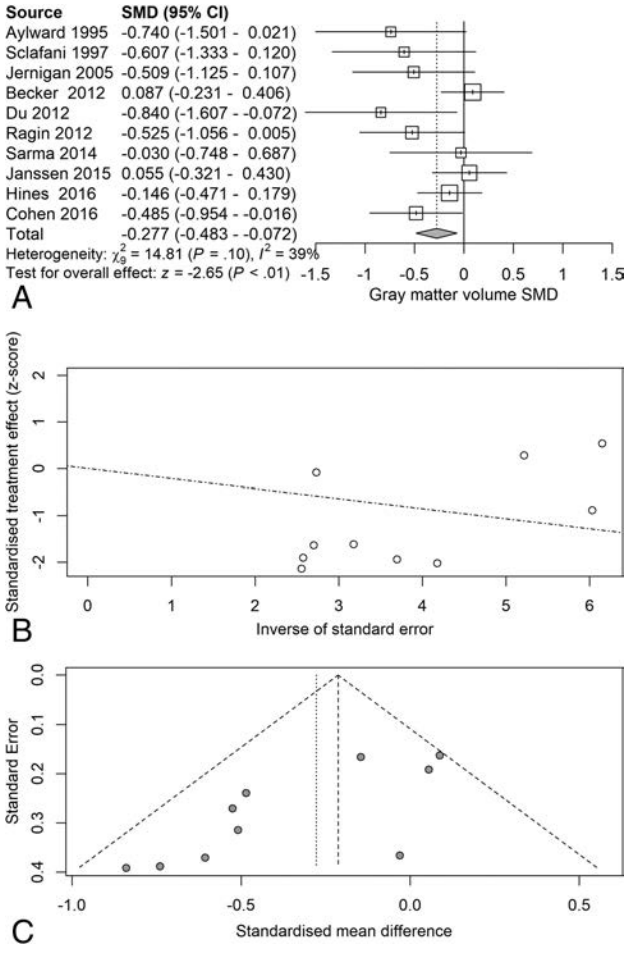

FIG 3. Gray matter standardized mean differences across studies comparing seropositive with seronegative participants. *A*, Forest plot. *B*, Funnel plot. *C*, Radial plot.

(On-line Table 2). Use of combined therapies makes treatment more effective and reduces the risk of developing drug resistance. While illegal drug use was an exclusion criterion in 7/19 studies, in 10/19 studies drug use was not described (On-line Table 3). In the 2 studies reporting hepatitis status, a single participant was affected.[7,8]

DISCUSSION

Summary of Results

In a quantitative meta-analysis of HIV neurostructural studies reported from 1993 to 2016, spanning the widespread introduction of antiretroviral treatment, we observed that serostatus was, on average, associated with decreases in TBv and GMv and concomitant CSFv increases. Serostatus effects in all tissue compartments, except gray matter, have diminished with time, suggesting that widespread use of ART has resulted in a decline in macroscopic neurostructural changes. Nevertheless, small effects in TBv, GMv, and CSFv do persist in treated seropositive patients.

HIV Effects on Total Brain and CSF Volume

TBv and CSFv in HIV are believed to reflect global atrophy. While qualitative and quantitative studies have demonstrated global atrophy in HIV, more recent studies have reported no differences in TBv,[11,29] one in subjects infected with HIV for <1 year,[11] suggesting that shorter illness duration before initiating treatment can decrease HIV-associated cerebral atrophy. HIV-associated global atrophy, however, may also be related to drug and alcohol abuse effects and other life stressors commonly seen in the HIV-infected population.[30-32]

HIV Effects on Gray Matter Volume

Effects of HIV infection on cortical gray matter are less well-documented in the neuropathologic literature but include astroglial proliferation and glial atrophy.[33] Cortical metabolite changes include NAA/Cr reductions[34] and mIns/Cr and Cho/Cr increases.[35]

The articles used in the meta-analysis of HIV effects on GMv incorporated both cortical and subcortical gray matter under gray matter volume. Nearly 80% of post-antiretroviral therapy era studies assessed for eligibility in our analyses reported HIV-associated decreases in GMv, with several specifically reporting HIV-related cortical GMv reductions.[10,11] Nevertheless, more recent literature includes multiple studies that find no HIV GMv effects, suggesting that ART treatment initiation diminishes gray matter loss. While GMv loss does persist in the ART era, there are strong

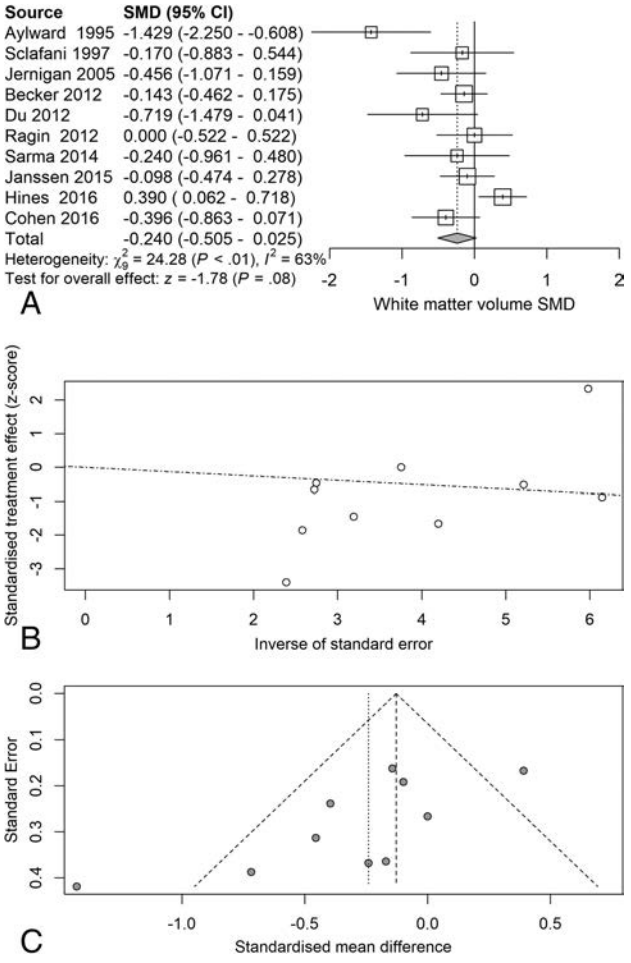

FIG 4. White matter standardized mean differences across studies comparing seropositive with seronegative participants. *A*, Forest plot. *B*, Funnel plot. *C*, Radial plot.

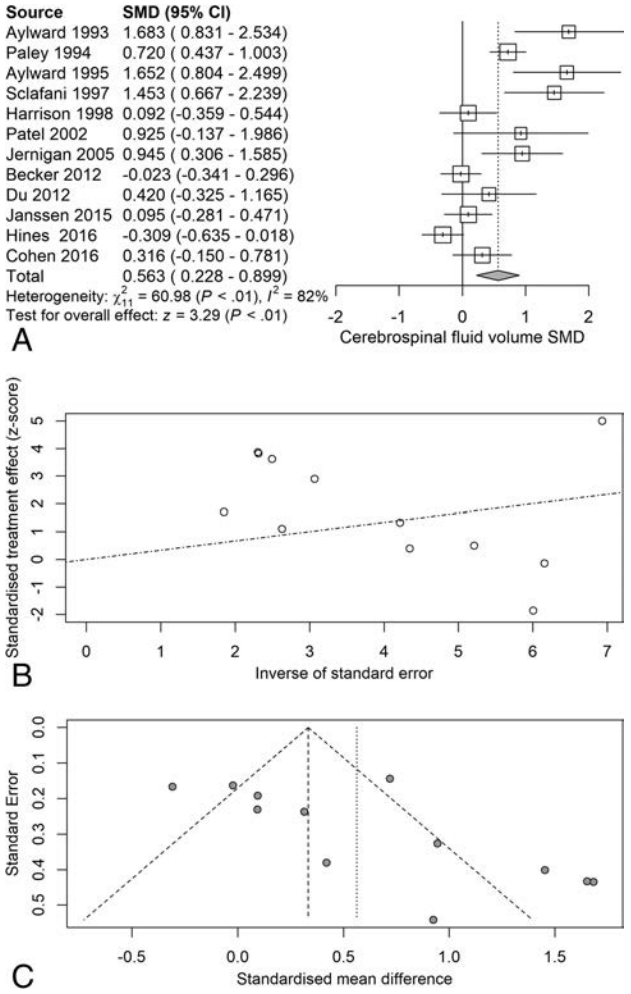

FIG 5. CSF standardized mean differences across studies comparing seropositive with seronegative participants. *A*, Forest plot. *B*, Funnel plot. *C*, Radial plot.

associations between decreasing serostatus effects and more recent publication.

HIV Effects on White Matter Volume

Of the studies meeting eligibility requirements, our analysis found that ART may have a weak influence on HIV-associated WMv reductions. Our meta-analysis confirms that the degree of macrostructural WMv loss diminishes rapidly in the ART era. Nevertheless, there is evidence of microstructural changes persisting in HIV infection in the ART era,[3] suggesting that DTI may be more sensitive in detecting HIV white matter serostatus effects.[3]

HIV Effects on Basal Ganglia Volume

There is ample evidence of the early and enduring influence of HIV on the basal ganglia. Neuropathologic findings demonstrate macrophages, microglia, and high concentrations of viral proteins in the basal ganglia.[36] Metabolic studies found basal ganglia hypermetabolism in the early and middle stages of HIV infection,[37] followed by hypometabolism with disease progression.[38] Behavioral manifestations reflecting HIV effects on the basal ganglia included voluntary movement impairment and compromised executive function.[39,40]

Before the introduction of ART, structural HIV studies reported decreased basal ganglia volumes,[7] particularly in the caudate nuclei, that were associated with dementia.[41] Viral load has been reported to be highest in the caudate nuclei,[42] possibly due to the proximity to the virus-enriched CSF. Dopaminergic neurons are particularly susceptible to HIV neurotoxic effects.[43] Basal ganglia volume loss is associated with psychomotor slowing[44] and may be an important predictor of cognitive impairment. While HIV-associated reductions in basal ganglia volume are still reported in the ART era,[45] more recent studies failed to demonstrate serostatus effects on the basal ganglia, likely related to earlier and more effective treatments. Nevertheless, to isolate possible serostatus effects on basal ganglia structure in the setting of the observed high between-study heterogeneity, further work using aggregated multisite data with subject-level information allowing estimation and isolation of comorbid neurostructural moderating influences is warranted.

Sources of Between-Study Variability

Several potential sources contributed to the variability in the study effects included in our meta-analysis. First, differences in MR imaging acquisition parameters included field strengths ranging from 1.5T to 3T and voxel volumes ranging from 5.5 to

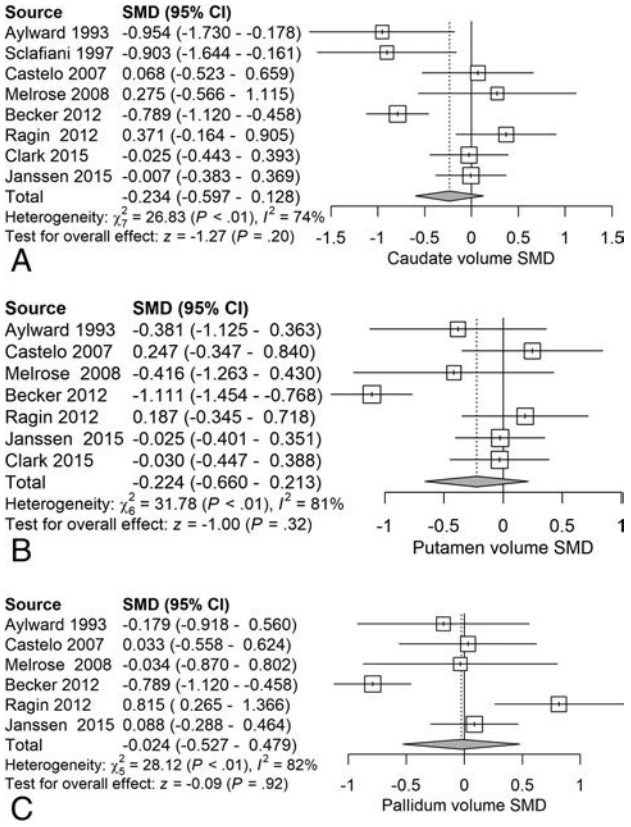

FIG 6. Forest plots of basal ganglia gray matter showing standardized mean differences across studies comparing seropositive with seronegative participants *A*, Caudate volume. *B*, Putamen volume. *C*, Pallidal volume.

0.647 mm^3. Second, there was wide variation in the demographic characteristics of the study cohort. For example, Sarma et al[16] and Cohen et al[22] examined TBv in young perinatally infected adolescents with mean ages of 17 and 13 years, respectively, while the cohort studied by Hines et al[21] had a mean age of 59 years. Third, variation in sample comorbidities, including recreational drug use and antiretroviral therapy treatment type, was high. While ART effects on brain structure are difficult to isolate in cross-sectional studies with wide ranges of disease and treatment duration, our data suggest that ART does have a strong protective effect on brain macrostructure.

Temporal Variation in HIV-Related Brain Atrophy

The serostatus-associated reductions in TBv, GMv, and WMv and increases in CSFv effects vary with study age. Older studies demonstrated larger effects, with differences in WMv and subcortical GMv virtually disappearing in recent years. One possible explanation for this variation is the difference in field strengths. Earlier studies used 1.5T systems, and later studies predominantly used 3T systems. Another possible explanation is differences in voxel size, with later studies having smaller voxel sizes. Meta-regression, however, revealed that there were no independent effects of field strength and voxel size. It is unlikely that these acquisition changes contributed to the progressive reduction in serostatus effects observed because brain structure quantification would be expected to be more accurate in studies using smaller voxels, with diminished partial volume effects. The most likely explanation for

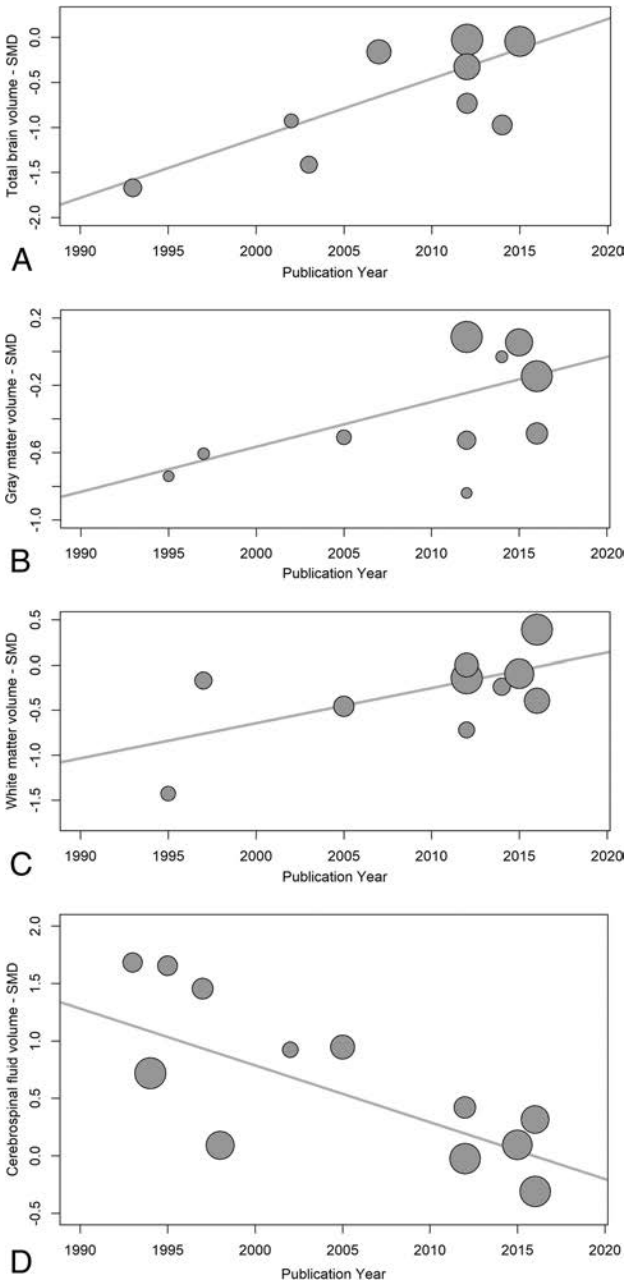

FIG 7. Publication year influence on serostatus effects. These are plots of structural brain measure standardized mean differences and their corresponding regression lines, for total brain volume (*A*) $P = .001$, gray matter volume (*B*) $P = .086$, white matter volume (*C*) $P < .001$, and CSF volume (*D*) $P < .001$. The plot *circle area* is inversely proportional to the estimated SMD variance.

the temporal variation in HIV-related brain atrophy is the duration of untreated or partially treated illness. In the oldest study included in our meta-analysis,[7] which also had the greatest HIV-related brain atrophy, 62.5% of participants were treated with zidovudine or didanosine single therapy and 37.5% were untreated. In more recent studies, almost all subjects were treated with combination ART, implying that subjects are on a combination of at least 3 different drugs from 2 of the major antiretroviral therapy classes. Combined therapies make treatment more effective and reduce the risk of developing drug resistance. While the associated reductions in viral load and immune reconstitution do

appear to have a role in preservation of brain structure,[5] brain volume losses are still evident in treated seropositive patients.

There are several potential etiologies of the persistent volume losses in treated HIV-infected participants. Irreversible pretreatment CNS damage is a possibility. Alternatively, chronic subclinical CNS inflammation despite ART has been documented[46] and may contribute to progressive brain atrophy. Neurotoxicity associated with ART, relatively underexplored, is another potential mechanism for progressive brain atrophy,[47] a possibility that might be explored using longitudinal designs. With other measures, there is weak evidence of progressive HIV-induced CNS changes during ART. One study that examined treated seropositive subjects using DTI demonstrated greater-than-normal age-related increases in diffusion in the corpus callosum for 1 year compared with seronegative controls, indicating progressive white matter microstructural changes in HIV.[48] Another DTI study looking at a small longitudinal HIV-infected cohort observed increased corpus callosum and centum semiovale diffusion after 6 months of ART.[49]

The comorbidities commonly associated with HIV may also contribute to brain atrophy in treated HIV infection. Illicit drug use such as methamphetamines, cocaine, opiates, and cannabinoids, common in HIV-infected participants,[50] has been associated with structural brain abnormalities.[30,31] In the studies included in the meta-analyses, many did not address drug use. Fifty-three percent of studies did not have drug use as an exclusion criterion, and inclusion of participants who used drugs was only described in 47% of studies. Although concomitant or previous drug use may have contributed to the observed structural changes, any quantitative effects could not be determined from the available data. Although it has been suggested that comorbid hepatitis C infection may contribute to HIV-associated neurostructural abnormalities, hepatitis C status was not reported by most articles. HIV infection predominates in lower socioeconomic groups who may have brain structure differences arising from other sources.[32] Finally, HIV infection is associated with an increased incidence of cardiovascular risk factors such as diabetes, smoking,[51,52] and chronic obstructive pulmonary disease,[53] all associated with accelerated brain aging.[51,54]

Relation to Cognitive Effects

HIV-associated structural effects persist in treated cohorts, particularly in total GMv, albeit to a decreased degree. There is also evidence that progressive regional changes in GMv and WMv are associated with cognitive decline in treated HIV participants. In a study with 94% of participants treated with ART, impaired motor function was associated with basal ganglia gray matter atrophy.[55] A study with 100% ART-treated subjects demonstrated a correlation between cortical thinning and reduced psychomotor speed.[56] Another study of 100% ART-treated subjects revealed correlations between decreased TBv and reduced motor function and processing speed, and decreased thalamic volumes with reduced motor function.[18] Impaired executive function correlated with decreased basal ganglia volumes in another study of treated subjects with HIV.[9] Regional structural effects may therefore potentially serve as markers of fixed or progressive cognitive motor impairment, but this possibility may be best explored using longitudinal designs.

Study Limitations

As with most meta-analyses, not all eligible studies were included in this study due to inaccessibility of data. Publication bias resulting from the tendency not to publish negative results from small imaging studies may also be a factor. There were many sources of demographic variability among the included studies, such as participants' infection duration, treatment status, age, educational level, and the presence of comorbidities that may also affect brain structure. Finally, there were MR imaging acquisition parameter differences across the included studies. Nevertheless, meta-regression results did not suggest that these acquisition differences contributed to serostatus effects on brain macrostructure.

CONCLUSIONS

Published studies indicate that regional brain atrophy results from HIV infection, with serostatus effects often more pronounced in neurologically impaired subjects. This study provides a quantitative meta-analysis of neurostructural changes related to serostatus in HIV-infected participants, with TBv, GMv, and CSFv all showing reliable serostatus effects. While older studies in our meta-analysis demonstrated larger effect sizes, smaller HIV-related volume change was still seen in more recent studies in which all or most participants received ART. HIV effects on brain structure showed substantial between-study variation, which likely resulted from changes in HIV treatment practice during the study period. It remains unclear whether the persistent neurostructural effects of HIV infection are secondary to the following: 1) initial brain injury occurring before ART treatment; 2) subclinical neuroinflammation persisting despite ART; 3) ART neurotoxicity; or 4) common HIV comorbidities. Longitudinal studies of HIV-infected participants and meta-analysis approaches incorporating subject-level data are needed to pursue these possibilities in more detail.

ACKNOWLEDGMENTS

We gratefully acknowledge the assistance of Drs Becker, Ragin, Jernigan, Archibald, Cohen, and Janssen for providing information not given in the original articles.

REFERENCES

1. Levy RM, Bredesen DE. **Central nervous system dysfunction in acquired immunodeficiency syndrome.** *J Acquir Immune Defic Syndr* 1988;1:41–64 Medline
2. d'Arminio Monforte A, Cinque P, Mocroft A, et al; EuroSIDA Study Group. **Changing incidence of central nervous system diseases in the EuroSIDA cohort.** *Ann Neurol* 2004;55:320–28 CrossRef Medline
3. O'Connor EE, Jaillard A, Renard F, et al. **Reliability of white matter microstructural changes in HIV infection: meta-analysis and confirmation.** *AJNR Am J Neuroradiol* 2017;38:1510–19 CrossRef Medline
4. Clark US, Walker KA, Cohen RA, et al. **Facial emotion recognition impairments are associated with brain volume abnormalities in individuals with HIV.** *Neuropsychologia* 2015;70:263–71 CrossRef Medline
5. Pfefferbaum A, Rogosa DA, Rosenbloom MJ, et al. **Accelerated aging of selective brain structures in human immunodeficiency virus**

infection: a controlled, longitudinal magnetic resonance imaging study. *Neurobiol Aging* 2014;35:1755–68 CrossRef Medline
6. Bonnet F, Amieva H, Marquant F, et al; S CO3 Aquitaine Cohort. **Cognitive disorders in HIV-infected patients: are they HIV-related?** *AIDS* 2013;27:391–400 CrossRef Medline
7. Aylward EH, Henderer JD, McArthur JC, et al. **Reduced basal ganglia volume in HIV-1-associated dementia: results from quantitative neuroimaging.** *Neurology* 1993;43:2099–104 CrossRef Medline
8. Aylward EH, Brettschneider PD, McArthur JC, et al. **Magnetic resonance imaging measurement of gray matter volume reductions in HIV dementia.** *Am J Psychiatry* 1995;152:987–94 CrossRef Medline
9. Corrêa DG, Zimmermann N, Netto TM, et al. **Regional cerebral gray matter volume in HIV-positive patients with executive function deficits.** *J Neuroimaging* 2016;26:450–57 CrossRef Medline
10. Becker JT, Maruca V, Kingsley LA, et al; Multicenter AIDS Cohort Study. **Factors affecting brain structure in men with HIV disease in the post-HAART era.** *Neuroradiology* 2012;54:113–21 CrossRef Medline
11. Ragin AB, Du H, Ochs R, et al. **Structural brain alterations can be detected early in HIV infection.** *Neurology* 2012;79:2328–34 CrossRef Medline
12. Moher D, Liberati A, Tetzlaff J, et al; the PRISMA Group. **Preferred reporting items for systematic reviews and meta-analyses: the PRISMA statement.** *PLoS Med* 2009;6:e1000097 CrossRef
13. Jernigan TL, Gamst AC, Archibald SL, et al. **Effects of methamphetamine dependence and HIV infection on cerebral morphology.** *Am J Psychiatry* 2005;162:1461–72 CrossRef Medline
14. Patel SH, Kolson DL, Glosser G, et al. **Correlation between percentage of brain parenchymal volume and neurocognitive performance in HIV-infected patients.** *AJNR Am J Neuroradiol* 2002;23:543–49 Medline
15. Ge Y, Kolson DL, Babb JS, et al. **Whole brain imaging of HIV-infected patients: quantitative analysis of magnetization transfer ratio histogram and fractional brain volume.** *AJNR Am J Neuroradiol* 2003;24:82–87 Medline
16. Sarma MK, Nagarajan R, Keller MA, et al. **Regional brain gray and white matter changes in perinatally HIV-infected adolescents.** *Neuroimage Clin* 2014;4:29–34 CrossRef Medline
17. Du H, Wu Y, Ochs R, et al. **A comparative evaluation of quantitative neuroimaging measurements of brain status in HIV infection.** *Psychiatry Res* 2012;203:95–99 CrossRef Medline
18. Janssen MA, Meulenbroek O, Steens SC, et al. **Cognitive functioning, wellbeing and brain correlates in HIV-1 infected patients on long-term combination antiretroviral therapy.** *AIDS* 2015;29:2139–48 CrossRef Medline
19. Castelo JM, Courtney MG, Melrose RJ, et al. **Putamen hypertrophy in nondemented patients with human immunodeficiency virus infection and cognitive compromise.** *Arch Neurol* 2007;64:1275–80 CrossRef Medline
20. Di Sclafani V, Mackay RD, Meyerhoff DJ, et al. **Brain atrophy in HIV infection is more strongly associated with CDC clinical stage than with cognitive impairment.** *J Int Neuropsychol Soc* 1997;3:276–87 Medline
21. Hines LJ, Miller EN, Hinkin CH, et al; Multicenter AIDS Cohort Study. **Cortical brain atrophy and intra-individual variability in neuropsychological test performance in HIV disease.** *Brain Imaging Behav* 2016;10:640–51 CrossRef Medline
22. Cohen S, Caan MW, Mutsaerts HJ, et al. **Cerebral injury in perinatally HIV-infected children compared to matched healthy controls.** *Neurology* 2016;86:19–27 CrossRef Medline
23. Paley M, Chong WK, Wilkinson ID, et al. **Cerebrospinal fluid-intracranial volume ratio measurements in patients with HIV infection: CLASS image analysis technique.** *Radiology* 1994;190:879–86 CrossRef Medline
24. Harrison MJ, Newman SP, Hall-Craggs MA, et al. **Evidence of CNS impairment in HIV infection: clinical, neuropsychological, EEG, and MRI/MRS study.** *J Neurol Neurosurg Psychiatry* 1998;65:301–07 CrossRef Medline
25. Melrose RJ, Tinaz S, Castelo JM, et al. **Compromised fronto-striatal functioning in HIV: an fMRI investigation of semantic event sequencing.** *Behav Brain Res* 2008;188:337–47 CrossRef Medline
26. Becker JT, Sanders J, Madsen SK, et al; Multicenter AIDS Cohort Study. **Subcortical brain atrophy persists even in HAART-regulated HIV disease.** *Brain Imaging Behav* 2011;5:77–85 CrossRef Medline
27. Schwarzer G, Carpenter JR, Rücker G. *Meta-analysis with R.* Cham: Springer-Verlag; 2015
28. Higgins JP, Thompson SG, Deeks JJ, et al. **Measuring inconsistency in meta-analyses.** *BMJ* 2003;327:557–60 CrossRef Medline
29. Thompson PM, Dutton RA, Hayashi KM, et al. **3D mapping of ventricular and corpus callosum abnormalities in HIV/AIDS.** *Neuroimage* 2006;31:12–23 CrossRef Medline
30. Yücel M, Solowij N, Respondek C, et al. **Regional brain abnormalities associated with long-term heavy cannabis use.** *Arch Gen Psychiatry* 2008;65:694–701 CrossRef Medline
31. Thompson PM, Hayashi KM, Simon SL, et al. **Structural abnormalities in the brains of human subjects who use methamphetamine.** *J Neurosci* 2004;24:6028–36 CrossRef Medline
32. Hanson JL, Chandra A, Wolfe BL, et al. **Association between income and the hippocampus.** *PLoS One* 2011;6:e18712 CrossRef Medline
33. Budka H, Costanzi G, Cristina S, et al. **Brain pathology induced by infection with the human immunodeficiency virus (HIV): a histological, immunocytochemical, and electron microscopical study of 100 autopsy cases.** *Acta Neuropathol* 1987;75:185–98 CrossRef Medline
34. Yiannoutsos CT, Ernst T, Chang L, et al. **Regional patterns of brain metabolites in AIDS dementia complex.** *Neuroimage* 2004;23:928–35 CrossRef Medline
35. Laubenberger J, Häussinger D, Bayer S, et al. **HIV-related metabolic abnormalities in the brain: depiction with proton MR spectroscopy with short echo times.** *Radiology* 1996;199:805–10 CrossRef Medline
36. Berger JR, Nath A. **HIV dementia and the basal ganglia.** *Intervirology* 1997;40:122–31 CrossRef Medline
37. Hinkin CH, van Gorp WG, Mandelkern MA, et al. **Cerebral metabolic change in patients with AIDS: report of a six-month follow-up using positron-emission tomography.** *J Neuropsychiatry Clin Neurosci* 1995;7:180–87 CrossRef Medline
38. Rottenberg DA, Moeller JR, Strother SC, et al. **The metabolic pathology of the AIDS dementia complex.** *Ann Neurol* 1987;22:700–06 CrossRef Medline
39. Robinson-Papp J, Byrd D, Mindt MR, et al; Manhattan HIV Brain Bank. **Motor function and human immunodeficiency virus–associated cognitive impairment in a highly active antiretroviral therapy-era cohort.** *Arch Neurol* 2008;65:1096–101 CrossRef Medline
40. Reger M, Welsh R, Razani J, et al. **A meta-analysis of the neuropsychological sequelae of HIV infection.** *J Int Neuropsychol Soc* 2002;8:410–24 CrossRef Medline
41. Hestad K, McArthur JH, Dal Pan GJ, et al. **Regional brain atrophy in HIV-1 infection: association with specific neuropsychological test performance.** *Acta Neurol Scand* 1993;88:112–18 Medline
42. Kumar AM, Borodowsky I, Fernandez B, et al. **Human immunodeficiency virus type 1 RNA levels in different regions of human brain: quantification using real-time reverse transcriptase-polymerase chain reaction.** *J Neurovirol* 2007;13:210–24 CrossRef Medline
43. Nath A, Anderson C, Jones M, et al. **Neurotoxicity and dysfunction of dopaminergic systems associated with AIDS dementia.** *J Psychopharmacol* 2000;14:222–27 CrossRef Medline
44. Wright PW, Pyakurel A, Vaida FF, et al. **Putamen volume and its clinical and neurological correlates in primary HIV infection.** *AIDS* 2016;30:1789–94 CrossRef Medline
45. Ances BM, Ortega M, Vaida F, et al. **Independent effects of HIV, aging, and HAART on brain volumetric measures.** *J Acquir Immune Defic Syndr* 2012;59:469–77 CrossRef Medline
46. Anthony IC, Ramage SN, Carnie FW, et al. **Influence of HAART on HIV-related CNS disease and neuroinflammation.** *J Neuropathol Exp Neurol* 2005;64:529–36 CrossRef Medline

47. Robertson K, Liner J, Meeker RB. **Antiretroviral neurotoxicity.** *J Neurovirol* 2012;18:388–99 CrossRef Medline
48. Chang L, Wong V, Nakama H, et al. **Greater than age-related changes in brain diffusion of HIV patients after 1 year.** *J Neuroimmune Pharmacol* 2008;3:265–74 CrossRef Medline
49. Wright P, Heaps J, Shimony JS, et al. **The effects of HIV and combination antiretroviral therapy on white matter integrity.** *AIDS* 2012; 26:1501–08 CrossRef Medline
50. Mimiaga MJ, Reisner SL, Grasso C, et al. **Substance use among HIV-infected patients engaged in primary care in the United States: findings from the Centers for AIDS Research Network of Integrated Clinical Systems cohort.** *Am J Public Health* 2013;103:1457–67 CrossRef Medline
51. Debette S, Seshadri S, Beiser A, et al. **Midlife vascular risk factor exposure accelerates structural brain aging and cognitive decline.** *Neurology* 2011;77:461–68 CrossRef Medline
52. Currier JS, Lundgren JD, Carr A, et al; Working Group 2. **Epidemiological evidence for cardiovascular disease in HIV-infected patients and relationship to highly active antiretroviral therapy.** *Circulation* 2008;118:e29–35 CrossRef Medline
53. Crothers K, Butt AA, Gibert CL, et al. **Increased COPD among HIV-positive compared to HIV-negative veterans.** *Chest J* 2006;130: 1326–33 CrossRef
54. Esser RW, Stoeckel MC, Kirsten A, et al. **Structural brain changes in patients with COPD.** *Chest* 2016;149:426–34 CrossRef Medline
55. Küper M, Rabe K, Esser S, et al. **Structural gray and white matter changes in patients with HIV.** *J Neurol* 2011;258:1066–75 CrossRef Medline
56. Kallianpur KJ, Kirk GR, Sailasuta N, et al. **Regional cortical thinning associated with detectable levels of HIV DNA.** *Cereb Cortex* 2012;22: 2065–75 CrossRef Medline

Semiautomated Evaluation of the Primary Motor Cortex in Patients with Amyotrophic Lateral Sclerosis at 3T

G. Donatelli, A. Retico, E. Caldarazzo Ienco, P. Cecchi, M. Costagli, D. Frosini, L. Biagi, M. Tosetti, G. Siciliano, and M. Cosottini

ABSTRACT

BACKGROUND AND PURPOSE: Amyotrophic lateral sclerosis is a neurodegenerative disease involving the upper and lower motor neurons. In amyotrophic lateral sclerosis, pathologic changes in the primary motor cortex include Betz cell depletion and the presence of reactive iron-loaded microglia, detectable on 7T MR images as atrophy and T2*-hypointensity. Our purposes were the following: 1) to investigate the signal hypointensity-to-thickness ratio of the primary motor cortex as a radiologic marker of upper motor neuron involvement in amyotrophic lateral sclerosis with a semiautomated method at 3T, 2) to compare 3T and 7T results, and 3) to evaluate whether semiautomated measurement outperforms visual image assessment.

MATERIALS AND METHODS: We investigated 27 patients and 13 healthy subjects at 3T, and 19 patients and 18 healthy subjects at 7T, performing a high-resolution 3D multiecho T2*-weighted sequence targeting the primary motor cortex. The signal hypointensity-to-thickness ratio of the primary motor cortex was calculated with a semiautomated method depicting signal intensity profiles of the cortex. Images were also visually classified as "pathologic" or "nonpathologic" based on the primary motor cortex signal intensity and thickness.

RESULTS: The signal hypointensity-to-thickness ratio of the primary motor cortex was greater in patients than in controls ($P < .001$), and it correlated with upper motor neuron impairment in patients ($\rho = 0.57$, $P < .001$). The diagnostic accuracy of the signal hypointensity-to-thickness ratio was high at 3T (area under the curve = 0.89) and even higher at 7T (area under the curve = 0.94). The sensitivity of the semiautomated method (0.81) outperformed the sensitivity of the visual assessment (0.56–0.63) at 3T.

CONCLUSIONS: The signal hypointensity-to-thickness ratio of the primary motor cortex calculated with a semiautomated method is suggested as a radiologic marker of upper motor neuron burden in patients with amyotrophic lateral sclerosis. This semiautomated method may be useful for improving the subjective radiologic evaluation of upper motor neuron pathology in patients suspected of having amyotrophic lateral sclerosis.

ABBREVIATIONS: ALS = amyotrophic lateral sclerosis; HS = healthy subjects; M1 = primary motor cortex; ROC = receiver operating characteristic; SH/Thk = signal hypointensity-to-thickness ratio; UMN = upper motor neuron

Amyotrophic lateral sclerosis (ALS) is a progressive and clinically heterogeneous neurodegenerative disease involving both upper and lower motor neurons,[1,2] having different prognoses[3] and, perhaps, different responses to possible therapies, even in the experimental scenario. Different from the lower motor neuron impairment that can be carefully investigated with electrophysiologic tests,[4] the evaluation of upper motor neuron (UMN) burden is mainly clinical[1,5] and is partially confounded by signs related to lower motor neuron degeneration.[4] Moreover, at the time of the diagnosis, the UMN impairment can range widely from faint to severe, and the variability in signs and symptoms at disease onset[3] makes early diagnosis and correct phenotypic characterization of the disease difficult.

In ALS, the main pathologic changes in the primary motor

Received May 3, 2017; accepted after revision August 13.

From the Department of Translational Research and New Technologies in Medicine and Surgery (G.D., P.C., M. Cosottini) and Neurology Unit, Department of Clinical and Experimental Medicine (E.C.I., D.F., G.S.), University of Pisa, Pisa, Italy; National Institute for Nuclear Physics (A.R.), Pisa Division, Pisa, Italy; Imago7 Research Foundation (M. Costagli, L.B., M.T.), Pisa, Italy; and Laboratory of Medical Physics and Biotechnologies for Magnetic Resonance (M. Costagli, L.B., M.T.), Istituto di Ricovero e Cura a Carattere Scientifico Stella Maris, Pisa, Italy.

This work is part of the experimental protocol "Clinical Impact of Ultra-High-Field MRI in Neurodegenerative Diseases Diagnosis" (RF RF-2009-1546281) approved and funded by the Italian Ministry of Health and cofunded by the Health Service of Tuscany.

Paper previously presented at: European Congress of Radiology, March 1–5, 2017; Vienna, Austria.

Please address correspondence to Graziella Donatelli, MD, Neuroradiology Unit, Via Paradisa 2, 56124, Pisa, Italy; e-mail: graziella_donatelli@hotmail.com

Indicates open access to non-subscribers at www.ajnr.org
Indicates article with supplemental on-line tables.
Indicates article with supplemental on-line photos.
http://dx.doi.org/10.3174/ajnr.A5423

cortex (M1) include the loss of Betz cells in the layer V[6] and the presence of reactive iron-loaded microglia,[6,7] visible on MR images as cortical atrophy[8-10] and T2* hypointensity,[7] respectively. In recent years, several conventional and nonconventional MR imaging techniques have been used to look for a biomarker of UMN impairment at both cortical and subcortical levels with variable results, and quantitative measurements of cortical atrophy were performed at a group level.[11] Despite such effort, a definite and reliable marker of UMN degeneration is not yet available. As a result, while MR imaging of the brain is currently used to exclude mimic pathology and the detection of the T2 hypointensity of M1 can support suspicion of ALS, the specific search for this abnormality is not recommended for ALS diagnosis.[12]

The first attempt to move toward the radiologic diagnosis at the single-subject level was recently performed with an ultra-high-field MR imaging system (7T).[13] Taking advantage of the very high sensitivity of ultra-high-field strength to the magnetic susceptibility of microglial ferritin, the authors localized pathologic cortical thinning and T2* hypointensity in the deep layers of M1, and they were shown to significantly correlate with the clinical UMN burden. In light of these results, the T2* hyopintensity of M1 was suggested as a possible marker of neuroinflammation and UMN impairment in patients with ALS rather than a marker of the disease. Unfortunately, the T2* sensitivity to microglial ferritin depends on the magnetic field strength, and M1 assessment in patients with ALS can be a challenge in clinical practice using MR imaging systems up to 1.5T also in patients with a severe UMN impairment. On the contrary, 3T scanners may change the radiologic approach to patients with pyramidal symptoms and signs in motor neuron diseases. Therefore, our main aim was to investigate the signal hypointensity-to-thickness ratio (SH/Thk) of the deep layers of the M1 as a radiologic marker of UMN burden in patients with ALS with a semiautomated method at 3T. Secondary aims were to evaluate whether the results obtained with a clinical scanner (3T) were comparable with those achieved with a research scanner (7T) and whether the semiautomated measurements improved the sensitivity of the visual radiologic assessment.

MATERIALS AND METHODS

Patients with ALS and Healthy Subjects

Twenty-seven patients with ALS (18 men and 9 women; mean age, 58 ± 11 years) and 13 healthy subjects (HS; 6 men and 7 women; mean age, 56 ± 15 years) underwent brain MR imaging with a 3T system.

Nineteen patients with ALS (14 men and 5 women; mean age, 63 ± 10 years), different from the patients with ALS investigated at 3T, and 18 HS (9 men and 9 women; mean age, 56 ± 13 years) underwent brain MR imaging with a 7T system.

Five of the above-mentioned HS underwent both examinations to compare the performance of the 3T and 7T systems in the assessment of signal intensity and thickness of the deep layers of M1.

All patients had a diagnosis of definite ALS according to the revised El Escorial criteria[1] and were consecutively enrolled by the neurology unit of the University Hospital of Pisa. They were clinically evaluated by an experienced neurologist on the day of enrollment, and the UMN impairment was quantified for each limb using a clinical composite semiquantitative arbitrary score of UMN burden (UMN score), according to that previously used by Cosottini et al.[13] For each patient, the total UMN score (range, 0–33) and the UMN score of each limb (range, 0–8) were recorded; then, the average UMN score was calculated as the mean of UMN scores of both arms and legs. Clinical and demographic data of patients are reported in On-line Tables 1–3. Exclusion criteria for enrollment were the presence of neurologic comorbidities. HS were enrolled from among relatives and spouses of patients with ALS and radiology department staff; none had any history of neurologic or psychiatric diseases.

All patients and controls gave their written informed consent for the enrollment. This study was performed as part of the experimental protocol called "Clinical Impact of Ultra-High-Field MRI in Neurodegenerative Diseases Diagnosis," RF-2009-1546281, approved by Italian Ministry of Health and by the local ethics committee. The project was founded by the Italian Ministry of Health and cofunded by the Health Service of Tuscany.

MR Imaging Acquisition

The MR imaging protocol at both 3T and 7T included a 3D multiecho T2*-weighted sequence prescribed axially and covering the brain from the vertex to the splenium of the corpus callosum.

MR imaging examinations at 3T were performed with a Discovery MR 750 (GE Healthcare, Milwaukee, Wisconsin) scanner equipped with an 8-channel head coil. Acquisition parameters of the 3D multiecho T2*-weighted sequence were the following: TR = 68.3 ms; TEs = 13, 18.6, 24.3, 29.9, 35.5, 41.2, 46.8, 52.4, 58.1, 63.7 ms; flip angle = 15°; NEX = 0.70; acquisition matrix = 448 × 384; FOV = 20 × 20 cm; spatial resolution of reconstructed images = 0.39 × 0.39 × 1 mm^3; scan duration = 4 minutes 22 seconds.

MR imaging examinations at 7T were performed with a Discovery MR 950 scanner (GE Healthcare) equipped with a 2CH-TX/32CH-RX head coil (Nova Medical, Wilmington, Massachusetts). Technical parameters of the 3D multiecho T2*-weighted sequence were the following: TR = 54.1 ms; TEs = 5.6, 12, 18.3, 24.7, 31.1, 37.5, 43.9 ms; flip angle = 15°; NEX = 0.70; acquisition matrix = 448 × 448; FOV = 22.4 × 22.4 cm; spatial resolution of reconstructed images = 0.5 × 0.5 × 1 mm^3; scan duration = 6 minutes 59 seconds.

Semiautomated Image Assessment

In each hemisphere of all subjects, the thickness and signal intensity of the regions of M1 corresponding to Penfield areas of the upper[14] and lower[15] limbs were assessed with an in-house-developed, semiautomated tool for image processing. Given the wide cortical extension of the upper and lower limb motor areas, to increase the reliability of the ROI position among subjects, we selected 2 smaller M1 subregions for the ROI positioning; thus, ROIs of the upper limbs were positioned in the hand knob, whereas ROIs of the lower limbs were positioned in the most cranial and lateral part of the paracentral lobule. In each set of images, a neuroradiologist blinded to the clinical diagnosis identified the sections that best represented each M1 target region and an additional section including the splenium of the corpus callo-

sum, which served to obtain 1 region of reference for the M1 signal intensity measures.[16] The interactive image-processing tools were run according to the steps described in detail in On-line Fig 1. The observer is prompted to draw a polygonal ROI (not <5 mm^2) in the splenium of the corpus callosum, whose average intensity was retained to normalize the intensity values of the cortex ROIs. For each M1 target region, the observer manually draws the profile of the interface between the M1 and the neighboring subarachnoid space, which is interpolated by the software with a spline function to make it smoother. The directions normal to the spline are computed, and the trend of the signal intensity (y-axis) is reported as the function of the distance along the normal direction to the cortex (x-axis) in physical units (millimeter). The signal intensity profiles are then averaged and the absolute value is considered. A baseline intensity value corresponding to the average signal intensity of the subcortical white matter, computed in a region chosen by the observer, is then subtracted. The hypointensity profile is then fitted with a double sigmoid function F that can be expressed as the difference between 2 sigmoid function as follows: $F(x; a, b_1, b_2, c_1, c_2) = a\,[f_1(x; b_1, c_1) - f_2(x; b_2, c_2)]$, where $f(x; b, c) = 1/\{1 + e\hat{}[-b\,(x - c)]\}$. The thickness and the height of the final intensity profile, which was normalized with respect to the signal intensity of the splenium of the corpus callosum, are recorded as measures of the mean thickness and signal hypointensity of M1 deep layers, respectively. In particular, the depth of the curve and the width at 25% of the height are taken as measures of signal hypointensity and thickness of the deep layers of the M1, respectively.

The semiautomated tool for image processing was implemented in Matlab (MathWorks, Natick, Massachusetts) and runs on different operating systems (Windows, MacOS, Linux). It receives input MR images in the NIfTI or Analyze (Analyze-Direct, Overland Park, Kansas) file format and returns the measures of the cortex hypointensity and thickness as well as several graphic representations of intermediate steps of the interactive image processing.

For each target region of every subject, the SH/Thk was calculated to put together and maximize the contribution of both parameters in the morphometric assessment of the cortex. In the comparison between patients and HS and in the computation of the receiver operating characteristic (ROC) curve, we included in the analysis all data of all HS and, for each patient, only the greatest SH/Thk value recorded between the 2 hemispheres. The choice of selecting only 1 measure for each patient was based on the possible asymmetry in the pathologic involvement of the M1.[17-19] On the contrary, all measures of all patients were used in assessing the correlation between the SH/Thk of the M1 subregions and the UMN scores of the corresponding limbs.

Visual Image Assessment

All images were randomly evaluated by 2 neuroradiologists (M. Cosottini and G.D., with 26 and 7 years of experience, respectively) blinded to the clinical diagnosis. The observers were asked to visually evaluate each series of images on the basis of the signal intensity and thickness of the deep layers of M1 compared with those of neighboring cortices. Images were labeled as "nonpathologic" if M1 deep layers were judged to be similar to those of other cortices or "pathologic" if they were markedly more hypointense and thin.[13] After 1 month from the first reading, the same neuroradiologists were asked to again assess the whole set of images.

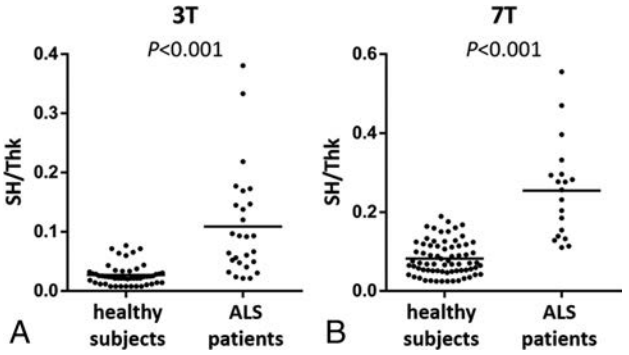

FIG 1. Boxplot of the SH/Thk measured in the deep layers of the primary motor cortex in healthy subjects and patients with ALS at 3T (*A*) and 7T (*B*). At both magnetic fields, the ratio is significantly greater in patients than in subjects ($P < .001$).

Statistical Analysis

Quantitative and semiquantitative data were analyzed using nonparametric statistical tests with the significance level set to .05. In more detail, 3T and 7T data concerning HS who underwent both MR imaging examinations were compared using the Wilcoxon test. The SH/Thk comparison between patients with ALS and HS was performed using the Friedman test, whereas all other intergroup comparisons were investigated using the Mann-Whitney U test. Relationships between variables were investigated with the Spearman rank test, and ROC analysis was used as a binary classifier system to evaluate the performance of the SH/Thk in distinguishing patients from HS.

Using the clinical diagnosis as the criterion standard, we calculated the sensitivity, specificity, positive predictive value, negative predictive value, and diagnostic accuracy of the visual assessment of images for both reading sessions of both observers (for each reader, data shown in the "Results" section refer to the reading session with the best diagnostic accuracy). The Cohen κ statistic was used to calculate intra- and interrater reliability.

RESULTS

Epidemiologic and Clinical Data Analysis

The age of patients was not significantly different from that of HS at both 7T and 3T ($P = .12$ and $P = .64$, respectively). Total UMN scores and mean UMN scores did not significantly differ between patients investigated at 3T and patients assessed at 7T ($P = .87$ and $P = .86$, respectively).

Semiautomated Image Assessment

SH/Thk of the Primary Motor Cortex.

3T. SH/Thk was significantly higher in patients than in HS (mean, 0.11 ± 0.09; 95% CI, 0.07–0.14 for patients; and mean, 0.03 ± 0.02; 95% CI, 0.02–0.03 for HS; $P < .001$) (Fig 1*A*).

7T. SH/Thk was significantly higher in patients than in HS (mean, 0.25 ± 0.12; 95% CI, 0.20–0.31 for patients; and mean, 0.08 ± 0.04; 95% CI, 0.07–0.09 for HS; $P < .001$) (Fig 1*B*).

In the subgroup of HS who underwent MR imaging at both 3T and 7T, the SH/Thk of the deep layers of the M1 was significantly ($P < .001$) higher at 7T than at 3T.

Correlation of the SH/Thk with UMN Score.

3T. In patients with ALS, the SH/Thk of the deep layers of M1 significantly correlated with the UMN score of the corresponding limbs ($\rho = 0.57$, $P < .001$; 95% CI, 0.42–0.69) (Fig 2*A*).

7T. In patients with ALS, the SH/Thk measured in the M1 deep layers showed a significant correlation with the UMN score of the corresponding limbs ($\rho = 0.57$, $P < .001$; 95% CI, 0.39–0.71) (Fig 2*B*).

The measures of signal intensity and thickness of M1 subregions of HS overlapped those recorded in cortical subregions of patients corresponding to limbs with UMN scores of up to 3. On the contrary, the dataset of HS was more clearly distinguishable from that concerning cortical subregions of patients corresponding to limbs with UMN scores of >3. This observation was seen with both 3T and 7T data (On-line Figs 2 and 3).

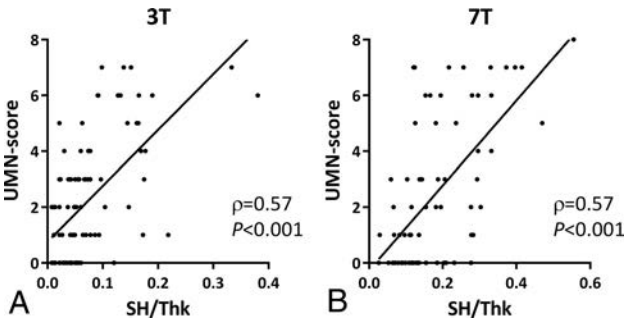

FIG 2. Correlation between the SH/Thk measured in the deep layers of the primary motor cortex of patients with ALS (hand knob and paracentral lobule of both hemispheres) and the UMN scores of the corresponding limbs. Correlations are moderate and significant at both 3T and 7T ($\rho = 0.57$, $P < .001$).

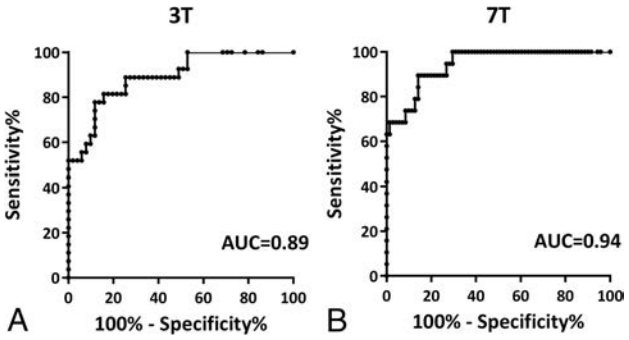

FIG 3. ROC curves elaborated with 3T (*A*) and 7T (*B*) data pool. The curves show, respectively, a good and an excellent accuracy to discriminate pathologic and nonpathologic values of SH/Thk.

Diagnostic Performance of SH/Thk.

3T. ROC analysis of 3T data showed a good accuracy (area under the curve = 0.89) in differentiating pathologic from nonpathologic data, with a sensitivity of 0.81 and a specificity of 0.84 (Fig 3*A*).

7T. ROC analysis of 7T data showed an excellent accuracy (area under the curve = 0.94) as binary classifiers of data as pathologic or nonpathologic, with a sensitivity of 0.89 and a specificity of 0.86 (Fig 3*B*).

Visual Image Assessment

3T. Sensitivity, specificity, and diagnostic accuracy were, respectively, 0.56, 0.92, and 0.68 for the first reader and 0.63, 0.85, and 0.70 for the second reader (Table). The intrarater agreement was good for the first reader and very good for the second reader (0.74 and 0.85, respectively), and the interrater agreement was good for both reading sessions (0.80 and 0.70). The mean values of the total UMN scores of patients correctly diagnosed and patients misdiagnosed were, respectively, 11 and 5 for the first reader and 12 and 3 for the second reader.

7T. Sensitivity, specificity, and diagnostic accuracy were, respectively, 0.68, 0.89, and 0.78 for the first reader and 0.63, 1.00, and 0.81 for the second reader (Table). The intrarater agreement was very good for both readers (0.83 and 0.81), and the interrater agreement was good for both reading sessions (0.65 and 0.77). The mean values of the total UMN scores of patients correctly diagnosed and patients misdiagnosed were, respectively, 13 and 2 for the first reader and 13 and 4 for the second reader.

DISCUSSION

SH/Thk Changes in Patients with ALS and Correlation with Clinical UMN Impairment

The magnetic susceptibility of the deep layers of the M1, revealed by 3D multiecho T2*-weighted images and related to cortical content of nonheme iron,[7,16,20] can be used to assess both their signal intensity and thickness. The distinction between the superficial and deep layers of the M1 is also often detectable on 3T images of patients and HS (On-line Fig 1 and Fig 4) and depends on the amount of myelinated fibers, deep layers being more myelinated than superficial ones. The gray-white matter junction in the M1 is sometimes hardly distinguishable in HS and in patients with mild UMN impairment because of the heavily myelinated deep layers of M1.[13] On the contrary, in patients with ALS with moderate-to-severe UMN impairment, the deep layers of the M1 appear mark-

Results of visual assessment of 3T and 7T images

	3T				7T			
	First Reader		Second Reader		First Reader		Second Reader	
	First Reading	Second Reading	First Reading	Second Reading	First Reading	Second Reading	First Reading	Second Reading
Sensitivity	0.52	0.56	0.63	0.59	0.63	0.68	0.63	0.58
Specificity	0.92	0.92	0.85	0.85	0.89	0.89	1.00	1.00
Positive predictive value	0.93	0.94	0.89	0.89	0.86	0.87	1.00	1.00
Negative predictive value	0.48	0.50	0.52	0.50	0.70	0.73	0.72	0.69
Diagnostic accuracy	0.65	0.68	0.70	0.68	0.76	0.78	0.81	0.78

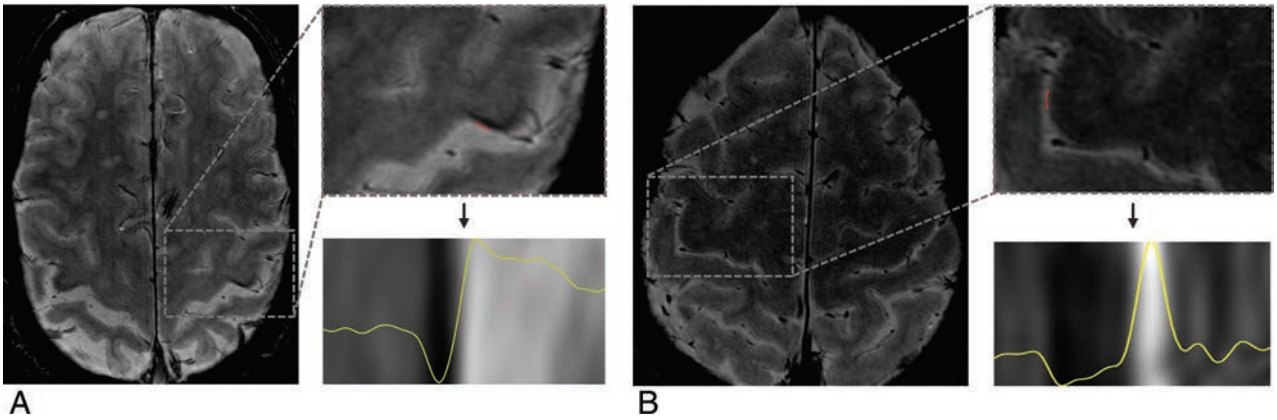

FIG 4. The signal profile of the M1 containing the intensity and thickness information is shown for the left knob of a patient with ALS (*A*) and the right knob of a healthy subject (*B*), where the deep layers of the cortex are clearly visible.

edly more hypointense than the underlying white matter (On-line Fig 1 and Fig 4).

When we used such cortical features in the semiautomated analysis, the SH/Thk was significantly higher in patients than in HS. This finding confirmed its usefulness in the correct assessment of M1 morphology at the group level. However, as shown in Fig 1, SH/Thk values were more scattered in patients than in HS, and there was a partial overlap between the 2 groups. Such distribution of patient data was most likely due to the nonuniform UMN burden among patients. In fact, as shown in On-line Fig 3, a greater UMN score corresponded to a greater ability to distinguish patients from HS, mainly for UMN scores of >3. From a clinical point of view, in the group of patients with ALS, there was a significant positive correlation between the SH/Thk of the deep layers of M1 and the UMN score of the corresponding limbs: the greater the SH/Thk, the greater the clinical limb impairment. In other words, the cortical hypointensity ranged from being very pronounced to being seemingly indistinguishable from that of an unaffected cortex in patients with severe or light UMN impairment, respectively.

The hypothesis of a direct link between the location of cortical atrophy within the motor homunculus and clinical signs of UMN impairment was proposed >20 years ago on the basis of pathologic studies,[17] but until now, only a few MR imaging studies investigated such a correlation using scores of functional disability[9,10,21] or UMN impairment.[13] Our results agree with previous findings at ultra-high-field MR imaging[13] and confirm the link between the degree of focal cortical atrophy and hypointensity in the motor homunculus and the degree of signs of UMN degeneration in the corresponding limbs. Such results explain why neuroradiologists can correctly diagnose patients with ALS with moderate-to-severe UMN impairment, whereas patients with low or very low UMN burden are misdiagnosed. Moreover, the pattern of T2* hypointensity can be different among patients. In fact, according to the UMN burden, the extension of M1 signal hypointensity ranges from being localized to a small region of the M1 to bilaterally involving its full length, from the interhemispheric fissure to the lateral sulcus.

The marked T2* hypointensity of the deep layers of M1 in some patients with ALS compared with HS was demonstrated to be the expression of the greater magnetic susceptibility related to the abundant intracortical deposition of iron in the form of microglial ferritin.[7,16] With the magnetic susceptibility having a positive and strict dependence on the magnetic field strength, T2* sensitivity to paramagnetic substances is lower at 3T than at 7T, as demonstrated in the subgroup of HS who underwent MR imaging examinations at both magnetic fields, thus reducing the ability to detect small collections of intracortical ferritin in patients with ALS with moderate-to-low UMN impairment. Such findings explain why the sensitivity, negative predictive value, and diagnostic accuracy in the visual imaging assessment were lower at 3T than at 7T. In line with this result, the performance of ROC analysis was also slightly better at 7T than at 3T. However, the accuracy in distinguishing pathologic and nonpathologic images using the semiautomated method was also high at 3T.

ROC data can be used in the assessment of subjects referred from neurologists with suspected motor neuron disease. In this scenario, the choice of a cutoff that improves sensitivity though affecting specificity can result in a more accurate M1 evaluation of patients. In fact, in our population, the use of the semiautomated method showed an increased sensitivity in evaluating M1 morphologic changes compared with visual imaging assessment. Therefore, besides visual image evaluation, after data collection from healthy subjects and the definition of a cutoff value, the use of the SH/Thk in clinical practice can contribute to the radiologic evaluation of images, mainly in patients with mild UMN burden, confirming morphologic changes that are only slightly visible on visual inspection. More interesting prospects are to increase the sensitivity of neuroimages in the detection of UMN pathology, allowing the identification of very small M1 changes and reducing the false-negative rate, and to estimate the UMN burden, thus supporting the clinical evaluation of patients and contributing to their phenotypical classification. To further support this hypothesis, one could confirm, in a larger sample, that the UMN score of patients correctly classified at visual assessment is higher than that of patients in whom visual and semiautomated assessments disagree in the classification of images.

One should note the following aspects of the present study. First, different from studies investigating cortical thickness, which assessed the cortex in a full-thickness fashion,[8-10] here we evaluated only the deep layers of M1, known to be the location of pathologic changes. Second, contrary to cortical thickness and

voxel-based morphometry studies,[8-10,18,19] after having collected some data from HS, the presented method could be applied not only at the group level but also at the single-subject level to estimate the UMN burden in each patient with pyramidal signs and symptoms. Third, until now, MR imaging studies investigated, individually, cortical atrophy[8-10,18,19] or hypointensity.[7,22] To the best of our knowledge, this is the first study assessing the combination of both parameters, thus improving the radiologic evaluation of M1. Compared with the assessment of a single parameter (SH or Thk), the use of the SH/Thk gives us 3 main advantages: 1) to assess simultaneously 2 different radiologic features related to the cortical neurodegeneration; 2) to find a radiologic tool that correlates with clinical UMN impairment; and 3) to reduce the false-positive ratio related to the increase in T2* hypointensity of M1 in the elderly. Furthermore, because the SH/Thk is semiquantitative data measured in each single subject, it could be used for the phenotypic stratification of UMN involvement in longitudinal studies aiming at investigating the spread of cortical changes across time[2] or the efficacy of neuronal and nonneuronal therapies.

Methodologic Considerations

T2* signal features within the cortex allow distinguishing superficial and deep layers, thus measuring only the thickness of M1 deep layers, where the atrophy seems to be localized. By contrast, sequences commonly used for cortical thickness measurements, such as inversion recovery T1-weighted sequences, provide better gray-white matter contrast but are used only for full-thickness cortical measurements and do not allow more targeted measurements.

For evaluation of cortical thinning and signal hypointensity of the deep layers of the primary motor cortex at 7T, 2D gradient recalled sequences with high in-plane resolution have previously been used.[13] However, in clinical settings on high-field MR imaging systems (3T), 2D gradient recalled-echo sequences are not as efficient as 3D multiecho T2*-weighted techniques, which were proved to be the most sensitive in the detection of the low signal intensity in the precentral cortex of patients with ALS, due to the higher sensitivity of multiecho T2*-weighted imaging to iron in the form of ferritin[23]; hence, their use was preferred in this study.

The sequence used in this study has often been used in the assessment of brain iron deposits[24,25]; however, it has recently been demonstrated that techniques that rely on the signal phase, namely quantitative susceptibility mapping, are more accurate than transverse relaxation times in terms of iron quantification.[26,27] Nevertheless, the production of susceptibility maps requires particular acquisition settings: in most quantitative susceptibility mapping implementations such as ours, the MR imaging system is programmed to provide the complex MR imaging data divided into real and imaginary parts, which are of no radiologic use. In fact, quantitative susceptibility mapping requires additional scan time in addition to the conventional 3D T2* multiecho sequence that is included in the clinical protocol. Quantitative susceptibility mapping also requires time-consuming postprocessing.

A limitation of this study was that patients with ALS investigated at 3T and 7T were not the same; hence, a direct comparison of the diagnostic accuracies obtained with the systems working at different magnetic field strengths would be unfair. However, on the basis of the absence of significant differences in total and mean UMN scores between the 2 groups of patients and on the significant correlation of signal intensity and thickness with UMN scores,[13] we could hypothesize that MR imaging morphologic changes of M1 are comparable between groups, and a cautious comparison of MR diagnostic accuracy between different magnetic fields could be made. A further limitation is the number of subjects enrolled. Considering that ALS is a rare disease, the population we investigated is quite large, but the potential clinical applications described above need to be tested on a larger group of subjects or, at least, on a different cohort of patients to confirm the feasibility and reproducibility of results.

CONCLUSIONS

The SH/Thk of the deep layers of the M1 measured with a semiautomated method at 3T seems to be a radiologic marker of upper motor neuron burden in patients with ALS, though with less accuracy than at 7T.

Despite the heterogeneous magnitude of the UMN burden of patients, the combination of visual imaging assessment and the use of a semiautomated algorithm able to assess both thickness and T2* hypointensity of the deep layers of M1 could increase the sensitivity in evaluating images of patients referred with suspected motor neuron disease.

Disclosures: Mirco Cosottini—*RELATED*: *Grant*: Italian Ministry of Health, *Comments*: This study has received funding (RF-2009-1546281) to Mirco Cosottini as Principal Investigator by the Italian Ministry of Health (www.salute.gov.it) and the Health Service of Tuscany (www.regione.toscana.it/sst). The funders had no role in study design, data collection and analysis, decision to publish, or preparation of the manuscript.* *Money paid to the institution.

REFERENCES

1. Brooks BR, Miller RG, Swash M, et al; World Federation of Neurology Research Group on Motor Neuron Diseases. **El Escorial revisited: revised criteria for the diagnosis of amyotrophic lateral sclerosis.** *Amyotroph Lateral Scler Other Motor Neuron Disord* 2000;1:293–99 CrossRef Medline
2. Ravits JM, La Spada AR. **ALS motor phenotype heterogeneity, focality, and spread: deconstructing motor neuron degeneration.** *Neurology* 2009;73:805–11 CrossRef Medline
3. Kiernan MC, Vucic S, Cheah BC, et al. **Amyotrophic lateral sclerosis.** *Lancet* 2011;377:942–55 CrossRef Medline
4. Eisen A, Swash M. **Clinical neurophysiology of ALS.** *Clin Neurophysiol* 2001;112:2190–201 CrossRef Medline
5. de Carvalho M, Dengler R, Eisen A, et al. **Electrodiagnostic criteria for diagnosis of ALS.** *Clin Neurophysiol* 2008;119:497–503 CrossRef Medline
6. Kawamata T, Akiyama H, Yamada T, et al. **Immunologic reactions in amyotrophic lateral sclerosis brain and spinal cord tissue.** *Am J Pathol* 1992;140:691–707 Medline
7. Kwan JY, Jeong SY, Van Gelderen P, et al. **Iron accumulation in deep cortical layers accounts for MRI signal abnormalities in ALS: correlating 7 Tesla MRI and pathology.** *PLoS One* 2012;7:e35241 CrossRef Medline
8. Verstraete E, Veldink JH, Hendrikse J, et al. **Structural MRI reveals cortical thinning in amyotrophic lateral sclerosis.** *J Neurol Neurosurg Psychiatry* 2012;83:383–88 CrossRef Medline
9. Schuster C, Kasper E, Machts J, et al. **Focal thinning of the motor cortex mirrors clinical features of amyotrophic lateral sclerosis and**

their phenotypes: a neuroimaging study. *J Neurol* 2013;260: 2856–64 CrossRef Medline
10. Walhout R, Westeneng HJ, Verstraete E, et al. **Cortical thickness in ALS: towards a marker for upper motor neuron involvement.** *J Neurol Neurosurg Psychiatry* 2015;86:288–94 CrossRef Medline
11. Foerster BR, Welsh RC, Feldman EL. **25 years of neuroimaging in amyotrophic lateral sclerosis.** *Nat Rev Neurol* 2013;9:513–24 CrossRef Medline
12. Filippi M, Agosta F, Abrahams S, et al; European Federation of Neurological Societies. **EFNS guidelines on the use of neuroimaging in the management of motor neuron diseases.** *Eur J Neurol* 2010;17: 526-e20 CrossRef Medline
13. Cosottini M, Donatelli G, Costagli M, et al. **High-resolution 7T MR imaging of the motor cortex in amyotrophic lateral sclerosis.** *AJNR Am J Neuroradiol* 2016;37:455–61 CrossRef Medline
14. Yousry TA, Schmid UD, Alkadhi H, et al. **Localization of the motor hand area to a knob on the precentral gyrus: a new landmark.** *Brain* 1997;120:141–57 CrossRef Medline
15. Penfield W, Rasmussen T. *The Cerebral Cortex of Man: A Clinical Study of Localization of Function.* New York: Macmillan; 1950
16. Costagli M, Donatelli G, Biagi L, et al. **Magnetic susceptibility in the deep layers of the primary motor cortex in amyotrophic lateral sclerosis.** *Neuroimage Clin* 2016;12:965–69 CrossRef Medline
17. Mochizuki Y, Mizutani T, Takasu T. **Amyotrophic lateral sclerosis with marked neurological asymmetry: clinicopathological study.** *Acta Neuropathol* 1995;90:44–50 CrossRef Medline
18. Kassubek J, Unrath A, Huppertz HJ, et al. **Global brain atrophy and corticospinal tract alterations in ALS, as investigated by voxel-based morphometry of 3-D MRI.** *Amyotroph Lateral Scler Other Motor Neuron Disord* 2005;6:213–20 CrossRef Medline
19. Devine MS, Pannek K, Coulthard A, et al. **Exposing asymmetric gray matter vulnerability in amyotrophic lateral sclerosis.** *Neuroimage Clin* 2015;7:782–87 CrossRef Medline
20. Hallgren B, Sourander P. **The effect of age on the non-haemin iron in the human brain.** *J Neurochem* 1958;3:41–51 CrossRef Medline
21. Bede P, Bokde A, Elamin M, et al. **Grey matter correlates of clinical variables in amyotrophic lateral sclerosis (ALS): a neuroimaging study of ALS motor phenotype heterogeneity and cortical focality.** *J Neurol Neurosurg Psychiatry* 2013;84:766–73 CrossRef Medline
22. Ignjatović A, Stević Z, Lavrnić S, et al. **Brain iron MRI: a biomarker for amyotrophic lateral sclerosis.** *J Magn Reson Imaging* 2013;38: 1472–79 CrossRef Medline
23. Adachi Y, Sato N, Saito Y, et al. **Usefulness of SWI for the detection of iron in the motor cortex in amyotrophic lateral sclerosis.** *J Neuroimaging* 2015;25:443–51 CrossRef Medline
24. Du G, Lewis MM, Styner M, et al. **Combined R2* and diffusion tensor imaging changes in the substantia nigra in Parkinson's disease.** *Mov Disord* 2011;26:1627–32 CrossRef Medline
25. Baudrexel S, Nürnberger L, Rüb U, et al. **Quantitative mapping of T1 and T2* discloses nigral and brainstem pathology in early Parkinson's disease.** *Neuroimage* 2010;51:512–20 CrossRef Medline
26. Schweser F, Deistung A, Lehr BW, et al. **Quantitative imaging of intrinsic magnetic tissue properties using MRI signal phase: an approach to in vivo brain iron metabolism?** *Neuroimage* 2011;54: 2789–807 CrossRef Medline
27. Barbosa JH, Santos AC, Tumas V, et al. **Quantifying brain iron deposition in patients with Parkinson's disease using quantitative susceptibility mapping, R2 and R2.** *Magn Reson Imaging* 2015;33: 559–65 CrossRef Medline

Perivascular Spaces in Old Age: Assessment, Distribution, and Correlation with White Matter Hyperintensities

A. Laveskog, R. Wang, L. Bronge, L.-O. Wahlund, and C. Qiu

ABSTRACT

BACKGROUND AND PURPOSE: The visual rating scales for perivascular spaces vary considerably. We sought to develop a new scale for visual assessment of perivascular spaces and to further describe their distribution and association with white matter hyperintensities in old age.

MATERIALS AND METHODS: This population-based study included 530 individuals who did not have dementia and were not institutionalized (age, ≥60 years or older; mean age, 70.7 years; 58.9% women) who were living in central Stockholm, Sweden. A semiquantitative visual rating scale was developed to score the number and size of visible perivascular spaces in 7 brain regions in each hemisphere. A modified Scheltens visual rating scale was used to assess white matter hyperintensities.

RESULTS: The global scores for perivascular spaces ranged from 4–32 for number, 3–22 for size, and 7–54 for the combination of number and size. The weighted κ statistics for the intra- and interrater reliability both were 0.77. The global score for the number of perivascular spaces increased with advancing age ($P < .001$). The scores for the number of perivascular spaces in the basal ganglia and subinsular regions were significantly correlated with the load of white matter hyperintensities, especially in lobar and deep white matter regions (partial correlation coefficients, >0.223; $P < .01$).

CONCLUSIONS: The new visual rating scale for perivascular spaces shows excellent intra- and interrater reliability. The number of perivascular spaces globally and, especially, in the basal ganglia, is correlated with the load of lobar and deep white matter hyperintensities, supporting the view that perivascular spaces are a marker for cerebral small-vessel disease.

ABBREVIATIONS: ICD = International Classification of Diseases; PVH = periventricular hyperintensities; PVS = perivascular spaces; SNAC-K = Swedish National study on Aging and Care in Kungsholmen; STRIVE = STandards for Reporting Vascular changes on nEuroimaging; WMH = white matter hyperintensities

The perivascular spaces (PVS) are subpial virtual spaces between the adventitia of the vessel and the basal membrane of the glia limitans, involved in the lymphatic drainage of the brain.[1,2] PVS are now easily identifiable in vivo, owing to improved MR imaging techniques.[3] Since the late 1980s, different rating scales have been developed for the evaluation of PVS, depending on the purpose of the study.[4-9] However, very few scales have simultaneously taken the number, size, and location of PVS into consideration. This is important because it remains unclear whether the number or the size of PVS is clinically relevant. Also, PVS in various anatomic regions of the brain may differ in risk factors, neuropathologies, and functional consequences.[10,11] Thus, STandards for Reporting Vascular changes on nEuroimaging (STRIVE) have proposed to evaluate the number, size (maximum diameter), and anatomic location of PVS.[12]

PVS are common among elderly adults. Indeed, PVS are correlated with increasing age,[4,9,13] though some earlier studies have shown equal distribution of PVS through a range of ages.[14,15] In addition, a sex difference in the distribution of PVS in the basal

Received August 16, 2016; accepted after revision September 1, 2017.

From the Division of Radiology (A.L.), Department of Clinical Science, Intervention and Technology; Aging Research Center (R.W., C.Q.), Department of Neurobiology, Care Sciences and Society; and Department of Clinical Neuroscience (L.B.), Karolinska Institutet, Stockholm, Sweden; Department of Neuroradiology (A.L.), Karolinska University Hospital, Stockholm, Sweden; Aleris Diagnostics (L.B.), Sabbatsberg, Stockholm, Sweden; and Division of Clinical Geriatrics (L.-O.W.), Department of Neurobiology, Care Sciences and Society, Karolinska University Hospital at Huddinge, Stockholm, Sweden.

SNAC-K was supported by the Swedish Ministry of Health and Social Affairs, the Stockholm County Council, Stockholm Municipality, and the Swedish Research Council. This work was further supported, in part, by grants from the Swedish Research Council (grant Nos. 2015-02531 and 2016-06658); the Swedish Research Council for Health, Working Life and Welfare (grant No. 2014-01382); and the Karolinska Institutet, Stockholm, Sweden.

Please address correspondence to Anna Laveskog, MD, Department of Neuroradiology, Karolinska University Hospital, S-171 76 Stockholm, Sweden; e-mail: anna.laveskog@sll.se; Rui Wang, PhD, Aging Research Center, Karolinska Institutet, Gävlegatan 16, 113 30 Stockholm, Sweden; e-mail: rui.wang@ki.se; or Chengxuan Qiu, MD, Aging Research Center, Karolinska Institutet, Gävlegatan 16, 113 30 Stockholm, Sweden; e-mail: chengxuan.qiu@ki.se

Indicates open access to non-subscribers at www.ajnr.org
Indicates article with supplemental on-line tables.
Indicates article with supplemental on-line photo.
http://dx.doi.org/10.3174/ajnr.A5455

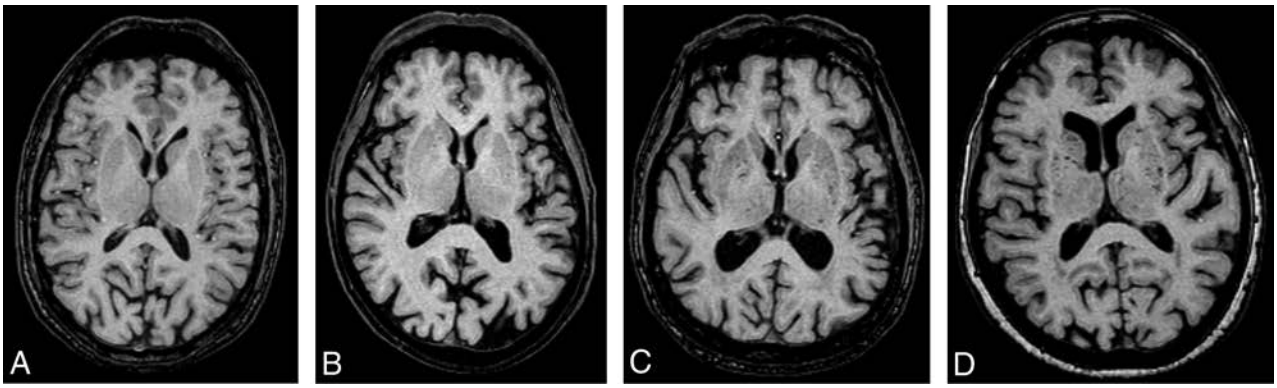

FIG 1. Sample images of grades 0–3 for the number of perivascular spaces bilaterally in the basal ganglia medial to the external capsule. The images indicate grade 0 (*A*), grade 1 (*B*), grade 2 (*C*), and grade 3 (*D*) in the basal ganglia. Note that the perivascular spaces contributing to the score might be in another level and thus not visible in the sample images.

ganglia has been reported, with men having more PVS than women.[11,13,16] The most common etiologies proposed for the widening of the originally virtual PVS to become visible on MR imaging are hypertension[13,17] and amyloid deposition, at least in patients with Alzheimer disease.[18] Some studies have suggested that PVS are associated with cognitive decline and dementia.[6,13]

In the past decade, studying PVS as an imaging marker for cerebral small-vessel disease represents one of the research frontiers in brain aging.[8] Some studies have reported that PVS are correlated with the load of both white matter hyperintensities (WMH) and periventricular hyperintensities (PVH) independent of age and vascular risk factors,[19] suggesting that PVS may be an imaging marker for cerebral small-vessel disease. However, it has been unclear whether PVS in various anatomic regions are differentially associated with global and regional WMH because PVS in different regions may have different origins and etiopathologies.[10]

Here we present data from a population-based MR imaging study within the Swedish National study on Aging and Care in Kungsholmen (SNAC-K) in central Stockholm, Sweden.[20] Within this study, we have the unique opportunity to describe a new visual rating scale for PVS by considering the number, size, and location of PVS. Furthermore, we sought to investigate the age- and sex-specific distribution of PVS in older individuals and to explore whether global and regional PVS are associated with the load of global and regional WMH.

MATERIALS AND METHODS

Study Participants

Participants were derived from the SNAC-K study, a multidisciplinary study of aging and health, as fully reported elsewhere.[20] Briefly, the SNAC-K study included 4 younger cohorts with 6-year intervals (60, 66, 72, and 78 years of age) and 7 older cohorts with 3-year intervals (81, 84, 87, 90, 93, 96, and 99 and older years of age). Of all 4590 persons who were eligible to participate in SNAC-K, 3363 (73.3%) were eventually examined at baseline (March 2001 to June 2004). From September 2001 to October 2003, five hundred fifty-five SNAC-K participants who were not institutionalized or disabled and who did not have dementia also underwent brain MR imaging examinations.[20] Of these, 2 persons did not complete the entire examination owing to claustrophobia, 4 had suboptimal MR imaging because of motion artifacts, 2 were excluded because of large meningiomas, and images for 17 persons were lost due to technical problems. Therefore, 530 subjects were included in this study. All the participants had a Mini-Mental State Examination score of ≥21 (mean score, 29). Fifteen brain regions in 6 subjects were impossible to assess because of large infarcts. Therefore, these regions, but not other regions in these subjects, were excluded from our analysis.

SNAC-K was approved by the regional ethics review board in Stockholm, Sweden. Written informed consent was collected from all participants in the SNAC-K MR imaging sample.

MR Imaging Acquisition

All participants were scanned on an Intera 1.5T system (Philips Healthcare, Best, the Netherlands). For the visual assessment of PVS, a T1-weighted sequence (MPRAGE; TR, 15 ms; TE, 7 ms; flip angle, 15°) consisting of one hundred fifty 1.5-mm axial sequential images without angulation; a FLAIR sequence (TR, 6000 ms; TI, 1900 ms; TE, 100 ms; echo-train length, 21; flip angle 90°) of twenty 5-mm sequential images, with a gap of 1 mm, angled to the subcallosal line; and a proton-density/T2-weighted sequence (TR, 3995 ms; TE, 18/90 ms; echo-train length, 6; flip angle, 90°) of sixty 3-mm sequential images without a gap or angulation were used. All images were reviewed on a clinical PACS system.

Visual Assessment of PVS

We constructed a visual rating scale while considering the number, size, and location of PVS. The assessment was performed separately for each hemisphere, and the different locations of the brain were chosen on the basis of the regions used in earlier studies.[6,7,21] In each region of both hemispheres, the number and maximum diameter of PVS were scored and recorded separately. The scores for both the number and size were then summed up to obtain a global semiquantitative measurement of visible PVS, with a maximum score of 84.

The brain regions scored were the cerebellum, mesencephalon (including the upper part of pons), hippocampus, subinsular territory (external capsule, claustrum, and extreme capsule), basal ganglia (medial to external capsule, including the thalamus and internal capsule), frontal lobe, and parieto-occipital lobe. Visible PVS in each region were counted and then scored as 0 (no visible PVS), 1 (1–5 PVS), 2 (6–10 PVS), or 3 (>10 PVS) (Fig 1 and

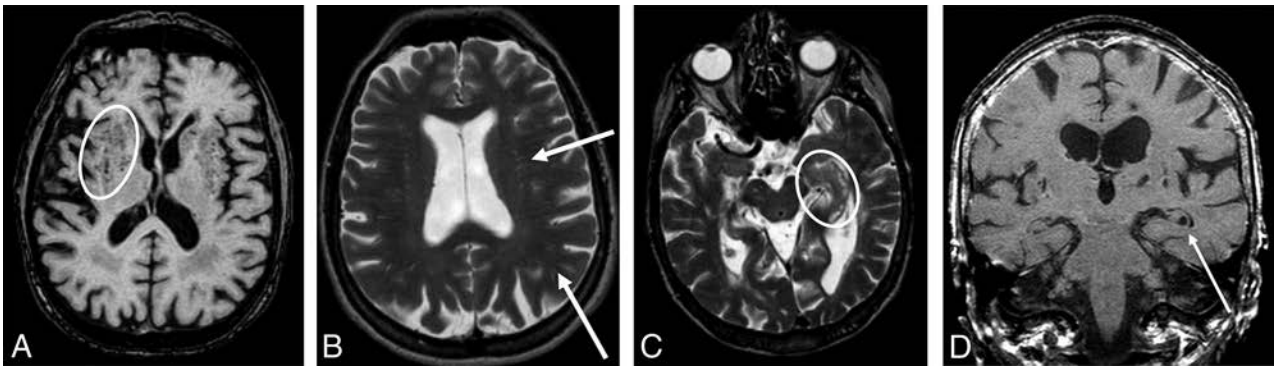

FIG 2. Sample images of PVS with different grades. *A* and *B*, Grade 3 in number and grade 1 in size of PVS in the subinsular, basal ganglia, frontal, and parietal regions. There are >10 PVS in each region, but none of the PVS are wider than 2 mm. In the basal ganglia, PVS are seen as dots (*oval*) because the image is acquired cross-sectional to the vessels (*A*, axial T1), while PVS are linear in the frontal and parietal lobe (*arrows*), where the vessels are in a plane with the image (*B*, axial T2). *C*, Grade 3 in number and grade 1 in size in the left hippocampus (*oval*, axial T2). PVS in the hippocampus are really hippocampal sulcus remnants, which can be clearly seen in *D* (*arrow*, coronal T1).

On-line Table 1). When we measured the diameter of obliquely imaged PVS, the smallest diameter of each periventricular space was used. The maximum diameter of PVS was scored as 0 (no visible PVS), 1 (1–2 mm), 2 (3–4 mm), and 3 (>4 mm). All images were assessed by an experienced clinical neuroradiologist (A.L.). Six months after the initial reading, MR images of 20 randomly selected subjects were re-evaluated for PVS, which yielded a weighted κ statistic of 0.77 (intrarater reliability). In addition, MR images of 18 subjects were evaluated for PVS by an experienced general radiologist (L.B.); this evaluation yielded a weighted κ statistic of 0.77 (interrater reliability).

We used the T1-weighted 3D volume images to count the total number of PVS in the basal ganglia and subinsular region and followed them through the sections, which facilitated separating PVS from lacunes and choroidal fissure cysts and avoided counting the same space twice. With T1, instead of T2, images for the basal ganglia also diminished the disturbance from WMH common in this region that might be confused with PVS. The PVS in the frontal and parietal lobes were more easily assessed on the axial T2 images as well as hippocampal sulcus remnants and PVS in cerebellum and mesencephalon (Fig 2). The FLAIR images were used to distinguish PVS from lacunes. The changes were considered to constitute lacunes if they were surrounded by a high signal on FLAIR images or if they did not have a rounded elongated shape. However, because the scale is based on counting the number and measuring the diameters of PVS, different sequences with thin sections might be used.

Visual Assessment of WMH and PVH

WMH were defined as hyperintense signal on FLAIR images. The load of WMH was rated using a modified Scheltens rating scale (On-line Table 2).[22] The rating scale is the same as the original Scheltens scale, but the regionalization is different. First, we rated the 2 hemispheres separately. Second, due to very few white matter changes in the thalami and the cognitive importance of the external capsule, the basal ganglia and thalami were divided into subinsular region (external capsule, claustrum, and extreme capsule) and basal ganglia (medial to external capsule, including the thalamus and internal capsule). Hyperintense changes in the basal ganglia and thalami were included in the WMH, as previously suggested.[23] Finally, we combined the parietal and occipital lobes into 1 region due to the low number of WMH in the occipital lobe. PVH were rated according to the original Scheltens scale.[22]

All assessments of WMH were completed by a clinical neuroradiologist (A.L.) without knowledge of subjects' clinical characteristics. The intrarater reliability for WMH was good, with the weighted κ statistic of 0.67.

Assessment of Cardiovascular Health

Data on demographics (eg, age, sex, and education) and cardiovascular risk factors and disorders were collected through face-to-face interviews, clinical examinations, laboratory tests, and patient registers.[20] Hypertension was defined as arterial blood pressure of ≥140/90 mm Hg or current use of antihypertensive agents. Obesity was defined as a body mass index of ≥30 kg/m^2. High total cholesterol was defined as a total serum cholesterol of ≥6.22 mmol/L or use of cholesterol-lowing agents. Diabetes was defined as having a self-reported history of diabetes, a record of diabetes in the patient register, use of hypoglycemic agents, or an HbA1c of ≥5.4%.

A history of heart disease was ascertained according to medical records in the Stockholm patient register. We included coronary heart disease (International Classification of Diseases, Ninth Revision [ICD-9] codes 410–414; ICD-10 codes I20-I25); heart failure (ICD-9 code 428 and ICD-10 code I50); and atrial fibrillation (ICD-9 code 427.8 and ICD-10 code I48).

Statistical Analysis

Demographic characteristics of study participants by sex were compared using the *t* test for continuous variables and the χ^2 test for categoric variables. We used a scatterplot to show the distribution of global PVS scores by age, and the correlations of PVS scores with age were explored with the general linear regression model. To demonstrate the distribution of the regional PVS load, we presented the number and proportion of subjects according to the scores of PVS in each brain region for both hemispheres. Partial correlation was used to investigate the correlation between PVS scores and WMH scores globally and by regions, controlling for age, sex, and education. STATA, Version 12.0 for Windows (StataCorp, College Station, Texas) was used for all analyses.

Table 1: Demographic and clinical characteristics of study participants by sex

Characteristics	Total Sample	Men	Women	*P* Value[a]
No. of subjects	530	218	312	
Age (yr) (No.) (%)				
60	141 (26.6)	66 (30.3)	75 (24.0)	
66	123 (23.2)	51 (23.4)	72 (23.1)	
72	84 (15.8)	30 (13.8)	54 (17.3)	
78	73 (13.8)	29 (13.3)	44 (14.1)	
81	49 (9.2)	18 (8.3)	31 (9.9)	
84	26 (4.9)	9 (4.1)	17 (5.4)	
87	18 (3.4)	9 (4.1)	9 (2.9)	
90 or older	16 (3.0)	6 (2.8)	10 (3.2)	.72
Age (yr), mean (SD)	70.7 (9.1)	70.1 (9.2)	71.1 (9.0)	.20
Education (No.) (%)				
Primary school	67 (12.6)	26 (11.9)	41 (13.1)	
Middle school	246 (46.4)	78 (35.8)	168 (53.8)	
University	217 (40.9)	114 (52.3)	103 (33.0)	<.01
Hypertension (No.) (%)	383 (72.3)	165 (75.7)	218 (69.9)	.14
Diabetes (No.) (%)	41 (7.7)	25 (11.5)	16 (5.1)	<.01
High cholesterol (No.) (%)	295 (56.4)	118 (55.7)	177 (56.9)	.78
Obesity (No.) (%)	72 (13.6)	30 (13.8)	42 (13.5)	.93
Atrial fibrillation (No.) (%)	11 (2.1)	7 (3.2)	4 (1.3)	.13
Coronary heart disease (No.) (%)	53 (10.0)	30 (13.8)	23 (7.4)	.02
Heart failure (No.) (%)	12 (2.3)	5 (2.3)	7 (2.2)	.97
PVH (median) (IQR)	8 (6–9)	8 (6–10)	8 (6–9)	.56
WMH (median) (IQR)	16 (5–29)	16 (4–26)	16 (6–30)	.56

Note:—IQR indicates interquartile range.
[a] *P* value was for the test of sex differences.

RESULTS

Characteristics of Study Participants

Table 1 shows the demographic and clinical characteristics of the 530 participants by sex. The mean age of the sample was 70.7 ± 9.1 years, and 58.9% were women. Men were more likely than women to have a higher level of education ($P < .01$), diabetes ($P < .01$), and coronary heart disease ($P = .02$). There were no significant sex differences in the mean age, prevalence of hypertension, high total cholesterol, obesity, atrial fibrillation, and heart failure or in the severity of WMH and PVH ($P > .10$) (Table 1).

Distribution of Global PVS

The means of the global score for the number of PVS were 18.7 ± 5.2 (range, 4–32); 10.7 ± 2.6 for the size of PVS (range, 3–22); and 29.3 ± 7.4 for combining the number and size of PVS (range, 7–54). The PVS total score shows approximately normal distribution (On-line Figure). Large PVS (>4 mm) were detected in only 6 individuals (1.1%) of all the 530 participants or in 29 regions (0.4%) of a total number of 7405 brain regions (each person having 7 regions in each hemisphere).

The global score for the combination of both the number and size of PVS increased with advancing age (β coefficient = 0.218, $P < .01$) as did the global score for the number of PVS (β coefficient = 0.162, $P < .01$). The global score for PVS size did not vary substantially with age, though the correlation was statistically significant (β coefficient = 0.057, $P < .01$) (Fig 3). There was no significant sex difference in the distribution of global scores for either the number or size of PVS.

Distribution Patterns of Regional PVS

Around 60% of the subjects showed >10 PVS in the frontal and parieto-occipital lobes; ~45% showed 6–10 PVS in the basal ganglia; >50% showed 1–5 PVS in the subinsular, hippocampus, or mesencephalon regions; and >85% of the subjects did not have any PVS in the cerebellum region (Table 2).

For distribution of regional PVS by size, >80% of the subjects had a PVS size of 1–2 mm in the frontal lobe, parieto-occipital lobe, or basal ganglia. The most common region for having PVS of ≥3 mm was the basal ganglia (~15% in both hemispheres). The distribution of PVS by both number and size appeared to be symmetric in both hemispheres.

Correlation between WMH and PVS

After we controlled for demographics, the global scores for the number, size, and both the number and size of PVS were all positively correlated with the WMH score in lobar and deep white matter areas ($P < .05$ or $P < .01$), whereas there was no significant correlation between global PVS and PVH scores (Table 3).

Higher scores for the number of PVS in the basal ganglia and subinsular areas were significantly associated with a higher global WMH score and a higher WMH score in the lobar, deep, and periventricular areas. Furthermore, a higher score for the number or size of PVS in the hippocampus was significantly associated with higher WMH scores in lobar areas. Finally, PVS scores in the frontal lobe, parieto-occipital lobe, mesencephalon, and cerebellum were largely not correlated with WMH scores.

DISCUSSION

In this population-based study of older adults, we have developed a new rating scale for visual assessment of PVS, considering the number, size, and location, which meets the requirements of STRIVE, the neuroimaging standards for research into cerebral small-vessel disease.[12] With this scale, we show evidence that PVS are an imaging marker for cerebral small-vessel disease and that the number, rather than the size, might be a more important measure for PVS. In addition, using this scale, we will be able to investigate different risk factors for and functional consequences of PVS by various brain areas.

When we started studying PVS, there were several scales for visual assessment available, even though few scales have been used in >1 study, probably because most of these scales had great benefits, but also drawbacks. Most of the previous scales were only concerned with the PVS number and used a fixed diameter of 2[24] or 3 mm[19] to separate PVS from lacunes, even though PVS can sometimes grow very large.[25] For instance, one scale measured the mean diameters of all PVS in 1 axial section at the level of the cella media of the lateral ventricles, which means that the scale mainly evaluated the frontal and parietal white matter.[5] This scale left out the basal ganglia, where many PVS are located. In another scale, the PVS both along the lenticulostriate arteries (in the basal gan-

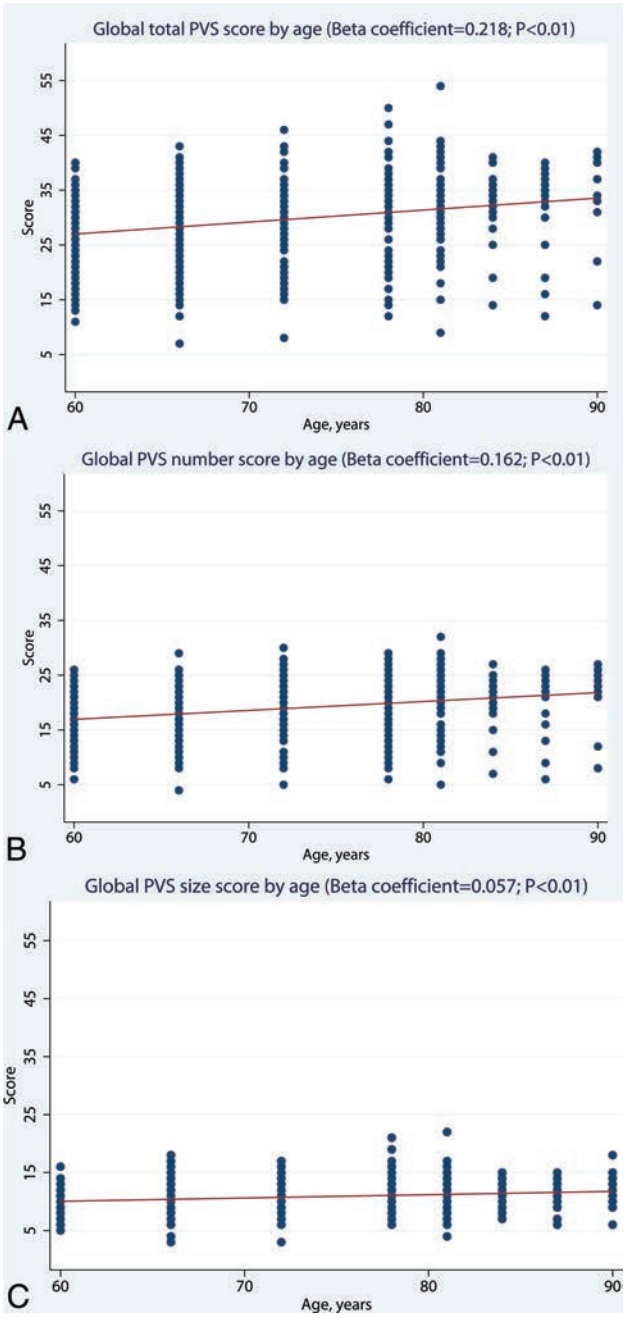

FIG 3. Age-specific distribution of global scores for the number, size, and a combination of both number and size of PVS. Note that there are 3 subjects with missing values in the global PVS score for size.

glia) and in the high convexities were assessed.[4] The scale was based on the width of PVS but was also given 1 point if there were >4 PVS in each region. Thus, the scale did not really separate the diameter from the number of PVS. The third scale rated the number of PVS only in the most affected hemisphere but combined the basal ganglia with the centrum semiovale and rated only the hippocampus separately.[6] Thus, this scale could not differentiate PVS in the basal ganglia from those in the centrum semiovale. This drawback was overcome in a later study.[19]

The scale by Patankar et al[7] rated the number of PVS in 4 different regions, which makes this scale very appealing; thus, it has been used by other groups.[26,27] However, this scale has a great disadvantage in a complicated grading, where each region has a different grading scale with 2 different schemes for the basal ganglia. Because we aimed to develop a rating scale that was easy to use, we decided to use the grades 0–3 for both the diameter and number of PVS. Our rating scale is in line with the requirements of the STRIVE in terms of rating both the number and size in different locations.[12]

We found a slight increase in the global score for PVS number with advancing age, which is in accordance with most other studies.[4,8,9,13,28-31] Our study sample was relatively healthy,[20] which might partly explain a smaller increase with age than expected, because PVS are presumably correlated with the degree of cerebral small-vessel disease and amyloid deposition with increasing age.[17,18] We did not find a sex difference in the distribution of PVS, even though it has been reported in earlier studies[11,13,16]; notably, one of these studies comprised a very large population-based sample ($n = \sim 1800$), in which men were found to have more PVS in the basal ganglia than women,[13] while another large-scale study of patients with ischemic stroke ($n = 1090$) found that men had more PVS in the white matter than women, but there was no sex difference in the distribution of PVS in the basal ganglia.[11] The discrepancies in the findings may be partly attributable to the differences in characteristics of the study populations.

In our sample, we found very few PVS >4 mm (1.1% of all subjects or 0.4% of all the examined brain regions), which is in accordance with the traditional view that PVS should be <5 mm.[32] In addition, our data showed rather limited variation in the size of PVS by age. This appears to be contradictory to a clinically based study, which showed a strong correlation of the width of the PVS with increasing age.[4] However, because the scale in that study yielded a higher score if there were many PVS, it might have reflected an increasing number, rather than size, of PVS with age. Given that the width of PVS has been correlated with advancing age,[4] it might still be important to also include the diameter when assessing PVS.

A higher global PVS score was correlated with a greater burden of WMH in lobar regions and the basal ganglia, which supports the view that PVS, along with WMH, are markers for cerebral small-vessel disease.[9,19,33] More interesting, we found a correlation between the PVS score in the basal ganglia and WMH load not only in the same region but also in lobar areas, while we did not find any correlation between the lobar PVS score and WMH load either in the lobar areas or in the basal ganglia. This is in line with the view that PVS, especially in the basal ganglia, are caused mainly by hypertensive arteriopathy, like WMH, while lobar PVS are mainly due to cerebral amyloid angiopathy or amyloid accumulation in the brain with normal aging.[10,30]

A major strength of our study is the large sample from the general population. To date, only very few studies have had such a large sample of community dwellers.[4,13,29] In addition, because our scale is based on counting the number and measuring the diameter of PVS, it can be used on different MR imaging sequences, as opposed to the visual impression–based rating scales. Furthermore, the regionalization in the assessments of both PVS and WMH is of relevance when studying their correlations with vascular risk factors and cognitive aging.

Table 2: Distribution of regional perivascular spaces by number and size[a]

Hemispheres and Regions	No. of Perivascular Spaces				Size (mm in Diameter) of Perivascular Spaces[b]			
	None	1–5	6–10	>10	None	1–2	3–4	>4
Left								
Frontal	32 (6.0)	70 (13.2)	107 (20.2)	321 (60.6)	32 (6.0)	473 (89.3)	25 (4.7)	0
Parieto-occipital	25 (4.7)	68 (12.8)	116 (21.9)	321 (60.6)	25 (4.7)	486 (91.7)	16 (3.0)	3 (0.6)
Basal ganglia	0	85 (16.0)	240 (45.3)	205 (38.7)	0	443 (83.6)	80 (15.1)	7 (1.3)
Subinsular	128 (24.2)	277 (52.3)	107 (20.2)	18 (3.4)	128 (24.2)	370 (69.9)	30 (5.7)	1 (0.2)
Hippocampus	156 (29.4)	328 (61.9)	46 (8.7)	0	156 (29.4)	348 (65.7)	26 (4.9)	0
Mesencephalon	255 (48.1)	274 (51.9)	0	0	254 (47.9)	273 (51.5)	3 (0.6)	0
Cerebellum	456 (86.0)	74 (14.0)	0	0	456 (86.0)	74 (14.0)	0	0
Right								
Frontal	28 (5.3)	64 (12.1)	94 (17.7)	344 (64.9)	28 (5.3)	474 (89.4)	27 (5.1)	1 (0.2)
Parieto-occipital	29 (5.5)	79 (14.9)	106 (20.0)	316 (59.6)	29 (5.5)	487 (91.9)	14 (2.6)	0
Basal ganglia	1 (0.2)	103 (19.4)	231 (43.6)	195 (36.8)	1 (0.2)	452 (85.3)	63 (11.9)	14 (2.6)
Subinsular	131 (24.7)	280 (52.8)	103 (19.4)	16 (3.0)	131 (24.7)	369 (69.6)	29 (5.5)	1 (0.2)
Hippocampus	210 (39.6)	284 (53.6)	35 (6.6)	1 (0.2)	209 (39.5)	292 (55.2)	26 (4.9)	2 (0.4)
Mesencephalon	263 (49.6)	265 (50.0)	2 (0.4)	0	262 (49.5)	263 (49.7)	4 (0.8)	0
Cerebellum	462 (87.2)	68 (12.8)	0	0	463 (87.4)	67 (12.6)	0	0

[a] Data are No. (%).

[b] There were missing values of perivascular space size in 1 subject in the mesencephalon (right hemisphere), 1 in the hippocampus (right hemisphere), and 1 in the basal ganglia (left hemisphere).

Table 3: Partial correlation coefficients between PVS and WMH scores[a]

Global and Regional PVS Scores	WMH Scores			
	Global	Lobar White Matter Areas[b]	Deep White Matter Areas[b]	Periventricular Regions[b]
PVS score, total				
Global region	0.204[c]	0.182[c]	0.171[c]	0.066
Frontal region	0.040	0.048	0.011	0.007
Parieto-occipital region	0.028	0.017	0.028	0.031
Basal ganglia	0.318[c]	0.256[c]	0.292[c]	0.160[c]
Subinsular region	0.228[c]	0.206[c]	0.173[c]	0.101[d]
Hippocampus	0.127[c]	0.137[c]	0.072	0.021
Mesencephalon	0.044	0.044	0.073	−0.077
Cerebellum	0.071	0.034	0.110[d]	0.039
PVS score (No.)				
Global region	0.206[c]	0.177[c]	0.183[c]	0.074
Frontal region	0.034	0.039	0.015	0.001
Parieto-occipital region	0.002	−0.013	0.018	0.022
Basal ganglia	0.355[c]	0.295[c]	0.303[c]	0.194[c]
Subinsular region	0.263[c]	0.223[c]	0.233[c]	0.111[d]
Hippocampus	0.101[d]	0.117[c]	0.051	−0.004
Mesencephalon	0.041	0.044	0.067	−0.081
Cerebellum	0.071	0.034	0.11[d]	0.037
PVS score (size)				
Global region	0.184[c]	0.177[c]	0.140[c]	0.042
Frontal region	0.046	0.061	−0.004	0.023
Parieto-occipital region	0.109[d]	0.113[d]	0.052	0.053
Basal ganglia	0.070	0.042	0.107[d]	0.008
Subinsular region	0.143[d]	0.152[d]	0.059	0.073
Hippocampus	0.151[c]	0.154[c]	0.092[d]	0.043
Mesencephalon	0.002	0.012	0.029	−0.096[d]
Cerebellum	0.071	0.033	0.111	0.041

[a] The correlation coefficients were adjusted for age, sex, and education.

[b] Lobar white matter areas include the frontal, parieto-occipital, and temporal lobes in both hemispheres; deep white matter areas include the basal ganglia, capsular, thalami, pons, and mesencephalon; and periventricular areas include the frontal, lateral, and occipital periventricular areas.

[c] $P < .01$.

[d] $P < .05$.

Our study also has limitations. First, we used diameter to measure the severity of PVS, which may be less precise than the direct measurement of PVS volume. Indeed, semiautomatic approaches for assessing PVS volume are being developed,[16] though current volumetric methods do not cover the entire brain or work as fast as visual rating approaches.[34,35] Second, our scale includes 2 parameters (number and size) of PVS in 14 regions, which is rather time-consuming (on average 6 minutes per examination). This means that our study has an advantage for research purposes. For visual assessment of several imaging markers (eg, WMH, microbleeds, and brain atrophy) or for clinical use, however, the scale of Potter et al[9] may be easier to use for rating PVS in the most important regions such as the basal ganglia and centrum semiovale.

CONCLUSIONS

We describe a new semiquantitative scale for visual assessment of PVS that considers the number and diameter of PVS as well as location. This rating scale has excellent intra- and interrater reliability. Using this scale, we found that the global number of PVS increased with age and correlated with increasing load of WMH in lobar and deep white matter regions. This rating scale will be useful for future research on PVS, especially regarding risk factors and functional consequences of PVS by region. We plan to further investigate vascular risk factors and cognitive decline associated with global and regional PVS. A potential implication of linking global and regional PVS to functional outcomes is that the presence of visible PVS may be important to include in clinical reports on brain MR imaging examinations in the future, as we currently do for WMH in our clinical reports.

ACKNOWLEDGMENTS

We are grateful to all the SNAC-K participants and to our colleagues in the SNAC-K group for their collaboration in data collection and management. We thank Dr Heather Martin from the Department of Neuroradiology, Karolinska University Hospital, Stockholm, Sweden, for careful editing of our manuscript.

Disclosures: Rui Wang—*RELATED*: *Grant*: The Swedish Ministry of Health and Social Affairs, the participating County Councils and Municipalities, and the Swedish Research Council. Chengxuan Qui—*RELATED*: *Grant*: The Swedish Ministry of Health and Social Affairs, the participating County Councils and Municipalities, the Swedish Research Council, and the Swedish Research Council for Health, Working Life and Welfare.* *Money paid to the institution.

REFERENCES

1. Esiri MM, Gay D. **Immunological and neuropathological significance of the Virchow-Robin space.** *J Neurol Sci* 1990;100:3–8 CrossRef Medline
2. Weller RO, Subash M, Preston SD, et al. **Perivascular drainage of amyloid-beta peptides from the brain and its failure in cerebral amyloid angiopathy and Alzheimer's disease.** *Brain Path* 2008;18:253–66 CrossRef Medline
3. Groeschel S, Chong WK, Surtees R, et al. **Virchow-Robin spaces on magnetic resonance images: normative data, their dilatation, and a review of the literature.** *Neuroradiology* 2006;48:745–54 CrossRef Medline
4. Heier LA, Bauer CJ, Schwartz L, et al. **Large Virchow-Robin spaces: MR-clinical correlation.** *AJNR Am J Neuroradiol* 1989;10:929–36 Medline
5. Hiroki M, Miyashita K. **Linear hyperintensity objects on magnetic resonance imaging related to hypertension.** *Cerebrovasc Dis* 2001;11:164–68 CrossRef Medline
6. Maclullich AM, Wardlaw JM, Ferguson KJ, et al. **Enlarged perivascular spaces are associated with cognitive function in healthy elderly men.** *J Neurol Neurosurg Psychiatry* 2004;75:1519–23 CrossRef Medline
7. Patankar TF, Mitra D, Varma A, et al. **Dilatation of the Virchow-Robin space is a sensitive indicator of cerebral microvascular disease: study in elderly patients with dementia.** *AJNR Am J Neuroradiol* 2005;26:1512–20 Medline
8. Rouhl RP, van Oostenbrugge RJ, Knottnerus IL, et al. **Virchow-Robin spaces relate to cerebral small vessel disease severity.** *J Neurol* 2008;255:692–96 CrossRef Medline
9. Potter GM, Chappell FM, Morris Z, et al. **Cerebral perivascular spaces visible on magnetic resonance imaging: development of a qualitative rating scale and its observer reliability.** *Cerebrovasc Dis* 2015;39:224–31 CrossRef Medline
10. Charidimou A, Jaunmuktane Z, Baron JC, et al. **White matter perivascular spaces: an MRI marker in pathology-proven cerebral amyloid angiopathy?** *Neurology* 2014;82:57–62 CrossRef Medline
11. Zhang C, Chen Q, Wang Y, et al; Chinese IntraCranial AtheroSclerosis (CICAS) Study Group. **Risk factors of dilated Virchow-Robin spaces are different in various brain regions.** *PLoS One* 2014;9:e105505 CrossRef Medline
12. Wardlaw JM, Smith EE, Biessels GJ, et al; STandards for ReportIng Vascular changes on nEuroimaging (STRIVE v1). **Neuroimaging standards for research into small vessel disease and its contribution to ageing and neurodegeneration.** *Lancet Neurol* 2013;12:822–38 CrossRef Medline
13. Zhu YC, Dufouil C, Soumare A, et al. **High degree of dilated Virchow-Robin spaces on MRI is associated with increased risk of dementia.** *J Alzheimers Dis* 2010;22:663–72 CrossRef Medline
14. Jungreis CA, Kanal E, Hirsch WL, et al. **Normal perivascular spaces mimicking lacunar infarction: MR imaging.** *Radiology* 1988;169:101–04 CrossRef Medline
15. Song CJ, Kim JH, Kier EL, et al. **MR imaging and histologic features of subinsular bright spots on T2-weighted MR images: Virchow-Robin spaces of the extreme capsule and insular cortex.** *Radiology* 2000;214:671–77 CrossRef Medline
16. Ramirez J, Berezuk C, McNeely AA, et al. **Visible Virchow-Robin spaces on magnetic resonance imaging of Alzheimer's disease patients and normal elderly from the Sunnybrook Dementia Study.** *J Alzheimers Dis* 2015;43:415–24 CrossRef Medline
17. Hiroki M, Miyashita K, Oda M. **Tortuosity of the white matter medullary arterioles is related to the severity of hypertension.** *Cerebrovasc Dis* 2002;13:242–50 CrossRef Medline
18. Roher AE, Kuo YM, Esh C, et al. **Cortical and leptomeningeal cerebrovascular amyloid and white matter pathology in Alzheimer's disease.** *Mol Med* 2003;9:112–22 Medline
19. Doubal FN, MacLullich AM, Ferguson KJ, et al. **Enlarged perivascular spaces on MRI are a feature of cerebral small vessel disease.** *Stroke* 2010;41:450–54 CrossRef Medline
20. Wang R, Fratiglioni L, Laveskog A, et al. **Do cardiovascular risk factors explain the link between white matter hyperintensities and brain volumes in old age? A population-based study.** *Eur J Neurol* 2014;21:1076–82 CrossRef Medline
21. Rollins NK, Deline C, Morriss MC. **Prevalence and clinical significance of dilated Virchow-Robin spaces in childhood.** *Radiology* 1993;189:53–57 CrossRef Medline
22. Scheltens P, Barkhof F, Leys D, et al. **A semiquantative rating scale for the assessment of signal hyperintensities on magnetic resonance imaging.** *J Neurol Sci* 1993;114:7–12 CrossRef Medline
23. Wahlund LO, Barkhof F, Fazekas F, et al; European Task Force on Age-Related White Matter Changes. **A new rating scale for age-related white matter changes applicable to MRI and CT.** *Stroke* 2001;32:1318–22 CrossRef Medline
24. Achiron A, Faibel M. **Sandlike appearance of Virchow-Robin spaces in early multiple sclerosis: a novel neuroradiologic marker.** *AJNR Am J Neuroradiol* 2002;23:376–80 Medline
25. Salzman KL, Osborn AG, House P, et al. **Giant tumefactive perivascular spaces.** *AJNR Am J Neuroradiol* 2005;26:298–305 Medline
26. Selvarajah J, Scott M, Stivaros S, et al. **Potential surrogate markers of cerebral microvascular angiopathy in asymptomatic subjects at risk of stroke.** *Eur Radiol* 2009;19:1011–18 CrossRef Medline
27. Tarnaris A, Tamangani J, Fayeye O, et al. **Virchow-Robin spaces in idiopathic normal pressure hydrocephalus: a surrogate imaging marker for coexisting microvascular disease?** *Acta Neurochir Suppl* 2012;113:33–37 CrossRef Medline
28. Chen W, Song X, Zhang Y. **Assessment of the Virchow-Robin spaces in Alzheimer disease, mild cognitive impairment, and normal aging, using high-field MR imaging.** *AJNR Am J Neuroradiol* 2011;32:1490–95 CrossRef Medline
29. Gutierrez J, Rundek T, Ekind MS, et al. **Perivascular spaces are associated with atherosclerosis: an insight from the Northern Manhattan Study.** *AJNR Am J Neuroradiol* 2013;34:1711–16 CrossRef Medline
30. Yakushiji Y, Charidimou A, Hara M, et al. **Topography and associations of perivascular spaces in healthy adults: the Kashima scan study.** *Neurology* 2014;83:2116–23 CrossRef Medline
31. Shimada K, Kawamoto A, Matsubayashi K, et al. **Silent cerebrovascular disease in the elderly: correlation with ambulatory pressure.** *Hypertension* 1990;16:692–99 CrossRef Medline
32. Osborn AG, Preece MT. **Intracranial cysts: radiologic-pathologic correlation and imaging approach.** *Radiology* 2006;239:650–64 CrossRef Medline
33. Hansen TP, Cain J, Thomas O, et al. **Dilated perivascular spaces in the basal ganglia are a biomarker of small-vessel disease in a very elderly population with dementia.** *AJNR Am J Neuroradiol* 2015;36:893–98 CrossRef Medline
34. Hernández Mdel C, Piper RJ, Wang X, et al. **Towards the automatic computational assessment of enlarged perivascular spaces on brain magnetic resonance images: a systematic review.** *J Magn Reson Imaging* 2013;38:774–85 CrossRef Medline
35. Wang X, Valdés Hernández Mdel C, Doubal F, et al. **Development and initial evaluation of a semi-automatic approach to assess perivascular spaces on conventional magnetic resonance images.** *J Neurosci Methods* 2016;257:34–44 CrossRef Medline

Do Fluid-Attenuated Inversion Recovery Vascular Hyperintensities Represent Good Collaterals before Reperfusion Therapy?

E. Mahdjoub, G. Turc, L. Legrand, J. Benzakoun, M. Edjlali, P. Seners, S. Charron, W. Ben Hassen, O. Naggara, J.-F. Meder, J.-L. Mas, J.-C. Baron, and C. Oppenheim

ABSTRACT

BACKGROUND AND PURPOSE: In acute ischemic stroke, whether FLAIR vascular hyperintensities represent good or poor collaterals remains controversial. We hypothesized that extensive FLAIR vascular hyperintensities correspond to good collaterals, as indirectly assessed by the hypoperfusion intensity ratio.

MATERIALS AND METHODS: We included 244 consecutive patients eligible for reperfusion therapy with MCA stroke and pretreatment MR imaging with both FLAIR and PWI. The FLAIR vascular hyperintensity score was based on ASPECTS, ranging from 0 (no FLAIR vascular hyperintensity) to 7 (FLAIR vascular hyperintensities abutting all ASPECTS cortical areas). The hypoperfusion intensity ratio was defined as the ratio of the time-to-maximum >10-second over time-to-maximum >6-second lesion volumes. The median hypoperfusion intensity ratio was used to dichotomize good (low hypoperfusion intensity ratio) versus poor (high hypoperfusion intensity ratio) collaterals. We then studied the association between FLAIR vascular hyperintensity extent and hypoperfusion intensity ratio.

RESULTS: Hypoperfusion was present in all patients, with a median hypoperfusion intensity ratio of 0.35 (interquartile range, 0.19–0.48). The median FLAIR vascular hyperintensity score was 4 (interquartile range, 3–5). The FLAIR vascular hyperintensities were more extensive in patients with good collaterals (hypoperfusion intensity ratio ≤0.35) than with poor collaterals (hypoperfusion intensity ratio >0.35; *P for Trend* = .016). The FLAIR vascular hyperintensity score was independently associated with good collaterals (*P for Trend* = .002).

CONCLUSIONS: In patients eligible for reperfusion therapy, FLAIR vascular hyperintensity extent was associated with good collaterals, as assessed by the pretreatment hypoperfusion intensity ratio. The ASPECTS assessment of FLAIR vascular hyperintensities could be used to rapidly identify patients more likely to benefit from reperfusion therapy.

ABBREVIATIONS: FVH = FLAIR vascular hyperintensity; HIR = hypoperfusion intensity ratio; IQR = interquartile range; Tmax = time-to-maximum

Collateral circulation plays an important role in stroke pathophysiology.[1] In response to a middle cerebral artery occlusion, flow in leptomeningeal anastomoses from anterior and posterior cerebral arteries reverts and pial collaterals dilate, providing blood supply to maintain tissue viability. Assessing collateral status has direct applications for decision-making and predicting outcome after acute ischemic stroke. Using collateral-based imaging as an entry selection criterion, a recent trial showed that rapid endovascular treatment dramatically improved functional outcome in patients with proximal vessel occlusion, small infarct core, and moderate-to-good collateral circulation.[2] DSA remains the reference to assess collateral status,[1] but less invasive methods based on postcontrast CT[2] or MR imaging[3,4] have been developed. On the basis of first-pass gadolinium PWI, the hypoperfusion intensity ratio (HIR) has been creatively proposed to assess the severity of hypoperfusion.[5] Defined as the proportion of the time-to-maximum (Tmax) >10-second over the Tmax >6-second lesion volumes, the HIR is a good predictor of collateral status, as demonstrated by correlations with DSA: A low HIR corresponded to good collaterals and predicted smaller infarct growth and better clinical outcome than a high HIR.[5,6]

A means to assess collateral status without the need for contrast agent, additional scanning time, or automated perfusion software would be desirable for patient management. FLAIR, which is part of most stroke MR imaging protocols, provides information about vessel status. High signal intensities within blood vessels, in subarachnoid spaces, distal to arterial occlusion,[7]

Received March 17, 2017; accepted after revision August 24.

From the Departments of Radiology (E.M., L.L., J.B., M.E., S.C., W.B.H., O.N., J.-F.M., C.O.) and Neurology (G.T., P.S., J.-L.M., J.-C.B.), Université Paris Descartes, Institut national de la santé et de la recherche médicale S894, Département Hospitalo-Universitaire Neurovasc, Centre Hospitalier Sainte-Anne, Paris, France.

Please address correspondence to Catherine Oppenheim, MD, PhD, CH Sainte-Anne, 1 rue Cabanis, 75014 Paris, France; e-mail: c.oppenheim@ch-sainte-anne.fr

Indicates article with supplemental on-line table.

http://dx.doi.org/10.3174/ajnr.A5431

termed FLAIR vascular hyperintensities (FVHs),[8,9] are related to hemodynamic impairment and represent slow retrograde flow in leptomeningeal collaterals.[10] However, whether they reflect good or poor collaterals remains controversial. For some authors, FVHs represent poor collaterals and predict larger infarct growth[11,12] and worse clinical outcome.[12-14] In the only study using the HIR to assess collaterals, extensive FVHs, assessed dichotomously as FVHs visible in >4 axial sections, were associated with high HIR (ie, poor collaterals) in 62 patients with arterial occlusion in any territory on prethrombolysis MRA.[12] Conversely, other studies found that FVHs indicate good collaterals, with extensive FVHs associated with smaller baseline DWI lesions,[15-18] less severe neurologic deficits,[15-17] smaller infarct growth,[16,18,19] and better clinical outcome.[15,18] We previously reported similar findings based on FVH presence beyond the boundaries of the cortical DWI lesion in patients with proximal MCA occlusion,[9] which also predicted a better clinical response to recanalization.[20] This accumulated evidence indirectly suggests that FVHs represent good collaterals. Accordingly, we aimed to determine whether extensive FVHs are associated with good collaterals, using HIR as a surrogate marker for collaterals, in a large cohort of patients with MCA territory stroke eligible for reperfusion therapy.

MATERIALS AND METHODS

This retrospective study was based on a prospectively collected monocentric register of consecutive (2003–2015) patients treated by intravenous thrombolysis and/or thrombectomy. The inclusion criteria were acute ischemia in the MCA territory; pretreatment MR imaging with DWI, FLAIR, and PWI; and 24-hour follow-up MR imaging to assess infarct growth. Patients with anterior cerebral artery or posterior circulation strokes were excluded because the ASPECTS was originally designed for the MCA territory. Patients with severe artifacts on DWI, FLAIR, or PWI were also excluded. Early neurologic improvement was defined as a ≥8-point decrease in the NIHSS score within the first 24 hours or an NIHSS score ≤1 at 24 hours. Excellent or favorable outcomes were defined as 3-month mRS ≤ 1 or ≤ 2, respectively. In accordance with French legislation, ethics committee approval was not required because our study only implied retrospective analysis of anonymized data collected as part of routine clinical care.

MR imaging has been systematically implemented in our center as first-line diagnostic imaging in candidates for reperfusion therapies. Pretreatment and 24-hour follow-up MR imaging were performed on a 1.5T scanner (Signa; GE Healthcare, Milwaukee, Wisconsin) using a standardized protocol,[9] including DWI, FLAIR, T2*, intracranial 3D-TOF MRA, and an additional PWI sequence for pretreatment MR imaging. FLAIR parameters were TR/TE/TI, 8277–9802/155.5–159.4/2093–2300 ms; FOV, 24 × 24 cm^2; matrix, 256 × 192; 1 excitation; 24 contiguous axial sections, 6-mm thick; 2-minute18-second maximal duration. PWI consisted of a T2*-weighted echo-planar sequence with TR/TE, 2000/60 ms; FOV, 24 × 24 cm^2; matrix, 64 × 96; 1 excitation; repetition, 50 times after a bolus (5–7 mL/s) of 20 mL of gadoteric acid.

FVHs were defined as focal, tubular, or serpentine hyperintensities in subarachnoid spaces with a typical arterial course.[8] Blinded to PWI and clinical data, we semiquantitatively assessed FVHs using the FVH score, according to their spatial distribution in the 7 ASPECTS cortical areas (insula, M1–M6).[9] An ASPECTS cortical area was considered positive when it coincided with an FVH. The FVH score ranged from 0 (no FVH) to 7 (FVHs abutting all ASPECTS cortical areas). The FVH score was additionally rated by a second reader in half of the population.

BrainStat arterial input function software (READY View; GE Healthcare) was used to generate Tmax maps. An automated 3D rigid registration (FMRIB Linear Image Registration Tool, FLIRT, Version 5.5; http://www.fmrib.ox.ac.uk/fsl/fslwiki/FLIRT) between Tmax maps and DWI was performed and manually corrected whenever necessary. MANGO software (Version 3.8; Research Imaging Institute, UTHSCSA; http://ric.uthscsa.edu/mango/) was used to successively extract a brain mask of ADC < $1.3 \times 10^{-3} mm^2/s$ to remove CSF voxels, project it onto Tmax maps, and extract brain voxels with Tmax >6 seconds and >10 seconds. HIR was computed as the ratio between the Tmax >10-second over Tmax >6-second volumes. Pretreatment (DWI_1) and follow-up (DWI_2) volumes were manually segmented using interactive tools based on DWI signal intensity.[21] Infarct growth was defined as the difference between DWI_2 and DWI_1 volumes. A PWI-DWI mismatch was considered present when Tmax >6-second volume exceeded 1.8 × DWI_1 volume.[6] The occlusion site was categorized into proximal (internal carotid artery and/or M1 segment of the MCA) or distal. Complete recanalization was defined as an arterial occlusive lesion score of 3 on 24-hour MRA.

The intraclass correlation coefficient was used to assess interobserver agreement for the FVH score. For further analyses, the FVH score was considered in 4 categories (ASPECTS = 0–1, 2–3, 4–5, or 6–7) to avoid small numbers in extreme FVH scores. The median HIR in our cohort was used to dichotomize good (low HIR) versus poor (high HIR) collaterals.[6,12] A univariable analysis comparing patients with low and high HIRs was used to test our hypothesis that extensive FVHs represent good collaterals (Student *t* or Mann-Whitney *U* test for continuous variables; χ^2 or the Fisher exact test for categoric variables, as appropriate; and the Cochran-Armitage test for ordinal variables). Considering potential collinearity, baseline variables with a *P* value < .10 in the univariable analysis were entered into a multivariable binary logistic regression model with a dichotomized HIR as the dependent variable. All the above analyses were repeated using the median HIR threshold of 0.4, derived from the Diffusion Weighted Imaging Evaluation for Understanding Stroke Evolution 2 (DEFUSE 2) cohort and found to be a good predictor of collateral status.[6] In an additional univariable analysis, we further compared patients according to FVH extent for clinical and imaging data, 24-hour infarct growth, early neurologic improvement, and 3-month mRS (χ^2, Mann-Whitney *U*, or Jonckheere-Terpstra test, as appropriate). A *P* value < .05 was considered significant (SPSS, Version 19, IBM, Armonk, New York; SAS 9.4, SAS Institute, Cary, North Carolina).

RESULTS

During the study period, 777 patients underwent intravenous thrombolysis and/or thrombectomy; 533 patients were excluded

Table 1: Comparison of patients with low and high HIR[a]

Characteristics	Low HIR (n = 122)	High HIR (n = 122)	P Value
Age	70 (56–79)	71 (60–79)	.446
Male (No.) (%)	55 (45)	83 (68)	<.001
Hypertension (No.) (%)[b]	68 (57)	66 (55)	.685
Diabetes mellitus (No.) (%)[b]	12 (10)	20 (17)	.142
Hyperlipidemia (No.) (%)[b]	31 (26)	40 (33)	.251
Current smoking (No.) (%)[c]	23 (20)	25 (21)	.771
Systolic BP (mm Hg)	149 (139–163)	156 (139–173)	.141
Diastolic BP (mm Hg)	82 (71–89)	81 (70–93)	.990
Serum glucose (mmol/L)[d]	6.1 (5.4–7.0)	6.5 (5.5–7.9)	.038
NIHSS[b] score	11 (7–17)	16 (11–21)	<.001
Baseline MRI			
Onset-to-MRI time (min)	112 (86–153)	112 (84–156)	.838
Proximal occlusion (No.) (%)	81 (66)	80 (66)	.893
DWI_1 volume (mL)	8 (4–19)	41 (16–96)	<.001
Tmax >6-sec volume (mL)	44 (17–85)	115 (56–147)	<.001
Tmax >10-sec volume (mL)	9 (2–22)	52 (27–75)	<.001
PWI-DWI mismatch (No.) (%)	85 (70)	59 (48)	<.001
FVH score (No.) (%)			.016[e]
0–1	6 (5)	13 (11)	
2–3	30 (25)	33 (27)	
4–5	54 (44)	59 (48)	
6–7	32 (26)	17 (14)	
24-hr follow-up			
NIHSS score[f]	6 (2–15)	14 (7–20)	<.001
ENI (No.) (%)[f]	51 (42)	27 (22)	.001
DWI_2 volume (Ml)	18 (9–45)	87 (33–161)	<.001
Infarct growth (Ml)	6 (1–26)	29 (10–75)	<.001
Complete recanalization (No.) (%)	40 (33)	45 (37)	.502
3-mo mRS ≤ 1 (No.) (%)[g]	49 (45)	25 (21)	<.001
3-mo mRS ≤ 2 (No.) (%)[g]	63 (58)	51 (44)	.033

Note:—BP indicates blood pressure; ENI, early neurologic improvement.
[a] Unless specified, numbers are median (interquartile range).
[b] Missing data for 4 patients.
[c] Missing data for 9 patients.
[d] Missing data for 13 patients.
[e] *P for Trend*.
[f] Missing data for 5 patients.
[g] Missing data for 18 patients.

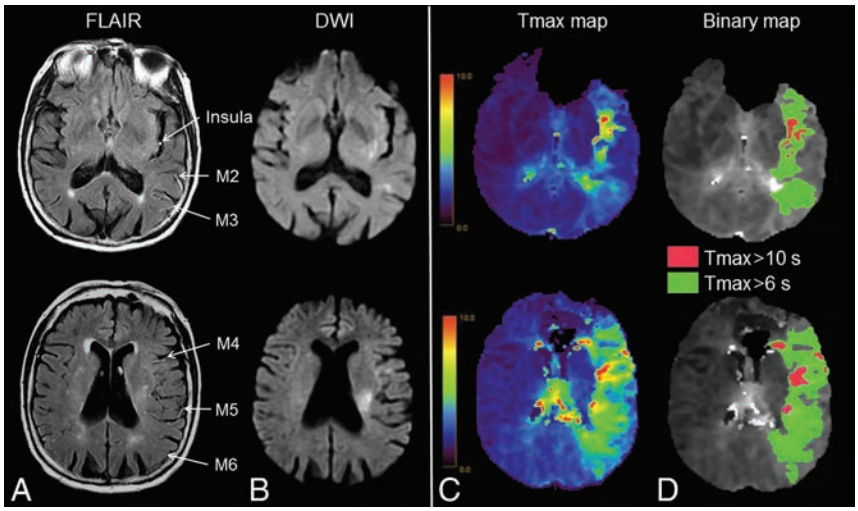

FIG 1. Extensive FVHs and low hypoperfusion intensity ratio. MR imaging obtained 110 minutes after stroke onset (NIHSS score = 12) in an 88-year-old woman. *A*, FVHs in 6 ASPECTS areas (insula, M2–M6), corresponding to a 6-point FVH-score. *B*, Thirteen-milliliter diffusion-weighted imaging lesion. Tmax map (*C*) with 85-mL Tmax >6-second lesion and 15-mL Tmax >10-second lesion (*D*) (HIR = 0.18). After intravenous thrombolysis, the 24-hour NIHSS score was 1, and the DWI lesion was 12 mL (not shown). The 3-month mRS was 1.

(pretreatment CT scan, n = 85; pretreatment MR imaging not available in DICOM format, n = 49; PWI not performed, n = 272; severe artifacts on DWI, FLAIR, or PWI, n = 26; non-MCA stroke, n = 84; no follow-up MR imaging, n = 14; or pretreatment 3T MR imaging, n = 3). They did not differ from the 244 included patients as to sex (P = .45), age (P = .46), or baseline NIHSS scores (P = .19). Two-hundred eight (85.3%) patients were treated by intravenous thrombolysis; 23 (9.4%), by thrombectomy; and 13 (5.3%), by bridging therapy. Median time to treatment was 150 minutes (interquartile range [IQR], 120–189) for thrombolysis and 230 minutes (IQR, 149–401) for thrombectomy. One hundred sixty-one (66%) patients had a proximal occlusion (internal carotid artery, n = 47, or M1, n = 114).

Interobserver agreement for the FVH score was excellent (intraclass correlation coefficient, 0.88; 95% CI, 0.84–0.91). The median FVH score in the whole population was 4 (IQR, 3–5). FVHs were abutting the insula, M2, M3, M5, M1, M6, and M4 ASPECTS areas in 240 (98%), 209 (86%), 156 (64%), 150 (61%), 126 (52%), 125 (51%), and 59 (24%) patients. Hypoperfusion was present in all patients with median Tmax >6-second and >10-second volumes of 74 mL (minimum, 0.95; maximum, 258) and 24 mL (minimum, 0.06; maximum, 160), respectively. The median HIR was 0.35 (IQR, 0.19–0.48).

In univariable analysis (Table 1), patients with good collaterals (HIR ≤ 0.35, Fig 1) had higher FVH scores (*P for Trend* = .016) than those with poor collaterals (HIR > 0.35, Fig 2). Patients with good collaterals also had lower baseline NIHSS scores, smaller DWI_1 volumes, smaller Tmax >10-second and Tmax >6-second volumes, and more frequently had a PWI-DWI mismatch (P < .001). In multivariable analysis (Table 2), the FVH score remained significantly associated with a low HIR (*P for Trend* = .002), after adjustment of potential confounders. Results were similar using the alternative HIR threshold of 0.4[6,22] for dichotomization between good and poor collaterals (data not shown).

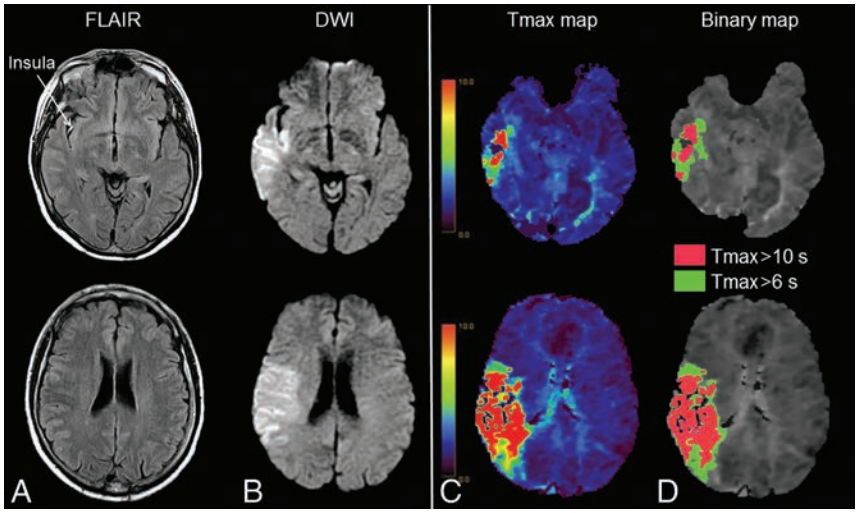

FIG 2. Few FVHs and high hypoperfusion intensity ratio. MR imaging obtained 180 minutes after stroke onset (NIHSS score = 12) in a 56-year-old man. *A*, FVHs in the insula, corresponding to a 1-point FVH score. *B*, Ninety-four milliliter diffusion-weighted imaging lesion. Tmax map (*C*) with 91-mL Tmax >6-second lesion and 53-mL Tmax >10-second lesion (*D*) (HIR = 0.58). After intravenous thrombolysis, the 24-hour NIHSS score was 14, and the DWI lesion was 150 mL (not shown). The 3-month mRS was 3.

Table 2: Factors associated with a low HIR in multivariable analysis

Characteristics	Adjusted OR (95% CI)	*P* Value
Male	0.98 (0.42–2.29)	.953
Serum glucose, per 1-mmol/L increase[a]	0.99 (0.83–1.18)	.882
Baseline NIHSS score, per 1-point increase[b]	1.04 (0.96–1.12)	.343
DWI_1 volume, per 1-mL increase	1.01 (0.99–1.03)	.446
Tmax >10-sec volume, per 1-mL increase[c]	0.89 (0.85–0.92)	<.001
PWI-DWI mismatch	8.95 (2.65–30.22)	<.001
FVH-score	–	.002[d]
0–1	1	–
2–3	1.17 (0.25–5.50)	.844
4–5	2.39 (0.56–10.22)	.242
6–7	34.20 (4.35–268.60)	.001

[a] Missing data for 13 patients.
[b] Missing data for 4 patients.
[c] Tmax >6 sec was not selected with Tmax >10 sec to avoid collinearity.
[d] *P for Trend*.

When we compared patients according to their FVH scores (Table 3), patients with extensive FVHs were imaged earlier ($P = .007$) and had more proximal occlusions ($P < .001$), more PWI-DWI mismatch ($P = .011$), and lower HIR, considered as a continuous variable ($P = .049$). Despite similar baseline NIHSS scores and recanalization rates, patients with extensive FVHs tended to have smaller infarct growth ($P = .125$) and more frequently experienced an early neurologic improvement ($P < .001$) or an excellent 3-month mRS ($P = .039$) than those with fewer FVHs.

To rule out the potential influence of the occlusion site on our main findings, we analyzed post hoc the subset of 161 proximal occlusions, with similar results in univariable analysis (On-line Table), and again found an independent association between a high FVH score and a low HIR in multivariable analysis (*P for Trend* = .031). Of note, when we compared patients with proximal occlusion according to their FVH scores, patients with extensive FVHs had smaller DWI volumes ($P = .003$) and higher DWI-ASPECTS scores ($P = .006$) on pretreatment MR imaging.

DISCUSSION

In a large population of patients with MCA stroke who underwent MR imaging with PWI before reperfusion therapy, we found the following: 1) FVH extent was independently associated with a low HIR (ie, proportionally milder hypoperfusion and hence good collaterals); and 2) patients with extensive FVHs more frequently experienced early neurologic improvement and excellent 3-month outcome, despite similar initial stroke severity and recanalization rates. These findings strengthen the notion that extensive FVHs represent a reliable surrogate for good collaterals, which maintain the viability of the ischemic tissue while awaiting reperfusion.

The presence of FVHs is considered a reliable marker of arterial occlusion[7,13,23-25] and, consequently, is associated with more severe admission neurologic deficits than its absence. Like others,[17] we found FVHs in most patients (99%) with arterial occlusion. Besides their dichotomous presence or absence, FVH extent has been quantitated with various methods. In one method, FVHs were rated as involving less than or more than one-third of the MCA territory or the hypoperfused area,[16,19] but determining this cutoff is notoriously difficult. FVHs have also been graded according to their sulcal location[26] or by counting their number,[11] which is cumbersome in the hyperacute clinical setting. Finally, counting axial FLAIR sections with FVHs has recently been proposed,[12] but this does not account for the actual extent within each section and depends on the section number and thickness. We, like others, have previously assessed FVH topography relative to the DWI lesion, considering their rostrocaudal and anteroposterior distributions, but this approach depends on the size of the DWI lesion and does not yield the total extent of all FVHs.[9,17,20] Our simple approach overcomes most of these limitations, affords an excellent interobserver concordance, and improves feasibility relative to manually counting all FVHs for clinical implementation.

Only a few studies have focused on the significance of FVH extent in the early time window. One study did not find an association between FVH extent and clinical outcome,[25] while several others reported that extensive FVHs were associated with smaller baseline DWI lesions,[9,15-17] larger PWI-DWI mismatch,[9,16] smaller infarct growth,[16,18,19] and better clinical outcome.[15,17,18] Similarly, we showed an independent association between extensive FVHs and a low HIR (ie, good collaterals). Patients with extensive FVHs also had a larger PWI-DWI mismatch, suggesting larger penumbra due to robust collaterals protecting the penumbra from rapidly decaying while awaiting reperfusion. Accord-

Table 3: Comparison of patients according to FVH score[a]

	FVH Score				
	0–1 (*n* = 19)	2–3 (*n* = 63)	4–5 (*n* = 113)	6–7 (*n* = 49)	*P* Value
Age (yr)	73 (60–80)	70 (57–79)	71 (56–80)	67 (62–77)	.339
Male (No.) (%)	12 (63)	31 (49)	68 (60)	27 (55)	.500
Hypertension (No.) (%)[b]	12 (63)	38 (60)	58 (51)	26 (53)	.537
Diabetes mellitus (No.) (%)[b]	4 (21)	9 (14)	13 (12)	6 (12)	.708
Hyperlipidemia (No.) (%)[b]	9 (47)	18 (29)	43 (38)	18 (37)	.477
Current smoking (No.) (%)[c]	3 (16)	12 (19)	23 (20)	10 (20)	.954
Systolic BP (mm Hg)	148 (140–172)	159 (142–173)	151 (139–167)	148 (134–160)	.071
Diastolic BP (mm Hg)	87 (76–93)	84 (69–95)	80 (70–89)	80 (72–90)	.334
Serum glucose (mmol/L)[d]	6.6 (5.5–8.1)	6.7 (5.4–7.3)	6.4 (5.5–7.6)	6.0 (5.3–7.0)	.189
Baseline NIHSS score[b]	13 (8–20)	13 (7–18)	15 (8–20)	15 (11–21)	.321
Onset-to-MRI time (min)	142 (84–196)	115 (89–176)	115 (91–151)	97 (83–130)	.007
Proximal occlusion (No.) (%)	6 (31)	31 (49)	81 (72)	43 (88)	<.001
DWI_1 volume (mL)	24 (12–102)	19 (5–67)	18 (7–49)	12 (6–34)	.077
Tmax >10-sec volume (mL)	26 (5–76)	17 (4–43)	24 (11–53)	30 (11–64)	.200
Tmax >6-sec volume (mL)	65 (19–133)	47 (19–102)	78 (40–123)	96 (66–134)	.002
HIR ≤ 0.35 (No.) (%)	6 (32)	30 (48)	54 (47)	32 (65)	.057
HIR	0.44 (0.30–0.54)	0.39 (0.19–0.48)	0.33 (0.19–0.47)	0.32 (0.14–0.44)	.049
PWI-DWI mismatch (No.) (%)	6 (32)	32 (51)	71 (63)	35 (51)	.011
DWI_2 volume (mL)	73 (14–150)	43 (13–147)	37 (13–104)	29 (12–52)	.075
24-hr infarct growth (mL)	27 (2–87)	19 (4–57)	14 (1–45)	13 (4–28)	.125
Complete recanalization (No.) (%)	7 (37)	19 (30)	38 (34)	21 (43)	.551
ENI (No.) (%)[e]	7 (37)	12 (20)	30 (27)	29 (53)	<.001
3-mo mRS ≤ 1 (No.) (%)[f]	3 (17)	14 (24)	35 (34)	22 (45)	.039
3-mo mRS ≤ 2 (No.) (%)[f]	9 (47)	26 (41)	47 (42)	32 (65)	.057

Note:—ENI indicates early neurologic improvement; BP, blood pressure.

[a] Unless specified, numbers are median (interquartile range).

[b] Missing data for 4 patients.

[c] Missing data for 9 patients.

[d] Missing data for 13 patients.

[e] Missing data for 5 patients.

[f] Missing data for 18 patients.

ingly, extensive FVHs were associated with smaller ischemic lesions before treatment in patients with proximal occlusion, reinforcing our hypothesis that FVHs represent good collaterals.

The benefit of FVH-ASPECTS over simple DWI-ASPECTS for the assessment of collateral status remains to be evaluated. Most important, patients with extensive FVHs more frequently experienced early neurologic improvement and excellent 3-month outcome in contrast to those with fewer FVHs, despite more proximal occlusions and similar recanalization rates. Conversely, our findings stand in apparent contradiction to other studies suggesting that FVHs represent poor collaterals.[7,12,13,23,24] However, these studies either dichotomously categorized patients into the presence or absence of FVHs[7,13,23] rather than analyzing FVH extent and/or were conducted in patients not eligible for thrombolysis.[24] These differences might explain the discrepancy with our findings. Perhaps more surprising are the results from Kufner et al,[12] who found that FVHs rather reflected poor collaterals using the HIR in patients with arterial occlusion before thrombolysis. This discrepancy might result from several differences between this study and ours. First, Kufner et al used a 3T scanner compared with 1.5T here, and the significance of FVHs may depend on magnetic field strength and sequence parameters.[27] Second, we studied a larger and more homogeneous population of overall severe anterior circulation strokes, as opposed to mixed anterior and posterior milder strokes in the Kufner et al study. The unreported proportion of posterior circulation strokes might have influenced their results because the reliability of HIR as a surrogate for good-versus-poor collaterals in this stroke subtype is unknown. Third, Kufner et al dichotomized their sample according to whether FVHs were visible over at least four 5-mm thick FLAIR sections, and such a cutoff might not have equal meaning for anterior-versus-posterior circulation strokes. Fourth, they merged patients with M1, M2, P1, P2, and vertebral occlusions into a single "medium vessel occlusion" group with an unreported proportion of distal occlusions.

FVHs might, however, be a marker for proximal occlusion[23] rather than an indicator of collateral flow. Distal occlusions are indeed unlikely to result in extensive FVHs, irrespective of the quality of collaterals. However, the independent association between the FVH score and the low HIR we found in the population mixing distal and proximal occlusions remained significant in the 161 patients with proximal occlusion. This strengthens the link between FVH visibility and the quality of collaterals, irrespective of the occlusion type. Finally, the definition of HIR differed between our study and that of Kufner et al[12] (Tmax 10/6 seconds here versus Tmax 8/2 seconds), but the definition we used predicted rates of collateral flow, infarct growth, and clinical outcome in the DEFUSE 2 cohort.[6] Further studies are needed to determine which of the above differences accounts best for the discrepancy between the 2 studies.

Direct comparisons between FVH extent and DSA are limited.[10,15,26,28] Except from a seminal study in which only 8 patients underwent DSA,[7] others consistently reported FVHs to be associated with good collaterals.[10,15,26,28] Our results are consistent with the latter DSA-FLAIR correlations. Although the HIR is an indirect marker of collateral status,[5,6] PWI is obtained within

minutes of FLAIR, thereby overcoming the issue of the delay between MR imaging and DSA inherent in all MR imaging–DSA comparisons. Given the transient nature of FVHs,[7] correlation between MR images obtained nearly simultaneously provides new insights into the debated significance of FVHs.

That numerous well-developed collaterals appear as extensive FVHs deserves attention. In ischemic stroke, FVHs are undoubtedly related to retrograde collateral flow, which reaches cortical areas later than anterograde flow, often during the venous angiographic phase. This sluggish flow likely explains, at least in part, FVH visibility.[10] A recent study showed that FVHs were more prominent when the arterial circulation time on DSA was neither too short (>1 second) nor too long (<7.98 seconds).[28] Given that prominent FVHs are observed in a wide range of intermediate time delays of retrograde collateral filling,[28] FVH visibility might depend on not only flow speed but also the amount of recruitable collaterals. Extensive FVHs could reflect the recruitment of numerous well-developed collaterals from both the anterior cerebral artery and posterior cerebral arteries (which can cover the entire ischemic bed). FVHs abutting anterosuperior ASPECTS areas may correspond to leptomeningeal collaterals from the anterior cerebral artery to the MCA, and FVHs abutting posteroinferior ASPECTS areas may correspond to leptomeningeal collaterals from the posterior cerebral artery to the MCA.[26]

This retrospective study has several limitations. First, collateral status was indirectly based on the HIR. The validity of the dichotomization at the median to categorize into good and poor collaterals can also be questioned. Our median HIR was, however, identical to that observed in the study of Bang et al.[5] We also checked that our results were not affected by using the median HIR value of 0.4 derived from the DEFUSE 2 cohort.[6] Second, despite similar recanalization rates in patients with low/high HIRs or in those with few/extensive FVHs, we cannot exclude some patients having futile recanalization because the latter was assessed on the 24-hour MRA. Third, our results are based on 1.5T MR imaging data from the same manufacturer with standardized parameters. Although this ensures data homogeneity, it prevents extrapolating to other magnetic fields, coil systems, or FLAIR parameters that may influence FVH visibility.[27] Fourth, we collapsed FVH data as a single score, assuming that each ASPECTS area had the same significance. However, FVHs in different ASPECTS locations may not share the same pathophysiology.[15,17,24,26] Further studies are needed to determine the implications of FVH location, if any. Last, most patients were treated by thrombolysis alone, following guidelines at the time they had a stroke. Although the association between the FVH score and HIR is independent of the type of treatment, the association with outcome might differ in patients treated according to current state-of-the-art guidelines. Because we found that extensive FVHs represented good collaterals, their link with early neurologic improvement and favorable outcome could be stronger if recanalization rates increase, as expected with bridging therapy.

CONCLUSIONS

Using quantitative assessment of FVHs and the HIR as a marker of collateral status, we found a significant association between FVH extent and good collaterals in patients with MCA stroke before reperfusion therapy. Thus, to rapidly identify patients more likely to benefit from reperfusion therapy, ASPECTS assessment of FVHs might serve as a surrogate for collateral status whenever perfusion data or fast postprocessing software is not available.

REFERENCES

1. McVerry F, Liebeskind DS, Muir KW. **Systematic review of methods for assessing leptomeningeal collateral flow.** *AJNR Am J Neuroradiol* 2012;33:576–82 CrossRef Medline
2. Goyal M, Demchuk AM, Menon BK, et al; ESCAPE Trial Investigators. **Randomized assessment of rapid endovascular treatment of ischemic stroke.** *N Engl J Med* 2015;372:1019–30 CrossRef Medline
3. Campbell BC, Christensen S, Tress BM, et al; EPITHET Investigators. **Failure of collateral blood flow is associated with infarct growth in ischemic stroke.** *J Cereb Blood Flow Metab* 2013;33:1168–72 CrossRef Medline
4. Kim SJ, Son JP, Ryoo S, et al. **A novel magnetic resonance imaging approach to collateral flow imaging in ischemic stroke.** *Ann Neurol* 2014;76:356–69 CrossRef Medline
5. Bang OY, Saver JL, Alger JR, et al; UCLA Collateral Investigators. **Determinants of the distribution and severity of hypoperfusion in patients with ischemic stroke.** *Neurology* 2008;71:1804–11 CrossRef Medline
6. Olivot JM, Mlynash M, Inoue M, et al; DEFUSE 2 Investigators. **Hypoperfusion intensity ratio predicts infarct progression and functional outcome in the DEFUSE 2 cohort.** *Stroke* 2014;45:1018–23 CrossRef Medline
7. Kamran S, Bates V, Bakshi R, et al. **Significance of hyperintense vessels on FLAIR MRI in acute stroke.** *Neurology* 2000;55:265–69 CrossRef Medline
8. Azizyan A, Sanossian N, Mogensen MA, et al. **Fluid-attenuated inversion recovery vascular hyperintensities: an important imaging marker for cerebrovascular disease.** *AJNR Am J Neuroradiol* 2011;32:1771–75 CrossRef Medline
9. Legrand L, Tisserand M, Turc G, et al. **Do FLAIR vascular hyperintensities beyond the DWI lesion represent the ischemic penumbra?** *AJNR Am J Neuroradiol* 2015;36:269–74 CrossRef Medline
10. Sanossian N, Saver JL, Alger JR, et al. **Angiography reveals that fluid-attenuated inversion recovery vascular hyperintensities are due to slow flow, not thrombus.** *AJNR Am J Neuroradiol* 2009;30:564–68 CrossRef Medline
11. Hohenhaus M, Schmidt WU, Brunecker P, et al. **FLAIR vascular hyperintensities in acute ICA and MCA infarction: a marker for mismatch and stroke severity?** *Cerebrovasc Dis* 2012;34:63–69 CrossRef Medline
12. Kufner A, Galinovic I, Ambrosi V, et al. **Hyperintense vessels on FLAIR: hemodynamic correlates and response to thrombolysis.** *AJNR Am J Neuroradiol* 2015;36:1426–30 CrossRef Medline
13. Ebinger M, Kufner A, Galinovic I, et al. **Fluid-attenuated inversion recovery images and stroke outcome after thrombolysis.** *Stroke* 2012;43:539–42 CrossRef Medline
14. Girot M, Gauvrit JY, Cordonnier C, et al. **Prognostic value of hyperintense vessel signals on fluid-attenuated inversion recovery sequences in acute cerebral ischemia.** *Eur Neurol* 2007;57:75–79 Medline
15. Huang X, Liu W, Zhu W, et al. **Distal hyperintense vessels on FLAIR: a prognostic indicator of acute ischemic stroke.** *Eur Neurol* 2012;68:214–20 CrossRef Medline
16. Lee KY, Latour LL, Luby M, et al. **Distal hyperintense vessels on FLAIR: an MRI marker for collateral circulation in acute stroke?** *Neurology* 2009;72:1134–39 CrossRef Medline
17. Liu D, Scalzo F, Rao NM, et al. **Fluid-attenuated inversion recovery vascular hyperintensity topography, novel imaging marker for revascularization in middle cerebral artery occlusion.** *Stroke* 2016;47:2763–69 CrossRef Medline
18. Olindo S, Chausson N, Joux J, et al. **Fluid-attenuated inversion recovery vascular hyperintensity: an early predictor of clinical out-**

come in proximal middle cerebral artery occlusion. *Arch Neurol* 2012;69:1462–68 CrossRef Medline

19. Pérez de la Ossa N, Hernández-Perez M, Domènech S, et al. **Hyperintensity of distal vessels on FLAIR is associated with slow progression of the infarction in acute ischemic stroke.** *Cerebrovasc Dis* 2012; 34:376–84 CrossRef Medline
20. Legrand L, Tisserand M, Turc G, et al. **Fluid-attenuated inversion recovery vascular hyperintensities-diffusion-weighted imaging mismatch identifies acute stroke patients most likely to benefit from recanalization.** *Stroke* 2016;47:424–27 CrossRef Medline
21. Hassen WB, Tisserand M, Turc G, et al. **Comparison between voxel-based and subtraction methods for measuring diffusion-weighted imaging lesion growth after thrombolysis.** *Int J Stroke* 2016;11: 221–28 CrossRef Medline
22. Wouters A, Dupont P, Christensen S, et al. **Association between time from stroke onset and fluid-attenuated inversion recovery lesion intensity is modified by status of collateral circulation.** *Stroke* 2016; 47:1018–22 CrossRef Medline
23. Cheng B, Ebinger M, Kufner A, et al; Stroke Imaging Repository (STIR) Investigators. **Hyperintense vessels on acute stroke fluid-attenuated inversion recovery imaging: associations with clinical and other MRI findings.** *Stroke* 2012;43:2957–61 CrossRef Medline
24. Kono T, Naka H, Nomura E, et al. **The association between hyperintense vessel sign and final ischemic lesion differ in its location.** *J Stroke Cerebrovasc Dis* 2014;23:1337–43 CrossRef Medline
25. Schellinger PD, Chalela JA, Kang DW, et al. **Diagnostic and prognostic value of early MR imaging vessel signs in hyperacute stroke patients imaged <3 hours and treated with recombinant tissue plasminogen activator.** *AJNR Am J Neuroradiol* 2005;26: 618–24 Medline
26. Liu W, Xu G, Yue X, et al. **Hyperintense vessels on FLAIR: a useful non-invasive method for assessing intracerebral collaterals.** *Eur J Radiol* 2011;80:786–91 CrossRef Medline
27. Ahn SJ, Lee KY, Ahn SS, et al. **Can FLAIR hyperintense vessel (FHV) signs be influenced by varying MR parameters and flow velocities? A flow phantom analysis.** *Acta Radiol* 2016;57:580–86 CrossRef Medline
28. Lee SH, Seo KD, Kim JH, et al. **Correlation between hyperintense vessels on FLAIR imaging and arterial circulation time on cerebral angiography.** *Magn Reson Med Sci* 2016;15:105–10 CrossRef Medline

Can Arterial Spin-Labeling with Multiple Postlabeling Delays Predict Cerebrovascular Reserve?

H.J. Choi, C.-H. Sohn, S.-H. You, R.-E. Yoo, K.M. Kang, T.J. Yun, S.H. Choi, J.-H. Kim, W.-S. Cho, and J.E. Kim

ABSTRACT

BACKGROUND AND PURPOSE: The effect of delayed transit time is the main source of error in the quantitative measurement of CBF in arterial spin-labeling. In the present study, we evaluated the usefulness of the transit time–corrected CBF and arterial transit time delay from multiple postlabeling delays arterial spin-labeling compared with basal/acetazolamide stress technetium Tc99m-hexamethylpropylene amineoxime (Tc99m-HMPAO) SPECT in predicting impairment in the cerebrovascular reserve.

MATERIALS AND METHODS: Transit time–corrected CBF maps and arterial transit time maps were acquired in 30 consecutive patients with unilateral ICA or MCA steno-occlusive disease (severe stenosis or occlusion). Internal carotid artery territory–based ROIs were applied to both perfusion maps. Additionally, impairment in the cerebrovascular reserve was evaluated according to both qualitative and quantitative analyses of the ROIs on basal/acetazolamide stress Tc99m-HMPAO SPECT using a previously described method. The area under the receiver operating characteristic curve was used to evaluate the diagnostic accuracy of arterial spin-labeling in depicting impairment of the cerebrovascular reserve. The correlation between arterial spin-labeling and cerebrovascular reserve was evaluated.

RESULTS: The affected hemisphere had a decreased transit time–corrected CBF and increased arterial transit time compared with the corresponding values of the contralateral normal hemisphere, which were statistically significant ($P < .001$). The percentage change of transit time–corrected CBF and the percentage change of arterial transit time were independently differentiating variables ($P < .001$) for predicting cerebrovascular reserve impairment. The correlation coefficient between the arterial transit time and cerebrovascular reserve index ratio was −0.511.

CONCLUSIONS: Our results demonstrate that the transit time–corrected CBF and arterial transit time based on arterial spin-labeling perfusion MR imaging can predict cerebrovascular reserve impairment.

ABBREVIATIONS: ASL = arterial spin-labeling; ATT = arterial transit time; CVR = cerebrovascular reserve; MP-ASL = multiphase ASL (Hadamard-encoded pseudocontinuous ASL with multiple postlabeling delays); PLD = postlabeling delay; rCVR= cerebrovascular reserve ratio; ROC = receiver operating characteristic; TCF = transit time–corrected CBF; technetium Tc99m hexamethylpropylene amineoxime = Tc99m HMPAO

Assessment of hemodynamic abnormalities is important for managing cerebral ischemia and patients with Moyamoya disease, and the cerebrovascular reserve (CVR) has been considered the most useful predictor of cerebral hemodynamics.[1] Several brain perfusion imaging techniques have been used to evaluate the CVR, including PET, SPECT, CTP, and DSC perfusion MR imaging.[2,3] However, all these techniques require bolus injections of a contrast medium or radioactive tracers.

Basal/acetazolamide stress perfusion SPECT using an intravenous radiotracer, commonly technetium Tc99m-hexamethylpropylene amineoxime (Tc99m-HMPAO), is widely used because it can measure highly sensitive CVR in cerebral hemodynamics.[4] Generally, acetazolamide is safe to administer and is well-tolerated[5]; however, in one study, adverse reactions were reported in almost all healthy subjects (32 of 33 healthy subjects) following acetazolamide injection, such as headache or flushing.[6] Moreover, severe or life-threatening adverse events have been reported, including reversible pontine ischemia, pulmonary edema, Stevens–Johnson syndrome, and anaphylaxis with the risk of morbidity

Received May 25, 2017; accepted after revision September 4.

From the Department of Radiology (H.J.C.), CHA Bundang Medical Center, CHA University, Seongnam, Korea; Departments of Radiology (C.-H.S., R.-E.Y., K.M.K., T.J.Y., S.H.C., J.-H.K.) and Neurosurgery (W.-S.C., J.E.K.), Seoul National University Hospital, Seoul, Korea; and Department of Radiology (S.-H.Y.), Korea University Hospital, Seoul, Korea.

This study was supported by a grant from the Korean Health Technology R&D Project, Ministry for Health, Welfare and Family Affairs, South Korea (A070001).

Paper previously presented at: Annual Meeting of the American Society of Neuroradiology, April 22-27, 2017; Long Beach, California.

Please address correspondence to Chul-Ho Sohn, MD, Department of Radiology, Seoul National University Hospital, 101, Daehangno, Jongno-gu, Seoul 110-744, Korea; e-mail: neurorad63@gmail.com

Indicates open access to non-subscribers at www.ajnr.org

http://dx.doi.org/10.3174/ajnr.A5439

and mortality.[7-11] Several contraindications to acetazolamide also exist, including hypersensitivity to other sulfonamides or severe hepatic and renal disease.[5]

Arterial spin-labeling (ASL) perfusion MR imaging provides a noninvasive, repeatable method for quantifying the CBF using magnetically labeled arterial blood as an endogenous tracer without exposure to radiation and also provides higher spatial resolution than SPECT.[12-14] However, ASL has certain drawbacks. The main problem is a time delay between the inversion of blood spins passing through the labeling plane in the neck and the images in any plane in the head after labeled blood flows into brain tissue.[12,15] Cerebral steno-occlusive diseases, however, are generally accompanied by an elongation of the transit time because of the formation of collateral blood flow, which limits the validity of CBF determined by ASL.[16-18] Thus, the postlabeling delay (PLD) is the most important parameter, and clinical studies have been performed with multiple PLDs with arterial transit time (ATT) correction to improve the quantification of CBF.[16,18,19] With continuous ASL, direct measurement of the ATT could help improve perfusion quantification, particularly for vascular diseases with multiple different labeling times. However, these measurements can be very time-consuming and tend to have a low SNR.[15,19-22] Hadamard-encoded pseudocontinuous ASL with multiple PLDs (multiphase ASL [MP-ASL]) was recently proposed as an approach to increase the SNR and time efficiency of multiple-labeling time acquisitions.[22]

In this study, we present MP-ASL perfusion in unilateral steno-occlusive disease to predict the CVR relative to the widely used Tc99m-HMPAO basal/acetazolamide stress perfusion SPECT.

MATERIALS AND METHODS

Patients

This retrospective study was approved by the Seoul National University Hospital institutional review board. Between June 2015 and December 2016, ninety-eight consecutive patients with unilateral ICA or MCA steno-occlusive disease (severe stenosis [>70%] or occlusion) who had undergone ASL perfusion MR imaging and SPECT were included in this study. The exclusion criteria were as follows: 1) patients with contralateral moderate or severe stenosis, 2) a time interval between ASL perfusion MR imaging and SPECT of >1 month, and 3) poor image quality because of a previous hemorrhage or operation. Thirty patients were ultimately enrolled in this study. Eleven patients had undergone superficial temporal artery–middle cerebral artery anastomosis, and 1 patient had undergone proximal ICA stent placement. Four patients who had anastomosis surgery had preoperative and postoperative examination sets (preoperative ASL and SPECT and postoperative ASL and SPECT), and their images were analyzed separately. Consequently, 34 ASL and SPECT images from 30 patients were analyzed in this study. Two patients were diagnosed with unilateral Moyamoya disease, and 28 patients were diagnosed with non-Moyamoya steno-occlusive disease. All patients had severe stenosis or total occlusion of the unilateral ICAs or MCAs, as determined by MRA or DSA. There were 12 female and 18 male patients (a total of 30 patients with a mean age of 55.5 years and an age range of 16–82 years [male patients had a mean age of 59.2 years and age range of 48–82 years, and female patients had a mean age of 49.2 years and age range of 16–72 years]), with no significant difference in the age between male and female patients ($P = .12$). Patients had either distal ICA occlusion ($n = 5$), proximal ICA occlusion ($n = 12$), proximal ICA severe stenosis ($n = 2$), proximal MCA occlusion ($n = 8$), or proximal MCA/anterior cerebral artery occlusion ($n = 3$).

MR Imaging Protocol and Postprocessing

MR images were obtained with a 3T MR imaging scanner (Discovery MR750w; GE Healthcare, Milwaukee, Wisconsin) with a 32-channel head coil. We used the following 3D ASL protocol: TR, 5868.0 ms; TE, 11.0 ms; section thickness, 6 mm; NEX, 1; readout, 4 arms × 640 samples; 26 sections; FOV, 24 × 24 cm^2; and reconstructed in a plane voxel resolution, 1.88 × 1.88 mm^2. The total examination time for the ASL protocol was 3 minutes 57 seconds. All patients who underwent perfusion studies could tolerate MR imaging. This protocol encodes 7 different PLD times into a single acquisition. With the parameters tabulated above, images with PLD times of 1.00, 1.22, 1.48, 1.78, 2.15, 2.63, and 3.32 seconds and effective label durations of 0.22, 0.26, 0.30, 0.37, 0.48, 0.68, and 1.18 seconds were reconstructed. These PLD times were intended to probe the bolus arrival time. The ATT map (δ) and perfusion map (f) were calculated by fitting the 7-delays ASL difference signals as a function of the PLD (w) to the following equation:

$$\Delta M = 2M_t^0 \times \beta \times \alpha \times T1t \times f \times e^{-\delta/T1a} \times [e^{-\max(w-\delta,0)/T1t} - e^{-\max(\tau+w-\delta,0)/T1t}]/\lambda,^{23}$$

where ΔM is the ASL difference signal, f is the perfusion rate, $T1a$ and $T1t$ are the longitudinal relaxation times of blood and tissue, M_t^0 is the fully relaxed equilibrium magnetization of brain tissue, α is the efficiency of the labeling sequence, λ is the tissue-to-blood partition coefficient of water, δ is the transit delay, τ is the labeling duration, and w is the PLD. Vascular signal suppression is assumed in this model. β has been added to the kinetic model to compensate for any static tissue signal loss caused by the vessel-suppression pulses. Notice that for δ less than w, δ completely disappears from the equation.[22-26]

SPECT Imaging Protocol

Basal/acetazolamide brain perfusion SPECT was performed with a 1-day protocol. Basal SPECT images were acquired 5 minutes after intravenous injection of Tc99m-HMPAO (9.25 MBq per kilogram of body weight) using a triple-headed gamma camera (Triad XLT 9; Trionix Research Laboratory, Twinsburg, Ohio) equipped with low-energy ultra-high-resolution fan-beam collimators. Image acquisition was performed with a step-and-shoot mode with 40 steps for 20 seconds per step (total duration, 13.3 minutes). Ten minutes before the end of the basal SPECT, 14 mg/kg of acetazolamide was intravenously injected. Another dose of Tc99m-HMPAO (18.5 MBq per kilogram of body weight) was injected at the end of basal SPECT, and a second acquisition of SPECT was started 5 minutes later. The acetazolamide stress perfusion images were generated by using decay-corrected subtraction of the basal images from the corresponding stress images. All SPECT images were reconstructed on 128 × 128 matrices by using a filtered back-projection method with a Butterworth filter.

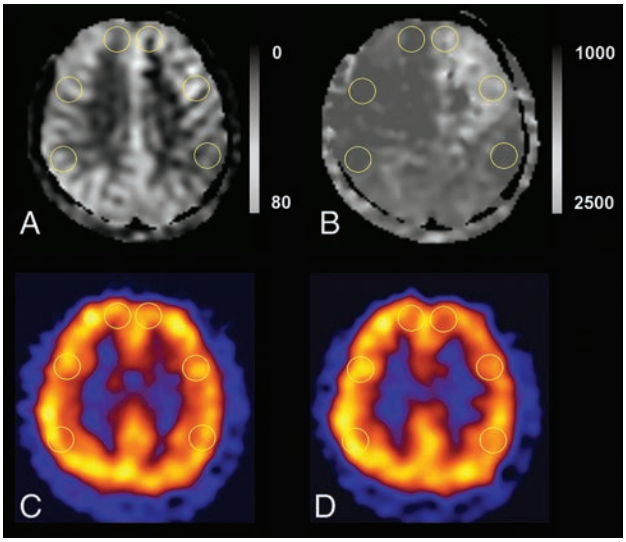

FIG 1. ROI placements in supraventricular levels on ASL and SPECT. We drew the ROIs in the bilateral anterior cerebral artery territories and anterior and posterior MCA territories in TCF (*A*), ATT (*B*), baseline SPECT (*C*), and acetazolamide challenge SPECT (*D*). We also drew an ROI in the ipsilateral cerebellum with the highest uptake on visual assessment for normalization of SPECT values.

ASL MR Imaging and SPECT Imaging Analysis

All MR imaging and basal/acetazolamide SPECT scans were reviewed by board-certified reviewer 1 (H.J.C. with 6 years of experience in radiology). Unclear interpretations were subsequently resolved in consensus with board-certified reviewer 2 (C.H.S. with >20 years of experience in radiology). The same analysis was performed by board-certified reviewer 3 (S.H.Y. with 6 years of experience in radiology).

Quantitative Assessment of ASL-Derived ATT and Transit Time–Corrected CBF

On ASL MR imaging, ROIs were drawn in the gray matter of the major territories of the intracranial arteries and the equivalent site on the contralateral normal side on the ATT and transit time–corrected CBF (TCF) maps directly in the workstation (Fig 1). The ROIs were placed in 6 locations (2 bilateral anterior cerebral artery territories and 4 bilateral MCA territories) on the supraventricular level over a fixed territory in all patients to avoid the infarcted area. ATT [ms] and TCF [mL/100 g/min] were obtained in each territory. The percentage change of TCF is calculated as $100 \times [(TCF_{\text{contralateral normal}} - TCF_{\text{ipsilateral affected}})/TCF_{\text{contralateral normal}}]$, and the percentage change of ATT is calculated as $100 \times [(ATT_{\text{contralateral normal}} - ATT_{\text{ipsilateral affected}})/ATT_{\text{contralateral normal}}]$.

Qualitative and Quantitative Assessment of SPECT-Derived CVR and Cerebrovascular Reserve Index

The SPECT data were assessed qualitatively and quantitatively. Regions of known old infarction with perfusion defects were not included for visual grading. The visual grades of reduced CVR were classified into 1 of 2 grades, preserved or impaired. Impairment of the CVR was defined as no increase or decrease in perfusion in acetazolamide stress SPECT compared with basal SPECT. Visual grading was performed on each side of the hemispheres relative to the normal contralateral side.

Table 1: ASL parameter values of each ROI[a]

ASL Parameters	Absolute Values		
	Contralateral Unaffected ROIs	Ipsilateral Affected ROIs	*P*
TCF (mL/100 g/min)	46.00 ± 8.89	34.81 ± 14.58	<.001
ATT (ms)	1235.49 ± 142.40	1643.71 ± 240.03	<.001

[a] Values are means.

For quantitative analysis, reviewers created 7 ROIs in the major arterial territories with an equivalent location on ASL images (2 bilateral anterior cerebral artery territories, 4 bilateral MCA territories, and 1 ipsilateral cerebellum for normalization), which were the same locations examined in the ASL images. The cerebrovascular reserve index (CVR_{index}) in each arterial territory was defined as $100 \times [(CBF_{\text{Acetazolamide}} - CBF_{\text{Baseline}}) / CBF_{\text{Baseline}}]$, where $CBF_{\text{Acetazolamide}}$ and CBF_{Baseline} were normalized by the ipsilateral cerebellar CBF, which was measured by drawing an ROI in the highest uptake on visual inspection.[27] Furthermore, the cerebrovascular reserve index ratio ($rCVR_{\text{index}}$) was defined as $100 \times [(rCBF_{\text{Acetazolamide}} - rCBF_{\text{Baseline}}) / rCBF_{\text{Baseline}}]$. The rCBF indicates the asymmetric ratio, which is normalized CBF value by the contralateral unaffected side.[27]

Statistical Analysis

To evaluate the ability of the ATT delay and TCF to predict impairment of the CVR, we performed a receiver operating characteristic (ROC) curve analysis to identify the optimal threshold for maximizing the sensitivity and specificity. In addition, pair-wise comparisons of the ROC curves were performed to compare the diagnostic accuracy of TCF, the percentage change of TCF ATT, and the percentage change of ATT. The correlation between ASL parameters and SPECT-derived CVR_{index} was determined by the Pearson correlation coefficient. Interobserver agreement for qualitative analysis of CVR in SPECT was evaluated by the weighted κ coefficient. The quantitative analysis for the CVR_{index} on SPECT and the quantitative analysis for ATT and TCF on ASL were assessed with the intraclass correlation coefficient. Weighted κ values or intraclass correlation coefficient of <0.20, 0.21–0.40, 0.41–0.60, 0.61–0.80, and 0.81–1.00 represented poor, fair, moderate, good, and excellent agreement, respectively.[28] All statistical analyses were performed with SPSS statistics, Version 20.0 (IBM, Armonk, New York); R statistical and computing software (http://www.r-project.org/); and MedCalc Statistical Software, Version 17.1 (MedCalc Software, Mariakerke, Belgium). A P value $< .05$ was considered statistically significant.

RESULTS

Time Interval between Examinations

The mean interval between ASL and SPECT examinations was 1.7 ± 4.9 days (range, 0–28 days).

Comparison of ASL Parameters between the Affected and Contralateral Unaffected ROIs

Table 1 shows the mean absolute values of ASL parameters of the affected and contralateral unaffected ROIs. The affected ROIs had a decreased TCF and increased ATT compared with the corresponding values of the contralateral normal unaffected ROIs, which were statistically significant ($P < .001$). Because a higher correlation was

Table 2: Diagnostic performance of the ASL parameters for predicting CVR impairment

	Mean	Area under ROC Curve	Associated Criterion	Sensitivity	Specificity	*P*
TCF (mL/100 g/min)	40.40 ± 13.27[a]	0.822 (0.747–0.882)[b]	≤33.00	62.00	93.02	<.001
Percentage change of TCF (%)	12.55 ± 21.86[a]	0.905 (0.843–0.949)[b]	>7.14	84.00	97.67	<.001
ATT (ms)	1439.59 ± 283.95[a]	0.891 (0.826–0.938)[b]	>1527	82.00	88.37	<.001
Percentage change of ATT (%)	−17.57 ± 26.24[a]	0.889 (0.823–0.936)[b]	≤−8.86	94.00	87.21	<.001

[a] Data are means.

[b] Data in parentheses are 95% confidence intervals.

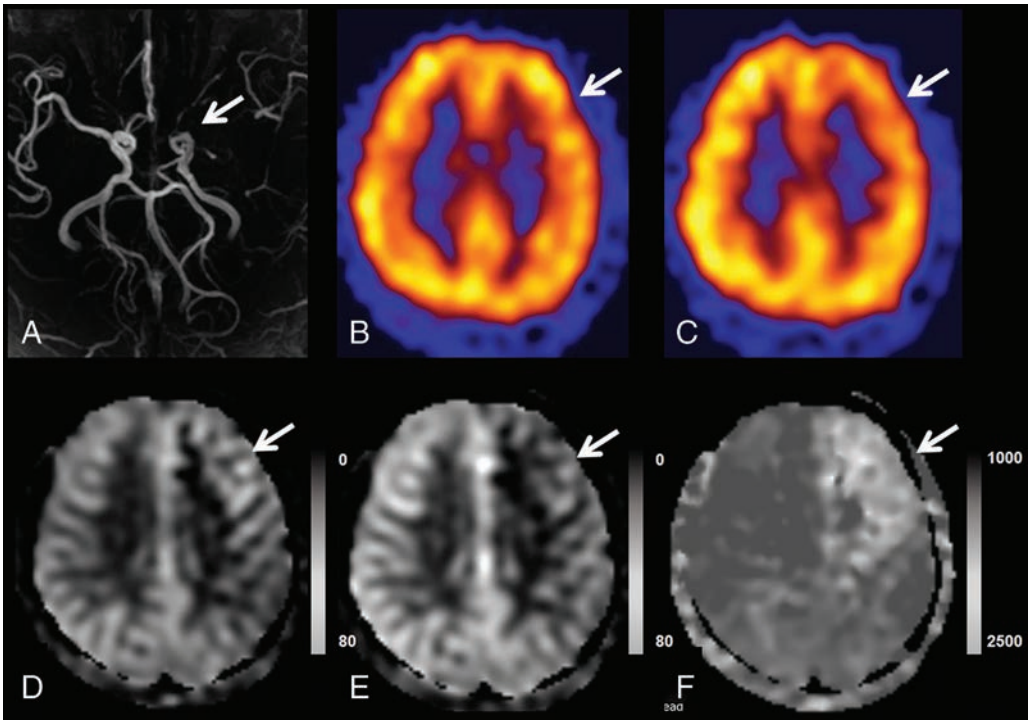

FIG 2. A representative case of the use of the TCF and ATT maps in depicting CVR impairment. TOF MRA (*A*) demonstrates left proximal MCA occlusion. Basal/acetazolamide Tc99m-HMPAO SPECT images (*B* and *C*) show normal perfusion on basal SPECT and decreased perfusion in the left frontal lobe (MCA M2, superior division territory) on acetazolamide challenge SPECT, which indicates impairment of the CVR in this region. In ASL without a time correction (*D*), there is no hypoperfusion; however, TCF from MP-ASL (*E*) demonstrates decreased perfusion and delayed ATT (*F*).

noted in the MCA territory than in the anterior cerebral artery territory, we focused on the MCA territory in subsequent results.

Diagnostic Performance of ASL Parameters in the Prediction of CVR Impairment

In qualitative assessment of baseline and acetazolamide challenge SPECT, 20 patients (66.67%) showed impairment of CVR on the affected side. Eight patients (26.67%) showed preserved CVR even in ipsilateral steno-occlusive disease. In addition, we evaluated 136 ROIs: Fifty ROIs showed impaired CVR and 86 ROIs showed preserved CVR. Four patients who had bypass surgery showed impaired CVR on qualitative assessment in preoperative and postoperative SPECT. Results pertaining to the diagnostic performance of TCF and ATT in predicting CVR impairment based on a qualitative assessment of SPECT data are summarized in Table 2. The percentage change of TCF showed the best area under the curve value (0.905) in predicting CVR impairment. A significant difference was found in the pair-wise comparison of the areas under the ROC curve between TCF and the percentage change of transit time (difference between areas = 0.083, P = .015). Otherwise, there was no significant difference among the areas under the ROC curve. A representative case of TCF and ATT used in depicting the CVR impairment is shown in Fig 2.

Correlation between ASL Parameters and SPECT-Derived Parameters

The correlation between ASL parameters and SPECT-derived parameters is summarized in Fig 3. The TCF showed a positive correlation with the CVR_{index} or $rCVR_{index}$, and the ATT showed a negative correlation with the CVR_{index} or $rCVR_{index}$ ($P < .001$, respectively).

Interobserver Agreement for MP-ASL Parameters, Qualitative Assessment of CVR, and Quantitative Assessment of CVR Based on SPECT

Interobserver agreement for the visual assessment of the impairment of CVR based on SPECT (weighted $\kappa = 0.950$), measurement of the basal CBF in SPECT (intraclass correlation coefficient = 0.964), acetazolamide challenge CBF in SPECT (intraclass correlation coefficient = 0.968), TCF in ASL (intraclass correlation coefficient = 0.902), and the ATT in ASL (intraclass correlation coefficient = 0.966) was excellent.

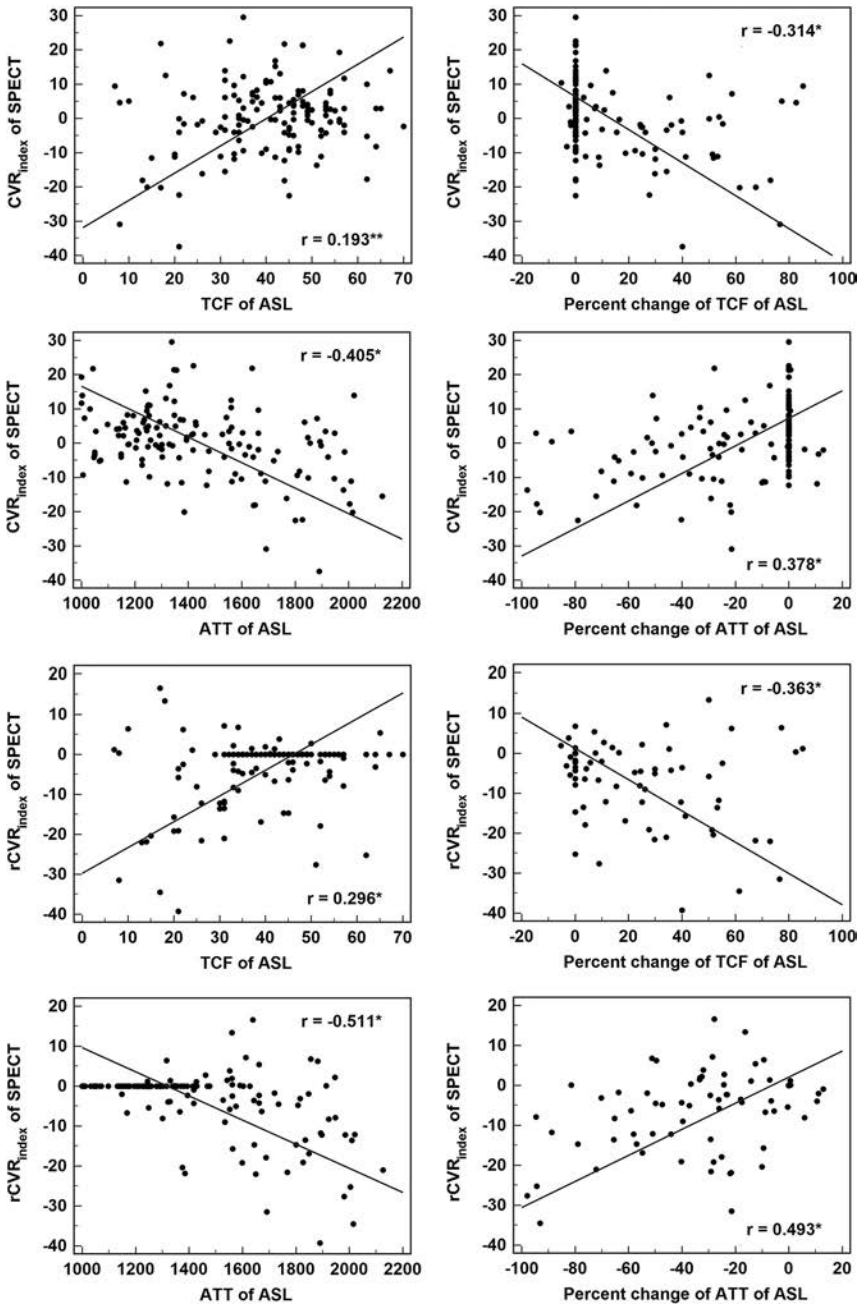

FIG 3. Scatterplots and Pearson correlation coefficients between values of ASL and SPECT of MCA territories (the *asterisk* indicates $P < .001$; *double asterisks*, $P = .007$).

DISCUSSION

The present study demonstrated that TCF and ATT measurements made by MP-ASL can predict CVR without acetazolamide in patients with unilateral steno-occlusive disease. Therefore, ASL can reduce the number of examinations for patients who require frequent follow-up to evaluate CVR without the acetazolamide challenge SPECT.

Many studies have examined the relationship between hemodynamic parameters and metabolic reserve. Based on a PET study, Gibbs et al[29] suggested that the ratio CBF/CBV (reciprocal of the MTT) is an index of diminishing cerebral perfusion pressure, and even without a measurement of the regional oxygen extraction ratio, the MTT can provide the best predictive value for cerebrovascular reserve. Schumann et al[30] also demonstrated that the MTT was linearly correlated with cerebral perfusion pressure under physiologic conditions and may be sensitive to metabolic reserve consumption. Vagal et al[5] reported that the MTT is 1 of 3 general approaches for assessing CVR in the same position as CBF measurements by the acetazolamide challenge and direct oxygen extraction fraction measurements. The MTT determination based on perfusion CT or DSC-MR imaging showed a strong correlation with CVR in patients with chronic vascular occlusive disease.[31-33] The ATT is different from the MTT; however, it has been reported that there was significant correlation between the ATT and MTT ($r = 0.604$, $P = .01$).[16] To the best of our knowledge, there is no prior study about the correlation between the ATT and the CVR based on SPECT with acetazolamide challenge. With respect to predicting the CVR from baseline SPECT CBF scans, we found a poorer correlation between baseline CBF and CVR_{index} ($r = -0.279$, $P = .021$) than for ATT or TCF and no significant correlation between baseline CBF and $rCVR_{index}$ ($r = -0.058$, $P = .637$). These results are like those of studies indicating that CBF has no correlation with CVR or a poorer correlation than the MTT.[3,34] However, we observed a better correlation between the percentage change in the TCF and $rCVR_{index}$ ($r = -0.363$, $P < .001$). The percentage change in the TCF showed excellent diagnostic performance in predicting CVR with a sensitivity of 84.00%, specificity of 97.67%, and an area under the ROC curve of 0.905. In addition, the correlation between the ATT and $rCVR_{index}$ was moderate ($r = -0.511$, $P < .001$). The ATT showed excellent diagnostic performance in predicting CVR with a sensitivity of 82.00%, specificity of 88.37%, and an area under the ROC curve of 0.891. According to our results, the TCF and ATT have potential value in predicting CVR.

In a previous study, the CVR index by ASL with an acetazolamide challenge in monitoring Moyamoya disease showed excellent performance in the identification of impaired CVR, which was based on single postlabeling delay ASL and the use of acetazolamide.[35] Comparable results have been reported for respiratory challenge MR imaging in hypercapnia or breathing control in the assessment of CVR with use of ASL and blood oxygen level–dependent techniques.[36] Although these methods provide useful

information about CVR in a safe, noninvasive, and repeatable manner at high temporal and spatial resolution, there may be restrictions on the use of the complex equipment associated with the procedure, such as gas concentration control, the use of a mask or ventilator, the use of visual cueing or a pneumatic belt for paced breathing, and patient-training before the MRI scan.[36]

Single PLD ASL imaging provides rapid and robust measurements of CBF. However, the method does not provide measurements of the ATT. ATT prolongation causes underestimation of CBF, and such effects might be particularly important in patients with steno-occlusive diseases. In a recent recommendation for the clinical application of ASL from the International Society for Magnetic Resonance in Medicine consensus, the authors mentioned that the complex-but-efficient Hadamard time-encoding strategies of ASL can provide additional information of the estimation of ATT and the most precise quantitation of CBF, especially in steno-occlusive disease.[12] The MP-ASL speeds imaging and efficiently improves the SNR.[22] Additionally, we found the feasibility of MP-ASL in predicting CVR in patients with steno-occlusive disease who had a long transit time from labeling to scanning without the use of a vasodilatory stimulus (such as acetazolamide) or contrast (iodinate or gadolinium base). This protocol encoded 7 different PLD times with the application of 7 effective label durations. Because the ASL signal increases with label duration, Alsop et al[12] suggested a labeling duration of 1.8 seconds as a compromise between an increase in the SNR and the disadvantage of greater power deposition and T1 sensitivity in a single postlabeling delay ASL. We used 7 shorter effective label durations (range, 0.22–1.18 seconds) than the duration recommended by Alsop et al. A previous study demonstrated a trade-off between systematic error and the SNR using standard continuous ASL versus the Hadamard continuous arterial spin-labeling method.[22] Because Hadamard encoding can remove transit time–related systematic errors, it holds an advantage for clinical applications, particularly for patients with steno-occlusive disease, for whom the range of prolonged ATT values is variable or unknown.

Acetazolamide acts quickly: an increase of CBF up to 53% ± 24% in 3 minutes after 1 g of acetazolamide administration.[37] The SPECT protocol in this study was administration of acetazolamide 10 minutes before the end of baseline SPECT. One of the purposes of the protocol is to save time to avoid motion artifacts. Acetazolamide can be injected during the baseline scan to optimize the effect of the drug at the end of the test. The Tc99m-HMPAO that we use for imaging is characterized by being fixed in the brain within 2 minutes after injection.[38] Even if other medications are introduced in the middle of the scan (and even if the blood flow is changed), the fixed status does not change.

This study has a few limitations. First, we did not divide the patient group into atherosclerotic stenosis and unilateral Moyamoya disease groups, which are different pathophysiologies of vascular stenosis, collateral formation, and consequent arterial transit delay.[39] However, this protocol covered a long PLD (the longest postlabeling time was 3.32 seconds), which would not be affected by the long ATT. Second, we used SPECT as a reference standard for CVR impairment rather than PET, which has usually been considered a standard for CBF quantification. However, some studies have shown that SPECT can be an alternative method for CBF assessment in patients with cerebrovascular disease.[40] Third, because the measurements of CVR and CVR_{index} were made via a 1-day protocol of Tc99m-HMPAO SPECT with a split dose, we should normalize the values by the ipsilateral cerebellum or contralateral equivalent normal side to obtain the adjusted quantification. Fourth, we did not control for conditions that could cause variations in CBF, such as caffeine, time of day, or diet, and the examinations were not performed back to back.[41] We used percent change of values and asymmetric ratio in addition to the absolute values to reduce uncontrolled variations.

CONCLUSIONS

MP-ASL can predict cerebrovascular reserve without acetazolamide in patients with unilateral steno-occlusive disease. ASL can provide a potential noninvasive imaging tool for measuring CVR impairment.

REFERENCES

1. Derdeyn CP, Grubb RL Jr, Powers WJ. **Cerebral hemodynamic impairment: methods of measurement and association with stroke risk.** *Neurology* 1999;53:251–59 CrossRef Medline
2. Wintermark M, Sesay M, Barbier E, et al. **Comparative overview of brain perfusion imaging techniques.** *Stroke* 2005;36:e83–99 CrossRef Medline
3. Kim E, Sohn CH, Na DG, et al. **Perfusion computed tomography evaluation of cerebral hemodynamic impairment in patients with unilateral chronic steno-occlusive disease: a comparison with the acetazolamide challenge 99mTc-hexamethylpropyleneamine oxime single-photon emission computed tomography.** *J Comput Assist Tomogr* 2009;33:546–51 CrossRef Medline
4. Barber PA, Consolo HK, Yang Q, et al. **Comparison of MRI perfusion imaging and single photon emission computed tomography in chronic stroke.** *Cerebrovasc Dis* 2001;11:128–36 CrossRef Medline
5. Vagal AS, Leach JL, Fernandez-Ulloa M, et al. **The acetazolamide challenge: techniques and applications in the evaluation of chronic cerebral ischemia.** *AJNR Am J Neuroradiol* 2009;30:876–84 CrossRef Medline
6. Sullivan HG, Kingsbury TB 4th, Morgan ME, et al. **The rCBF response to Diamox in normal subjects and cerebrovascular disease patients.** *J Neurosurg* 1987;67:525–34 CrossRef Medline
7. Komiyama M, Nishikawa M, Yasui T, et al. **Reversible pontine ischemia caused by acetazolamide challenge.** *AJNR Am J Neuroradiol* 1997;18:1782–84 Medline
8. Zimmermann S, Achenbach S, Wolf M, et al. **Recurrent shock and pulmonary edema due to acetazolamide medication after cataract surgery.** *Heart Lung* 2014;43:124–26 CrossRef Medline
9. Her Y, Kil MS, Park JH, et al. **Stevens-Johnson syndrome induced by acetazolamide.** *J Dermatol* 2011;38:272–75 CrossRef Medline
10. Hu CY, Lee BJ, Cheng HF, et al. **Acetazolamide-related life-threatening hypophosphatemia in a glaucoma patient.** *J Glaucoma* 2015;24:e31–33 CrossRef Medline
11. Kelly TE, Hackett PH. **Acetazolamide and sulfonamide allergy: a not so simple story.** *High Alt Med Biol* 2010;11:319–23 CrossRef Medline
12. Alsop DC, Detre JA, Golay X, et al. **Recommended implementation of arterial spin-labeled perfusion MRI for clinical applications: a consensus of the ISMRM perfusion study group and the European consortium for ASL in dementia.** *Magn Reson Med* 2015;73:102–16 CrossRef Medline
13. Deibler AR, Pollock JM, Kraft RA, et al. **Arterial spin-labeling in routine clinical practice, Part 1: technique and artifacts.** *AJNR Am J Neuroradiol* 2008;29:1228–34 CrossRef Medline
14. Alsop DC, Detre JA, Grossman M. **Assessment of cerebral blood flow in Alzheimer's disease by spin-labeled magnetic resonance imaging.** *Ann Neurol* 2000;47:93–100 Medline
15. Haga S, Morioka T, Shimogawa T, et al. **Arterial spin labeling perfu-**

sion magnetic resonance image with dual postlabeling delay: a correlative study with acetazolamide loading (123)I-iodoamphetamine single-photon emission computed tomography. *J Stroke Cerebrovasc Dis* 2016;25:1–6 CrossRef Medline
16. Wang R, Yu S, Alger JR, et al. **Multi-delay arterial spin labeling perfusion MRI in Moyamoya disease–comparison with CT perfusion imaging.** *Eur Radiol* 2014;24:1135–44 CrossRef Medline
17. Yun TJ, Sohn CH, Han MH, et al. **Effect of delayed transit time on arterial spin labeling: correlation with dynamic susceptibility contrast perfusion magnetic resonance in Moyamoya disease.** *Invest Radiol* 2013;48:795–802 CrossRef Medline
18. MacIntosh BJ, Lindsay AC, Kylintireas I, et al. **Multiple inflow pulsed arterial spin-labeling reveals delays in the arterial arrival time in minor stroke and transient ischemic attack.** *AJNR Am J Neuroradiol* 2010;31:1892–94 CrossRef Medline
19. Wang DJ, Alger JR, Qiao JX, et al; UCLA Stroke Investigators. **Multi-delay multi-parametric arterial spin-labeled perfusion MRI in acute ischemic stroke: comparison with dynamic susceptibility contrast enhanced perfusion imaging.** *Neuroimage Clin* 2013;3:1–7 CrossRef Medline
20. Bokkers RP, Bremmer JP, van Berckel BN, et al. **Arterial spin labeling perfusion MRI at multiple delay times: a correlative study with H(2)(15)O positron emission tomography in patients with symptomatic carotid artery occlusion.** *J Cereb Blood Flow Metab* 2010;30:222–29 CrossRef Medline
21. Chalela JA, Alsop DC, Gonzalez-Atavales JB, et al. **Magnetic resonance perfusion imaging in acute ischemic stroke using continuous arterial spin labeling.** *Stroke* 2000;31:680–87 CrossRef Medline
22. Dai W, Shankaranarayanan A, Alsop DC. **Volumetric measurement of perfusion and arterial transit delay using Hadamard encoded continuous arterial spin labeling.** *Magn Reson Med* 2013;69:1014–22 CrossRef Medline
23. Alsop DC, Detre JA. **Reduced transit-time sensitivity in noninvasive magnetic resonance imaging of human cerebral blood flow.** *J Cereb Blood Flow Metab* 1996;16:1236–49 CrossRef Medline
24. Dai W, Robson PM, Shankaranarayanan A, et al. **Reduced resolution transit delay prescan for quantitative continuous arterial spin labeling perfusion imaging.** *Magn Reson Med* 2012;67:1252–65 CrossRef Medline
25. Buxton RB, Frank LR, Wong EC, et al. **A general kinetic model for quantitative perfusion imaging with arterial spin labeling.** *Magn Reson Med* 1998;40:383–96 CrossRef Medline
26. Wang J, Alsop DC, Li L, et al. **Comparison of quantitative perfusion imaging using arterial spin labeling at 1.5 and 4.0 Tesla.** *Magn Reson Med* 2002;48:242–54 CrossRef Medline
27. Martí-Fàbregas JA, Catafau AM, Marí C, et al. **Cerebral perfusion and haemodynamics measured by SPET in symptom-free patients with transient ischaemic attack: clinical implications.** *Eur J Nucl Med* 2001;28:1828–35 CrossRef Medline
28. Landis JR, Koch GG. **The measurement of observer agreement for categorical data.** *Biometrics* 1977;33:159–74 CrossRef Medline
29. Gibbs JM, Wise RJ, Leenders KL, et al. **Evaluation of cerebral perfusion reserve in patients with carotid-artery occlusion.** *Lancet* 1984;1:310–14 Medline
30. Schumann P, Touzani O, Young AR, et al. **Evaluation of the ratio of cerebral blood flow to cerebral blood volume as an index of local cerebral perfusion pressure.** *Brain* 1998;121(pt 7):1369–79 CrossRef Medline
31. Eicker SO, Turowski B, Heiroth HJ, et al. **A comparative study of perfusion CT and 99m Tc-HMPAO SPECT measurement to assess cerebrovascular reserve capacity in patients with internal carotid artery occlusion.** *Eur J Med Res* 2011;16:484–90 CrossRef Medline
32. Kawano T, Ohmori Y, Kaku Y, et al. **Prolonged mean transit time detected by dynamic susceptibility contrast magnetic resonance imaging predicts cerebrovascular reserve impairment in patients with Moyamoya disease.** *Cerebrovasc Dis* 2016;42:131–38 CrossRef Medline
33. Park JC, Kim JE, Kang HS, et al. **CT perfusion with angiography as a substitute for both conventional digital subtraction angiography and acetazolamide-challenged SPECT in the follow-up of postbypass patients.** *Cerebrovasc Dis* 2010;30:547–55 CrossRef Medline
34. Kim JH, Lee SJ, Shin T, et al. **Correlative assessment of hemodynamic parameters obtained with T2*-weighted perfusion MR imaging and SPECT in symptomatic carotid artery occlusion.** *AJNR Am J Neuroradiol* 2000;21:1450–56 Medline
35. Yun TJ, Paeng JC, Sohn CH, et al. **Monitoring cerebrovascular reactivity through the use of arterial spin labeling in patients with Moyamoya disease.** *Radiology* 2016;278:205–13 CrossRef Medline
36. Moreton FC, Dani KA, Goutcher C, et al. **Respiratory challenge MRI: practical aspects.** *Neuroimage Clin* 2016;11:667–77 CrossRef Medline
37. Vorstrup S, Henriksen L, Paulson OB. **Effect of acetazolamide on cerebral blood flow and cerebral metabolic rate for oxygen.** *J Clin Invest* 1984;74:1634–39 CrossRef Medline
38. Murase K, Tanada S, Fujita H, et al. **Kinetic behavior of technetium-99m-HMPAO in the human brain and quantification of cerebral blood flow using dynamic SPECT.** *J Nucl Med* 1992;33:135–43 Medline
39. Martin SZ, Madai VI, von Samson-Himmelstjerna FC, et al. **3D GRASE pulsed arterial spin labeling at multiple inflow times in patients with long arterial transit times: comparison with dynamic susceptibility-weighted contrast-enhanced MRI at 3 Tesla.** *J Cereb Blood Flow Metab* 2015;35:392–401 CrossRef Medline
40. Inugami A, Kanno I, Uemura K, et al. **Linearization correction of 99mTc-labeled hexamethyl-propylene amine oxime (HM-PAO) image in terms of regional CBF distribution: comparison to C15O2 inhalation steady-state method measured by positron emission tomography.** *J Cereb Blood Flow Metab* 1988;8:S52–60 CrossRef Medline
41. Fan AP, Jahanian H, Holdsworth SJ, et al. **Comparison of cerebral blood flow measurement with [15O]-water positron emission tomography and arterial spin labeling magnetic resonance imaging: a systematic review.** *J Cereb Blood Flow Metab* 2016;36:842–61 CrossRef Medline

Spatial Correlation of Pathology and Perfusion Changes within the Cortex and White Matter in Multiple Sclerosis

A.D. Mulholland, R. Vitorino, S.-P. Hojjat, A.Y. Ma, L. Zhang, L. Lee, T.J. Carroll, C.G. Cantrell, C.R. Figley, and R.I. Aviv

ABSTRACT

BACKGROUND AND PURPOSE: The spatial correlation between WM and cortical GM disease in multiple sclerosis is controversial and has not been previously assessed with perfusion MR imaging. We sought to determine the nature of association between lobar WM, cortical GM, volume and perfusion.

MATERIALS AND METHODS: Nineteen individuals with secondary-progressive multiple sclerosis, 19 with relapsing-remitting multiple sclerosis, and 19 age-matched healthy controls were recruited. Quantitative MR perfusion imaging was used to derive CBF, CBV, and MTT within cortical GM, WM, and T2-hyperintense lesions. A 2-step multivariate linear regression (corrected for age, disease duration, and Expanded Disability Status Scale) was used to assess correlations between perfusion and volume measures in global and lobar normal-appearing WM, cortical GM, and T2-hyperintense lesions. The Bonferroni adjustment was applied as appropriate.

RESULTS: Global cortical GM and WM volume was significantly reduced for each group comparison, except cortical GM volume of those with relapsing-remitting multiple sclerosis versus controls. Global and lobar cortical GM CBF and CBV were reduced in secondary-progressive multiple sclerosis compared with other groups but not for relapsing-remitting multiple sclerosis versus controls. Global and lobar WM CBF and CBV were not significantly different across groups. The distribution of lobar cortical GM and WM volume reduction was disparate, except for the occipital lobes in patients with secondary-progressive multiple sclerosis versus those with relapsing-remitting multiple sclerosis. Moderate associations were identified between lobar cortical GM and lobar normal-appearing WM volume in controls and in the left temporal lobe in relapsing-remitting multiple sclerosis. No significant associations occurred between cortical GM and WM perfusion or volume. Strong correlations were observed between cortical-GM perfusion, normal appearing WM and lesional perfusion, with respect to each global and lobar region within HC, and RRMS and SPMS patients ($R^2 \leq 0.96$, $P < .006$ and $R^2 \leq 0.738$, $P < .006$).

CONCLUSIONS: The weak correlation between lobar WM and cortical GM volume loss and perfusion reduction suggests the independent pathophysiology of WM and cortical GM disease.

ABBREVIATIONS: cGM = cortical GM; EDSS = Expanded Disability Status Scale; HC = healthy control; NAWM = normal-appearing white matter; RRMS = relapsing-remitting multiple sclerosis; SPMS = secondary-progressive multiple sclerosis; T2h-1 = T2-hyperintense lesions

MS is a notable cause of neurologic and cognitive disability in young people. Pathologically, it is characterized by inflammatory demyelination and, in chronic lesions, axonal loss.[1] The cause of reduced cortical metabolism described in MS remains uncertain.[2,3] While MS is typically regarded as a disease primarily affecting WM, cortical GM (cGM) is increasingly complicit in physical and cognitive disease progression. However, the relationships between WM and cGM disease progression remain controversial. Although some studies have suggested a relationship between normal-appearing WM (NAWM) atrophy and cGM damage,[4,5] others suggested that cGM disease progression is either independent from or only partly related to WM abnormali-

Received November 15, 2016; accepted after revision August 4, 2017.

From the Department of Physical Sciences (A.D.M., R.V., S.-P.H., A.Y.M., L.Z.), Sunnybrook Research Institute, Toronto, Ontario, Canada; Departments of Medical Imaging (L.Z., R.I.A.) and Neurology (L.L.), Sunnybrook Health Sciences Centre, Toronto, Ontario, Canada; Department of Biomedical Engineering and Radiology (T.J.C.), University of Chicago, Chicago, Illinois; Department of Biomedical Engineering (C.G.C.), Northwestern University, Chicago, Illinois; Department of Radiology and Biomedical Engineering (C.R.F.), University of Manitoba, Winnipeg, Manitoba, Canada; and Department of Medical Imaging (R.I.A.), University of Toronto, Toronto, Ontario, Canada.

This work was supported by the Canadian Institutes of Health Research operating grant No. 130366; National Institutes of Health, EB017928; American Heart Association grants 20380798 and 14PRE20380810; and a Biogen fellowship funding award.

Please address correspondence to Richard I. Aviv, MD, Sunnybrook Health Sciences Centre, 2075 Bayview Ave, Room AG-31, Toronto, ON, M4N 3M5 Canada; e-mail: Richard.aviv@sunnybrook.ca

Indicates open access to non-subscribers at www.ajnr.org
Indicates article with supplemental on-line table.
Indicates article with supplemental on-line photos.

http://dx.doi.org/10.3174/ajnr.A5410

ties.[6,7] Louapre et al,[8] using DTI at 7T, found a lack of spatial specificity between NAWM tracts and the overlying cGM. Steenwijk et al[9] reported a stronger relationship between cGM atrophy and WM tract pathology in patients with relapsing-remitting multiple sclerosis (RRMS) compared with those with secondary-progressive multiple sclerosis (SPMS), concluding that the association between NAWM and cGM becomes increasingly independent with disease progression. The assertion that cGM and WM progression is either dependent or partly independent is supported by histopathologic and radiologic series demonstrating the role of meningeal mediated processes in both cortical and leucocortical lesions but not WM T2-hyperintense lesion (T2h-l) development.[10,11]

Although few studies[4,5,9] have examined the regional relationship between cortical structure and WM disease, the association between regional WM volume and perfusion and cortical volume and perfusion has not been previously studied. CBF and CBV reduction have been previously shown either in the absence of, or adjusting for, intergroup structural differences, suggesting that cortical perfusion could serve as a surrogate of disease severity and tissue integrity under specific conditions.[12-14] Aviv et al[12] demonstrated focal cGM CBV reduction in cognitively impaired compared with preserved patients with SPMS after adjusting for global WM T2h-l volumes. Hojjat et al[15] demonstrated significant CBF reduction in the absence of structural differences in impaired compared with cognitively preserved patients with RRMS. Last, Debernard et al[14] found CBF reduction in the absence of cGM volume differences in unimpaired patients with RRMS compared with healthy controls (HCs) using pseudocontinuous arterial spin-labeled/labeling perfusion. While prior studies reported regional variation in CBF and CBV, none examined the regional associations between lobar WM (normal-appearing and lesional) and cGM volume and perfusion reduction. Consistent with growing evidence for partly independent mechanisms of disease progression in WM and cGM, we hypothesized that an independent association would be found between lobar WM disease and cGM volume and perfusion.

MATERIALS AND METHODS

Study Participants

Thirty-eight patients with MS (19 with SPMS and 19 with RRMS) from 2 tertiary referral MS clinics and 19 healthy, age-matched controls were prospectively recruited during a 1-year period. Exclusion criteria were a history of drug/alcohol abuse, relapse or steroid use in <6 months, pre-MS psychiatric history, head injuries involving loss of consciousness, cardiac disease, and MR imaging contraindications. Demographic data were obtained for each subject. This study was approved by both local ethics committees (Sunnybrook Health Sciences Centre and St. Michael's Hospital, Toronto), and written consent was obtained from each participant before study enrollment.

Cognitive Testing

All patients and HCs underwent MR imaging, neurologic examination, and Expanded Disability Status Scale (EDSS) assessment within 1 week. Patients were tested with the Minimal Assessment of Cognitive Function in Multiple Sclerosis battery comprising 7 tests covering 5 cognitive domains, including processing speed, memory, executive function, visuospatial perception, and verbal fluency. Only cognitively preserved patients were enrolled in the study, given the greater potential for confounding pathophysiologic factors, with greater disease progression characterized by cognitive impairment and the previously published association between cognitive impairment, disease progression, and hypoperfusion.[9,15,16]

Image Acquisition

All MR imaging data were acquired on a 3T MR imaging system (Achieva; Philips Healthcare, Best, the Netherlands) with an 8-channel phased array coil. The MR imaging sequences included: axial proton density/T2 (TR/TE/flip angle = 2500/10.7ms/90°; FOV = 230 × 230 mm^2; acquisition matrix = 256 × 263; section thickness = 3 mm); axial T1-weighted TSE (TR/TE/flip angle = 9.5/2.3ms/12°; FOV = 240 × 240 mm^2; acquisition matrix = 256 × 219; section thickness = 1.2 mm); axial phase-sensitive inversion recovery (TR/TE = 3374/15 ms; FOV = 230 × 230 mm^2; acquisition matrix = 400 × 255; section thickness = 3 mm); axial field-echo, echo-planar dynamic susceptibility contrast perfusion (TR/TE/flip angle = 1633/30ms/60°; FOV = 220 × 220 mm^2; acquisition matrix = 96 × 93; section thickness = 4 mm; no gap; signal bandwidth = 1260 Hz/pixel; sections = 24). During the perfusion scan, 10 mL of 1-mmol/mL concentrated gadobutrol (Gadovist; Bayer Schering Pharma, Berlin, Germany) was administered by a power injector at a rate of 5 mL/s, followed by a 25-mL bolus of saline at 5 mL/s. Sixty images were acquired with the injection occurring at the fifth volume. A segmented inversion recovery Look-Locker EPI sequence was performed immediately before and after the axial DSC sequence (TR/TE/flip angle = 29/14ms/20°; TI = 15.8 ms; FOV = 220 × 220 mm^2; acquisition matrix = 128 × 126; 15 *k*-space lines per acquisition; section thickness = 4 mm; time points = 60). A 3-second delay occurred following the last imaging time point to facilitate longitudinal magnetization recovery.

Quantitative MR Perfusion

Quantitative CBF (milliliter/100 gram/minute), quantitative CBV (milliliter/100 gram), and MTT (second) were obtained using bookend MR imaging perfusion as previously published.[17] The technique uses pre- and postgadolinium bookend scans to calculate WM quantitative CBV without the need for an arterial input function while accounting for the effects of intravascular-to-extravascular water exchange. The tissue concentration–time curve is calculated through arterial input function sampling, allowing relative CBV and relative CBF determination. The central volume principle was used to calculate MTT.

Image Processing

Structural T1- and proton-density/T2-weighted images were coregistered using linear registration (SPM8; http://www.fil.ion.ucl.ac.uk/spm/software/spm12). T2h-l and deep GM structures were segmented by a board-certified neuroradiologist (>10 years' experience) using the trace function in Analyze 8.0 (Mayo Clinic, Rochester, Minnesota). T1-weighted structural images were first segmented into GM and WM masks using the unified segmen-

Table 1: Comparison of demographic and clinical data for HCs and subjects with RRMS and SPMS[a]

Parameter	HC (n = 19)	RRMS (n = 19)	SPMS (n = 20)	RRMS vs HC (P Value)	SPMS vs HC (P Value)	SPMS vs RRMS (P Value)
Age (yr)	49.0 ± 7.1	46.4 ± 7.2	55.2 ± 6.5	.27	.0168[b]	.0041[b]
Sex (F/M)	14:5	15:4	11:9	.70	.23	.12
Education (yr)	16.9 ± 2.9	16.1 ± 1.3	15.1 ± 2.6	.22	.051	.15
Disease duration (yr)	0.00	11.8 ± 5.4	16.7 ± 6.5	NA	NA	.0234
EDSS (median) (IQR)	0.00	1.5 (1–2)	6 (6–6.5)	NA	NA	.0006[b]

Note:—IQR indicates interquartile range; NA, not applicable.

[a] All values are mean (SD) except where indicated. Bonferroni corrected $P < .017$ is considered statistically significant.

[b] Significant.

tation model in SPM8 and checked for accuracy before creating subject-specific NAWM masks by subtracting T2h-l from the automated WM segmentation. For cortical volumetric analysis, the International Consortium for Brain Mapping lobar templates (Laboratory of Neuroimaging, Keck School of Medicine, Los Angeles, California) and MRIcro Brodmann templates (Neuropsychology Laboratory, Columbia, South Carolina) were registered to Montreal Neurological Institute 152 space using the normalize function in SPM. Structural T1-weighted images and associated lesional ROIs and lobar templates were coregistered to the EPI DSC pregadolinium images with linear registration (FMRIB Linear Image Registration Tool, FLIRT; https://fsl.fmrib.ox.ac.uk/fsl/fslwiki/FLIRT) and nonlinear intensity modulation and multiresolution, nonlinear registration with 4 subsampling levels (FMRIB Nonlinear Registration Tool, FNIRT; http://fsl.fmrib.ox.ac.uk/fsl/fslwiki/FNIRT). Global and lobar cGM and WM volumetric and perfusion metrics were then quantified separately for bilateral frontal, parietal, temporal, and occipital lobes, as previously described.[18]

Statistical Analysis

Demographic, clinical, volumetric, and perfusion data were summarized for HCs and patients with RRMS, and SPMS using the mean and SD for continuous variables and proportions for categoric variables. To compare RRMS versus HC, SPMS versus HC, and SPMS versus RRMS for demographic variables (ie, age, sex, educational years, disease duration, and EDSS), we used the univariate logistic regression model. Significant confounding factors were determined and used for perfusion data analysis. A Bonferroni-corrected P value < .017 (.05/3) was considered statistically significant for controlling for multiple comparisons among the 3 groups. To compare HC, RRMS, and SPMS cohort differences for the imaging parameter covariates (ie, CBF, CBV, MTT, lobar GM, and WM volume), we used a generalized linear model with a logit link function after adjusting for confounding factors. The GENMOD procedure in Statistical Analysis Software (SAS, Version 9.4 for Windows; SAS Institute, Cary, North Carolina) was performed to fit the model, with a Bonferroni-adjusted P value < .017 considered statistically significant. Confounding factors of age, disease duration, and EDSS were assessed for multicollinearity by examining tolerance and variance inflation factors (1/tolerance) in a regression model using SPSS (IBM, Armonk, New York). A tolerance value of <0.1 and a variance inflation factor of >10 were regarded as indicating multicollinearity. Normality was determined with the Shapiro-Wilk test, and anomalous dependent variables were log-transformed to fit the data to a normal distribution. Natural log-transformation was applied as appropriate for normalizing the distributions. A general linear regression was implemented to assess the association between GM and WM regional perfusion data, between GM and T2h-l regional perfusion data, between WM and T2h-l regional perfusion data, and between lobar GM and lobar WM volume data while considering confounding factors and expressed as R^2.

RESULTS

Clinical Characteristics, Global Volumes, and Perfusion

The MS subgroups did not significantly differ in sex, disease duration, and years of education, though the SPMS cohort was older (P = .0041) and had higher EDSS (P = .0006) scores than the RRMS cohort (Table 1). Patients with SPMS demonstrated a longer disease duration, but this did not reach statistical significance (P = .02). The SPMS cohort had greater global atrophy in cGM and WM compared with the RRMS group and HC subjects (P = .002, P = .0026 and P = .0049, and P = .0011, respectively; Table 2). Those with RRMS exhibited lower global WM (P = .0115) but not GM volume compared with HCs. GM and WM CBF and CBV were reduced and MTT was prolonged in subjects with SPMS compared with those with RRMS. GM CBF reduction and MTT prolongation were present in RRMS and SPMS compared with HCs. No significant WM CBF or CBV difference was observed for any RRMS/SPMS comparison with HCs. WM MTT was significantly prolonged for those with SPMS versus HCs. No significant T2h-l volume, CBF, or MTT differences were seen between patients with RRMS and those with SPMS, though patients with SPMS had higher T2h-l CBV than those with RRMS.

Lobar Volumetric Group Comparisons

Patients with SPMS had reduced cGM volumes in the temporal and occipital lobes and reduced WM volumes in the occipital lobe compared with those with RRMS (Table 3). Patients with SPMS also demonstrated reduced occipital lobe WM and temporal and occipital cGM compared with HCs. Frontal and parietal lobe WM volume reduction was observed for all comparisons, and patients with RRMS also demonstrated a reduced temporal WM volume compared with HCs. Overall, a weak association was present between lobar cGM and lobar NAWM volume (On-line Table and On-line Fig 1) in patients with both RRMS (R^2 0.14–0.65) and SPMS (R^2 = 0.16–0.62), with no statistical significance achieved for any lobar region. Association was stronger in HCs (R^2 = 0.53–0.79).

Lobar Perfusion Group Comparisons

The distribution of significant lobar cortical perfusion differences between group comparisons is demonstrated in the Figure. Lobar cGM CBF reduction and MTT increase were present in all lobes in

Table 2: Comparison of perfusion and volumetric data for cGM, NAWM, and T2h-l between HCs and subjects with RRMS and SPMS after adjusting for confounding factors[a]

Parameter	Median (Interquartiles)			*P* Value		
	HC (*n* = 19)	RRMS (*n* = 19)	SPMS (*n* = 20)	RRMS vs HC	SPMS vs HC	SPMS vs RRMS
cGM						
Global volume	890 (869–914)	864 (827–895)	673 (646–697)	.10	.0026[b]	.0020[b]
CBF	43.20 (33.91–54.49)	41.07 (29.85–55.68)	34.05 (27.19–43.68)	<.0001[b]	<.0001[b]	.0011[b]
CBV	2.64 (2.02–3.29)	2.53 (1.94–3.37)	2.40 (1.92–3.07)	.078	.046	.0062[b]
MTT	3.77 (3.20–4.31)	3.90 (3.32–4.41)	4.30 (3.66–4.99)	.0001[b]	<.0001[b]	<.0001[b]
NAWM						
Global volume	878 (812–894)	818 (738–850)	697 (669–729)	.0115[b]	.0011[b]	.0049[b]
CBF	23.49 (18.69–27.78)	21.55 (16.05–29.50)	19.54 (16.74–24.92)	.68	.58	.0080[b]
CBV	1.59 (1.28–2.00)	1.57 (1.17–2.15)	1.51 (1.30–1.98)	.89	.16	.0103[b]
MTT	4.51 (4.09–5.10)	4.62 (4.08–5.20)	4.86 (4.28–5.41)	.25	.0005[b]	.0094[b]
T2h-l						
Global volume	0.00	5.4 (1.2–9.3)	6.4 (1.0–10.9)	NA	NA	.82
CBF	0.00	12.77 (8.23–17.24)	11.15 (8.95–15.71)	NA	NA	.049
CBV	0.00	0.99 (0–1.32)	1.08 (0.83–1.47)	NA	NA	.0026[b]
MTT	0.00	4.91 (4.00–5.63)	5.64 (4.82–6.30)	NA	NA	.43

Note:—NA, not applicable.

[a] Bonferroni-corrected $P < .017$ is considered statistically significant. Age was considered a confounding factor for comparing RRMS vs HC and SPMS vs HC; age, EDSS, and disease duration were considered confounding factors for comparing SPMS vs RRMS. All volumes are in cubic centimeters; CBF, milliliter/100 gram/meter; CBV, milliliter/100 gram; MTT, second.

[b] Significant.

Table 3: Lobar GM and WM volume differences among HCs and subjects with RRMS and SPMS after adjusting for confounding factors[a]

Parameter	Median (Interquartiles)			*P* Value		
	HC (*n* = 19)	RRMS (*n* = 19)	SPMS (*n* = 19)	RRMS vs HC (*n* = 19)	SPMS vs HC (*n* = 19)	SPMS vs RRMS (*n* = 19)
Gray matter						
Frontal lobe	200.040 (190.352–167.944)	199.248 (192.480–207.896)	200.352 (193.500–207.540)	.69	.60	.22
Parietal lobe	90.296 (83.992–94.512)	89.824 (85.048–95.176)	93.368 (88.956–96.352)	.72	.03	.095
Temporal lobe	122.740 (110.640–130.560)	121.336 (114.672–128.544)	106.892 (99.432–112.928)	.86	.0044[b]	.0073[b]
Occipital lobe	101.088 (98.536–106.272)	97.160 (95.728–102.960)	72.792 (69.868–75.196)	.10	.0030[b]	.0033[b]
White matter						
Frontal lobe	190.568 (170.368–201.528)	170.316 (159.520–189.112)	146.260 (134.908–157.136)	<.0001[b]	.0006[b]	<.0001[b]
Parietal lobe	101.200 (94.536–109.152)	93.272 (84.944–97.208)	81.952 (77.736–87.532)	.0001[b]	.0018[b]	<.0001[b]
Temporal lobe	70.132 (56.648–79.352)	68.512 (64.116–74.016)	61.208 (51.576–71.720)	.026	.98	.0026[b]
Occipital lobe	32.024 (30.248–35.092)	29.092 (24.136–33.768)	26.864 (23.552–31.832)	.65	.0098[b]	.0003[b]

[a] Bonferroni-corrected $P < .017$ is considered statistically significant. Age was considered a confounding factor for comparing RRMS vs HC and SPMS vs HC; age, EDSS, and disease duration were considered confounding factors for comparing SPMS vs RRMS. All volumes are in cubic centimeters.

[b] Significant.

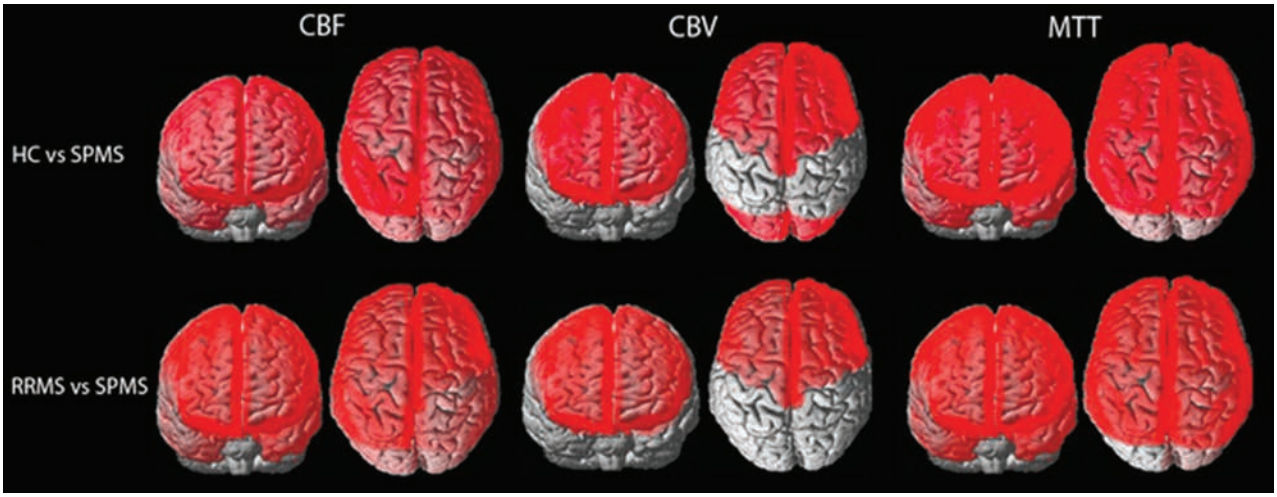

FIGURE. Whole-brain depiction of perfusion differences in cortical gray matter among HCs and patients with RRMS and SPMS. Units for CBF are milliliter/100 gram/minute; CBV, milliliter/100 gram; MTT, second.

patients with SPMS compared with the other groups, except for MTT increase within the left occipital lobe for the SPMS versus RRMS comparison, which did not reach statistical significance. Lobar cGM CBV reduction was present in the bilateral frontal lobes of patients with SPMS compared with the other groups and in the bilateral occipital lobes of SPMS versus HCs. No significant lobar cGM CBF, CBV reduction, or MTT prolongation was found between subjects with RRMS and HCs. No significant lobar perfusion differences were observed between any group comparison for NAWM. A strong association was shown between cGM and NAWM global and lobar perfusion for all group comparisons and lobes ($R^2 = 0.77–0.98$, $P < .0001$; On-line Table and On-line Fig 2). Overall, patients with SPMS demonstrated stronger associations between lobar T2h-l and cGM and NAWM perfusion compared with those with RRMS (On-line Table and On-line Figs 3 and 4; cGM CBF, $R^2 = 0.31–0.77$; NAWM CBF, $R^2 = 0.35–0.85$ versus cGM CBF, $R^2 = 0.07–0.61$; and NAWM CBF, $R^2 = 0.06–0.69$, respectively).

Associations between Perfusion and Volumetric Data

No significant associations were found between perfusion and volumetric data in any regression analysis (ie, for cGM, T2h-l, or NAWM).

DISCUSSION

We demonstrated a weak association between lobar volumes of cGM and NAWM in patients with MS despite cGM and NAWM volume reduction with increasing disease severity. Similarly, although lobar NAWM and cGM perfusion were highly correlated, the distribution of lobar cGM perfusion reduction was distinct from that of underlying lobar NAWM perfusion, which showed no significant between-group differences. These results do not conflict with the notion that the pathophysiology of WM and cGM disease may occur independently and that the strength of association varies relative to the disease severity. The strong association between cGM and NAWM perfusion and the lack of association with volumetric measures suggest a potential role for perfusion as an independent surrogate of disease activity.

Weak associations between NAWM volume and GM volume and perfusion in the present study argue against a mechanism of secondary cGM anterograde or retrograde axonal degeneration and suggest independent pathophysiologic processes acting on WM and GM. This assertion is supported by various pathologic and imaging studies,[8,19-21] which have shown that cGM lesions may develop before the appearance of WM plaques[19] and arise independent of and are poorly correlated with T2h-l formation.[20,21] A number of pathologic and imaging articles have increasingly implicated an independent etiology for cGM lesion formation attributed to either the direct presence of meningeal-derived neurotoxic substances or secondary microglial activation mediated through meningeal/subpial inflammation and manifest as a gradient of demyelination centered on the subpial cortex.[21,22]

Numerous articles have examined the spatial relationship between lobar T2h-l and cGM integrity using quantitative and functional parameters other than perfusion. A recent correlative study of quantitative cortical T2* at 7T- and 3T-derived surface- and tract-based analyses found a correlation between WM tract DTI and cGM integrity, though this was not spatially specific, reflecting a common sensitivity to MS pathologic changes.[8] Steenwijk et al[9] used DTI at 3T to investigate the association between regional GM atrophy and pathology in anatomically connected WM tracts in patients with RRMS, SPMS, and primary-progressive MS, demonstrating a relationship between NAWM tract fractional anisotropy and deep GM and cGM. The model of variance associated with cGM thickness was greatest in patients with RRMS but declined in those with SPMS and primary-progressive MS. A strong association between NAWM integrity and cGM thickness was found only in the mildly impaired group when patients were dichotomized by EDSS category 4. The authors concluded that NAWM integrity contributes to cGM atrophy only in early MS. Bodini et al[4] used Tract-Based Spatial Statistics (TBSS; https://fsl.fmrib.ox.ac.uk/fsl/fslwiki/TBSS) to explore the relationship between cGM atrophy and fractional anisotropy in connected NAWM tracts in patients with primary-progressive MS and found that only 4/11 regions studied showed a quantitative association between reduced NAWM fractional anisotropy and GM atrophy.

Jehna et al[5] found spatial interdependence among focal cortical volumes, lesion location, and probabilistic fiber pathways, suggesting that WM tracts and cGM volume are regionally dependent and injured due to similar disease processes, suggesting that lesional axonal transaction[23] leads to Wallerian degeneration and retrograde GM atrophy. Their study was performed in "low disabled" individuals with significantly lower ages (29.5 years) and disease duration (7.3 years) compared with the present cohort. In contradistinction, we did not demonstrate a stronger association between NAWM/T2h-l and cGM volume or perfusion with earlier disease, likely explained by longer disease duration and older age in our RRMS group compared with the cohort of Jehna et al and the different functional techniques used. The near-universally stronger cGM and NAWM perfusion association and deteriorating perfusion metrics with disease progression also confirmed in prior studies[12,14,16,22,24] suggest that perfusion is sensitive to a common pathophysiologic mechanism reflecting concomitant but not necessarily codependent cGM and WM pathology in MS. Findings are supported by a recently reported DTI study,[8] suggesting that perfusion could serve as a useful surrogate of disease activity in addition to routine structural imaging.

Limitations of the study are the lobar rather than functional domain approach adopted to examine associations among NAWM, T2h-l, and cGM. This could result in functionally unrelated regions being included in the lobar cGM assessed. However, a lobar approach was previously used in a recent publication showing that the presence of juxtacortical T2h-l may affect the degree of lobar cortical thinning.[25] Alternative approaches assessing the association between large-scale functional brain networks and cGM integrity may provide greater insight into the volumetric and functional spatial relationship and the effect on cognition.[26] Greater insight into the association among NAWM, T2h-l, and cGM may be illustrated by a longitudinal rather than a cross-sectional study design, therefore representing a limitation of the present study. Last, the small sample size is relatively modest, limiting generalizability to a broader population of patients with

MS. Despite these sample size limitations, we could demonstrate important differences in associations between volumetric and perfusion variables.

CONCLUSIONS

The weak spatial association between WM disease and cGM atrophy does not conflict with the notion of an independent pathophysiology of WM and cGM disease. Perfusion reduction with disease severity, particularly in cGM, suggests that perfusion is sensitive to the pathophysiologic mechanism of MS disease severity and may be a useful surrogate of cortical disease progression.

Disclosures: Seyed-Parsa Hojjat—*RELATED*: *Grant*: Biogen fellowship funding award. Timothy J. Carroll—*RELATED*: *Grant*: National Institutes of Health (1R21EB017928–01A1). Charles G. Cantrell—*RELATED*: *Grant*: American Heart Association (14PRE20380310). Richard I. Aviv—*RELATED*: *Grant*: Canadian Institutes of Health Research (130366), Biogen fellowship funding award.

REFERENCES

1. Rashid W, Parkes LM, Ingle GT, et al. **Abnormalities of cerebral perfusion in multiple sclerosis.** *J Neurol Neurosurg Psychiatry* 2004; 75:1288–93 CrossRef Medline
2. De Keyser J, Steen C, Mostert JP, et al. **Hypoperfusion of the cerebral white matter in multiple sclerosis: possible mechanisms and pathophysiological significance.** *J Cereb Blood Flow Metab* 2008; 28:1645–51 CrossRef Medline
3. Sun X, Tanaka M, Kondo S, et al. **Clinical significance of reduced cerebral metabolism in multiple sclerosis: a combined PET and MRI study.** *Ann Nucl Med* 1998;12:89–94 CrossRef Medline
4. Bodini B, Khaleeli Z, Cercignani M, et al. **Exploring the relationship between white matter and gray matter damage in early primary progressive multiple sclerosis: an in vivo study with TBSS and VBM.** *Hum Brain Map* 2009;30:2852–61 CrossRef Medline
5. Jehna M, Langkammer C, Khalil M, et al. **An exploratory study on the spatial relationship between regional cortical volume changes and white matter integrity in multiple sclerosis.** *Brain Connect* 2013; 3:255–64 CrossRef Medline
6. Calabrese M, Gallo P. **Magnetic resonance evidence of cortical onset of multiple sclerosis.** *Mult Scler* 2009;15:933–41 CrossRef Medline
7. Fisher E, Lee JC, Nakamura K, et al. **Gray matter atrophy in multiple sclerosis: a longitudinal study.** *Ann Neurol* 2008;64:255–65 CrossRef Medline
8. Louapre C, Govindarajan ST, Gianni C, et al. **Is the relationship between cortical and white matter pathologic changes in multiple sclerosis spatially specific? A multimodal 7-T and 3-T MR imaging study with surface and tract-based analysis.** *Radiology* 2016;278: 524–35 CrossRef Medline
9. Steenwijk MD, Daams M, Pouwels PJ, et al. **Unraveling the relationship between regional gray matter atrophy and pathology in connected white matter tracts in long-standing multiple sclerosis.** *Hum Brain Map* 2015;36:1796–807 CrossRef Medline
10. Mainero C, Louapre C, Govindarajan ST, et al. **A gradient in cortical pathology in multiple sclerosis by in vivo quantitative 7 T imaging.** *Brain* 2015;138:932–45 CrossRef Medline
11. Klaver R, De Vries HE, Schenk GJ, et al. **Grey matter damage in multiple sclerosis: a pathology perspective.** *Prion* 2013;7:66–75 CrossRef Medline
12. Aviv RI, Francis PL, Tenenbein R, et al. **Decreased frontal lobe gray matter perfusion in cognitively impaired patients with secondary-progressive multiple sclerosis detected by the bookend technique.** *AJNR Am J Neuroradiol* 2012;33:1779–85 CrossRef Medline
13. Peruzzo D, Castellaro M, Calabrese M, et al. **Heterogeneity of cortical lesions in multiple sclerosis: an MRI perfusion study.** *J Cereb Blood Flow Metab* 2013;33:457–63 CrossRef Medline
14. Debernard L, Melzer TR, Van Stockum S, et al. **Reduced grey matter perfusion without volume loss in early relapsing-remitting multiple sclerosis.** *J Neurol Neurosurg Psychiatry* 2014;85:544–51 CrossRef Medline
15. Hojjat SP, Cantrell CG, Vitorino R, et al. **Regional reduction in cortical blood flow among cognitively impaired adults with relapsing-remitting multiple sclerosis patients.** *Mult Scler* 2016;11:1421–28 CrossRef Medline
16. Hojjat SP, Cantrell CG, Carroll TJ, et al. **Perfusion reduction in the absence of structural differences in cognitively impaired versus unimpaired RRMS patients.** *Mult Scler* 2016;22:1685–94 CrossRef Medline
17. Vakil P, Lee JJ, Mouannes-Srour JJ, et al. **Cerebrovascular occlusive disease: quantitative cerebral blood flow using dynamic susceptibility contrast MR imaging correlates with quantitative H2[150] PET.** *Radiology* 2013;266:879–86 CrossRef Medline
18. Shah MK, Shin W, Parikh VS, et al. **Quantitative MR perfusion imaging: preliminary results in stroke.** *J Magn Reson Imaging* 2010; 32:796–802 CrossRef Medline
19. Popescu BF, Lucchinetti CF. **Meningeal and cortical grey matter pathology in multiple sclerosis.** *BMC Neurol* 2012;12:1l1 CrossRef Medline
20. Bö L, Geurts JJ, van der Valk P, et al. **Lack of correlation between cortical demyelination and white matter pathologic changes in multiple sclerosis.** *Arch Neurol* 2007;64:76–80 CrossRef Medline
21. Sethi V, Yousry T, Muhlert N, et al. **A longitudinal study of cortical grey matter lesion subtypes in relapse-onset multiple sclerosis.** *J Neurol Neurosurg Psychiatry* 2016;87:750–53 CrossRef Medline
22. Francis PL, Jakubovic R, O'Connor P, et al. **Robust perfusion deficits in cognitively impaired patients with secondary-progressive multiple sclerosis.** *AJNR Am J Neuroradiol* 2013;34: 62–67 CrossRef Medline
23. Trapp BD, Peterson J, Ransohoff RM, et al. **Axonal transection in the lesions of multiple sclerosis.** *N Engl J Med* 1998;338:278–85 CrossRef Medline
24. Francis PL, Chia TL, Jakubovic R, et al. **Extensive white matter dysfunction in cognitively impaired patients with secondary-progressive multiple sclerosis.** *AJNR Am J Neuroradiol* 2014;35:1910–15 CrossRef Medline
25. Pareto D, Sastre-Garriga J, Auger C, et al. **Juxtacortical lesions and cortical thinning in multiple sclerosis.** *AJNR Am J Neuroradiol* 2015; 36:2270–76 CrossRef Medline
26. Gläscher J, Rudrauf D, Colom R, et al. **Distributed neural system for general intelligence revealed by lesion mapping.** *Proc Natl Acad Sci U S A* 2010;107:4705–09 CrossRef Medline

Association of Developmental Venous Anomalies with Demyelinating Lesions in Patients with Multiple Sclerosis

D.M. Rogers, M.E. Peckham, L.M. Shah, and R.H. Wiggins III

ABSTRACT

SUMMARY: We present 5 cases of demyelination in patients diagnosed with multiple sclerosis that are closely associated with a developmental venous anomaly. Although the presence of a central vein is a known phenomenon with multiple sclerosis plaques, demyelination occurring around developmental venous anomalies is an underreported phenomenon. Tumefactive demyelination can cause a diagnostic dilemma because of its overlapping imaging findings with central nervous system neoplasm. The relationship of a tumefactive plaque with a central vein can be diagnostically useful, and we suggest that if such a lesion is closely associated with a developmental venous anomaly, an inflammatory or demyelinating etiology should be a leading consideration.

ABBREVIATION: DVA = developmental venous anomaly

The perivenular nature of demyelinating plaques in multiple sclerosis has been observed in many studies, with the earliest mention of this relationship found in an 1863 autopsy specimen.[1,2] The central veins within demyelinating lesions are not usually perceived on conventional T2 and FLAIR MR imaging sequences, but inferred anatomically; a classic example of this is the demyelination occurring along callosal-septal medullary veins known as "Dawson fingers." Advances in MR techniques, such as 3T FLAIR*, high-field 7T MR imaging, and susceptibility-weighted imaging, have helped to demonstrate that nearly all multiple sclerosis plaques are oriented along a central vein.[3-5] This has recently led the North American Imaging in Multiple Sclerosis Cooperative to propose that the "central vein sign" has potential diagnostic utility to prospectively diagnose multiple sclerosis.[6] Gaitán et al[7] used dynamic contrast-enhanced 7T MR to show that smaller multiple sclerosis lesions enhance centrifugally, suggesting that these lesions grow outward from this central vein.[7] Recently, Samaraweera et al[8] showed that a central vein can be identified on clinical 3T scanners by using T2* sequences with high echoplanar imaging.

Developmental venous anomalies (DVAs) have been found to be more prevalent in patients with multiple sclerosis.[9] Despite this relationship, there is little research regarding the spatial proximity between DVAs and demyelinating plaques. A single published case report describes a focus of acute demyelination surrounding a DVA in the cerebellum, which was confirmed histologically.[10] Strengthening this association may provide a useful clue in the diagnosis of tumefactive demyelination in the setting of confounding imaging findings.

We present 5 cases of demyelination in patients diagnosed with multiple sclerosis that are closely associated with a DVA.

CASE SERIES

Case 1

A 56-year-old woman with a medical history of hypertension and chronic lymphocytic (Hashimoto) thyroiditis initially presented with left-sided facial numbness, word-finding difficulty, and ataxia. Contrast-enhanced MR imaging demonstrated enhancing lesions within the left middle cerebellar peduncle and right cerebellum. The right cerebellar lesion was closely associated with a large DVA (Fig 1). Follow-up MR imaging 1 month later showed enlargement of these lesions, along with a new enhancing lesion in the left pons.

The initial differential diagnoses included acute demyelination and metastatic disease from an unknown primary malignancy. A CT of chest/abdomen/pelvis in search of a source of malignancy was negative, as was a lumbar puncture for malignant cells and oligoclonal bands. MR imaging perfusion examination demonstrated decreased K^{trans}, increased Ve, and decreased Vp within these lesions, consistent with increased permeability, decreased cellularity, and decreased vascularity, respectively.

Received May 20, 2017; accepted after revision July 12.

From the Department of Radiology and Imaging Science, University of Utah Medical Center, Salt Lake City, Utah.

Please address correspondence to Douglas M. Rogers, MD, 1861 South 1500 East, Salt Lake City, UT 84105; e-mail: Douglas.rogers@hsc.utah.edu

http://dx.doi.org/10.3174/ajnr.A5374

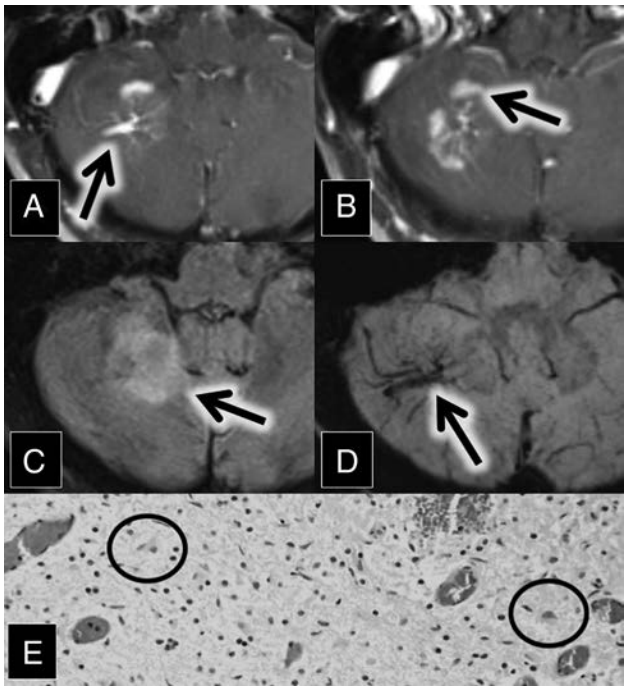

FIG 1. *A* and *B*, Axial contrast-enhanced and fat-saturated MR imaging show a right cerebellar DVA (*A*, *arrow*) surrounded by patchy parenchymal enhancement (*B*, *arrow*). *C*, Axial FLAIR MR imaging shows corresponding hyperintense lesion in the right cerebellum (*arrow*). *D*, Axial susceptibility-weighted imaging maximum intensity projection shows a large right cerebellar DVA (*arrow*). *E*, H&E staining 20× shows moderately hypercellular cerebellar white matter with infiltrating macrophages (*circled*). In addition, immunohistochemical staining demonstrated intact neurofilament and positive CD68 histiocytes, and Luxol fast blue stain showed myelin loss (*not pictured*).

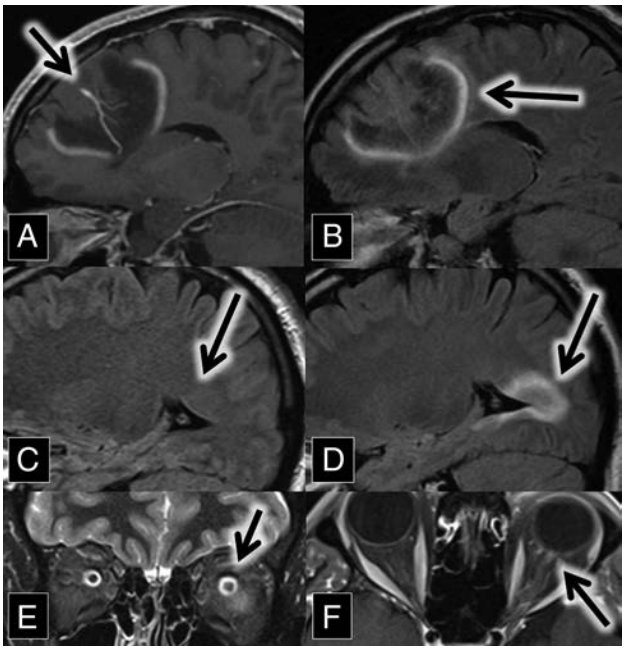

FIG 2. *A* and *B*, Sagittal contrast-enhanced T1 and FLAIR MR images show a large left frontal lobe DVA (*A*, *arrow*) surrounded by a lesion with discontinuous leading-edge enhancement (*B*, *arrow*), typical for tumefactive demyelination. *C* and *D*, Sagittal FLAIR MR images at the same anatomic location with a 15-month interval show the development of a demyelinating plaque adjacent to the occipital horn of the right lateral ventricle (*arrows*). *E*, Coronal T2 with fat-saturation MR imaging shows left optic nerve hyperintensity (*arrow*). The patient presented with optic neuritis 15 months before imaging in *A* and *B*. *F*, Axial contrast-enhanced T1 with fat saturation MR imaging shows left optic nerve enhancement (*arrow*) in the setting of optic neuritis.

Taken together, the findings were consistent with acute demyelination, and this was dictated and verbally reported to the referring neurosurgeons. Persistent clinical uncertainty led to an excisional biopsy of the right cerebellar lesion. Demyelination was histologically confirmed (Fig 1). Imaging performed 3 months postoperatively demonstrated decreased size and enhancement of the pontine and left middle cerebellar peduncle lesions. A year later, her facial numbness and ataxia resolved, and she subsequently developed increased fatigue and lack of concentration. Based on the imaging and the pathologic findings, the patient was diagnosed by her neurologist with multiple sclerosis and has not had a relapse while on fingolimod therapy.

Case 2

A 37-year-old man with a medical history of transverse myelitis presented with gradually increasing blurry vision of his left eye, which was mildly painful. MR imaging and ophthalmologic examination were consistent with left optic neuritis (Fig 2).

After treatment with steroids, the patient improved. He did not tolerate treatment with natalizumab because of an allergic reaction, so he was started on dimethyl fumarate. He returned 15 months later with left homonymous hemianopsia and right visual field constriction. MR imaging at this time demonstrated left frontal, left parietal, and right temporal lesions with discontinuous leading-edge enhancement, typical for acute tumefactive demyelination. Postcontrast images demonstrated that the left frontal lobe lesion was centered on a large DVA (Fig 2). Spectroscopy was obtained, which showed elevated choline and decreased *N*-acetyl aspartate, suggestive of active cell membrane turnover with underlying neuronal loss.

The patient was treated with methylprednisolone, leading to improvement of his vision to near baseline. Given the pathognomonic brain lesions with peripheral discontinuous enhancement, along with the preceding history of optic neuritis and transverse myelitis, a neurologist diagnosed the patient with relapsing-remitting multiple sclerosis.

Case 3

A 46-year-old man with a history of relapsing-remitting multiple sclerosis, renal stones, and gastric ulcers related to *Helicobacter pylori* infection presented for routine follow-up. MR imaging from 2 years prior demonstrated multiple white matter and spinal cord FLAIR hyperintense lesions, predominantly in a callosal and pericallosal distribution typical of multiple sclerosis. A new enhancing lesion was present in the left middle cerebellar peduncle, closely associated with a left cerebellar DVA (Fig 3). The T2 sequence demonstrated the central vein sign. The enhancement of this lesion was no longer present on the follow-up MR imaging 2 years later.

The patient had multiple relapses over several years, with tran-

sient symptoms including vertical diplopia, ataxia, and, most recently, left-sided extremity numbness. Despite this, he remains physically active. He continues to be followed by a neurologist and has avoided an exacerbation over the past 5 years on dimethyl fumarate therapy.

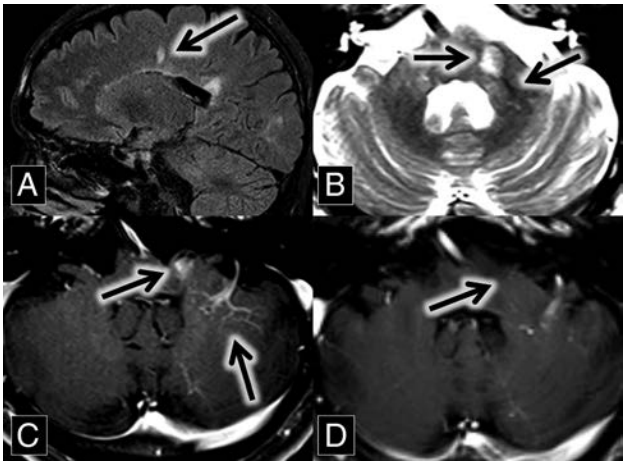

FIG 3. *A*, Sagittal FLAIR MR imaging shows multiple hyperintense callosal and pericallosal multiple sclerosis plaques (Dawson fingers; *arrow*) *B*, Axial T2 MR imaging shows a hyperintense left middle cerebellar peduncle lesion (*midline arrow*) associated with a flow void (central vein sign; *left lateral arrow*), which extends from the DVA better demonstrated in image *C*. *C* and *D*, Axial contrast-enhanced T1 MR images show an enhancing left middle cerebellar peduncle lesion (*midline arrow*) closely associated with a left cerebellar DVA (*left lateral arrow*). This enhancement was resolved on the follow-up scan at the same anatomic level 2 years later (*D*, *arrow*).

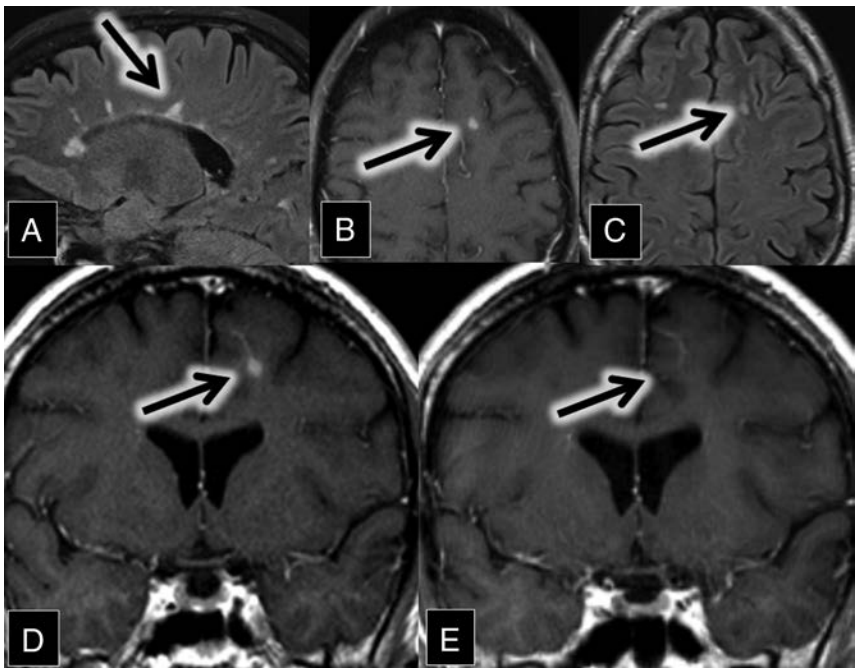

FIG 4. *A*, Sagittal FLAIR MR imaging shows multiple hyperintense callosal and pericallosal multiple sclerosis plaques (consistent with Dawson fingers; *arrow*). *B*, Axial contrast-enhanced T1 and *C*, FLAIR MR images show a FLAIR hyperintense (*C*, *arrow*) and enhancing (*B*, *arrow*) lesion in the left frontal lobe. *D* and *E*, Coronal contrast-enhanced T1 MR images show an enhancing left frontal lobe lesion (*D*, *arrow*) closely associated with a DVA. This enhancement was resolved on the follow-up scan 9 months later (*E*, *arrow*).

Case 4

A 47-year-old man with relapsing-remitting multiple sclerosis presented for evaluation of new diplopia secondary to internuclear ophthalmoplegia. MR imaging demonstrated numerous white matter and spinal cord FLAIR and T2 hyperintense lesions in a pattern typical of multiple sclerosis. A review of his imaging from 7 years prior showed an interim development of a new enhancing demyelinating lesion closely associated with a left frontal lobe DVA (Fig 4). The enhancement resolved on the follow-up MR imaging 9 months later.

A neurologist initially diagnosed him with multiple sclerosis in his early 20s after recurrent episodes of optic neuritis. Since then, he had multiple relapses, with symptoms dominated by progressive gait difficulty and spasticity, neuropathic pain, and depression. The patient continues to be followed by a neurologist and is currently being treated with rituximab.

Case 5

A 27-year-old woman with relapsing-remitting multiple sclerosis presented for routine follow-up. MR imaging demonstrated multiple subcortical and periventricular FLAIR hyperintense lesions, including callosal and pericallosal plaques typical of multiple sclerosis. A comparison of axial FLAIR and T1 contrast-enhanced images demonstrated a grouping of FLAIR hyperintense lesions around a right parietal DVA. These lesions were new compared with MR imaging from 8 months prior, most consistent with new demyelinating lesions (Fig 5).

The patient had no motor or sensory deficits, but she struggled with symptoms of chronic fatigue and cognitive dysfunction, with occasional word-finding difficulty. She continues to be followed by a neurologist and treated with maintenance therapy of interferon β-1a.

DISCUSSION

The relationship of demyelination and DVAs is underreported, despite the presence of a central vein as a known phenomenon with multiple sclerosis plaques. This may be due in part to limitations of conventional imaging because both abnormalities may not be apparent together on the same standard MR imaging sequence. DVAs are easily seen on contrast-enhanced images, whereas multiple sclerosis plaques are best seen on T2 and FLAIR sequences. Occasionally, demyelination is enhancing in its acute phase, allowing the association with a DVA to be demonstrated on contrast-enhanced images (as shown in cases 1–4). Sometimes, a DVA may be large enough that the flow void is clearly identified within the plaque on a T2 sequence. Although advanced MR imaging sequences such as 3T FLAIR* and high-field 7T MR imaging can improve the detection of the central vein in demyelinating plaques, the central vein

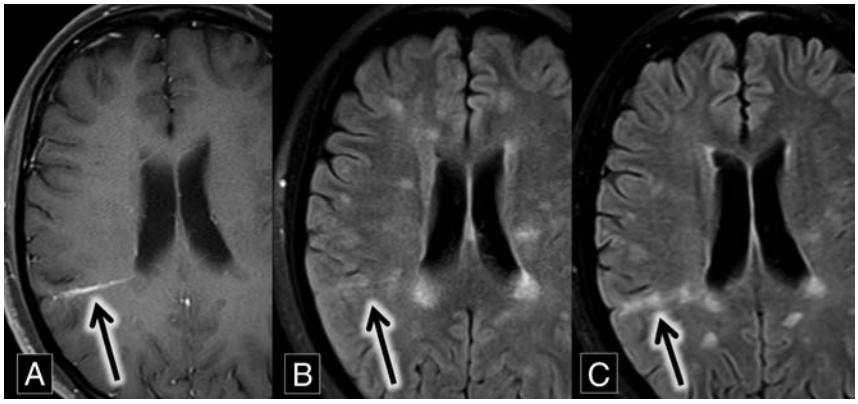

FIG 5. *A*, Axial contrast-enhanced T1 MR imaging shows a right parietal lobe DVA (*arrow*). *B* and *C*, Axial FLAIR MR images over an 8-month interval show development of right parietal lobe hyperintense plaques (*B* and *C*, *arrows*) oriented along the course of the DVA demonstrated in *A*.

can also be identified on clinical 3T scanners by using T2* sequences with high echo-planar imaging.[8] It should be acknowledged that although MR imaging is a useful tool in expediting the diagnosis of multiple sclerosis by demonstrating the dissemination of lesions in space and time, clinical criteria remain the criterion standard for diagnosis.[11]

Tumefactive demyelination can cause a diagnostic dilemma because of its overlapping imaging findings with central nervous system neoplasm. The relationship of a tumefactive plaque with a central vein can be diagnostically useful,[3-6,8,12-15] and we suggest that if such a lesion is closely associated with a DVA, an inflammatory or demyelinating etiology should be a leading consideration. In addition to correlation with other clinical and imaging clues, further evaluation with MR imaging perfusion and MR imaging spectroscopy can also aid in the diagnosis in such cases, distinguishing neoplastic from non-neoplastic lesions, thereby avoiding biopsy.[16] Biopsy in the presence of a DVA will carry an additional risk of infarction and/or hemorrhage beyond the surgical margin because the DVA may represent the sole venous outflow to adjacent normal brain parenchyma.[17-19] Another noninvasive strategy is short-term imaging follow-up because the enhancement of a demyelinating lesion should decrease and/or resolve over time.

The predisposition for demyelination to occur around normally distributed cerebral veins is well-known,[6] and we hypothesize that the medusa-like DVA may actually create an even more compelling milieu for this process to occur. Once thought to be benign and incidental findings, recent studies show that brain tissue surrounding DVAs is abnormal in most cases. A comparison of MR imaging and PET in patients with DVAs demonstrated surrounding hypometabolism in 75% of cases.[20] On MR imaging perfusion, MTT and TTP are prolonged around most DVAs, suggestive of venous congestion in these regions.[21]

The pathophysiology and histopathology of multiple sclerosis plaques is characterized by lymphocytes and monocytes crossing the blood-brain barrier via venous channels, causing perivenular cuffing in active lesions.[22,23] These lymphocytes interact with autoantigens such as myelin basic protein, leading to a local inflammatory response and subsequent demyelination.[6,24,25] We hypothesize that the rate and/or amount of lymphocytic infiltration may be accelerated in the setting of impaired venous drainage by a DVA. Further investigation is required to determine whether the demonstrated parenchymal abnormalities around DVAs increase the propensity to develop demyelination around these typically benign vascular lesions in the setting of multiple sclerosis.

CONCLUSIONS

Demyelination surrounding DVAs is an underreported and potentially dangerously unrecognized phenomenon. Tumefactive demyelination may be difficult to differentiate from central nervous system neoplasm on imaging, and an association of the demyelinating lesion with a DVA should instigate further noninvasive testing such as MR perfusion imaging in an attempt to avoid biopsy and possible associated complications. The presented cases support the perivenular nature of multiple sclerosis.

REFERENCES

1. Rindfleisch E. **Histologisches Detail zu der grauen Degeneration von Gehirn und Rückenmark. (Zugleich ein Beitrag zu der Lehre von der Entstehung und Verwandlung der Zelle.)** *Archiv für pathologische Anatomie und Physiologie und für klinische Medicin* 1863;26:474–83 CrossRef
2. Rae-Grant AD, Wong C, Bernatowicz R, et al. **Observations on the brain vasculature in multiple sclerosis: a historical perspective.** *Mult Scler Relat Disord* 2014;3:156–62 CrossRef Medline
3. Solomon AJ, Schindler MK, Howard DB, et al. **"Central vessel sign" on 3T FLAIR* MRI for the differentiation of multiple sclerosis from migraine.** *Ann Clin Transl Neurol* 2016;3:82–87 CrossRef Medline
4. Mistry N, Abdel-Fahim R, Samaraweera A, et al. **Imaging central veins in brain lesions with 3-T T2*-weighted magnetic resonance imaging differentiates multiple sclerosis from microangiopathic brain lesions.** *Mult Scler* 2016;22:1289–96 CrossRef Medline
5. Tallantyre EC, Brookes MJ, Dixon JE, et al. **Demonstrating the perivascular distribution of MS lesions in vivo with 7-Tesla MRI.** *Neurology* 2008;70:2076–78 CrossRef Medline
6. Sati P, Oh J, Constable RT, et al. **The central vein sign and its clinical evaluation for the diagnosis of multiple sclerosis: a consensus statement from the North American Imaging in Multiple Sclerosis Cooperative.** *Nat Rev Neurol* 2016;12:714–22 CrossRef Medline
7. Gaitán MI, Sati P, Inati SJ, et al. **Initial investigation of the blood-brain barrier in MS lesions at 7 Tesla.** *Mult Scler* 2013;19:1068–73 CrossRef Medline
8. Samaraweera AP, Clarke MA, Whitehead A, et al. **The central vein sign in multiple sclerosis lesions is present irrespective of the T2* sequence at 3 T.** *J Neuroimaging* 2017;27:114–21 CrossRef Medline
9. Zhao G, Li DK, Traboulsee T, et al. **Developmental venous anomalies (venous angiomas) on MRI are more common in patients with multiple sclerosis.** In: *Proceedings of the International Society for Magnetic Resonance in Medicine Twelfth Scientific Meeting*, Kyoto, Japan. May 15–21, 2004
10. Jung G, Schroder R, Lanfermann H, et al. **Evidence of acute demyelination around a developmental venous anomaly: magnetic resonance imaging findings.** *Invest Radiol* 1997;32:575–77 CrossRef Medline
11. Filippi M, Rocca MA, Ciccarelli O, et al. **MRI criteria for the diagnosis of multiple sclerosis: MAGNIMS consensus guidelines.** *Lancet Neurol* 2016;15:292–303 CrossRef Medline
12. Lane JI, Bolster B, Campeau NG, et al. **Characterization of multiple sclerosis plaques using susceptibility-weighted imaging at 1.5 T:**

can perivenular localization improve specificity of imaging criteria? *J Comput Assist Tomogr* 2015;39:317–20 CrossRef Medline
13. Zhang Y, Metz LM. **Dominant perivenular enhancement of tumefactive demyelinating lesions in multiple sclerosis.** *Neurology* 2010; 75:1396 CrossRef Medline
14. Tan IL, van Schijndel RA, Pouwels PJ, et al. **MR venography of multiple sclerosis.** *AJNR Am J Neuroradiol* 2000;21:1039–42 Medline
15. Dal-Bianco A, Hametner S, Grabner G, et al. **Veins in plaques of multiple sclerosis patients–a longitudinal magnetic resonance imaging study at 7 Tesla.** *Eur Radiol* 2015;25:2913–20 CrossRef Medline
16. Hourani R, Brant LJ, Rizk T, et al. **Can proton MR spectroscopic and perfusion imaging differentiate between neoplastic and nonneoplastic brain lesions in adults?** *AJNR Am J Neuroradiol* 2008;29: 366–72 CrossRef Medline
17. Nagatani K, Osada H, Takeuchi S, et al. **Surgical resection of developmental venous anomaly causing massive intracerebral haemorrhage: a case report.** *Br J Neurosurg* 2014;28:116–18 CrossRef Medline
18. Amuluru K, Al-Mufti F, Hannaford S, et al. **Symptomatic infratentorial thrombosed developmental venous anomaly: case report and review of the literature.** *Interv Neurol* 2016;4:130–37 CrossRef Medline
19. Rammos SK, Maina R, Lanzino G. **Developmental venous anomalies: current concepts and implications for management.** *Neurosurgery* 2009;65:20–29; discussion 29–30 CrossRef Medline
20. Larvie M, Timerman D, Thum JA. **Brain metabolic abnormalities associated with developmental venous anomalies.** *AJNR Am J Neuroradiol* 2015;36:475–80 CrossRef Medline
21. Jung HN, Kim ST, Cha J, et al. **Diffusion and perfusion MRI findings of the signal-intensity abnormalities of brain associated with developmental venous anomaly.** *AJNR Am J Neuroradiol* 2014;35: 1539–42 CrossRef Medline
22. Matthews PM, Roncaroli F, Waldman A, et al. **A practical review of the neuropathology and neuroimaging of multiple sclerosis.** *Pract Neurol* 2016;16:279–87 CrossRef Medline
23. Tanaka R, Iwasaki Y, Koprowski H. **Ultrastructural studies of perivascular cuffing cells in multiple sclerosis brain.** *Am J Pathol* 1975;81:467–78 Medline
24. Adams CW. **The onset and progression of the lesion in multiple sclerosis.** *J Neurol Sci* 1975;25:165–82 CrossRef Medline
25. Minagar A, Alexander JS. **Blood-brain barrier disruption in multiple sclerosis.** *Mult Scler* 2003;9:540–49 CrossRef Medline

Time for a Time Window Extension: Insights from Late Presenters in the ESCAPE Trial

J.W. Evans, B.R. Graham, P. Pordeli, F.S. Al-Ajlan, R. Willinsky, W.J. Montanera, J.L. Rempel, A. Shuaib, P. Brennan, D. Williams, D. Roy, A.Y. Poppe, T.G. Jovin, T. Devlin, B.W. Baxter, T. Krings, F.L. Silver, D.F. Frei, C. Fanale, D. Tampieri, J. Teitelbaum, D. Iancu, J. Shankar, P.A. Barber, A.M. Demchuk, M. Goyal, M.D. Hill, and B.K. Menon; for the ESCAPE Trial Investigators

ABSTRACT

BACKGROUND AND PURPOSE: The safety and efficacy of endovascular therapy for large-artery stroke in the extended time window is not yet well-established. We performed a subgroup analysis on subjects enrolled within an extended time window in the Endovascular Treatment for Small Core and Proximal Occlusion Ischemic Stroke (ESCAPE) trial.

MATERIALS AND METHODS: Fifty-nine of 315 subjects (33 in the intervention group and 26 in the control group) were randomized in the ESCAPE trial between 5.5 and 12 hours after last seen healthy (likely to have groin puncture administered 6 hours after that). Treatment effect sizes for all relevant outcomes (90-day mRS shift, mRS 0–2, mRS 0–1, and 24-hour NIHSS scores and intracerebral hemorrhage) were reported using unadjusted and adjusted analyses.

RESULTS: There was no evidence of treatment heterogeneity between subjects in the early and late windows. Treatment effect favoring intervention was seen across all clinical outcomes in the extended time window (absolute risk difference of 19.3% for mRS 0–2 at 90 days). There were more asymptomatic intracerebral hemorrhage events within the intervention arm (48.5% versus 11.5%, $P = .004$) but no difference in symptomatic intracerebral hemorrhage.

CONCLUSIONS: Patients with an extended time window could potentially benefit from endovascular treatment. Ongoing randomized controlled trials using imaging to identify late presenters with favorable brain physiology will help cement the paradigm of using time windows to select the population for acute imaging and imaging to select individual patients for therapy.

ABBREVIATION: ICH = intracerebral hemorrhage

Current guidelines recommend endovascular treatment in patients with ischemic stroke presenting within 6 hours from stroke-symptom onset.[1] One guideline allows treatment of selected patients in the 6- to 12-hour window.[2] A meta-analysis of the recent endovascular trials performed by the Highly Effective Reperfusion Evaluated in Multiple Endovascular Stroke trials (HERMES) collaboration showed the highest benefit of endovascular treatment among patients present-

Received April 17, 2017; accepted after revision August 15.

From the Departments of Clinical Neurosciences and Radiology (J.W.E., B.R.G., F.S.A.-A., P.A.B., A.M.D., M.G., M.D.H., B.K.M.) and Community Health Sciences and Department of Medicine (P.P., M.D.H., B.K.M.), Cumming School of Medicine, University of Calgary, Calgary, Alberta, Canada; Department of Medical Imaging (R.W., W.J.M.), Division of Radiology (T.K.), and Division of Neurology (F.L.S., C.F.), Department of Medicine, University Health Network, Toronto Western Hospital, Toronto, Ontario, Canada; Departments of Radiology (J.L.R.) and Medicine (Neurology) (A.S.), University of Alberta, Edmonton, Alberta, Canada; Departments of Neuroradiology (P.B.) and Geriatric and Stroke Medicine (D.W.), Beaumont Hospital and the Royal College of Surgeons in Ireland, Dublin, Ireland; Departments of Radiology (D.R.) and Neurosciences (A.Y.P.), Centre hospitalier de l'Université de Montréal, University of Montreal, Montreal, Quebec, Canada; Department of Neurology (T.G.J.), University of Pittsburgh Medical Center, Pittsburgh, Pennsylvania; Erlanger Medical Centre (T.D.) and Department of Radiology (B.W.B), Erlanger Hospital, University of Tennessee, Chattanooga, Tennessee; Colorado Neurological Institute (D.F.F., D.T.), Engelwood, Colorado; Montreal Neurological Institute (J.T.), McGill University, Montreal, Quebec, Canada; Department of Radiology (D.I.), The Ottawa Hospital, University of Ottawa, Ottawa, Ontario, Canada; Department of Neuroradiology (J.S.), Dalhousie University, Halifax, Nova Scotia, Canada; Hotchkiss Brain Institute (P.A.B., A.M.D., M.G., M.D.H., B.K.M.), University of Calgary, Calgary, Alberta, Canada; and Foothills Medical Centre (B.K.M.), Calgary, Alberta, Canada.

The study sponsor was the University of Calgary. Covidien provided major funding through an unrestricted grant to the University of Calgary. Additional active and in-kind support for the trial was from a consortium of funding public and charitable sources (Heart and Stroke Foundation Canada, Alberta Innovates Health Solutions, Alberta Health Services, Canadian Stroke Prevention Intervention Network through Canadian Institutes of Health Research) and the University of Calgary (Hotchkiss Brain Institute, Department of Clinical Neurosciences, Department of Radiology, and Calgary Stroke Program).

The sponsor of the trial was the Governors of the University of Calgary. The sponsor had no role in the design, data gathering, analysis, or reporting of the trial. The University of Calgary received unrestricted grants from Medtronic (Covidien), Alberta Innovates Health Solutions, Heart and Stroke Foundation Canada, Canadian Institute for Health Research through the Canadian Stroke Prevention Intervention Network, and Alberta Health Services. The University of Calgary provided internal funding from the Hotchkiss Brain Institute, the Department of Clinical Neurosciences, and Department of Radiology.

Clinical Trial Registration: www.clinicaltrials.gov NCT01778335.

Please address correspondence to Bijoy K. Menon, MD, MSc, Foothills Medical Centre, 1403 29th St NW, Calgary, AB T2N 2T9, Canada; e-mail: docbijoymenon@gmail.com

Indicates open access to non-subscribers at www.ajnr.org

http://dx.doi.org/10.3174/ajnr.A5462

Table 1: Baseline characteristics and workflow in subjects with last seen healthy to randomization time >5.5 hours

	Intervention (n = 33)	Control (n = 26)
Demographics		
Age (median) (IQR) (yr)	66.1 (15.2)	67.9 (21.9)
Female sex	60.6% (20)	42.3% (11)
Caucasian race	87.9% (29)	92.3% (24)
Medical history		
Hypertension	66.7% (22)	80.8% (21)
Diabetes mellitus	15.2% (5)	26.9% (7)
Atrial fibrillation	42.4% (14)	42.3% (11)
Clinical characteristics		
NIHSS score (median) (IQR)	14 (4)	17 (12)
Systolic blood pressure at hospital arrival (median) (IQR) (mm Hg)	143 (22)	138 (43)
Serum glucose at hospital arrival (median) (IQR) (mmol/L)	6.8 (2.2)	6.9 (2.0)
Imaging characteristics		
ASPECTS on baseline noncontrast CT (median) (IQR)	9 (2)	8.5 (3)
Location of occlusion on CTA[a]		
ICA with involvement of the M1 MCA segment (n = 16)	29.0% (9/31)	26.9% (7/26)
M1 or all M2 MCA segments (n = 40)	67.7% (21/31)	73.1% (19/26)
Single M2 MCA segment (n = 1)	3.2% (1/31)	0% (0/26)
Process time (min)		
Stroke onset to randomization (median) (IQR)	468 (179)	405 (107)
Treatment		
IV alteplase	24.2% (8/33)	57.8% (15/26)

Note:—IQR indicates interquartile range.

[a] Two scans missing or not scoreable reduces the denominator to 31 in the intervention group.

ing within 5 hours; however, a smaller benefit was seen in those presenting after 5 hours of symptom onset, with most of these patients presenting <8 hours after onset.[3] Another individual patient-level meta-analysis from the first 5 trials reported a benefit of endovascular therapy over standard medical therapy when arterial puncture was performed <7.3 hours from symptom onset.[4]

Currently, Endovascular Therapy Following Imaging Evaluation for Acute Ischemic Stroke 3 (DEFUSE 3) and Clinical Mismatch in the Triage of Wake Up and Late Presenting Strokes Undergoing Neurointervention with Trevo (DAWN) are 2 major multicenter randomized trials assessing the possible benefit of endovascular treatment in image-selected patients presenting in late time windows (6–24 hours in DAWN and 6–16 hours in DEFUSE 3). The recent presentation of positive data from the DAWN study highlights the importance of imaging in the selection of late-presenting patients.[5] The Endovascular Treatment for Small Core and Proximal Occlusion Ischemic Stroke (ESCAPE) trial used head CT and CT angiography as radiographic markers to enroll patients up to 12 hours from symptom onset (defined as the last known well time), thus providing a unique perspective on patients presenting to medical attention relatively late. We analyzed data from patients in the extended timeframe (6–12 hours) of the ESCAPE trial.[6]

MATERIALS AND METHODS

Data are from the ESCAPE trial. The ESCAPE trial was a prospective, multicenter, randomized, controlled, open-label trial design with blinded outcome assessment.[6,7] The trial enrolled patients presenting within 12 hours from last seen healthy with disabling ischemic stroke, a small core infarct on noncontrast head CT (ASPECTS 6–10), and moderate-to-good collaterals on CT angiography.[6,8] Because the 75th percentile for randomization to arterial access/groin puncture time was 28 minutes in the intervention group, patients randomized between 5.5 and 12 hours from last seen healthy (likely to undergo arterial access/groin puncture >6 hours from symptom onset/last seen healthy) were defined as the extended time window population for the current analyses.

The primary outcome was the modified Rankin Scale score at 90 days after stroke onset. Secondary outcomes were mRS 0–2, mRS 0–1 (all at 90 days), the proportion achieving NIHSS 0–2 at 24 hours, and the proportion developing intracerebral hemorrhage (ICH), reported both as symptomatic ICH and using the European Cooperative Acute Stroke Study 2 (ECASS 2) categories on follow-up imaging.[9] Reperfusion (modified TICI 2b–3) is reported for the intervention arm. Data are summarized using descriptive statistics, and the adjusted outcomes were assessed using both ordinal logistic regression and unconditional logistic regression with adjustment for key prognostic variables (age, sex, baseline NIHSS score, baseline site of occlusion, baseline NCCT ASPECTS, and intravenous alteplase treatment). Interaction was assessed using a likelihood ratio test within the logistic regression analysis with a multiplicative interaction term.

RESULTS

Fifty-nine of 315 (19%) subjects were randomized >5.5 hours from last seen healthy. There was no evidence of heterogeneity of treatment effect between the early presenters and subjects enrolled in the extended time window (P = .134, likelihood ratio test). Table 1 shows differences in demographics, baseline characteristics, and workflow between the intervention (n = 33) and control (n = 26) arms of subjects within the late time window. Patients in the control arm were more likely to receive intravenous alteplase; otherwise, the population characteristics were similar.

Clinical outcomes in late-window subjects are summarized in Table 2 and the Figure. A treatment effect favoring intervention is seen across all clinical outcomes. In this subgroup, intervention was superior to the best medical therapy for NIHSS 0–2 at 90 days (45.5% versus 13.6%, P = .019). The absolute risk difference favoring intervention was 19.3% on the mRS 0–2 at 90 days, and the shift analysis (proportional odds model) favored intervention (adjusted common OR = 2.61; 95% CI, 0.9–7.8). A higher rate of all types of ICH (including petechial hemorrhage) was noted in the intervention arm (Table 3), but not of symptomatic ICH.

Table 2: Clinical outcomes and treatment effect in subjects in the ESCAPE trial with last seen healthy to randomization time of >5.5 hours

Outcome	Intervention (*n* = 33)	Control (*n* = 26)	Risk Difference (Absolute)	*P* Value	Risk Ratio Unadjusted (95% CI)
mRS at 90 days, (median) (IQR)	3 (3)	4 (3)	–	.029[a]	–
mRS 0–2 at 90 days	48.5% (16/33)	29.2% (7/24)	19.3%	.178	1.7 (0.8–3.4)
mRS 0–1 at 90 days	39.3% (13/33)	20.1% (5/24)	18.6%	.161	1.89 (0.8–4.6)
NIHSS score 0–2 at 90 days	45.5 (15/33)	13.6 (3/22)	31.8%	.019	3.33 (1.1–10.2)
ICH any (all types)	48.5% (16/33)	11.5% (3/26)	36.9%	.004	4.2 (1.4–12.9)
ICH symptomatic	0%	0%	0%	1.000	–
mTICI 2b-3 (EVT group) or mAOL 2–3 (control group)[b]	87.5% (28/32)	13.0% (3/23)	74.5%	–	–

Note:—mTICI indicates modified Thrombolysis in Cerebral Infarction score; mAOL, modified Arterial Occlusive Lesion score; EVT, endovascular treatment.
[a] Parametric test of medians.
[b] Reperfusion assessed as mTICI 2b–3 at end of EVT in the intervention group or as recanalization with mAOL score 2–3 on repeat CTA in the control group.

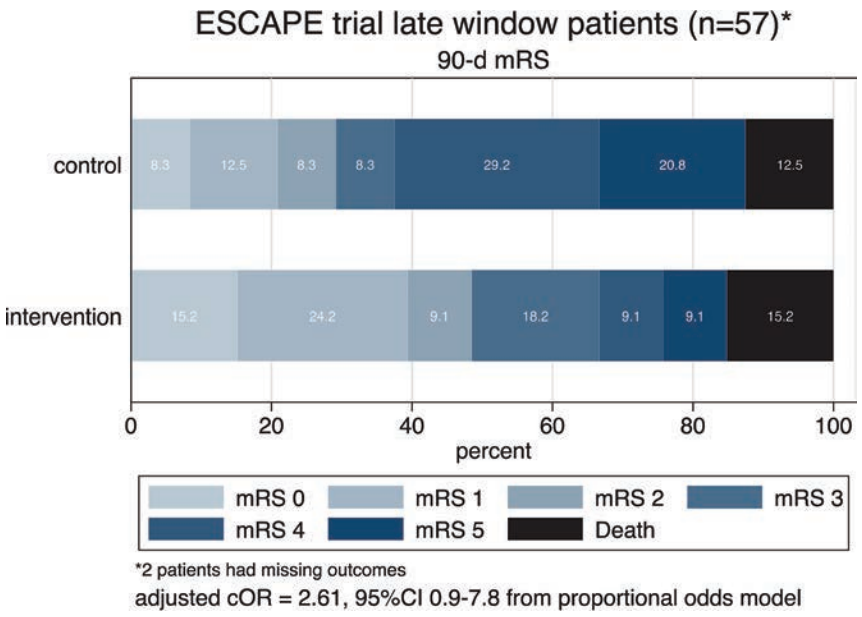

FIGURE. Ninety-day mRS distribution in the intervention ($n = 33$) and the control ($n = 26$) arms of the ESCAPE trial in subjects randomized >5.5 hours from last seen healthy. cOR indicates common odds ratio.

Table 3: Distribution of intracerebral hemorrhage using the ECASS radiologic classification on follow-up imaging in subjects with last seen healthy to randomization of >5.5 hours in the ESCAPE trial[a]

ICH Type	Intervention (*n* = 33)	Control (*n* = 26)
HI-1	18.1% (6)	3.8% (1)
HI-2	24.2% (8)	7.7% (2)
PH-1 or rPH-1	3.0% (1)	0 (0)
PH-2 or rPH-2	3.0% (1)	0 (0)
None	51% (17)	88.5% (23)

Note:—HI indicates hemorrhagic infarction; PH, parenchymal hematoma; rPH, remote parenchymal hematoma.
[a] Composite *P* value = .029.

DISCUSSION

The ESCAPE trial enrolled a small number of subjects in late time windows but showed no evidence of heterogeneity of treatment effect in subjects between the early and late time windows. In the late time window population, all clinical outcomes showed trends favoring the intervention arm, consistent with the recent meta-analyses of the endovascular trials.[3,4]

The ESCAPE trialists adopted a 2-stage screening paradigm to identify subjects for enrollment. The 12-hour window identified the population sampling frame and was an arbitrary threshold determined by consensus at the time of the study design. These subjects were then imaged using a CT/CTA metric to identify individuals for enrollment. Imaging served as a marker of favorable brain physiology instead of time.[10] This was a pragmatic choice because the patient is often unaware of stroke-onset time or is unable to communicate it clearly. Epidemiologic studies suggest that 1 of every 3 patients with stroke may either wake up with symptoms or have unwitnessed onset, and this proportion may increase with an aging population.[11-14] Patients with unwitnessed stroke onset may have a last known well time many hours before or immediately proximate to the time of stroke recognition. Among this group, 2 types of patients can be identified. Both patients with a true recent infarct onset and patients with good collaterals and slow infarct progression can be identified as ideal therapy candidates.[15,16] The change to a physiologic paradigm of using time windows to select which populations to screen and then imaging to select those eligible for acute treatment is actively supported by these results.

Because late presenters, on average, are more likely to have larger infarcts with more severe parenchymal and endothelial damage, these patients may be at higher risk of hemorrhage than early presenters. Our analysis showed an increased risk of occurrence of all ICHs in late presenters in the intervention group compared with best medical therapy; however, this risk applied to the clinically silent hemorrhagic infarction types and not to the clinically relevant parenchymal hematoma category. There was no difference in clinically defined symptomatic ICH.

Our study is limited by a small sample size and the post hoc nature of our analysis, but a major strength is that findings arise from a carefully controlled prospective randomized trial. Recently, the DAWN trial implemented an image-based patient selection with CT/MR imaging perfusion to provide randomized controlled trial data to support endovascular treatment in the extended time window and to further support the paradigm of using imaging selection of patients for treatment.

CONCLUSIONS

While the results of the DAWN study are not yet published, some limited comparisons can be made with recent preliminary data. Among the 206 patients enrolled in the DAWN trial, the median age was 72 and 73 years in the intervention and control arms, respectively, and the median baseline NIHSS of 17 in both treatment groups was like that in our analysis. The last seen healthy time to randomization was greater in the DAWN trial (13.4 ± 4.1 hours; median, 12.2 hours in the treatment arm; and 13.0 ± 4.5 hours; median, 13.2 hours in the control arm).[17] The reported weighted-based coprimary outcome of the mean mRS was 5.5 versus 3.4 in the control and intervention groups, respectively, in DAWN.[5] Although not directly comparable with our post hoc subgroup analysis, the positive signal seen in our results appears to be supported by this randomized controlled trial data. We await the formal publication of the DAWN and DEFUSE 3 trials to provide further opportunity for comparison with these data.

ACKNOWLEDGMENTS

The ESCAPE trialists would like to acknowledge the contribution of Dr Cheemun Lum, a key member of the ESCAPE trial team at the University of Ottawa and a dedicated and talented neurointerventionalist, who passed away suddenly during the completion of this work.

Disclosures: Jeremy L. Rempel—*UNRELATED*: *Consulting Fee or Honorarium*: Memorial University, *Comments*: speaking honorarium. Ashfaq Shuaib—*UNRELATED*: *Board Membership*: Canadian Stroke Consortium*; *Employment*: University of Alberta. David Williams—*RELATED*: *Grant*: University of Calgary, *Comments*: I was a site investigator (Ireland) for the ESCAPE study*; *Support for Travel to Meetings for the Study or Other Purposes*: University of Calgary, *Comments*: I was a site investigator (Ireland) for the ESCAPE study and was supported to attend investigator meetings*; *UNRELATED*: *Board Membership*: Boehringer Ingelheim, Bayer, Bristol Myers Squibb, Daiichi Sankyo, *Comments*: member of the Advisory Board on the safe use of novel anticoagulants. Daniel F. Roy—*RELATED*: *Grant*: University of Calgary, *Comments*: Angiography Core Lab for the ESCAPE trial. Alexander Y. Poppe—*RELATED*: *Grant*: University of Calgary, *Comments*: fees paid per patient enrolled for participation of our center in the ESCAPE trial*; *UNRELATED*: *Board Membership*: Bayer, Bristol-Myers Squibb–Pfizer, *Comments*: Advisory Boards 2016; *Grants/Grants Pending*: CaSTOR, The Canadian Stroke Trials for Optimized Results, *Comments*: catalyst grant for developing a study network on tandem carotid lesions in acute stroke; *Payment for Lectures Including Service on Speakers Bureaus*: Medtronic, *Comments*: speaker fees 2016; *Payment for Development of Educational Presentations*: EMD Serono, *Comments*: examiner in mock exam for neurology residents. Tudor G. Jovin—*UNRELATED*: *Consultancy*: Neuravi, Codman Neurovascular, *Comments*: Neuravi, Steering Committee member; Codman Neurovascular, Data and Safety Monitoring Board member; *Stock/Stock Options*: Anaconda, Silk Road, Route 92, Blockade Medical; *Travel/Accommodations/Meeting Expenses Unrelated to Activities Listed*: Stryker* (Principal Investigator DAWN). Thomas Devlin—*RELATED*: *Grant*: Medtronic, *Comments*: research support; *UNRELATED*: *Consultancy*: BrainsGate, San Bio, Ornim Medical, Daiichi Sankyo, *Comments*: research support*; *Payment for Lectures Including Service on Speakers Bureaus*: Medtronic, *Comments*: speakers bureau.* Michael D. Hill—*RELATED*: *Grant*: Medtronic, University of Calgary, Alberta Innovates, Heart and Stroke Foundation, Canadian Institutes of Health Research, Alberta Health Services, *Comments*: grants or support-in-kind to the University of Calgary for the ESCAPE trial*; *UNRELATED*: *Board Membership*: Canadian Neuroscience Federation, *Comments*: volunteer governance board for a not-for-profit organization; *Consultancy*: Merck, *Comments*: remuneration for clinical trial adjudication of outcomes panel; *Grants/Grants Pending*: Medtronic, *Comments*: grant support for the HERMES collaboration; *Stock/Stock Options*: Calgary Scientific, *Comments*: stock ownership in a Calgary imaging and data company. Philip A. Barber—*UNRELATED*: *Consultancy*: Ablynx Pharmaceutical*; *Employment*: University of Calgary; *Grants/Grants Pending*: Heart and Stroke Foundation of Canada*. Daniela Iancu—*RELATED*: *Grant*, *Comments*: ESCAPE Trial*. Bijoy K. Menon—*RELATED*: *Grant*: Covidien*; *UNRELATED*: *Patents (Planned, Pending or Issued)*, *Comments*: US patent pending, patent on systems of triage for stroke; *Stock/Stock Options*: Quikflo Health. Blaise W. Baxter—*UNRELATED*: *Consultancy/Speakers Bureau*: Penumbra, Medtronic, Stryker, Pulsar, Route 92; *Patents (Planned, Pending or Issued)*: Advanced Catheter Therapies, *Comments*: Patent US8622992, no royalties. Mayank Goyal—*RELATED*: *Grant*: Medtronic, *Comments*: part funding of the ESCAPE trial, funding for HERMES collaboration*; *Consulting Fee or Honorarium*: Medtronic, *Comments*: consulting fee for design and conduct of SWIFT PRIME trial; *UNRELATED*: *Consultancy*: Stryker, MicroVention, Ablynx, *Comments*: for educational activities and product advice; *Patents (Planned, Pending or Issued)*: GE Healthcare, MicroVention, *Comments*: licensing agreement for systems of stroke diagnosis and systems of intracranial access. Donald F. Frei—*UNRELATED*: *Consultancy*: Stryker, MicroVention, Penumbra; *Payment for Lectures Including Service on Speakers Bureaus*: Stryker, MicroVention, Penumbra; *Stock/Stock Options*: Penumbra. Donatella Tampieri—*UNRELATED*: *Consultancy*: Canadian Medical Protective Association; *Grants/Grants Pending*: Fonds de recherche du Québec.* Andrew M. Demchuk—*RELATED*: *Grant*: Medtronic, *Comments*: unrestricted grant to support enrollment and coordination of the ESCAPE trial*; *Consulting Fee or Honorarium*: Medtronic, *Comments*: honoraria for Continuing Medical Education events. Frank L. Silver—*UNRELATED*: *Consultancy*: Boehringer Ingelheim Canada, *Comments*: National Coordinator, REPECT ESUS clinical trial. *Money paid to the institution.

REFERENCES

1. Powers WJ, Derdeyn CP, Biller J, et al; American Heart Association Stroke Council. **2015 American Heart Association/American Stroke Association Focused Update of the 2013 Guidelines for the Early Management of Patients with Acute Ischemic Stroke Regarding Endovascular Treatment: A Guideline for Healthcare Professionals from the American Heart Association/American Stroke Association.** *Stroke* 2015;46:3020–35 CrossRef Medline
2. Casaubon LK, Boulanger JM, Glasser E, et al; Heart and Stroke Foundation of Canada Canadian Stroke Best Practices Advisory Committee. **Canadian Stroke Best Practice Recommendations: Acute Inpatient Stroke Care Guidelines, update 2015.** *Int J Stroke* 2016;11:239–52 CrossRef Medline
3. Goyal M, Menon BK, van Zwam WH, et al; HERMES collaborators. **Endovascular thrombectomy after large-vessel ischaemic stroke: a meta-analysis of individual patient data from five randomised trials.** *Lancet* 2016;387:1723–31 CrossRef Medline
4. Saver JL, Goyal M, van der Lugt A, et al; HERMES collaborators. **Time to treatment with endovascular thrombectomy and outcomes from ischemic stroke: a meta-analysis.** *JAMA* 2016;316:1279–88 CrossRef Medline
5. Jovin TG, Nogueira RG. **Dawn in full daylight.** In: *Proceedings of the 3rd European Stroke Organisation Conference,* Prague, Czech Republic; May 16–18, 2017
6. Goyal M, Demchuk AM, Menon BK, et al; ESCAPE Trial Investigators. **Randomized assessment of rapid endovascular treatment of ischemic stroke.** *N Engl J Med* 2015;372:1019–30 CrossRef Medline
7. Demchuk AM, Goyal M, Menon BK, et al; ESCAPE Trial Investigators. **Endovascular treatment for Small Core and Anterior circulation Proximal occlusion with Emphasis on minimizing CT to recanalization times (ESCAPE) trial: methodology.** *Int J Stroke* 2015;10:429–38 CrossRef Medline
8. Menon BK, Sajobi TT, Zhang Y, et al. **Analysis of workflow and time to treatment on thrombectomy outcome in the endovascular treatment for small core and proximal occlusion ischemic stroke (ESCAPE) randomized, controlled trial.** *Circulation* 2016;133:2279–86 CrossRef Medline
9. Hacke W, Kaste M, Fieschi C, et al; Second European-Australasian Acute Stroke Study Investigators. **Randomised double-blind placebo-controlled trial of thrombolytic therapy with intravenous alteplase in acute ischaemic stroke (ECASS II).** *Lancet* 1998;352:1245–51 CrossRef Medline
10. Hill MD, Goyal M, Demchuk AM, et al. **Ischemic stroke tissue-window in the new era of endovascular treatment.** *Stroke* 2015;46:2332–34 CrossRef Medline
11. Thomalla G, Gerloff C. **Treatment concepts for wake-up stroke and stroke with unknown time of symptom onset.** *Stroke* 2015;46:2707–13 CrossRef Medline
12. Nadeau JO, Fang J, Kapral MK, et al; Registry of the Canadian Stroke

Network. **Outcome after stroke upon awakening.** *Can J Neurol Sci* 2005;32:232–36 Medline
13. Bal S, Bhatia R, Shobha N, et al. **Stroke-on-awakening: Safety of CT-CTA based selection for reperfusion therapy.** *Can J Neurol Sci* 2014;41:182–86 CrossRef
14. Hill MD, Kenney C, Dzialowski I, et al. **Tissue Window in Stroke Thrombolysis study (TWIST): a safety study.** *Can J Neurol Sci* 2013; 40:17–20 CrossRef Medline
15. Menon BK, Qazi E, Nambiar V, et al; Interventional Management of Stroke III Investigators. **Differential effect of baseline computed tomographic angiography collaterals on clinical outcome in patients enrolled in the Interventional Management of Stroke III trial.** *Stroke* 2015;46:1239–44 CrossRef Medline
16. Hwang YH, Kang DH, Kim YW, et al. **Impact of time-to-reperfusion on outcome in patients with poor collaterals.** *AJNR Am J Neuroradiol* 2015;36:495–500 CrossRef Medline
17. Nogueira RG, Jadhav AP, Haussen DC, et al; DAWN Trial Investigators. **Thrombectomy 6 to 24 hours after stroke with a mismatch between deficit and infarct.** *N Engl J Med* 2017 Nov 11. [Epub ahead of print] CrossRef Medline

Posttreatment Infarct Volumes when Compared with 24-Hour and 90-Day Clinical Outcomes: Insights from the REVASCAT Randomized Controlled Trial

F.S. Al-Ajlan, A.S. Al Sultan, P. Minhas, Z. Assis, M.A. de Miquel, M. Millán, L. San Román, A. Tomassello, A.M. Demchuk, T.G. Jovin, P. Cuadras, A. Dávalos, M. Goyal, and B.K. Menon; for the REVASCAT Investigators

ABSTRACT

BACKGROUND AND PURPOSE: Endovascular therapy has become the standard of care for patients with disabling anterior circulation ischemic stroke due to proximal intracranial thrombi. Our aim was to determine whether the beneficial effect of endovascular treatment on functional outcome could be explained by a reduction in posttreatment infarct volume in the Endovascular Revascularization With Solitaire Device Versus Best Medical Therapy in Anterior Circulation Stroke Within 8 Hours (REVASCAT) trial.

MATERIALS AND METHODS: The REVASCAT trial was a multicenter randomized open-label trial with blinded outcome evaluation. Among 206 enrolled subjects (endovascular treatment, $n = 103$; control, $n = 103$), posttreatment infarct volume was measured in 204 subjects. Posttreatment infarct volumes were compared with treatment assignment and recanalization status. Appropriate statistical models were used to assess the relationship among baseline clinical and imaging variables, posttreatment infarct volume, the 24-hour NIHSS score, and functional status with the 90-day modified Rankin Scale score.

RESULTS: The median posttreatment infarct volume in all subjects was 23.7 mL (interquartile range = 68.9 mL) and 16.3 mL (interquartile range = 50.2 mL) in the endovascular treatment arm and 38.6 mL (interquartile range = 74.9 mL) in the control arm ($P = .02$ for endovascular treatment versus control subjects). Baseline NIHSS ($P < .01$), site of occlusion ($P < .03$), baseline NCCT ASPECTS ($P < .01$), and recanalization status ($P = .02$) were independently associated with posttreatment infarct volume. Baseline NIHSS ($P < .01$), time from symptom onset to randomization ($P = .02$), treatment type ($P = .04$), and recanalization status ($P < .01$) were independently associated with the 24-hour NIHSS scores. The 24-hour NIHSS score strongly mediated the relationship between treatment type and 90-day mRS ($P < .01$ for indirect effect when adjusted for age), while posttreatment infarct volume did not ($P = .26$).

CONCLUSIONS: Endovascular treatment saves brain and improves 90-day clinical outcomes primarily through a beneficial effect on the 24-hour stroke severity.

ABBREVIATIONS: EVT = endovascular treatment; IQR = interquartile range

In 2015, five randomized clinical trials revolutionized stroke care by confirming the benefit of modern endovascular therapy (EVT) in patients with acute ischemic stroke due to proximal anterior circulation occlusion.[1-5] Fast reperfusion played an important role in the success of these trials, likely by saving brain that would otherwise have infarcted without reperfusion.

Although posttreatment infarct volumes are routinely used in experimental models of focal cerebral ischemia,[6] human clinical trials have preferred to use ordinal scales like the modified Rankin Scale, the National Institutes of Health Stroke Scale, or the Barthel Index to primarily measure posttreatment outcomes.[7-9] This preference is, in part, because past human studies attempting to correlate posttreatment infarct volumes to clinical outcomes have

Received June 11, 2017; accepted after revision August 16.

From the Department of Clinical Neurosciences and Department of Radiology (F.S.A.-A., A.S.A.S., P.M., Z.A., A.M.D., M.G., B.K.M.), Cumming School of Medicine, University of Calgary, Calgary, Alberta, Canada; Department of Neurosciences at King Faisal Specialist Hospital and Research Centre (F.S.A.-A.), Riyadh, Saudi Arabia; Stroke Unit (M.A.d.M.), Neurology Department, Hospital de Bellvitge, L'Hospitalet de Llobregat, Barcelona, Spain; Stroke Unit (M.M., P.C., A.D.), Department of Neurosciences and Department of Radiology, Hospital Germans Trias, Universitat Autosome de Barcelona, Badalona (Barcelona), Spain; Stroke Unit (L.S.R.), Neurology Department, Hospital Clínic, Barcelona, Spain; Stroke Unit (A.T.), Neurology Department, Hospital Vall d'Hebron, Barcelona, Spain; and Stroke Institute (T.G.J.), Department of Neurology, University of Pittsburgh Medical Center, Pittsburgh, Pennsylvania.

REVASCAT was funded by a local independent Catalan institution (Fundació Ictus Malaltia Vascular) through an unrestricted grant from the manufacturer of the device (Covidien). This project has been partially supported by a grant from the Spanish Ministry of Health cofinanced by FEDER (Instituto de Salud Carlos III, RETICS-INVICTUS PLUS, RD 16/0019).

Clinical Trial Registration: https://clinicaltrials.gov/ct2/show/NCT01692379.

Please address correspondence to Bijoy K. Menon, MD, MSc, Foothills Medical Centre, 1403 29th St NW, Calgary, AB T2N 2T9 Canada; e-mail: docbijoymenon@gmail.com; @bijoymenon

Indicates open access to non-subscribers at www.ajnr.org

http://dx.doi.org/10.3174/ajnr.A5463

yielded contradictory results.[10,11-13] On the other hand, successful recanalization has been shown to be strongly associated with improved functional outcomes and reduced mortality.[14] Data from the recent Endovascular Treatment for Small Core and Proximal Occlusion Ischemic Stroke (ESCAPE) trial showed that the successful recanalization and reduction in posttreatment infarct volume were associated with better clinical outcome.[15] The purpose of this analysis was to analyze the relationship among baseline clinical characteristics, type of treatment, recanalization status, posttreatment infarct volumes, and the 24-hour and 90-day clinical outcomes from the Endovascular Revascularization With Solitaire Device Versus Best Medical Therapy in Anterior Circulation Stroke Within 8 Hours (REVASCAT) trial.[5]

MATERIALS AND METHODS

Methodologic details of the REVASCAT trial have been reported elsewhere.[5] Briefly, the REVASCAT trial was a prospective, multicenter, randomized, controlled, open, blinded–end point trial. Patients were randomized 1:1 to mechanical embolectomy with the stent retriever Solitaire FR (Covidien, Irvine, California) versus best medical management alone. Eligible patients were between 18 and 80 years of age, had an occlusion in the proximal anterior circulation and could be treated within 8 hours of symptom onset, and had a prestroke modified Rankin Scale score of ≤1 and a baseline score of at least 6 points on the National Institutes of Health Stroke Scale score. The main exclusion criteria on imaging were evidence of a large ischemic core, as indicated by an Alberta Stroke Program Early CT Score of <7 on CT or a score of <6 on diffusion-weighted MR imaging. All patients or their surrogates provided written informed consent. The primary outcome was disability at 90 days on the mRS.[16] Secondary outcomes included centrally adjudicated infarct volumes on CT or MR imaging at 24–36 hours and vessel recanalization on CT angiography or MR angiography at 24–36 hours.

Imaging

The trial protocol included follow-up MR imaging with MR angiography or noncontrast CT with CT angiography at 24–36 hours from stroke-symptom onset.

Diffusion-weighted imaging was the technique of choice for measurement of posttreatment infarct volume. If DWI was not available, an NCCT scan was chosen for measurement. Two readers (F.S.A.-A. and P.M.) used Quantomo (Cybertrial, Calgary, Alberta, Canada)[17] to delineate infarct and measure posttreatment infarct volumes (in milliliters) while being blinded to all other clinical and imaging information. Manual adjustments to delineate infarct boundaries were performed when necessary. If the infarct showed hemorrhagic conversion, the hemorrhage regions were incorporated within the boundaries of the infarct. Posttreatment infarct volume was measured with NCCT in 189 subjects and with MR imaging in 15 subjects. Successful recanalization was defined with the modified Thrombolysis in Cerebral Infarction score (2b or 3) on conventional angiography in the intervention arm and the modified arterial occlusive lesion core (2 or 3) on 24-hour CTA or MRA among subjects in the control arm.[18]

Statistical Analysis

Because posttreatment infarct volume did not have a normal distribution, the Wilcoxon rank sum test was used to test for differences in volumes between treatment and control subjects and between subjects achieving and not achieving recanalization.

Generalized linear regression was used to model the association between treatment and posttreatment infarct volume, adjusting for prespecified variables (age, sex, baseline NIHSS, baseline site of occlusion [internal carotid artery versus M1 or M2 of the middle cerebral artery], intravenous alteplase [yes versus no], and time from stroke onset to randomization). A cube root transformation of posttreatment infarct volume best satisfied the assumptions of this model (normality of residuals and homoscedasticity) and was used for this analysis. A similar model was used to model the association between treatment and the 24-hour NIHSS score.

A generalized linear model with log-link was used to report rate/risk ratios for functional independence (mRS 0–2 at 90 days) and 90-day mortality in the highest-versus-lowest posttreatment infarct volume quartile. Generalized linear regression with backward elimination was used to arrive at a final parsimonious model that reports the association between treatment type and 90-day mRS after adjusting for the 24-hour NIHSS score and posttreatment infarct volume. The template of Baron and Kenny[19] was used to perform mediational analysis (http://www.ats.ucla.edu/stat/stata/faq/mulmediation.htm), testing whether the 24-hour NIHSS score and posttreatment infarct volume (potential mediating variables) mediate partially or completely (indirect effect) the association between treatment type and 90-day mRS. All 3 causal steps necessary for mediation analysis as proposed by Baron and Kenny were satisfied (Fig 1). All statistical analyses were performed in STATA/MP version 14.0 (StataCorp, College Station, Texas). Statistical significance was assessed at $\alpha < .05$ in all analyses.

RESULTS

A total of 206 patients (103 in the EVT arm versus 103 in the control arm) were enrolled in the study. Median baseline NCCT ASPECTS was 7 in the EVT group and 8 in the control group. Intravenous alteplase was administered to 68.0% of patients in the EVT group and 77.7% of those in the control group. The median time from stroke onset to randomization was 225 minutes.

Median posttreatment infarct volume in all study participants was 23.7 mL (interquartile range [IQR] = 68.9 mL) and 16.3 mL (IQR = 50.2 mL) in the EVT arm and 38.6 mL (IQR = 74.9 mL) in the control arm ($P = .02$). Median posttreatment infarct volume in the EVT arm in recanalizers was 14.6 mL (IQR = 7.8–46.2 mL) versus 92.9 mL (IQR = 14.6–233.1 mL) in the nonrecanalizers ($P = .05$). The median posttreatment infarct volume in the control arm in recanalizers was 18.1 mL (IQR = 8.4–76.7 mL) versus 52.8 mL (IQR = 18.5–109.5 mL) in the nonrecanalizers ($P = .02$).

Baseline NIHSS score ($P < .01$), site of occlusion ($P < .03$), baseline NCCT ASPECTS ($P < .01$), and recanalization status ($P = .02$) were independently associated with posttreatment infarct volume (cube root–transformed), while age, sex, treatment type, intravenous alteplase, and time from symptom onset to randomization were not ($P > .05$). The baseline NIHSS score ($P <$

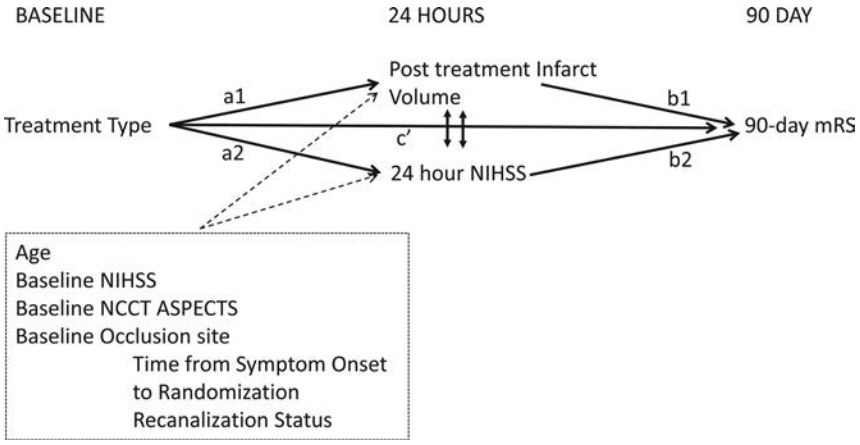

FIG 1. A pictorial representation of the causal pathway in patients with acute ischemic stroke. Treatment type (EVT or control) determines posttreatment infarct volume and the 24-hour NIHSS score along with other variables such as age, sex, baseline clinical and imaging markers of stroke severity, time to treatment, and recanalization status (independent variables). Posttreatment infarct volume and the 24-hour NIHSS score (mediator variables) likely then determine 90-day mRS (dependent variable). The total effect of the independent variables on the dependent variables consists of a direct effect c′ (as shown in the image) and indirect effects.[1] The indirect or mediating effect of each mediator variable on the association between independent variables and dependent variables is determined by computing the product of the regression coefficients a1 × b1 or a2 × b2 as appropriate. In our study, the 2 mediator variables (posttreatment infarct volume and the 24-hour NIHSS score) are significantly correlated. Analysis suggests that the age-adjusted 24-hour NIHSS score mediates strongly the relationship between treatment type and 90-day mRS ($P < .01$ for indirect effect when adjusted for age), while posttreatment infarct volume does not ($P = .26$).

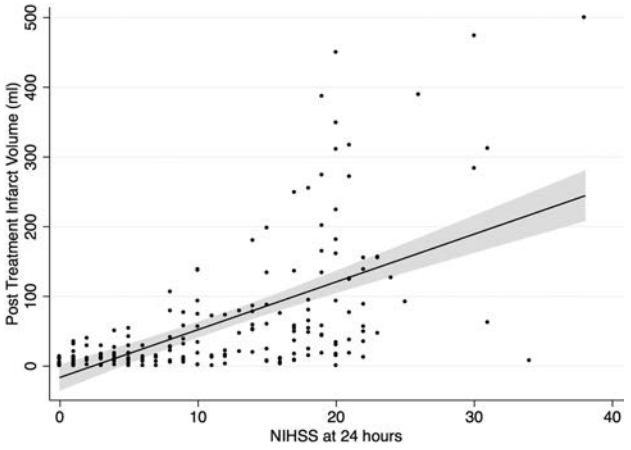

FIG 2. Relationship between the 24-hour NIHSS score and posttreatment infarct volume in milliliters.

.01), time from symptom onset to randomization ($P = .02$), treatment type ($P = .04$), and recanalization status ($P < .01$) were independently associated with the 24-hour NIHSS score, while age, sex, site of occlusion, baseline NCCT ASPECTS, and intravenous alteplase were not ($P > .05$). A significant correlation was seen between posttreatment infarct volume and the 24-hour NIHSS score ($P < .01$, Fig 2).

Distribution of posttreatment infarct volume versus 90-day mRS is shown in Fig 3. Patients in the lowest quartile for posttreatment infarct volume were 4 times more likely to achieve functional independence at 90 days (mRS 0–2) compared with patients in the highest quartile (rate ratio = 3.92; 95% CI, 0.66-23.16). Patients in the highest quartile of posttreatment infarct volume were 4 times more likely to die at 90 days (mRS 6) compared with patients in the lowest quartile (risk ratio = 3.88; 95% CI, 1.39–10.77). In a parsimonious model obtained after including all baseline clinical and imaging variables, treatment type, and recanalization status with 90-day mRS as outcome, treatment type was not independently associated with 90-day mRS ($P = .81$) after adjusting for posttreatment infarct volume ($P = .12$), the 24-hour NIHSS score ($P < .01$), and age ($P = .01$). The Baron and Kenny mediational analysis model suggests that the 24-hour NIHSS score strongly mediates the relationship between treatment type and 90-day mRS ($P < .01$ for indirect effect when adjusted for age), while posttreatment infarct volume does not ($P = .26$).

DISCUSSION

Our results show that endovascular treatment in subjects with acute ischemic stroke and proximal anterior circulation occlusions was associated with significantly smaller posttreatment infarct volumes only when recanalization was achieved. Subjects in the control arm also achieved smaller posttreatment infarct volumes with recanalization. Our results are therefore consistent with the analysis from the ESCAPE trial that showed similar findings.[15] We also found that NIHSS measured at 24 hours, though significantly correlated with posttreatment infarct volume, is a better determinant of 90-day mRS than the posttreatment infarct volume.

The causal chain in acute ischemic stroke that explains 90-day clinical outcome is complex. Baseline clinical variables such as age and baseline stroke severity as measured clinically (NIHSS) or on imaging (NCCT ASPECTS and site of occlusion) are known prognostic determinants. Early recanalization as a result of treatment (EVT, intravenous alteplase) also affects 90-day clinical outcomes. Outcomes measured earlier such as posttreatment infarct volume or the 24-hour NIHSS score may only be used as surrogates for 90-day clinical outcome if they capture the effect of these baseline clinical, imaging, and treatment variables on 90-day clinical outcome almost entirely. Our analysis shows that the age-adjusted 24-hour NIHSS score strongly mediates the relationship between treatment type and 90-day outcome and that posttreatment infarct volume does not contribute any further to mediating this relationship. Although we found a robust relationship between the 24-hour NIHSS score and posttreatment infarct volume (Fig 2), the effects of brain eloquence and other prognostic determinants such as diabetes, hypertension, or other medical comorbidities are more likely to be captured by a clinical measure such as the NIHSS compared with an imaging measure like posttreatment infarct volume. Of note, recent analysis from the ESCAPE trial showed that analysis of NIHSS trajectories from baseline to day 5 may be better than the 24-hour NIHSS score alone in determining 90-day mRS.[20]

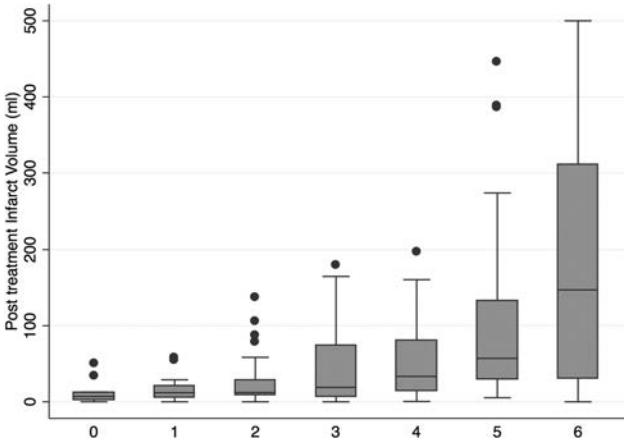

FIG 3. Relationship between 90-day mRS and posttreatment infarct volume in milliliters.

Aging is a complex medical phenomenon having effects on health beyond direct effects exerted through increasing prevalence of known diseases.[21] Aging is an important determinant of clinical outcomes in patients with acute ischemic stroke. Our analysis shows that age influences 90-day clinical outcome that is independent of posttreatment infarct volume and the 24-hour NIHSS score. Our analysis therefore emphasizes that surrogate outcomes in stroke such as the 24-hour NIHSS score or even posttreatment infarct volume will lose precision if patient age is not considered.

Our study has limitations. We could not do a complete exploration of the effect of all independent and mediating variables on 90-day clinical outcomes due to the limited sample size. Posttreatment infarct volumes were measured using 24- to 48-hour MR imaging or CT. MR imaging may be more sensitive than CT, and measuring infarct volumes late (even at 30 days) may offer more precise estimates of dead tissue than at 24–48 hours. Finally, although the 24-hour NIHSS score captures brain eloquence, we did not use imaging measures to better delineate eloquence.

CONCLUSIONS

Our results support primary findings from the REVASCAT trial that endovascular treatment saves brain and improves 24-hour (imaging and clinical outcomes) and 90-day clinical outcomes. The effect of EVT on 90-day clinical outcome is primarily mediated through an effect on the 24-hour NIHSS score.

Disclosures: Maria A. de Miquel—*UNRELATED*: *Board Membership*: Fundació Ictus. Andrew M. Demchuk—*RELATED*: *Consulting Fee or Honorarium*: Medtronic, *Comments*: honorarium for Continuing Medical Education events. Tudor G. Jovin—*RELATED*: *Support for Travel to Meetings for the Study or Other Purposes*: Fundació Ictus; *UNRELATED*: *Consultancy*: Neuravi, Johnson & Johnson; *Employment*: Stryker; *Stock/Stock Options*: FreeOx Biotech, Blockade Medical, Anaconda, Silk Road; *Travel/Accommodations/Meeting Expenses Unrelated to Activities Listed*: Stryker Neurovascular. Antoni Dávalos—*RELATED*: *Grant*: Covidien-Medtronic, *Comments*: unrestricted grant for conducting the REVASCAT trial*; *UNRELATED*: *Payment for Lectures Including Service on Speakers Bureaus*: Medtronic, *Comments*: less than US $2000. Mayank Goyal—*UNRELATED*: *Grant*: Medtronic, *Comments*: part funding for the ESCAPE trial and funding for the HERMES collaboration*; *Consulting Fee or Honorarium*: Medtronic, Stryker, MicroVention, *Comments*: for education and advice related to acute stroke; *Other*: GE Healthcare, *Comments*: licensing agreement for systems of stroke diagnosis. *Money paid to the institution.

REFERENCES

1. Berkhemer OA, Fransen PS, Beumer D, et al. **A randomized trial of intraarterial treatment for acute ischemic stroke**. *N Engl J Med* 2015; 372:11–20 CrossRef Medline
2. Goyal M, Demchuk AM, Menon BK, et al; ESCAPE Trial Investigators. **Randomized assessment of rapid endovascular treatment of ischemic stroke.** *N Engl J Med* 2015;372:1019–30 CrossRef Medline
3. Campbell BC, Mitchell PJ, Kleinig TJ, et al; EXTEND-IA Investigators. **Endovascular therapy for ischemic stroke with perfusion-imaging selection.** *N Engl J Med* 2015;372:1009–18 CrossRef Medline
4. Saver JL, Goyal M, Bonafe A, et al; SWIFT PRIME Investigators. **Stent-retriever thrombectomy after intravenous t-PA vs. t-PA alone in stroke.** *N Engl J Med* 2015;372:2285–95 CrossRef Medline
5. Jovin TG, Chamorro A, Cobo E, et al; REVASCAT Trial Investigators. **Thrombectomy within 8 hours after symptom onset in ischemic stroke.** *N Engl J Med* 2015;372:2296–306 CrossRef Medline
6. Macrae IM. **Preclinical stroke research: advantages and disadvantages of the most common rodent models of focal ischaemia.** *Br J Pharmacol* 2011;164:1062–78 CrossRef Medline
7. Duncan PW, Jorgensen HS, Wade DT. **Outcome measures in acute stroke trials: a systematic review and some recommendations to improve practice.** *Stroke* 2000;31:1429–38 CrossRef Medline
8. Quinn TJ, Dawson J, Walters MR, et al. **Functional outcome measures in contemporary stroke trials.** *Int J Stroke* 2009;4:200–05 Medline
9. Banks JL, Marotta CA. **Outcomes validity and reliability of the modified Rankin scale: implications for stroke clinical trials: a literature review and synthesis.** *Stroke* 2007;38:1091–96 CrossRef Medline
10. Thijs VN, Lansberg MG, Beaulieu C, et al. **Is early ischemic lesion volume on diffusion-weighted imaging an independent predictor of stroke outcome? A multivariable analysis.** *Stroke* 2000;31:2597–602 CrossRef Medline
11. Wardlaw JM, Keir SL, Bastin ME, et al. **Is diffusion imaging appearance an independent predictor of outcome after ischemic stroke?** *Neurology* 2002;59:1381–87 CrossRef Medline
12. Saver JL, Johnston KC, Homer D, et al. **Infarct volume as a surrogate or auxiliary outcome measure in ischemic stroke clinical trials: the RANTTAS investigators.** *Stroke* 1999;30:293–98 CrossRef Medline
13. Kimura K, Sakamoto Y, Iguchi Y, et al, **Serial changes in ischemic lesion volume and neurological recovery after t-PA therapy.** *J Neurol Sci* 2011;304:35–39 CrossRef Medline
14. Rha JH, Saver JL. **The impact of recanalization on ischemic stroke outcome: a meta-analysis.** *Stroke* 2007;38:967–73 CrossRef Medline
15. Al-Ajlan FS, Goyal M, Demchuk AM, et al; ESCAPE Trial Investigators. **Intra-arterial therapy and post-treatment infarct volumes: insights from the ESCAPE randomized controlled trial.** *Stroke* 2016; 47:777–81 CrossRef Medline
16. Saver JL. **Novel end point analytic techniques and interpreting shifts across the entire range of outcome scales in acute stroke trials.** *Stroke* 2007;38:3055–62 CrossRef Medline
17. Kosior JC, Idris S, Dowlatshahi D, et al; PREDICT/Sunnybrook CTA ICH study investigators. **Quantomo: validation of a computer-assisted methodology for the volumetric analysis of intracerebral haemorrhage.** *Int J Stroke* 2011;6:302–05 CrossRef Medline
18. Zaidat OO, Yoo AJ, Khatri P, et al; STIR Thrombolysis in Cerebral Infarction (TICI) Task Force. **Recommendations on angiographic revascularization grading standards for acute ischemic stroke: a consensus statement.** *Stroke* 2013;44:2650–63 CrossRef Medline
19. Baron RM, Kenny DA. **The moderator-mediator variable distinction in social psychological research: conceptual, strategic, and statistical considerations.** *J Pers Soc Psychol* 1986;51:1173–82 CrossRef Medline
20. Sajobi TT, Menon BK, Wang M, et al; ESCAPE Trial Investigators. **Early trajectory of stroke severity predicts long-term functional outcomes in ischemic stroke subjects: results from the ESCAPE Trial (Endovascular Treatment for Small Core and Anterior Circulation Proximal Occlusion With Emphasis on Minimizing CT to Recanalization Times).** *Stroke* 2017;48:105–10 CrossRef Medline
21. Bulterijs S, Hull RS, Björk VC et al. **It is time to classify biological aging as a disease.** *Front Genet* 2015;6:205 CrossRef Medline

Two-Center Experience in the Endovascular Treatment of Ruptured and Unruptured Intracranial Aneurysms Using the WEB Device: A Retrospective Analysis

J. Popielski, A. Berlis, W. Weber, and S. Fischer

ABSTRACT

BACKGROUND AND PURPOSE: The safety and efficacy of the Woven EndoBridge (WEB) device for the treatment of cerebral aneurysms has been investigated in several studies. Our objective was to report the experience of 2 neurovascular centers with the WEB device in the treatment of broad-based intracranial aneurysms, including the technical feasibility and safety as well as short- and midterm angiographic and clinical follow-up-results.

MATERIALS AND METHODS: We performed a retrospective analysis of all ruptured and unruptured aneurysms treated with a WEB device (WEB Single-Layer and Single-Layer Sphere) between August 2014 and February 2017. Primary outcome measures included the feasibility of implantation and the angiographic outcome. Secondary outcome measures included the clinical outcome at discharge and procedural complications.

RESULTS: One hundred two aneurysms in 101 patients, including 37 (36.3%) ruptured aneurysms, were treated with the WEB device. Implantation was successful in 98 (96.1%) aneurysms. Additional devices (stents/coils) were necessary in 15.3% (15/98) of aneurysms. Procedural complications occurred in 4.9% (5/102). Of these, 4 were thromboembolic events and 1 was an intraprocedural rupture. Angiographic follow-up at 3 and 12 months was available for 79.6% (78/98) and 50.0% (49/98) of all aneurysms to date, respectively, showing a sufficient aneurysm occlusion in 80.7% (63/78) at 3 months and 77.6% (38/49) at 12 months. Delayed aneurysm ruptures have not been observed during the follow-up period to date.

CONCLUSIONS: The WEB device offers a safe and effective treatment option for broad-based intracranial aneurysms without the need for dual antiplatelet therapy.

ABBREVIATIONS: ASA = acetylsalicylic acid; WEB = Woven EndoBridge; DL = Dual-Layer; SL = Single-Layer; SLS = Single-Layer Sphere

Endovascular occlusion of both ruptured and unruptured intracranial aneurysms has developed to a standard treatment with favorable results during the past decades.[1-3] Standard coiling of wide-neck bifurcation aneurysms has a relevant risk of thromboembolic complications with lower occlusion rates.[4] Several endovascular concepts address the problem of wide-neck aneurysms, whereas stent-assisted coiling and flow diversion represent the most popular techniques besides a growing number of innovative endovascular concepts.[5,6]

Received May 4, 2017; accepted after revision August 7.

From the Institut für Diagnostische und Interventionelle Radiologie, Neuroradiologie, Nuklearmedizin (J.P., W.W., S.F.), Knappschaftskrankenhaus Bochum-Langendreer, Universitätsklinik, Bochum, Germany; and Klinik für Diagnostische Radiologie und Neuroradiologie (A.B.), Klinikum Augsburg, Augsburg, Germany.

Please address correspondence to Sebastian Fischer, MD, Knappschaftskrankenhaus Bochum-Langendreer, Universitätsklinik, Institut für Diagnostische und Interventionelle Radiologie, Neuroradiologie, Nuklearmedizin, In der Schornau 23–25, 44892 Bochum, Germany; e-mail: sebif101@googlemail.com

http://dx.doi.org/10.3174/ajnr.A5413

Techniques that aim to reconstruct the parent artery with neointimal growth over the aneurysmal orifice require an implant inside the parent artery, with the imperative of using antiplatelet medications. Stent-assisted coiling or flow diversion is therefore limited to unruptured aneurysms in most cases.[7] Piotin et al[8] reported that stents were associated with increased morbidity compared with standard coiling. While extra-aneurysmal flow diverters have proved their effectiveness in sidewall aneurysms, the concept remains challenging in bifurcation aneurysms because 1 branch is covered by the device. Nevertheless, Yavuz et al[9] presented a series of 25 MCA bifurcation aneurysms treated with the Pipeline Embolization Device (Covidien, Irvine, California).

The introduction of the Woven EndoBridge (WEB) aneurysm embolization system (Sequent Medical, Aliso Viejo, California) as a self-expanding intra-aneurysmal flow diverter in 2010 offered an innovative option for broad-based intracranial aneurysms without the need for concomitant dual antiplatelet therapy.

Here we report our experience with the WEB Single-Layer

(SL) and Single-Layer Sphere (SLS) devices in the endovascular treatment of ruptured and nonruptured intracranial aneurysms.

MATERIALS AND METHODS

WEB Devices Used in This Series

The WEB device is an intra-aneurysmal implant consisting of a self-expanding nitinol braid. The device is electrothermally detachable and is introduced through microcatheters with diameters dependent on the size of the device. The initial version was introduced as the WEB Dual-Layer (DL) in 2010, with a second mesh placed inside the primary braid to achieve increased coverage at the neck region of the aneurysm. This version was replaced by the WEB SL and WEB SLS in 2013, which are devices with a single-layer mesh, whereas the SLS version has a more spheric shape, designed for the treatment of rounded aneurysms compared with the barrel-like shape of the SL version. The available diameters of the recent versions range from 4 (144 wires) to 11 mm (216 wires) in 1-mm increments, with lengths ranging from 3 to 7 mm for the SL version. The length of the SLS device is determined by its diameter and results from a subtraction of 1.6 mm. Devices up to a diameter of 7 mm have been compatible with a 0.021-inch microcatheter since 2015, whereas diameters of 8 and 9 mm need an 0.027-inch microcatheter, and the largest sizes of 10–11 mm require a 0.033-inch microcatheter.[6,10] The VIA Microcatheter (Sequent Medical) is designed for the delivery of the WEB device.

The aneurysms analyzed in the present study were exclusively treated with WEB SL and SLS versions.

Inclusion and Exclusion Criteria

Each case was discussed at an institutional neurovascular board, including neurosurgical, neurologic, and neurointerventional experts at the 2 participating neurointerventional centers. The decision for endovascular treatment was reached by consensus. The final endovascular treatment strategy was determined by the operator.

Criteria to use the WEB device were a wide neck and a fundus width between 3 and 10 mm. Arguments in favor of endovascular treatment compared with neurosurgical clipping were an aneurysm location in the posterior circulation and an anticipated surgical difficulty. Saccular aneurysms with a maximum width below 3 mm or above 10 mm (+1/−1 rule described below), those with a dome-to-neck ratio of <1 (missing stability for the WEB device), and fusiform and extradural aneurysms were not considered.

All patients were informed of the planned treatment usually before admission but at least 1 day before the procedure, except those with an acute SAH. The clinical status of each patient with an unruptured aneurysm was graded by the modified Rankin Scale on admission, at discharge, and at each follow-up visit by a neurovascular team member. Patients with an acute SAH were graded by the Hunt and Hess scale initially. All clinical and radiographic data were analyzed in retrospect. Complications that resulted in a permanent clinical decline were defined as relevant and were analyzed separately. The study was approved by the local ethics committee.

Endovascular Procedure and Device Selection

Procedures were performed with the patient under general anesthesia by 4 experienced interventionalists. In elective procedures, a dual antiplatelet medication with acetylsalicylic acid (ASA) and clopidogrel was initiated at least 1 day before the procedure (500 mg of ASA and 600 mg of clopidogrel followed by a daily dose of 100 mg of ASA and 75 mg of clopidogrel) to permit the possibility of stent-assisted coiling, if needed. The response to the antiplatelet medication was not routinely tested. Single antiplatelet therapy with 100 mg of ASA daily was continued for at least 1 month. All procedures were performed with an initial intravenous bolus of heparin (5000 IU).

An 8F/6F combination of guiding catheters or a 6F catheter alone was introduced into the target artery. The aneurysm was visualized in an angulation without superimposition of surrounding branches.

Size selection of the WEB resulted from exact calibrated measurements of the aneurysm (width and height of the fundus, width of the neck) in 2 orthogonal projections based on a 3D rotational angiographic dataset. Because a stable position of the WEB inside the aneurysm results from a slight oversizing of the device, 1 mm was added to the average width of the aneurysms to assure good wall apposition of the device inside the aneurysm. The height of the selected device was therefore 1 mm lower than the average height of the aneurysm to adjust for the longitudinal increase caused by the horizontal compression (+1/−1 rule).[11]

An appropriate VIA microcatheter was placed inside the aneurysmal fundus followed by the deployment of the WEB, which results from a combination of forward pushing of the device with simultaneous withdrawal of the microcatheter.

At this point in the procedure, the appropriate position of the WEB device was documented under fluoroscopy or an additional angiographic run including 3D angiography. In procedures with residual contrast filling between the device and the aneurysmal wall (radial flow), the WEB was withdrawn and a larger device was implanted. A slight extension of the mesh and the proximal detachment marker into the parent artery was tolerated if no evidence of flow compromise or thrombus formation occurred during an observational period of at least 10 minutes. The device was removed or a self-expanding stent was implanted to protect the parent artery in cases of distinct malposition. The stable position of the WEB was documented on a final angiographic run after detachment under continuous fluoroscopy.

Follow-Up Schedule

Angiographic follow-up examinations were scheduled at 3 and 12 months after treatment. The angiographic results were evaluated independently by 2 neuroradiologists on the basis of a 5-grade scale as described by Caroff et al[12]: 1, no residual flow in aneurysm/WEB; 2, opacification of the proximal recess of WEB; 3, neck remnant; 4, residual flow inside the WEB; 5, aneurysm remnant. Grades 1 and 2 were considered complete occlusion. Grades 1–3 indicated a sufficient aneurysm occlusion.

Statistical Analysis

The statistical analysis of all variables was performed independently with Excel (Microsoft, Redmond, Washington). Continuous variables were described by median and range. Independent variables were characterized as percentages.

Ethical Standards and Patient Consent

We declare that all human and animal studies have been approved by the ethics committee of Ruhr Universität Bochum, Germany, and have therefore been performed in accordance with the ethical standards laid down in the 1964 Declaration of Helsinki and its later amendments. A separate informed consent from each patient before inclusion in this study was not required due to the design of the study.

RESULTS

Patient Population

Between August 2014 and February 2017, one hundred one patients (median age, 58.6 years; range, 28–89 years) with 102 intracranial aneurysms were treated.

Aneurysm Characteristics

Of the 102 aneurysms treated in this series, 37 were acutely ruptured (maximum of 7 days from SAH to treatment), 60 were incidental findings, and 5 were remnants of previously coiled or clipped aneurysms. The median fundus width of all aneurysms was 6.0 mm (range, 4–10 mm) with a median neck width of 4.6 mm (range, 4–7 mm). Tables 1 and 2 summarize the locations and baseline characteristics.

Table 1: Baseline patient ($n = 101$) characteristics

Without Hemorrhage		SAH	
Total	64 (100%)		37 (100%)
mRS 0	52 (81.3%)	HH 1	10 (27.1%)
mRS 1	6 (9.4%)	HH 2	9 (24.3%)
mRS 2	2 (3.1%)	HH 3	5 (13.5%)
mRS 3	2 (3.1%)	HH 4	5 (13.5%)
mRS 4	2 (3.1%)	HH 5	8 (21.6%)
mRS 5	0 (0.0%)		

Note:—HH indicates Hunt and Hess.

Table 2: Baseline aneurysm ($n = 102$) characteristics

Aneurysm	No. (%)	Unruptured	Ruptured
Total	102 (100%)	65 (100%)	37 (100%)
Anterior circulation	88 (86.3%)	60 (92.3%)	28 (75.7%)
Posterior circulation	14 (13.7%)	5 (7.7%)	9 (24.3%)
AcomA	33 (32.4%)	21 (32.3%)	12 (32.4%)
MCA	44 (43.1%)	34 (52.3%)	10 (27.1%)
AchA	1 (1.0%)	0 (0.0%)	1 (2.7%)
ICA-T	7 (6.9%)	5 (7.7%)	2 (5.4%)
PcomA	3 (2.9%)	0 (0.0%)	3 (8.1%)
BA tip	12 (11.8%)	4 (6.2%)	8 (21.6%)
SCA	2 (1.9%)	1 (1.5%)	1 (2.7%)

Note:—AchA indicates anterior choroidal artery; AcomA, anterior communicating artery; BA, basilar artery; ICA-T, terminus of internal carotid artery; PcomA, posterior communicating artery; SCA, superior cerebellar artery.

Procedural Results

Implantation was successful in all except 4 aneurysms (3.9%), which were excluded from the follow-up analysis. In 2 cases of MCA aneurysms, the WEB was withdrawn due to a flow deceleration in the MCA branch originating from the aneurysm base. Another MCA aneurysm was not accessible with the microcatheter because of a severe elongation of the ICA, and 1 anterior communicating artery aneurysm was in a very tight angulation to the parent artery. The treatment strategy was changed to stent-assisted coiling in 3 procedures, and 1 aneurysm was finally clipped.

The procedure was completed with a WEB device only as intended in 83 (81.4%) aneurysms (Fig 1), whereas in 7 (6.9%), additional coils were necessary to completely fill the aneurysm. In another 8 (7.8%) procedures, a self-expanding stent was implanted to guarantee a stable position of the WEB. This was combined with additional coiling in 1 aneurysm.

Immediate and Follow-Up Angiographic Results

In the Entire Series. A first follow-up angiography was available for 78/98 (79.6%) aneurysms to date after a median of 3.5 months (range, 1.0–21.0 months), showing complete occlusion (grades 1 and 2) in 47/78 (60.2%) and sufficient aneurysm occlusion (grades 1–3) in 63/78 (80.7%). Of the remaining 20 patients, 9 died as consequence of their SAH, 9 were lost to follow-up, 1 died of causes unrelated to the treated aneurysm, and 1 died of causes related to the procedure (see below). A second follow-up angiography was performed in 49/98 (50.0%) after a median of 8.6 months (range, 2.0–20.0 months), showing complete occlusion in 29/49 (59.2%) and sufficient occlusion in 38/49 aneurysms (77.6%). Retreatment has been necessary in 10 aneurysms to date due to a regrowth of the aneurysms or a clustering of the WEB.

In Unruptured Aneurysms. At least 1 follow-up angiography was performed in 91.8% (56/61) of all unruptured aneurysms, showing complete occlusion in 60.8% (34/56) and sufficient occlusion in 82.2% (46/56). Thirty-seven of the 61 aneurysms (60.7%) were evaluated in a second angiography to date. Of those, 59.4% (22/37) were completely occluded and 78.3% (29/37) showed sufficient occlusion.

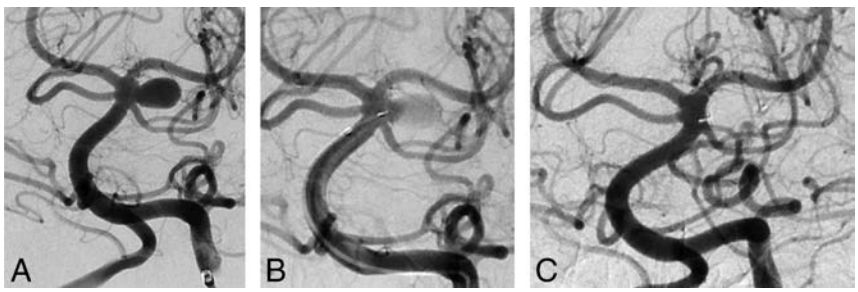

FIG 1. *A*, Incidental finding of an aneurysm of the origin of the superior cerebellar artery (anteroposterior view). *B*, Implantation of a WEB SL 7–4 without flow disturbance in the parent arteries (anteroposterior view). *C*, Three-month follow-up angiography with complete occlusion of the aneurysm and reconstruction of the neck area (anteroposterior view).

In Ruptured Aneurysms. Of the 37 aneurysms treated in the acute phase, 22 (59.5%) and 12 (32.4%) were examined at the first and second follow-ups. At the first follow-up, complete occlusion was 59.1% (13/22) compared with 58.3% (7/12) at the second follow-up. Accordingly, sufficient occlusion was 77.3% (17/22) and 75.0% (9/12).

Tables 3–5 summarize the immediate and follow-up angiographic results depending on the status of rupture.

Table 3: Immediate and follow-up results of ruptured aneurysms[a]

	Immediate	3-Month Follow-Up	12-Month Follow-Up
Total	37 (100%)	22 (59.5%)	12 (32.4%)
Grade			
1	5 (13.5%)	11 (50.0%)	6 (50.0%)
2	1 (2.7%)	2 (9.1%)	1 (8.3%)
3	2 (5.4%)	4 (18.2%)	2 (16.7%)
4	29 (78.4%)	2 (9.1%)	1 (8.3%)
5	0 (0.0%)	3 (13.6%)	2 (16.7%)
Complete occlusion (grades 1 and 2)		13 (59.1%)	7 (58.3%)
Sufficient occlusion (grades 1–3)		17 (77.3%)	9 (75.0%)

[a] 1 indicates no residual flow in aneurysm/WEB; 2, opacification of the proximal recess of the WEB; 3, neck remnant; 4, residual flow inside the WEB; 5, aneurysm remnant.

Table 4: Immediate and follow-up results of unruptured aneurysms[a]

	Immediate	3-Month Follow-Up	12-Month Follow-Up
Total	61 (100%)	56 (91.8%)	37 (60.7%)
Grade			
1	3 (4.9%)	22 (39.4%)	15 (40.5%)
2	5 (8.2%)	12 (21.4%)	7 (18.9%)
3	0 (0.0%)	12 (21.4%)	7 (18.9%)
4	53 (86.9%)	5 (8.9%)	3 (8.2%)
5	0 (0.0%)	5 (8.9%)	5 (13.5%)
Complete occlusion (grades 1 and 2)		34 (60.8%)	22 (59.4%)
Sufficient occlusion (grades 1–3)		46 (82.2%)	29 (78.3%)

[a] 1 indicates no residual flow in aneurysm/WEB; 2, opacification of the proximal recess of the WEB; 3, neck remnant; 4, residual flow inside the WEB; 5, aneurysm remnant.

Table 5: Immediate and follow-up results of ruptured and unruptured aneurysms[a]

	Immediate	3-Month Follow-Up	12-Month Follow-Up
Total	98 (100%)	78 (79.6%)	49 (50.0%)
Grade			
1	8 (8.2%)	33 (42.3%)	21 (42.9%)
2	6 (6.1%)	14 (17.9%)	8 (16.3%)
3	2 (2.0%)	16 (20.5%)	9 (18.4%)
4	82 (83.7%)	7 (9.0%)	4 (8.1%)
5	0 (0.0%)	8 (10.3%)	7 (14.3%)
Complete occlusion (grades 1 and 2)		47 (60.2%)	29 (59.2%)
Sufficient occlusion (grades 1–3)		63 (80.7%)	38 (77.6%)

[a] 1 indicates no residual flow in aneurysm/WEB; 2, opacification of the proximal recess of the WEB; 3, neck remnant; 4, residual flow inside the WEB; 5, aneurysm remnant.

Peri- and Early Postprocedural Clinically Relevant Complications

Clinically relevant complications occurred in 5 patients (4.9%), resulting in morbidity and mortality rates of 4.0% (4/101 patients) and 1.0% (1/101 patients), respectively.

Of those, 4 were thromboembolic compared with 1 intraprocedural rupture. One patient with an incidental middle cerebral artery aneurysm (M1 segment) and the temporal branch arising close to the aneurysm neck was treated with a WEB SL (6 × 3) device. The proximal part of the device slightly extended into the parent artery without evidence of thrombus formation. Nevertheless, the operator decided to place a self-expanding stent (LVIS; MicroVention, Tustin, California) to stabilize the device. The procedure was finished without flow compromise in the parent artery or the temporal branch. Approximately 30 minutes later, the patient developed a hemiparesis of the left arm. Angiography revealed a thrombotic occlusion of the temporal branch with no flow compromise in the M1 segment. The aneurysm showed complete occlusion. After an interdisciplinary discussion, 20 mL of alteplase (Actilyse; Boehringer Ingelheim Pharma, Germany) was infused for 30 minutes with a microcatheter placed in the proximal M1 segment, which resulted in a complete recanalization of the branch. The decision to use alteplase was derived by consensus, even though a recently published meta-analysis showed lower morbidity rates with glycoprotein IIb/IIIa inhibitors.[13] The paresis of the left arm remained unchanged (mRS 3). MR imaging performed 2 days later revealed an ischemic lesion in the right MCA territory.

Another 89-year-old patient with a ruptured ICA posterior communicating artery aneurysm was treated with a WEB SL (5 × 3) without extension into the ICA; 30 minutes after the procedure, the patient showed a left-sided hemiplegia. Angiography revealed a thrombotic occlusion of the terminal ICA, treated by an intra-arterial infusion of 33 mL of tirofiban without complete resolution of the thrombus after an observational period of 120 minutes. A mechanical thrombectomy with a pREset system (phenox, Bochum, Germany) resulted in complete recanalization. Another 20 minutes later, angiography showed a recurrent thrombus formation at the aneurysm orifice, which was successfully treated with a self-expanding stent (Neuroform Atlas; Stryker Neurovascular, Kalamazoo, Michigan). The patient was placed on ticagrelor thereafter. The procedure was terminated without evidence of further thrombus formation or an intracranial hemorrhage. The hemiplegia remained. One day later the patient declined finally to a comatose status. CT revealed a complete infarction of the right MCA and anterior cerebral artery territory with massive swelling. A day later, the patient died.

The remaining thromboembolic complications both occurred in incidental aneurysms (MCA and anterior cerebral artery) treated with additional self-expanding stents (LVIS). Both patients showed clinically relevant strokes on postprocedural CT scans without evidence of in-stent thrombosis, probably related to distal emboli caused by the stent implantation resulting in an mRS grade of 3.

In 1 case of a ruptured ICA aneurysm, a rerupture occurred with a VIA 27 microcatheter. The microcatheter was left in place followed by the implantation of a WEB (SL 8 × 6) partially outside the aneurysm, which resulted in prompt hemostasis. The remaining aneurysm was then occluded by stent-assisted coiling (Neuroform Atlas). A left-sided hemiparesis resolved completely (Fig 2*A*–*D*).

Delayed Complications

Neither delayed aneurysm ruptures nor thromboembolic complications have been observed during the follow-up period to date.

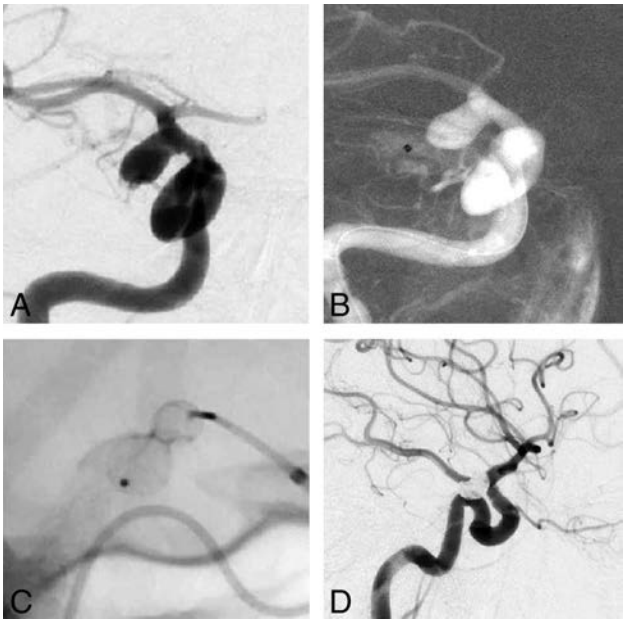

FIG 2. *A*, Acutely ruptured broad-based ICA posterior communicating artery aneurysm (anteroposterior view). *B*, Catheterization followed by aneurysm rupture; VIA 27 microcatheter outside the aneurysm (roadmap in the anteroposterior view). *C*, Placement of a WEB SL 8–6 partly outside the aneurysm showing a constriction of the WEB at the point of rupture (single image without subtraction). *D*, Final complete occlusion of the aneurysm by stent-assisted coiling (lateral view).

DISCUSSION

In this retrospective study, we analyzed the angiographic and clinical results in the treatment of both ruptured and unruptured intracranial aneurysms with the WEB device.

The technical success rate of 96.1% and the rate of thromboembolic complications (3.9%) are comparable with those reported in the literature.[14-21]

The main drawback of stent-assisted coiling is the need for dual antiplatelet medication. Nishido et al[22] compared the clinical and angiographic results of 1815 saccular aneurysms treated with stents ($n = 299$) with those treated without ($n = 1492$). They found a lower rate of recurrence in the group treated with stents, while the rate of complications was significantly higher (9.4% versus 5.6%). Adeeb et al,[23] in their series of 74 aneurysms treated with a single stent, observed an immediate complete occlusion rate of 52.7% with an improvement to 70.3% during the follow-up period of 15.2 months. These results are comparable with those in our series.

Our results are in line with those of previously published series: Pierot et al[17] presented the results of 55 aneurysms treated at 10 neurointerventional centers. They found a 1-year complete occlusion rate of 54.0% and a neck remnant in 26.0%. The rate of ruptured aneurysms in this series was 7.3% ($n = 4$). The mortality rate at 1 year was 2.0%. The results of 2 good clinical practice studies with the WEB device (WEBCAST and French Observatory) are analyzed in another publication of Pierot et al.[24] In the cumulated series of 114 aneurysms treated with the WEB DL ($n = 82$) and the WEB SL/SLS ($n = 32$), 10 aneurysms were ruptured. The rate of thromboembolic events was significantly higher in the group of 16 patients without a prophylactic antiplatelet medication (56.3%) compared with those with 1 antiplatelet agent 12% (6/50). These data might diminish the advantage of the WEB device against stent-assisted coiling and indicate the need for at least 1 antiplatelet agent in elective procedures, but 71.9% of all aneurysms in this series were treated with the WEB DL version, which might be of a higher thrombogenicity, probability due to the double-layer surface at the aneurysm orifice.

A dual antiplatelet therapy was initiated in all elective patients of our series. The medication with ASA, 100 mg, was continued for at least 4 weeks as described above. In patients with an acute SAH, the procedure was performed without a periprocedural antiplatelet medication followed by a monotherapy with 100 mg of ASA for at least 4 weeks.

Fiorella et al[18] presented the 30-day safety results of the WEB Intrasaccular Therapy (WEB-IT) study. They recommended a monotherapy with 100 mg of ASA before the procedure in less complex cases, while in broad-based anatomies, they initiated a dual antiplatelet therapy continued for 90 days if a protrusion of the WEB into the parent artery occurred. They observed 7 minor ischemic strokes during the follow-up period, with 2 of them resulting in an mRS of 1. Adjunctive devices were used in 7 aneurysms (2 stents, 7 balloons). Treatment with the WEB device failed in 2 patients. The mortality rate in the entire series is 0% to date.

Technical Aspects

As described above, we encountered 1 intraprocedural rupture. Van Rooij et al[21] in their series of 32 acutely ruptured aneurysms treated with the WEB device observed no procedural perforation. However, acutely ruptured aneurysms are generally known for their higher risk of procedural perforations.[16,25] Deployment of the WEB should be performed without contact of the device to the aneurysm wall until two-thirds of the mesh is unfolded. At this point, the device engages a centered position inside the aneurysm with invagination of its tip. The possibility of implanting a WEB device with a 0.017-inch microcatheter (not used in our study) might ease the procedure.

Thromboembolic Complications

The rate of thromboembolic complications in our cohort is similar to that in other studies. Pierot et al[17] observed thromboembolic events in 9 of 51 (17.7%) patients. They found a trend toward lower thromboembolic complications with the WEB SL/SLS compared with the WEB DL version, which was not used in our series. Most interesting, 3 of the thromboembolic complications in our series occurred with self-expanding stents. This might indicate the positive relation between adjunctive devices and thromboembolic complications.

The importance of a meticulous case and device selection becomes clear against these findings because the need for additional devices will be lower with an exact fitting between the aneurysm and the WEB device.

Lawson et al[15] in their series of 22 aneurysms treated with the WEB device observed 1 symptomatic ischemic event. The WEB used is this case was oversized. These findings are similar to those of Caroff et al,[20] who found 2 strokes in their series due to the use

of oversized WEB devices. The authors concluded that undersizing can lead to recurrence and residual aneurysm, while excessive oversizing may promote clot formation and thromboembolism.

Follow-Up Results

While standard coiling procedures result in an absence of contrast media, aneurysms treated with the WEB frequently show a remaining perfusion after implantation. This impedes a direct comparison between the techniques and raises the question of sufficient protection from further ruptures. We did not observe any cases of aneurysm rupture during the follow-up period either in the incidental or ruptured group.

We classified the angiographic results on the basis of a 5-point scale as suggested by Caroff et al.[12] This, in contrast to a 3-point scale, allows differentiation between a typical aneurysm remnant, which might require retreatment in the future, and an opacification inside the mesh of the WEB, which might result in a contemporary intra-aneurysmal thrombosis without additional treatment.[26] Mine et al,[27] in their recently published series of 49 aneurysms treated with the WEB device, demonstrated that a small proximal recess related to the device should not be considered a remnant and remains stable with time. According to these findings, the rate of complete aneurysm occlusion at 3 and 12 months is 60.2% (47/78) and 59.2% (29/49), respectively, in our series.

Our results with a sufficient occlusion of almost 80% are comparable with those in previously published series. We have observed no major difference between ruptured and unruptured aneurysms during the follow-up period to date, though the comparability of the 2 groups is restricted due to the different sample sizes.

Advantages and Disadvantages in Ruptured Aneurysms

The main advantage is the possibility of treating ruptured aneurysms without periprocedural antiplatelet medication. Another major benefit consists of the reduced overall procedure time. An analysis of the WEB-IT study showed that one-third of all procedures were completed in <20 minutes.[18] This is in line with our experience, though we did not analyze the procedure times. We observed 1 intraprocedural rupture that was rapidly stopped by the implantation of the WEB, similar to the findings in the WEB-IT cohort with 2 hemorrhages. The capability of the WEB to induce hemostasis promptly is another advantage. The limitation in size and the learning curve with this new device might be considered a temporary drawback compared with standard concepts.

Limitations of the Study

Our study has several limitations. The retrospective character of the study with 2 different centers might cause inhomogeneity of the data. Factors such as the number of attempts before implantation of the device, duration of the procedure, and the learning curve were not considered. The limited number of treated aneurysms and follow-up data impedes a separate analysis of ruptured and unruptured aneurysms. The angiographic results were classified without an independent assessment.[28]

CONCLUSIONS

The WEB device offers a safe and effective treatment option for broad-based aneurysms, independent of the status of rupture, without the need for a dual antiplatelet therapy. Proper device selection appears to be a key factor in minimizing the risk of thromboembolic complications and may increase the rate of sufficient aneurysm occlusion. Further studies with longer follow-up data will prove the significance of the presented therapy.

Disclosures: Ansgar Berlis—*RELATED*: *Consulting Fee or Honorarium*: Sequent Medical, MicroVention, *Comments*: proctor contract; *UNRELATED*: *Consultancy*: Stryker, Medtronic, *Comments*: proctor contract; *Payment for Lectures Including Service on Speakers Bureaus*: Penumbra. Werner Weber—*RELATED*: *Consultancy:* R&D team of Sequent, MicroVention; *Payment for Lectures Including Service on Speakers Bureaus*: MicroVention; *Other*: proctoring the WEB device in Europe and Germany.* Sebastian Fischer—*UNRELATED*: *Board Membership*: Codman Neurovascular, *Comments*: Advisory Board; *Payment for Lectures Including Service on Speakers Bureaus*: Sequent Medical, *Comments*: speaking honorarium. *Money paid to the institution.

REFERENCES

1. Sorenson T, Lanzino G. **Trials and tribulations: an evidence-based approach to aneurysm treatment.** *J Neurosurg Sci* 2016;60:22–26 Medline
2. Falk Delgado A, Andersson T, Falk Delgado A. **Clinical outcome after surgical clipping or endovascular coiling for cerebral aneurysms: a pragmatic meta-analysis of randomized and non-randomized trials with short- and long-term follow-up.** *J Neurointerv Surg* 2017;9:264–77 CrossRef Medline
3. Henkes H, Fischer S, Weber W, et al. **Endovascular coil occlusion of 1811 intracranial aneurysms: early angiographic and clinical results.** *Neurosurgery* 2004;54:268–80; discussion 280–85 CrossRef Medline
4. Zhao B, Yin R, Lanzino G, et al. **Endovascular coiling of wide-neck and wide-neck bifurcation aneurysms: a systematic review and meta-analysis.** *AJNR Am J Neuroradiol* 2016;37:1700–05 CrossRef Medline
5. Pierot L, Biondi A. **Endovascular techniques for the management of wide-neck intracaranial bifurcation aneurysms: a critical review of the literature.** *J Neuroradiol* 2016;43:167–75 CrossRef Medline
6. Henkes H, Weber W. **The past, present and future of endovascular aneurysm treatment.** *Clin Neuroradiol* 2015;25(suppl 2):317–22 CrossRef Medline
7. Zhao B, Tan X, Yang H, et al. **Stent-assisted coiling versus coiling alone of poor-grade ruptured intracranial aneurysms: a multicenter study.** *J Neurointervent Surg* 2017;9:165–68 CrossRef Medline
8. Piotin M, Blanc R, Spelle L, et al. **Stent-assisted coiling of intracranial aneurysms: clinical and angiographic results in 216 consecutive aneurysms.** *Stroke* 2010;41:110–15 CrossRef Medline
9. Yavuz K, Geyik S, Saatci I, et al. **Endovascular treatment of middle cerebral artery aneurysms with flow modification with the use of the Pipeline embolization device.** *AJNR Am J Neuroradiol* 2014;35:529–35 CrossRef Medline
10. Armoiry X, Turjman F, Hartmann DJ, et al. **Endovascular treatment of intracranial aneurysms with the WEB device: a systematic review of clinical outcomes.** *AJNR Am J Neuroradiol* 2016;37:868–72 CrossRef Medline
11. Lescher S, du Mensil de Rochemont R, Berkefeld J. **Woven Endobridge (WEB) device for endovascular treatment of complex unruptured aneurysms: a single center experience.** *Neuroradiology* 2016;58:883–90 CrossRef Medline
12. Caroff J, Mihalea C, Klisch C, et al. **Single-layer WEBs: intrasaccular flow disrupters for aneurysm treatment—feasibility results from a European study.** *AJNR Am J Neuroradiol* 2015;36:1942–46 CrossRef Medline
13. Brinjikji W, Morales-Valero SF, Murad MH, et al. **Rescue treatment**

of thromboembolic complications during endovascular treatment of cerebral aneurysms: a meta-analysis. *AJNR Am J Neuroradiol* 2015;36:121–25 CrossRef Medline
14. Pierot L, Costalat V, Moret J, et al. **Safety and efficacy of aneurysm treatment with WEB: results of the WEBCAST study.** *J Neurosurg* 2016;214:1250–56 CrossRef Medline
15. Lawson A, Goddard T, Ross S, et al. **Endovascular treatment of cerebral aneurysms using the Woven Endo Bridge technique in a single center: preliminary results.** *J Neurosurg* 2017;126:17–28 CrossRef Medline
16. Asnafi S, Rouchaud A, Pierot L, et al. **Efficacy and safety of the Woven EndoBridge (WEB) device for the treatment of intracranial aneurysms: a systematic review and meta-analysis.** *AJNR Am J Neuroradiol* 2016;37:2287–92 CrossRef Medline
17. Pierot L, Gubucz I, Buhk JH, et al. **Safety and efficacy of aneurysm treatment with the WEB: results of the WEBCAST 2 study.** *AJNR Am J Neuroradiol* 2017;38:1151–55 CrossRef Medline
18. Fiorella D, Molineux A, Coon A, et al. **Demographic, procedural and 30-day safety results from the WEB Intra-saccular Therapy Study (WEB-IT).** *J Neurointerv Surg* 2017 Jan 17. [Epub ahead of print] CrossRef Medline
19. Clajus C, Strasilla C, Fiebig T, et al. **Initial and mid-term results from 108 consecutive patients with cerebral aneurysms treated with the WEB device.** *J Neurointerv Surg* 2017;9:411–47 CrossRef Medline
20. Caroff J, Mihaela C, Dargento F, et al. **Woven Endobridge (WEB) device for endovascular treatment of ruptured intracranial wide-neck aneurysms: a single center experience.** *Neuroradiology* 2014;56:755–61 CrossRef Medline
21. van Rooj WJ, Peluso JP, Bechan RS, et al. **WEB treatment of ruptured intracranial aneurysms.** *AJNR Am J Neuroradiol* 2016;37:1679–83 CrossRef Medline
22. Nishido H, Piotin M, Bartolini B, et al. **Analysis of complications and recurrences of aneurysm coiling with special emphasis on the stent-assisted technique.** *AJNR Am J Neuroradiol* 2014;35:339–44 CrossRef Medline
23. Adeeb N, Grissenauer C, Patel A, et al. **The use of single stent-assisted coiling in treatment of bifurcation aneurysms: a multicenter cohort study with proposal of a scoring system to predict complete occlusion.** *Neurosurgery* 2017 Jun 8. [Epub ahead of print] CrossRef Medline
24. Pierot L, Spelle L, Molyneux A, et al. **Clinical and anatomical follow-up in patients with aneurysms treated with the WEB device: 1-year follow-up report in the cumulated population of 2 prospective, multicenter series (WEBCAST and French Observatory).** *Neurosurgery* 2016;78:133–41 CrossRef Medline
25. Orrù E, Roccatagliata L, Cester G, et al. **Complications of endovascular treatment of cerebral aneurysms.** *Eur J Radiol* 2013;82:1653–58 CrossRef Medline
26. Fiorella D, Arthur A, Byrne J, et al. **Interobserver variability in the assessment of aneurysm occlusion with the WEB aneurysm embolization system.** *J Neurointerv Surg* 2015;7:591–95 CrossRef Medline
27. Mine B, Goutte A, Brisbois D, et al. **Endovascular treatment of intracranial aneurysms with the Woven EndoBridge device: mid term and long term results.** *J Neurointerv Surg* 2017 Feb 20. [Epub ahead of print] CrossRef Medline
28. Rezek I, Mousan G, Wang Z, et al. **Effect of core laboratory and multiple reader interpretation of angiographic images on follow-up outcomes of coiled cerebral aneurysms: a systematic review and meta-analysis.** *AJNR Am J Neuroradiol* 2013;34:1380–84 CrossRef Medline

Hemodynamic Changes Caused by Multiple Stenting in Vertebral Artery Fusiform Aneurysms: A Patient-Specific Computational Fluid Dynamics Study

N. Lv, W. Cao, I. Larrabide, C. Karmonik, D. Zhu, J. Liu, Q. Huang, and Y. Fang

ABSTRACT

BACKGROUND AND PURPOSE: The multiple stent placement technique has largely improved the long-term outcomes of intracranial fusiform aneurysms, but the hemodynamic mechanisms remain unclear. In this study, we analyzed the hemodynamic changes caused by different stent-placement strategies in patient-specific models using the computational fluid dynamics technique, aiming to provide evidence for clinical decision-making.

MATERIALS AND METHODS: Ten vertebral artery fusiform aneurysms were included, and their patient-specific computational fluid dynamics models were reconstructed. A fast virtual stent placement technique was used to simulate sequential multiple stent placements (from a single stent to triple stents) in the vertebral artery fusiform aneurysm models. Hemodynamic parameters, including wall shear stress, pressure, oscillatory shear index, relative residence time, and flow pattern, were calculated and compared among groups with different numbers of stents.

RESULTS: Virtual stents were deployed in all 10 cases successfully, consistent with the real stent configuration. Wall shear stress decreased progressively by 7.2%, 20.6%, and 25.8% as the number of stents increased. Meanwhile, relative residence time and pressure increased on average by 11.3%, 15.4%, and 45.0% and by 15.7%, 21.5%, and 28.2%. The oscillatory shear index showed no stable variation trend. Flow patterns improved by weakening the intensity of the vortices and displacing the vortex center from the aneurysmal wall.

CONCLUSIONS: Stent placement modifies hemodynamic patterns in vertebral artery fusiform aneurysms, which might favor thrombosis formation in the aneurysmal sac. This effect is amplified with the number of stents deployed. However, a potential risk of rupture or recanalization exists and should be considered when planning to use the multiple stent placement technique in vertebral artery fusiform aneurysms.

ABBREVIATIONS: CFD = computational fluid dynamics; OSI = oscillatory shear index; RRT = relative residence time; VAFA = vertebral artery fusiform aneurysm; WSS = wall shear stress

Vertebral artery fusiform aneurysm (VAFA) is the most frequent type of intracranial fusiform aneurysm, which is often associated with nerve compression or ischemia, but bleeding is relatively rare.[1,2] However, in case of rupture, the mortality and early rebleeding rate of fusiform aneurysms are even higher than for saccular aneurysms.[3] Since the development of neuroimaging techniques and interventional devices, endovascular treatment has been the primary method for VAFAs. Although flow diverters have shown their effectiveness in treating aneurysms, the risk of ischemic events in posterior circulation cannot be ignored, especially when vital branches are covered.[4] Therefore, stepwise overlapping stent placement is still a safer and more effective choice for VAFAs than flow diverters, and the long-term improvement has been demonstrated.[5]

Hemodynamic studies of saccular aneurysms have revealed that stent placement can reduce the impinge flow and wall shear stress (WSS); this effect may favor thrombus formation and consequently cure the aneurysm.[6] However, the morphology of fusiform aneurysms is entirely different from that of saccular aneurysms; this difference may result in unique flow patterns before and after stent placement. Most important, gaining knowledge of

Received February 14, 2017; accepted after revision August 4.

From the Department of Neurosurgery (N.V., W.C., D.Z., Y.F., Q.H., J.L.), Changhai Hospital, Second Military Medical University, Shanghai, China; National Scientific and Technical Research Council of Argentina (I.L.), Buenos Aires, Argentina; and MRI Core (C.K.), Houston Methodist Research Institute, Houston, Texas.

Nan Lv and Wei Cao contributed equally to this work and should be regarded as co-first authors.

This work was supported by the National Natural Science Foundation of China (grant Nos. 81571118 and 81301004), the National Research and Development Project of Key Chronic Diseases (grant No. 2016YFC1300700), and National Scientific and Technical Research Council of Argentina (grant Nos. PICT 2014-1730 and PICT 2015-0006).

Please address correspondence to Qinghai Huang, MD, and Yibin Fang, MD, Department of Neurosurgery, Changhai Hospital, Changhai Rd 168, Shanghai, 200433, China; e-mail: ocinhqh@163.com; fangyibin@vip.163.com

Indicates open access to non-subscribers at www.ajnr.org

http://dx.doi.org/10.3174/ajnr.A5452

Table 1: Clinical data of 10 patients with VAFAs

Patient No.	Age (yr)	Sex	Ruptured	Treatment	Follow-Up
Case 1	46	Male	No	3 EP	8 mo, cured
Case 2	53	Male	No	2 EP	12 mo, thrombosis formation
Case 3	39	Female	Yes	2 EP+coils	Withdraw
Case 4	37	Male	Yes	2 EP+coils	6 mo, cured
Case 5	51	Male	No	2 EP+coils	7 mo, thrombosis formation
Case 6	59	Male	No	3 EP	13 mo, cured
Case 7	49	Female	Yes	2 EP+coils	12 mo, cured
Case 8	46	Male	Yes	3 EP+coils	12 mo, cured
Case 9	60	Male	No	2 EP	6 mo, stable
Case10	46	Male	No	2 EP	12 mo, thrombosis formation

Note:—EP indicates Enterprise self-expanding stent.

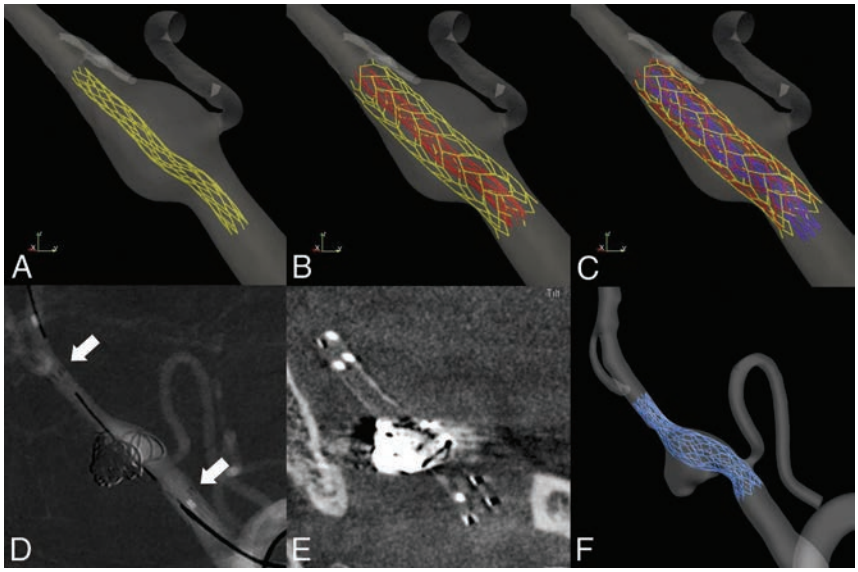

FIG 1. Process of virtual stent deployment. *A–C*, Three virtual Enterprise stents were deployed one by one. *D* and *E*, Location of real stents in 2D angiography and DynaCT (Siemens). *F*, Virtual stents deployed in a similar location with the real counterparts.

how intra-aneurysmal flow patterns change when the number of overlapping stents increases is of great importance because it may provide some evidence for optimizing stent-placement strategies.

In this study, we compared the hemodynamic changes caused by an increasing number of stents in patient-specific cases with measured boundary conditions with the computational fluid dynamics (CFD) technique, aiming to provide evidence for clinical decision-making for fusiform aneurysms.

MATERIALS AND METHODS

The institutional review board of the Second Military Medical University–affiliated Changhai Hospital approved this retrospective study, and the requirement for informed consent was waived. In addition, we have not conducted research outside our country of residence.

Patients and Imaging Acquisition

From January 2015 to December 2015, nineteen VAFAs in 19 patients were diagnosed in our hospital by 3D rotational angiography. Four patients were excluded because the lesion involved the extracranial V3 portion or basilar artery; and 5 patients were excluded because a double lumen sign was observed by DSA. Finally, 10 patients (male/female ratio = 8:2; mean age, 48.6 years) with 4 ruptured and 6 unruptured VAFAs were included in the study. The clinical data of the patients are shown in Table 1.

3D rotational angiography was performed with the Artis zee biplane angiographic system (Siemens, Erlangen, Germany). A 5-second DSA acquisition protocol was adopted, and 18 mL of contrast agent was injected through the vertebral artery at a rate of 3 mL/s. During the 5-second acquisition after a 1-second delay, a 200° rotation of the C-arm was performed to obtain 133 frames. All acquired 5-second DSA data were transferred to the syngo X Workplace (Siemens) for reconstruction of the 3D artery vessel tree and exported into a stereolithography format.

Models of VAFAs and Stents

The stereolithography models were segmented and smoothed by Geomagic Studio 9.0 software (Geomagic, Morrisville, North Carolina) and then imported into ICEM CFD 11.0 (ANSYS, Canonsburg, Pennsylvania) to create volume grids for the CFD simulations. The vessel wall was divided into 3 parts: aneurysm, parent artery, and other vessels.

The virtual stent model simulated the Enterprise self-expanding stent (Codman & Shurtleff, Raynham, Massachusetts), which is one of the most widely used commercial self-expanding stents. Three different stent sizes were constructed, including 4.5 mm (diameter)/22 mm (length), 4.5/28 mm, and 4.5/37 mm. The porosity and metal-coverage rates were 94% and 6%, respectively. The stents were reconstructed using the fast virtual stent method and deployed in the VAFA models as previously described by Larrabide et al.[7] The proximal and distal ends of the virtual stents were determined according to the realistic locations on 2D angiographic imaging of each patient. We simulated 3 scenarios: single stent, 2 overlapping stents, and 3 overlapping stents, as well as the presenting status (Fig 1).

CFD Analysis and Hemodynamic Parameters

CFD simulations were performed by CFX 11.0 (ANSYS). The vessel was considered a rigid wall with no-slip boundary conditions. The governing equations underlying the calculation were the Navier-Stokes formulations, with an assumption of a laminar and incompressible blood flow (density, $\rho = 1050$ kg/m^3; dynamic viscosity, $\mu = 0.00345$ Pa $\times$ s). Inlet boundary conditions for all scenarios were imposed by a pulsatile velocity waveform obtained from transcranial Doppler sonography, and to account for the effect of autoregulation of flow in the brain, we defined the outlet

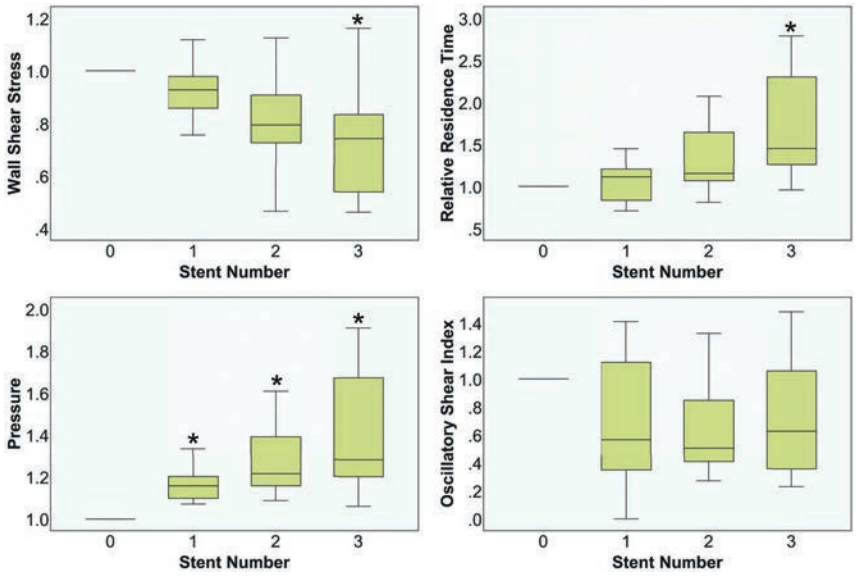

FIG 2. Box figure of hemodynamic analysis results. The *asterisk* indicates that the parameter was significantly different from the prestenting status.

Table 2: Hemodynamic parameters of VAFAs with different stenting strategies[a]

Parameters	0 Stent	1 Stent	2 Stents	3 Stents	*P* Value
Wall shear stress (%) ($n = 10$)	100	92.8	79.4	74.2	.003
Oscillatory shear index (%) ($n = 10$)	100	56.5	50.5	62.6	.169
Pressure (%) ($n = 10$)	100	115.7	121.5	128.2	<.001
Relative residence time (%) ($n = 10$)	100	111.3	115.4	145.0	.004

[a] Data are expressed as the median of the variation rate.

Table 3: *P* values of multiple comparisons among different stenting strategies

Parameters	0 Stent vs 1 Stent	0 Stent vs 2 Stents	0 Stent vs 3 Stents
WSS ($n = 10$)	.498	.063	.007
Pressure ($n = 10$)	.037	.001	<.001
RRT ($n = 10$)	.904	.251	.009

as the opening boundary condition with zero static pressure, assuming no downstream hemodynamic resistance. The cardiac cycle of 0.8 seconds was discretized at a time-step of 0.001 seconds for the numeric simulations. For each model, we simulated 3 continuous cardiac cycles to ensure the numeric stability of the simulation, and results are reported from the last cycle. The results were postprocessed and visualized with CFX 11.0.

Several hemodynamic parameters were calculated in this study: normalized wall shear stress, pressure of the aneurysmal wall, oscillatory shear index (OSI), and relative residence time (RRT). The time-averaged WSS was further averaged over the dome area (the entire luminal surface of the aneurysm sac) and then normalized by the average parent vessel WSS in the same patient to allow comparison among different patients. OSI, a nondimensional parameter, measures the directional change of WSS during the cardiac cycle. RRT, a combination of WSS and OSI, reflects the residence time of blood near the wall:

$$1)\qquad WSS = \frac{1}{T}\int_0^T |WSS_i|\, dt,$$

$$2)\qquad OSI = \frac{1}{2}\left\{1 - \frac{\left|\int_0^T WSS_i\, dt\right|}{\int_0^T |WSS_i|\, dt}\right\},$$

$$3)\qquad RRT = \frac{1}{(1 - 2 \times OSI) \times WSS} = \frac{1}{\frac{1}{T}\left|\int_0^T wss_i\, dt\right|},$$

where wss_i is the instantaneous *WSS* vector and *T* is the duration of the cycle. The *OSI* was averaged over the dome area.

Statistical Analysis

Statistical analyses were performed by using Excel 2003 (Microsoft, Redmond, Washington) and SAS 9.1 (SAS Institute, Cary, North Carolina). Hemodynamic parameters were normalized by the prestenting status values in each case to investigate the rate of variation caused by different stent placement strategies. Then the Kruskal-Wallis *H* test was used, followed by the Nemenyi test for multiple comparisons. $P < .05$ (2-sided) was the criterion for statistical significance.

RESULTS

All the virtual stents were deployed successfully in the 10 VAFA models with the 3 different strategies. Their locations (beginning and end of the stent) were consistent with the realistic stents derived from the 2D DSA images (Fig 1).

As the number of stents increased, WSS was observed to decrease gradually by 7.2%, 20.6%, and 25.8%; and after the third stent was implanted, the variation reached a significantly different level compared with the prestenting status. Meanwhile, the RRT revealed progressive elevation by 11.3%, 15.4%, and 45.0% and obtained a significant difference after the third stent used. The pressure on the aneurysmal wall increased by 15.7%, 21.5%, and 28.2% as 3 stents were implanted sequentially. The variation rate of the pressure was significantly different from the prestenting status, even when only 1 stent was deployed. As to the OSI, the modification was revealed to be fluctuant, without any significant difference compared with the prestenting status (Fig 2). The median variation of each parameter is shown in Table 2. Further comparison of different stent placement strategies with the prestenting status is shown in Table 3.

Changes of the flow patterns before and after stent implantation were observed by plotting the speed vector field. The results showed that the flow patterns were not significantly changed after stent implantation. However, the intensities of the vortices were

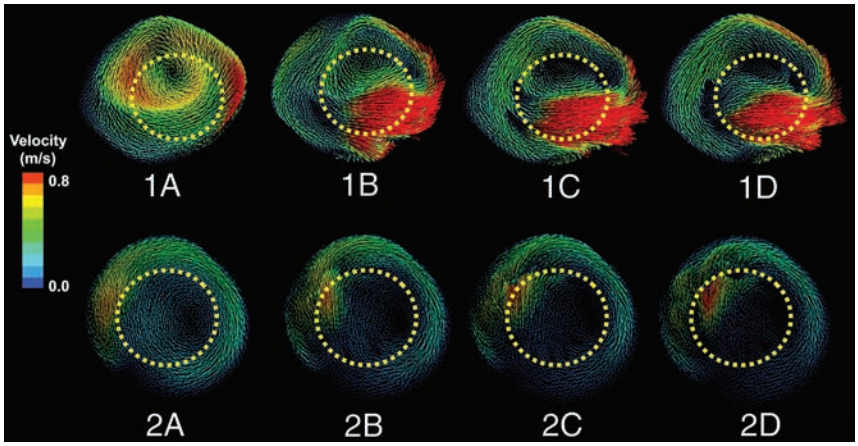

FIG 3. Flow patterns of 2 vertebral artery fusiform cases with different stent-placement strategies. One and 2 represent 2 individual cases. From left to right, flow patterns before and after implantation of 1–3 stents. The *yellow dotted lines* represent the positions of the stents. As the number of stents increased, blood flow inside the stent lumen concentrated and the flow rate accelerated, while the flow rate inside the aneurysmal sacs slowed and the vortex intensity weakened.

reduced, and the number of vortices in some cases was decreased (Fig 3).

DISCUSSION

Intracranial fusiform aneurysms are dilations of the parent artery without a clear aneurysmal neck. Similar to the widespread application of intracranial stent placement, endovascular treatment of fusiform aneurysms has been an important method and has greatly improved the long-term prognosis.[8] This effect was even more significant when multiple overlapping stents were used.[9,10] Although flow-diverter stents have been demonstrated to be an efficient treatment for aneurysms, their safety in posterior fusiform aneurysms still needs to be established by more evidence, especially because some important branches of smaller arteries might become covered.[11] Therefore, stepwise overlapping stent placement is still a safe and feasible choice when dealing with posterior fusiform aneurysms.

In saccular aneurysm studies, both in vivo and in silico experiments have demonstrated that multiple stent implantations can reduce injective blood flow and create a hemodynamic environment, which will promote thrombus formation and finally cure the aneurysm.[12] However, few hemodynamic studies have focused on intracranial fusiform aneurysms, in which hemodynamic patterns are different from those of saccular lesions. The application of the CFD technique makes hemodynamic studies in aneurysms more feasible and measurable. The fast virtual stent technique, first introduced by Larrabide et al,[7] provides an accurate and efficient method to consider the behavior of stents in patient-specific aneurysm models. Being different from previous finite element analysis and porous medium methods, the fast virtual stent method shows a high consistency with real stents and an impressive efficiency.[5,13] On the basis of this technique, we simulated the Enterprise stent and investigated the performance of different stent-placement strategies in 10 patient-specific VAFA models, aiming to obtain more evidence for clinical decision-making.

Thrombus formation in the aneurysm sac and consequent reconstruction of the parent artery are the primary goals of stent placement in fusiform aneurysms. The stents should increase the time of blood flow staying in the aneurysm to create an environment for thrombosis, to achieve these goals.[14] RRT is an important parameter that reflects the disturbed blood flow and its prolonged residence time in the aneurysmal sac. Tanemura et al[6] demonstrated that a single Enterprise stent could increase the RRT by 20% in a previous CFD study. Our study further demonstrated that the RRT gradually increases by sequential stent placements, which would likely provide a better environment for thrombus formation.

WSS is the most studied hemodynamic parameter that has been demonstrated to play an important role in aneurysm initiation, rupture, and recanalization.[15] Previous studies on saccular aneurysms suggested that stent implantation can lead to reduction of WSS and that this effect is related to the stent porosity—the lower the stent porosity, the more significantly the WSS decreased, and the distribution of WSS of the aneurysm became more uniform.[16] In our study, progressive reduction of WSS was observed in VAFAs as the number of stents increased, which was similar to that in saccular aneurysms. However, lower WSS might also increase the risk of aneurysmal growth and even rupture, which has been shown in our previous CFD studies in saccular lesions. We therefore deduce that if thrombosis does not occur in a relatively short time, the aneurysms would be at risk of deterioration.

Another concern is the observed elevation of the pressure in every case and even for only a single stent. In a hemodynamic study of flow diverters by Cebral et al,[17] a significant increase in pressure in some cases was observed after flow-diverter implantation, which, as those authors wrote, might lead to aneurysm rupture. However, some researchers had reported controversial results of a pressure decrease through virtual stent implantation in a fusiform aneurysm.[18] These findings indicate that the modification of pressure may be related to patient-specific characteristics, which, in turn, might be related to the morphologic differences of aneurysms and stents. The average elevation of pressure in this study was 28.2%. Coils might play a protective role in these VAFAs and should be considered, especially in cases in which CFD indicates a pressure increase.

The intra-aneurysmal flow pattern, reflecting the overall hemodynamic characteristics of an intracranial aneurysm, is reported to be more complex in ruptured aneurysms.[17] Stent implantation might modify the complex flow pattern into a simplified pattern by reducing the power of vortices and secondary flows, which may create favorable conditions for intra-aneurysmal thrombosis. In the present study, most of the cases had >2 independent vortices before stent placement and the number of

vortices changed during the cardiac cycle in the most complex situations. After stent deployment, weakening of the intensity of the vortices and shifting of the vortex center from the aneurysmal wall were observed in most cases, indicating an improvement of the flow pattern.

According to the results of multiple comparisons among different groups, single stents might not affect the hemodynamics as significantly as multiple stents. This possibility is consistent with clinical experience in that multiple stents improved the long-term results in VAFAs. However, as the number of stents increases, lower WSS and higher pressure might amplify the risk of rupture and recanalization; moreover, there was a greater theoretic chance for occlusion of some vital perforating branches. Although no hemorrhage or ischemic events were encountered in these patients, careful decision-making for the stent-placement strategy and timely follow-up are required.

There are several limitations in this study that might influence the results. First, because this is a patient-specific study and each case might have its own characteristics, the small sample size may be the main limitation. Second, the boundary conditions of the simulations were unified, and some perforating branches were neglected artificially. We did not consider potential changes of the inflow and outflow conditions, which might occur after stent placement. Changes of these boundary conditions will modify the absolute values of the investigated hemodynamic parameters. The observed trends however (ie, decrease in WSS, OSI, and RRT and an increase in pressure) are mostly driven by the separation of the hemodynamic environment of the aneurysmal sac from the parent artery and therefore should remain valid in a small or moderate variation of the boundary conditions. Absolute values derived from computational simulations should always be considered with caution and should be confirmed with actual measurements. In addition, the biologic process of thrombosis formation was too complex to simulate and was omitted.

CONCLUSIONS

The hemodynamic mechanism of endovascular stent placement in treating fusiform aneurysms can be explored with the virtual stent-placement technique. Stent placement modified hemodynamic patterns in VAFAs toward favoring thrombosis conditions in the aneurysmal sac. This effect was amplified with increasing numbers of stents. However, the potential risk of rupture or recanalization exists and should be considered when planning to use the multiple-stent technique in VAFAs.

Disclosures: Ignacio Larrabide—*RELATED: Support for Travel to Meetings for the Study or Other Purposes*: Agencia Nacional de Promoción Científica y Tecnológica, *Comments*: grant PICT 2015-0006*; *UNRELATED: Employment*: Consejo Nacional de Investigaciones Científicas Y Técnicas, *Comments*: Research Fellow. *Money paid to the institution.

REFERENCES

1. Drake CG, Peerless SJ. **Giant fusiform intracranial aneurysms: review of 120 patients treated surgically from 1965 to 1992.** *J Neurosurg* 1997;87:141–62 CrossRef Medline
2. Echiverri HC, Rubino FA, Gupta SR, et al. **Fusiform aneurysm of the vertebrobasilar arterial system.** *Stroke* 1989;20:1741–47 CrossRef Medline
3. Yoon W, Seo JJ, Kim TS, et al. **Dissection of the V4 segment of the vertebral artery: clinicoradiologic manifestations and endovascular treatment.** *Eur Radiol* 2007;17:983–93 CrossRef Medline
4. Siddiqui AH, Abla AA, Kan P, et al. **Panacea or problem: flow diverters in the treatment of symptomatic large or giant fusiform vertebrobasilar aneurysms.** *J Neurosurg* 2012;116:1258–66 CrossRef Medline
5. Augsburger L, Reymond P, Rufenacht DA, et al. **Intracranial stents being modeled as a porous medium: flow simulation in stented cerebral aneurysms.** *Ann Biomed Eng* 2011;39:850–63 CrossRef Medline
6. Tanemura H, Ishida F, Miura Y, et al. **Changes in hemodynamics after placing intracranial stents.** *Neurol Med Chir (Tokyo)* 2013;53:171–78 CrossRef Medline
7. Larrabide I, Kim M, Augsburger L, et al. **Fast virtual deployment of self-expandable stents: method and in vitro evaluation for intracranial aneurysmal stenting.** *Med Image Anal* 2012;16:721–30 CrossRef Medline
8. Yang P, Zhao K, Zhou Y, et al. **Stent-assisted coil placement for the treatment of 211 acutely ruptured wide-necked intracranial aneurysms: a single-center 11-year experience.** *Radiology* 2015;276:619 CrossRef Medline
9. Mehta B, Burke T, Kole M, et al. **Stent-within-a-stent technique for the treatment of dissecting vertebral artery aneurysms.** *AJNR Am J Neuroradiol* 2003;24:1814–18 Medline
10. Won YS, Rho MH, Chung EC, et al. **Multiple overlapping stent-assisted coiling of complex aneurysms: a single-center experience.** *Neurol Res* 2015;37:189–96 CrossRef Medline
11. Bhogal P, Pérez MA, Ganslandt O, et al. **Treatment of posterior circulation non-saccular aneurysms with flow diverters: a single-center experience and review of 56 patients.** *J Neurointerv Surg* 2017;9:471–81 CrossRef Medline
12. Hashimoto T, Meng H, Young WL. **Intracranial aneurysms: links among inflammation, hemodynamics and vascular remodeling.** *Neurol Res* 2006;28:372–80 CrossRef Medline
13. Thériault P, Terriault P, Brailovski V, et al. **Finite element modeling of a progressively expanding shape memory stent.** *J Biomech* 2006;39:2837–44 CrossRef Medline
14. Cantón G, Levy DI, Lasheras JC, et al. **Flow changes caused by the sequential placement of stents across the neck of sidewall cerebral aneurysms.** *J Neurosurg* 2005;103:891–902 CrossRef Medline
15. Lv N, Wang C, Karmonik C, et al. **Morphological and hemodynamic discriminators for rupture status in posterior communicating artery aneurysms.** *PLoS One* 2016;11:e0149906 CrossRef Medline
16. Liou TM, Li YC. **Effects of stent porosity on hemodynamics in a sidewall aneurysm model.** *J Biomech* 2008;41:1174–83 CrossRef Medline
17. Cebral JR, Mut F, Raschi M, et al. **Aneurysm rupture following treatment with flow-diverting stents: computational hemodynamics analysis of treatment.** *AJNR Am J Neuroradiol* 2011;32:27–33 CrossRef Medline
18. Tremmel M, Xiang J, Natarajan SK, et al. **Alteration of intra-aneurysmal hemodynamics for flow diversion using Enterprise and Vision stents.** *World Neurosurg* 2010;74:306–15 CrossRef Medline

Lower Arterial Cross-Sectional Area of Carotid and Vertebral Arteries and Higher Frequency of Secondary Neck Vessels Are Associated with Multiple Sclerosis

P. Belov, D. Jakimovski, J. Krawiecki, C. Magnano, J. Hagemeier, L. Pelizzari, B. Weinstock-Guttman, and R. Zivadinov

ABSTRACT

BACKGROUND AND PURPOSE: Arterial and neck vessel system characteristics of patients with multiple sclerosis have not been previously investigated. Therefore, the aim of this study was to examine the frequency of neck vessels and their cross-sectional areas (in square millimeters) between patients with MS and healthy controls.

MATERIALS AND METHODS: In this study, 193 patients with MS and 193 age- and sex-matched healthy controls underwent 2D TOF venography at 3T. The main arterial (carotid and vertebral), venous (internal jugular), and secondary neck vessels were examined at 4 separate cervical levels (C2/3, C4, C5/6, and C7/T1). The ANCOVA adjusted for age, body mass index, smoking status, hypertension, and heart disease was used to compare the differences between patients with MS and healthy controls.

RESULTS: After controlling for all confounding factors, patients with MS had significantly lower cross-sectional areas of the carotid arteries at the C2/3 ($P = .03$), C5/6 ($P = .026$), and C7/T1 ($P = .005$) levels as well as of the vertebral arteries at the C2/3 ($P = .02$), C4 ($P = .012$), and C7/T1 ($P = .006$) levels, compared with healthy controls. A higher frequency of secondary neck vessels was found at all 4 levels in patients with MS: C2/3 (12.9 versus 10, $P < .001$), C4 (9.1 versus 7.5, $P < .001$), C5/6 (7.8 versus 6.8, $P = .012$), and C7/T1 (8.8 versus 6, $P < .001$). The total cross-sectional areas of secondary neck vessels were also significantly higher at all 4 levels ($P < .03$). No significant differences in the cross-sectional areas of jugular veins were found between patients with MS and healthy controls.

CONCLUSIONS: Patients with MS showed lower cross-sectional areas of the carotid and vertebral arteries and a higher frequency of secondary neck vessels and their cross-sectional areas compared with healthy controls.

ABBREVIATIONS: BMI = body mass index; CCA = common carotid artery; CSA = cross-sectional area; ECA = external carotid artery; HC = healthy controls; IJV = internal jugular vein; VA = vertebral artery

Multiple sclerosis is the most common neurologic disease responsible for disability in the active working population. Overlapping mechanisms of chronic autoimmune demyelination and progressive neurodegeneration are hallmarks of the disease pathophysiology, which is highly variable through the spectrum of the MS course.[1] Due to the vast heterogeneity of the disease presentation, research has taken different routes to understanding the potential multifactorial interplay of the autoimmune, degenerative, environmental, genetic, and cardiovascular factors.[2]

Evidence is mounting that increased MS prevalence and disease severity are associated with more frequent cardiovascular risk factors, such as obesity and hypertension.[3] Sedentary lifestyle, lack of exercise,[4] hypertension,[5,6] smoking status,[7] altered lipid metabolism,[8] and especially obesity in the early developmental stages[9] have all been consistently associated with an earlier MS disease onset, accelerated disability progression, and worse inflammatory and neurodegenerative disease outcomes. A recent

Received May 23, 2017; accepted after revision August 17.

From the Buffalo Neuroimaging Analysis Center, Department of Neurology (P.B., D.J., J.K., C.M., J.H., R.Z.), Jacobs MS Center, Department of Neurology (B.W.-G.), and Center for Biomedical Imaging at Clinical Translational Science Institute (R.Z.), University at Buffalo, State University of New York, Buffalo, New York; Department of Electronics, Information and Bioengineering (L.P.), Politecnico di Milano, Milan, Italy; and Fondazione Don Carlo Gnocchi Organizzazione Non Lucrativa di Utilita' Sociae (L.P.), Milan, Italy.

This study was funded, in part, by The Annette Funicello Research Fund for Neurological Diseases and internal resources of the Buffalo Neuroimaging Analysis Center. In addition, we received support from the Jacquemin Family Foundation. Research reported in this publication was also funded, in part, by the National Center for Advancing Translational Sciences of the National Institutes of Health under award No. ULITR001412. The content is solely the responsibility of the authors and does not necessarily represent the official views of the National Institutes of Health.

Please address correspondence to Robert Zivadinov, MD, PhD, FAAN, FEAN, FANA, Translational Imaging Center at Clinical Translational Science Institute, Buffalo Neuroimaging Analysis Center, Jacobs School of Medicine and Biomedical Sciences, University at Buffalo, State University of New York, 100 High St, Buffalo, NY 14203; e-mail: rzivadinov@bnac.net

Indicates open access to non-subscribers at www.ajnr.org
Indicates article with supplemental on-line tables.
Indicates article with supplemental on-line photo.

http://dx.doi.org/10.3174/ajnr.A5469

nationwide study in Denmark that included 8947 patients with MS and 44,735 healthy controls (HC) showed a lower occurrence of cerebrovascular comorbidities before MS onset, followed by a higher occurrence after the MS disease onset.[10] Therefore, there is an increasing interest in understanding pathophysiologic mechanisms by which cardiovascular factors may influence the MS disease course and severity.

Investigating the head and neck vascular circulation is the crucial common ground for better understanding of the association between cardiovascular comorbidities and MS. Because this system is a constitutional member of the blood-brain barrier, any alteration in its integrity may have a deleterious impact on both systems. Therefore, examining information about the neck vessel cross-sectional area (CSA) is crucial to further understanding the associations between the extracranial and intracranial vascular changes observed in MS. However, a comprehensive all-inclusive approach to studying the CSA of the arterial and venous systems of neck vessels is generally lacking. In addition, the extent of normal vascular variation due to age, sex, and body mass index (BMI) has not been fully investigated, to our knowledge.

Previous studies examined the importance of some vascular aspects of MS using perfusion imaging.[11] Both positron-emission tomography[12] and dynamic-susceptibility contrast perfusion MR imaging studies showed a widespread reduction in cerebral blood flow affecting both the white and gray matter.[11] Reports of impairment in cerebrovascular coupling and reactivity[13] may additionally explain the cause of the neurodegenerative processes in MS. Patients with MS also demonstrated cerebrovascular reactivity impairment in different brain networks, notably within the default mode networks.[14] While the pathogenesis of these intracerebral perfusion alterations is unknown, it may be due to cardiovascular comorbidities or chronic high nitric oxide levels associated with the disease pathology.[15]

Against this background, we aimed to examine the frequency of the neck vessels and their CSA (in square millimeters) between patients with MS and HC. Additionally, we explored possible confounding factors such as age, vascular comorbidities, and BMI in comparing the neck vascular systems in patients with MS and HC.

MATERIALS AND METHODS

Study Participants

Study participants included in this study are part of an ongoing prospective study of the cardiovascular, environmental, and genetic risk factors in MS that enrolled >1000 subjects with MS and HC.[16] Inclusion criteria for this substudy investigating the characteristics of neck vessels in MS were the following: 1) MR venography examination performed within 30 days of the clinical examination, 2) age range of 18–80 years, 3) MS defined by the 2010 revised McDonald criteria,[17] or 4) being a healthy control without a known history of neurologic disorder. Exclusion criteria were the following: 1) known history of morphologic vascular abnormalities (Klippel-Trenaunay-Weber, Parkes Weber, Servelle-Martorell, or Budd-Chiari syndromes), 2) secondary-progressive or primary-progressive MS, and 3) pregnant or nursing mothers.

One hundred ninety-three patients with MS and 193 age- and sex-matched HC underwent health screening and physical, neurologic, and MR imaging examinations. Histories of smoking, heart disease, and hypertension were also collected using structured questionnaires in concordance with cross-examination of hospital medical records for all subjects. The subjects were divided into never/ever smokers. Active smokers were classified as individuals who smoked >10 cigarettes per day in the 3 months before the start of the study. Subjects were classified as past smokers if they smoked consecutively for a minimum of 6 months at some point in the past.[7] Heart disease included diagnosis of congestive heart failure, heart attack, arrhythmia, valvar disorders, heart murmurs, or heart surgery. Diagnosis of hypertension was performed according to the Seventh Report of the Joint National Committee on Prevention, Detection, Evaluation, and Treatment of High Blood Pressure.[18] Subjects with stage 1 (systolic blood pressure of 140–159 mm Hg or diastolic blood pressure of 90–99 mm Hg) and stage 2 (systolic blood pressure ≥160 mm Hg or diastolic blood pressure of ≥100 mm Hg) were classified as hypertense. BMI was assessed in all subjects. Patients with MS were examined using the Expanded Disability Status Scale by an experienced neurologist.

The study was approved by the institutional review board of State University of New York at Buffalo, and all subjects signed the written informed consent form.

MR Imaging Acquisition and Analysis

All scans were acquired on a 3T Signa Excite HD 12.0 Twin Speed scanner (GE Healthcare, Milwaukee, Wisconsin) using an 8-channel head and neck coil. Both neck vessel frequency and the CSAs of the vessels were measured using a 2D-MRV sequence that consisted of 150 slices (1.5 mm thick) using a 320 × 192 matrix and a 22.0-cm FOV. The phase FOV was 75% for a resolution of 0.69 × 1.15 × 1.5 mm^3. Imaging parameters were TE/TR/flip angle of 4.3 ms/14 ms/70° and total acquisition time of 5 minutes 19 seconds.

Neck vessels were examined at 4 separate cervical levels, including C2/C3, C4, C5/C6, and C7/T1. At first, 2 trained operators (P.B. and C.M., each with a minimum of 5 years of experience) determined the CSA of the common carotid (CCA), internal carotid, external carotid (ECA), and vertebral arteries (VA) and the internal jugular veins (IJVs). In cervical sections above the bifurcation of the CCA (C4 or C2/C3), the CSAs of both the ICA and the ECA were added together. The total CSA of each vessel was calculated by summing values from both the corresponding left- and right-sided measurements. Because the vertebral vein is not commonly present in all subjects,[19] it was classified as an accessory drainage pathway and included in the segmentation of secondary vessels. Due to the possible presence of slow and tortuous flow that might create signal saturation within very small vessels, the secondary vessel inclusion threshold was set to 2.0 mm^2. All visible neck vessels at the 4 cervical levels were marked, their frequencies were manually counted, and their CSAs were assessed. Additional vessel exclusion criteria were the following: 1) vessels that created loops in the rostrocaudal direction, and 2) the operator not being able to trace the detected signal on slices above and below the designated level.

The CSAs of all neck vessels were determined with the Java Image Manipulation Tool (JIM), Version 7.0 (http://www.xinapse.com) ROI Toolkit. For the best edge selection, the Contour ROI Tool, a

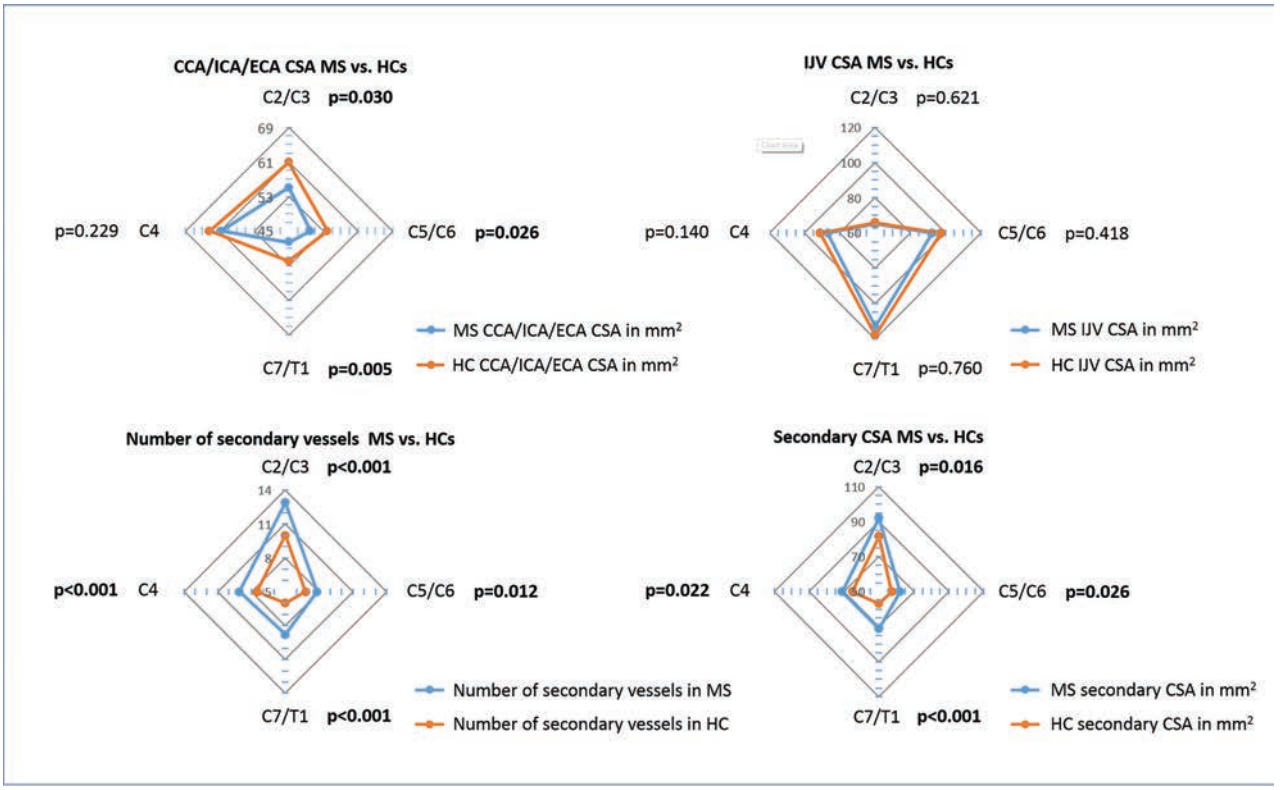

FIG 1. Radar plot representation of the neck vessel differences between patients with multiple sclerosis and healthy controls. Significant correlations are in boldface.

part of the automated Preview Contours Toolbox was used. If necessary, the operator manually adjusted the ROI boundary. The manual adjustment was mainly used in the following: 1) MRV scans with substantial image noise on the predetermined contrast, 2) to separate 2 close-but-different vessels when the automated contouring tool highlighted both, and 3) to exclude signal from arising vessel branches. The maximum contrast was preset at a 900 intensity. The general rule of determining the ideal analysis contrast was based on the stability of the signal boundaries. Meticulous segmentation of the main arterial, venous, and secondary vessels at the 4 cervical levels was performed, with high reproducibility (interclass correlation, >0.818; $P < .001$) (On-line Table 1).[20] The On-line Figure shows an example of corresponding vessel selection and representative CSA measurements in a healthy control.

Statistical Analysis

Statistical analyses were performed using SPSS, Version 24.0 (IBM, Armonk, New York). For clinical and demographic comparisons between the groups, χ^2 cross-tabulation and the Student *t* test were used accordingly. To determine associations between number of neck vessels and their cross-sectional areas with age and BMI, we used a Spearman rank correlation.

The ordinal variables regarding the secondary vessel frequency were transformed into a ranked-order type. Differences in neck vessel frequency and size (CSA) between MS and HC groups were assessed with analysis of covariance adjusted for age, BMI, smoking history, heart disease, and hypertension. Radar plots were used to visualize the data in a comprehensive manner (Fig 1). All analyses were additionally repeated in subgroups of subjects without the presence of cardiovascular comorbidities (obesity, heart disease, hypertension, diabetes mellitus type 1), to further control whether the findings were related to cardiovascular comorbidities. To examine the smoking effect on the CSA measures, we performed additional supplemental analysis in patients with MS who were smokers and nonsmokers.

In all analyses, a minimum significance level of $P \leq .05$ based on a 2-tailed test was considered statistically significant.

RESULTS

Demographic and Clinical Characteristics

All 193 patients with MS had relapsing-remitting MS. Demographic and clinical information is summarized in Table 1. The ratio of women within both groups was 130/193 (67.4%). Patients with MS were 42.2 ± 13.9 years of age, with a mean BMI of 26.8 ± 5.8, a mean disease duration of 12 ± 9.4 years, and a median Expanded Disability Status Scale score of 2.0. The HC group was 42.9 ± 17.5 years of age and had an average BMI of 26.8 ± 5.7. There were no significant differences between both groups regarding age ($P = .676$), sex ($P = 1.000$), and BMI ($P = .940$). Only 2 patients with MS and 1 healthy control had a diagnosis of type 1 diabetes mellitus. However, the cardiovascular burden was higher in the MS group versus HC, including smoking history ($P = .005$) and hypertension ($P = .001$), and there was a trend toward an increased prevalence of heart disease ($P = .053$). The demographic and clinical information regarding the subgroup of subjects without hypertension and heart disease is summarized in On-line Table 2.

Age and BMI Associations with the Size and the Number of Secondary Neck Vessels

The relationship between age and neck vessels is depicted in Table 2. Age showed a significant inverse correlation with the number of secondary neck vessels in HC. The older HC population had fewer vessels measured at the C2/3 ($P = .039$), C4 ($P = .003$), C5/6 ($P = .05$), and C7/T1 ($P = .031$) levels. On the contrary, no significant association of age and frequency of secondary neck vessels was found in patients with MS. Age was not associated with total secondary vessel CSA in either patients with MS or HC. As shown for the secondary vessels, the same analysis of correlations between the arterial CSA and age was performed. No association was found between age and arterial CSA at any cervical level, except at the C2/3 level in both MS and HC cohorts ($P = .031$ and $P = .023$, respectively). On the contrary, both patients with MS and HC showed a significant association of age and increased IJV CSA.

BMI showed an even stronger inverse association with the frequency of secondary neck vessels in HC and patients with MS (Table 2). HC with lower BMIs had a higher frequency of secondary vessels measured at the C2/3 ($P = .05$), C4 ($P < .001$), C5/6 l ($P = .001$), and C7/T1 ($P = .025$) levels. Similarly, a lower BMI in patients with MS was associated with a higher frequency of secondary neck vessels at the C2/3 level ($P = .007$), C4 level ($P < .001$), C5/6 level ($P < .001$), and C7/T1 level ($P = .017$). The CSA of the secondary neck vessels showed an inverse association with BMI in patients with MS at the C2/3, C4, and C5/6 levels ($P < .01$).

Differences between MS and HC Cohorts in Arterial, Venous, and Secondary Neck Vessel Frequency and Cross-Sectional Area

The frequency and size of the arterial, venous, and secondary neck vessels in both MS and HC groups are summarized in Tables 3 and 4 and Fig 1. Due to the age and BMI dependency exhibited by the size and number of the secondary vessels in patients with MS and HC, as well as cardiovascular risk factor differences between the 2 groups, all comparisons were adjusted for age, BMI, smoking history, heart disease, and hypertension.

After we controlled for these confounding factors, patients with MS had a significantly lower CSA of the carotid arteries at C2/3 (55.1 ± 16.4 versus 60.9 ± 17.9, $P = .03$), C5/6 (50.1 ± 10.1 versus 53.9 ± 12.5, $P = .026$), and C7/T1 (47.6 ± 9.8 versus 52 ± 9.9, $P = .005$) levels, as well as of the vertebral arteries at the C2/3 (20.1 ± 4.4 versus 21.8 ± 5.8, $P = .02$), C4 (18.6 ± 4.2 versus 20.3 ± 5, $P = .012$), and C7/T1 (16.3 ± 4.5 versus 18.4 ± 5.9, $P = .006$) levels, compared with HC. A higher frequency of secondary neck vessels was found at all 4 levels in patients with MS: C2/3 (12.9 versus 10, $P < .001$), C4 (9.1 versus 7.5, $P < .001$), C5/6 (7.8 versus 6.8, $P = .012$), and C7/T1 (8.8 versus 6, $P < .001$). The total CSA of

Table 1: Demographic and clinical characteristics of patients with multiple sclerosis ($n = 193$) and healthy controls ($n = 193$)[a]

	MS ($n = 193$)	HC ($n = 193$)	*P* Value
Female (No.) (%)	130 (67.4)	130 (67.4)	1.000
Age (mean) (SD) (yr)	42.2 (13.9)	42.9 (17.5)	.676
BMI (mean) (SD)	26.8 (5.8)	26.8 (5.7)	.94
Disease duration (mean) (SD) (yr)	12.0 (9.4)	NA	–
EDSS (median) (range)	2 (0.0–6.5)	NA	–
Smoking history (No.) (%)	73 (46.8)	58 (32.4)	.005[b]
Heart disease (No.) (%)	30 (19.7)	20 (12.4)	.053
Hypertension (No.) (%)	38 (25.3)	19 (11.3)	.001[b]

Note:—EDSS indicates Expanded Disability Status Scale; IQR, interquartile range; NA, not applicable.
[a] χ^2 and Student *t* test were used for comparing variables between groups.
[b] An α level of .05 was considered significant.

Table 2: Correlations of arterial, venous, and secondary neck vessel frequency and the cross-sectional area with age and BMI in study groups[a]

	Age				Body Mass Index			
	MS ($n = 193$)		HC ($n = 193$)		MS ($n = 193$)		HC ($n = 193$)	
	R Value	*P* Value	*R* Value	*P* Value	*R* Value	*P* Value	*R* Value	*P* Value
Arterial CSA (mm^2)								
C2/3	−0.156	.031[b]	−0.163	.023[b]	0.130	.085	0.059	.449
C4	0.075	.298	0.045	.534	0.037	.626	−0.017	.830
C5/6	0.103	.156	0.122	.092	0.136	.073	0.095	.224
C7/T1	−0.049	.502	−0.003	.968	0.085	.266	0.047	.548
IJV CSA (mm^2)								
C2/3	0.257	<.001[b]	0.150	.37	0.098	.198	0.083	.287
C4	0.255	<.001[b]	0.177	.14[b]	0.146	.054	0.139	.075
C5/6	0.196	.006[b]	0.252	<.001[b]	0.339	<.001[b]	0.231	.003[b]
C7/T1	0.187	.009[b]	0.327	<.001[b]	0.375	<.001[b]	0.344	<.001[b]
Secondary CSA (mm^2)								
C2/3	0.039	.594	−0.060	.404	−0.192	.011[b]	−0.074	.347
C4	0.112	.122	−0.040	.584	−0.229	.002[b]	−0.121	.121
C5/6	0.047	.518	0.028	.696	−0.214	.004[b]	−0.064	.417
C7/T1	0.061	.398	−0.049	.498	−0.078	.307	−0.065	.405
No. of vessels								
C2/3	0.013	.860	−0.149	.039[b]	−0.204	.007[b]	−0.153	.050[b]
C4	−0.460	.527	−0.211	.003[b]	−0.292	<.001[b]	−0.316	<.001[b]
C5/6	−0.076	.294	−0.141	.050[b]	−0.333	<.001[b]	−0.251	.001[b]
C7/T1	−0.060	.406	−0.155	.031[b]	−0.180	.017[b]	−0.174	.025[b]

[a] Spearman ranked correlations between age/BMI and the corresponding vascular variable were used.
[b] An α level of .05 was considered significant.

Table 3: Arterial, venous, and secondary neck vessel frequency and the cross-sectional area in the study groups[a]

	Primary Vessel (CSA) (mm^2)					
	Arterial and Venous			Arterial (VAs)		
	MS (n = 193)	HC (n = 193)	P Value	MS (n = 193)	HC (n = 193)	P Value
Arterial (CCA/ICA/ECA)						
C2/C3	55.1 (16.4)	60.9 (17.9)	.030[b]	20.1 (4.4)	21.8 (5.8)	.02[b]
C4	60.8 (15.7)	63.4 (16.3)	.229	18.6 (4.2)	20.3 (5.0)	.012[b]
C5/C6	50.1 (10.1)	53.9 (12.5)	.026[b]	18.1 (6.9)	19.3 (4.7)	.341
C7/T1	47.6 (9.8)	52 (9.9)	.005[b]	16.3 (4.5)	18.4 (5.9)	.006[b]
Venous (IJVs)						
C2/C3	64.9 (27.4)	66.0 (31.6)	.621			
C4	86.9 (35.9)	91.1 (41.0)	.140			
C5/C6	92.3 (57.1)	97.4 (60.2)	.418			
C7/T1	113.3 (67.0)	117.9 (79.3)	.790			

[a] Analysis of covariance adjusted for age and BMI, smoking history, heart disease, and hypertension was used. In the ANCOVA for frequency of vessels, ranked variables were used.
[b] An α level of .05 was considered significant.

Table 4: Secondary neck vessel frequency and the cross-sectional area in the study groups[a]

	No. of Vessels			CSA (mm^2)		
	MS (n = 193)	HC (n = 193)	P Value	MS (n = 193)	HC (n = 193)	P Value
Secondary vessels						
C2/C3	12.9 (5.4)	10 (4.2)	<.001[b]	92.1 (40.6)	81.6 (35.5)	.016[b]
C4	9.1 (4.2)	7.5 (3.3)	<.001[b]	71.0 (33.7)	65.3 (28.7)	.022[b]
C5/C6	7.8 (3.9)	6.8 (3.4)	.012[b]	61.9 (32.2)	57.2 (28.2)	.028[b]
C7/T1	8.8 (4.9)	6 (3.5)	<.001[b]	71.1 (40.5)	56.7 (32.5)	<.001[b]

[a] Analysis of covariance adjusted for age and BMI, smoking history, heart disease, and hypertension was used. In the ANCOVA for frequency of vessels, ranked variables were used.
[b] An α level of .05 was considered significant.

secondary vessels was also significantly higher at all 4 levels in patients with MS ($P < .03$). The difference was most significant at the C7/T1 level where the CSA of patients with MS was 71.1 ± 40.5 mm^2 compared with 56.7 ± 32.5 mm^2 in HC ($P < .001$). No significant differences in the CSA of the IJVs were found between MS and HC cohorts. Figure 2 shows an example of the differences in vessel number and CSA observed in patients with MS and age- and sex-matched HC.

In a subgroup of subjects without cardiovascular risk factors, the comparison between patients with MS ($n = 135$) and HC ($n = 142$) yielded results like those in the main analyses for arterial, venous, and secondary vessel frequency and their CSAs (On-line Tables 3 and 4). Except for the number of secondary vessels on the C5/C6 level (7.0 versus 8.3, $P = .034$), MS smokers showed no significant differences compared with MS nonsmokers (On-line Tables 5 and 6).

DISCUSSION

Two main findings were identified in this study. First, even after adjusting for all cardiovascular factors including BMI, hypertension, heart disease, smoking history, and age, the MS cohort showed a higher frequency of secondary neck vessels and larger CSAs compared with HC. This finding was consistent through all cervical levels examined. Most interesting, the patients with MS also had a smaller arterial CSA of the main and secondary arterial vessels (CCA, ICA, ECA, and VA, respectively). Furthermore, these findings were reconfirmed in a subgroup of subjects (70%) without the presence of cardiovascular comorbidities. In addition, we showed that demographic factors, such as age and BMI, are essential confounders between patients with MS and HC when considering the morphology of neck vessels and should be controlled for in future studies.

The finding that patients with MS show different patterns of vascular neck vessel morphology with respect to aging compared with HC would suggest that MS and cardiovascular disease have intertwining pathways.[10] Cardiovascular risk factors are known to contribute to MS disease severity. For example, smoking has been associated with higher lesion burden and more severe brain atrophy in patients with MS.[7] When several cardiovascular comorbidities are combined, this relationship becomes even more robust.[6] Two independent epidemiologic studies showed an interesting disparity of decreased prevalence of ischemic heart disease and an increased prevalence of stroke in patients with MS compared with HC.[21,22] This finding would suggest that the arterial vessels supplying the central nervous system are possibly subject to particular atherosclerotic harm.[23] In fact, 1 study showed that patients with MS had decreased carotid compliance compared with HC.[23] Although the decreased arterial lumen of the carotid and vertebral arteries found in MS patients may suggest that inflammatory mechanisms contribute to early atherosclerosis in MS patients,[24] we found similar results in the subgroup of MS patients without presence of cardiovascular diseases. Other authors have also shown lower CCA values in patients with MS compared with HC (65 versus 78 mm^2).[25] Another MS study that used a phase-contrast MRV technique showed a somewhat higher CSA CCA area compared with our measurements using time-of-flight MRV (65 versus 48.9 mm^2, respectively).[26] Heterogeneity of the population of patients with MS between the 2 studies can also contribute to explanation of these findings. Therefore, future studies should investigate this issue in more detail at disease onset, when the presence of cardiovascular risks is minimal.

The hypoperfusion of the normal-appearing white matter commonly detected in patients with MS may be partially linked to the anatomic differences of the neck arterial system observed in the present study.[27] Decreased cerebral blood flow in both the normal-appearing white matter and the gray matter has been previously reported.[11] Distinct perfusion clusters in patients with MS

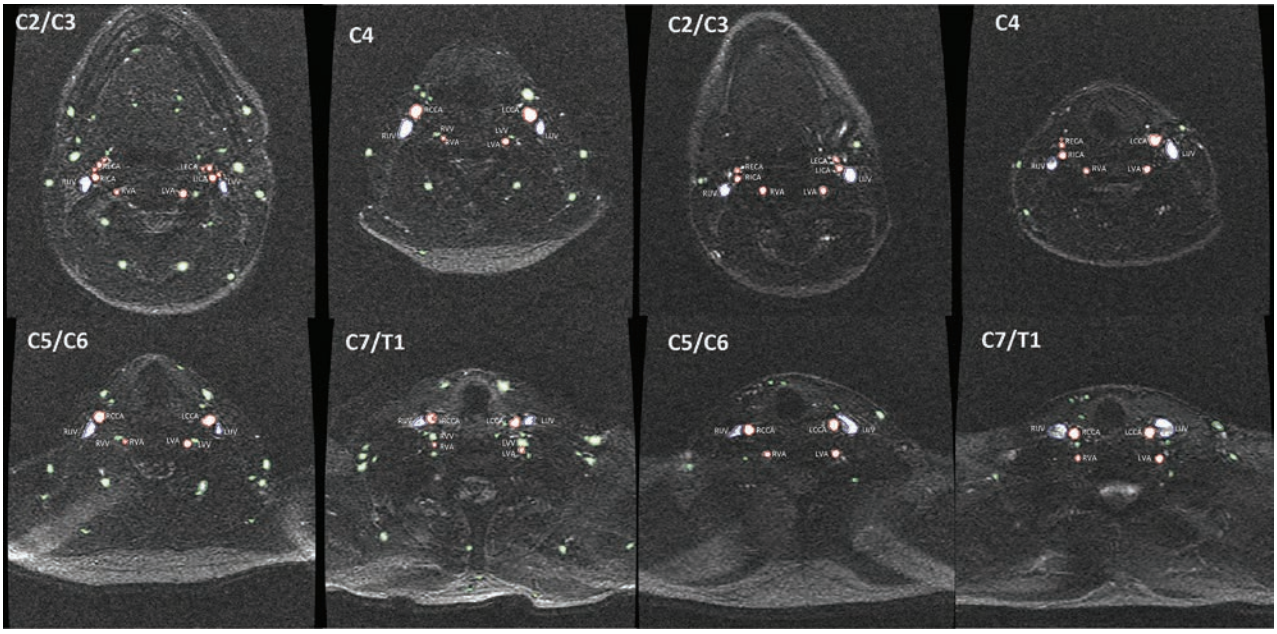

FIG 2. Comparison of main and secondary vessel number and cross-sectional area on a 2D-MRV sequence at 4 cervical levels in patients with multiple sclerosis (4 corresponding panels on the left) and age- and sex-matched healthy controls (4 corresponding panels on the right). VV indicates vertebral vein; L, left; R, right. Green color represents the secondary vessels, red color represents the CCA, ICA, EAC, and VA, while blue represents the IJV.

showed associations of local hypoperfusion and formation of T1-hypointense lesions, highlighting the need for better perfusion in lesion repair.[28] Most important, the hypoperfusion observed in the GM, in an absence of volume loss, indicates that decreased brain perfusion might be a temporal predecessor to brain atrophy development in MS.[29] Even though there is growing evidence of coexisting vascular pathology in MS, the current perfusion studies are generally of small sample size and limited effect size. Therefore, caution in any interpretation of direct causality is warranted.

Neurovascular coupling is a physiologic mechanism responsible for increasing the cortical blood flow due to cell activation.[30] In healthy individuals, this results in cerebral vasodilation that is compensating for the increased demand of glucose and oxygen.[31] A hypocapnic study showed that patients with MS are unable to physiologically increase cerebral blood flow, which, in turn, leads to global diffuse hypoperfusion.[13] This abnormality has been previously linked as a triggering factor for MS lesion formation and may explain, to some extent, the neurodegenerative aspect of the MS disease process.[32] Overall, the morphologic changes to the neck arteries supplying the brain that were observed in this study may be a consequence of prolonged normal-appearing white matter/GM hypoperfusion and impaired cerebrovascular reactivity, which leads to accelerated neurodegeneration in MS.

An alternative inverse explanation for the decrease of arterial CSA observed in this study could be related to the increase of disability, which causes less physical activity in patients with MS.[4] Because worsening disability causes a sedentary lifestyle, this will eventually lead to an increase of the cardiovascular burden and vascular complications.[4] Additionally, measures to improve the reserve-related activities and maintaining strenuous activities have resulted in better clinical and MR imaging–derived MS outcomes. While the present study cannot answer whether the morphologic changes of the neck arteries observed are secondary or primary to the MS disease process, future studies should extend our preliminary findings in early and more advanced MS disease stages using a longitudinal study design.

When the size of IJVs between the MS and HC cohorts was compared, no differences were found between the 2 groups at any cervical level. Therefore, our findings are in line with several recent MRV studies showing no IJV anatomic differences between patients with MS and HC,[33,34] but contrary to some other studies showing the opposite findings.[26,35,36] Several recent studies demonstrated that the IJV CSA has marked variability in its course through the neck and increased narrowing with aging.[20,37]

Several studies used MRV to examine the prevalence and the extent of secondary vessels in the necks of patients with MS. One study showed an increased frequency of posterior paraspinal collaterals in patients with MS.[36] In another study, there was a trend toward greater occurrence of non-IJV collaterals.[35] Yet another study reported no differences between patients with MS and HC in the secondary neck vessels using 5 mm^2 as their cutoff for identification.[33] On the contrary, using 2 mm^2 as a cutoff in the present study, we showed that patients with MS had a significantly increased frequency of secondary neck vessels and their CSAs. In the present study, no phase-contrast imaging was used, which did not allow us to characterize the secondary neck vessels with respect to their arterial or venous components; therefore, the increased frequency of secondary neck vessels may represent arterial or venous collateralization. On the other hand, a large phase-contrast MRV study showed that patients with MS had lower IJV and higher paraspinal venous flow, compared with HC.[38] While our study cannot answer this question, one of the possible hypotheses could be that the decreased size of the carotid and vertebral arterial supply to the CNS could result in secondary arterial compensation mechanisms.

Age is an important factor in the development of venous he-

modynamic changes in the neck. In this study, increased age showed an association with fewer secondary vessels in the neck of HC. In addition, an increase in the BMI showed an association with a decreased frequency of neck vessels measured at all levels in both MS and HC groups. The effects of age and BMI on morphologic changes of the IJVs in a healthy aging population have been previously described.[20,39] Even when we corrected for the previously aforementioned risk factors, the MS cohort displayed an increased secondary neck vessel frequency and secondary vessel CSA, compared with HC. The differences were the most robust both at the C2/C3 level, representing vessels at the base of the skull, and at C7/T1 level, representing the level of the superior thoracic outlet. Therefore, while in HC we found a decrease of the number of secondary vessels with aging, this association was lacking in patients with MS; this finding suggests a possible disease effect on vascular recruitment.

The additional vascularization may be triggered by either the recurrent hypoperfusion of the brain or inflammatory factors involved in the complex remodeling of preexisting conduits running alongside the main arteries.[40,41] For example, the T helper 17 cell subset and interleukin 17 have been linked as essential in both the severity of MS and as an important factor in neovascularization.[41]

Dynamic flow quantification of the secondary vasculature could further aid in understanding the anatomic flow differences of secondary neck vessels observed in this study, providing flow data rather than purely structural measurements. Furthermore, the current time-of-flight MRV technique allows segmentation of only the luminal aspect of the vessel and not of the anatomic CSA. Any regions of bidirectional flow, absence of flow, and flow nonhomogeneity may create partially inaccurate vessel-size estimation. Regarding the hemodynamic properties, measuring the luminal CSA might be a better anatomic proxy than inclusion of the thickness of the vessel wall. Additionally, studies associating the morphology of the neck vasculature with dynamic brain perfusion will provide an important answer to the anatomic and dynamic vascular role of these vessels in the complex pathogenesis of MS. The major strength of the study is the use of a large 1:1 matched sample of HC and patients with MS, which decreased the potential comparison bias between the 2 study populations. An additional longitudinal study, using phase contrast and examining the atherosclerotic burden, should further address the limitations of the current study design. Because this was an observational study, we did not adjust for multiple comparisons in our statistical analyses. Therefore, larger longitudinal studies should confirm our preliminary findings.

CONCLUSIONS

Patients with MS showed lower CSAs of the carotid and vertebral arteries and a higher frequency of secondary neck vessels and their CSAs compared with HC. These findings may suggest that the inflammatory mechanisms, which are present in patients with MS from early onset, may contribute to accelerated atherosclerosis in patients with MS. The higher frequency of secondary neck vessels may suggest that the decreased size of the carotid and vertebral arterial supply to the CNS could lead to the formation of secondary arterial compensation mechanisms. However, further replication and continuation of the research are warranted before final conclusions can be drawn.

Disclosures: Christopher Magnano—*UNRELATED*: *Employment*: General Electric, *Comments*: independent of the work presented in this article. Bianca Weinstock-Guttman—*UNRELATED*: *Consultancy*: Biogen Idec, Teva Neuroscience, EMD Serono, Novartis, Genzyme & Sanofi, Genetech*; *Grants/Grants Pending*: Biogen Idec, Teva Neuroscience, EMD Serono, Novartis, Genzyme & Sanofi*; *Payment for Lectures Including Service on Speakers Bureaus*: Biogen Idec, Teva Neuroscience, EMD Serono, Novartis, Genzyme & Sanofi, Genentech. Robert Zivadinov—*UNRELATED*: *Consultancy*: Genzyme-Sanofi, Novartis; *Grants/Grants Pending*: Genzyme-Sanofi, Intekrin-Coherus, Novartis, IMS Health*; *Payment for Lectures Including Service on Speakers Bureaus*: Genzyme-Sanofi, Novartis*. *Money paid to the institution.

REFERENCES

1. Lucchinetti CF, Bruck W, Lassmann H. **Evidence for pathogenic heterogeneity in multiple sclerosis.** *Ann Neurol* 2004;56:308 CrossRef Medline
2. Xia Z, White CC, Owen EK, et al. **Genes and Environment in Multiple Sclerosis project: a platform to investigate multiple sclerosis risk.** *Ann Neurol* 2016;79:178–89 CrossRef Medline
3. Marrie RA, Reider N, Cohen J, et al. **A systematic review of the incidence and prevalence of cardiac, cerebrovascular, and peripheral vascular disease in multiple sclerosis.** *Mult Scler* 2015;21:318–31 CrossRef Medline
4. Klaren RE, Hubbard EA, Wetter NC, et al. **Objectively measured sedentary behavior and brain volumetric measurements in multiple sclerosis.** *Neurodegener Dis Manag* 2017;7:31–37 CrossRef Medline
5. Dagan A, Gringouz I, Kliers I, et al. **Disability progression in multiple sclerosis is affected by the emergence of comorbid arterial hypertension.** *J Clin Neurol* 2016;12:345–50 CrossRef Medline
6. Kappus N, Weinstock-Guttman B, Hagemeier J, et al. **Cardiovascular risk factors are associated with increased lesion burden and brain atrophy in multiple sclerosis.** *J Neurol Neurosurg Psychiatry* 2016;87:181–87 CrossRef Medline
7. Zivadinov R, Weinstock-Guttman B, Hashmi K, et al. **Smoking is associated with increased lesion volumes and brain atrophy in multiple sclerosis.** *Neurology* 2009;73:504–10 CrossRef Medline
8. Weinstock-Guttman B, Zivadinov R, Mahfooz N, et al. **Serum lipid profiles are associated with disability and MRI outcomes in multiple sclerosis.** *J Neuroinflammation* 2011;8:127 CrossRef Medline
9. Kavak KS, Teter BE, Hagemeier J, et al; New York State Multiple Sclerosis Consortium. **Higher weight in adolescence and young adulthood is associated with an earlier age at multiple sclerosis onset.** *Mult Scler* 2015;21:858–65 CrossRef Medline
10. Thormann A, Magyari M, Koch-Henriksen N, et al. **Vascular comorbidities in multiple sclerosis: a nationwide study from Denmark.** *J Neurol* 2016;263:2484–93 CrossRef Medline
11. D'Haeseleer M, Hostenbach S, Peeters I, et al. **Cerebral hypoperfusion: a new pathophysiologic concept in multiple sclerosis?** *J Cereb Blood Flow Metab* 2015;35:1406–10 CrossRef Medline
12. Sun X, Tanaka M, Kondo S, et al. **Clinical significance of reduced cerebral metabolism in multiple sclerosis: a combined PET and MRI study.** *Ann Nucl Med* 1998;12:89–94 CrossRef Medline
13. Marshall O, Lu H, Brisset JC, et al. **Impaired cerebrovascular reactivity in multiple sclerosis.** *JAMA Neurol* 2014;71:1275–81 CrossRef Medline
14. Marshall O, Chawla S, Lu H, et al. **Cerebral blood flow modulation insufficiency in brain networks in multiple sclerosis: a hypercapnia MRI study.** *J Cereb Blood Flow Metab* 2016;36:2087–95 CrossRef Medline
15. Sadeghian M, Mastrolia V, Rezaei Haddad A, et al. **Mitochondrial dysfunction is an important cause of neurological deficits in an inflammatory model of multiple sclerosis.** *Sci Rep* 2016;6:33249 CrossRef Medline
16. Zivadinov R, Ramasamy DP, Benedict RR, et al. **Cerebral microbleeds in multiple sclerosis evaluated on susceptibility-weighted im-**

ages and quantitative susceptibility maps: a case-control study. *Radiology* 2016;281:884–95 CrossRef Medline
17. Polman CH, Reingold SC, Banwell B, et al. **Diagnostic criteria for multiple sclerosis: 2010 revisions to the McDonald criteria.** *Ann Neurol* 2011;69:292–302 CrossRef Medline
18. Chobanian AV, Bakris GL, Black HR, et al; Joint National Committee on Prevention, Detection, Evaluation, and Treatment of High Blood Pressure. National Heart, Lung, and Blood Institute, National High Blood Pressure Education Program Coordinating Committee. **Seventh Report of the Joint National Committee on Prevention, Detection, Evaluation, and Treatment of High Blood Pressure.** *Hypertension* 2003;42:1206–52 CrossRef Medline
19. Gisolf J, van Lieshout JJ, van Heusden K, et al. **Human cerebral venous outflow pathway depends on posture and central venous pressure.** *J Physiol* 2004;560:317–27 CrossRef Medline
20. Magnano, Belov, Krawiecki J, et al. **Internal jugular vein cross-sectional area enlargement is associated with aging in healthy individuals.** *PLoS One* 2016;11:e0149532 CrossRef Medline
21. Allen NB, Lichtman JH, Cohen HW, et al. **Vascular disease among hospitalized multiple sclerosis patients.** *Neuroepidemiology* 2008;30:234–38 CrossRef Medline
22. Christiansen CF. **Risk of vascular disease in patients with multiple sclerosis: a review.** *Neurol Res* 2012;34:746–53 CrossRef Medline
23. Ranadive SM, Yan H, Weikert M, et al. **Vascular dysfunction and physical activity in multiple sclerosis.** *Med Sci Sports Exerc* 2012;44:238–43 CrossRef Medline
24. Minagar A, Jy W, Jimenez JJ, et al. **Multiple sclerosis as a vascular disease.** *Neurol Res* 2006;28:230–35 CrossRef Medline
25. Feng W, Utriainen D, Trifan G, et al. **Quantitative flow measurements in the internal jugular veins of multiple sclerosis patients using magnetic resonance imaging.** *Rev Recent Clin Trials* 2012;7:117–26 CrossRef Medline
26. Haacke EM, Feng W, Utriainen D, et al. **Patients with multiple sclerosis with structural venous abnormalities on MR imaging exhibit an abnormal flow distribution of the internal jugular veins.** *J Vasc Interv Radiol* 2012;23:60–68.e1–3 CrossRef Medline
27. ElSankari S, Balédent O, van Pesch V, et al. **Concomitant analysis of arterial, venous, and CSF flows using phase-contrast MRI: a quantitative comparison between MS patients and healthy controls.** *J Cereb Blood Flow Metab* 2013;33:1314–21 CrossRef Medline
28. Narayana PA, Zhou Y, Hasan KM, et al. **Hypoperfusion and T1-hypointense lesions in white matter in multiple sclerosis.** *Mult Scler* 2014;20:365–73 CrossRef Medline
29. Debernard L, Melzer TR, Van Stockum S, et al. **Reduced grey matter perfusion without volume loss in early relapsing-remitting multiple sclerosis.** *J Neurol Neurosurg Psychiatry* 2014;85:544–51 CrossRef Medline
30. Salinet AS, Robinson TG, Panerai RB. **Effects of cerebral ischemia on human neurovascular coupling, CO2 reactivity, and dynamic cerebral autoregulation.** *J Appl Physiol (1985)* 2015;118:170–77 CrossRef Medline
31. Lu H, Xu F, Rodrigue KM, et al. **Alterations in cerebral metabolic rate and blood supply across the adult lifespan.** *Cereb Cortex* 2011;21:1426–34 CrossRef Medline
32. Prinster A, Quarantelli M, Orefice G, et al. **Grey matter loss in relapsing-remitting multiple sclerosis: a voxel-based morphometry study.** *Neuroimage* 2006;29:859–67 CrossRef Medline
33. Zivadinov R, Lopez-Soriano A, Weinstock-Guttman B, et al. **Use of MR venography for characterization of the extracranial venous system in patients with multiple sclerosis and healthy control subjects.** *Radiology* 2011;258:562–70 CrossRef Medline
34. Wattjes MP, van Oosten BW, de Graaf WL, et al. **No association of abnormal cranial venous drainage with multiple sclerosis: a magnetic resonance venography and flow-quantification study.** *J Neurol Neurosurg Psychiatry* 2011;82:429–35 CrossRef Medline
35. McTaggart RA, Fischbein NJ, Elkins CJ, et al. **Extracranial venous drainage patterns in patients with multiple sclerosis and healthy controls.** *AJNR Am J Neuroradiol* 2012;33:1615–20 CrossRef Medline
36. Zaharchuk G, Fischbein NJ, Rosenberg J, et al. **Comparison of MR and contrast venography of the cervical venous system in multiple sclerosis.** *AJNR Am J Neuroradiol* 2011;32:1482–89 CrossRef Medline
37. Buch K, Groller R, Nadgir RN, et al. **Variability in the cross-sectional area and narrowing of the internal jugular vein in patients without multiple sclerosis.** *AJR Am J Roentgenol* 2016;206:1082–86 Medline
38. Sethi SK, Daugherty AM, Gadda G, et al. **Jugular anomalies in multiple sclerosis are associated with increased collateral venous flow.** *AJNR Am J Neuroradiol* 2017;38:1617–22 CrossRef Medline
39. Magnano C, Belov P, Krawiecki J, et al. **Internal jugular vein narrowing and body mass index in healthy individuals and multiple sclerosis patients.** *Veins and Lymphatics* 2014;3:4632 CrossRef
40. Koerselman J, van der Graaf Y, de Jaegere PP, et al. **Coronary collaterals: an important and underexposed aspect of coronary artery disease.** *Circulation* 2003;107:2507–11 Medline
41. la Sala A, Pontecorvo L, Agresta A, et al. **Regulation of collateral blood vessel development by the innate and adaptive immune system.** *Trends Mol Med* 2012;18:494–501 CrossRef Medline

CT Attenuation Analysis of Carotid Intraplaque Hemorrhage

L. Saba, M. Francone, P.P. Bassareo, L. Lai, R. Sanfilippo, R. Montisci, J.S. Suri, C.N. De Cecco, and G. Faa

ABSTRACT

BACKGROUND AND PURPOSE: Intraplaque hemorrhage is considered a leading parameter of carotid plaque vulnerability. Our purpose was to assess the CT characteristics of intraplaque hemorrhage with histopathologic correlation to identify features that allow for confirming or ruling out the intraplaque hemorrhage.

MATERIALS AND METHODS: This retrospective study included 91 patients (67 men; median age, 65 ± 7 years; age range, 41–83 years) who underwent CT angiography and carotid endarterectomy from March 2010 to May 2013. Histopathologic analysis was performed for the tissue characterization and identification of intraplaque hemorrhage. Two observers assessed the plaque's attenuation values by using an ROI (≥ 1 and ≤ 2 mm^2). Receiver operating characteristic curve, Mann-Whitney, and Wilcoxon analyses were performed.

RESULTS: A total of 169 slices were assessed (59 intraplaque hemorrhage, 63 lipid-rich necrotic core, and 47 fibrous); the average values of the intraplaque hemorrhage, lipid-rich necrotic core, and fibrous tissue were 17.475 Hounsfield units (HU) and 18.407 HU, 39.476 HU and 48.048 HU, and 91.66 HU and 93.128 HU, respectively, before and after the administration of contrast medium. The Mann-Whitney test showed a statistically significant difference of HU values both in basal and after the administration of contrast material phase. Receiver operating characteristic analysis showed a statistical association between intraplaque hemorrhage and low HU values, and a threshold of 25 HU demonstrated the presence of intraplaque hemorrhage with a sensitivity and specificity of 93.22% and 92.73%, respectively. The Wilcoxon test showed that the attenuation of the plaque before and after administration of contrast material is different (intraplaque hemorrhage, lipid-rich necrotic core, and fibrous tissue had *P* values of .006, .0001, and .018, respectively).

CONCLUSIONS: The results of this preliminary study suggest that CT can be used to identify the presence of intraplaque hemorrhage according to the attenuation. A threshold of 25 HU in the volume acquired after the administration of contrast medium is associated with an optimal sensitivity and specificity. Special care should be given to the correct identification of the ROI.

ABBREVIATIONS: Az = area under the receiver operating characteristic curve; CEA = carotid endarterectomy; HU = Hounsfield unit; IPH = intraplaque hemorrhage; LRNC = lipid-rich necrotic core

During the past few years, several studies have demonstrated that the occurrence of intraplaque hemorrhage (IPH) in the carotid artery is linked with an increased risk of plaque rupture,[1-3] and therefore, IPH is considered a fundamental parameter of the so-called plaque vulnerability.[4]

Most of the research performed in the past 20 years was based on results from autopsy studies or on the specimens taken from carotid endarterectomies.[5,6] With the introduction of high-resolution black-blood MRI,[7,8] it has become possible to identify noninvasively the IPH with optimal correlation to histology, and past literature has suggested an association between IPH and the occurrence of cerebrovascular events.[9] In a recently published meta-analysis by Saam et al,[10] it was demonstrated that the presence of IPH is associated with a 5- to 7-fold higher risk of cerebrovascular events.

However, carotid arteries are frequently imaged by using CT, which allows for characterizing the degree of stenosis[11,12] with an excellent level of detail. Further, it offers information related to the risk of the plaque vulnerability such as the volume of the

Received April 10, 2017; accepted after revision August 20.

From the Departments of Radiology (L.S.), Cardiology (M.F., P.P.B., G.F.), and Vascular Surgery (R.S., R.M.), Azienda Ospedaliero Universitaria of Cagliari – Polo di Monserrato, Cagliari, Italy; Department of Radiological, Oncological, and Pathological Sciences (L.L.), Sapienza University of Rome, Rome, Italy; Point of Care Devices (J.S.S.), Global Biomedical Technologies, Roseville, California; AtheroPoint (J.S.S.), Roseville, California; Department of Electrical Engineering (J.S.S.), Idaho State University, Pocatello, Idaho; and Department of Radiology and Radiological Science (C.N.D.C.), Division of Cardiovascular Imaging, Medical University of South Carolina, Charleston, South Carolina.

Please address correspondence to Luca Saba, MD, Department of Radiology, Azienda Ospedaliero Universitaria (A.O.U.), di Cagliari – Polo di Monserrato s.s. 554 Monserrato (Cagliari) 09045, Italy; e-mail: lucasaba@tiscali.it

http://dx.doi.org/10.3174/ajnr.A5461

plaque and it subcomponents[13,14] or the identification of ulcers in the plaque.[15,16] Moreover, CT provides a unique option in some categories of patients who cannot be imaged by using MR imaging (eg, those with a prosthesis or pacemaker). Therefore, the identification of the determinants of plaque vulnerability, and in particular IPH, could be extremely important.

The purpose of this study was to assess the CT characteristics of the IPH with histopathologic correlation to identify features that allow for confirming or ruling out the IPH.

MATERIALS AND METHODS

Study Design and Patient Population

The institutional review board of our hospital (Azienda Ospedaliera Universitaria di Cagliari) approved this retrospective study protocol, and we included all the patients who underwent carotid endarterectomy (CEA) and whose carotid specimen was analyzed by histologists. Therefore, 91 patients (67 men; median age, 65 ± 7 years; age range, 41–83 years) who underwent CEA from March 2010 to May 2013 were included. This research was conducted in accordance with the guidelines of our institution's research committee, and because of the retrospective nature of the analysis, patient consent was waived.

We considered as an inclusion criterion that the CEA was performed within 10 days after the CTA, whereas we excluded those patients who underwent CEA for restenosis or radiation therapy–induced carotid stenosis. A further exclusion criterion was the plaque's rupture or fragmentation during the CEA procedure and/or manipulation.

In our hospital, the quantification of the degree of stenosis and the carotid artery plaque analysis is performed by using CTA according to previously published inclusion criteria.[17,18] Carotid sonography is used as the first-line technique to assess the presence of atherosclerosis, and briefly, CTA of carotid arteries is performed when 1) carotid sonography shows a pathologic stenosis (> 50% measured with the NASCET criteria[19]) or features related to plaque vulnerability (eg, ulcerations, irregular surface) and 2) sonography cannot adequately assess the degree of stenosis and the plaque's characteristics because of anatomic conditions. Patients were also classified as symptomatic or asymptomatic according to the neurologic assessment documented in the clinical chart review by using the Trial of ORG 10172 in Acute Stroke Treatment (TOAST) criteria. Part of the study population (n = 58) of this research was included in previously published papers.[20,21]

CTA Technique

Patients were studied by using a 16–multidetector row CT system (Brilliance; Philips Healthcare, Best, the Netherlands). CT images were obtained with coverage from the aortic arch to the carotid siphon with caudocranial direction. Examinations were performed before and after the administration of contrast material. Angiographic phase was obtained with the administration of 80 mL of prewarmed contrast medium (Ultravist 370; Bayer HealthCare, Berlin, Germany). CT technical parameters included: slice thickness, 0.6 mm; interval, 0.3 mm; matrix size, 512 × 512; and field of view, 14–19 cm. A C-filter algorithm of reconstruction was applied.

Carotid Endarterectomy

Two vascular surgeons (R.M. and R.S., with 25 and 16 years of experience, respectively) performed all the CEA procedures by using the "en-bloc" technique by scoring the outer media and adventitia with a scalpel and then removing the plaque as an intact tube. This approach was adopted to reduce the manipulation of the carotid artery and avoid the potential rupture/fragmentation of the plaque.

In our hospital, patients underwent CEA according to the recommendations by the Asymptomatic Carotid Atherosclerosis Study (ACAS),[22] NASCET,[19] Stroke Prevention and Educational Awareness Diffusion (SPREAD),[23] and European Carotid Surgery Trial (ECST)[3] after the exclusion of a cardioembolic source of embolism.

Histologic Analysis of the Plaque

The methods used for the plaque processing and histologic analysis have been described in a previously published paper.[20] In summary, the histologic analysis was performed by 2 histologists (G.F. and L.L., with 22 and 5 years of experience, respectively) who were blinded to the radiologic findings. After the CEA, the excised "en-bloc" plaque is immediately fixed in formalin, and it is sent to the laboratory directly after the surgical procedure. Carotid plaques were decalcified and embedded in paraffin wax. None of the CEA specimens showed disruption of the luminal surface of the plaque. The portion of the specimen that showed the carotid plaque was divided transversely in sections having 3 mm intervals that were air-dried at 60°C for 45 minutes. After this phase, paraffin was removed by xylol, and the sections were hydrated. Finally, endogenous peroxidase activity was blocked by 2% hydrogen peroxide (H_2O_2). The transverse sections were subjected to histologic examination to identify the plaque components. Because the main focus of the study was to assess the attenuation characteristics of IPH, special care was used in the identification of IPH. Finally, according to the histologic characteristics, the plaque of each slice was categorized into one of 4 groups: IPH, lipid-rich necrotic core (LRNC), fibrous, and calcified.

Co-Registration and Histology Matching

The co-registration between CTA and histologic slices represents a key point of this paper, and special care was dedicated to avoid misregistration. After the selection of the CTA slice, the corresponding histologic section was identified by considering the following parameters: distance from the carotid bifurcation, lumen shape, and presence of prominent areas of calcification. In particular, the location of the bifurcation was identified to measure the length in the z-axis correctly. Moreover, given the difference in thickness between the MDCTA image sections (0.625 mm) and the histologic cross sections (5 μm), to further validate, 2–3 histologic sections were compared with 1 cross-sectional MDCTA image on the basis of the relative distance from the bifurcation.

IPH and Plaque Analysis Quantification

Two radiologists (L.S. and M.F., with 11 and 8 years of experience in CTA, respectively) performed all measurements of Hounsfield units (HU) by using as window-level settings a width of 850 and

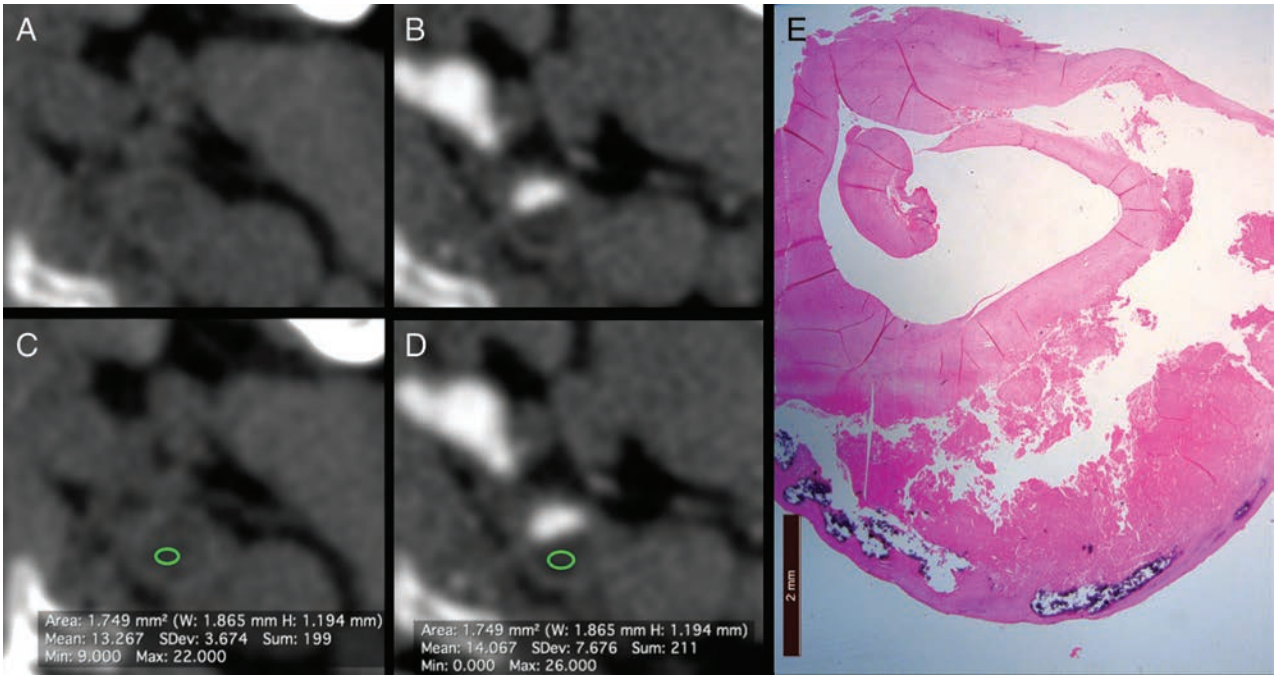

FIG 1. A 67-year-old male patient. The images acquired before (*A*) and after the administration of contrast material (*B*) clearly show the carotid artery plaques. The ROI analyses before (*C*) and after the administration of contrast material (*D*) show the HU attenuation of the plaque (13.267 HU and 14.067 HU, respectively). In panel *E*, the corresponding histologic slice is given.

length of 300.[24] In this study, the registration phase between CT and histologic slices was fundamental, and special care was used. The CT analysis was performed in 3 different phases. The first one was conducted with both radiologists in consensus to assess the image quality of the datasets and exclude those carotid arteries that showed dental streak artifacts or movement artifacts that reduced the image quality. The second and third phases were performed with radiologists who worked independently.

In the second phase, the angiographic dataset was assessed; radiologists had histopathologic sections as well as the spatial coordinates (slice number – Z distance from the carotid bifurcation), and they were asked to trace a circular or elliptical ROI ($\geq$ 1 mm^2 and $\leq$2 mm^2) in the plaque and to quantify the HU attenuation values in the analyzed slice. The shape of the vessel wall and the lumen as well as the location of the bifurcation and the presence of calcifications in the plaque were used for matching. The procedures were repeated for each slice of each patient where it was possible to trace an ROI of at least 1 mm^2.

In the third phase, radiologists selected the basal scan dataset and identified the same slice corresponding to the angiographic phase. To reach a correct registration between basal and angiographic datasets, they visually verified if the slices were registered or if it was necessary to select another slice along the z-axis. After this "matching phase," the same ROI used in the contrast phase (duplicate option) was positioned in the same position of the plaque to measure the attenuation values (Fig 1).

Statistical Analysis

In this study, the normality of each continuous variable group was tested by using the Kolmogorov-Smirnov *Z* test, and appropriate tests for Gaussian or non-Gaussian values were selected. The Bland-Altman plot was calculated between the 2 readers to test the attenuation values, and the averaged value for each section was considered for the analysis. The Mann-Whitney test was calculated to test the difference of attenuation values between the different categories (IPH, LRNC, and fibrous tissue). Receiver operating characteristic curve analysis was performed, and the model was characterized by the area under the receiver operating characteristic curve (Az) with 95% CIs to test the relationship between HU attenuation values in the ROI and IPH. Moreover, thresholds derived from the ROC analysis were calculated. The Wilcoxon test was applied to test the difference of attenuation values before and after administration of contrast material for the plaques (IPH, LRNC, and fibrous).

A *P* value $<$.05 was regarded as indicating a statistically significant association, and all values were calculated by using a 2-tailed significance level. *R* statistical and computing software (www.r-project.org) was used for statistical analyses.

RESULTS

General Results

The mean time interval between CT and CEA was 9 days (range, 3–14 days). No patients were excluded from the analysis. Twenty-six cases of IPH were found (prevalence of 23.08%), and another 21 had LRNC without IPH (prevalence 23.07%). In 5 cases, along the length of the plaque, there were histologic slices with LRNC and other slices with IPH (prevalence of 5.45%). The other 39 plaques did not show IPH or LRNC and were mainly calcified ($n = 24$) or characterized by fibrous tissue or myofibroblast proliferation ($n = 15$).

In our cohort, we found 29 asymptomatic patients and 62 symptomatic patients. (In the 62 symptomatic patients, 25 strokes, 24 transient ischemic attacks, and 13 cases of amaurosis fugax were observed.) The analysis of the association between IPH

Table 1: Summary of attenuation values

Type of Tissue	*N*	Mean HU	SD	Median	2.5–97.5 Percentiles	Normal Distribution
Basal						
Fibrous	47	91.66	17.7474	93	47.525–121.400	0.0052
LRNC	63	39.476	19.4529	34	16.075–87.625	0.0355
IPH	59	17.475	4.9283	17	8.975–26.025	0.0668
Contrast						
Fibrous	47	93.128	16.3609	94	49.875–120.775	0.0003
LRNC	63	48.048	19.3811	43	21.000–85.925	0.1446
IPH	59	18.407	4.8428	18	10.975–27.000	0.0021

Table 2: Mann-Whitney analysis

Type of Tissue	IPH	LRNC	Fibrous
Basal			
IPH	x	0.001	0.001
LRNC	0.001	x	0.001
Fibrous	0.001	0.001	x
Contrast			
IPH	x	0.001	0.001
LRNC	0.001	x	0.001
Fibrous	0.001	0.001	x

Note:—x indicates test is not applicable.

and the presence of cerebrovascular symptoms (including the 5 plaques where some histologic slices had LRNC and others had IPH for a total of 31 subjects with IPH) revealed an association between plaques with IPH and symptoms with a *P* value of .02 (17% of IPH in asymptomatic subjects [5/29] and 42% of IPH in symptomatic subjects [26/62]).

A total of 435 histologic slices were recorded and measured (the median number for each plaque was 5, ranging from 3–12). We excluded 61 histologic sections because of suboptimal quality. Another 129 histologic sections were excluded because they were mainly calcified plaques, and in another 63 cases, a small amount of calcium was found in the histopathologic examinations. Therefore, 253 histologic sections were excluded.

Radiologists performed the CT matching in the remaining 182 histologic slices. They excluded 2 patients (with a total of 7 histologic slices) because of streak artifacts and 1 patient who had movement artifacts (6 histologic slices). The final number of assessed slices was 169 (59 IPH, 63 LRNC, and 47 fibrous).

Plaque Analysis

Table 1 summarizes the results of the attenuation values according to the histologic types in the arterial and venous phases. The average values of the IPH were 17.475 HU and 18.407 HU before and after the administration of contrast material, respectively. The average values of the LRNC were 39.476 HU and 48.048 HU before and after the administration of contrast material, respectively, whereas for the fibrous plaque, the average values were 91.66 HU and 93.128 HU before and after the administration of contrast material.

We found that the category that showed the bigger enhancement was the LRNC (average increase of 8.54 HU) followed by fibrous tissue (1.468 HU), whereas the IPH showed the smaller variation (average increase, 0.932). The concordance between the readers (measured by Bland-Altman plots) was good, with a systematic error (1.96 SD) between −2 HU and +3 HU for IPH, between −4 HU and +5 HU for LRNC, and between −6 HU and +12 for fibrous tissue.

Mann-Whitney Test

By comparing the attenuation values among the 3 different analyzed categories (IPH, LRNC, and fibrous), we found that there was a statistically significant difference of HU values both before and after the administration of contrast material (Table 2). In Fig 2 a boxplot shows the attenuation values according to the category.

Receiver Operating Characteristic Curve Analysis

The receiver operating characteristic curve analysis was performed to test the association between the HU attenuation and the presence or absence of IPH, shown in Fig 3. The Az for the attenuation analysis performed in the basal scan was 0.944, whereas the Az after the administration of contrast medium was 0.978 (difference between the Az; $P = .026$). From the receiver operating characteristic curve analysis, we also tested multiple thresholds to identify the best combination of sensitivity and specificity value (Table 3). We found that a threshold of 25 HU in the plaque (in the dataset after administration of contrast material) has a sensitivity of 93.22% and a specificity of 92.73% for the presence of IPH.

Wilcoxon Analysis

This test was used to check the effect of the contrast material in the plaque categories. By comparing the overall attenuation of the plaques (IPH, LRNC, and fibrous) before and after the administration of contrast medium, we found a statistically significant difference ($P = .001$). By assessing the attenuation of IPH, LRNC, and fibrous tissue before and after contrast medium, we found *P* values of .006, .0001, and .018, respectively, demonstrating that the attenuation of the plaque before and after administration of contrast material is different.

DISCUSSION

Recent published studies have demonstrated that the presence of IPH is related to an increased risk of stroke independent of the severity of luminal stenosis.[25,26] Therefore, the identification of IPH represents an important step to correctly stratify the risk of potential cerebrovascular events of a subject.

CT is a widely used technique for the preoperative assessment of the subject, which allows for obtaining information related to other features related to the plaque's vulnerability such as the presence of ulcerations or large plaque volume.[13,27] It is important to remember that because of the radiation delivered, CT is not considered the best tool for follow-up of patients with carotid artery stenosis (unlike ultrasound), and that is one of its main limitations as a diagnostic tool; however, the improvement in CT technology with the introduction of dose-reduction techniques results in a viable option. The purpose of this study was to assess the CT characteristics of IPH with histopathologic correlation to identify features that allow for confirming or ruling out the IPH.

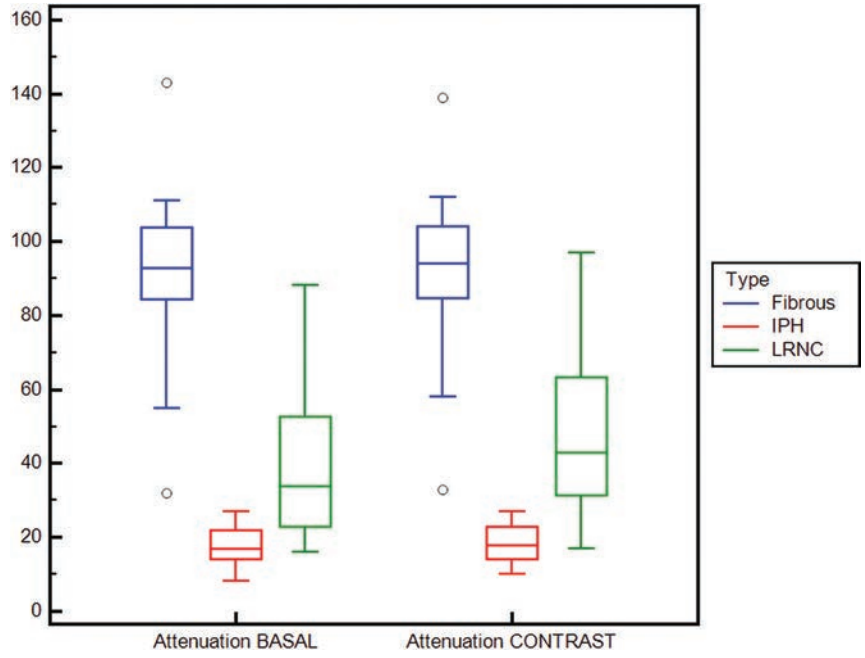

FIG 2. Boxplot with the attenuation values before and after the administration of contrast material according to the type of tissue.

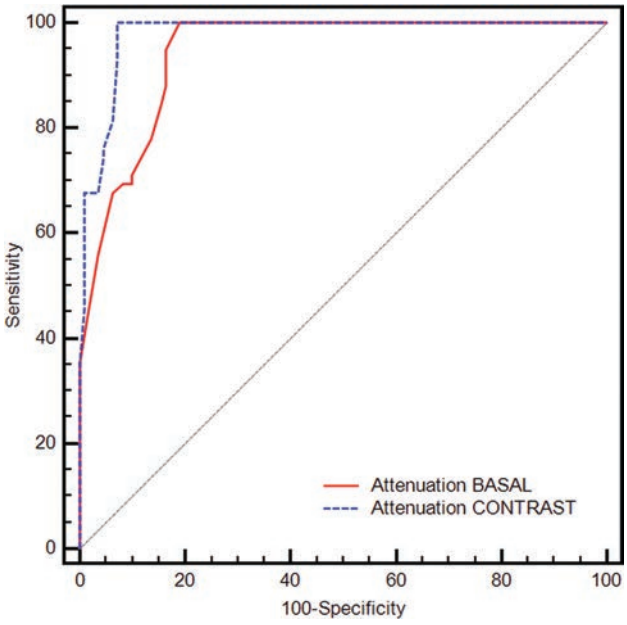

FIG 3. Receiver operating characteristic curve analysis that shows the Az of the attenuation (basal and after the administration of contrast medium) versus the presence/absence of IPH.

To obtain correct data, our readers (histologists and radiologists) gave special attention to excluding all those slices or CT datasets that were not optimal from a technical point of view. Moreover, the calcified plaques or those plaques with a visible cluster of calcium were excluded. First, the identification of the calcium is extremely easy thanks to the big attenuation that this tissue produces in the x-rays. For the same reason, those histologic slices where calcium was visible in small amounts were excluded. From the original 435 histologic slices, radiologists analyzed 169 slices (38.9%).

We found that the average value of the IPH was extremely low, with an average basal value of 17.475 HU and average value of 18.407 HU after the administration of contrast medium. In 2009, Adjuk et al[28] found that the attenuation values of the American Heart Association plaque VIb (confluent extracellular lipid core complicated by hemorrhage) was lower compared with the other types of plaque, with an average value of 22 HU compared with 59 HU for the other types of plaques, and these data were confirmed in a further publication performed by the same group in 2013.[29] Our values are lower compared with those found by Adjuk et al,[28,29] and we think that this can be attributed to 2 different causes. First, the different selection criteria; in fact, we excluded all those plaques that also had a small cluster of calcium that can justify the raised attenuation values in the work of Adjuk et al.[28,29] Second, we did not considered histologic slices with LRNC and IPH, but only those 2 features independently; this approach may explain the lower attenuation values of our observations. In addition, a study published by de Weert et al[30] in 2006 demonstrated that the presence of very hypoattenuated areas was associated with the presence of plaques complicated by hemorrhage (<30 HU).

We also compared the attenuation values among the 3 different analyzed categories (IPH, LRNC, and fibrous), and we found that there was a statistically significant difference of HU values (Table 2). This result demonstrates that the attenuation values are different from the attenuation of LRNC and fibrous tissue. In particular, hemorrhage has significantly lower attenuation values compared with the other categories of tissues.

The receiver operating characteristic curve analysis confirmed the strength of the association between the hypoattenuated values and presence of IPH (Az = 0.944 in basal analysis and 0.978 after contrast medium), and by considering a threshold value of 25 HU (in the scans obtained after the administration of contrast material), we obtained a sensitivity of 93.22% and a specificity of 92.73% for the presence of IPH. These results demonstrated that it is possible to identify an attenuation threshold by identifying the presence of IPH.

Our results are different from those observed by U-King-Im et al[31] where the authors compared CTA and IPH detected by MR imaging and found that mean CT plaque attenuation was higher for plaques with MR imaging–defined IPH (47 HU) compared with plaques without IPH (43 HU). Moreover, they found a significant overlap between the distributions of plaque densities by concluding that mean plaque attenuation is of limited value in distinguishing between the 2 groups. The differences between our results and the paper by U-King-Im et al[31] can be explained by the different methodology applied. They used as reference standard MR-defined IPH, whereas we considered the histopathologic

Table 3: Threshold analysis

HU Value	Basal Values				After Contrast Medium Values			
	Sensitivity	Specificity	+LR	−LR	Sensitivity	Specificity	+LR	−LR
<0	0.00	100.00	NC	1.00	0.00	100.00	NC	1.00
≤2	55.93	96.36	15.38	0.46	35.59	100.00	NC	0.64
≤4	67.80	93.64	10.65	0.34	45.76	99.09	50.34	0.55
≤8	69.49	90.00	6.95	0.34	67.80	99.09	74.58	0.32
≤12	71.19	90.00	7.12	0.32	67.80	96.36	18.64	0.33
≤16	77.97	86.36	5.72	0.26	74.58	95.45	16.41	0.27
≤20	84.75	84.55	5.48	0.18	76.27	95.45	16.78	0.25
≤22	88.14	83.64	5.39	0.14	81.36	93.64	12.78	0.20
≤25	94.92	83.64	5.80	0.061	93.22	92.73	12.82	0.073
≤30	100.00	80.91	5.24	0.00	100.00	92.73	13.75	0.00
≤120	100.00	0.00	1.00	NC	100.00	0.00	1.00	NC

Note:—+LR indicates positive likelihood ratio; −LR, negative likelihood ratio; NC, not classifiable.

slices. We excluded from the analysis all the slices where a cluster of calcium was identified, and this explains the average lower CT values found in our study in those plaques with IPH. Moreover, we considered multiple sections for each plaque according to the histopathologic category, and this is important because we found 10 plaques where there were areas with IPH and others without IPH. These findings confirm that in the same plaques, there exist different tissues, and they are not always represented in a single axial section. For this reason, we suggest readers check the entire length of the plaque and not only the thickened point and assess with ROIs having different levels of the plaque. This is a significant point because the plaques show a spatial heterogeneity other than a temporal variability; therefore, the plaque should be considered a dynamic process, and lack of IPH doesn't mean that sometime in the future IPH cannot appear.

We also tested the difference in attenuation before and after the administration of contrast medium and found that there was a statistically significant difference (.006, .0001, and .018 for IPH, LRNC, and fibrous tissue, respectively), by confirming the fact that the contrast material plays an important role in the attenuation values of the carotid artery plaques.[32-34]

In this study, there are some limitations. First, this is a retrospective study, and this approach may determine a bias; however, it is our opinion this can be a considered a minor limitation because our focus was to assess the attenuation value of the IPH, and we would use the same paradigm in prospective approach. Second, the registration between histologic sections and the CT dataset is fundamental to obtain correct as well as relevant data. We tried to use our experience and all the potential tools to overcome the problems related to the registration (spatial registration features, manual and experienced correction, and the use of 2 different readers). However, there are some limits that are not possible to solve, in particular, the fact that the histologic preparation leads to plaque shrinkage[35]; in the study by de Weert et al,[30] the total plaque area acquired in MDCTA images was 30% larger than the histologic total plaque area.

CONCLUSIONS

The results of this preliminary study suggest that CT can be used to identify the presence of IPH according to the attenuation. A threshold of 25 HU in the volume acquired after the administration of contrast medium is associated with an optimal sensitivity and specificity. Special care should be given to the correct identification of the area to place the ROI.

Disclosures: Marco Francone—*UNRELATED: Payment for Lectures Including Service On Speakers Bureaus*: Bracco Medical Imaging. Carlo Nicola De Cecco—*UNRELATED: Grants/Grants Pending*: Siemens*. *Money paid to the institution.

REFERENCES

1. Kwee RM, van Oostenbrugge RJ, Mess WH, et al. **MRI of carotid atherosclerosis to identify TIA and stroke patients who are at risk of a recurrence.** *J Magn Reson Imaging* 2013;37:1189–94 CrossRef Medline
2. Mono ML, Karameshev A, Slotboom J, et al. **Plaque characteristics of asymptomatic carotid stenosis and risk of stroke.** *Cerebrovasc Dis* 2012;34:343–50 CrossRef Medline
3. Kurosaki Y, Yoshida K, Endo H, et al. **Association between carotid atherosclerosis plaque with high signal intensity on T1-weighted imaging and subsequent ipsilateral ischemic events.** *Neurosurgery* 2011;68:62–67; discussion 67 CrossRef Medline
4. Demarco JK, Huston J 3rd. **Imaging of high-risk carotid artery plaques: current status and future directions.** *Neurosurg Focus* 2014; 36:E1 CrossRef Medline
5. Peeters W, Hellings WE, de Kleijn DP, et al. **Carotid atherosclerotic plaques stabilize after stroke: insights into the natural process of atherosclerotic plaque stabilization.** *Arterioscler Thromb Vasc Biol* 2009;29:128–33 CrossRef Medline
6. Hellings WE, Peeters W, Moll FL, et al. **Composition of carotid atherosclerotic plaque is associated with cardiovascular outcome: a prognostic study.** *Circulation* 2010;121:1941–50 CrossRef Medline
7. Moody AR, Allder S, Lennox G, et al. **Direct magnetic resonance imaging of carotid artery thrombus in acute stroke.** *Lancet* 1999; 353:122–23 CrossRef Medline
8. Daniels LR, Gladman JR, Altaf N, et al. **Magnetic resonance direct thrombus imaging in moderate carotid artery stenosis.** *Stroke* 2006; 37:767–68 CrossRef Medline
9. Millon A, Mathevet JL, Boussel L, et al. **High-resolution magnetic resonance imaging of carotid atherosclerosis identifies vulnerable carotid plaques.** *J Vasc Surg* 2013;57:1046–51.e2 CrossRef Medline
10. Saam T, Hetterich H, Hoffmann V, et al. **Meta-analysis and systematic review of the predictive value of carotid plaque hemorrhage on cerebrovascular events by magnetic resonance imaging.** *J Am Coll Cardiol* 2013;62:1081–91 CrossRef Medline
11. Anzidei M, Napoli A, Zaccagna F, et al. **Diagnostic accuracy of colour Doppler ultrasonography, CT angiography and blood-pool-enhanced MR angiography in assessing carotid stenosis: a comparative study with DSA in 170 patients.** *Radiol Med* 2012;117:54–71 CrossRef Medline
12. Lell M, Fellner C, Baum U, et al. **Evaluation of carotid artery stenosis with multisection CT and MR imaging: influence of imaging mo-**

dality and postprocessing. *AJNR Am J Neuroradiol* 2007;28:104–10 Medline
13. van den Bouwhuijsen QJ, Bos D, Ikram MA, et al. **Coexistence of calcification, intraplaque hemorrhage and lipid core within the asymptomatic atherosclerotic carotid plaque: The Rotterdam Study.** *Cerebrovasc Dis* 2015;39:319–24 CrossRef Medline
14. Saba L, Raz E, Anzidei M, et al. **Differences in plaque morphology and correlation of stenosis at the carotid artery bifurcation and the carotid siphon.** *AJR Am J Roentgenol* 2013;201:1108–14 CrossRef Medline
15. Homburg PJ, Rozie S, van Gils MJ, et al. **Atherosclerotic plaque ulceration in the symptomatic internal carotid artery is associated with nonlacunar ischemic stroke.** *Stroke* 2010;41:1151–56 CrossRef Medline
16. Saba L, Caddeo G, Sanfilippo R, et al. **CT and ultrasound in the study of ulcerated carotid plaque compared with surgical results: potentialities and advantages of multidetector row CT angiography.** *AJNR Am J Neuroradiol* 2007;28:1061–66 CrossRef Medline
17. Saba L, Sanfilippo R, Montisci R, et al. **Agreement between multidetector-row CT angiography and ultrasound echo-color Doppler in the evaluation of carotid artery stenosis.** *Cerebrovasc Dis* 2008;26:525–32 CrossRef Medline
18. Saba L, Sanfilippo R, Pascalis L, et al. **Carotid artery wall thickness and ischemic symptoms: evaluation using multi-detector-row CT angiography.** *Eur Radiol* 2008;18:1962–71 CrossRef Medline
19. North American Symptomatic Carotid Endarterectomy Trial Collaborators. **Beneficial effect of carotid endarterectomy in symptomatic patients with high-grade carotid stenosis.** *N Engl J Med* 1991;325:445–53 CrossRef Medline
20. Saba L, Tamponi E, Raz E, et al. **Correlation between fissured fibrous cap and contrast enhancement: preliminary results with the use of CTA and histologic validation.** *AJNR Am J Neuroradiol* 2014;35:754–59 CrossRef Medline
21. Saba L, Raz E, Grassi R, et al. **Association between the volume of carotid artery plaque and its subcomponents and the volume of white matter lesions in patients selected for endarterectomy.** *AJR Am J Roentgenol* 2013;201:W747–52 CrossRef Medline
22. Executive Committee for the Asymptomatic Carotid Atherosclerosis Study. **Endarterectomy for asymptomatic carotid artery stenosis.** *JAMA* 1995;273:1421–28 CrossRef Medline
23. Setacci C, Lanza G, Ricci S, et al. **SPREAD Italian guidelines for stroke. Indications for carotid endarterectomy and stenting.** *J Cardiovasc Surg (Torino)* 2009;50:171–82 Medline
24. Saba L, Mallarin G. **Window settings for the study of calcified carotid plaques with multidetector CT angiography.** *AJNR Am J Neuroradiol* 2009;30:1445–50 CrossRef Medline
25. Parmar JP, Rogers WJ, Mugler JP 3rd, et al. **Magnetic resonance imaging of carotid atherosclerotic plaque in clinically suspected acute transient ischemic attack and acute ischemic stroke.** *Circulation* 2010;122:2031–38 CrossRef Medline
26. Takaya N, Yuan C, Chu B, et al. **Presence of intraplaque hemorrhage stimulates progression of carotid atherosclerotic plaques: a high-resolution magnetic resonance imaging study.** *Circulation* 2005;111:2768–75 CrossRef Medline
27. Rozie S, de Weert TT, de Monyé C, et al. **Atherosclerotic plaque volume and composition in symptomatic carotid arteries assessed with multidetector CT angiography; relationship with severity of stenosis and cardiovascular risk factors.** *Eur Radiol* 2009;19:2294–301 CrossRef Medline
28. Ajduk M, Pavić L, Bulimbasić S, et al. **Multidetector-row computed tomography in evaluation of atherosclerotic carotid plaques complicated with intraplaque hemorrhage.** *Ann Vasc Surg* 2009;23:186–93 CrossRef Medline
29. Ajduk M, Bulimbasić S, Pavić L, et al. **Comparison of multidetector-row computed tomography and duplex Doppler ultrasonography in detecting atherosclerotic carotid plaques complicated with intraplaque hemorrhage.** *Coll Antropol* 2013;37:213–29 Medline
30. de Weert TT, Ouhlous M, Meijering E, et al. **In vivo characterization and quantification of atherosclerotic carotid plaque components with multidetector computed tomography and histopathological correlation.** *Arterioscler Thromb Vasc Biol* 2006;26:2366–72 CrossRef Medline
31. U-King-Im JM, Fox AJ, Aviv RI, et al. **Characterization of carotid plaque hemorrhage: a CT angiography and MR intraplaque hemorrhage study.** *Stroke* 2010;41:1623–29 CrossRef Medline
32. Saba L, Lai ML, Montisci R, et al. **Association between carotid plaque enhancement shown by multidetector CT angiography and histologically validated microvessel density.** *Eur Radiol* 2012;22:2237–45 CrossRef Medline
33. Saba L, Piga M, Raz E, et al. **Carotid artery plaque classification: does contrast enhancement play a significant role?** *AJNR Am J Neuroradiol* 2012;33:1814–17 CrossRef Medline
34. Saba L, Mallarini G. **Carotid plaque enhancement and symptom correlations: an evaluation by using multidetector row CT angiography.** *AJNR Am J Neuroradiol* 2011;32:1919–25 CrossRef Medline
35. Dobrin PB. **Effect of histologic preparation on the cross-sectional area of arterial rings.** *J Surg Res* 1996;61:413–15 CrossRef Medline

Dynamic Contrast-Enhanced MRI–Derived Intracellular Water Lifetime (τ_i): A Prognostic Marker for Patients with Head and Neck Squamous Cell Carcinomas

S. Chawla, L.A. Loevner, S.G. Kim, W.-T. Hwang, S. Wang, G. Verma, S. Mohan, V. LiVolsi, H. Quon, and H. Poptani

ABSTRACT

BACKGROUND AND PURPOSE: Shutter-speed model analysis of dynamic contrast-enhanced MR imaging allows estimation of mean intracellular water molecule lifetime (a measure of cellular energy metabolism) and volume transfer constant (a measure of hemodynamics). The purpose of this study was to investigate the prognostic utility of pretreatment mean intracellular water molecule lifetime and volume transfer constant in predicting overall survival in patients with squamous cell carcinomas of the head and neck and to stratify p16-positive patients based upon survival outcome.

MATERIALS AND METHODS: A cohort of 60 patients underwent dynamic contrast-enhanced MR imaging before treatment. Median, mean intracellular water molecule lifetime and volume transfer constant values from metastatic nodes were computed from each patient. Kaplan-Meier analyses were performed to associate mean intracellular water molecule lifetime and volume transfer constant and their combination with overall survival for the first 2 years, 5 years, and beyond (median duration, >7 years).

RESULTS: By the last date of observation, 18 patients had died, and median follow-up for surviving patients ($n = 42$) was 8.32 years. Patients with high mean intracellular water molecule lifetime (4 deaths) had significantly ($P = .01$) prolonged overall survival by 5 years compared with those with low mean intracellular water molecule lifetime (13 deaths). Similarly, patients with high mean intracellular water molecule lifetime (4 deaths) had significantly ($P = .006$) longer overall survival at long-term duration than those with low mean intracellular water molecule lifetime (14 deaths). However, volume transfer constant was a significant predictor for only the 5-year follow-up period. There was some evidence ($P < .10$) to suggest that mean intracellular water molecule lifetime and volume transfer constant were associated with overall survival for the first 2 years. Patients with high mean intracellular water molecule lifetime and high volume transfer constant were associated with significantly ($P < .01$) longer overall survival compared with other groups for all follow-up periods. In addition, p16-positive patients with high mean intracellular water molecule lifetime and high volume transfer constant demonstrated a trend toward the longest overall survival.

CONCLUSIONS: A combined analysis of mean intracellular water molecule lifetime and volume transfer constant provided the best model to predict overall survival in patients with squamous cell carcinomas of the head and neck.

ABBREVIATIONS: CRT = chemoradiation therapy; DCE-MRI = dynamic contrast-enhanced MR imaging; HNSCC = squamous cell carcinomas of the head and neck; HPV = human papillomavirus; HR = hazard ratio; K^{trans} = volume transfer constant; OS = overall survival; τ_i = mean intracellular water molecule lifetime

Patients with squamous cell carcinomas of the head and neck (HNSCC) are usually associated with a poor prognosis, and the presence of metastatic lymph nodes is considered a negative prognostic indicator.[1] Consequently, there is an unmet need to understand the tumor biology to improve clinical management.

Dynamic contrast-enhanced MR imaging (DCE-MRI) allows estimation of volume transfer constant (K^{trans}),[2,3] an efflux rate constant of gadolinium-based contrast agent from the intravas-

Received February 21, 2017; accepted after revision September 4.

From the Departments of Radiology (S.C., L.A.L., S.G.K., S.W., G.V., S.M., H.P.), Radiation Oncology (H.Q.), Biostatistics and Epidemiology (W.-T.H.), and Pathology and Lab Medicine (V.L.), Perelman School of Medicine, University of Pennsylvania, Philadelphia, Pennsylvania; Department of Radiology (S.G.K.), New York University, New York, New York; Department of Radiation Oncology and Molecular Radiation Sciences (H.Q.), Johns Hopkins University, Baltimore, Maryland; and Department of Cellular and Molecular Physiology (H.P.), University of Liverpool, Liverpool, United Kingdom.

This work was supported by National Institutes of Health grant R01-CA102756 (H.P.).

Paper previously presented at: American Society of Neuroradiology Annual Meeting and the Foundation of the ASNR Symposium, May 21–26, 2016; Washington, D.C.

Please address correspondence to Harish Poptani, PhD, Centre for Pre-Clinical Imaging, Department of Cellular and Molecular Physiology, University of Liverpool, Crown St, Liverpool L69 3BX, United Kingdom; e-mail: Harish.Poptani@liverpool.ac.uk

Indicates open access to non-subscribers at www.ajnr.org

http://dx.doi.org/10.3174/ajnr.A5440

cular compartment to tumor interstitium. The potential of pretreatment K^{trans} in predicting short-term response[4-7] as well as overall survival (OS) in patients with HNSCC has been reported.[8,9] Patients treated with chemoradiation therapy (CRT) and with high baseline K^{trans} from metastatic nodes were associated with an improved prognosis compared with patients with low baseline K^{trans}.[8,9] In addition to K^{trans}, shutter-speed model analysis of DCE-MRI derives a novel imaging biomarker known as mean intracellular water lifetime (τ_i),[10-12] which has been suggested to be a metabolic marker.[12] The unique strength of τ_i lies in the fact that it is less sensitive to arterial input function scaling variations than K^{trans},[13] indicating that τ_i is a more reproducible and reliable marker. The parameter τ_i has been used to characterize breast,[14] prostate,[15,16] esophageal,[17] and hepatocellular cancer.[18] A recent study[19] also demonstrated the prognostic utility of τ_i in predicting survival in patients with hepatocellular carcinomas.

Although K^{trans} reflects tumor perfusion and vascular permeability,[3] τ_i provides unique information related to tumor cell characteristics such as cell size, cell membrane permeability, and cellular metabolic activity.[12] Given that K^{trans} and τ_i provide complementary information about the tumor microenvironment, we believe that a combined analysis may be more useful than individual parameters in predicting prognosis in patients with HNSCC.

Thus, the purpose of the present study was to assess the prognostic value of pretreatment τ_i and K^{trans} in predicting OS in patients with HNSCC. In addition, in a subset of patients, we explored the prognostic potential of τ_i and K^{trans} in p16-associated HNSCC given the fundamental differences in tumor biology and prognosis of these patients.[20-22]

Patient characteristics and treatment modalities

Characteristics	
Number of patients	60
Mean age, yrs ± SD	62.34 ± 9.18
Sex	
Male	49 (81.7%)
Female	11 (18.3%)
Primary tumor site	
Base of tongue	24 (40.0%)
Tonsil	14 (23.3%)
Larynx	7 (11.7%)
Less common/unknown sites	15 (25.0%)
T staging	
Tx	14 (23.3%)
T0	2 (3.3%)
T1	2 (3.3%)
T2	15 (25.0%)
T3	9 (15.0%)
T4	18 (30.0%)
N staging	
N1	2 (3.3%)
N2	51 (85.0%)
N3	7 (11.7%)
M staging	
M0	60 (100%)
p16 expression	
Positive	21 (35.0%)
Negative	11 (18.3%)
Unknown (insufficient specimen)	28 (46.7%)
Treatment	
Radiotherapy + concurrent chemotherapy	39 (65.0%)
Induction chemotherapy + radiotherapy + concurrent chemotherapy	21 (35.0%)

MATERIALS AND METHODS

Patients

This retrospective analysis of pre-existing imaging and clinical data was institutional review board–approved and was compliant with the Health Insurance Portability and Accountability Act. On the basis of previous CT/MR imaging reports, all patients were assessed for the presence of at least 1 metastatic cervical lymph node measuring >1 cm^3 and biopsy-proved histopathologic diagnosis of HNSCC. The exclusion criteria included prior CRT or a history of cancer other than HNSCC. A total of 72 patients with newly diagnosed HNSCC met the inclusion criteria and were recruited between January 2005 and August 2009. TNM staging was used to determine the disease status. Each patient received appropriate therapy to deliver the maximum clinical benefit, which included upfront neck dissection ($n = 3$), concurrent CRT ($n = 46$), or induction chemotherapy followed by CRT ($n = 23$). Three patients who underwent upfront neck dissection and 9 patients who had either corrupted MR imaging data or insufficient clinical data were excluded from the data analysis. Therefore, OS analyses were performed on the remaining 60 patients (mean age ± SD, 62.34 ± 9.18 years; 49 men, 11 women). Tumor location and staging from these patients at the initial presentation are summarized in the Table.

Data Acquisition

All patients underwent MR imaging before surgery and CRT on a 1.5T Sonata scanner (Siemens, Erlangen, Germany; $n = 37$) or on a 3T Magnetom Trio scanner (Siemens; $n = 35$). Structural imaging included axial T2-weighted and T1-weighted images with standard parameters. Inversion-recovery–prepared T1-weighted images were acquired by using TIs of 60, 200, 400, 800, and 1600 ms before the acquisition of DCE-MRI data for T1 quantification.

As described previously,[5] DCE-MRI was performed by using a rapid 3D-spoiled gradient-echo sequence modified to acquire 8 angle-interleaved subaperture images from the full-echo radial data.[23] Imaging parameters were: TR, 5.0 ms; TE, 4.2 ms; 256 readout points per view; 256 views (32 views per subaperture, 8 subapertures); field of view, 260 × 260 mm^2; number of sections, 8; section thickness, 5 mm. Fat saturation was applied once every 8 excitations. Spatial saturation was applied once every 32 excitations to minimize the flow effect while minimizing acquisition time. This scheme resulted in a temporal resolution of 2.5 seconds for each subaperture image with full spatial resolution of 256 × 256 by using a dynamic *k*-space–weighted image reconstruction contrast algorithm.

Image Processing

All images (T2, T1, postcontrast T1-weighted, and DCE-MRI) were coregistered by using a 2-step nonrigid image registration technique.[5] The ROIs were drawn on the solid portion of the largest nodal mass by using anatomic images. Care was taken to avoid necrotic/cystic or hemorrhagic parts as well as surrounding blood vessels. Pharmacokinetic analysis of DCE-MRI data was performed for each voxel in the selected ROIs by using a shutter-speed model.[5,10] Estimation of arterial input function was per-

formed semiautomatically from an ROI on one of the carotid arteries located near the metastatic lymph node.[5,10] Median pretreatment τ_i and K^{trans} were computed by using only the central 4 sections to avoid erroneous results from wraparound artifacts in the edge sections.

Clinical Follow-Up and Data Analysis

The clinical follow-up period was measured from the end date of CRT to the date of death for deceased patients or to the date of last observation for surviving patients.

Median pretreatment τ_i and K^{trans} values were 0.125 seconds and 0.409 minutes^{-1}, respectively, and were used as thresholds to divide patients into 2 groups (at or above and below the threshold value). Patients in the high τ_i group had a mean ± SD τ_i of 0.276 ± 0.086 seconds and a median of 0.269 seconds. Patients in the low τ_i group had a mean ± SD τ_i of 0.070 ± 0.028 seconds and a median of 0.071 seconds. Similarly, patients in the high K^{trans} group had a mean ± SD K^{trans} of 0.90 ± 0.54 minutes^{-1} with a median of 0.88 minutes^{-1}, whereas patients in the low K^{trans} group had a mean ± SD K^{trans} of 0.188 ± 0.108 minutes^{-1} and a median of 0.196 minutes^{-1}.

Using the 2-year (short-term), 5-year (intermediate-term), and all available follow-up (long-term [median, 7.83 years; range, 0.07–10.7 years]) as clinical end points, OS was analyzed. In addition to using τ_i and K^{trans} as independent predictors, combinations of these parameters (high τ_i/high K^{trans}, high τ_i/low K^{trans}, low τ_i/high K^{trans}, and low τ_i/low K^{trans}) were used. Kaplan-Meier survival curves were plotted and compared by using log-rank tests. Using a Cox regression model, hazard ratios (HRs) of deaths and associated 95% CI were estimated for τ_i and K^{trans} first separately, and then for the different combinations of these parameters (high τ_i/high K^{trans}, high τ_i/low K^{trans}, low τ_i/high K^{trans}, and low τ_i/low K^{trans}). In addition, a Wald test was performed to evaluate the joint effect of these combinations. A P value <.05 was considered significant. All data analyses were performed by using SPSS for Windows version 18.0 (IBM, Armonk, New York).

Stratifying HPV/p16-Positive and p16-Negative Patients

Human papillomavirus (HPV) status was determined from tissue specimens by immunohistochemical evaluation of p16 expression by using a commercially available monoclonal antibody. Tissue samples were available from only 32 patients, and these were divided into 2 groups: positive (n = 21) or negative (n = 11) for p16 expression.[24] There were no significant differences (P > .05) in age, treatment regimen, τ_i, and K^{trans} between patients who had and those who did not have tissue specimens for p16 expression. Using p16 as an independent variable, OS analyses were performed from these 32 patients. To further stratify p16-positive and p16-negative patients, separate OS analyses were performed by using τ_i and K^{trans} as independent variables and by using combinations of these parameters.

RESULTS

Representative anatomic images and τ_i and K^{trans} maps from a patient who was alive by the last date of observation with a follow-up duration of 8.19 years and from a patient who died 2.12 years after the end of CRT are shown in Figs 1 and 2, respectively.

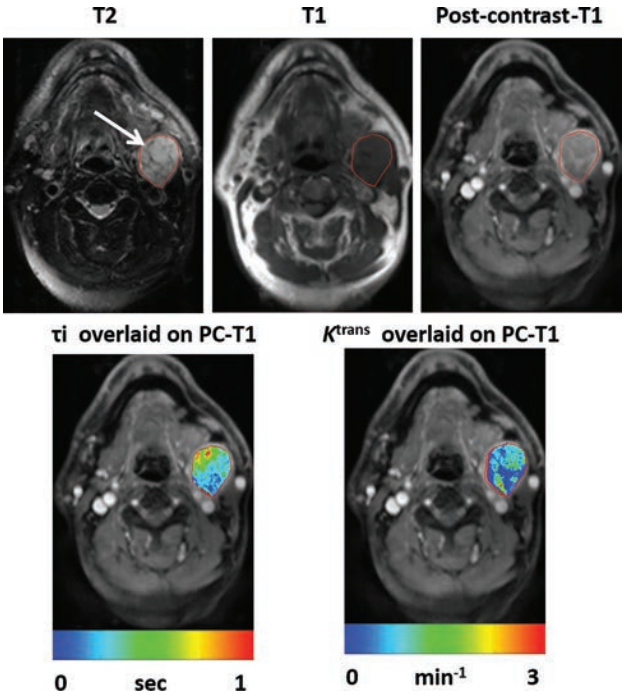

FIG 1. Representative images from a patient exhibiting long survival (follow-up duration of 8.19 years). Axial T2-weighted image (*A*) demonstrates an enlarged heterogeneous hyperintense metastatic left level IIa lymph node (*arrow*). This appears hypointense on a coregistered T1-weighted image (*B*), with heterogeneous enhancement on the corresponding postcontrast T1-weighted image (*C*). DCE-MRI–derived τ_i (0.136 seconds [*D*]) and K^{trans} (0.882 minutes^{-1} [*E*]) maps are shown as color images overlaid on postcontrast T1-weighted images.

In the first 2-year follow-up period, 13 of 60 patients died of the disease. In 5 years, the number of deceased patients was 17, whereas a total of 18 patients died by the last date of observation. The median follow-up for surviving patients (n = 42) was 8.32 years (range, 5.42–10.7 years).

Prognostic Utility of τ_i

In the first 2 years, a trend toward longer OS was noted for patients with higher τ_i (4 deaths) compared with those with lower τ_i (9 deaths; log-rank P = .09). The probability for survival in patients with high τ_i was 86.7% (95% CI, 68.3%–94.8%), whereas it was 70% (95% CI, 60.3%–83.1%) for patients with low τ_i.

Interestingly, by 5 years, significantly longer OS was observed for patients with higher τ_i (4 deaths) compared with those with lower τ_i (13 deaths; log-rank P = .01). Similarly, patients with higher τ_i (4 deaths) had significantly prolonged OS compared with those with lower τ_i (14 deaths; log-rank P = .006; Fig 3) when long-term follow-up duration was considered (median duration, >7 years). At 5 years, survival probability for patients with high τ_i was 86.7% (95% CI, 68.3%– 94.8%), and for patients with low τ_i, it was 56.8% (95% CI, 37.4%–72.1%).

Cox regression analysis demonstrated a nonsignificant difference (P = .13) in OS between the 2 groups for the 2-year follow-up period, with an HR of 2.43 (95% CI, 0.75–7.92). However, a P value of .02 with HR of 3.71 (95% CI, 1.20–11.39) for 5 years and a P value of .01 with HR of 4.24 (95% CI, 1.38–12.97) were observed in predicting long-term OS.

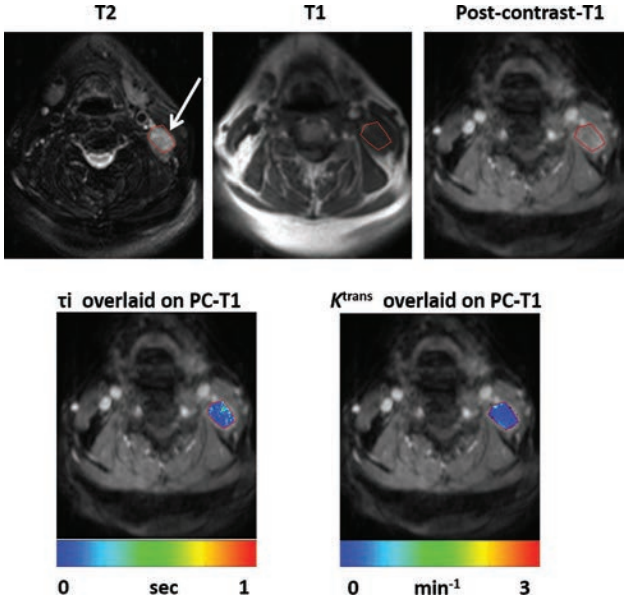

FIG 2. Representative images from a patient who died 2.12 years after the end of CRT. Axial T2-weighted image (*A*) demonstrates a heterogeneous hyperintense metastatic left level IIb lymph node (*arrow*). It appears hypointense on a coregistered T1-weighted image (*B*) with heterogeneous enhancement on postcontrast T1-weighted image (*C*). DCE-MRI–derived τ_i (0.031 seconds; [*D*]) and K^{trans} (0.135 minutes^{-1} [*E*]) maps overlaid on postcontrast T1-weighted images demonstrating lower τ_i and K^{trans} values from the node compared with the patient with longer survival as shown in Fig 1.

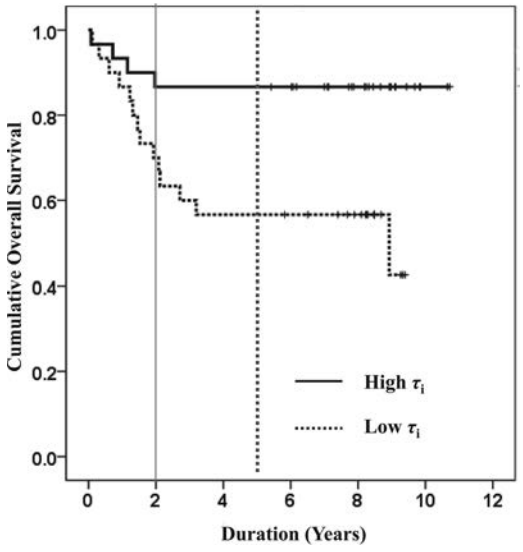

FIG 3. Kaplan-Meier plot for τ_i. Patients with higher pretreatment τ_i (*solid curves*) demonstrate longer OS compared with patients with lower τ_i (*broken curves*) for first 2-year (solid vertical line, $P = .09$), 5-year (dotted vertical line, $P = .01$), and long-term (median duration, >7 years; $P = .006$) follow-up periods.

Prognostic Utility of K^{trans}

At 2 years, patients with higher K^{trans} (4 deaths) had longer but nonsignificant OS compared with those with lower K^{trans} (9 deaths; log-rank $P = .07$). At 2 years, survival probability was 87.1% (95% CI, 69.2%–95.0%) for patients with high K^{trans} and 69.0% (95% CI, 48.8%–82.5%) for patients with low K^{trans}.

By 5 years, significantly prolonged OS for patients with higher K^{trans} (5 deaths) was noted compared with those with lower K^{trans} (12 deaths; log-rank $P = .03$). Survival probability for patients with high K^{trans} was 83.9% (95% CI, 65.5%–93.0%) and for patients with low K^{trans} was 58.6% (95% CI, 38.8%–74.0%). However, only a trend toward prolonged OS was observed for patients with higher K^{trans} (6 deaths) compared with those with lower K^{trans} (12 deaths; log-rank $P = .06$) when long-term OS was evaluated (Fig 4).

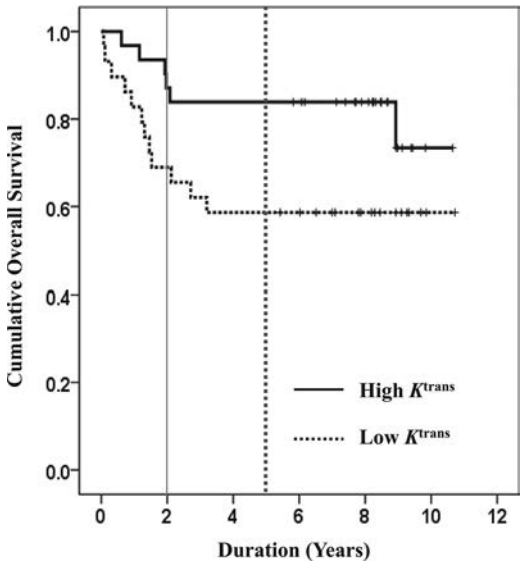

FIG 4. Kaplan-Meier plots for K^{trans}. Patients with higher pretreatment K^{trans} (*solid curves*) demonstrate longer OS compared with patients with lower K^{trans} (*broken curves*) at the 2-year (*solid vertical line*; $P = .07$), 5-year (*dotted vertical line*; $P = .028$), and long-term (median duration, >7 years; $P = .06$) follow-up periods.

Cox regression analyses showed nonsignificant differences between the 2 groups for 2 years ($P = .09$) with HR of 2.78 (95% CI, 0.85–9.05) and for long-term periods ($P = .06$) with HR of 2.52 (95% CI, 0.94–6.72). However, a *P* value of .04 with HR of 3.04 (95% CI, 1.07–8.64) was observed in predicting 5-year OS.

Prognostic Utility of Combined Analysis Involving τ_i and K^{trans}

By 2 years, the longest OS was observed for patients with high τ_i/high K^{trans} ($n = 15$, 2 deaths). On the other hand, patients with low τ_i/low K^{trans} ($n = 14$, 7 deaths) had the shortest OS (log-rank $P = .02$). In the group of patients ($n = 31$) who had either high τ_i/low K^{trans} or low τ_i/high K^{trans}, 4 patients died. Moreover, patients with high τ_i/low K^{trans} had longer OS than patients with low τ_i/high K^{trans}. Similarly, at 5 years, patients with high τ_i/high K^{trans} ($n = 15$, 2 deaths) had the longest OS, whereas patients with low τ_i/low K^{trans} ($n = 14$, 10 deaths) had the shortest OS (log-rank $P < .0001$). Of the remaining 31 patients, 5 patients were deceased and patients with high τ_i/low K^{trans} had longer OS than patients with low τ_i/high K^{trans}.

A similar pattern was observed for long-term analysis. Patients with high τ_i/high K^{trans} ($n = 15$, 2 deaths) had the longest OS, and patients with low τ_i/low K^{trans} ($n = 14$, 10 deaths) had the shortest OS (log-rank $P < .0001$). Of the remaining 31 patients, 6 died, and again, patients with high τ_i/low K^{trans} had longer OS than patients with low τ_i/high K^{trans} (Fig 5).

For the first 2-year follow-up period, multivariate Cox regression analyses revealed a P value of .048 with HRs of 0.21 (95% CI, 0.04–1.00; $P = .05$), 0.22 (95% CI, 0.05–1.07; $P = .06$), and 0.20 (95% CI, 0.04–0.95; $P = .04$) for patients with high τ_i/high K^{trans}, high τ_i/low K^{trans}, and low τ_i/high K^{trans}, respectively, with respect to patients with low τ_i/low K^{trans}. Similarly, a P value of .003 with HRs of 0.13 (95% CI, 0.03–0.60; $P = .009$), 0.14 (95% CI, 0.03–0.63; $P = .01$), and 0.19 (95% CI, 0.05–0.69; $P = .01$) for the first 5 years, and P value of .003 with HRs of 0.12 (95% CI, 0.03–0.58; $P = .007$), 0.13 (95% CI, 0.03–0.61; $P = .01$), and 0.26 (95% CI, 0.08–0.82; $P = .02$) for long-term OS were observed.

When all the combinations of variables (high τ_i/high K^{trans}, high τ_i/low K^{trans}, low τ_i/high K^{trans}) were considered together, HRs of 1.84 (95% CI, 1.05–3.23; $P = .03$), 2.32 (95% CI, 1.35–3.97; $P = .002$), and 2.31 (95% CI, 1.38–3.87; $P = .001$) for the first 2 years, 5 years, and long-term OS, respectively, were observed. Overall, combination of the τ_i and K^{trans} groups demonstrated differential OS (Wald test, $P = .003$).

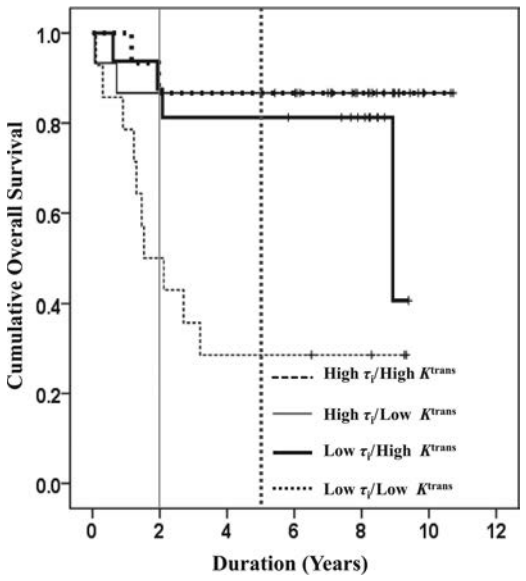

FIG 5. Kaplan-Meier plots for combinations of τ_i and K^{trans}. Patients with high τ_i/K^{trans} (*thick broken curve*) had the longest OS, and patients with low τ_i/K^{trans} (*thin broken curve*) had the shortest OS for the first 2-year (*solid vertical line*; $P = .02$), 5-year (*dotted vertical line*; $P < .0001$), and long-term (median duration, >7 years; $P < .0001$) follow-up periods. In addition, patients with high τ_i/low K^{trans} (*thick solid curve*) exhibited longer OS than patients with low τ_i/high K^{trans} (*thin solid curve*) at all clinical end points.

Stratifying HPV/p16-Positive and p16-Negative Patients

Of 32 patients with the availability of p16 status, 13 died by the date of last observation. Patients with p16-positive status had significantly longer OS than p16-negative patients ($P = .05$; Fig 6*A*). Noticeably, no significant difference ($P = .17$) in OS was observed between patients in whom p16-expression data were or were not available.

Patients with p16-positive status with higher τ_i demonstrated nonsignificantly longer OS ($P = .20$) than patients with lower τ_i. Similarly, nonsignificant ($P = .61$) differences were observed for K^{trans}. Moreover, p16-positive patients with high τ_i/high K^{trans} had the longest OS, and patients with low τ_i/low K^{trans} had the shortest OS. However, these findings were also not significant (Fig 6*B*; $P > .05$). In addition, patients with p16-negative status and higher τ_i demonstrated nonsignificantly ($P = .12$) longer OS than those with lower τ_i. We could not compare OS by using K^{trans} because all patients in this subgroup had K^{trans} higher than the median value.

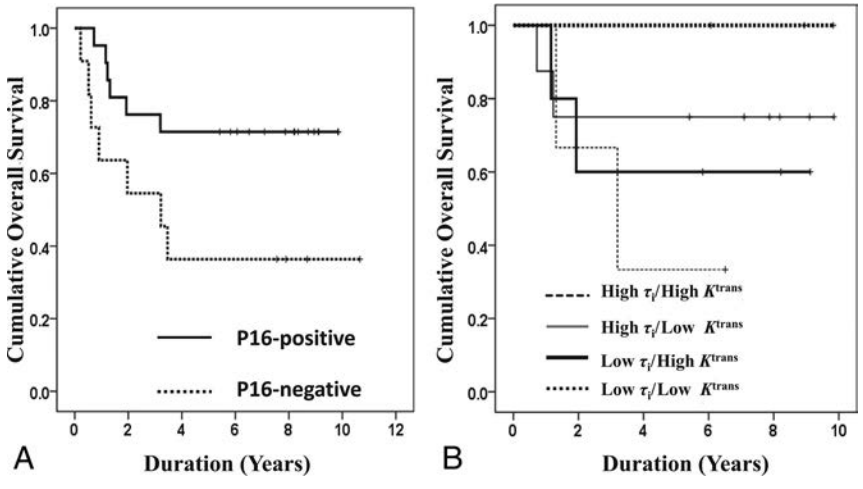

FIG 6. Kaplan-Meier plots for p16 expression. (*A*) Patients with p16-positive expression (solid curve) exhibited significantly longer long-term (median duration, >7 years) OS ($P < .05$) than patients with p16-negative expression (*broken curve*) (*B*). Patients with positive p16 expression and high τ_i/high K^{trans} (*thick broken curve*) had longer OS than p16-positive patients with low τ_i/low K^{trans} (*thin broken curve*). In addition, patients with high τ_i/low K^{trans} (*gray solid curve*) exhibited longer OS than patients with low τ_i/high K^{trans} (*black solid curve*) at all clinical end points. However, these differences were not significant ($P > .05$).

DISCUSSION

Our observations suggest that patients with higher pretreatment τ_i and K^{trans} from metastatic nodes exhibit longer OS. These results are particularly encouraging given the adverse prognosis associated with nodal metastases and offer potential opportunities to develop alternative therapeutic approaches in the poor prognosis cohort.

Earlier studies[12,25,26] have reported that τ_i is inversely correlated with cell membrane ion-pump activity, a measure of mitochondrial metabolism

suggesting that τ_i might be a sensitive indicator of cellular energy turnover. Similarly, some studies have reported that increased metabolic activity is associated with lower τ_i (median, 0.16–1.03 seconds) in regions of prostrate[15,16] and esophageal cancer[17] compared with normal tissues. In yet another study,[18] lower τ_i (0.11 ± 0.02 seconds versus 0.29 ± 0.53 seconds) was observed from normal liver parenchyma (a metabolically more active region) compared with hepatocellular carcinomas. The inverse correlation between τ_i and tumor metabolism was corroborated when higher τ_i was observed in complete responders compared with poor responders with breast carcinomas.[12,14] Taken together, these studies imply that malignant cells

from tumors with high τ_i have reduced metabolic energy available for their growth relative to malignant cells from tumors with low τ_i.

In the present study, patients with HNSCC with higher pretreatment τ_i from the metastatic nodes were associated with prolonged OS measured at 3 different clinical end points, suggesting that malignant cells were associated with reduced metabolic energy. An inverse correlation of τ_i with EF5, a marker of hypoxia, and direct correlation of elevated τ_i regions with high blood flow have been reported.[27] An earlier study[28] reported that tumors with relatively higher blood flow and reduced hypoxia are associated with increased oxygenation, resulting in better access to chemotherapeutic drugs and radiosensitivity. Taken together, these studies and our observations suggest that tumors with higher τ_i may harbor a favorable microenvironment for CRT. We postulate that the combined effect of lower hypoxia and reduced metabolic activity of the tumor cells might have contributed to higher pretreatment τ_i that led to better treatment response and prolonged OS in patients with HNSCC. This notion is supported by a HR of 4.24 that was observed at the long-term follow-up period, implying a 4-fold higher risk of death in patients with low τ_i than in patients with high τ_i.

Pretreatment K^{trans} (median value, 0.19–0.64 minutes^{-1}) has been reported to predict treatment response to CRT,[4-6] induction therapy,[7] and short-term survival in patients with HNSCC.[8,9] We also observed that higher pretreatment K^{trans} was associated with better OS. Because K^{trans} reflects a combination of tumor perfusion and microvascular permeability, our results and those of earlier published reports support the notion that tumor vascularity might be an important predictor of disease control in HNSCC. The fact that K^{trans} predicted only 5-year OS while τ_i was useful in predicting both 5-year and long-term OS suggests that τ_i is a more robust prognostic imaging biomarker in evaluating HNSCC.

When τ_i and K^{trans} were combined, significantly longer OS was observed for patients with high τ_i/high K^{trans} for all clinical end points. We believe that synergistic interaction between these 2 parameters in predicting OS was greater than what would be expected from an individual parameter. The fact that patients with high τ_i/high K^{trans} demonstrated the longest OS agrees with the hypothesis that these patients may have had the most favorable conditions such as elevated tumor blood flow, lower hypoxia, and lower cellular metabolic energy for optimal therapeutic benefit of CRT. Another interesting finding was that patients with high τ_i/low K^{trans} exhibited longer OS than patients with low τ_i/high K^{trans} at all clinical end points. This indicates that τ_i was a more dominant factor than K^{trans} in the synergistic interaction leading to longer OS, further substantiating that τ_i is a robust prognostic indicator in HNSCC.

We performed an exploratory analysis to investigate if τ_i and K^{trans} could predict OS in HPV/p16 patients because HPV/p16 is a key etiological factor in HNSCC, with distinct epidemiologic, clinical, and molecular characteristics.[21,22] Patients harboring the *p16* gene are generally more sensitive to CRT and are associated with improved prognosis and prolonged survival.[20] The favorable outcome in p16-positive patients may be attributed to fewer and distinct somatic genetic alterations and positive immunologic response.[21,22] In agreement with prior studies,[20,21] significantly longer OS was observed for p16-positive patients compared with p16-negative patients in our study. A nonsignificant, but positive trend toward longer OS for p16-positive patients harboring high τ_i and K^{trans} suggests the prognostic utility of τ_i and K^{trans} may also be valid in stratifying p16-positive patients. We recognize that these results may be subject to selection bias inherent to the availability of tissue specimens. However, a nonsignificant difference in OS between patients who had and those who did not have tissues for p16 expression indicated that there was a minimal influence of sample size in the determination of OS.

While predicting short-term (6 months) treatment response to CRT, no significant differences in pretreatment τ_i were observed between complete and partial responders.[5] However, in the present study, patients who had higher pretreatment τ_i were associated with prolonged OS. The difference might be related to different follow-up duration, assessment of clinical outcome (local regional recurrence/evidence of residual disease on pathology versus OS), and different number of patients ($n = 33$ versus $n = 60$) enrolled between these 2 studies. We focused on assessing nodal metastases in predicting OS because lymphadenopathy in the neck is a well-known prognostic determinant in patients with HNSCC.[29] A DCE-MRI analysis of primary tumors would also be important; however, artifacts induced by physiologic motion precluded the analysis of primary tumors. We combined DCE-MRI data from MR systems with 2 different field strengths (1.5T and 3T). To account for this variability, blood T1 and contrast agent relaxivities corresponding to the field strengths were used for converting signal intensity curves to concentration curves and estimating pharmacokinetic parameters. Previously,[5] we reported similar trends for K^{trans} in predicting treatment response in patients scanned at 2 different field strengths, suggesting that DCE-MRI–derived parameters are independent of magnetic field. Our supposition is corroborated by a study[30] in which no significant differences in signal enhancement ratio, time to peak enhancement, uptake, and washout rates were observed for breast lesions scanned with 1.5T and 3T MR systems.

CONCLUSIONS

Our data indicate that shutter-speed model analysis of DCE-MRI provides 2 important imaging biomarkers (τ_i and K^{trans}) presenting complementary physiologic information about the tumor microenvironment. Although τ_i may be a potential independent prognostic imaging biomarker for predicting OS, combined analysis of τ_i and K^{trans} greatly improves the predictive power of these parameters in determining OS in HNSCC. Future prospective trials involving a larger patient population are required to confirm our findings.

Disclosures: Suyash Mohan—*UNRELATED*: *Grants/Grants Pending*: Galileo, CDS, NovoCure*. Virginia LiVolsi—*RELATED*: *Grants/Grants Pending*: National Institutes of Health, *Comments*: grant R01-CA102756 (Harish Poptani)*. Harry Quon—*UNRELATED: Grants/Grants Pending*: University of Pennsylvania*. Harish Poptani—*RELATED: Grants/Grants Pending*: National Institutes of Health*; *UNRELATED*: *Employment*: University of Liverpool. *Money paid to the institution.

REFERENCES

1. Chen CC, Lin JC, Chen KW. **Lymph node ratio as a prognostic factor in head and neck cancer patients.** *Radiat Oncol* 2015;10:181 CrossRef Medline

2. Tofts PS, Kermode AG. **Measurement of the blood-brain barrier permeability and leakage space using dynamic MR imaging. 1. Fundamental concepts.** *Magn Reson Med* 1991;17:357–67 CrossRef Medline
3. Tofts PS, Brix G, Buckley DL, et al. **Estimating kinetic parameters from dynamic contrast-enhanced T(1)-weighted MRI of a diffusable tracer: standardized quantities and symbols.** *J Magn Reson Imaging* 1999;10:223–32 CrossRef Medline
4. Chawla S, Kim S, Dougherty L, et al. **Pretreatment diffusion-weighted and dynamic contrast-enhanced MRI for prediction of local treatment response in squamous cell carcinomas of the head and neck.** *AJR Am J Roentgenol* 2013;200:35–43 CrossRef Medline
5. Kim S, Loevner LA, Quon H, et al. **Prediction of response to chemoradiation therapy in squamous cell carcinomas of the head and neck using dynamic contrast-enhanced MR imaging.** *AJNR Am J Neuroradiol* 2010;31:262–68 CrossRef Medline
6. Jansen JF, Schöder H, Lee NY, et al. **Tumor metabolism and perfusion in head and neck squamous cell carcinoma: pretreatment multimodality imaging with 1H magnetic resonance spectroscopy, dynamic contrast-enhanced MRI, and [18F]FDG-PET.** *Int J Radiat Oncol Biol Phys* 2012;82:299–307 CrossRef Medline
7. Bernstein JM, Kershaw LE, Withey SB, et al. **Tumor plasma flow determined by dynamic contrast-enhanced MRI predicts response to induction chemotherapy in head and neck cancer.** *Oral Oncol* 2015;51:508–13 CrossRef Medline
8. Chawla S, Kim S, Loevner LA, et al. **Prediction of disease-free survival in patients with squamous cell carcinomas of the head and neck using dynamic contrast-enhanced MR imaging.** *AJNR Am J Neuroradiol* 2011;32:778–84 CrossRef Medline
9. Shukla-Dave A, Lee NY, Jansen JF, et al. **Dynamic contrast-enhanced magnetic resonance imaging as a predictor of outcome in head-and-neck squamous cell carcinoma patients with nodal metastases.** *Int J Radiat Oncol Biol Phys* 2012;82:1837–44 CrossRef Medline
10. Kim S, Quon H, Loevner LA, et al. **Transcytolemmal water exchange in pharmacokinetic analysis of dynamic contrast-enhanced MRI data in squamous cell carcinoma of the head and neck.** *J Magn Reson Imaging* 2007;26:1607–17 CrossRef Medline
11. Yankeelov TE, Lepage M, Chakravarthy A, et al. **Integration of quantitative DCE-MRI and ADC mapping to monitor treatment response in human breast cancer: initial results.** *Magn Reson Imaging* 2007;25:1–13 CrossRef Medline
12. Springer CS Jr, Li X, Tudorica LA, et al. **Intratumor mapping of intracellular water lifetime: metabolic images of breast cancer?** *NMR Biomed* 2014;27:760–73 CrossRef Medline
13. Li X, Cai Y, Moloney B, et al. **Relative sensitivities of DCE-MRI pharmacokinetic parameters to arterial input function (AIF) scaling.** *J Magn Reson* 2016;269:104–12 CrossRef Medline
14. Tudorica A, Oh KY, Chui SY, et al. **Early prediction and evaluation of breast cancer response to neoadjuvant chemotherapy using quantitative DCE-MRI.** *Transl Oncol* 2016;9:8–17 CrossRef Medline
15. Li X, Priest RA, Woodward WJ, et al. **Cell membrane water exchange effects in prostate DCE-MRI.** *J Magn Reson* 2012;218:77–85 CrossRef Medline
16. Lowry M, Zelhof B, Liney GP, et al. **Analysis of prostate DCE-MRI: comparison of fast exchange limit and fast exchange regimen pharmacokinetic models in the discrimination of malignant from normal tissue.** *Invest Radiol* 2009;44:577–84 CrossRef Medline
17. Chang EY, Li X, Jerosch-Herold M, et al. **The evaluation of esophageal adenocarcinoma using dynamic contrast-enhanced magnetic resonance imaging.** *J Gastrointest Surg* 2008;12:166–75 CrossRef Medline
18. Jajamovich GH, Huang W, Besa C, et al. **DCE-MRI of hepatocellular carcinoma: perfusion quantification with Tofts model versus shutter-speed model–initial experience.** *MAGMA* 2016;29:49–58 CrossRef Medline
19. Lee SH, Hayano K, Zhu AX, et al. **Water-exchange-modified kinetic parameters from dynamic contrast-enhanced MRI as prognostic biomarkers of survival in advanced hepatocellular carcinoma treated with antiangiogenic monotherapy.** *PLoS One* 2015;10:e0136725 CrossRef Medline
20. Ang KK, Harris J, Wheeler R, et al. **Human papillomavirus and survival of patients with oropharyngeal cancer.** *N Engl J Med* 2010;363:24–35 CrossRef Medline
21. Klussmann JP, Mooren JJ, Lehnen M, et al. **Genetic signatures of HPV-related and unrelated oropharyngeal carcinoma and their prognostic implications.** *Clin Cancer Res* 2009;15:1779–86 CrossRef Medline
22. Elrefaey S, Massaro MA, Chiocca S, et al. **HPV in oropharyngeal cancer: the basics to know in clinical practice.** *Acta Otorhinolaryngol Ital* 2014;34:299–309 Medline
23. Song HK, Dougherty L. **Dynamic MRI with projection reconstruction and KWIC processing for simultaneous high spatial and temporal resolution.** *Magn Reson Med* 2004;52:815–24 CrossRef Medline
24. Klaes R, Friedrich T, Spitkovsky D, et al. **Overexpression of p16(INK4A) as a specific marker for dysplastic and neoplastic epithelial cells of the cervix uteri.** *Int J Cancer* 2001;92:276–84 CrossRef Medline
25. Zhang Y, Poirier-Quinot M, Springer CS Jr., et al. **Active transplasma membrane water cycling in yeast is revealed by NMR.** *Biophys J* 2011;101:2833–42 CrossRef Medline
26. Nath KPR, Nelson DS, Pickup S, et al. **Acute changes in cellular-interstitial water exchange rate in DB-1 melanoma xenografts after lonidamine administration as a marker of tumor energetics and ion transport.** *Proc Intl Soc Magn Reson Med* 2014;22:2757
27. Koch CJ, Jenkins WT, Jenkins KW, et al. **Mechanisms of blood flow and hypoxia production in rat 9L-epigastric tumors.** *Tumor Microenviron Ther* 2013;1:1–13 CrossRef Medline
28. Cooper RA, Carrington BM, Loncaster JA, et al. **Tumour oxygenation levels correlate with dynamic contrast-enhanced magnetic resonance imaging parameters in carcinoma of the cervix.** *Radiother Oncol* 2000;57:53–59 CrossRef Medline
29. Layland MK, Sessions DG, Lenox J. **The influence of lymph node metastasis in the treatment of squamous cell carcinoma of the oral cavity, oropharynx, larynx, and hypopharynx: N0 versus N+.** *Laryngoscope* 2005;115:629–39 CrossRef Medline
30. Pineda FD, Medved M, Fan X, et al. **Comparison of dynamic contrast-enhanced MRI parameters of breast lesions at 1.5 and 3.0 T: a pilot study.** *Br J Radiol* 2015;88:20150021 CrossRef Medline

Diffusion-Weighted Imaging of the Head and Neck: Influence of Fat-Suppression Technique and Multishot 2D Navigated Interleaved Acquisitions

Y.J. Bae, B.S. Choi, H.-K. Jeong, L. Sunwoo, C. Jung, and J.H. Kim

ABSTRACT

BACKGROUND AND PURPOSE: DWI of the head and neck can reveal valuable information, but the effects of fat suppression and multishot acquisition on image quality have not been thoroughly investigated. We aimed to comprehensively compare the quality of head and neck DWI at 3T using 2 fat-suppression techniques, STIR, and spectral presaturation with inversion recovery, which were used with both single- and multishot EPI.

MATERIALS AND METHODS: Sixty-five study participants underwent 3 DWI sequences of single-shot EPI–STIR, single-shot EPI–spectral presaturation with inversion recovery, and multishot EPI–spectral presaturation with inversion recovery of the head and neck. In multiple anatomic regions, 2 independent readers assessed 5-point visual scores for fat-suppression uniformity and image distortion, and 1 reader measured the contrast-to-noise ratio and ADC.

RESULTS: The mean visual score for fat-suppression uniformity was higher in single-shot EPI–STIR than in other sequences (all regions except for the orbital region, $P < .05$). The mean visual score for image distortion was higher in multishot EPI–spectral presaturation with inversion recovery than in single-shot EPI sequences (all regions, $P < .001$). Contrast-to-noise ratio was mostly lower in single-shot EPI–STIR than in other sequences ($P < .001$), and ADC was significantly higher in multishot EPI–spectral presaturation with inversion recovery than in single-shot EPI sequences ($P \leq .001$).

CONCLUSIONS: Overall, multishot EPI–spectral presaturation with inversion recovery provided the best image quality, with relatively homogeneous fat suppression, less image distortion than single-shot EPI sequences, and higher contrast-to-noise ratio than single-shot EPI–STIR. The measured ADC values can be higher in multishot EPI–spectral presaturation with inversion recovery, which necessitates cautious application of the previously reported ADC values to clinical settings.

ABBREVIATIONS: IRIS = image reconstruction using image-space sampling; msEPI = multishot EPI; RESOLVE = readout-segmented EPI using parallel imaging and a 2D navigator; SPIR = spectral presaturation with inversion recovery; ssEPI = single-shot EPI; CNR = contrast-to-noise ratio

DWI can measure differences in tissue microstructure based on the random displacement of water molecules.[1,2] The differences in water mobility are quantified by the ADC, which is inversely correlated with tissue cellularity.[2,3] Using this property, DWI can offer additional information about lesion characteristics in different regions of the body, including the head and neck.[2,4-8]

In clinical practice, DWI is usually performed with a single-shot EPI (ssEPI) sequence.[2,4-8] To obtain good ssEPI quality, effective fat suppression is essential to eliminate the lipid signal and reduce ghost artifacts.[4] Previous studies conducted on breast tissue have demonstrated that uniformity of fat suppression, SNR, contrast-to-noise ratio (CNR), and even ADC are affected by the choice of the fat-suppression technique.[4,9-13] There has been only 1 study of the head and neck region that evaluated the effect of the fat-suppression technique on ssEPI-DWI.[4] The authors suggested that STIR offered better image quality, but they assessed the images on a single level using an ROI covering the entire area of the depicted structure, a technique that failed to consider the complex anatomy of the head and neck.[4] In addition, they did not compare the ADC among different fat-suppression techniques.

Multishot EPI (msEPI) is an imaging technique that reduces magnetic susceptibility artifacts and T2* blurring in DWI.[5,14-16] Because the head and neck region has substantial magnetic field inhomogeneity due to air-containing structures, the utility of

Received February 17, 2017; accepted after revision August 19.

From the Department of Radiology (Y.J.B., B.S.C., L.S., C.J., J.H.K.), Seoul National University Bundang Hospital, Seongnam, Republic of Korea; and Philips Korea (H.-K.J.), Seoul, Republic of Korea.

Please address correspondence to Byung Se Choi, MD, PhD, Department of Radiology, Seoul National University Bundang Hospital, 82, Gumi-ro 173 beon-gil, Bundang-gu, Seongnam, 13620, Republic of Korea; e-mail: byungse.choi@gmail.com

Indicates article with supplemental on-line appendix and tables.

Indicates article with supplemental on-line photo.

http://dx.doi.org/10.3174/ajnr.A5426

msEPI-DWI has been proved effective in decreasing geometric distortion.[5,17] However, msEPI-DWI requires spectral-selective saturation such as spectral presaturation with inversion recovery (SPIR) for optimal fat suppression, not STIR.[15] Two studies have compared the image quality between ssEPI-DWI and msEPI-DWI in the head and neck,[5,17] but neither considered fat-suppression techniques.

The aim of this study was to perform a comprehensive comparison of the quality of DWI in the head and neck using different fat-suppression techniques and to determine the utility of the msEPI sequence. Specifically, we adopted 2D navigated interleaved msEPI-DWI with image reconstruction using image-space sampling (IRIS) functions,[15,16] which has been known to reduce ghosts and off-resonance artifacts but has not yet been used to study the head and neck region. We performed ssEPI-DWI with STIR (ssEPI-STIR), ssEPI-DWI with SPIR (ssEPI-SPIR), and msEPI-DWI with SPIR (msEPI-SPIR) in the head and neck region using a 3T MR imaging scanner. The purpose of our study was to compare both qualitative and quantitative measurements of the image qualities of the above 3 sequences.

MATERIALS AND METHODS

Subjects

The institutional review board of our hospital approved this retrospective study; the requirement for informed consent was waived. Between July and December of 2016, one hundred thirty-nine subjects with various pathologies underwent head and neck MR imaging at our institution. We excluded subjects who did not undergo the 3 DWI sequences of interest (ssEPI-STIR, ssEPI-SPIR, and msEPI-SPIR) ($n = 69$), and who were younger than 19 years of age ($n = 5$). As a result, 65 subjects (43 men and 22 women; age range, 26–85 years; mean age, 57.4 years) were included. The underlying pathologies of the included subjects were as follows: abscess ($n = 2$), dentigerous cyst ($n = 1$), invasive fungal sinusitis and/or skull base osteomyelitis ($n = 3$), inverted papilloma ($n = 2$), lipogranuloma ($n = 1$), metastatic squamous cell carcinoma ($n = 2$), nasal hemangioma ($n = 1$), neurogenic tumor ($n = 2$), squamous papilloma ($n = 1$), parapharyngeal tumor ($n = 2$), parotid tumor ($n = 7$), posttreatment status of cancer including basal cell carcinoma ($n = 1$), lymphoma ($n = 3$), malignant melanoma ($n = 1$), maxillary sinus cancer ($n = 2$), nasal cavity cancer ($n = 3$), nasopharynx cancer ($n = 11$), olfactory neuroblastoma ($n = 1$), oral cavity cancer ($n = 11$), temporal bone metastasis ($n = 1$), and tonsillar cancer ($n = 7$).

MR Imaging Protocol

MR imaging was performed with a 3T instrument (Ingenia; Philips Healthcare, Best, the Netherlands) with a 32-channel sensitivity encoding head coil. DWI was performed in the axial plane using b-values of 0 and 1000 s/mm^2, and 3 orthogonal directions of diffusion gradients. Other imaging parameters for ssEPI-STIR, ssEPI-SPIR, and msEPI-SPIR are summarized in On-line Table 1. Regarding z-axis scan coverage, we obtained axial images centering the lesion of interest depending on each subject. Therefore, the scan range for the z-axis varied among the subjects. Thus, we did not fully cover the following structures: the orbital region in 15 subjects, the pons in 7 subjects, and the cerebellum in 3 subjects. In addition, the larynx was covered in 21 subjects, and the shoulder was covered in 12 subjects, respectively. Besides the DWI, the following sequences were obtained using routine protocols for head and neck MR imaging: axial TSE T2WI with and without fat suppression, axial TSE T1WI, coronal TSE T2WI with fat suppression, and axial/coronal/sagittal TSE post-contrast-enhanced T1WI with fat suppression.

Qualitative Imaging Analysis

Image quality in relation to the means of fat-suppression uniformity and image distortion was evaluated with a 5-point visual scale. Two board-certified neuroradiologists (Y.J.B. and B.S.C, with 8 and 18 years of experience, respectively), who were blinded to the clinical information and the imaging methods, independently visually inspected the 3 DWI sequences from all study subjects.

Visual scoring for fat-suppression uniformity was as follows: 5, homogeneous fat suppression; 4, a few artifacts from insufficient fat suppression; 3, heterogeneous fat suppression without impairment of lesion analysis; 2, mostly not suppressed, making lesion identification unfeasible due to ghost artifacts; 1, no fat suppression. Fat-suppression uniformity was assessed in the anatomic orbital, buccal, and mental regions and the posterior neck and shoulder. A 5-point scale for image distortion was as follows: 5, excellent image quality with no geometric distortion or susceptibility artifacts; 4, good image quality with little distortion and few artifacts; 3, fair image quality, some distortion and artifacts; 2, poor image quality, with substantial distortion and many artifacts; 1, unacceptable. The anatomic regions for the assessment of image distortion were the orbit–sphenoethmoid sinus level, posterior fossa, nasal cavity–maxillary sinus level, pharynx, oral cavity, larynx, posterior neck, and shoulder. Due to short scan coverage, the assessment of the orbital region failed in 15 subjects, and the larynx and shoulder were assessed in 21 and 15 subjects.

Quantitative Imaging Analysis

CNR Calculation. The ROI allocation for quantitative imaging analysis was performed by 1 neuroradiologist (Y.J.B). On ssEPI-STIR, ssEPI-SPIR, and msEPI-SPIR with a b-value of 1000 s/mm^2, smoothed polygonal ROIs were drawn in the pons, cerebellar white matter, parotid gland, lymph node, palatine tonsil, semispinalis capitis muscle, and orbital fat, while attempting to include as much of the anatomic structure as possible (On-line Fig 1). The B_0 maps of the 3 DWI sequences and the axial T2WIs were used as references to identify the anatomic points for ROI placement. The CNR was calculated using the automatically measured signal intensities in each ROI as follows: CNR = (Signal Intensity in Targeted Structure − Signal Intensity in Orbital Fat)/Signal Intensity in Orbital Fat.

Among the study subjects, ROI placement failed in the pons of 7 subjects and in the cerebellum of 3 subjects due to short scan coverage, in the lymph node of 2 subjects due to lack of the presence of a feasible lesion, in the palatine tonsil of 26 subjects due to the small volume of tonsillar tissue or posttreatment status, and in the orbital fat of 15 subjects due to short scan coverage.

ADC Measurement. The above ROIs were copied and pasted

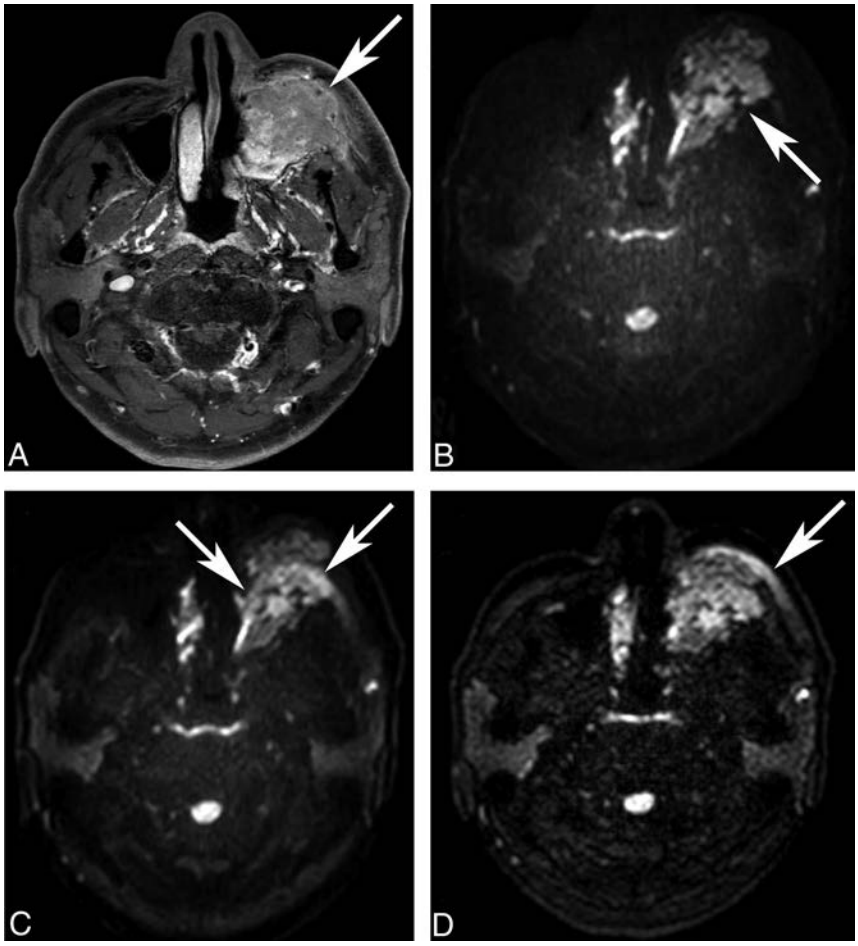

FIG 1. Fat-suppression uniformity of DWI. A 49-year-old man underwent MR imaging for staging of left maxillary sinus cancer (*A*, post-contrast-enhanced T1WI, *arrow*). On ssEPI-STIR (*B*), fat suppression is homogeneous without disrupting the original mass (*arrow*). On ssEPI-SPIR (*C*), unsuppressed fat signal (*arrows*) in the subcutaneous layer creates ghost artifacts that obscure the original mass, making the lesion assessment unfeasible. Unlike ssEPI-SPIR, unsuppressed fat signal (*arrow*) does not shift much to cover the mass on msEPI-SPIR (*D*).

onto the corresponding ADC maps from 3 DWI sequences with the same coordinates and areas, excluding orbital fat. The ADC was measured automatically; however, for the same reasons, it was not possible to measure the ADC in the pons of 7 subjects, the cerebellum of 3 subjects, the lymph nodes of 2 subjects, and the palatine tonsil of 26 subjects.

Statistical Analysis

Continuous variables were expressed as mean ± SD. κ statistics and the McNemar test were performed to assess the interobserver agreement of the 5-point scale visual scores between the 2 readers. We considered κ of >0.75 as excellent agreement, 0.40–0.75 as fair to good, and <0.40 as poor.[18] Visual scores for fat-suppression uniformity and image distortion among the 3 DWI sequences were compared using repeated-measures ANOVA. Then, pair-wise comparison was performed using the paired *t* test with a Bonferroni correction among 1) ssEPI-STIR and ssEPI-SPIR, 2) ssEPI-STIR and msEPI-SPIR, and 3) ssEPI-SPIR and msEPI-SPIR. The CNR and ADC of the 3 DWI sequences were compared using repeated-measures ANOVA. The Mauchly test of sphericity was used to test the assumption of the repeated-measures ANOVA, and the Greenhouse-Geissler correction method was considered if sphericity was violated. Pair-wise comparison was also performed using a paired *t* test with a Bonferroni correction between each 2 DWI sequences. A *P* value < .05 indicated statistical significance, and for pair-wise comparison, a *P* value < .017 was considered statistically significant based on the Bonferroni correction. All statistical analyses were performed with SPSS software (Version 24.0; IBM, Armonk, New York).

RESULTS

Qualitative Assessment

Reliabilities of visual scores are explained in the On-line Appendix (On-line Tables 2 and 3).

Visual scores for fat-suppression uniformity are summarized in On-line Table 4. In both readers, the mean visual score was higher in ssEPI-STIR than in msEPI-SPIR and ssEPI-SPIR in all regions (all, $P < .05$) (Fig 1) except for the orbital region. In the orbital region, all 3 sequences showed excellent fat-suppression uniformity with visual scores higher than 4, which made no significant difference (reader 1, $P = .370$; reader 2, $P = .363$). In the buccal and mental regions, mean scores were significantly higher in msEPI-SPIR than in ssEPI-SPIR (reader 1, $P = .005$ and <.001; reader 2, $P = .008$ and <.001). Mean scores in the posterior neck and shoulder were not significantly different between msEPI-SPIR and ssEPI-SPIR in both readers (all, $P > .05$).

On-line Table 5 summarizes visual scores for image distortion. Mean visual scores for image distortion were significantly higher in msEPI-SPIR than in ssEPI-STIR and ssEPI-SPIR (both readers, all regions, $P < .001$) (Fig 2). The mean scores between ssEPI-STIR and ssEPI-SPIR showed no significant differences for both readers (all, $P > .05$).

Quantitative Assessment

Quantitative results for CNR and ADC measurements are provided in Table 1.

CNR. CNR was significantly lower in ssEPI-STIR than in ssEPI-SPIR and msEPI-SPIR in all targeted structures (all, $P < .001$). There was no significant difference in CNR between msEPI-SPIR and ssEPI-SPIR in all regions other than the parotid gland where CNR was significantly higher in msEPI-SPIR than in ssEPI-SPIR ($P < .001$).

ADC. ADC was significantly higher in msEPI-SPIR than in ssEPI-STIR and in ssEPI-SPIR in all targeted structures (all, $P \leq .001$). In the cerebellar white matter, parotid gland, and semispi-

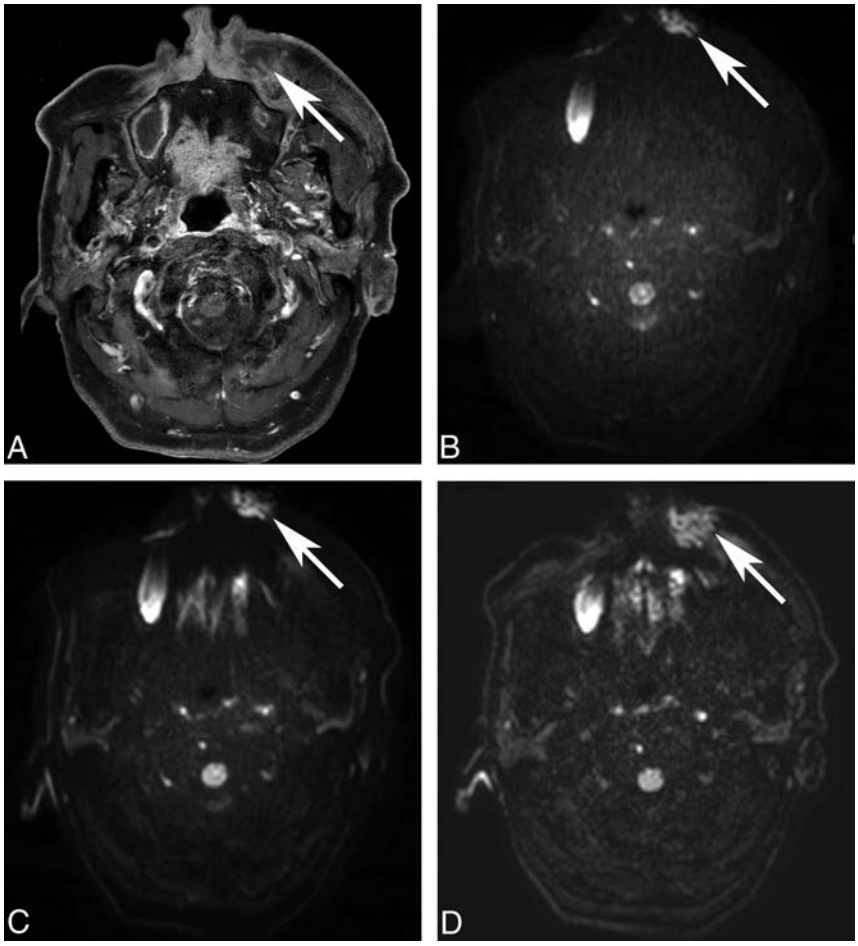

FIG 2. Image distortion of DWI. An 85-year-old man underwent MR imaging for the evaluation of a left premaxillary abscess (*A*, post-contrast-enhanced TIWI, *arrow*). Image distortion is increased on ssEPI-STIR (*B*, *arrow*) and ssEPI-SPIR (*C*, *arrow*) and decreased on msEPI-SPIR (*D*, *arrow*). The left premaxillary abscess is not distorted by the susceptibility artifacts only on msEPI-SPIR.

Table 1: Quantitative assessment of DWI[a]

	ssEPI-STIR	ssEPI-SPIR	msEPI-SPIR	*P* Values[b]
CNR				
Pons	4.45 ± 0.84	8.29 ± 1.62	7.69 ± 1.90	.001/.001/.022
Cerebellar white matter	3.86 ± 0.73	8.78 ± 1.53	8.52 ± 2.13	.001/.001/.294
Parotid gland	0.43 ± 0.41	1.21 ± 0.68	1.74 ± 0.82	.001/.001/.001
Lymph node	4.55 ± 1.59	6.61 ± 2.02	7.06 ± 2.56	.001/.001/.104
Palatine tonsil	4.46 ± 2.47	6.37 ± 2.27	6.55 ± 2.12	.001/.001/.61
Semispinalis muscle	0.40 ± 0.22	0.87 ± 0.31	1.00 ± 0.50	.001/.001/.05
ADC ($\times 10^{-3}$ mm^2/s)				
Pons	0.737 ± 0.042	0.743 ± 0.033	0.799 ± 0.083	.236/.001/.001
Cerebellar white matter	0.636 ± 0.039	0.655 ± 0.030	0.691 ± 0.061	.001/.001/.001
Parotid gland	0.771 ± 0.170	0.867 ± 0.147	0.907 ± 0.141	.001/.001/.001
Lymph node	0.900 ± 0.321	0.915 ± 0.349	1.028 ± 0.341	.300/.001/.001
Palatine tonsil	0.753 ± 0.325	0.748 ± 0.321	0.846 ± 0.310	.818/.001/.001
Semispinalis muscle	0.881 ± 0.187	1.118 ± 0.115	1.360 ± 0.107	.001/.001/.001

[a] Data are given as mean ± SD.

[b] *P* values are derived from pair-wise comparison using a paired *t* test with a Bonferroni correction among ssEPI-STIR and ssEPI-SPIR/ssEPI-STIR and msEPI-SPIR/ssEPI-SPIR and msEPI-SPIR.

nalis muscle, the ADC was highest in msEPI-SPIR, lower in ssEPI-SPIR, and lowest in ssEPI-STIR with statistical significance (all, $P \leq .001$). There was no significant difference in the ADC between ssEPI-STIR and ssEPI-SPIR in the pons, lymph nodes, and tonsil (all, $P > .017$).

DISCUSSION

This study was a comprehensive comparison among 3 DWI sequences, ssEPI-STIR, ssEPI-SPIR, and msEPI-SPIR, in the head and neck using both qualitative and quantitative measurements. Our results showed that fat-suppression uniformity was significantly better in ssEPI-STIR than in the 2 sequences using SPIR, but image distortion was significantly improved in msEPI-SPIR compared with ssEPI sequences. The CNR was significantly lower in ssEPI-STIR than in msEPI-SPIR and ssEPI-SPIR. The ADC was significantly higher in msEPI-SPIR than ssEPI sequences.

Homogeneous fat suppression in DWI is essential to avoid ghost artifacts.[4,19] Another concern regarding fat suppression in DWI is that not only visual quality but also SNR, CNR, and even ADC could be altered according to the choice of fat-suppression technique.[4,10-13,19] Thus, selecting the optimal fat-suppression technique is a major determinant of the image quality of DWI.

Among fat-suppression techniques, SPIR is widely used on the basis of the frequency-selective radiofrequency pulse that excites only fat spins using chemical shift differences between lipid and water protons.[4,10,11,13] However, this technique often fails to provide homogeneous fat suppression in regions of the body where field inhomogeneity is substantial.[4,10-12,20,21] On the other hand, the STIR method uses a nonselective 180° inversion pulse and the relatively short T1 relaxation time of the lipid proton to nullify the fat signal. Thus, it is less sensitive to field heterogeneity.[4,10-12] Therefore, STIR is known to be a more reliable imaging technique for large body parts such as the breast.[4,10,11]

The head and neck region has large susceptibility effects due to air-containing structures. However, few studies have investigated the effects of fat-suppression techniques on the image quality of DWI. In 2014, Maehara et al[4] reported that STIR provided good image quality for visual inspection, despite SNR and CNR being higher when the chemical shift selective method, based on frequency-selective pulse, was used. However, this study had several limitations that could hamper its general application. First, the number of study subjects was relatively small ($n = 25$). Second, the authors did not consider the complex

anatomy of the head and neck; instead, they measured SNR and CNR in 2 ROIs allocated in the semispinalis capitis muscle and the whole area of depicted structures. Third, they did not measure and compare the ADC according to fat-suppression techniques, which could be affected by fat suppression.[12,13,21]

We must also consider msEPI when evaluating the image quality of head and neck DWI. The msEPI technique acquires only a subset of *k*-space samples per each excitation, thereby reducing bandwidth-related EPI artifacts and phase errors.[5,15-17] Two previous studies have used readout-segmented EPI using parallel imaging and a 2D navigator (RESOLVE) to assess its advantage when applied to head and neck DWI.[5,17] These studies have discovered that image quality was significantly improved in RESOLVE by reducing susceptibility artifacts, geometric distortion, and blurring, resulting in homogeneous images.[5,17] Nevertheless, we should consider that msEPI should be coupled with the fat-suppression technique SPIR, not STIR.[15,16] The use of STIR for each shot on msEPI would cause substantial signal loss or a significant increase in scan time.

Our study was the first to consider both fat suppression and msEPI acquisition when performing a comprehensive comparison of the quality of DWI in the head and neck. In addition, our study has several other advantages. We enrolled by far the largest number of study subjects among head and neck DWI studies, and we assessed both qualitative and quantitative measurements in multiple segmented regions of the head and neck with consideration of anatomic structures. Our study was also the first to adopt the 2D navigated interleaved msEPI-DWI with IRIS of the head and neck. Similar to RESOLVE, msEPI-DWI with IRIS acquires 2D navigator echoes to permit further correction of motion-induced phase errors.[15,16] Moreover, when used in conjunction with parallel imaging methods, an efficient reconstruction method for interleaved msEPI acquisitions (ie, IRIS) was provided to enhance phase correction and achieve high spatial resolution.[15,16]

Our results of the qualitative imaging assessment showed that fat suppression was more homogeneous in ssEPI-STIR than in msEPI-SPIR and ssEPI-SPIR (On-line Table 4). This result agrees with previous studies, which reported that STIR could provide more homogeneous fat suppression in body parts with severe field inhomogeneity than SPIR.[4,10-12,19] With the same use of SPIR, msEPI-SPIR had a higher visual score for fat-suppression uniformity than ssEPI-SPIR in the buccal and mental regions. We believe that this result was due to the reduction of ghost artifacts from unsuppressed fat signals on the msEPI sequence compared with the ssEPI sequence (Fig 1).[5,15-17] Unlike ssEPI-SPIR, the reduction of ghost artifacts could eliminate the obscuring of targeted structures by unsuppressed fat signals on msEPI-SPIR. The difference between msEPI-SPIR and ssEPI-SPIR was not significant in the orbital region and posterior neck where fat suppression was equally excellent and in the shoulder where both sequences failed in homogeneous fat suppression. In the orbital region, all 3 sequences showed comparably excellent fat-suppression homogeneity. More important, regarding image distortion, the distortion was much more reduced in msEPI-SPIR than in ssEPI-STIR and ssEPI-SPIR (On-line Table 5 and Fig 2). Taken together with the above results, we concluded through visual assessment that msEPI-SPIR provided the best image quality with relatively homogeneous fat suppression and less image distortion compared with ssEPI-STIR and ssEPI-SPIR, but for imaging the shoulder region, msEPI-SPIR could be more limited than ssEPI-STIR.

In quantitative measurements, CNR was significantly lower in ssEPI-STIR than in msEPI-SPIR and in ssEPI-SPIR, regardless of the anatomic structures (Table 1). With the STIR method, the SNR and CNR are lower than with the spectral-selective presaturation methods because the STIR method uses a nonselective 180° inversion pulse and most tissues recover more slowly than fat.[4,10,12] In accordance with previous reports of head and neck DWI,[5,17] no significant difference in CNR between msEPI-SPIR and ssEPI-SPIR was observed in most anatomic structures. However, in the parotid gland, CNR was significantly higher in msEPI-SPIR than in ssEPI-SPIR. Because our study included a much larger number of study subjects than previous reports and we were the first to use interleaved msEPI-DWI with IRIS in lieu of RESOLVE, the difference in the CNR result may be acceptable with the following explanation: We assumed that the higher CNR in the msEPI sequence was due to the reduction of the blurring effect from T2 decay in the msEPI sequence, which resulted from a smaller echo-train length than in the ssEPI sequence.[15,16] Along with the qualitative assessment, we could certify that msEPI-SPIR provided the best image quality for head and neck DWI.

The ADC was significantly higher in msEPI-SPIR than in ssEPI-STIR and ssEPI-SPIR. This result also seemed to contradict previous reports,[5,17] but it may be explained in several ways. First, the STIR method may lead to an underestimation of measured ADC values due to lower SNR than the SPIR method.[12,13,21] In addition, considering the possibility of a higher CNR of the msEPI-SPIR than of the ssEPI sequence, we could easily assume that the ADC could be higher in msEPI-SPIR than in ssEPI-SPIR. Second, various motion artifacts from cardiac motion, respiratory movement, or swallowing could affect the measurement of ADC values. Our msEPI sequence used a 2D navigator to correct in-plane motion, but it could be affected by through-plane motion along the z-axis.[15,16] In fact, 1 study applying the msEPI sequence in DWI of the liver[22] resulted in a higher value of ADC in msEPI than in ssEPI, which is in accordance with our results. Because the head and neck region has a high possibility of motion artifacts, motion artifacts may be the causative factor for determining ADC values. Last, interleaved msEPI-SPIR with IRIS and RESOLVE are applicable in different vendors that use different diffusion gradients. Different imaging gradients can influence the actual b-values and subsequently the ADC, due to so-called cross-term interactions.[23] As a result, the ADC value could vary depending on the choice of fat-suppression technique and msEPI acquisition, and we should be cautious when applying the previously reported ADC values to lesion characterization in our own DWI.

Our study has some limitations. First, the number of study subjects whose DWI scans covered the larynx and shoulder was small. Further study with larger numbers of DWI scans including the lower neck area will be needed. Second, the 3 DWI sequences have not been applied in clinical usage such as the characterization between benign and malignant lesions or monitoring responses after cancer treatment. Thus, future studies regarding the

clinical use of the 3 DWI sequences should be performed to further evaluate their diagnostic values. Third, we used a b-value of 1000 s/mm^2 in our study. To our knowledge, there has been no study regarding the optimal b-value for DWI in the head and neck. Therefore, future studies are needed to verify this issue.

CONCLUSIONS

Our results indicate that msEPI-SPIR could provide the best image quality with relatively few artifacts from insufficient fat suppression except for the shoulder region, less image distortion than ssEPI sequences, and higher CNR than ssEPI-STIR and/or ssEPI-SPIR. The measured ADC values can be higher in msEPI-SPIR than in other sequences depending on the effect of the fat-suppression technique used and the msEPI acquisition, which necessitates cautious application of the previously reported ADC values in the individual clinical settings.

ACKNOWLEDGMENTS

The authors thank the Medical Research Collaborating Center at Seoul National University Bundang Hospital for consultation on the statistical analyses.

Disclosures: Ha-Kyu Jeong—*UNRELATED*: *Employment*: Philips Korea, *Comments*: regular salary.

REFERENCES

1. Le Bihan D, Breton E, Lallemand D, et al. **Separation of diffusion and perfusion in intravoxel incoherent motion MR imaging.** *Radiology* 1988;168:497–505 CrossRef Medline
2. Vandecaveye V, De Keyzer F, Vander Poorten V, et al. **Head and neck squamous cell carcinoma: value of diffusion-weighted MR imaging for nodal staging.** *Radiology* 2009;251:134–46 CrossRef Medline
3. Herneth AM, Guccione S, Bednarski M. **Apparent diffusion coefficient: a quantitative parameter for in vivo tumor characterization.** *Eur J Radiol* 2003;45:208–13 CrossRef Medline
4. Maehara M, Ikeda K, Kurokawa H, et al. **Diffusion-weighted echo-planar imaging of the head and neck using 3-T MRI: investigation into the usefulness of liquid perfluorocarbon pads and choice of optimal fat suppression method.** *Magn Reson Imaging* 2014;32:440–45 CrossRef Medline
5. Zhao M, Liu Z, Sha Y, et al. **Readout-segmented echo-planar imaging in the evaluation of sinonasal lesions: a comprehensive comparison of image quality in single-shot echo-planar imaging.** *Magn Reson Imaging* 2016;34:166–72 CrossRef Medline
6. Thoeny HC, De Keyzer F, King AD. **Diffusion-weighted MR imaging in the head and neck.** *Radiology* 2012;263:19–32 CrossRef Medline
7. Srinivasan A, Dvorak R, Perni K, et al. **Differentiation of benign and malignant pathology in the head and neck using 3T apparent diffusion coefficient values: early experience.** *AJNR Am J Neuroradiol* 2008;29:40–44 CrossRef Medline
8. Abdel Razek AA, Kandeel AY, Soliman N, et al. **Role of diffusion-weighted echo-planar MR imaging in differentiation of residual or recurrent head and neck tumors and posttreatment changes.** *AJNR Am J Neuroradiol* 2007;28:1146–52 CrossRef Medline
9. Woodhams R, Ramadan S, Stanwell P, et al. **Diffusion-weighted imaging of the breast: principles and clinical applications.** *Radiographics* 2011;31:1059–84 CrossRef Medline
10. Mürtz P, Tsesarskiy M, Kowal A, et al. **Diffusion-weighted magnetic resonance imaging of breast lesions: the influence of different fat-suppression techniques on quantitative measurements and their reproducibility.** *Eur Radiol* 2014;24:2540–51 CrossRef Medline
11. Brandão S, Nogueira L, Matos E, et al. **Fat suppression techniques (STIR vs. SPAIR) on diffusion-weighted imaging of breast lesions at 3.0 T: preliminary experience.** *Radiol Med* 2015;120:705–13 CrossRef Medline
12. Baron P, Dorrius MD, Kappert P, et al. **Diffusion-weighted imaging of normal fibroglandular breast tissue: influence of microperfusion and fat suppression technique on the apparent diffusion coefficient.** *NMR Biomed* 2010;23:399–405 CrossRef Medline
13. Wenkel E, Geppert C, Schulz-Wendtland R, et al. **Diffusion weighted imaging in breast MRI: comparison of two different pulse sequences.** *Acad Radiol* 2007;14:1077–83 CrossRef Medline
14. Porter DA, Heidemann RM. **High resolution diffusion-weighted imaging using readout-segmented echo-planar imaging, parallel imaging and a two-dimensional navigator-based reacquisition.** *Magn Reson Med* 2009;62:468–75 CrossRef Medline
15. Jeong HK, Dewey BE, Hirtle JA, et al. **Improved diffusion tensor imaging of the optic nerve using multishot two-dimensional navigated acquisitions.** *Magn Reson Med* 2015;74:953–63 CrossRef Medline
16. Jeong HK, Gore JC, Anderson AW. **High-resolution human diffusion tensor imaging using 2-D navigated multishot SENSE EPI at 7 T.** *Magn Reson Med* 2013;69:793–802 CrossRef Medline
17. Koyasu S, Iima M, Umeoka S, et al. **The clinical utility of reduced-distortion readout-segmented echo-planar imaging in the head and neck region: initial experience.** *Eur Radiol* 2014;24:3088–96 CrossRef Medline
18. Fleiss JL. *Statistical Methods for Rates and Proportions*. 2nd ed. New York: John Wiley; 1981
19. Kazama T, Nasu K, Kuroki Y, et al. **Comparison of diffusion-weighted images using short inversion time inversion recovery or chemical shift selective pulse as fat suppression in patients with breast cancer.** *Jpn J Radiol* 2009;27:163–67 CrossRef Medline
20. Koç O, Paksoy Y, Erayman I, et al. **Role of diffusion weighted MR in the discrimination diagnosis of the cystic and/or necrotic head and neck lesions.** *Eur J Radiol* 2007;62:205–13 CrossRef Medline
21. Nakatsu M, Hatabu H, Itoh H, et al. **Comparison of short inversion time inversion recovery (STIR) and fat-saturated (chemsat) techniques for background fat intensity suppression in cervical and thoracic MR imaging.** *J Magn Reson Imaging* 2000;11:56–60 Medline
22. Deng J, Miller FH, Salem R, et al. **Multishot diffusion-weighted PROPELLER magnetic resonance imaging of the abdomen.** *Invest Radiol* 2006;41:769–75 CrossRef Medline
23. Brihuega-Moreno O, Heese FP, Tejos C, et al. **Effects of, and corrections for, cross-term interactions in Q-space MRI.** *Magn Reson Med* 2004;51:1048–54 CrossRef Medline

Effect of an Arm Traction Device on Image Quality and Radiation Exposure during Neck CT: A Prospective Study

Y.J. Choi, J.H. Lee, D.H. Yoon, H.J. Kim, K.J. Seo, K.-H. Do, and J.H. Baek

ABSTRACT

BACKGROUND AND PURPOSE: The image quality of neck CT is frequently disturbed by streak artifact from the shoulder girdles. Our aim was to determine the effects of an arm traction device on image quality and radiation exposure in neck CT.

MATERIALS AND METHODS: Patients with lymphoma with complete remission who were scheduled to undergo 2 consecutive follow-up neck CT scans for surveillance within a 1-year interval were enrolled in this prospective study. They underwent 2 consecutive neck CT scans (intervention protocol: patients with an arm traction device; standard protocol: no positioning optimization) on the same CT system. The primary outcome measures were image noise in the lower neck and dose-length product. Secondary outcomes were streak artifacts in the supraclavicular fossa, volume CT dose index, and the extent of the biacromial line shift.

RESULTS: Seventy-three patients were enrolled and underwent 2 consecutive CT scans with a mean interval of 155 days. In the intervention protocol, a mean noise reduction in the lower neck of 25.2%–28.5% ($P < .001$) was achieved, and a significant decrease in dose-length product (413 versus 397, $P < .001$) was observed. The intervention protocol significantly decreased streak artifacts ($P < .001$) and volume CT dose index (13.9 versus 13.4, $P < .001$) and could lower the biacromial line an average of 2.1 cm.

CONCLUSIONS: An arm traction device can improve image quality and reduce radiation exposure during neck CT. The device can be simply applied in cooperative patients with suspected lower neck lesions, and the approach offers distinct advantages over the conventional imaging protocol.

ABBREVIATIONS: $CTDI_{vol}$ = volume CT dose index; DLP = dose-length product

The image quality of CT in the lower neck is frequently disturbed by streak artifacts from the shoulder girdles and iodinated contrast media remaining in the subclavian vein. CT image-quality improvement strategies can involve trade-offs, including factors that increase the radiation exposure or the manufacturing cost related to CT hardware or software improvement.[1-7] Previous studies have tried to improve image quality by optimization of the shoulder position without the need for increased radiation exposure or the additional cost requirements of complex data processing.[8-11] One such study demonstrated that an arm traction device combined with automatic tube current modulation reduced the image noise and streak artifacts in the lower neck, while also decreasing the radiation exposure level.[9] Although the authors suggested the potential utility of an arm traction device that worked by lowering the shoulder level, the patient characteristics demonstrated considerable heterogeneity and the CT machines varied between the control and intervention groups; it is possible that these may have influenced the study results. Therefore, the purpose of this study was to prospectively determine any additive effects of an arm traction device and automatic tube current modulation on the image quality and radiation exposure of CT of the neck region. This was performed by imaging the same subjects in both the intervention protocol (using the arm traction device) and the standard protocol and performing all acquisitions on the same CT scanner.

Received April 24, 2017; accepted after revision August 14.

From the Departments of Radiology and Research Institute of Radiology (Y.J.C., J.H.L., K.J.S., K.-H.D., J.H.B.), Oncology (D.H.Y.), and Clinical Epidemiology and Biostatistics (H.J.K.), University of Ulsan College of Medicine, Asan Medical Center, Seoul, Korea.

Please address correspondence to Jeong Hyun Lee, MD, PhD, Department of Radiology and Research Institute of Radiology, University of Ulsan College of Medicine, Asan Medical Center, 86 Asanbyeongwon-Gil, Songpa-Gu, Seoul 138-736, Republic of Korea; e-mail: jeonghlee@amc.seoul.kr

http://dx.doi.org/10.3174/ajnr.A5418

MATERIALS AND METHODS

The prospective study protocol was reviewed and approved by the hospital review board, and the requirement for informed consent for data evaluation was waived. Written informed consent to un-

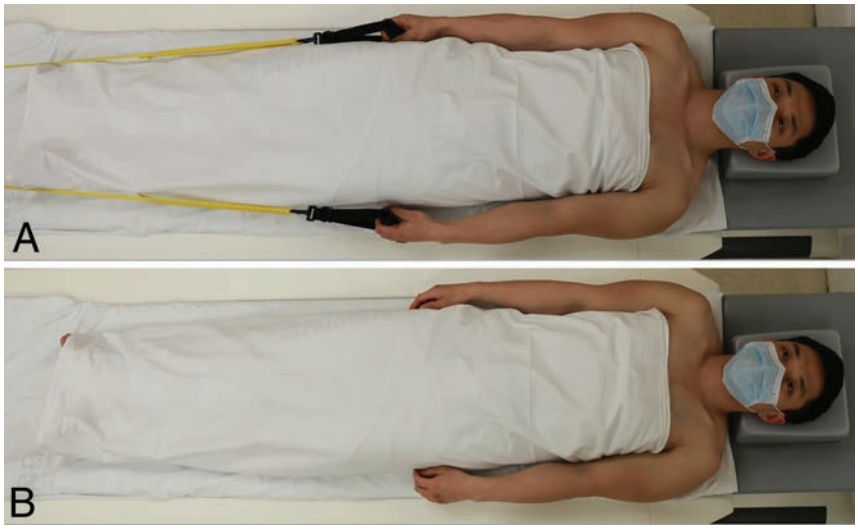

FIG 1. Patient position for neck CT imaging. Patients in the intervention CT protocol were examined with the arm traction device (*A*). Patients in the standard CT protocol were examined in a relaxed supine position (*B*). Reprinted with permission from Choi et al.[9]

dergo the CT protocol was obtained from all patients before each examination.

Study Patients

Patients were eligible if they met the following criteria: older than 18 years of age; able to follow commands and cooperate with the use of the arm traction device; and patients with lymphoma with complete remission who were scheduled to undergo 2 consecutive follow-up neck CT scans within a 1-year interval for surveillance purposes. Complete remission of lymphoma was defined as no evidence of disease, as indicated by radiologic imaging, such as CT or [^{18}F]fluorodeoxyglucose positron-emission tomography. Patients were excluded from the study if they met any of the following criteria: a previous history of surgery or radiation therapy to the neck; vascular or bone-related medical implants such as a central line or a metallic plate in the neck, upper arms, or shoulder; suspicious disease progression on follow-up CT; or an interval of >1 year between the 2 consecutive CT scans.

Outcome Measures

This study had 2 primary outcomes: the image quality and radiation exposure from the CT scan. CT image quality was measured by image noise at the level of the lower neck, while radiation exposure was measured by the dose-length product (DLP). Secondary outcomes were streak artifacts in the supraclavicular fossa, image noise in the midneck, volume CT dose index ($CTDI_{vol}$), effective diameter, and the extent of shoulder level lowering measured by the extent of the biacromial line shift.

CT Protocol and Analysis

Patients underwent 2 consecutive neck CT scans (intervention and standard protocol). In the standard protocol, patients were positioned on the CT table with the shoulders lowered as much as possible and told to maintain the position throughout the scan. In the intervention protocol, a custom-made arm traction device was applied to the patients. This device was placed and secured by a radiologic technologist (Fig 1).

All patients underwent CT examinations on the same 128-channel multidetector CT system (Somatom Definition Edge; Siemens, Erlangen, Germany). Imaging variables were as follows: 120 kV; 200 effective mAs; axial scan mode; display FOV, 22 cm; large-body scan FOV, 50 cm; pitch, 1; gantry rotation time, 0.5 seconds; detector collimation, 128 × 0.6 mm; and 3-mm axial reconstructed section thickness with a soft-tissue algorithm. Real-time automatic tube current modulation software (CARE Dose 4D; Siemens) was used to regulate the tube current, depending on the patient's anatomy. Images were obtained from the upper margin of the frontal sinus to the top of the aortic arch, either with or without an IV injection of contrast media. Contrast-enhanced CT scans were acquired after 70 seconds following the administration of 150 mL of intravenous ioversol (Optiray-320; Mallinckrodt, St. Louis, Missouri) at a rate of 2.5 mL/s via the right antecubital vein. Radiologic images were reviewed with a PACS.

One neuroradiologist with 7 years of dedicated head and neck experience assessed the image noise by calculating the SD of the CT values in Hounsfield units for pixels within an ROI fitted within the relevant structures (as outlined below). CT values were measured at the mid- and lower neck levels contralateral to the side used for the intravenous contrast media administration. The ROIs were placed on the internal jugular vein and sternocleidomastoid muscle at the level of the cricoid cartilage (midneck) and the thyroid gland and internal jugular vein at the level of the first costovertebral joint (lower neck).

For the evaluation of streak artifacts, 2 board-certified neuroradiologists with 15 and 8 years of experience independently analyzed the axial CT images on a PACS screen, with the scanning parameters removed from the screen to blind the reviewers to whether the arm traction device was being used. All image assessment was performed with a standard soft-tissue setting (window width: 300/window level: 35). The degree of streak artifacts in the supraclavicular fossa was evaluated and scored as follows: 1, no or minimal artifacts with no image obscuration; 2, mild artifacts causing partial obscuration of subcutaneous fat or skin without diagnostic interference; and 3, severe artifacts causing obscuration of deep cervical structures with diagnostic interference.[9] The supraclavicular fossa was defined on each axial scan when any portion of the clavicle was identified on 1 side of the neck.[12]

Radiation exposure was evaluated with DLP and $CTDI_{vol}$. Potential confounds, including the effective diameter of the neck and the z-axis scan range, were also assessed. The effective diameter of the neck was calculated from an axial CT image at the level of the lower margin of the cricoid cartilage using the following equation: Effective Diameter = $\sqrt{}$Anteroposterior Diameter ×

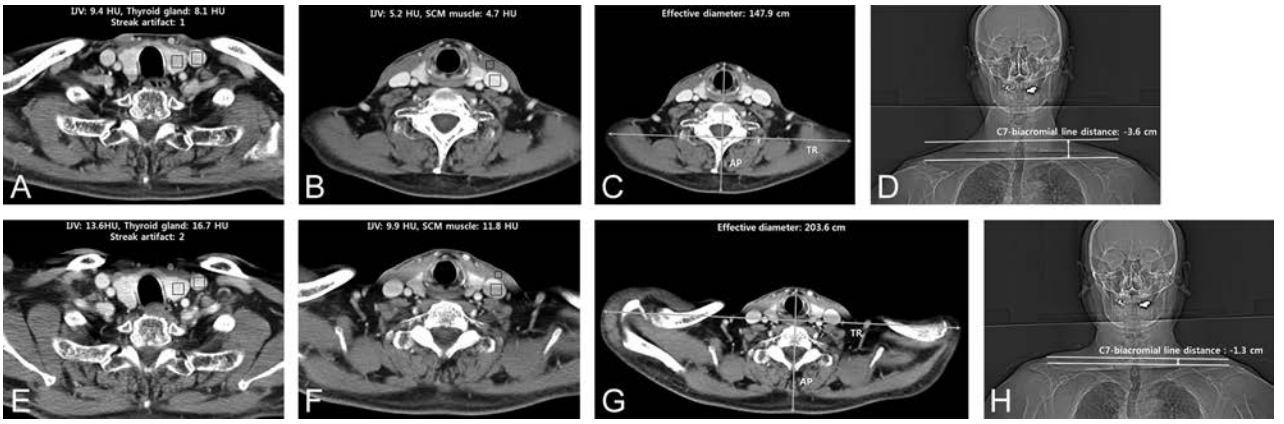

FIG 2. Representative neck CT images obtained with the intervention (*A–D*) and standard (*E–H*) protocols. The images demonstrate the measurements for image noise at the lower neck (first costovertebral joint level, *A* and *E*) and midneck (cricoid cartilage level, *B* and *F*), and the effective diameter measurement at the midneck (*C* and *G*). The C7-biacromial line distance was determined as illustrated on images *D* and *H*. The *white line* indicates the biacromial line; *arrow*, the C7-biacromial line distance; SCM, sternocleidomastoid; IJV, internal jugular vein; HU, Hounsfield units.

Transverse Diameter.[13] The total scan length was assessed for each patient by multiplying the total number of axial images acquired by the section thickness. To measure the degree of shoulder-level shift, we determined the C7-biacromial line distance. Two straight lines were drawn on the anteroposterior scout image: One was the line connecting the upper margin of the shoulder acromion bilaterally (biacromial line),[14] while the other line was parallel to the middle of the upper endplate of C7. The C7-biacromial line distance was defined as the distance between the 2 straight lines (Fig 2). The measurement was expressed as negative if the biacromial line was located caudal to the upper margin of C7 and positive if the line was located cranial to the upper margin of C7.

After the CT scans with the intervention protocol, the patients were asked to fill in a questionnaire and rate the discomfort on a 10-cm visual analog scale (grades 0–10), with 0 representing "no discomfort" and 10 representing "the worst discomfort imaginable." Patients were also asked if they would be willing to accept the arm traction device at the next CT follow-up.

Statistical Analysis

A sample size of 59 would achieve 80% power to detect a mean of paired differences of −9.0 with an estimated SD of differences of 20.0 and a significance level (α) of .0125 using a 2-sided paired *t* test (ie, the paired difference of DLP between the standard and intervention protocols). This sample size would achieve 89% power to detect a mean of paired differences of −3.5 with an estimated SD of differences of 7.0 and a significance level (α) of .0125 using a 2-sided paired *t* test (ie, the paired difference between the standard and intervention protocols of the image noise on the thyroid gland at the position of the lower neck). Therefore, with consideration of a 15% follow-up loss, we planned to collect data from 70 patients to estimate the double primary end points (DLP and image noise on the thyroid gland at the lower neck) in each subject from application of the intervention and standard CT protocols.

Data for continuous variables were presented as means and SDs, and for categoric variables, as the number of subjects. Paired *t* tests were used to analyze the differences between the 2 protocols with respect to image noise, DLP, $CTDI_{vol}$, effective diameter, C7-biacromial line distance, and z-axis scan range. A marginal homogeneity test and visual grade characteristics method were used to compare the streak artifact levels between the 2 protocols. The interobserver agreement for subjective evaluation of streak artifacts was calculated with κ statistics, and estimation of the overall κ was as follows: slight agreement (0–0.20), fair agreement (0.21–0.40), moderate agreement (0.41–0.60), substantial agreement (0.61–0.80), and almost perfect agreement (0.81–1.00). All statistical analyses were performed with MedCalc for Windows, Version 15.0 (MedCalc Software, Mariakerke, Belgium) and SPSS, Version 23.0 for Windows (SPSS, Armonk, New York), with a *P* value of .05 considered statistically significant.

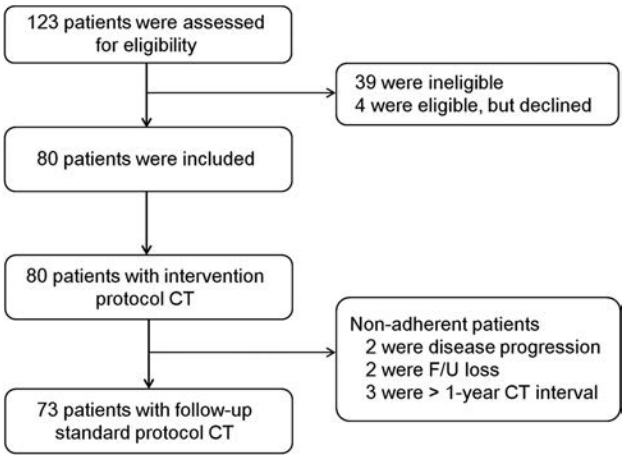

FIG 3. Study flow diagram.

RESULTS

From March 2015 to April 2016, we screened 123 patients, of whom 84 were eligible. After we excluded 4 patients who declined to use the arm traction device, 80 patients were included and underwent CT with the intervention protocol. Seven of these patients (8.8%) who were nonadherent to the study protocol for measurement of study outcomes were excluded. Finally, 73 patients (mean age, 50.6 years; age range, 19–76 years) were enrolled and underwent consecutive CT scans with the standard protocol (Fig 3). The baseline characteristics of the patients enrolled in this

study are summarized in Table 1. Among 73 patients, 4 patients (5.5%) underwent nonenhanced CT, with a mean interval between the intervention and standard CT protocol of 155 days.

Primary and Secondary Outcomes

Image-quality measures based on the assessment of image noise showed that the intervention protocol resulted in statistically significant improvement in CT image quality in the lower neck in comparison with the standard protocol ($P < .001$). A mean noise reduction of 28.5% (from 17.2 to 12.3 HU; group mean SD of the values within the ROI) was measured at the thyroid gland and 25.2% (from 14.3 to 10.7 HU) at the internal jugular vein in the lower neck. A statistically significant decrease in the DLP was also measured in the intervention protocol compared with the standard protocol ($P < .001$, Table 2).

The evaluation of the streak artifacts in the supraclavicular fossa showed a significant decrease in the intervention protocol in comparison with the standard protocol (a mean score of 1.6 versus 1.9; test of marginal homogeneity, $P < .001$). The area under the visual grade characteristics curve was determined as 0.61 (95% confidence interval, 0.519–0.702) and was statistically significant ($P = .02$). The interobserver agreement for streak artifacts was substantial (κ value = 0.66; 95% confidence interval, 0.537–0.794). $CTDI_{vol}$ and effective diameter were also significantly lower in the intervention protocol than in the standard protocol (for both, $P < .001$; Table 2). The intervention protocol could lower the biacromial line by an average of 2.1 cm in comparison with the standard protocol ($P < .001$). There was no statistical difference in the z-axis scan range between the 2 protocols (intervention versus standard, 27.2 ± 3.1 cm versus 26.8 ± 2.7 cm; $P = .14$; Table 2). A representative case is illustrated in Fig 2.

Questionnaire on Intervention Protocol

All 80 patients filled out the questionnaire given after the neck CT that used the intervention protocol. The mean score on the visual analog scale was 0.6 (range, 0–8). Sixty-two patients (77.5%) showed no discomfort (score 0), while 3 patients (3.8%) rated discomfort as >3. Seventy-seven patients (96.2%) responded that they would be willing to accept the intervention CT protocol again.

Table 1: Baseline characteristics of the patients enrolled in the study

Parameter	Value
Age (yr)	
Mean	50.6
Range	19–76
Sex (No.) (%)	
Men	39 (53.4)
Women	34 (46.6)
Body weight (kg)	
Mean	64.7
Range	35.7–98.1
Interval of CT scans (days)	
Mean	155
Range	58–355

Table 2: Clinical outcomes in the intervention and standard CT protocols[a]

Outcome	Intervention CT Protocol (*n* = 73)	Standard CT Protocol (*n* = 73)	*P* Value
Primary end points			
Image noise, lower neck[b]			
Thyroid gland	12.3 ± 5.1	17.2 ± 5.5	<.001
Internal jugular vein	10.7 ± 4.4	14.3 ± 5.1	<.001
DLP (mGy × cm)	397.6 ± 52.8	413.9 ± 56.3	<.001
Secondary end points			
Streak artifacts[c]	1.6 ± 0.5	1.9 ± 0.4	<.001
1	26 (35.6%)	11 (15.1%)	
2	46 (63.0%)	59 (80.8%)	
3	1 (1.4%)	3 (4.1%)	
Image noise, midneck[b]			
Internal jugular vein	7.1 ± 3.7	9.1 ± 5.8	.009
SCM muscle	5.6 ± 2.4	7.3 ± 4.0	<.001
$CTDI_{vol}$ (mGy)	13.4 ± 0.9	13.9 ± 0.9	<.001
Effective diameter (cm)[d]	16.2 ± 4.4	19.6 ± 4.9	<.001
C7-biacromial line distance (cm)[e]	−2.4 ± 1.1	−0.3 ± 1.1	<.001

Note:—SCM indicates sternocleidomastoid.
[a] Data are expressed as mean ± SD.
[b] Based on the evaluation of image noise, by measurement of the SD of the CT values in Hounsfield units.
[c] Streak artifacts at the supraclavicular fossa (1, none or minimal; 2, mild; and 3, severe).
[d] Effective diameter of the neck at the level of the lower margin of the cricoid cartilage.
[e] The C7-biacromial line distance was defined as the distance from the intersection of a line connecting the acromion processes to the upper endplate of C7. Negative values indicate that the biacromial line was located caudal to the upper margin of C7, and positive values, that it was located cranial of the upper margin of C7.

DISCUSSION

We prospectively assessed the effect of an arm traction device combined with automatic tube current modulation on the image quality and radiation exposure level of neck CT. Application of the arm traction device lowered the shoulder level and reduced both the dimension of the volume of tissue of imaging interest and the radiation attenuation from the shoulder and upper thorax. As a result, we could reduce not only the image noise and streak artifacts in the mid- and lower neck but also the radiation exposure level. Our current results suggest that the use of an arm traction device in routine practice could easily improve neck CT image quality while, at the same time, reducing radiation exposure.

In the present study, the main eligibility criterion was patients with lymphoma with complete remission who were scheduled to undergo consecutive neck CT scans within a 1-year interval. The National Comprehensive Cancer Network guidelines for patients with lymphoma recommend surveillance CT scans every 6 or 12 months for 2 years after completion of treatment.[15] We therefore considered these patients ideal for our study design—that is, the same patients would be eligible for both intervention and standard CT protocols. Even though the main eligibility criterion in this study was patients with lymphoma with complete remission, the arm traction device could be applied to any patient who would be cooperative in routine practice because this device is easy to use and causes little discomfort for most patients.

Previous studies have investigated several techniques to prevent image degradation in the lower neck and supracla-

vicular fossa. Some of the studies suggested the potential utility of lowering the shoulder level to reduce image degradation. However, the subjects or CT machines used in the studies demonstrated considerable heterogeneity between the control and intervention groups,[8-10] which may have greatly influenced the study results. We therefore designed a prospective study that used the same CT scanner for all acquisitions and enrolled the identical study subjects in both the intervention and control groups, to test the exact effect of the arm traction device on CT image quality and radiation exposure. This study revealed that the arm traction device we designed lowered the biacromial line an average of 2.1 cm, which lessened image degradation from the bony shoulder girdles and the abrupt size increase from the circular neck to the broadened chest in the mid- and lower neck scan sections. Given that the automatic tube current modulation technique allows maintenance of constant image quality within a maximum radiation exposure level by rapidly responding to large variations in beam attenuation, reducing the dimensions of the tissue of interest to be scanned (ie, effective diameter) should be a basic step toward the reduction of radiation exposure, as demonstrated in this study.

This study has several limitations. First, our subjects underwent imaging with a single CT machine to reduce any influence on the results related to the intrinsic properties of different CT systems. To generalize the study results, further studies on different CT machines are required, even though we speculate that future study results will be similar to ours, because the basic principle is similar across CT machines. Second, we did not consider the possibility of thyroiditis in the measurement of the ROIs. Any chronologic changes in thyroiditis could have influenced the image noise in the thyroid gland. However, we believe that any effects from thyroiditis must be extremely small because the image noise of both the thyroid gland and the internal jugular vein in the lower neck showed similar tendencies (reductions of 25.2%–28.5% in the intervention protocol). Third, we could not assess the size-specific dose estimate, which is the estimate of the absorbed radiation dose in an individual patient. A recent recommendation for studies evaluating the CT dose level suggested that the following 4 parameters be assessed to provide an accurate estimation of the dose absorbed by an individual patient: 1) $CTDI_{vol}$, 2) DLP, 3) effective diameter, and 4) size-specific dose estimates.[13] However, we did not report the size-specific dose estimates in the present investigation because conversion factors for this calculation are currently available for only the torso (chest-abdomen and/or pelvis), not for the neck region.[16,17] Finally, the clinical applicability of the arm traction device is limited to cooperative patients with no physical disability in either arm.

CONCLUSIONS

An arm traction device improves the image quality and reduces radiation exposure during neck CT. This arm traction device can be simply applied in cooperative patients with suspected lower neck lesions, and the approach offers distinct advantages over the conventional imaging protocol.

Disclosures: Jung Hwan Baek—*UNRELATED: Consultancy*: STARmed, RF Medical Co.

REFERENCES

1. Kalra MK, Maher MM, Toth TL, et al. **Strategies for CT radiation dose optimization.** *Radiology* 2004;230:619–28 CrossRef Medline
2. Russell M, Fink J, Rebeles F, et al. **Balancing radiation dose and image quality: clinical applications of neck volume CT.** *AJNR Am J Neuroradiol* 2008;29:727–31 CrossRef Medline
3. Tamm EP, Rong XJ, Cody DD, et al. **Quality initiatives: CT radiation dose reduction: how to implement change without sacrificing diagnostic quality.** *Radiographics* 2011;31:1823–32 CrossRef Medline
4. Parakh A, Kortesniemi M, Schindera ST. **CT radiation dose management: a comprehensive optimization process for improving patient safety.** *Radiology* 2016;280:663–73 CrossRef Medline
5. Goenka AH, Herts BR, Dong F, et al. **Image noise, CNR, and detectability of low-contrast, low-attenuation liver lesions in a phantom: effects of radiation exposure, phantom size, integrated circuit detector, and iterative reconstruction.** *Radiology* 2016;280:475–82 CrossRef Medline
6. Kim JH, Choo KS, Moon TY, et al. **Comparison of the image qualities of filtered back-projection, adaptive statistical iterative reconstruction, and model-based iterative reconstruction for CT venography at 80 kVp.** *Eur Radiol* 2016;26:2055–63 CrossRef Medline
7. Yoon HJ, Chung MJ, Hwang HS, et al. **Adaptive statistical iterative reconstruction-applied ultra-low-dose CT with radiography-comparable radiation dose: usefulness for lung nodule detection.** *Korean J Radiol* 2015;16:1132–41 CrossRef Medline
8. Wirth S, Meindl T, Treitl M, et al. **Comparison of different patient positioning strategies to minimize shoulder girdle artifacts in head and neck CT.** *Eur Radiol* 2006;16:1757–62 CrossRef Medline
9. Choi YJ, Lee JH, Cho WY, et al. **Effect of an arm traction device on image quality and radiation exposure during neck computed tomography.** *Eur J Radiol* 2016;85:68–72 CrossRef Medline
10. Kranz PG, Wylie JD, Hoang JK, et al. **Effect of the CT table strap on radiation exposure and image quality during cervical spine CT.** *AJNR Am J Neuroradiol* 2014;35:1870–76 CrossRef Medline
11. Brink M, de Lange F, Oostveen LJ, et al. **Arm raising at exposure-controlled multidetector trauma CT of thoracoabdominal region: higher image quality, lower radiation dose.** *Radiology* 2008;249:661–70 CrossRef Medline
12. Som PM, Curtin HD, Mancuso AA. **Imaging-based nodal classification for evaluation of neck metastatic adenopathy.** *AJR Am J Roentgenol* 2000;174:837–44 CrossRef Medline
13. Bankier AA, Kressel HY. **Through the Looking Glass revisited: the need for more meaning and less drama in the reporting of dose and dose reduction in CT.** *Radiology* 2012;265:4–8 CrossRef Medline
14. Korovessis P, Koureas G, Zacharatos S, et al. **Backpacks, back pain, sagittal spinal curves and trunk alignment in adolescents: a logistic and multinomial logistic analysis.** *Spine (Phila Pa 1976)* 2005;30:247–55 CrossRef Medline
15. Zelenetz AD, Gordon LI, Wierda WG, et al. **Diffuse Large B-Cell Lymphoma Version 1.2016.** *J Natl Compr Canc Netw* 2016;14:196–231 Medline
16. American Association of Physicists in Medicine. Size-specific dose estimates (SSDE) in pediatric and adult body CT examinations. AAPM Report 204. College Park, Maryland: American Association of Physicists in Medicine; 2011
17. Christner JA, Braun NN, Jacobsen MC, et al. **Size-specific dose estimates for adult patients at CT of the torso.** *Radiology* 2012;265:841–47 CrossRef Medline

Patterns of Sonographically Detectable Echogenic Foci in Pediatric Thyroid Carcinoma with Corresponding Histopathology: An Observational Study

I. Erdem Toslak, B. Martin, G.A. Barkan, A.I. Kılıç, and J.E. Lim-Dunham

ABSTRACT

BACKGROUND AND PURPOSE: Small echogenic foci within pediatric thyroid nodules are commonly seen by ultrasound and are one of the features used to determine the level of suspicion for malignancy. These are sometimes termed "microcalcifications," but their relation with malignancy is controversial due to the lack of standard terminology. Our aim was to evaluate sonographic patterns of echogenic foci in malignant pediatric thyroid nodules and describe the distribution of corresponding psammoma bodies and other histopathologic findings in thyroidectomy specimens.

MATERIALS AND METHODS: Ultrasounds of 15 pathologically proved malignant thyroid nodules in children were retrospectively reviewed by 2 radiologists who separately classified echogenic foci into the 4 morphologic patterns described in the American College of Radiology Thyroid Imaging, Reporting and Data System and noted their presence and distribution. Interobserver agreement was assessed, and consensus was reached for nodules for which there was disagreement. Surgical pathology findings from thyroidectomy specimens were retrospectively reviewed for the presence and distribution of psammomatous and dystrophic/stromal calcifications and eosinophilic/sticky colloid. Ultrasound and histopathologic ratings were compared, and frequencies and percentages corresponding to observed agreement levels were calculated.

RESULTS: Interobserver agreement between radiologists' sonographic assessments for the presence and distribution of echogenic foci ranged from 53% to 100% for all categories. Punctate echogenic foci were present in all nodules, and macrocalcifications, in 27%. Histopathology of the 15 nodules revealed that only 4 (27%) had psammomatous calcifications, while 9 (60%) had stromal calcifications and 8 (53%) had sticky colloid.

CONCLUSIONS: Sonographically detectable echogenic foci in malignant pediatric thyroid nodules can be reliably classified on the basis of American College of Radiology Thyroid Imaging, Reporting and Data System, with punctate echogenic foci composing the most common subtype. These echogenic foci do not represent psammomatous calcifications most of the time; instead, more than half of the malignant thyroid nodules with echogenic foci contained stromal calcifications or sticky colloid.

ABBREVIATIONS: ACR TI-RADS = American College of Radiology Thyroid Imaging, Reporting and Data System; PTC = papillary thyroid carcinoma; US = ultrasound; USFNAB = US-guided fine-needle aspiration biopsy

Punctate echogenic foci of <1 mm are commonly seen by ultrasound (US) in thyroid nodules. These are often termed "microcalcifications" and are relevant because their presence within a nodule is one of several US features known to increase the likelihood of malignancy in both the pediatric and adult populations.[1-4] Microcalcifications are generally assumed to represent psammoma bodies, which are considered specific for papillary thyroid carcinoma (PTC) but may also be found in follicular or medullary thyroid carcinoma and thyrotoxicosis.[5] Nevertheless, many PTCs do not contain psammoma bodies, which are found in only 25%–37% of PTCs.[5,6] Moreover, other histologic features such as dystrophic or stromal calcifications and eosinophilic or "sticky colloid" may be seen in PTC and other types of thyroid malignancies.[5-7]

The importance of sonographically detectable microcalcifications in thyroid nodules is controversial.[3,8-12] This controversy may be partially due to lack of standard terminology and of proper subclassification of the calcifications on the basis of morphologic features. Several US categorization systems for echo-

Received April 24, 2017; accepted after revision August 13.

From the Departments of Radiology (I.E.T., J.E.L.-D.) and Pathology (G.A.B., A.I.K.), Loyola University Medical Center, Maywood, Illinois; and Clinical Research Office (B.M.), Loyola University Chicago Health Sciences Division, Loyola University Chicago Stritch School of Medicine, Maywood, Illinois.

Please address correspondence to Jennifer E. Lim-Dunham, MD, Department of Radiology, Loyola University Medical Center, 2160 S 1st Ave, Maywood, IL 60153; e-mail jlim2@lumc.edu

http://dx.doi.org/10.3174/ajnr.A5419

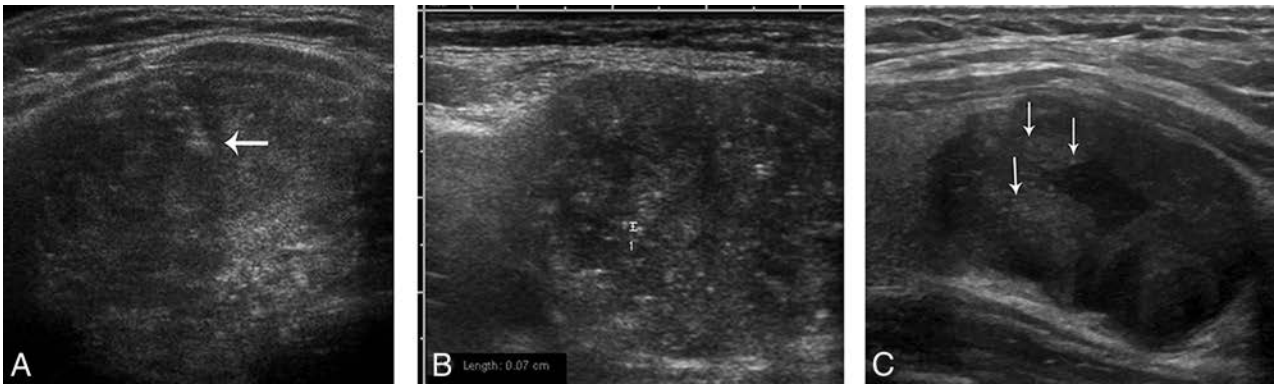

FIG 1. Typical sonography samples of categories of ACR TI-RADS echogenic foci and types of distribution. *A*, Macrocalcifications with posterior acoustic shadowing (*arrow*) in a left-sided 4.7-cm thyroid nodule in an 18-year-old girl with histologically proved papillary thyroid carcinoma. The distribution is classified as sparse. *B*, Punctate echogenic foci with small, 0.7-mm comet-tail artifacts in the same patient as in *A*. The distribution is diffuse. Pathology revealed stromal calcifications and sticky colloid, both sparsely distributed, and the absence of psammomatous calcifications. *C*, Punctate echogenic foci with no posterior artifacts (*arrows*) in a left-sided 3.5-cm thyroid nodule in a 12-year-old girl with a histologically proved follicular variant of papillary thyroid carcinoma. The distribution is sparse. Histology revealed no corresponding calcifications or sticky colloid.

genic foci in thyroid nodules have been developed, with some studies showing that echogenic foci previously termed "microcalcifications" were present not only in malignant thyroid nodules but also in benign nodules.[11,12] A recent study on adults that subclassified echogenic foci reported that what many authors called microcalcifications did not exclusively represent psammoma bodies, but rather other entities including stromal calcifications and sticky colloid.[7] On the basis of these findings, the recently proposed American College of Radiology Thyroid Imaging, Reporting and Data System (ACR TI-RADS) terminology used to describe echogenic foci in thyroid nodules has removed the word "microcalcification" from its lexicon and replaced it with more precise descriptors.[4]

To our knowledge, no dedicated study has previously been undertaken in the pediatric population of patterns of sonographic echogenic foci and corresponding histopathology. We hypothesized that as in adults, echogenic foci in malignant thyroid nodules may not always represent psammomatous calcifications. Therefore, the aim of this observational investigation was to evaluate echogenic foci in malignant pediatric thyroid nodules according to ACR TI-RADS and to describe the distribution of corresponding psammoma bodies and other histopathologic findings in thyroidectomy specimens.

MATERIALS AND METHODS

Ethics Statement

This retrospective study was approved by the institutional review board of Loyola University Medical Center, and written informed consent was waived. Patient records and information were anonymized and randomized before analysis.

Patient Selection

The study cohort included 29 consecutive pediatric patients, 18 years of age and younger, who underwent total thyroidectomy for thyroid malignancy between 1996 and 2016. Ten patients were excluded due to the lack of preoperative US images, and 4 patients were excluded due to the lack of surgical specimens, leaving 15 patients composing the final study group.

Ultrasonography and Image Analysis

All individuals underwent diagnostic gray-scale ultrasonography performed on a variety of US systems (Acuson Sequoia 512, XP128 and Aspen, Siemens, Erlangen, Germany; and Logic E9, GE Healthcare, Milwaukee, Wisconsin) using high-frequency (8–15 MHz) linear array transducers. Still and cine US images of the thyroid, including any focal nodules, were stored electronically in DICOM format on the PACS server. These images were independently evaluated by 2 radiologists (J.E.L.-D., I.E.T.), each with >10 years of experience and each blinded to the pathologic diagnosis. For nodules for which there was disagreement, consensus was reached in a separate session.

Echogenic foci in each nodule were classified into 1 of 4 morphologic categories on the basis of ACR TI-RADS lexicon descriptions[4,13]: echogenic foci with large V-shaped comet-tail artifacts measuring >1 mm; macrocalcifications, defined as coarse echogenic foci accompanied by acoustic shadowing; peripheral rim calcifications located along the margin of the nodule; and punctate echogenic foci with no or small (<1-mm) comet-tail artifacts. Typical examples of each category found in our patient population are illustrated in Fig 1. Examples of echogenic foci with large comet-tail artifacts and peripheral calcifications were not included because these were not found in any of our patients. If a nodule contained >1 type of echogenic focus, all relevant categories were applied.

The distribution of the echogenic foci was then analyzed. Sparse was defined as 1–3 scattered echogenic foci; focal, as >3 foci in a local cluster; and diffuse, as innumerable echogenic foci scattered throughout the nodule, in accordance with the system described by Tahvildari et al.[7] Typical examples of distribution are also demonstrated in Fig 1.

Tissue Diagnosis

Before thyroidectomy, 14 of the 15 nodules underwent US-guided fine-needle aspiration biopsy (USFNAB). The decision to proceed to thyroidectomy was made by the endocrine surgeon on the basis of USFNAB results for 12 patients. For the other 3 patients, including the patient who did not undergo USFNAB, thyroidec-

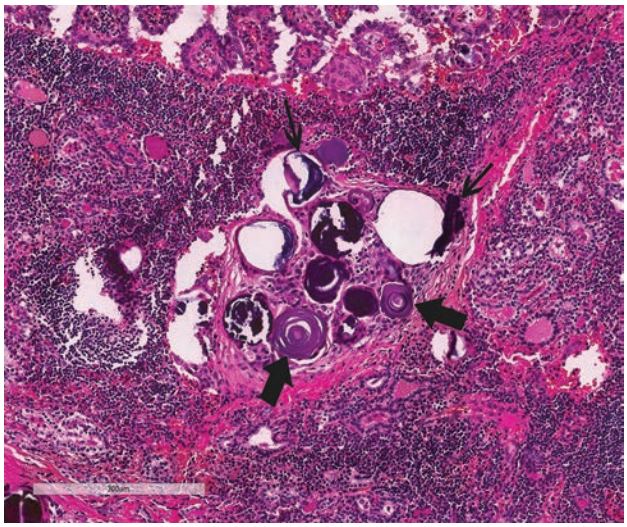

FIG 2. Examples of psammomatous (*thick arrows*) and stromal calcifications (*thin arrows*) from a thyroidectomy specimen of a 16-year-old girl showing papillary thyroid carcinoma in a background of lymphocytic thyroiditis (hematoxylin-eosin stain, 20×).

tomy was performed according to clinical and US findings. USFNAB cytology results were retrieved from the medical records; 9 (60%) of the cytology slides were available for review by a board-certified pathologist (G.A.B.).

The Bethesda System for Reporting Thyroid Cytopathology was used to classify the thyroid nodules as follows: nondiagnostic, benign, atypia or follicular lesion of undetermined significance, follicular neoplasm/suspicious for follicular neoplasm, suspicious for malignancy, or malignant.[14] Surgical pathology slides of the thyroidectomy specimens were retrospectively reviewed by the same pathologist. Care was taken to ensure that each surgical pathology sample corresponded in size and location to the designated nodule noted on the US evaluation. Histology samples were evaluated for the presence of psammomatous and stromal calcifications based on the previous descriptions in the literature, with a typical example demonstrated in Fig 2.[6] The distribution of each type of calcification was characterized as sparse, focal, or diffuse. Sparse was defined as rare calcifications that were detected only on close screening; focal, as calcifications easily identified but localized to 1 area; and diffuse, as calcifications scattered throughout the tumor, as described by Tahvildari et al.[7] Colloid, if present, was characterized as thin versus "sticky."[5]

Statistical Analysis

Descriptive statistics included a demographic analysis by patient sex, age, histology outcome, and nodule size. Patient age and nodule size were expressed as medians and interquartile ranges due to the small sample size.

Weighted κ coefficients were initially generated with Cicchetti-Allison weights to assess interobserver reliability between the 2 radiologists' ordinal ratings of the sonographic echogenic foci morphologic type and distribution of each nodule. However, the small sample size coupled with high levels of observed agreement ultimately precluded the use of κ coefficients in the final analysis. Thus, frequencies and percentages corresponding to observed agreement levels were reported for this observational study.

Table 1: Observed agreement between radiologists for presence and distribution of thyroid nodule echogenic foci[a]

US Classification	Agreement for Presence or Absence (No.) (%)	Agreement for Distribution (No.) (%)
Punctate echogenic foci	15/15 (100%)	14/15 (93%)
Echogenic foci with large comet-tail artifacts	11/15 (73%)	11/15 (73%)
Macrocalcifications	8/15 (53%)	8/15 (53%)
Peripheral rim calcifications	15/15 (100%)	15/15 (100%)

Note:—No. indicates number of nodules.
[a] The valid number of observations is 15.

Radiologists' consensus ratings for the presence and distribution of echogenic foci of the various morphologic types on US were then compared with the observation of psammomatous calcifications, stromal calcifications, and sticky colloid on the surgical specimens. As before, these findings were presented as cross-tabulations of patient counts due to the small sample size and substantial levels of observed agreement. All statistical analyses were conducted with SAS 9.4 (SAS Institute, Cary, North Carolina).

RESULTS

The 15 patients (14 female and 1 male) included in the study each had 1 thyroid nodule. The median age was 15 years (interquartile range, 13–18 years), and the median nodule size was 3.2 cm (interquartile range, 2.1–4.7 cm). Of the 14 nodules that underwent USFNAB, results were classified according to the Bethesda System as malignant in 9 (60%), follicular neoplasm/suspicious for follicular neoplasm in 3 (20%), and benign in 2 (13%). Diagnosis on thyroidectomy specimens was as follows: PTC in 10 (67%), follicular variant of PTC in 1 (6.5%), follicular thyroid carcinoma in 3 (20%), and poorly differentiated carcinoma in 1 (6.5%). Two cases reported as benign on cytology were identified on thyroidectomy specimens as PTC in one case and poorly differentiated carcinoma in the other. On retrospective review of the slides, this discrepancy was attributed to sampling error.

Observed agreement between the radiologists for the presence of echogenic foci ranged from 53% to 100%, with agreement lowest for macrocalcifications and highest for punctate echogenic foci and peripheral rim calcifications (Table 1). Both raters agreed in 14 nodules (93%) on the distribution of the punctate echogenic foci and agreed in all 15 nodules that peripheral rim calcifications were absent. There was a lower concordance for the macrocalcification subtype (8/15, 53%) (Table 1).

The radiologists' consensus rating regarding the presence of echogenic foci revealed that all 15 nodules contained punctate echogenic foci, of which 14 were diffusely distributed. Four nodules (27%) had macrocalcifications, of which 3 were sparsely distributed. Considering all patterns of echogenic foci and that some nodules contained >1 type of echogenic focus, there were 19 unique occurrences of echogenic foci; of these, 14 (74%) were rated as diffusely distributed, and 4 (21%), as sparsely distributed. There were no echogenic foci with large comet-tail artifacts or peripheral rim calcifications detected in any of the nodules.

Histologic examination revealed that 12 of the 15 (80%) nod-

Table 2: Thyroid nodule pathology as a function of US patterns[a]

Pathology Finding (No.)	Punctate Echogenic Foci (No.)		Macrocalcifications (No.)	
	Present (*n* = 15)	Absent (*n* = 0)	Present (*n* = 4)	Absent (*n* = 11)
Stromal calcification present (9)	9 (60%)	0 (0%)	4 (100%)	5 (45%)
Stromal calcification absent (6)	6 (40%)	0 (0%)	0 (0%)	6 (55%)
Psammomatous calcification present (4)	4 (27%)	0 (0%)	1 (25%)	3 (27%)
Psammomatous calcification absent (11)	11 (73%)	0 (0%)	3 (75%)	8 (73%)
Sticky colloid present (8)	8 (53%)	0 (0%)	3 (75%)	5 (45%)
Sticky colloid absent (7)	7 (47%)	0 (0%)	1 (25%)	6 (55%)

Note:—No. indicates number of nodules.
[a] The valid number of observations is 15.

ules had some type of calcification or sticky colloid, while 3 (20%) nodules had none. Nine (60%) nodules had stromal calcifications, of which 4 were diffusely distributed and 4 were sparsely distributed. All 4 (27%) nodules that contained psammomatous calcifications were rated as diffusely distributed. Eight (53%) nodules had sticky colloid, which was sparsely distributed in all. Considering all patterns of calcification or sticky colloid and that some nodules contained >1 type of abnormality, there were 21 unique occurrences; of these, 8 (38%) were rated as diffusely distributed, and 12 (57%), as sparsely distributed.

Radiologists' consensus ratings for the presence of sonographic echogenic foci were then compared with histologic findings (Table 2). Radiologists detected the punctate echogenic foci subtype in all 15 nodules. Histopathology revealed that among these 15 nodules, 9 (60%) had stromal calcifications, 4 (27%) had psammomatous calcifications, and 8 (53%) had eosinophilic/sticky colloid. Thus, most (11/15, 73%) patients determined to have punctate echogenic foci did not have psammomatous calcifications.

The subtype of macrocalcifications were less commonly seen by US (4/15, 27%) (Table 2). Pathology revealed that among these nodules, all 4 (100%) had stromal calcification, 1 (25%) had psammomatous calcifications, and 3 (75%) had sticky colloid. Results confirmed the absence of psammomatous calcifications in 3 of the 4 (75%) patients determined to have macrocalcifications.

Analysis of sonographic patterns by final pathologic diagnosis showed that all 10 PTC nodules were determined by US to have punctate echogenic foci, while 4 of them (40%) had macrocalcifications. Of the 3 follicular thyroid carcinoma nodules, all had punctate echogenic foci.

Analysis of histologic findings segregated by final pathologic diagnosis showed that though all 4 psammomatous calcifications detected by histopathology were present in PTC nodules, of the 10 PTC nodules, most (6/10, 60%) lacked psammomatous calcifications. This was the case even though all 10 nodules were rated by radiologists' consensus as having punctate echogenic foci. Instead, 9 (90%) of the PTC nodules were found to have stromal calcifications, and 6 (60%), to have sticky colloid. Sticky colloid was found in 1 of the 3 follicular thyroid carcinoma nodules and in the single poorly differentiated carcinoma nodule. The nodule with the follicular variant of PTC did not have any type of calcification. None of the follicular thyroid carcinomas, poorly differentiated carcinomas, or follicular variant of PTC nodules had stromal or psammomatous calcifications.

DISCUSSION

As recommended by the 2015 American Thyroid Association Management Guidelines for Children with Thyroid Nodules and Differentiated Thyroid Cancer, small echogenic foci seen within thyroid nodules by US are one of the features used to determine the level of suspicion for malignancy.[1] These are considered in conjunction with other features like margin irregularity and solid composition.[3] These echogenic foci are often termed "microcalcifications," though exact definitions are often not stated or vary from study to study.[3,8,10-12] Publications describing systems to standardize terminology include Beland et al[11] and the ACR TI-RADS,[4,13] both of which subclassified echogenic foci into 4 patterns, and the study of Malhi et al,[12] which classified echogenic foci into 5 patterns.

Our study used the ACR TI-RADS lexicon for subclassification of echogenic foci because the system is simple and widely accepted. We found high interrater observed agreements up to 100% for the presence of almost all echogenic foci subtypes, indicating that the application of TI-RADS was a reproducible method.

Psammoma bodies are lamellated calcifications that may be found in papillary types of tumors and are one of the features used to make the histologic diagnosis of PTC.[6] This type of calcification is also important because PTC nodules that contain psammoma bodies are associated with lower disease-free survival rates, higher rates of lymph node metastasis, and a higher risk of pulmonary metastasis.[6] Stromal calcifications without lamellated morphology did not have any impact on disease-free survival.[6] Another diagnostic feature that may be found in up to 13% of PTCs is so-called "sticky colloid," which stains more densely and deeply eosinophilic than the typical "thin" or "watery" colloid, normally found in benign thyroid conditions.[5]

Our study revealed that even though most malignant pediatric nodules with punctate echogenic foci subtype were PTC, more than half (11/15, 73%) lacked psammomatous calcifications on pathologic examination. The absence of psammomatous calcifications by histology was also true for those with the macrocalcification subtype (3/4, 75%). We conclude that in children, sonographically detected punctate echogenic foci in malignant thyroid nodules do not always represent psammomatous calcifications; therefore, the term "punctate echogenic foci" may be more accurate than "microcalcification."

These results are like those from a recent study by Tahvildari et al[7] of 29 adult PTC nodules with sonographically detected punctate echogenic foci classic for microcalcifications that showed that

6 (21%) did not contain any calcifications by histology. Only 14 (48%) contained psammomatous calcifications, either alone or in combination with coarse calcifications; therefore, in more than half (52%), psammoma bodies were absent.

Of the pathologic features examined in our thyroid nodules, the most common was stromal calcifications, which were detected in 9/15 (60%). Less commonly seen were sticky colloid in 8/15 (53%) and psammomatous calcifications in 4/15 (27%). Tahvildari et al[7] reported rates of 38%, 100%, and 42%, respectively, indicating a similar low percentage of nodules containing psammomatous calcifications. Our study suggests that in children, like adults, punctate echogenic foci in malignant nodules are more often associated with, and presumably sometimes represent, sticky colloid and stromal calcifications, rather than exclusively psammoma bodies.[6,7] A possible explanation for this pathologic correspondence is that stromal calcifications and sticky colloid may cause US artifacts like those caused by psammomatous calcifications. Additionally, it has been proposed that in the absence of any pathologically proved calcifications or sticky colloid, such as observed in 3 (20%) of our patients, the presence of tiny cysts beyond the resolution of US may cause specular reflection from the cyst walls, thus producing bright echogenic foci on US.[7,12,15]

In addition to the lack of US and histologic concordance for the presence of punctate echogenic foci, we also noted a mismatch in the distribution. Most of our sonographically detected echogenic foci were diffusely distributed, while less than half of the pathologically detected calcifications were diffusely distributed. Prior studies found a similar overestimation of diffuse distribution of echogenic foci on US compared with histology.[7] The discrepancy might be partly due to inherent technical differences between histology and radiology. During US examination, the entirety of a nodule can be visualized in a global fashion on a cine loop sweep, whereas histologic examination is limited to selected sections of surgical specimens.

All 15 nodules, which were all malignant, contained punctate echogenic foci. The observed rate of this pattern in children agrees with the rate of 96% in adults reported previously.[12] Past studies concerning US of pediatric thyroid nodules reported rates of microcalcifications in malignant nodules ranging from 25% to 44%, which are much lower than the rates found in our study.[10,16] This discrepancy might be due to variation in histologic types in the study populations or sample size. Additionally, the US resolution and/or definition of what constituted microcalcification may have differed between the studies because the type of US equipment and terminology used were not always explicitly stated.[10,16]

Because psammomatous calcifications are generally associated with the PTC type of thyroid malignancy, we also analyzed our data for PTC nodules only. Ten nodules (67%) were PTC, which is different from the past literature indicating that PTC composes 92%–100% of pediatric thyroid malignancies.[10,16] Of our PTC nodules, psammomatous calcifications were seen in only 40%. This number agrees with the rates of 25%–37% reported in the adult literature and argues against the assumption that psammomatous calcifications are a specific feature of PTC.[5,6] On the other hand, stromal calcifications were seen in 90% of our malignant thyroid nodules, which underscores the standing of stromal calcifications as a common finding in pediatric PTC nodules. The preponderance of stromal calcifications in our pediatric population is larger than the reported range in adults of 47%–48% and is at odds with the previously reported association between these calcifications and advanced age.[6,7]

The retrospective nature and small sample size were restrictions of our study. Additionally, the study was confined to evaluation of echogenic foci, and the influence of other nodule features to assess malignancy risk, including shape, margin, echogenicity, and composition, was not studied.[3,4] Finally, the pathologic examination of the nodules involved selective sampling. This is an inherent limitation of the histologic examination technique because even if the entire nodule is sampled, only the most superficial sections of the tissue block are examined routinely. Therefore, there may have been unrecognized calcifications or sticky colloid within the tissue blocks, resulting in underestimation of both the presence and distribution.

CONCLUSIONS

Our study shows that sonographically detectable echogenic foci in malignant pediatric thyroid nodules can be reliably classified into morphologic patterns on the basis of ACR TI-RADS descriptions, with punctate echogenic foci being the most common subtype. Contrary to general knowledge, sonographically detectable echogenic foci within pediatric thyroid carcinoma do not correspond to histopathologic findings of psammomatous calcifications most of the time; instead, more than half of the nodules contained stromal calcifications or sticky colloid. This was true for all types of thyroid malignancy, not only for PTC. These results argue against using the presence of echogenic foci alone as a predictor of malignancy in pediatric thyroid nodules. Rather, when determining of the level of suspicion for malignancy, one should also consider the subtype and the presence of echogenic foci in the context of other features such as margin irregularity and solid composition.

REFERENCES

1. Francis GL, Waguespack SG, Bauer AJ, et al; American Thyroid Association Guidelines Task Force. **Management Guidelines for Children with Thyroid Nodules and Differentiated Thyroid Cancer.** *Thyroid* 2015;25:716–59 CrossRef Medline
2. Haugen B, Alexander EK, Bible KC, et al. **2015 American Thyroid Association Management Guidelines for Adult Patients with Thyroid Nodules and Differentiated Thyroid Cancer: the American Thyroid Association Guidelines Task Force on Thyroid Nodules and Differentiated Thyroid Cancer.** *Thyroid* 2016;26:1–133 CrossRef Medline
3. Lim-Dunham JE, Erdem Toslak I, Alsabban K, et al. **Ultrasound risk stratification for malignancy using the 2015 American Thyroid Association Management Guidelines for Children with Thyroid Nodules and Differentiated Thyroid Cancer.** *Pediatr Radiol* 2017;47:429–36 CrossRef Medline
4. Grant EG, Tessler FN, Hoang JK, et al. **Thyroid ultrasound reporting lexicon: white paper of the ACR Thyroid Imaging, Reporting and Data System (TIRADS) committee.** *J Am Coll Radiol* 2015;12:1272–79 CrossRef Medline
5. Miller TR, Bottles K, Holly EA, et al. **A step-wise logistic regression analysis of papillary carcinoma of the thyroid.** *Acta Cytol* 1986;30:285–93 Medline
6. Bai Y, Zhou G, Nakamura M, et al. **Survival impact of psammoma body, stromal calcification, and bone formation in papillary thyroid carcinoma.** *Mod Pathol* 2009;22:887–94 CrossRef Medline

7. Tahvildari AM, Pan L, Kong CS, et al. **Sonographic-pathologic correlation for punctate echogenic reflectors in papillary thyroid carcinoma: what are they?** *J Ultrasound Med* 2016;35:1645–52 CrossRef Medline
8. Moon WJ, Jung SL, Lee JH, et al; Thyroid Study Group, Korean Society of Neuro- and Head and Neck Radiology. **Benign and malignant thyroid nodules: US differentiation–multicenter retrospective study.** *Radiology* 2008;247:762–70 CrossRef Medline
9. Khoo ML, Asa SL, Witterick IJ, et al. **Thyroid calcification and its association with thyroid carcinoma.** *Head Neck* 2002;24:651–55 CrossRef Medline
10. Moudgil P, Vellody R, Heider A, et al. **Ultrasound-guided fine-needle aspiration biopsy of pediatric thyroid nodules.** *Pediatr Radiol* 2016;46:365–71 CrossRef Medline
11. Beland MD, Kwon L, Delellis R a, et al. **Nonshadowing echogenic foci in thyroid nodules: are certain appearances enough to avoid thyroid biopsy?** *J Ultrasound Med* 2011;30:753–60 CrossRef Medline
12. Malhi H, Beland MD, Cen SY, et al. **Echogenic foci in thyroid nodules: significance of posterior acoustic artifacts.** *AJR Am J Roentgenol* 2014;203:1310–16 CrossRef Medline
13. Tessler FN, Middleton WD, Grant EG, et al. **ACR Thyroid Imaging, Reporting and Data System (TI-RADS): white paper of the ACR TI-RADS Committee.** *J Am Coll Radiol* 2017;14:587–95 CrossRef Medline
14. Cibas ES, Ali SZ. **The Bethesda System for Reporting Thyroid Cytopathology.** *Am J Clin Pathol* 2009;132:658–65 CrossRef Medline
15. Muradali D, Colgan T, Hayeems E, et al. **Echogenic ovarian foci without shadowing: are they caused by psammomatous calcifications?** *Radiology* 2002;224:429–35 CrossRef Medline
16. Karnak I, Ardiçli B, Ekinci S, et al. **Papillary thyroid carcinoma does not have standard course in children.** *Pediatr Surg Int* 2011;27:931–36 CrossRef Medline

Role of MR Neurography for the Diagnosis of Peripheral Trigeminal Nerve Injuries in Patients with Prior Molar Tooth Extraction

R. Dessouky, Y. Xi, J. Zuniga, and A. Chhabra

ABSTRACT

BACKGROUND AND PURPOSE: Clinical neurosensory testing is an imperfect reference standard to evaluate molar tooth extraction related peripheral trigeminal neuropathy. The purpose was to evaluate the diagnostic accuracy of MR neurography in this domain and correlation with neurosensory testing and surgery.

MATERIALS AND METHODS: In this retrospective study, nerve caliber, T2 signal intensity ratio, and contrast-to-noise ratios were recorded by 2 observers using MR neurography for bilateral branches of the peripheral trigeminal nerve, the inferior alveolar and lingual nerves. Patient demographics and correlation of the MR neurography findings with the Sunderland classification of nerve injury and intraoperative findings of surgical patients were obtained.

RESULTS: Among 42 patients, the mean ± SD age for case and control patients were 35.8 ± 10.2 years and 43.2 ± 11.5 years, respectively, with male-to-female ratios of 1:1.4 and 1:5, respectively. Case subjects (peripheral trigeminal neuropathy or injury) had significantly larger differences in nerve thickness, T2 signal intensity ratio, and contrast-to-noise ratios than control patients for the inferior alveolar nerve and lingual nerve (P = .01 and .0001, .012 and .005, and .01 and .01, respectively). Receiver operating characteristic analysis showed a significant association among differences in nerve thickness, T2 signal intensity ratio, and contrast-to-noise ratios and nerve injury (area under the curve, 0.83–0.84 for the inferior alveolar nerve and 0.77–0.78 for the lingual nerve). Interobserver agreement was good for the inferior alveolar nerve (intraclass correlation coefficient, 0.70–0.79) and good to excellent for the lingual nerve (intraclass correlation coefficient, 0.75–0.85). MR neurography correlations with respect to clinical neurosensory testing and surgical classifications were moderate to good. Pearson correlation coefficients of 0.68 and 0.81 and κ of 0.60 and 0.77 were observed for differences in nerve thickness.

CONCLUSIONS: MR neurography can be reliably used for the diagnosis of injuries to the peripheral trigeminal nerve related to molar tooth extractions, with good to excellent correlation of imaging with clinical findings and surgical results.

ABBREVIATIONS: IAN = inferior alveolar nerve; LN = lingual nerve; MRN = MR neurography; NST = neurosensory testing; PSIF = reversed fast imaging with steady state precession; PTN = peripheral trigeminal neuropathy; T2SIR = T2 signal intensity ratio; SI = signal intensity

Sensory innervation to the face is provided by 3 branches of the trigeminal nerve: the ophthalmic, maxillary, and mandibular nerves. During oral and maxillofacial treatments, the most commonly injured terminal branches are the inferior alveolar (IAN) and lingual (LN) nerves.[1,2] Among oral treatments, molar tooth extractions are very common, and up to 10 million third molars are extracted each year at a cost of more than US $3 billion.[3] Tooth extractions alone account for 60% of all nerve injuries in the jaw, with an incidence of permanent paresthesia in the lip, tongue, and cheek ranging from 11,500–35,000 per year.[4-6]

Currently, clinical neurosensory testing (NST) is used as the criterion standard to confirm the diagnosis of peripheral trigeminal neuropathy (PTN).[7] NST involves 3-level testing, with level A measuring spatiotemporal sensory perception, level B measuring contact detection with monofilament, and level C measuring pain threshold and tolerance. The 5 scores of sensory impairment denote normal, mild, moderate, severe, and complete loss (Table 1). Surgeons use clinical history and NST to diagnose neuropathy and stratify nerve injury with respect to the Sunderland classification. Initially described in 1951, this classification is based on the injury of individual structures of the organized nerve tissue

Received May 2, 2017; accepted after revision September 4.

From the Departments of Radiology (R.D., Y.X., A.C.) and Oral and Maxillofacial Surgery (J.Z.), University of Texas Southwestern Medical Center, Dallas, Texas; and Department of Radiodiagnosis (R.D.), Faculty of Medicine, Zagazig University, Zagazig, Egypt.

Please address correspondence to Avneesh Chhabra, MD, Musculoskeletal Radiology, UT Southwestern Medical Center, 5323 Harry Hines Blvd, Dallas, TX 75390-9178; e-mail: avneesh.chhabra@utsouthwestern.edu

Indicates article with supplemental on-line tables.

Indicates article with supplemental on-line photo.

http://dx.doi.org/10.3174/ajnr.A5438

Table 1: Clinical NST for trigeminal neuropathy[a]

	Level A: Spatiotemporal Sensory Perception Direction Sensitivity <90% Static 2-Point Discrimination <18 mm	Level B: Contact Detection with Monofilament <2.83	Level C: Pain Threshold and Tolerance Heat Temperature Threshold <47 Heat Temperature Tolerance <50 Pressure Pain Threshold <1.5 lb. Pressure Pain Tolerance <2.0 lb.
Normal	Present	Present	Present
Mild	Failed	Present	Present
Moderate	Failed	Failed	Present
Severe	Failed	Failed	Elevated
Complete	Failed	Failed	Absent

[a] Present: values recorded at test and control sites exhibit comparable sensitivity within published normative range. Failed: values recorded at test site sensitivity are less than that of control sites or published normative range. Elevated: values recorded at test site sensitivity are greater than that of control sites or published normative range but below maximum of test device (ie, 6 lbs.). Absent: values recorded at test site sensitivity are greater that maximum of test device (ie, 6 lbs.).

Table 2: Criteria for stratifying of nerve injuries on MRN and surgery based on Sunderland classification

Class	MRN	Surgical
I	Qualitative: Homogeneous increased T2 signal of nerve with no change in caliber Quantitative: No changes	Intact with no internal or external fibrosis, normal mobility and neuroarchitecture (visualize fascicles and Fanconi bands)
II	Qualitative: Homogeneous increased T2 signal of nerve and mild nerve thickening Perineural fibrosis Quantitative: <50% larger than contralateral /normal nerve	Intact with no internal fibrosis with external fibrosis, restricted mobility but neuroarchitecture intact (visualized fascicles and Fanconi bands once external scar removed)
III	Qualitative: Homogeneous increased T2 signal of nerve and moderate to marked nerve thickening Perineural fibrosis Quantitative: >50% larger than contralateral/normal nerve	Intact with both internal and external fibrosis, restricted mobility and disturbance of neuroarchitecture (abnormal fascicle patterns and/or Fanconi bands not visible)
IV	Qualitative: Heterogeneous increased T2 signal of nerve and focal enlargement in otherwise continuous nerve (neuroma in continuity) Perineural and intraneural fibrosis Quantitative: Focal swelling with heterogeneous T2 signal or fascicular disruption	Partial transected nerve, but some amount of distal nerve present with or without lateral neuroma
V	Qualitative: Discontinuous nerve with end-bulb neuroma Quantitative: Complete disruption with gap and end-bulb neuroma	Completely transected nerve with or without amputation (end-bulb) neuroma

(ie, myelin loss; axonal loss; and endoneurial, perineurial, and epineural injury, in that order).[8,9] The aims of surgical treatment are to repair the damaged nerve, maximize the number of axons that regenerate through the site of injury, and increase the proportion of axons that grow back to appropriate targets. Thus, timely decision making regarding surgical treatment and accurate presurgical planning is important for proper case management. Despite exhibiting high positive and negative predictive values for LN injuries, NST shows lower values for IAN injuries, with false-positive and false-negative rates of up to 23% and 40%, respectively.[7] NST results are not reliable in the first 3 months after the injury because of postoperative changes and the inability of patients and/or physicians to reproduce the sensory response. In addition, NST cannot determine the exact site of injury or delineate the anatomy for presurgical planning.[7,10] MR neurography (MRN), an imaging dedicated to the peripheral nerves, provides a noninvasive map of neuromuscular anatomy and resolves the intraneural architecture in multiple orthogonal planes.[11-14]

Currently, there are 2 different MR imaging methods available to study peripheral nerves: anatomic MRN and diffusion-based functional MRN, particularly DTI. MRN facilitates the detection of neuropathy by showing alterations of nerve caliber and abnormal intraneural T2 signal intensity ratio (T2SIR).[15] DTI aids in the functional evaluation of the intraneural pathophysiology, and altered diffusion characteristics correlate with axonal degeneration and demyelination.[16-19] The aim of our study was to evaluate the role and reliability of MRN for the diagnosis of injuries to the PTN in patients with prior molar tooth extraction to determine its accuracy with respect to the clinical and surgical staging. Our hypothesis was that MRN can quantitatively and reliably differentiate normal from injured nerves with high accuracy and that nerve injury classification on MRN correlates with clinical NST grading and surgical findings.

MATERIALS AND METHODS

This study was conducted at the University of Texas Southwestern Medical Center, Dallas, Texas, after institutional review board approval following Health Insurance Portability and Accountability Act guidelines. Informed consent was waived because of the retrospective nature of this study.

Patient Population

A retrospective review of charts of a consecutive series of 55 patients who were imaged with MRN for suspected PTN neuropathies over a 27-month period (January 2015 to March 2017) revealed 24 cases referred for clinically suspected PTN injury after

molar tooth extraction. All 24 patients exhibited NST evidence of injury of the IAN or LN and were referred from the institutional oral and maxillofacial surgery clinic. Others (31 patients) were referred for PTN injuries after dental or chin implants, teeth filling, or the extraction of maxillary or mandibular tumors and were not included in the final study sample. The control group consisted of 18 consecutive patients referred for suspected occipital neuralgia with no symptoms of trigeminal neuralgia, recent tooth extraction, facial pain, or previous oral/maxillofacial surgery. Patient demographics (age, sex) and laterality of the injury were recorded. The Sunderland class of nerve injury (Table 2) was prospectively documented by an experienced oral and maxillofacial surgeon as standard of care by using clinical and NST findings.[8,18] The patients who were not specifically stratified into 1 Sunderland class were recorded as indeterminate, and patients who could not be clinically tested for various reasons (eg, severe pain or inability to open the mouth in acute injury) were considered as unclassified for the purpose of the research study. Final Sunderland classification based on surgical findings was used for correlation with MRN and NST findings.

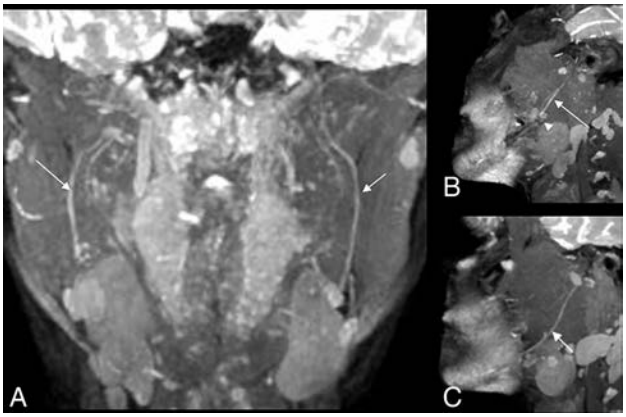

FIG 1. *A*, MIP coronal 3D PSIF image showing class II injury to the right IAN with mild increase in caliber (less than 50% of the left) and signal intensity of the right IAN (*long arrow*) in comparison with a normal left inferior alveolar nerve (*short arrow*). *B*, Sagittal reconstruction MIP 3D PSIF image showing increase in caliber and signal intensity of the right IAN (*long arrow*) proximal to injury site (*arrowhead*). *C*, Normal uniform caliber and signal intensity of the left IAN (*short arrow*).

Image Acquisition

From a total of 42 patients, 19 were imaged on 1.5T scanners (Avanto; Siemens, Erlangen, Germany), and 23 were imaged on 3T scanners (Achieva or Ingenia; Philips Healthcare, Best, the Netherlands). All patients were scanned supine in a multichannel head coil. Multiple pulse sequences were acquired by using the institutional MRN protocol (On-line Table 1), but only the 3D reversed fast imaging with steady state precession (PSIF) images were reviewed for study purposes.[11]

Image Interpretation and Analysis

All scans were prospectively reported by an experienced, fellowship-trained radiologist as part of routine patient care. Neuropathy was determined based on various qualitative (increased nerve T2 signal and perineural fibrosis) and quantitative (caliber alterations) criteria. Findings were confirmed on multiple sequences (T1, T2 fat-suppressed, PSIF, and DTI). A Sunderland classification was given to each nerve injury by using the qualitative criteria as described in Table 2 (Figs 1 and 2). When a single class could not be determined based on MRN (eg, report stated "Sunderland class III/IV or class IV/V injury"), the case was classified as indeterminate (On-line Table 2). All information was extracted from the formal reports and recorded for comparison with clinical NST and surgical findings.

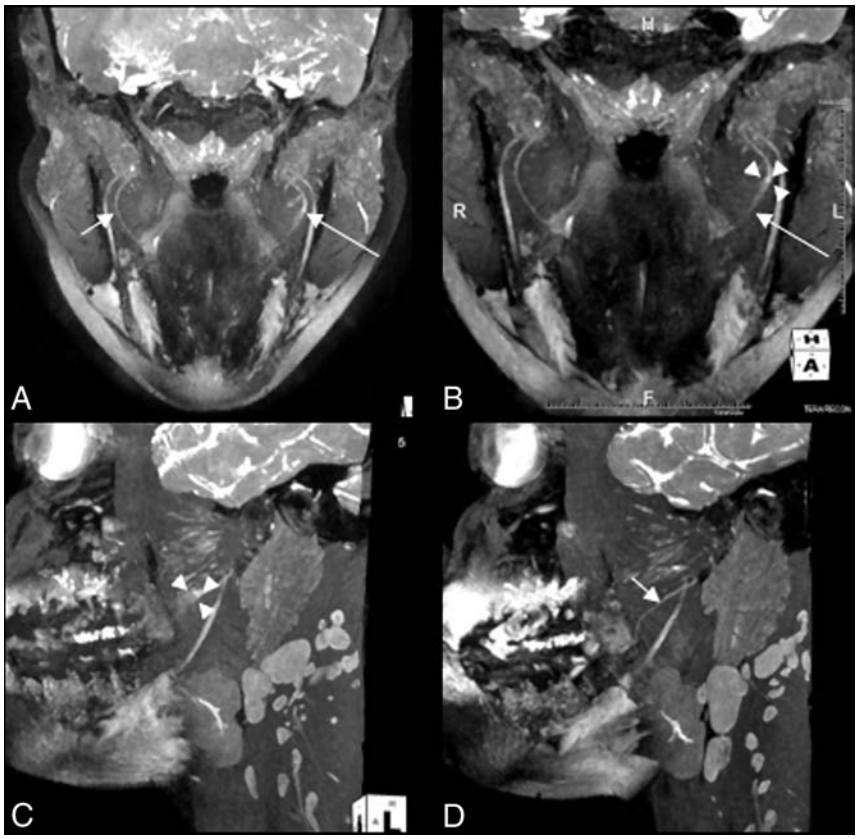

FIG 2. *A* and *B*, MIP 3D coronal PSIF images show a hyperintense left LN (*long arrow*) with a 3-mm neuroma in continuity (demarcated by 3 *arrowheads*) compatible with class IV injury. *C* and *D*, Sagittal reconstructions show the abnormal left LN neuroma (demarcated by 3 *arrowheads*) compared with a normal right LN (*short arrow*).

Nerve Measurements on MRN

Coronal 3D PSIF images were chosen to perform measurements on because they produce nerve-selective imaging.[20] Two readers with 20 and 5 years' experience in radiology, respectively, independently performed the measurements after a training set of 6 scans that included both case and control patients. The

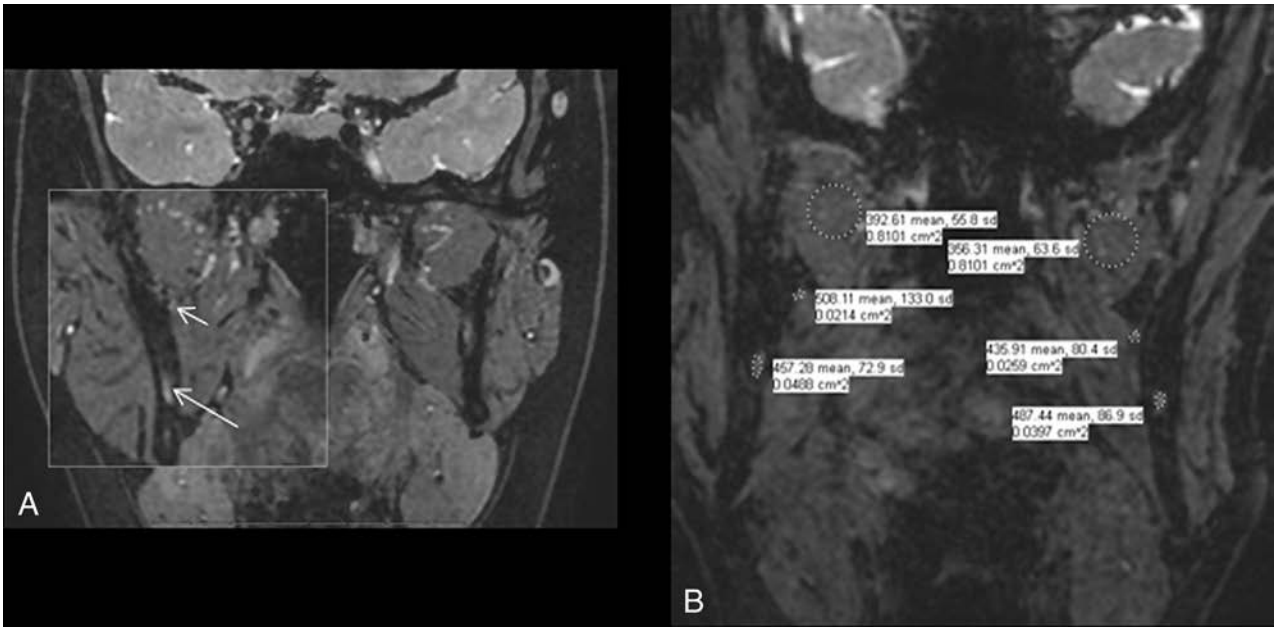

FIG 3. Coronal 3D PSIF images showing *A*, localization of the site of the LN and IAN (*short* and *long arrows*, respectively) and *B*, signal intensity measurements on both sides.

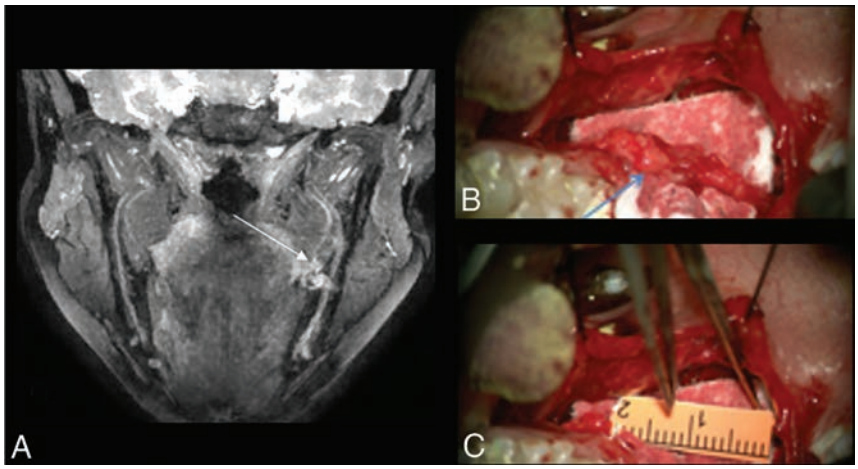

FIG 4. *A*, MIP 3D PSIF coronal image shows class IV/V injury of the left LN with excessive granulation and possible discontinuity of its distal end (*long arrow*). *B*, On surgery, it was also called class IV/V injury (*arrow*) with excessive scarring and granulation tissue and was resected. The final gap was 16 mm (*C*) and an allograft was placed for nerve reconstruction.

readers were blinded to the clinical history or prior MRN report. For the control group, a predefined bony landmark was used to identify both nerves for measurement. The midmandibular canal was chosen because the midlingual nerve can be easily identified medial to the medial cortex of the mandibular ramus, and the IAN lies within the bony mandibular canal (Fig 3*A*). Nerve thickness was recorded by measuring the maximum transverse dimension of the IAN in the midmandibular canal and the LN in its midcourse. T2 signal intensity was recorded in the same area by drawing a freehand ROI on each nerve (Fig 3*B*). In patients who underwent tooth extraction (the study group), the measurements were performed at the site of the most visible abnormality of the affected nerve. This was followed by calculation of T2SIR (SI nerve $\div \sqrt{}$SI nerve)[21] and CNR (SI nerve − SI pterygoid muscle $\div \sqrt{}$SI nerve) for each nerve in both groups. All data points, measurements, and calculations were recorded on a spreadsheet for data analysis.

Clinical and Surgical Classification

NST was performed by the same experienced oral and maxillofacial surgeon. Thirteen of 24 patients from this group underwent surgery of 13 nerves, and injuries were graded intraoperatively by using the Sunderland classification criteria in Table 2 (Fig 4). Unclassified nerve injuries or indeterminate findings on NST and intraoperatively were recorded (On-line Table 2).

Statistical Analysis

Descriptive statistics were used for the demographic data and Sunderland classifications on NST and MRN. Differences in sex and/or scanner between case and control patients were assessed by using the Fisher exact test, and the differences in median age and image measurements in case versus control patients were tested by using the Wilcoxon rank sum test. Area under the curve was calculated by using receiver operating characteristic for MRN accuracy in the detection of neuropathy. A κ analysis was performed to test correlations of Sunderland classification on independently performed NST, MRN, and surgical classifications in the group of cases (Fig 5). The Pearson correlation coefficient was used to investigate the association of differences in thickness between normal and injured nerves. Interobserver performance was assessed by using intraclass correlation coefficients. Agreement was classified as excellent ($>$ 0.80), good (0.61–0.80), moderate (0.41–0.60), fair (0.20–0.40), and poor ($<$ 0.20). Type I error was set at .05. R 3.3.2

(http://www.r-project.org/) and SAS 9.4 (SAS Institute, Cary, North Carolina) were used for statistical analysis.

RESULTS

Patient Population

Forty-two subjects were included in the final sample. Mean ± SD age of the case group with 24 patients was 35.8 ± 10.2 years, with a male-to-female ratio of 1:1.4. Mean ± SD age of the control group was 43.2 ± 11.5 years, with a male-to-female ratio of 1:5. Eight case group subjects and 11 controls were scanned on 1.5T scanners, and 16 case group subjects and 7 controls were scanned on 3T scanners. No significant difference was found in the distribution of sex or scanner between case and control groups ($P = 1$ for both sex and scanner for IAN; $P = .08$ for sex in LN and .18 for scanner in LN). No significant difference was found in the median age between case and control groups ($P = .20$ for IAN and $P = .06$ for LN).

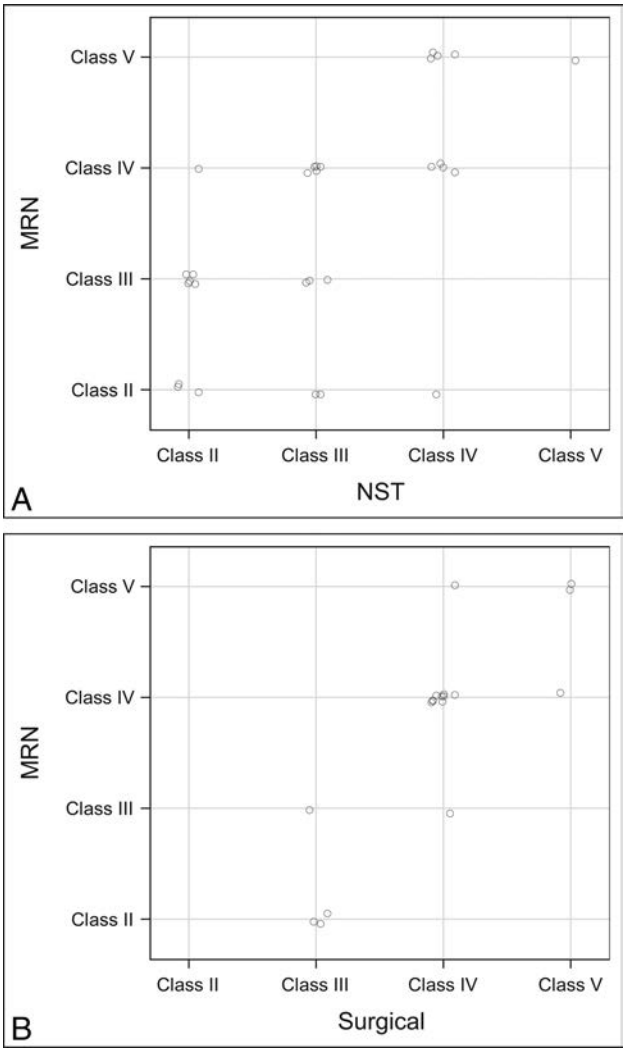

FIG 5. κ correlations for *A*, MRN versus NST and *B*, MRN versus surgical classifications.

Classification of Nerve Injuries on NST, MRN, and Surgery

In the case group, 25 nerve injuries were found in 24 patients (1 patient had both IAN and LN injuries). Eighteen were LN injuries (7 right and 11 left) and 7 were IAN injuries (3 right and 4 left). Sunderland classifications by NST included 2 class II, 2 class III, 4 class IV, and 1 class V injury (On-line Figure). Fourteen nerve injuries were indeterminate, and 2 were not classified. Sunderland classifications by MRN included 6 class II, 2 class III, 9 class IV, and 5 class V injuries, respectively. Three nerve injuries were indeterminate (On-line Table 2). Sunderland classifications on MRN were congruent with NST in 6 cases, upstaged in 9 cases and downstaged in 8 cases. Two cases that could not be classified on NST received a class on MRN. Thirteen of 24 patients underwent surgery for 13 nerve injuries. Sunderland classification on surgery included 2 class III, 7 class IV, and 3 class V injury. One was indeterminate when the surgeon could not decide between class IV and V injury, similar to MRN. Sunderland classifications on MRN were congruent with surgery in 10 cases and downstaged in 3 cases. No cases were upstaged. Assuming 1 nerve abnormality per patient (when classification was undetermined, the lower class was accepted), this study showed κ of 0.57 and 0.4 between MRN and NST classifications (Fig 5*A*) and MRN and surgical classifications (Fig 5*B*) with class IV and V combined, respectively.

Nerve Measurements on MRN

Bilateral IAN and LN measurements were performed. From a total of 168 nerves, nerve thickness and SI were measured in a total of 122 nerves. Ninety-seven nerves were normal (72 nerves bilaterally in the control group and 25 contralateral normal nerves in the case group) and 25 were abnormal. Forty-six nerves were excluded from the case group because a regional postsurgical inflammatory response may affect the other nerve(s) and confound the results. Mean ± SD of difference in thickness of IANs and LNs was 0.60 ± 0.33 mm and 0.87 ± 0.34 mm for the case group versus 0.22 ± 0.20 mm and 0.11 ± 0.12 mm for control patients, respectively (Table 3). The case group had significantly larger differences ($P = .01$ and .0001 for IAN and LN, respectively) of nerve thickness versus controls. Mean ± SD difference in T2SIR in IAN and LN was 3.15 ± 1.91 and 4.58 ± 3.40 × 10^{-3} mm^2/s, respectively, in the case group and 1.34 ± 1.09 and 1.92 ± 1.51 × 10^{-3} mm^2/s, respectively, in control patients ($P = .012$ and .005 for IAN and LN, respectively). On comparison of CNR for case and control patients, the mean ± SD difference in CNR in IAN and LN was 6.53 ± 4 and 6.93 ± 4.89 × 10^{-3} mm^2/s, respectively, in

Table 3: Differences in thickness, T2SIR, and CNR among the case and control groups

		Thickness			T2SIR			CNR		
Nerve	Group	Mean Difference	SD	*P* Value	Mean Difference	SD	*P* Value	Mean Difference	SD	*P* Value
IAN	Cases	0.60	0.33	.01	3.15	1.91	.012	6.53	4.00	.01
	Controls	0.22	0.20		1.34	1.09		2.20	1.89	
LN	Cases	0.87	0.34	.0001	4.58	3.40	.005	6.93	4.89	.01
	Controls	0.11	0.12		1.92	1.51		3.37	3.81	

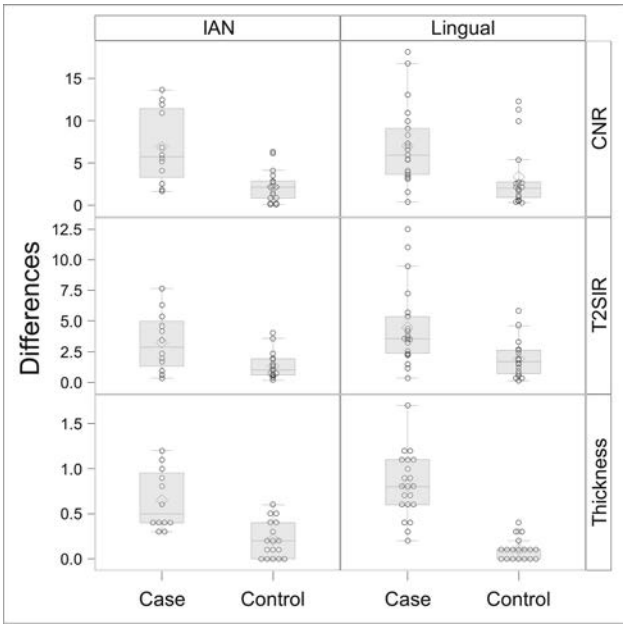

FIG 6. Differences in thickness, T2SIR, and CNR among the case and control groups.

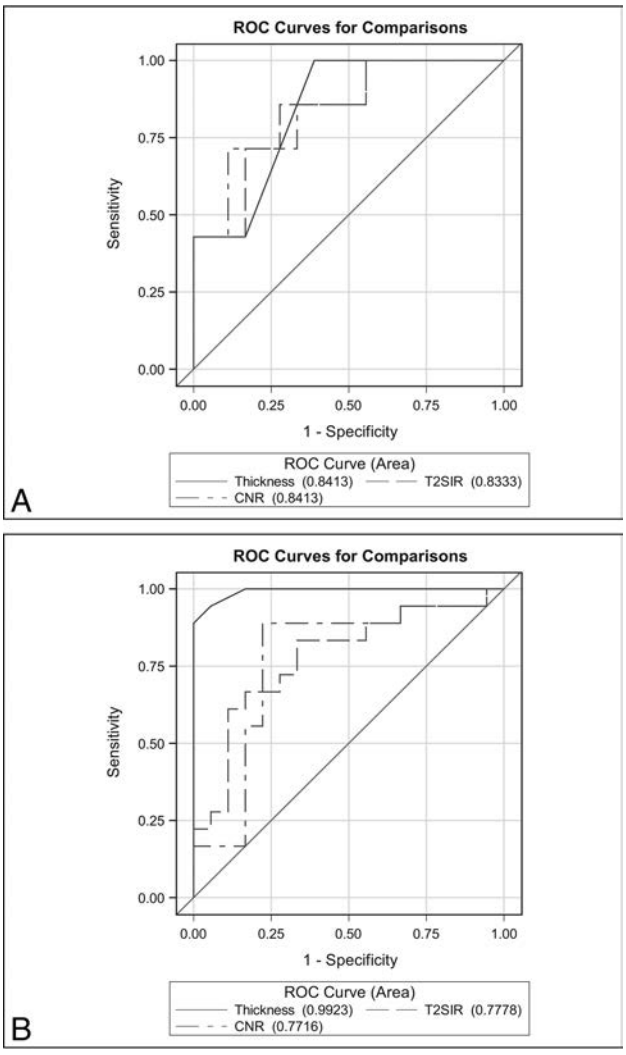

FIG 7. ROC curves for *A*, IAN and *B*, LN.

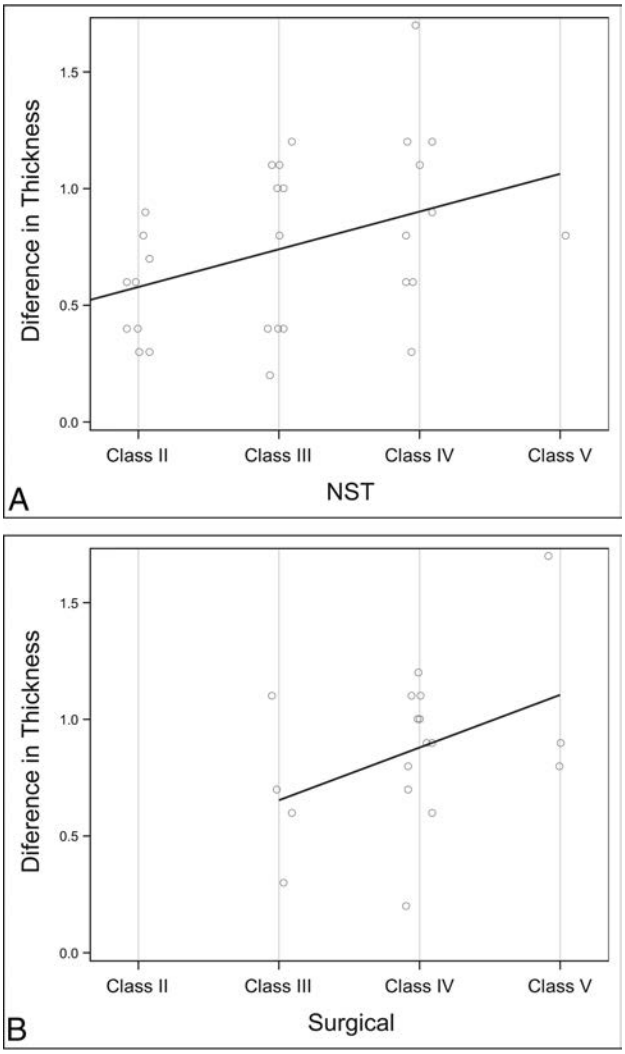

FIG 8. Correlations between differences in nerve thickness on MRN versus NST (*A*) and surgery (*B*).

the case group and 2.2 ± 1.89 and 3.37 ± 3.81 × 10^{-3}, mm^2/s, respectively, in controls ($P = .01$ for both IAN and LN) (Fig 6). The area under the curve revealed accuracy of 0.83–0.84 for IAN by using CNR, T2SIR, and thickness. For LN, the area under the curve revealed accuracy of 0.77–0.78 for CNR and T2SIR, whereas it was 0.99 for nerve thickness (Fig 7). Interobserver agreement was good for IAN (intraclass correlation coefficient, 0.70–0.79) and good to excellent for LN (intraclass correlation coefficient, 0.75–0.83) (On-line Table 3). The Pearson correlation coefficients were 0.68 and 0.81 for nerve injury classifications between MRN and NST (Fig 8*A*) and MRN and surgery (Fig 8*B*), respectively ($P = .0006$ and .0004, respectively).

DISCUSSION

The face is the fourth most common chronic pain site, contributing to substantial annual health care costs.[22] Molar tooth extractions result in facial and jaw pain caused by iatrogenic PTN injury and account for 60% of all nerve injuries of the jaw.[4] Persistent nerve damage results in disabling neuropathic pain and substantial oral dysfunction.[23] Early diagnosis and timely management are essential for both improved patient outcomes and prognosis.

The postoperative outcomes have been shown to be negatively affected by older age, delayed treatment (>3–6 months after injury), and a larger nerve gap.[10,24] The current diagnostic strategy of using NST as the criterion standard is limited. The subjective NST result delays the treatment of higher-class injury (patients who need surgical repair) and does not delineate the anatomy and exact location of injury for preoperative planning.[9]

The 3D PSIF sequence on MRN depicts the small PTN branches in their entirety because of vascular signal suppression and superior resolution (0.9 mm isotropic) (Figs 1–3).[11,20] In addition, findings of nerve injury, such as increased intraneural signal and alteration of the nerve caliber, are more conspicuous.[25] Similar to earlier studies on peripheral extremity nerves,[26] this study establishes that increased T2SIR can accurately diagnose nerve injury in the setting of neuropathy-related molar tooth extraction. Previous studies have shown correlation between changes in T2SIR and electrophysiology of the injured nerve.[16,17,19] Similar to results reported by Baumer et al,[26] the study confirms that alterations of nerve caliber can be accurately used to diagnose neuropathy. Thus, increased T2SIR and caliber of the injured nerve can be used as surrogate quantitative imaging markers for neuropathy.

Nerve injury stratification on imaging by using Sunderland classification has not been scientifically studied before. It is easy to identify a focal neuroma in continuity and complete transection with the nerve gap qualitatively. This study, in addition, has shown that using nerve thickness differences to classify nerve injuries in a quantitative manner is prudent and accurate. The measurements showed good to excellent interreader reliablity and there were good to excellent correlations with NST and surgery classifications when using nerve thickness differences. Thus, MRN can be used in practice to stratify nerve injuries.

When comparing Sunderland classifications on different modalities, NST was indeterminate in 56% (14/25), MRN was indeterminate in 12% (3/25), and surgery was indeterminate in 8% (1/13) of nerve injuries. MRN also detected 2 nerve abnormalities (IAN and LN) in 1 case where NST recorded only 1. Thus, MRN can provide incremental value over the current reference standard, NST. This result is not unexpected considering that MRN provides a more objective tool for 3D depiction of the nerve injury and can create a presurgical map for the surgeon.

The study has some limitations, including small sample size, retrospective nature, and differences among sex and age distribution between the case and control groups. These were unavoidable as we attempted to study a specific homogeneous group of patients compared with a previously published study in this domain.[27] Our controls were not healthy patients, but we made sure that none of them had symptoms, clinical findings, or surgery in the area of PTN. We did not evaluate other sequences, such as T1-weighted imaging for perineural scarring as it is difficult to evaluate the small nerve on T1-weighted images. We did not assess diffusion metric differences because of reproducibility issues with DTI. Finally, the same surgeon who documented NST results performed the final surgery, and not all patients underwent surgery because of various reasons.

In the future, the study can be performed in a larger sample and in a prospective fashion to address the above described limitations. In addition, the role of quantitative MRN imaging markers of nerve injury can be evaluated in determining patient outcomes and prognosis.

CONCLUSIONS

MRN is reliable and accurate for the diagnosis of PTN injuries related to molar tooth extractions, with good to excellent correlation of imaging findings with clinical findings and surgical results.

Disclosures: John Zuniga—*UNRELATED: Consultancy*: AxoGen, Comments: consultant for products application of nerve allografts. Avneesh Chhabra—*UNRELATED: Consultancy*: Icon Medical; *Royalties*: Jaypee Wolters.

REFERENCES

1. Jerjes W, Upile T, Shah P, et al. **Risk factors associated with injury to the inferior alveolar and lingual nerves following third molar surgery-revisited.** *Oral Surg Oral Med Oral Pathol Oral Radiol Endod* 2010;109:335–45 CrossRef Medline
2. Pogrel MA, Kaban LB. **Injuries to the inferior alveolar and lingual nerves.** *J Calif Dent Assoc* 1993;21:50–54 Medline
3. American Dental Association. **1999 survey of dental services rendered.** *ADA Catalog No SDSR-1999*
4. Friedman JW. **The prophylactic extraction of third molars: a public health hazard.** *Am J Public Health* 2007;97:1554–59 CrossRef Medline
5. Osborn TP, Frederickson G Jr., Small IA, et al. **A prospective study of complications related to mandibular third molar surgery.** *J Oral Maxillofac Surg* 1985;43:767–69 CrossRef Medline
6. Valmaseda-Castellón E, Berini-Aytés L, Gay-Escoda C. **Inferior alveolar nerve damage after lower third molar surgical extraction: a prospective study of 1117 surgical extractions.** *Oral Surg Oral Med Oral Pathol Oral Radiol Endod* 2001;92:377–83 CrossRef Medline
7. Zuniga JR, Meyer RA, Gregg JM, et al. **The accuracy of clinical neurosensory testing for nerve injury diagnosis.** *J Oral Maxillofac Surg* 1998;56:2–8 CrossRef Medline
8. Chhabra A, Ahlawat S, Belzberg A, et al. **Peripheral nerve injury grading simplified on MR neurography: as referenced to Seddon and Sunderland classifications.** *Indian J Radiol Imaging* 2014;24:217–24 CrossRef Medline
9. Sunderland S. **A classification of peripheral nerve injuries producing loss of function.** *Brain* 1951;74:491–516 CrossRef Medline
10. Robinson PP. **Observations on the recovery of sensation following inferior alveolar nerve injuries.** *Br J Oral Maxillofac Surg* 1988;26:177–89 CrossRef Medline
11. Manoliu A, Ho M, Nanz D, et al. **MR neurographic orthopantomogram: ultrashort echo-time imaging of mandibular bone and teeth complemented with high-resolution morphological and functional MR neurography.** *J Magn Reson Imaging* 2016;44:393–400 CrossRef Medline
12. Cho Sims G, Boothe E, Joodi R, et al. **3D MR neurography of the lumbosacral plexus: obtaining optimal images for selective longitudinal nerve depiction.** *AJNR Am J Neuroradiol* 2016 ;37:2158–62 CrossRef Medline
13. Bäumer P, Weiler M, Bendszus M, et al. **Somatotopic fascicular organization of the human sciatic nerve demonstrated by MR neurography.** *Neurology* 2015;84:1782–87 CrossRef Medline
14. Chhabra A, Thawait GK, Soldatos T, et al. **High-resolution 3T MR neurography of the brachial plexus and its branches, with emphasis on 3D imaging.** *AJNR Am J Neuroradiol* 2013;34:486–97 CrossRef Medline
15. Thawait SK, Chaudhry V, Thawait GK, et al. **High-resolution MR neurography of diffuse peripheral nerve lesions.** *AJNR Am J Neuroradiol* 2011;32:1365–72 CrossRef Medline
16. Bendszus M, Wessig C, Solymosi L, et al. **MRI of peripheral nerve**

degeneration and regeneration: correlation with electrophysiology and histology. *Exp Neurol* 2004;188:171–77 CrossRef Medline
17. Li X, Shen J, Chen J, et al. **Magnetic resonance imaging evaluation of acute crush injury of rabbit sciatic nerve: correlation with histology.** *Can Assoc Radiol J* 2008;59:123–30 Medline
18. Liu Y, Li J, Butzkueven H, et al. **Microstructural abnormalities in the trigeminal nerves of patients with trigeminal neuralgia revealed by multiple diffusion metrics.** *Eur J Radiol* 2013;82:783–86 CrossRef Medline
19. Shen J, Zhou CP, Zhong XM, et al. **MR neurography: T1 and T2 measurements in acute peripheral nerve traction injury in rabbits.** *Radiology* 2010;254:729–38 CrossRef Medline
20. Zhang Z, Meng Q, Chen Y, et al. **3-T imaging of the cranial nerves using three-dimensional reversed FISP with diffusion-weighted MR sequence.** *J Magn Reson Imaging* 2008;27:454–58 CrossRef Medline
21. Wikipedia contributors. **Signal-to-noise ratio.** Available at: https://en.wikipedia.org/wiki/Signal-to-noise_ratio. Accessed July 26, 2017
22. National Centers for Health Statistics. Chartbook on Trends in the Health of Americans 2006, Special Feature: Pain. Available at: http://www.cdc.gov/nchs/data/hus/hus06.pdf. Accessed December 1, 2016
23. Agbaje JO, Van de Casteele E, Hiel M, et al. **Neuropathy of trigeminal nerve branches after oral and maxillofacial treatment.** *J Maxillofac Oral Surg* 2016;15:321–27 CrossRef Medline
24. Bagheri SC, Meyer RA, Cho SH, et al. **Microsurgical repair of the inferior alveolar nerve: success rate and factors that adversely affect outcome.** *J Oral Maxillofac Surg* 2012;70:1978–90 CrossRef Medline
25. Qin BG, Yang JT, Yang Y, et al. **Diagnostic value and surgical implications of the 3D DW-SSFP MRI on the management of patients with brachial plexus injuries.** *Sci Rep* 2016;6:35999 CrossRef Medline
26. Bäumer PD, Dombert T, Staub F, et al. **Ulnar neuropathy at the elbow: MR neurography–nerve T2 signal increase and caliber.** *Radiology* 2011;260:199–206 CrossRef Medline
27. Cox B, Zuniga JR, Panchal N, et al. **Magnetic resonance neurography in the management of peripheral trigeminal neuropathy: experience in a tertiary care centre.** *Eur Radiol* 2016;26:3392–400 CrossRef Medline

MR Imaging of the Superior Cervical Ganglion and Inferior Ganglion of the Vagus Nerve: Structures That Can Mimic Pathologic Retropharyngeal Lymph Nodes

H. Yokota, H. Mukai, S. Hattori, K. Yamada, Y. Anzai, and T. Uno

ABSTRACT

BACKGROUND AND PURPOSE: The superior cervical ganglion and inferior ganglion of the vagus nerve can mimic pathologic retropharyngeal lymph nodes. We studied the cross-sectional anatomy of the superior cervical ganglion and inferior ganglion of the vagus nerve to evaluate how they can be differentiated from the retropharyngeal lymph nodes.

MATERIALS AND METHODS: This retrospective study consists of 2 parts. Cohort 1 concerned the signal intensity of routine neck MR imaging with 2D sequences, apparent diffusion coefficient, and contrast enhancement of the superior cervical ganglion compared with lymph nodes with or without metastasis in 30 patients. Cohort 2 used 3D neurography to assess the morphology and spatial relationships of the superior cervical ganglion, inferior ganglion of the vagus nerve, and the retropharyngeal lymph nodes in 50 other patients.

RESULTS: All superior cervical ganglions had homogeneously greater enhancement and lower signal on diffusion-weighted imaging than lymph nodes. Apparent diffusion coefficient values of the superior cervical ganglion ($1.80 \pm 0.28 \times 10^{-3}$mm^2/s) were significantly higher than normal and metastatic lymph nodes ($0.86 \pm 0.10 \times 10^{-3}$mm^2/s, $P < .001$, and $0.73 \pm 0.10 \times 10^{-3}$mm^2/s, $P < .001$). Ten and 13 of 60 superior cervical ganglions were hypointense on T2-weighted images and had hyperintense spots on both T1- and T2-weighted images, respectively. The latter was considered fat tissue. The largest was the superior cervical ganglion, followed in order by the retropharyngeal lymph node and the inferior ganglion of the vagus nerve ($P < .001$ to $P = .004$). The highest at vertebral level was the retropharyngeal lymph nodes, followed, in order, by the inferior ganglion of the vagus nerve and the superior cervical ganglion ($P < .001$ to $P = .001$). The retropharyngeal lymph node, superior cervical ganglion, and inferior ganglion of the vagus nerve formed a line from anteromedial to posterolateral.

CONCLUSIONS: The superior cervical ganglion and the inferior ganglion of the vagus nerve can be almost always differentiated from retropharyngeal lymph nodes on MR imaging by evaluating the signal, size, and position.

ABBREVIATIONS: CCAB = common carotid artery bifurcation; FS = fat-saturated; IGVN = inferior ganglion of the vagus nerve; RPLN = retropharyngeal lymph node; SCG = superior cervical ganglion

The autonomic nervous system is composed of 2 antagonistic sets of nerves: the sympathetic and parasympathetic nervous systems. The sympathetic efferent pathway starts at the posterolateral hypothalamic region and descends along the encephalic trunk to the intermediolateral horn cells of the thoracic spinal cord. The sympathetic nerves then form chain structures lying just lateral to the vertebral bodies. The structures of the sympathetic nervous system to date have not been characterized in detail with conventional neck imaging, to our knowledge.

The cervical sympathetic trunk lies on the prevertebral fascia medial to the carotid sheath and contains 3 interconnected ganglia: the stellate, middle cervical, and superior cervical ganglia.[1-7] The stellate ganglion is formed by the lower 2 cervical and first thoracic segmental ganglia. The middle cervical ganglion is the smallest one of the 3 ganglia. The superior cervical ganglia are elongated and cylindric and are the largest of the 3 ganglia (Fig 1). The size and location of the sympathetic ganglia have many variations. Although the stellate and middle cervical ganglia are occasionally divided into several parts,[1,3,4-6] the superior cervical ganglia are invariably detected bilaterally.[4-6] Imaging anatomy of the superior and stellate ganglia have only been reported in a few articles,[8-11] whereas the middle cervical ganglion has not been described.

Received April 27, 2017; accepted after revision August 28.

From Diagnostic Radiology and Radiation Oncology (H.Y., H.M., S.H., T.U.), Graduate School of Medicine, Chiba University, Chiba, Japan; Department of Radiology (K.Y.), Graduate School of Medical Science, Kyoto Prefectural University of Medicine, Kyoto, Japan; and Department of Radiology (Y.A.), University of Utah School of Medicine Health Sciences, Salt Lake City, Utah.

Please address correspondence to Hajime Yokota, MD, PhD, Diagnostic Radiology and Radiation Oncology, Graduate School of Medicine, Chiba University, 1-8-1, Inohana, Chuo-ku, Chiba City, Chiba, Japan, 260-8670; e-mail: yokotaha@gmail.com

Indicates article with supplemental on-line tables.

http://dx.doi.org/10.3174/ajnr.A5434

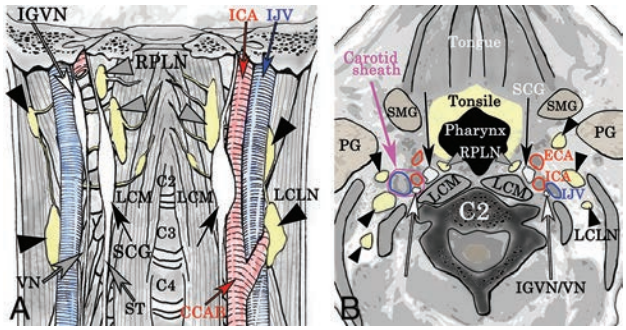

FIG 1. The coronal (*A*) and axial (*B*) views around the superior cervical ganglion according to anatomic reports show the superior cervical ganglion (*black arrow*), the inferior ganglion of the vagus nerve (*white arrow*), and the retropharyngeal lymph node (*gray arrowheads*). IJV indicates inferior jugular vein; ECA, external carotid artery; LCLN, lateral cervical lymph node (*black arrowheads*); LCM, longus capitis muscle; PG, parotid gland; SMG, submandibular gland; ST, sympathetic trunk; VN, vagus nerve. The *magenta circle* indicates the right carotid sheath.

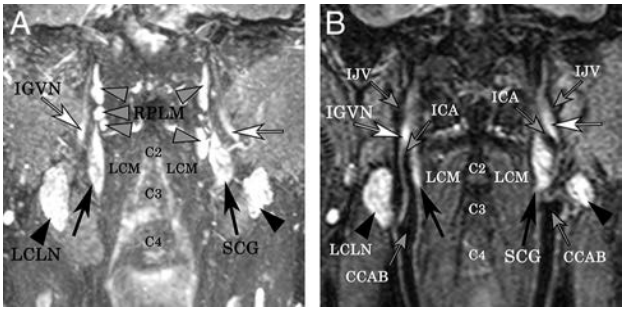

FIG 2. We assessed bilateral superior cervical ganglia (*black arrows*), the inferior ganglion of the vagus nerve (*white arrows*), and the retropharyngeal lymph nodes (*gray arrowheads*) using 3D-STIR (*A*, maximum-intensity-projection image; *B*, a section of original coronal images). The artery and vein clearly demonstrate flow voids. IJV indicates inferior jugular vein; LCLN, lateral cervical lymph node (*black arrowhead*); LCM, longus capitis muscle.

In a clinical setting such as cancer staging of the head and neck, it is problematic that the superior cervical ganglia (SCGs) can mimic retropharyngeal lymph nodes (RPLNs). In anatomic reports,[1-7] the SCGs are located at the side of the longus capitis or longus colli muscle around the C2 level. The lateral retropharyngeal lymph nodes are also distributed in the same region, extending from the level of the nasopharynx to the hyoid bone (the skull base to C3). The inferior ganglion of the vagus nerve (IGVN) is also along the internal carotid artery at approximately the same region, though there has been no imaging report of the IGVN, to our knowledge.

It is critical to focus on the SCG when performing interventional procedures of the neck, including open surgery and percutaneous local opioid anesthesia. Damage to this system can cause Horner syndrome. There is, however, no clear-cut method to differentiate SCGs from RPLNs and IGVNs during routine clinical imaging studies of the neck.

The purposes of this study were to describe the imaging anatomy of the SCG and IGVN and to propose methods to differentiate them from the RPLN. To accomplish this task, we performed studies on 2 separate cohorts. First, we investigated the signal intensity of these structures on routine 2D neck MR imaging. The second part of the study was conducted with MR neurography[12-15] to assess the morphology and spatial relationships of the SCG, IGVN, and RPLN.

MATERIALS AND METHODS

This retrospective study was approved by the institutional review board of Chiba University Hospital without additional informed consent. We searched cases from January 2016, retrospectively, according to the inclusion criteria listed below until reaching the required number of cases.

Power Analysis

Power analysis for paired and unpaired *t* tests among the SCG, IGVN, and RPLN indicated that 44 and 86 samples would be needed to detect type I error rates (α) of .05 to achieve a power of 90%, considering effect size as a medium effect of .5. A sample size of 60 and 100 SCGs and IGVNs of 30 and 50 cases were chosen for cohorts 1 and 2, respectively.

Structure Identification

Two board-certified neuroradiologists (with 12 and 10 years' experience) independently assessed the SCGs, IGVNs, and RPLNs and later evaluated them with consensus when necessary.

On the basis of previous anatomic reports (Fig 1),[1-7] we defined the SCGs as structures located symmetrically along the lateral edges of the longus capitis or longus colli muscle (Fig 2). An elongated cylindric or fusiform structure was searched cranially from the level of the common carotid artery bifurcation (CCAB).[16] A tapering shape of the superior and/or inferior poles, which presumably reflected the transitional zone between SCGs and the sympathetic trunk, was also used as a reference.

During the processes of identifying the SCG, there were objects with an MR imaging appearance like that of the SCG along the jugular vein, and we hypothesized that they represent the inferior ganglion of the vagus nerve. They had roughly the same size as the SCG as reported in previous anatomic studies (Fig 1).[1-7]

Nodular structures located from the suprahyoid retropharyngeal space to the skull base were identified to detect RPLNs. Lateral cervical lymph nodes were also detected.

Cohort 1: Signal Intensities of the SCG and Lymph Nodes Using Routine Neck MR Imaging

Subjects 1. From February 2015 to January 2016, eighty-four patients underwent neck MR imaging for the evaluation of both benign and malignant neoplasms of the head and neck before treatment. Fifty-four of 84 patients were excluded from this cohort because of an insufficient FOV ($n = 34$), inappropriate imaging protocol ($n = 9$), remarkable artifacts ($n = 6$), or tumor invasion or cervical vertebral body metastases with invasion in the retropharyngeal space ($n = 5$). Finally, this cohort included 30 patients (mean age, 63.0 ± 11.5 years; 9 women, 21 men). Twenty of 30 MRIs were performed for oral or pharyngeal cancers. Eleven of the 20 patients had unilateral lymph node metastasis from oral cancers or pharyngeal cancers on the internal jugular chain. Lymph node metastasis was determined by either pathologic examinations or interval changes after treatment.

Imaging Protocol 1. Neck MRIs were performed with a 1.5T scanner (Signa HDxt; GE Healthcare, Milwaukee, Wisconsin) using the following parameters: axial T1WI (TR/TE = 500/8.2 ms), axial and coronal T2WI (TR/TE = 3850–4075/85–88 ms), axial fat-saturated (FS)-T2WI (TR/TE = 3850/85 ms, squares estimation), axial and coronal gadolinium-enhanced FS-T1WI (TR/TE = 500–510/8.2–9.2 ms, chemical shift selective suppression, FOV = 220 × 220 mm, resolution = 0.430 × 0.430 × 5.000 mm, gap = 1.000 mm), sagittal 3D gadolinium-enhanced FS-T1WI (TR/TE = 8.1/3.6 ms, echo-spoiled gradient echo, squares estimation, FOV = 240 × 240 mm, resolution = 0.938 × 0.938 × 0.700 mm), and axial DWI (TR/TE = 7000/80.2 ms, b-value = 0 and 1000 s/cm^2, FOV = 280 × 280 mm, resolution = 1.094 × 1.094 × 5.000 mm, gap = 1.000 mm). All sequences used in-plane parallel imaging with an array spatial sensitivity encoding technique factor of 2.

Evaluation 1. Signal intensities of SCGs were evaluated and compared with those of lymph nodes with consensus. Each SCG was compared with an ipsilateral lymph node that was ≥5 mm and the largest in the scanned area. Apparent diffusion coefficient values of these structures were also measured. Metastatic and normal lymph nodes were evaluated separately.

Cohort 2: Morphology and Spatial Relationships of the SCG, IGVN, and RPLN on Neurography

Subjects 2. During the study period from September 2011 to January 2016, three hundred nineteen patients underwent MR neurography using 3D-STIR imaging to examine neuropathy or trauma of the brachial plexus before treatment. Two hundred sixty-nine of 319 cases were excluded from this cohort because of clinical symptoms related to the sympathetic and parasympathetic nervous systems (n = 10) or pathology that may lead to peripheral nerve hypertrophy or atrophy, such as chronic inflammatory demyelinating polyneuropathy and amyotrophic lateral sclerosis (n = 259). Finally, this cohort included 50 of 319 (mean age, 46.8 ± 19.9 years; 23 women; 27 men). These 50 patients had no disease that might account for abnormal retropharyngeal lymph nodes.

Imaging Protocol 2. 3D-STIR was acquired with a 1.5T scanner (Achieva; Philips Healthcare, Best, the Netherlands). The parameters of the 3D-STIR were the following: TR/TE/TI = 1600/200/180 ms, with coronal acquisitions along the cervical spine (FOV = 380 × 380 mm, resolution = 0.742 × 0.742 × 1.200 mm).

Evaluation 2. Two neuroradiologists tried detecting the SCG, IGVN, and RPLN independently. The length and width of each SCG, IGVN, and RPLN were measured by a single neuroradiologist. The ROI was drawn, and the volume of these structures was computed using Analysis of Functional Neuro Images (AFNI; http://afni.nimh.nih.gov/afni). The distance between the CCAB and the inferior pole of the SCG was also measured. The CCAB could be detected because arteries showed flow voids on 3D-STIR. The levels of the superior and posterior poles of the SCG, RPLN, and CCAB were defined by reference to the spinal column.

A probability map was created to reveal variations of SCGs. The location of SCGs was accessed relative to the location of 2 anatomic landmarks: the C2 transverse process and the CCAB.

Statistical Analysis

Power analysis was performed with G*Power 3.1.9.2 software (http://www.softpedia.com/get/Science-CAD/G-Power.shtml).[17] The other statistical analyses were performed with the SPSS 22.0 software package (IBM, Armonk New York). ADC values of the SCGs and lymph nodes were compared using a 2-tailed unpaired t test. Regarding the morphology and location, comparisons between the right and left and among SCGs, RPLNs, and IGVNs were also performed with paired and unpaired t tests for continuous variables and the Wilcoxon signed rank and Mann-Whitney U tests for categoric data.

RESULTS

Detectability and Interreader Agreement

In cohort 1, two radiologists identified bilateral SCGs and lymph nodes in all 30 cases. The lateral cervical lymph node was chosen for evaluation when RPLNs of >5 mm were not identified. Interobserver agreement was achieved in 57 of 60 SCGs (95.0%). Sixty bilateral SCGs were detected in all 30 cases with consensus. Forty-nine normal and 11 metastatic lymph nodes were also identified.

In cohort 2, two radiologists identified 100 bilateral SCGs and 100 IGVNs in all 50 cases and 104 RPLNs in 40 of 50 cases (0–5 RPLNs were detected in each case). At the independent reading, both readers concurred in 99 of 100 SCGs (99.0%), 96 of 100 IGVNs (96.0%), and 100 of 104 RPLNs (96.2%).

Signal Intensity and Contrast Enhancement

All SCGs had homogeneous, avid enhancement compared with normal and metastatic lymph nodes (Fig 3*A*). In contrast, it was difficult to differentiate SCGs from both normal and metastatic lymph nodes on the basis of the signal intensity of T1WI, T2WI, and FS-T2WI (Fig 3*B*, -*C*).

Some of the SCGs had 2 different types of spot or slit-shaped areas within them, which were not obvious in any of the lymph nodes. One was a hypointense area on T2WI and FS-T2WI and less evident on T1WI and gadolinium-enhanced FS-T1WI (Fig 4*A*, -*B*). The other was a hyperintense area on T1WI and T2WI that disappeared on FS-T2WI and gadolinium-enhanced FS-T1WI, indicative of fat tissue (Fig 4*C*, -*D*). The hypointense and hyperintense areas were seen in 10 (16.7%) and 13 (21.7%) of 60 SCGs, respectively. In 1 SCG, both of these structures were found. The IGVNs could not be detected on routine neck MR imaging with confidence.

ADC Values

The signal intensities of all SCGs on DWI were lower than those of both normal and metastatic lymph nodes (less restricted diffusion, Fig 3*D*). ADC values of the SCGs and normal and metastatic lymph nodes were 1.80 ± 0.28, 0.86 ± 0.10, and 0.73 ± 0.10 × 10^{-3}mm^2/s, respectively. ADC values of each SCG were significantly higher than observed in normal and metastatic lymph nodes (P < .001 and < .001). Metastatic lymph nodes showed higher signal intensity on DWI and lower ADC values (P = .001, more restricted) than those of normal lymph nodes.

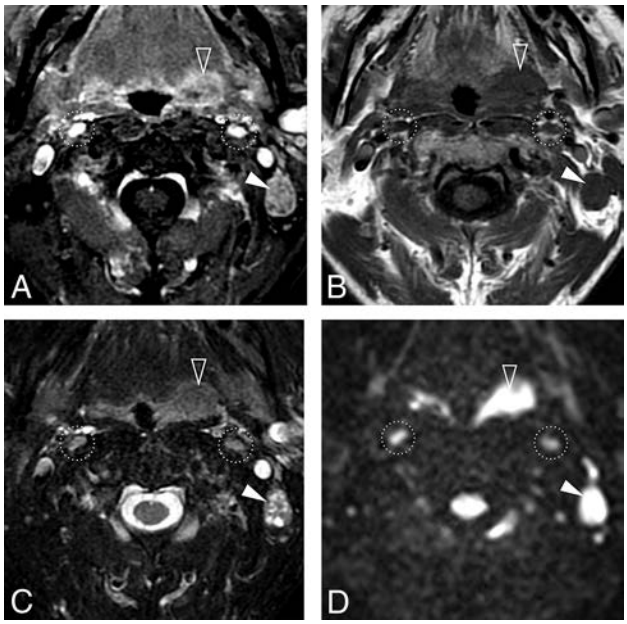

FIG 3. A 62-year-old man with oropharyngeal cancer with left lymph node metastasis. Bilateral superior cervical ganglia (*circles*), metastatic lymph node (*arrowhead*), and cancer (*open arrowhead*) are noted. Contrast-enhanced fat-saturated T1-wighted image (*A*) shows stronger enhancement of the SCG than the metastatic lymph node. The T1-weighted image (*B*) shows almost the same signals. Fat-saturated T2-weighted image (*C*) shows heterogeneous signal of the metastatic lymph node, whereas the SCG is homogeneous. Diffusion-weighted image shows that the signals of the SCGs are lower than those of the metastatic lymph node. ADC values of the right SCG, left SCG, and metastatic lymph nodes were 1.32, 1.54, and 0.90 $\times$ 10^{-3}mm^2/s, respectively.

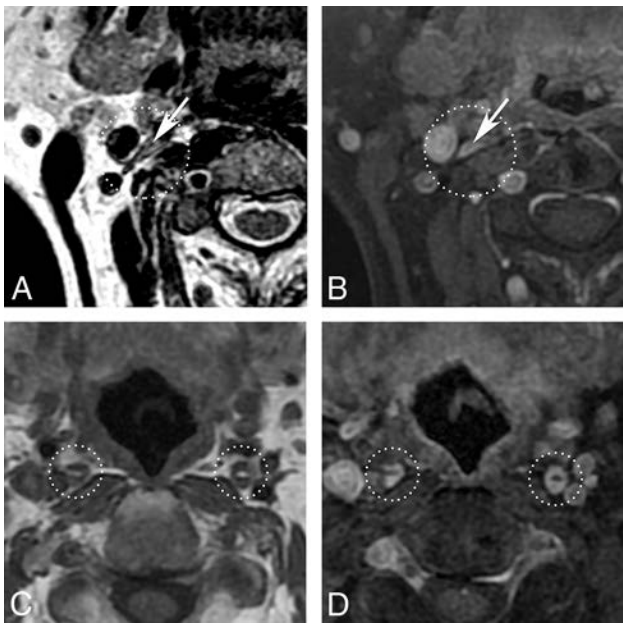

FIG 4. A 58-year-old woman with an intraganglionic hypointense spot (*arrow*) on the right on T2-weighted image (*A*). This spot is less evident (*arrow*) on the gadolinium-enhanced fat-saturated T1-weighted image (*B*). T1-weighted images in a 65-year-old man show slit-shaped hyperintense areas in the bilateral superior cervical ganglia (*C*, *circles*). Signals of these regions are suppressed on the gadolinium-enhanced fat-saturated T1-weighted image (*D*).

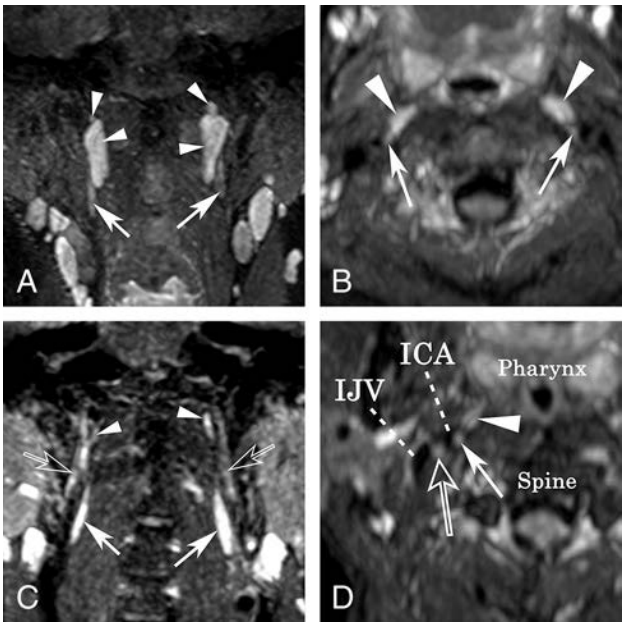

FIG 5. *A*, A 14-year-old adolescent with a prominent but normal RPLN. Coronal maximum-intensity-projection image shows the superior cervical ganglia (*arrows*) and the retropharyngeal lymph nodes (*arrowheads*). Each SCG was inferior to the RPLN. *B*, Reconstructed axial MIP image of 15-mm thickness shows that each SCG (*arrows*) is posterolateral to the RPLN (*arrowheads*). *C*, Coronal MIP image shows the SCG (*arrows*), inferior ganglia of vagus nerve (*open arrows*), and RPLN (*arrowheads*) in a 38-year-old man. The SCG is inferior to the IGVN. *D*, Reconstructed axial MIP image shows that the RPLN (*arrowhead*), SCG *(arrow*), internal carotid artery, IGVN (*open arrow*), and the internal jugular vein (IJV) form a line from anteromedial to posterolateral. *B* and *D*, Blurring on the images is because the MIP was used to superimpose the SCG, IGVN, and RPLN. IJV indicates inferior jugular vein.

Morphology

There were no significant differences between the right and left sides or of all morphologic parameters and vertebral levels of SCGs and RPLNs (On-line Tables 1 and 2). Most SCGs were significantly larger than RPLNs ($P < .001$/$P < .001$ on the right and left), though 26 RPLNs (25%) had higher volume than SCGs (Fig 5*A*). IGVNs also showed symmetric morphology between the right and left sides (On-line Table 3). The volume of the IGVNs was smaller than that of the SCGs and RPLNs ($P < .001$/$P <$. 001, and $P = .004$/$P = .018$, respectively).

Spatial Relationships

Ninety-three of 100 SCGs were located at the anteromedial or medial side of the internal carotid artery. Only 6 of 100 SCGs were located at the posterolateral side of the ICA, in which there was tortuosity of the vessels toward the medial side. The SCGs tended to be located caudal to the RPLNs ($P < .001$/$P < .001$), though 31 RPLNs (29.8%) partially overlapped the SCGs on the anteroposterior projection. All RPLNs were located anteromedial to the SCGs (Fig 5*B*).

The IGVNs tended to be located cranial to the SCGs ($P <$ .001). The center of the IGVNs tended to be located caudal to the RPLNs ($P = .001$/$P = 0.046$), though the superior pole of the IGVNs had no difference of vertebral level ($P = .062$/$P = .986$). Compared with the SCG, the IGVNs were located cranial to the

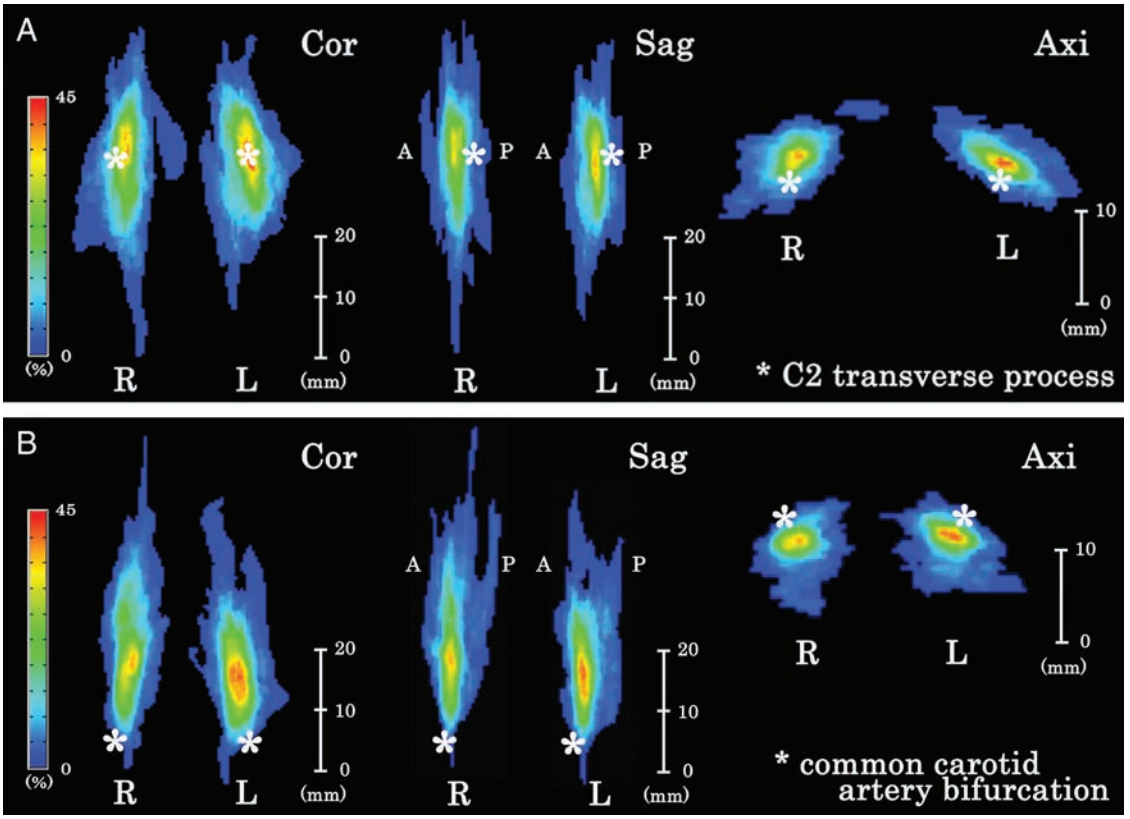

FIG 6. Probability maps of the superior cervical ganglion against the C2 transverse process (*A*, *asterisk*) and common carotid artery bifurcation (*B*, *asterisk*). The SCG was located at the anterior side against the C2 transverse process and superior and posterolateral to the CCAB. The location of bilateral SCGs is similar. R indicates right; L, left; Cor, coronal; Sag, sagittal; Axi, axial.

RPLNs ($P < .001$/$P < .001$). All IGVNs were located lateral or posterolateral to the SCGs and RPLNs.

Probability Map of SCGs

The probability map of SCGs showed them to be most commonly located in front of the C2 transverse process (Fig 6*A*) and superior to and posterolateral to the CCABs (Fig 6*B*). The maximum existence probabilities were 42% of the map (On-line Table 4). For example, 10% existence probability in this figure indicated that 10 of 100 SCGs existed in the area.

DISCUSSION

This is the first MR imaging analysis focused on identifying SCGs and IGVNs, to our knowledge. The SCG drew little attention in the past, and several previous reports mistakenly described it as retropharyngeal lymph node metastasis or tumor.[18,19] The results of the current study indicate that MR imaging can be useful in identifying these structures and would potentially facilitate safer and more accurate planning of surgical and interventional procedures such as SCG blocks for facial pain.

RPLNs are usually less evident in elderly populations than in children.[20] Because we assessed the MR imaging of elderly patients in cohort 1, most of whom presented with oral or pharyngeal cancers, the detection of SCGs was comparatively straightforward because of less evident RPLNs. The enhancement and DWI characteristics were most useful for differentiation in the analysis. The SCG has a large number of capillary vessels around the ganglion cells[8,21] and lacks a blood-nerve barrier.[22] These features might cause avid enhancement of the SCGs. Although metastatic lymph nodes can be strongly enhanced due to angiogenesis by cancer cells,[23] signals were often heterogeneous. Homogeneous enhancement was considered one of the characteristics of SCGs. The signal difference on DWI was likely due to differences in the ADC values because the signal intensity was visually about the same with conventional T2WI. ADC values can reflect histologic characteristics such as cell density. The SCG is constructed of ganglion cells, nerve fibers, vascular structures, and collagen fibers.[8,21] By contrast, lymph nodes show low ADC values due to lymphocyte accumulation.

Intraganglionic hypointense spots on T2WI might be consistent with the 2 previous reports that concluded that they represent venules.[8,9] Although this finding can be a characteristic feature of SCGs, metastatic lymph nodes were often heterogeneous in signal and might mimic this finding. In contrast, slits or spot-shaped fat tissue had not been previously described and were thought to be much more specific. The figure of T2WI presented by Loke et al[8] appeared to have FS-T2WI, presumably due to signal intensity changes caused by the low body temperature of the corpus. Our assumption is that the fat tissue in the SCGs may represent spaces among the neural branches. SCGs have many branches: superior, lateral, medial, and anterior. The superior branches enter the cranial cavities along with the ICA. The gray rami of the lateral branches communicate with the upper 4 cervical spinal nerves, as well as with some of the cranial nerves such as the vagus and hypoglossal nerves. The medial branches are laryngopharyngeal

and cardiac. The anterior branches are rami and those on the common and external carotid arteries. These branches may entrap fat tissue near the SCGs and mimic intraganglionic fat. Caution should be taken not to mistake fat tissue for lymph node hilum.

Cadaver studies have reported that the length and width of the SCGs are about 10–30 and 5–8 mm and are located posterior to the ICA.[1-7] The height of the SCGs varies in these reports from the level of C2–C3, just C2, just C4, and so forth.[1-7] Although our results were mostly consistent with these cadaveric studies, there were some discrepancies. Our results showed that SCGs were located not posterior to but anteromedial or medial to the ICA in almost all cases. In addition, SCGs were widely distributed from C1 to C5 in our study. Cadaveric studies potentially present a risk of artifactual changes in location due to postmortem procedures and postmortem changes. Only MR imaging can reveal precise shapes and locations of the SCGs in vivo.

MR imaging allowed detection of bilateral SCGs in all cases. SCGs have elongated, cylindric, and fusiform shapes, and the longus capitis muscle and ICA were landmarks to detect them. The RPLNs were also located along the longus capitis muscle and had an elongated appearance along the body axis; therefore, the size and positional relationships were the most important factors in assessing them correctly. While many SCGs were, in general, longer than the RPLNs in the craniocaudal direction, some of the RPLNs were larger than the SCGs. In such cases, focusing on the relative positions will be of pivotal importance. SCGs are usually located caudal to the RPLNs. IGVNs also have a fusiform shape; however, once again, the location was the most important key to differentiating IGVNs and SCGs. The RPLNs were located at the anteromedial side of the SCGs, and IGVNs were located lateral or posterolateral to the SCGs. As a result, the RPLN, SCG, the ICA, and IGVN formed a line on an axial plane from anteromedial to posterolateral (Fig 5*D*). In addition, IGVNs might not cause confusion using routine neck MR imaging. Although we attempted to detect IGVNs, retrospectively, in cases of routine neck MR imaging, IGVNs were difficult to detect with confidence, presumably because the volume of the IGVNs was small and the signals due to vascular structures compromised their detection.

Probability mapping showed that the positional relationship had a large degree of variation. If the sites with maximum probability were visually checked, the SCGs could not be detected in more than half of the cases. The SCGs are one of the targets for ganglionic local opioid injection for migraine, trigeminal neuralgia, postherpetic neuralgia, facial pain, complex regional pain syndrome, pain-associated depression, and vasospasms following subarachnoid hemorrhage.[24-26] Blinded or fluoroscopically guided approaches have been described.[24,27,28] These blinded techniques were expected to have a high risk of inaccurate localization of the targets. A potential risk of vertebral artery puncture and epi-/subdural injection has also been demonstrated.[26] Sonography-guided identification of the SCGs could be a potentially reliable technique, though this has only been validated in cadavers.[25] For the sonography study, the CCAB and transverse processes of the spinal bones were used as landmarks. The probability maps created do not favor one landmark over the other because the probability densities of SCGs showed no evident difference between the 2 maps. We believe that MR imaging–guided intervention might be one of the options for failed pain control under a blinded injection. Although an SCG block under MR imaging still requires controlled studies with blinded injection,[26,29] MR imaging may have a potential role in identifying the precise location of SCGs.

Limitations of this study include a lack of direct clinicopathologic correlation of the identified ganglia by either an operation or postmortem examination. Because one of our purposes was to characterize normal SCGs, invasive procedures for confirmation were not acceptable; however, our results were consistent with those of anatomic reports.[1-7] Also, as many participants as possible were examined to reveal the variations of morphology and location, minimizing the effects of misdetection for the ganglia and lymph nodes. Second, 2 different MR imaging instruments were used for this study because we assigned the specific protocols on separate instruments. The SCG signal was evaluated by thick sections of routine neck MR imaging. Evaluations using thin section thickness, such as neurography, might have been better to avoid partial volume effects and reveal detailed intraganglionic structures. Third, the lymph nodes that we classified into normal lymph nodes might have contained metastases, though there were significant differences in ADC values between normal and metastatic lymph node groups. Finally, we selected only adult cases. Our data might not be relevant to the pediatric population. In fact, the relative size of the SCGs and RPLNs may be different between adults and children because reactive retropharyngeal lymph nodes are more commonly seen in pediatric populations.

CONCLUSIONS

We have shown that MR imaging enables detection of SCGs. Although SCGs, IGVNs, and RPLNs showed similar shapes on cursory inspection, they can be differentiated individually by evaluating the signal intensity, size, and positional relationship. SCGs and RPLNs were on the lateral edges of the longus capitis muscle and the anteromedial side of the ICA, but RPLNs were smaller in volume, with a higher and more anteromedial position and lower contrast enhancement and ADC values than SCGs. IGVNs were smaller than SCGs and RPLNs and were located between the ICA and internal jugular vein. In other words, the RPLN, SCG, ICA, IGVN, and the internal jugular vein existed along a line from anteromedial to posterolateral on an axial section. Precise detection of them will lead to correct cancer staging and promote safe procedures such as lymph node biopsy and SCG block.

REFERENCES

1. Berkovitz B. **Cervical sympathetic trunk.** In: Standring S, ed. *Gray's Anatomy: The Anatomical Basis of Clinical Practice*. 39th ed. Edinburgh: Elsevier Churchill Livingstone; 2005:559–60
2. Fazliogullari Z, Kilic C, Karabulut AK, et al. **A morphometric analysis of the superior cervical ganglion and its surrounding structures.** *Surg Radiol Anat* 2016;38:299–302 CrossRef Medline
3. Yin Z, Yin J, Cai J, et al. **Neuroanatomy and clinical analysis of the cervical sympathetic trunk and longus colli.** *J Biomed Res* 2015;29:501–07 CrossRef Medline
4. Civelek E, Karasu A, Cansever T, et al. **Surgical anatomy of the cervical sympathetic trunk during anterolateral approach to cervical spine.** *Eur Spine J* 2008;17:991–95 CrossRef Medline
5. Saylam CY, Ozgiray E, Orhan M, et al. **Neuroanatomy of cervical sympathetic trunk: a cadaveric study.** *Clin Anat* 2009;22:324–30 CrossRef Medline

6. Kiray A, Arman C, Naderi S, et al. **Surgical anatomy of the cervical sympathetic trunk.** *Clin Anat* 2005;18:179–85 CrossRef Medline
7. Wisco JJ, Stark ME, Safir I, et al. **A heat map of superior cervical ganglion location relative to the common carotid artery bifurcation.** *Anesth Analg* 2012;114:462–65 CrossRef Medline
8. Loke SC, Karandikar A, Ravanelli M, et al. **Superior cervical ganglion mimicking retropharyngeal adenopathy in head and neck cancer patients: MRI features with anatomic, histologic, and surgical correlation.** *Neuroradiology* 2016;58:45–50 CrossRef Medline
9. Lee JY, Lee JH, Song JS, et al. **Superior cervical sympathetic ganglion: normal imaging appearance on 3T-MRI.** *Korean J Radiol* 2016;17:657–63 CrossRef Medline
10. Hogan QH, Erickson SJ. **MR imaging of the stellate ganglion: normal appearance.** *AJR Am J Roentgenol* 1992;158:655–59 CrossRef Medline
11. Slappendel R, Thijssen HO, Crul BJ, et al. **The stellate ganglion in magnetic resonance imaging: a quantification of the anatomic variability.** *Anesthesiology* 1995;83:424–26 CrossRef Medline
12. Vargas MI, Viallon M, Nguyen D, et al. **New approaches in imaging of the brachial plexus.** *Eur J Radiol* 2010;74:403–10 CrossRef Medline
13. Mallouhi A, Marik W, Prayer D, et al. **3T MR tomography of the brachial plexus: structural and microstructural evaluation.** *Eur J Radiol* 2012;81:2231–45 CrossRef Medline
14. Chhabra A, Thawait GK, Soldatos T, et al. **High-resolution 3T MR neurography of the brachial plexus and its branches, with emphasis on 3D imaging.** *AJNR Am J Neuroradiol* 2013;34:486–97 CrossRef Medline
15. Shibuya K, Sugiyama A, Ito S, et al. **Reconstruction magnetic resonance neurography in chronic inflammatory demyelinating polyneuropathy.** *Ann Neurol* 2015;77:333–37 CrossRef Medline
16. Zümre O, Salbacak A, Cicekcibasi AE, et al. **Investigation of the bifurcation level of the common carotid artery and variations of the branches of the external carotid artery in human fetuses.** *Ann Anat* 2005;187:361–69 CrossRef Medline
17. Faul F, Erdfelder E, Lang AG, et al. **G*Power 3: a flexible statistical power analysis program for the social, behavioral, and biomedical sciences.** *Behav Res Methods* 2007;39:175–91 CrossRef Medline
18. Yuen HW, Goh CH, Tan TY. **Enlarged cervical sympathetic ganglion: an unusual parapharyngeal space tumour.** *Singapore Med J* 2006;47:321–23 Medline
19. Anil G, Tan TY. **Imaging characteristics of schwannoma of the cervical sympathetic chain: a review of 12 cases.** *AJNR Am J Neuroradiol* 2010;31:1408–12 CrossRef Medline
20. Costa NS, Salisbury SR, Donnelly LF. **Retropharyngeal lymph nodes in children: a common imaging finding and potential source of misinterpretation.** *AJR Am J Roentgenol* 2011;196:W433–37 CrossRef Medline
21. Mitsuoka K, Kikutani T, Sato I. **Morphological relationship between the superior cervical ganglion and cervical nerves in Japanese cadaver donors.** *Brain Behav* 2016 29;7:e00619 CrossRef Medline
22. Kiernan JA. **Vascular permeability in the peripheral autonomic and somatic nervous systems: controversial aspects and comparisons with the blood-brain barrier.** *Microsc Res Tech* 1996;35:122–36 Medline
23. Wendl CM, Müller S, Meier J, et al. **High resolution contrast-enhanced ultrasound and 3-Tesla dynamic contrast-enhanced magnetic resonance imaging for the preoperative characterization of cervical lymph nodes: first results.** *Clin Hemorheol Microcirc* 2012; 52:153–66 CrossRef Medline
24. Treggiari MM, Romand JA, Martin JB, et al. **Cervical sympathetic block to reverse delayed ischemic neurological deficits after aneurysmal subarachnoid hemorrhage.** *Stroke* 2003;34:961–67 CrossRef Medline
25. Siegenthaler A, Haug M, Eichenberger U, et al. **Block of the superior cervical ganglion: description of a novel ultrasound-guided technique in human cadavers.** *Pain Med* 2013;14:646–49 CrossRef Medline
26. Jankovic D. **Superior cervical ganglion block.** In: Jankovic D, Peng P, eds. *Regional Nerve Blocks in Anesthesia and Pain Therapy*. 4th ed. Cham: Springer; 2015:201–09
27. Elias M. **Cervical sympathetic and stellate ganglion blocks.** *Pain Physician* 2000;3:294–304 Medline
28. Wirz S, Wartenberg HC, Nadstawek J, et al. **Superior cervical ganglion: an anatomical variant—are variations of the cranial carotid artery a risk factor for accidental intravascular injection?** [in German]. *Anaesthesist* 2008;57:689–92 CrossRef Medline
29. Liu SS, Ngeow JE, Yadeau JT. **Ultrasound-guided regional anesthesia and analgesia: a qualitative systematic review.** *Reg Anesth Pain Med* 2009;34:47–59 CrossRef Medline

Gadolinium DTPA Enhancement Characteristics of the Rat Sciatic Nerve after Crush Injury at 4.7T

B.J. Hill, K.R. Padgett, V. Kalra, A. Marcillo, B. Bowen, P. Pattany, D. Dietrich, and R. Quencer

ABSTRACT

BACKGROUND AND PURPOSE: Traumatic peripheral nerve injury is common and results in loss of function and/or neuropathic pain. MR neurography is a well-established technique for evaluating peripheral nerve anatomy and pathology. However, the Gd-DTPA enhancement characteristics of acutely injured peripheral nerves have not been fully examined. This study was performed to determine whether acutely crushed rat sciatic nerves demonstrate Gd-DTPA enhancement and, if so, to evaluate whether enhancement is affected by crush severity.

MATERIALS AND METHODS: In 26 rats, the sciatic nerve was crushed with either surgical forceps (6- to 20-N compressive force) or a microvascular/microaneurysm clip (0.1–0.6 N). Animals were longitudinally imaged at 4.7T for up to 30 days after injury. T1WI, T2WI, and T1WI with Gd-DTPA were performed.

RESULTS: Forceps crush injury caused robust enhancement between days 3 and 21, while clip crush injury resulted in minimal-to-no enhancement. Enhancement after forceps injury peaked at 7 days and was seen a few millimeters proximal to, in the region of, and several centimeters distal to the site of crush injury. Enhancement after forceps injury was statistically significant compared with clip injury between days 3 and 7 ($P < .04$).

CONCLUSIONS: Gd-DTPA enhancement of peripheral nerves may only occur above a certain crush-severity threshold. This phenomenon may explain the intermittent observation of Gd-DTPA enhancement of peripheral nerves after traumatic injury. The observation of enhancement may be useful in judging the severity of injury after nerve trauma.

ABBREVIATIONS: BNB = blood-nerve barrier; DCE = dynamic contrast-enhanced

Approximately 3% of trauma patients sustain an injury to the radial, median, ulnar, sciatic, femoral, tibial, or peroneal nerve.[1] The health care costs associated with traumatic peripheral nerve injury are approximately $150 billion per year in the United States alone.[2] Patients with traumatic nerve injury can have loss of motor function (up to complete paralysis), loss of sensation, and/or neuropathic pain.[3] Direct end-to-end epineurial repair remains the criterion standard treatment for high-grade nerve trauma and is often combined with autologous nerve grafting.[4] However, a recent meta-analysis of median and ulnar nerve repair showed that only 52% of patients achieved satisfactory motor recovery, while 43% achieved satisfactory sensory recovery.[5]

Peripheral nerve injury has been classified by Sunderland[6] on the basis of damage to Schwann cells/myelin, axons, endoneurium, perineurium, and epineurium (grades 1–5, respectively). Nerve conduction studies and electromyography are the standard diagnostic tests for grading traumatic mononeuropathy.[7] However, electrodiagnostics have limited ability to distinguish Sunderland grade 2, 3, and 4 injuries in the acute and subacute settings.[8] Because skeletal muscles begin to atrophy immediately after denervation and are permanently wasted by 18–24 months, and because axons regenerate at only millimeters per day, there is a clinical need to accurately grade nerve injuries in the acute setting so that surgical intervention can be expedited (when appropriate) to prevent permanent loss of function.[9] In addition, there is a clinical and scientific need for noninvasive diagnostic testing to monitor the effects of various novel medical and surgical interventions on nerve repair.[10,11] Diffusion tensor imaging has shown great promise in this realm in recent years[12] but remains a pri-

Received April 5, 2017; accepted after revision August 24.

From the Departments of Radiology (B.J.H., K.R.P., B.B., P.P., R.Q.), Radiation Oncology (K.R.P.), and Biomedical Engineering (K.R.P.), and Miami Project to Cure Paralysis (A.M., D.D.), Miller School of Medicine (V.K.), University of Miami, Miami, Florida.

Brook J. Hill and Kyle R. Padgett contributed equally to this work.

Paper previously presented in part at: Annual Meeting of the American Society of Neuroradiology, May 16–21, 2009; Vancouver, British Columbia, Canada.

Please address correspondence to Kyle R. Padgett, PhD, Department of Radiation Oncology, University of Miami Miller School of Medicine, 1475 NW 12th Ave, Suite 1500, Miami, FL 33136; e-mail: kpadgett@med.miami.edu; @brookjhill

Indicates article with supplemental on-line video.

http://dx.doi.org/10.3174/ajnr.A5437

Table 1: Number of MRI sessions at each time point after forceps (#5 jeweler or toothed Adson) crush injury

Forceps: Postop Day No.	No. MRI Sessions (with Limited DCE)
0	1 (0)
1	4 (0)
2	2 (0)
3	3 (2)
4	1 (0)
5	1 (0)
7	6 (5)
12	2 (0)
13	2 (1)
14	5 (4)
19	1 (1)
21	1 (1)
22	1 (1)
30	1 (1)
Total	31 (16)

Note:—Postop indicates postoperative.

Table 2: Number of MRI sessions at each time point after clip (10–60 g microvascular/microaneurysm) crush injury

Clip: Postop Day No.	No. MRI Sessions
1	3
2	4
3	2
4	3
5	4
6	1
7	2
Total	19

marily experimental technique and is technically challenging. Although Gd-DTPA is widely available with a well-defined safety profile, the Gd-DTPA enhancement characteristics of acutely injured peripheral nerves have not yet been fully examined. We performed this study to determine whether acutely crushed rat sciatic nerves demonstrate Gd-DTPA enhancement and, if so, to evaluate whether enhancement is affected by crush severity. On the basis of prior literature, we hypothesized that crushed nerves would not show Gd-DTPA enhancement.

MATERIALS AND METHODS

This study was approved by the University Animal Care and Use Committee (Protocol No. 06–172). Twenty-six male Sprague-Dawley rats were used for the study. In each rat, the left sciatic nerve was surgically exposed and crushed at the level of the midfemur by using either surgical forceps ($n = 14$) or a microvascular/microaneurysm clip ($n = 12$). Forceps used for the study included the #5 jeweler and toothed Adson, which were supplied by Fine Science Tools, Foster City, California. All forceps injuries were delivered for 60 seconds at maximum intensity, with the handles of the forceps completely opposed. Adson forceps injuries were delivered immediately adjacent to the forceps teeth, using the flat surface of the instrument. Forceps crush intensity was estimated in grams by using a 3-mm force-sensitive resistor (FlexiForce A101; Tekscan, South Boston, Massachusetts), a multimeter, and a set of scale calibration weights. The microvascular/microaneurysm clips (Harvard Apparatus, Holliston, Massachusetts) used for the study included 10- to 15-g microvascular ($n = 6$), 20- to 30-g microvascular ($n = 3$), and 60-g microaneurysm ($n = 3$) clips. Clip crush durations included 6 seconds ($n = 3$), 60 seconds ($n = 6$), and 600 seconds ($n = 3$). Sham surgery was performed on the right sciatic nerve in 4 animals; nonoperative right sciatic nerves in the remaining animals served as internal controls.

MR imaging was performed on a 4.7T dedicated animal magnet (47/40USR; Bruker Biospin, Ettlingen, Germany) using a 400-mT/m gradient coil with an inner diameter of 12 cm and a quadrature birdcage radiofrequency coil with an inner diameter of 7.2 cm. Animals were imaged between postoperative days 0 and 30; 50 MR imaging sessions were performed (Tables 1 and 2). Sequences included axial T1-weighted gradient-echo with fat saturation (TR, 235 ms; TE, 2.6 ms), axial T2-weighted rapid acquisition relaxation excitement with fat saturation (TR, 2500 ms; TE, 23 ms), and axial T1-weighted gradient-echo with fat saturation immediately after 0.1 mmol/kg of intravenous Gd-DTPA (Magnevist; Bayer HealthCare Pharmaceuticals, Wayne, New Jersey). Limited dynamic contrast-enhanced (DCE) T1-weighted gradient-echo imaging with fat saturation was performed on select animals, using the Bruker Small Animal MRI and Spectroscopy sequence (TR, 35 ms; TE, 3.5 ms). Sixteen MR imaging sessions included limited DCE imaging. All acquisitions had a section thickness of 0.8 mm without a gap, an FOV of 5 × 5 cm, and a matrix size of either 168 × 168 or 256 × 256. Gd-DTPA was administered through a surgically placed external jugular central venous catheter. Animals were sedated with isoflurane during imaging and positioned in the prone (normal upright) position, with hips and knees flexed at roughly 90°. Images were acquired in the axial plane, a few millimeters posterior to and roughly parallel to the femurs.

Image postprocessing included manual ROI selection and calculation of the signal-to-noise ratio in each ROI. ROIs included the injured sciatic nerve in the region of the crush injury, sham/nonoperative nerves in the corresponding contralateral location, normal muscle, and background air (Fig 1). The SNR was calculated as the quotient of the mean ROI signal divided by the SD of the noise of background air. Enhancement was calculated as the percentage increase in the SNR after the administration of contrast. Statistical analysis included comparison of enhancement after forceps injury with enhancement of clip injured nerves, sham nerves, nonoperative nerves, and normal muscle using a 2-tailed, 2-sample Student t test. As an internal control, enhancement of sham nerves was compared with enhancement of nonoperative nerves using the same statistical methodology. Significance was set at $P < .05$.

RESULTS

Forceps Crush Intensity

Measurements of the compressive force delivered by the #5 Jeweler forceps ranged between 650 and 750 g (6.4–7.4 N). Measurements of the compressive force delivered by the Toothed Adson forceps ranged between 750 g and 2.0 kg (7.4–20 N).

T2-Weighted MR Imaging

On T2WI, 14 of 14 (100%) forceps-injured nerves demonstrated increased caliber and signal proximal to, in the region of, and distal to the site of injury (Fig 2). Increased T2 signal extended

proximally as far as the sciatic notch and distally well into the tibial and peroneal nerve branches. In contrast, only 8 of 12 (67%) clip injured nerves demonstrated qualitative signal hyperintensity on T2WI.

Gadolinium-DTPA-Enhanced T1-Weighted MR Imaging

Qualitatively, 14 of 14 (100%) forceps-injured nerves demonstrated avid Gd-DTPA enhancement on T1WI. Enhancement was seen a few millimeters proximal to, in the region of, and several centimeters distal to the site of crush injury (Fig 3). Like T2 signal hyperintensity, Gd-DTPA enhancement extended distally into the tibial and peroneal nerve branches. However, Gd-DTPA enhancement did not extend as far proximally (toward the sciatic notch) as T2 signal hyperintensity. Robust Gd-DTPA enhancement was observed in forceps-injured nerves as early as 3 days after injury. Enhancement peaked at 7 days and subsequently diminished, but it was still evident on day 21 (Fig 4).

Quantitatively, enhancement of forceps-injured nerves was statistically significant ($P < .05$) compared with normal muscle at days 3, 7, and 14 (Fig 5). Enhancement of forceps-injured nerves was statistically significant compared with sham nerves ($P < .02$) as well as nonoperative nerves ($P < .01$) on day 7 only.

In contrast, only 1 of 12 (8%) clip-injured nerves demonstrated Gd-DTPA enhancement on T1WI. This nerve had been crushed with a 60-g microaneurysm clip for 60 seconds and showed Gd-DTPA enhancement only at the crush site on postoperative days 5 and 7. No qualitative enhancement was seen in the sciatic nerve distal to the crush site or the tibial or peroneal nerve branches. Quantitative enhancement of clip-injured nerves was significantly different from that of forceps-injured nerves when comparing all MR imaging sessions between days 3 and 7 ($P < .04$).

Forceps-injured nerves enhanced both internally and peripherally. Nonoperative nerves did not demonstrate internal Gd-DTPA enhancement. They did, however, demonstrate a thin rim of peripheral enhancement, presumably representing mesoneurium and/or external epineurium, both of which lack a blood-nerve barrier (BNB) (Fig 3*C*). Some sham nerves demonstrated faint qualitative enhancement only at the surgical site on days 7 ($n = 3$) and 14 ($n = 1$), though this was not statistically significant compared with nonoperative nerves at the same time points ($P > .15$).

Limited DCE MR neurography was performed on a select group of animals to better understand the kinetics of enhancement after contrast injection. On DCE T1WI, forceps-injured nerve SNR reached a plateau approximately 5–10 minutes after the administration of Gd-DTPA (Fig 6) and demonstrated a half-life of approximately 1 hour (Fig 7). Precise mathematic modeling of DCE data was not possible due to the limited temporal resolution and the lack of a reliable arterial input function in the FOV. However, the presence of a delayed, higher peak SNR in forceps-injured nerves compared with nonoperative nerves suggested an enlarged extravascular extracellular space after severe crush injury.[13]

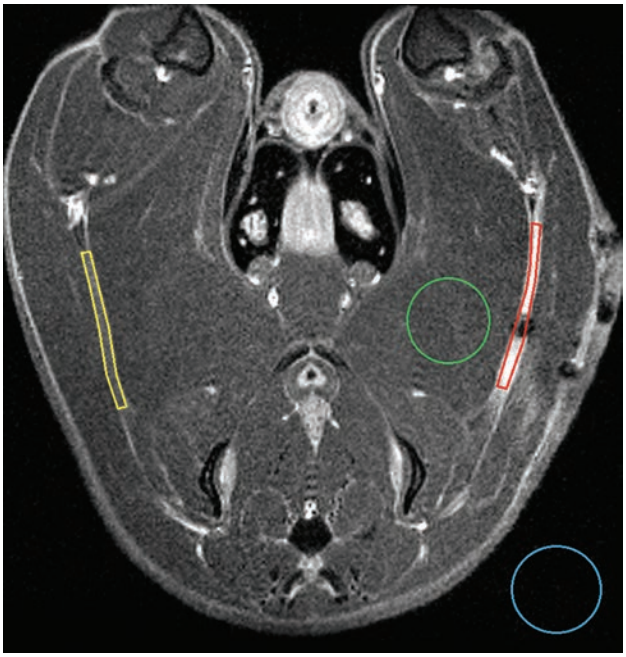

FIG 1. Axial T1WI with fat saturation after Gd-DTPA. Areas outlined in color represent manually defined ROIs corresponding to injured nerve (red), contralateral nerve (yellow), muscle (green), and background/air (blue). Precontrast and nonenhancing nerves were localized by correlating T1WI and T2WI findings.

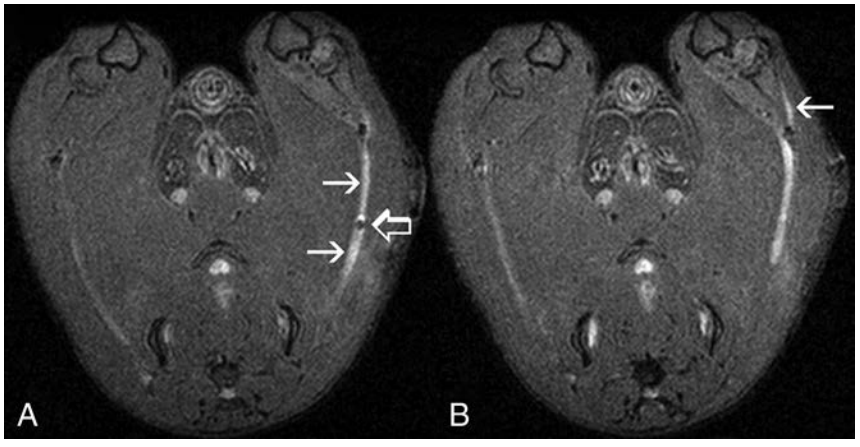

FIG 2. Axial T2WI with fat saturation (#5 Jeweler forceps injury, day 13). *A*, Injured sciatic nerve (*arrows*) shows increased caliber and signal compared with the nonoperative contralateral nerve. A small focus of susceptibility artifact (*open arrow*) is seen at the site of injury, presumably representing blood products. *B*, The adjacent section shows T2 hyperintensity in a distal branch (*arrow*) of the injured sciatic nerve.

DISCUSSION

Our results demonstrate that Gd-DTPA peripheral nerve enhancement after severe (forceps) crush injury is a robust phenomenon in the rat sciatic nerve at 4.7T. The relative absence of enhancement after mild (clip) crush injury suggests the presence of a crush-severity threshold, below which enhancement is not observed. Therefore, the observation of enhancement after nerve trauma could potentially be useful in judging the severity of injury. In addition, when one performs MR neurog-

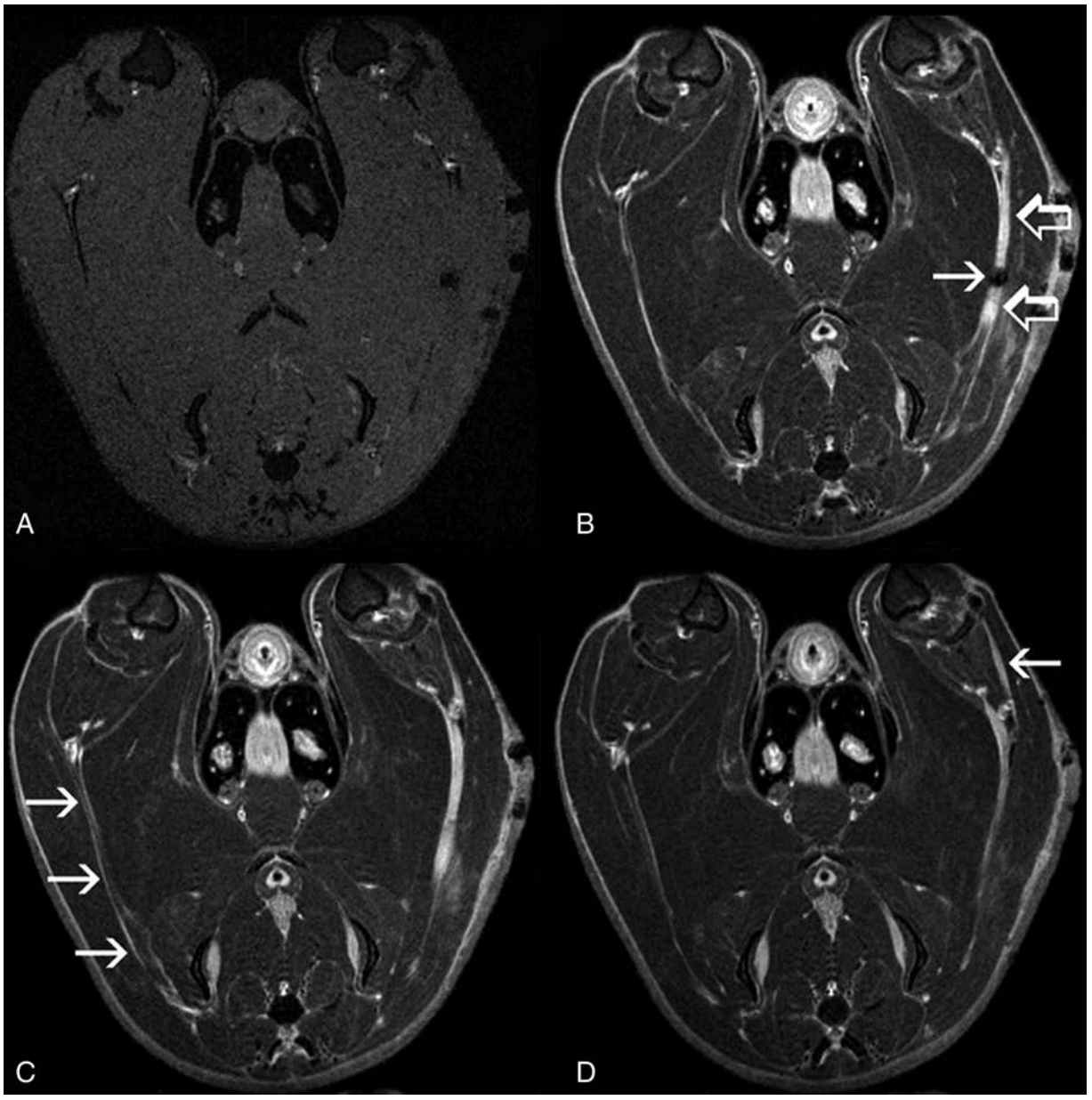

FIG 3. Axial T1WI with fat saturation, pre- (*A*) and post- (*B–D*) Gd-DTPA (same animal as in Fig 2). *A*, On precontrast images, both injured and nonoperative nerves are isointense to muscle. *B*, Intense Gd-DTPA enhancement (*open arrows*) is demonstrated a few millimeters proximal to, in the region of, and distal to the site of crush injury (*arrow*) (On-line Video 1). *C*, The nonoperative contralateral nerve (*arrows*) is well seen in this section and demonstrates a thin rim of peripheral enhancement but no internal enhancement (On-line Video 2). *D*, Enhancement is seen in a distal branch (*arrow*) of the injured sciatic nerve (On-line Video 3).

raphy for peripheral neuropathy of uncertain origin, the observation of enhancement may not exclude trauma from the differential diagnosis.

In our study, Gd-DTPA enhancement was more specific for higher grade injury compared with T2 hyperintensity. Also, Gd-DTPA enhancement more clearly localized the site of injury because T2 hyperintensity extended proximally to the sciatic notch, while Gd-DTPA enhancement extended only a few millimeters proximal to the site of the nerve crush. Gd-DTPA enhancement may provide additional information when added to routine MR neurography protocols in the posttraumatic setting.

Physiologically, peripheral nerve enhancement is a function of increased blood-nerve barrier permeability.[14] The BNB comprises tight junctions between endoneurial endothelial cells and perineurial myofibroblasts.[15] Increased BNB permeability can occur with demyelination (neurapraxia), Wallerian degeneration (axonotmesis), high-grade nerve trauma (neurotmesis), and numerous other causes of nerve injury.[16,17] In a rat sciatic model, Omura et al[18] observed increased BNB permeability 3 days after crush injury, with maximal BNB permeability after 7 days. Increased BNB permeability was observed 5 mm proximal to the site of injury, at the site of injury, and in the entire nerve distal to the site of injury. In a mouse sciatic model, Seitz et al[19] observed maximal BNB permeability distal to the site of injury 8 days after crush injury. These histologic results closely mirror our present imaging findings.

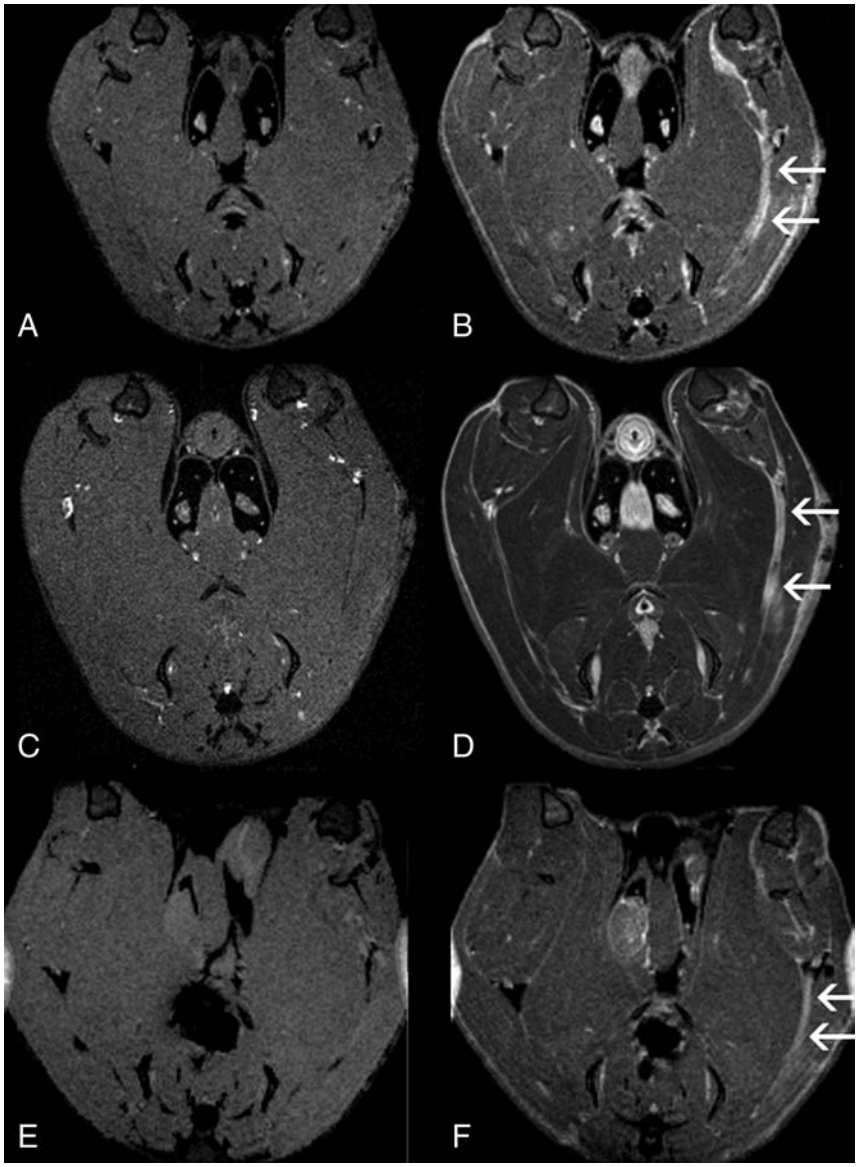

FIG 4. Axial T1WI pre- (left) and post- (right) Gd-DTPA with fat saturation acquired at days 7 (*A* and *B*), 13 (*C* and *D*), and 21 (*E* and *F*) after severe (forceps) crush injury. Robust enhancement of injured nerves is seen at all 3 time points (*arrows*).

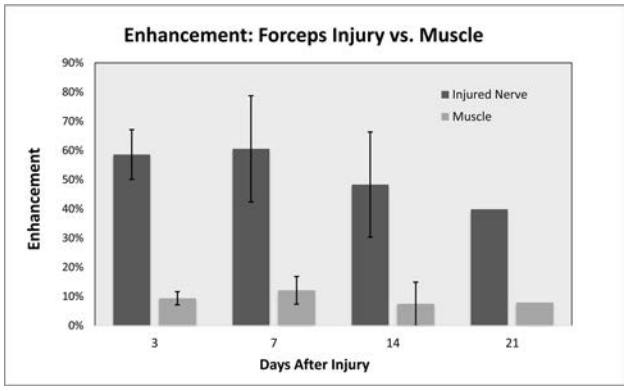

FIG 5. Peak enhancement after severe (forceps) crush injury compared with normal muscle between days 3 and 21. Enhancement is expressed as the percentage increase of the signal-to-noise ratio after Gd-DTPA administration. *Error bars* represent 1 SD.

Nerve crush is considered a model of axonotmesis (Sunderland grade 2 injury) with Wallerian degeneration followed by axonal regeneration.[20] Histologic studies have demonstrated a correlation between BNB permeability and axonal degeneration/regeneration.[16,18,19] By comparing histologic analysis of tight junction proteins with neurofilaments, Omura et al[18] demonstrated that both restoration of the BNB and axonal regeneration occur from proximal to distal and are closely related in time and space. Bouldin et al[16] have shown that increased BNB permeability persists beyond 14 weeks after complete transection as well as ricin injury; both models have no axonal regeneration. Further studies may be appropriate to determine whether resolution of enhancement after peripheral nerve trauma could be an indicator of axonal regeneration and whether the persistence of enhancement could indicate the absence of axonal regeneration.

Prior studies of Gd-DTPA-enhanced MR neurography after traumatic nerve injury have demonstrated mixed results. Gadolinium-DTPA enhancement has been reported in the facial nerve after crush injury[21] as well as in the median nerve after crush injury in an ex vivo model.[14] However, Aagaard et al[22] performed Gd-DTPA-enhanced MR neurography on 6 rats after sciatic nerve crush, and they were not able to reliably distinguish normal from crushed nerves. Furthermore, Bendszus et al[23] reported no Gd-DTPA enhancement of the rat sciatic nerve after ligation injury. Subsequent studies have also failed to demonstrate reliable Gd-DTPA enhancement in experimental autoimmune neuritis, focal demyelination induced by lysolecithin, and experimental Charcot–Marie-Tooth disease.[24-26] Our present observations of enhancement very closely parallel prior imaging findings after crush injury, using the nerve-specific contrast agent gadofluorine-M.[27] Possible explanations for prior mixed results with Gd-DTPA include varying injury mechanisms, crush forces, crush durations, magnetic field strengths (4.7T versus 1.5T), and MR imaging protocols. The interplay between crush force and crush duration is an obvious target for future investigation of the crush-severity enhancement threshold.

In recent years, diffusion tensor imaging has emerged as a potential new technique for evaluating injured nerves for evidence of axonal regeneration.[28-32] The loss and restoration of fractional anisotropy has been correlated with histologic and functional degeneration and recovery. Corresponding observations have been made regarding radial and axial diffusivity. How-

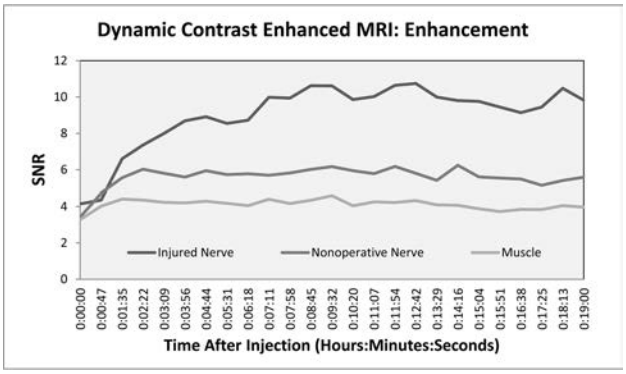

FIG 6. ROI signal-to-noise ratio as a function of time after the intravenous administration of Gd-DTPA (same animal as in Figs 2 and 3). The presence of a delayed, higher peak suggests an enlarged extravascular extracellular space after severe (forceps) crush injury (On-line Video 4).[13]

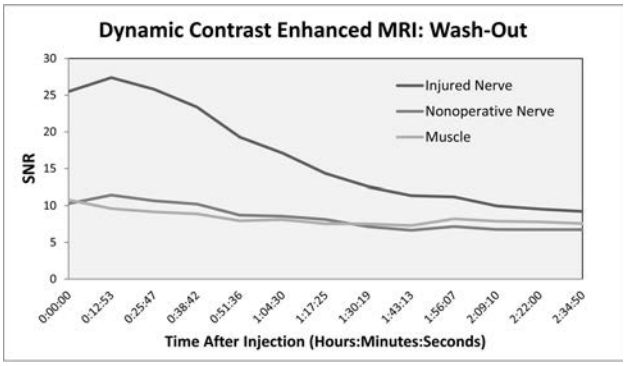

FIG 7. ROI signal-to-noise ratio as a function of time after the intravenous administration of Gd-DTPA (same animal as in Figs 2, 3, and 6). The half-life of Gd-DTPA enhancement was approximately 1 hour after severe (forceps) crush injury.

ever, incorporating DTI into clinical MR neurography protocols may be challenging due to the technical limitations of the technique and the relatively small size of peripheral nerves compared with CNS tissues that are typically investigated with DTI. Further studies may be appropriate to determine whether Gd-DTPA-enhanced MR neurography could supplement DTI, especially when also incorporating DCE.[33] Quantitative assessment of the resolution of enhancement could be particularly useful when monitoring mixed lesions (different grades of injury in different fascicles/segments of the same nerve) and subtle responses to medical intervention.

Limitations

This study has multiple limitations, most notably the lack of histologic and functional correlation. Although prior histologic studies have been rigorous, the correlation between BNB permeability and MR imaging enhancement is not necessarily linear. Further studies correlating enhancement with BNB permeability and axonal degeneration/regeneration should be performed to confirm the viability of this technique and to correlate the crush-severity threshold with the Sunderland classification of injury. Further studies should also evaluate the correlation between Gd-DTPA enhancement and functional deficits/recovery. Without functional correlation, it is impossible to ascertain whether nerve enhancement correlates with less favorable prognosis or whether the resolution of enhancement may herald eventual functional recovery.

This study has limited statistical power due to several experimental groups, some with small sample sizes. In addition, not every animal was imaged at every time point, and the number of MR imaging sessions per animal was limited. Although a larger experiment would have provided greater statistical power, the lack of clarity in the literature concerning the existence of Gd-DTPA enhancement and its temporal characteristics dictated the need for several experimental groups. We believe that our observation of statistically significant *P* values, despite these limitations, highlights the robust nature of Gd-DTPA enhancement after severe crush injury.

The mechanisms of injury used in this study, though reproducible and established in the literature, are only an approximation of human injuries encountered in clinical practice. However, the use of multiple injury severities more closely mimics a real-life clinical scenario, where injuries are highly variable from patient to patient. Because the exact severity and location of a human peripheral nerve crush injury are rarely known, it could be impossible to discover a crush severity threshold in humans and to correlate the spatial distribution of imaging findings with the precise location of injury. Future clinical studies will be necessary to determine the usefulness of this imaging technique in clinical practice.

This study was performed at 4.7T by using gradient-echo T1-weighted MR images, whereas clinical MR neurography typically is performed at 1.5T or 3T using spin-echo or fast spin-echo T1WI sequences. Theoretically, this difference could limit translation of our current findings into the clinical realm. However, we expect that T1 shortening on Gd-DTPA-enhanced studies should be readily identifiable on both gradient-echo and spin-echo pulse sequences at various field strengths. Most DCE studies quantify contrast concentration using gradient-echo or steady-state sampling techniques, and Gd-DTPA has a relatively constant r_1 relaxivity between 1.5T and 4.7T.[34]

Although qualitative DCE data were collected primarily to examine the kinetics of enhancement after contrast injection, our study was limited by the lack of formal DCE modeling. Future studies may seek to include formal DCE modeling, possibly using the reference region mathematic model,[33] given the potential scarcity of reliable arterial input functions surrounding peripheral nerve anatomy. Finally, potential errors in ROI selection may have influenced quantitative and/or statistical results in our study such as the following: scan obliquity, animal motion, difficulty distinguishing nonenhancing nerve tissue from adjacent muscle, partial volume averaging related to mesoneurial and/or external epineurial enhancement, and the presence of increased enhancement in the operative bed regardless of whether nerves were crushed. Errors in nerve contouring potentially could lead to false-positive results when comparing crushed and sham nerves with nonoperative nerves and normal muscle.

CONCLUSIONS

In our study, forceps crush injury (6- to 20-N compressive force) to the rat sciatic nerve caused robust Gd-DTPA enhancement between days 3 and 21, while clip crush injury (0.1–0.6 N) resulted in minimal-to-no enhancement. Enhancement after for-

ceps injury peaked at 7 days and was seen a few millimeters proximal to, in the region of, and several centimeters distal to the site of nerve crush. Compared with T2 signal hyperintensity, Gd-DTPA enhancement was more specific for higher grade injury and more clearly localized the site of injury. The spatial and temporal characteristics of Gd-DTPA enhancement in our study closely mirror prior histologic studies of blood-nerve barrier permeability after nerve injury. Further studies are needed to determine the scientific and clinical usefulness of this imaging technique.

ACKNOWLEDGMENTS

We thank Ramon German, Miguel Martinez, Paulo Diaz, Rosemarie Abril, and Monica Stagg for their hard work caring for the animals and assisting with surgery and Laura Blakemore, MD, and Paul Trombley, PhD, for their critical review of the manuscript.

REFERENCES

1. Noble J, Munro CA, Prasad VS. **Analysis of upper and lower extremity peripheral nerve injuries in a population of patients with multiple injuries.** *J Trauma* 1998;45:116–22 CrossRef Medline
2. Taylor CA, Braza D, Rice JB, et al. **The incidence of peripheral nerve injury in extremity trauma.** *Am J Phys Med Rehabil* 2008;87:381–85 CrossRef Medline
3. Schwartzman RJ, Grothusen J, Kiefer TR, et al. **Neuropathic central pain: epidemiology, etiology, and treatment options.** *Arch Neurol* 2001;58:1547–50 CrossRef Medline
4. Grinsell D, Keating CP. **Peripheral nerve reconstruction after injury: a review of clinical and experimental therapies.** *Biomed Res Int* 2014;2014:698256 CrossRef Medline
5. Ruijs AC, Jaquet JB, Kalmijn S, et al. **Median and ulnar nerve injuries: a meta-analysis of predictors of motor and sensory recovery after modern microsurgical nerve repair.** *Plast Reconstr Surg* 2005;116:484–94; discussion 495–96 CrossRef Medline
6. Sunderland S. *Nerve Injuries and Their Repair: A Critical Appraisal.* Edinburgh: Churchill Livingstone, 1991
7. Simon NG, Spinner RJ, Kline DG, et al. **Advances in the neurological and neurosurgical management of peripheral nerve trauma.** *J Neurol Neurosurg Psychiatry* 2016;87:198–208 CrossRef Medline
8. Feinberg J. **EMG: myths and facts.** *HSS J* 2006;2:19–21 CrossRef Medline
9. Chhabra A, Ahlawat S, Belzberg A, et al. **Peripheral nerve injury grading simplified on MR neurography: as referenced to Seddon and Sunderland classifications.** *Indian J Radiol Imaging* 2014;24:217–24 CrossRef Medline
10. Liao CD, Zhang F, Guo RM, et al. **Peripheral nerve repair: monitoring by using gadofluorine M-enhanced MR imaging with chitosan nerve conduits with cultured mesenchymal stem cells in rat model of neurotmesis.** *Radiology* 2012;262:161–71 CrossRef Medline
11. Li HJ, Zhang X, Zhang F, et al. **Enhanced repair effect of toll-like receptor 4 activation on neurotmesis: assessment using MR neurography.** *AJNR Am J Neuroradiol* 2014;35:1608–14 CrossRef Medline
12. Chen YY, Zhang X, Lin XF, et al. **DTI metrics can be used as biomarkers to determine the therapeutic effect of stem cells in acute peripheral nerve injury.** *J Magn Reson Imaging* 2017;45:855–62 CrossRef Medline
13. Tofts PS. **T1-weighted DCE imaging concepts: modelling, acquisition and analysis.** http://www.paul-tofts-phd.org.uk/DCE-MRI_siemens.pdf. Accessed May 30, 2017
14. Kobayashi S, Meir A, Baba H, et al. **Imaging of intraneural edema by using gadolinium-enhanced MR imaging: experimental compression injury.** *AJNR Am J Neuroradiol* 2005;26:973–80 Medline
15. Ubogu EE. **The molecular and biophysical characterization of the human blood-nerve barrier: current concepts.** *J Vasc Res* 2013;50:289–303 CrossRef Medline
16. Bouldin TW, Earnhardt TS, Goines ND. **Restoration of the blood-nerve barrier in neuropathy is associated with axonal regeneration and remyelination.** *J Neuropathol Exp Neurol* 1991;50:719–28 CrossRef Medline
17. Kanda T. **Biology of the blood-nerve barrier and its alteration in immune mediated neuropathies.** *J Neurol Neurosurg Psychiatry* 2013;84:208–12 CrossRef Medline
18. Omura K, Ohbayashi M, Sano M, et al. **The recovery of blood-nerve barrier in crush nerve injury: a quantitative analysis utilizing immunohistochemistry.** *Brain Res* 2004;1001:13–21 CrossRef Medline
19. Seitz RJ, Reiners K, Himmelmann F, et al. **The blood-nerve barrier in Wallerian degeneration: a sequential long-term study.** *Muscle Nerve* 1989;12:627–35 CrossRef Medline
20. Bridge PM, Ball DJ, Mackinnon SE, et al. **Nerve crush injuries: a model for axonotmesis.** *Exp Neurol* 1994;127:284–90 CrossRef Medline
21. Yanagida M. **MRI enhancement of the facial nerve with Gd-DTPA: first report—experimental study on the enhancement mechanism used in viewing vascular permeability of the facial nerve** [in Japanese]. *Nihon Jibiinkoka Gakkai Kaiho* 1993;96:1320–28 CrossRef Medline
22. Aagaard BD, Lazar DA, Lankerovich L, et al. **High-resolution magnetic resonance imaging is a noninvasive method of observing injury and recovery in the peripheral nervous system.** *Neurosurgery* 2003;53:199–203; discussion 203–04 CrossRef Medline
23. Bendszus M, Wessig C, Solymosi L, et al. **MRI of peripheral nerve degeneration and regeneration: correlation with electrophysiology and histology.** *Exp Neurol* 2004;188:171–77 CrossRef Medline
24. Stoll G, Wessig C, Gold R, et al. **Assessment of lesion evolution in experimental autoimmune neuritis by gadofluorine M-enhanced MR neurography.** *Exp Neurol* 2006;197:150–56 CrossRef Medline
25. Wessig C, Bendszus M, Stoll G. **In vivo visualization of focal demyelination in peripheral nerves by gadofluorine M-enhanced magnetic resonance imaging.** *Exp Neurol* 2007;204:14–19 CrossRef Medline
26. Wessig C, Jestaedt L, Sereda MW, et al. **Gadofluorine M-enhanced magnetic resonance nerve imaging: comparison between acute inflammatory and chronic degenerative demyelination in rats.** *Exp Neurol* 2008;210:137–43 CrossRef Medline
27. Bendszus M, Wessig C, Schütz A, et al. **Assessment of nerve degeneration by gadofluorine M-enhanced magnetic resonance imaging.** *Ann Neurol* 2005;57:388–95 CrossRef Medline
28. Skorpil M, Engström M, Nordell A. **Diffusion-direction-dependent imaging: a novel MRI approach for peripheral nerve imaging.** *Magn Reson Imaging* 2007;25:406–11 CrossRef Medline
29. Takagi T, Nakamura M, Yamada M, et al. **Visualization of peripheral nerve degeneration and regeneration: monitoring with diffusion tensor tractography.** *Neuroimage* 2009;44:884–92 CrossRef Medline
30. Morisaki S, Kawai Y, Umeda, et al. **In vivo assessment of peripheral nerve regeneration by diffusion tensor imaging.** *J Magn Reson Imaging* 2011;33:535–42 CrossRef Medline
31. Sun C, Hou Z, Hong G, et al. **In vivo evaluation of sciatic nerve crush injury using diffusion tensor imaging: correlation with nerve function and histology.** *J Comput Assist Tomogr* 2014;38:790–96 CrossRef Medline
32. Yamasaki T, Fujiwara H, Oda R, et al. **In vivo evaluation of rabbit sciatic nerve regeneration with diffusion tensor imaging (DTI): correlations with histology and behavior.** *Magn Reson Imaging* 2015;33:95–101 CrossRef Medline
33. Yankeelov TE, Luci JJ, Lepage M, et al. **Quantitative pharmacokinetic analysis of DCE-MRI data without an arterial input function: a reference region model.** *Magn Reson Imaging* 2005;23:519–29 CrossRef Medline
34. Rohrer M, Bauer H, Mintorovitch J, et al. **Comparison of magnetic properties of MRI contrast media solutions at different magnetic field strengths.** *Invest Radiol* 2005;40:715–24 CrossRef Medline

Spinal Cord Gray Matter Atrophy in Amyotrophic Lateral Sclerosis

M.-Ê. Paquin, M.M. El Mendili, C. Gros, S.M. Dupont, J. Cohen-Adad, and P.-F. Pradat

ABSTRACT

BACKGROUND AND PURPOSE: There is an emerging need for biomarkers to better categorize clinical phenotypes and predict progression in amyotrophic lateral sclerosis. This study aimed to quantify cervical spinal gray matter atrophy in amyotrophic lateral sclerosis and investigate its association with clinical disability at baseline and after 1 year.

MATERIALS AND METHODS: Twenty-nine patients with amyotrophic lateral sclerosis and 22 healthy controls were scanned with 3T MR imaging. Standard functional scale was recorded at the time of MR imaging and after 1 year. MR imaging data were processed automatically to measure the spinal cord, gray matter, and white matter cross-sectional areas. A statistical analysis assessed the difference in cross-sectional areas between patients with amyotrophic lateral sclerosis and controls, correlations between spinal cord and gray matter atrophy to clinical disability at baseline and at 1 year, and prediction of clinical disability at 1 year.

RESULTS: Gray matter atrophy was more sensitive to discriminate patients with amyotrophic lateral sclerosis from controls ($P = .004$) compared with spinal cord atrophy ($P = .02$). Gray matter and spinal cord cross-sectional areas showed good correlations with clinical scores at baseline ($R = 0.56$ for gray matter and $R = 0.55$ for spinal cord; $P < .01$). Prediction at 1 year with clinical scores ($R^2 = 0.54$) was improved when including a combination of gray matter and white matter cross-sectional areas ($R^2 = 0.74$).

CONCLUSIONS: Although improvements over spinal cord cross-sectional areas were modest, this study suggests the potential use of gray matter cross-sectional areas as an MR imaging structural biomarker to monitor the evolution of amyotrophic lateral sclerosis.

ABBREVIATIONS: ALS = amyotrophic lateral sclerosis; ALSFRS-R = arm-revised ALS Functional Rating Scale; CSA = cross-sectional area; GMCSA = gray matter cross-sectional area; SC = spinal cord; SCCSA = spinal cord cross-sectional area

Although amyotrophic lateral sclerosis (ALS) remains a relatively rare disease (median incidence rate was 2.08 per 100,000 in Europe for 2010,[1] the loss of autonomy, short survival rate (median survival from onset, 23–52 months),[1,2] and lack of proper treatment motivate the development of robust biomarkers to better categorize clinical phenotype and improve prognosis.[3,4] Common clinical manifestations include muscle weakness or clumsiness, atrophy, cramps, fasciculations, dysphagia, dysarthria, and respiratory symptoms such as dyspnea, orthopnea, and respiratory failure.[2] Because the clinical presentation and progression rate are highly heterogeneous,[5] it remains challenging to identify the true biologic effects of drug testing in clinical trials. Exploring new processing methods and hypotheses would promote a greater understanding of the physiopathologic processes.[6] In particular, imaging biomarkers of the spinal cord (SC) can potentially provide a relevant measure of the degeneration of lower motor neurons.[3,4]

A recent study showed that spinal cord cross-sectional area (SCCSA) measured with MR imaging improves prediction of the arm-revised ALS Functional Rating Scale (ALSFRS-R) subscore at 1 year.[3] Another study[7] established a strong link between SCCSA and the degeneration of lower motor neurons. The main limita-

Received March 30, 2017; accepted after revision August 17.

From the Faculté de Médecine (M.-Ê.P.) and Functional Neuroimaging Unit, CRIUGM (J.C.-A.), Université de Montréal, Montreal, Quebec, Canada; NeuroPoly Lab, Institute of Biomedical Engineering, Polytechnique Montreal (M.-Ê.P., C.G., S.M.D., J.C.-A.), Montreal, Quebec, Canada; Sorbonne Universités (M.M.E.M., P.-F.P.) UPMC Univ Paris 06, CNRS, INSERM, Laboratoire d'Imagerie Biomédicale, Paris, France; Department of Neurology (M.M.E.M.), Icahn School of Medicine, Mount Sinai, New York, New York; and Département des Maladies du Système Nerveux (P.-F.P.), Centre Référent Maladie Rare SLA, Hôpital de la Pitié-Salpêtrière, Paris, France.

This work was supported by the Canada Research Chair in Quantitative Magnetic Resonance Imaging (J.C.-A.), the Canadian Institute of Health Research (CIHR FDN-143263), the Canada Foundation for Innovation (32454), the Fonds de Recherche du Québec - Santé (28826), the Fonds de Recherche du Québec – Nature et Technologies (2015-PR-182754), the Natural Sciences and Engineering Research Council of Canada (435897-2013), the Quebec BioImaging Network and the Association Française contre les Myopathies, the Institut pour la Recherche sur la Moelle épinière et l'Encéphale, and the "Investissements d'avenir" (ANR-10-IAIHU-06).

Please address correspondence to Julien Cohen-Adad, PhD, Département Genie Electrique, L5610, Ecole Polytechnique, 2900 Edouard-Montpetit Blvd, Montreal, Quebec H3T 1J4, Canada; e-mail: jcohen@polymtl.ca

Indicates open access to non-subscribers at www.ajnr.org

http://dx.doi.org/10.3174/ajnr.A5427

tion of these studies is that they looked at cord atrophy, hindering the separation of the specific contribution of GM and WM atrophy. Recent advances in analysis tools for segmenting the SC GM[8] now permit such exploration.

The objective of the present study was to quantify spinal GM atrophy in ALS and to investigate its association with clinical disability at baseline and after 1 year.

MATERIALS AND METHODS

Patients

Twenty-nine patients with ALS and 22 age-matched controls were recruited at the ALS Center of the Pitié-Salpêtrière Hospital in Paris, France. Patients with ALS were diagnosed with probable ($n = 20$), laboratory probable or definite ($n = 9$) ALS according to the El Escorial criteria.[9] Exclusion criteria included important acute and chronic medical conditions interfering with the clinical evaluation, significant psychiatric or neurologic history (other than ALS for patients), and standard contraindications to MR imaging. Controls had no known neurologic disorder and no family history of neurologic diseases, and they were recruited to identify MR imaging markers in the SC that distinguish them from patients with ALS. The study was reviewed by the local ethics committee board, and written informed consent was obtained from each participant.

The following clinical assessments were conducted on patients with ALS: ALSFRS-R (total score and arm subscore [arm subscore included evaluation of handwriting, cutting food, and handling kitchen utensils]),[10] manual muscle testing (7 proximal and distal muscles of the arm were tested) by using the Medical Research Council score. The progression rate at baseline of the ALSFRS-R score was defined as Δ by the following equation:

$$\Delta = (\mathrm{ALSFRS}_{\mathrm{Max}} - \mathrm{ALSFRS}_{\mathrm{MRI}})/\tau$$

where $\mathrm{ALSFRS}_{\mathrm{Max}} = 48$, corresponding to the maximum ALSFRS-R score (ie, that of a healthy control); $\mathrm{ALSFRS}_{\mathrm{MRI}}$ is the ALSFRS-R score at the time of MR imaging; and τ is the delay (in months) between the first symptoms and the time of MR imaging. The progression rate Δ thus corresponds to the "speed" of the progression of the disease at the time of MR imaging (ie, baseline).

ALSFRS-R and manual muscle testing were performed on the same day as the MR imaging acquisition. Clinical evaluation was performed by an experienced neurologist specialized in ALS (P.-F.P., 15 years' experience).

One patient with ALS was excluded from the study because the MR imaging acquisition was interrupted for medical reasons, and 3 patients were excluded because of excessive motion during acquisition. The total number of patients used in this study was 25. Table 1 lists demographic data, Table 2 lists clinical data commonly used for prognosis, and Table 3 lists clinical scores at baseline and 1 year after.

MR Imaging Acquisition

Data were acquired on a 3T MR imaging system (Tim Trio; Siemens, Erlangen, Germany) by using the product 12-channel head, 4-channel neck, and the 3 most rostral elements of a spine coil for signal reception.

A 3D T2-weighted fast spin-echo sequence (sampling perfection with application-optimized contrasts by using different flip angle evolution, or SPACE) was acquired as an anatomic image for subsequent registration to a common template (see "Data Processing" section). Parameters were: TR, 1500 ms; TE, 120 ms; 52 sections; field of view, 280 × 280 mm^2; voxel size, 0.9 × 0.9 × 0.9 mm^3; acceleration factor, $R = 2$; and acquisition time, 3 minutes.

An axial 2D T2*-weighted multiecho gradient-echo sequence (multiecho data image combination, or MEDIC; Siemens proprietary sequence) was acquired for GM cross-sectional area (GMCSA) measurements thanks to the good white-to-gray matter contrast available in this type of sequence. Parameters were: TR, 470 ms; average TE, 17 ms; 23 sections; field of view, 180 ×

Table 1: Demographic data for the 25 patients with ALS and the 22 healthy controls

Characteristics	Controls	Patients with ALS	
		At Baseline	1-Year Follow-Up Subgroup
Number	22	25	19
Sex	11 F/11 M	6 F/19 M	3 F/16 M
Age at baseline, yr ± SD	50.9 ± 13.0	53.3 ± 10.1	52.8 ± 9.2

Note:—F indicates female; M, male.

Table 2: Clinical data commonly used as prognostic factors for the 25 patients with ALS

Clinical Data	Patients with ALS	
	Baseline	1-Year Follow-Up Subgroup
Body mass index at MRI (± SD)	23.7 ± 2.7	24.0 ± 2.7
Familial transmission	2 *SOD1* mutated	1 *SOD1* mutated
Site of onset	1 bulbar; 18 upper; 6 lower	1 bulbar; 12 upper; 6 lower
Delay from first symptom to diagnosis, mo ± SD	9.9 ± 5.6	10.7 ± 6.0

Note:—*SOD1* indicates *SuperOxide Dismutase 1* gene.

Table 3: Clinical scores[a]

	ALSFRS-R			MMT
	At MRI	Progression Rate at MRI Per Month	At 1 Year after MRI	At MRI
Total score, mean ± SD (/maximum)	37.96 ± 6.06 (/48)	0.59 ± 0.45	36.79 ± 4.84 (/48)	114.46 ± 24.36 (/140)
Arm subscore, mean ± SD (/maximum)	5.11 ± 2.20 (/8)	0.18 ± 0.14	5.74 ± 2.10 (/8)	53.71 ± 12.25 (/70)

Note:—MMT indicates manual muscle testing.

[a] Clinical scores are presented both in total (top row) and for the upper limbs only (arm subscore, bottom row). Presented clinical scores are, from left to right: the revised ALSFRS-R at the time of MRI, ALSFRS-R progression rate at MRI, ALSFRS-R at 1 year after MRI, and MMT at MRI. The progression rate represents the decline of ALSFRS-R score per month between the first onset of symptoms and the MRI.

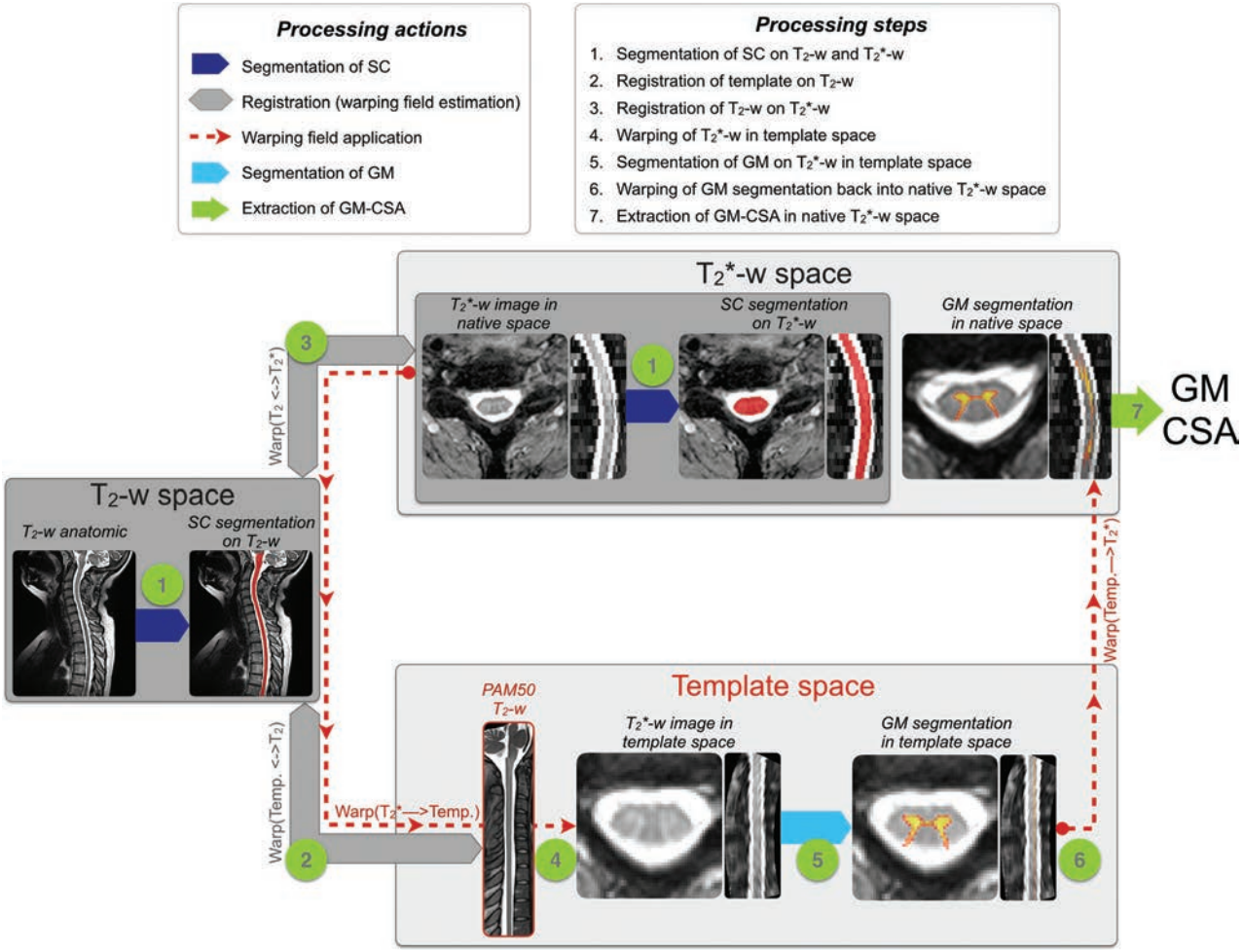

FIG 1. Processing pipeline for the GM segmentation and computation of the GMCSA.

180 mm^2; voxel size, 0.7 × 0.7 × 3 mm^3; acceleration factor, R = 2; acquisition time, 3 minutes; and intersection gap, 1.5 mm.

Acquisition parameters and .edx protocols can be downloaded from the Open Science Framework public repository (https://osf.io/9xkxx/).

Data Processing

All data were processed by using the open-source software Spinal Cord Toolbox v3.0.[11] All processing commands are available at the Open Science Framework public repository. In brief, T2-weighted and T2*-weighted images were automatically registered to a common template image, which was generated in a previous study by averaging spinal cord MRIs from 50 adult subjects.[12,13] The T2-weighted image was used to precisely identify vertebral levels, and the T2*-weighted image was used to automatically measure the GMCSA thanks to its good white-to-gray matter contrast. Figure 1 illustrates the processing pipeline, which can be broken down into 7 steps:

1) The spinal cord was automatically segmented by using "PropSeg"[14] on T2-weighted and T2*-weighted images. Note that the segmentation was slightly manually corrected when needed.

2) The PAM50 template[15] was registered to the T2-weighted anatomic data by using 3 consecutive steps: i) a section-wise rigid transformation (translation and rotation) based on the center of mass of the segmentations; ii) a nonrigid regularized registration by using the BSplineSyn algorithm[16] based on cord segmentations; and iii) a nonrigid registration by using the SyN algorithm[17] on the images (as implemented in Advanced Normalization Tools[18]).

3) The T2-weighted template registered into the T2-weighted anatomic space was then registered on the T2*-weighted image by using 3 consecutive steps: i) a section-wise regularized rigid registration[19] based on cord segmentations; ii) a nonrigid regularized registration by using the BSplineSyn algorithm on cord segmentations; and iii) a nonrigid registration by using the SyN algorithm on the images.

4) Both registrations (template to T2-weighted and T2-weighted space to T2*-weighted) output forward- and backward-warping fields. Concatenating the 2 forward-warping fields allows for warping the template (and all its elements) into the T2*-weighted space (WARP[template to T2*]), and concatenating all the backwards-warping fields allows for warping the T2*-weighted image into the template space (WARP[T2* to template]). Here, we took advantage of the second concatenation (WARP[T2* to template]) to warp the T2*-weighted image and the automatic SC segmentation into the template space.

5) The GM was automatically segmented on the T2*-weighted image in the template space. The GM segmentation was performed by using the multiatlas-based segmentation method in-

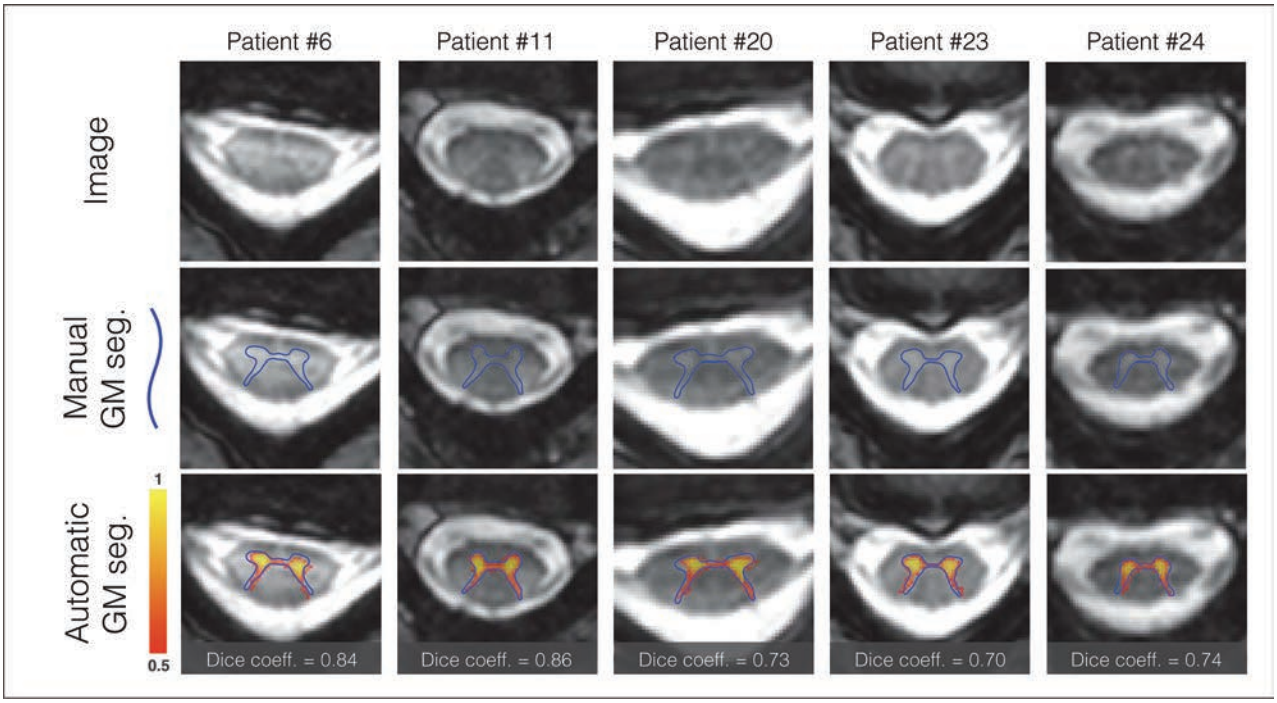

FIG 2. GM automatic segmentation and manual delineation patients with ALS. Manual delineation of the GM is displayed with the *blue line*, automatic probabilistic segmentation is shown in *red-to-yellow*. Dice coefficient comparing the automatic and manual segmentation is shown on the *bottom line*.

cluded in the Spinal Cord Toolbox.[8] The automatic GM segmentation was visually assessed for all patients. A more thorough quantitative validation has been conducted in a previous study.[8]

6) The GM segmentation was warped back into the T2*-weighted space by using the forward-warping field (WARP[template to T2*]).

7) The SCCSA and GMCSA were computed in the T2*-weighted space. The area computed for each section was corrected for the curvature of the spine by using the angle of the section with the SC centerline. Note that the cross-sectional area (CSA) was not normalized across subjects, as further discussed in the "Methodologic Considerations" section.

Statistical Analysis

Differences between Patients and Controls. All statistical analyses were performed with Python 2.7. A 1-sample Kolmogorov-Smirnov test was used to confirm that SCCSA and GMCSA followed a Gaussian distribution within the patients and controls groups. Consequently, a 2-sample Student *t* test assessed potential CSA differences between the 2 groups.

Correlation between GM Atrophy and Clinical Disability at MR Imaging (Baseline) and at 1 Year After. The association between spinal cord atrophy and clinical disability at baseline and at 1 year was investigated. The hypothesis was that atrophy of the cervical GM measured in MR imaging is associated with clinical outcome. At baseline, Pearson correlation coefficients between CSA of GM and SC and ALSFRS-R/manual muscle testing scores were computed. Similarly, Pearson correlation coefficients were computed between GMCSA and ALSFRS-R score and between SCCSA and ALSFRS-R score at 1 year after baseline with the 19 patients with ALS who were available to follow-up (referred to as the 1-year cohort). GMCSA and SCCSA values were averaged across the C4–C6 vertebral levels to be more specific with the arm subscore, which is associated with shoulder abduction (myotome C5), elbow flexion (myotome C6), and wrist extension (myotome C7).

Prediction of Clinical Disability at 1 Year After Baseline. The prediction of clinical disability was performed on the 1-year cohort. Regression trees[20] were used to evaluate the potential of MR imaging biomarkers to predict the total ALSFRS-R score at 1 year after MR imaging. Regression trees as used here are a supervised learning method aimed at predicting the ALSFRS-R score at 1 year by learning simple decision rules inferred from clinical predictors (sex, age, body mass index, site of onset, delay between first symptom and diagnosis, ALSFRS progression rate at baseline [see equation 1], and ALSFRS-R at baseline) and MR imaging measures. Several models were tested with 1) clinical predictors only; 2) clinical predictors and SCCSA; and 3) clinical predictors, GMCSA, and the ratio of WM CSA to GMCSA. MR imaging biomarkers were progressively added to the clinical predictors to test the impact of each MR imaging measure. The hypothesis was that at 1 year, the prediction score of disability would be higher when adding MR imaging measures at baseline to clinical predictors. Here, WM CSA was used instead of SCCSA to avoid colinearity between predictors (because SCCSA = WM CSA + GMCSA). As in the previous subsection, GMCSA and WM CSA values were averaged across the C4–C6 vertebral levels.

A leave-one-out cross-validation was performed to evaluate how each prediction model will generalize to a new dataset. A

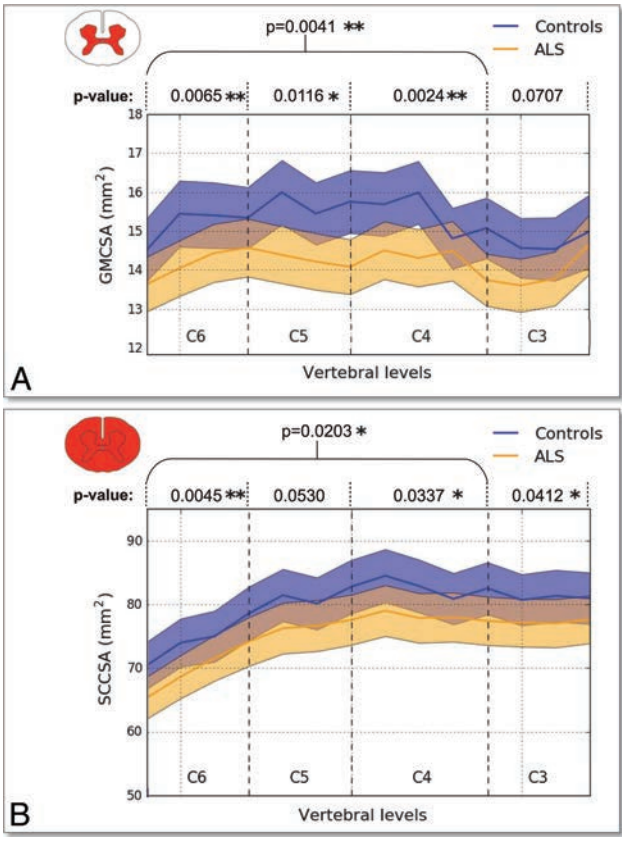

FIG 3. GMCSA and SCCSA measured on controls and patients with ALS between the C6–C3 vertebral levels. GMCSA (*A*) and SCCSA (*B*) averaged within group and plot against the cervical SC axis. Overall, a stronger intergroup difference can be observed for GMCSA. *Asterisk* ($P \leq .05$) and *double asterisk* ($P \leq .01$) at specific vertebral levels indicate significant differences between patients with ALS and controls according to Student *t* test *P* values representing control-to-patient differences in GMCSA and SCCSA for each cervical level between C6 and C3 and across levels.

patient was randomly discarded from the list of patients, and a new prediction model was created from the remaining $(n - 1)$ patients. From this model, we computed the prediction error, which is defined as the difference between the true and the predicted value of the ALSFRS-R score. This procedure was run 25 times, and the distribution of error was reported.

RESULTS

Data Processing

The proposed processing pipeline was fully automatic. The results have been visually inspected by an experimented rater, and a manual correction was only needed for the SC segmentation of 8 patients with ALS out of the 47 processed subjects (22 controls and 25 patients). The correction took approximately 1 minute per subject and consisted of a slight manual adjustment of the SC segmentation on $T2^*$-weighted images. The accuracy of the GM automatic segmentation has been validated in 5 randomly selected patients with ALS, with a Dice coefficient of 0.708. Figure 2 shows a visual illustration of the GM segmentation.

Differences between Patients and Controls

Figure 3 shows the average (± SD) of GMCSA (Fig 3*A*) and SCCSA (Fig 3*B*) in controls (*blue*) and patients with ALS (*orange*) across the SC cervical axis. Qualitatively, a larger difference between patients and controls is observed for GMCSA compared with SCCSA (7.2% difference for GMCSA versus 3.6% difference for SCCSA averaged between the C4–C6 vertebral levels, *t* test *P* values for each vertebral level are shown in Fig 3). Figure 4 shows a boxplot distribution of GMCSA and SCCSA averaged between the C4–C6 vertebral levels.

Correlation between GM Atrophy and Clinical Disability at MR Imaging (Baseline) and at 1 Year After

A correlation study was performed between clinical disability (at baseline, then at 1 year after MR imaging) and MR imaging biomarkers of grouped vertebral levels (C4–C6) (Table 4). GMCSA and SCCSA measures revealed significant correlations with the ALSFRS-R subscore at baseline and at 1 year after, suggesting an association between cervical GM atrophy and clinical disability of the upper limbs at baseline as well as after 1 year. For the manual muscle testing arm subscore at baseline, significant correlations were only found for GMCSA, although *P* values between GMCSA and SCCSA were very close (.049 versus .054 [Table 4]).

Prediction of Clinical Disability at 1 Year After Baseline

The purpose of this analysis was to investigate the benefits of adding MR imaging biomarkers to clinical predictors in a generalizable model of clinical disability prediction.

Table 5 shows the results of regression trees between total ALSFRS-R score at 1 year after baseline and several predictors frequently used in practice, with or without MR imaging biomarkers. Figure 5 shows the distribution of the prediction error for the 3 prediction models based on a leave-one-out cross-validation, suggesting that the prediction model including MR imaging biomarkers results in a more accurate score prediction. The model including all the proposed MR imaging biomarkers predicted the ALSFRS-R score with an average error of 1.63 ± 8.42 versus 2.05 ± 12.97 with clinical predictors only.

DISCUSSION

This study focused on using the CSA of the cervical SC GM in patients with ALS for 1) discriminating between patients with ALS and controls; 2) correlating CSA with clinical scores (ALSFRS-R and manual muscle testing); and 3) predicting clinical score (ALSFRS-R) at 1-year follow-up. The following subsections will compare our results with the previous literature and discuss their limitations and relevance for clinical implications.

GM Atrophy Detected in Patients with ALS

SCCSA exhibited significant differences between patients with ALS and healthy controls, confirming the results obtained by another study.[3] More interestingly, GMCSA showed larger differences between the 2 groups ($P = .004$ for GMCSA versus .02 for SCCSA at the C4–C6 vertebral levels), suggesting that GMCSA is a more sensitive marker of atrophy in ALS and that cord atrophy in ALS is predominantly driven by lower motor neuron degeneration. Although WM is expected to degenerate as a secondary effect of upper motor neuron degeneration, gliosis and myelin debris forming in the SC WM might somewhat lower the sensitivity of global cord atrophy.[21,22]

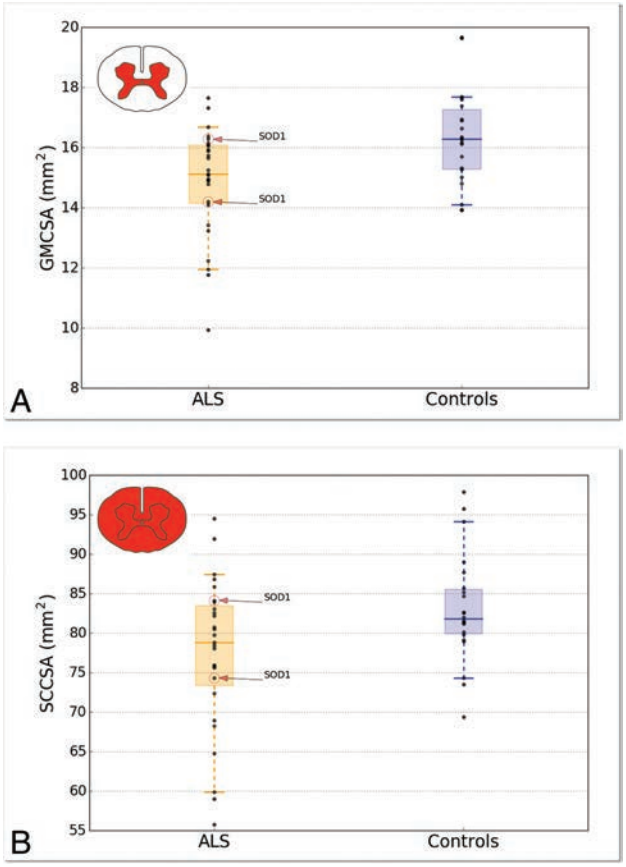

FIG 4. Boxplot distribution of GMCSA (*A*) and SCCSA (*B*) averaged between the C4–C6 vertebral levels. Each *dark point* represents an individual value. The median is represented as a *thick horizontal line* and the interquartile range as a *light rectangle*. The *horizontal bar* at both extremities of the whiskers represent the 5th and 95th percentiles. The 2 patients presenting the *SOD1* gene are identified in the plot.

In addition, the control-to-patient difference was larger at the C4–C6 vertebral level region (Fig 3), which is the site of large pools of motor neurons. Larger GM atrophy at the C4–C6 vertebral levels could be explained by a larger absolute number of atrophied motor neurons at this level and/or by a higher sensitivity of the MR imaging–based GMCSA measure at this level because of the increased size of the structure that facilitates delineation of the GM interface. Further studies covering a larger portion of the spinal cord would shed light on these possible explanations.

Table 4: Correlation coefficients between CSA (GM and SC) and clinical scores at baseline and at 1 year[a]

	At Baseline		At 1 Year
Predictors	ALSFRS-R Subscore	MMT Arm Subscore	ALSFRS-R Subscore
GMCSA	$R = 0.56$ $P = .004$[b]	$R = 0.40$ $P = .049$[a]	$R = 0.48$ $P = .035$[c]
SCCSA	$R = 0.55$ $P = .005$[b]	$R = 0.40$ $P = .054$	$R = 0.54$ $P = .017$[c]

Note:—MMT indicates manual muscle testing.
[a] CSA was averaged across the C4–C6 vertebral levels. Clinical scores included: 1) ALSFRS-R at baseline; 2) MMT subscores at baseline; and 3) ALSFRS-R subscore at 1 year.
[b] Significant ($P \leq .01$).
[c] Significant ($P \leq .05$).

From a clinical perspective, having SCCSA and GMCSA highly correlated raises the question of the relevance of measuring GMCSA in patients with ALS as a diagnostic measure, especially given that it is more difficult to reliably measure GMCSA from standard clinical scans because of the need for high axial resolution and sufficient GM/WM contrast-to-noise. Nevertheless, having access to a more specific assessment of GM atrophy still has potential for monitoring the efficiency of new drugs, though this has not been tested here.

GM Atrophy Correlates with Clinical Disability at MR Imaging and 1 Year After

As shown in Table 4, GMCSA seems to be a relevant biomarker of clinical disability at vertebral levels C4–C6 (ALSFRS-R and manual muscle testing arm at baseline, $P = .004$ and $P = .05$, respectively; ALSFRS-R at 1 year, $P = .03$). SCCSA also reflected clinical disability as previously shown,[3] though with lower sensitivity than GMCSA. A previous study[7] established a strong link between SCCSA and lower motor neuron degeneration by relating motor-evoked potential amplitude of the adductor digiti minimi and deltoid, respectively, with cord atrophy at spinal levels C8 and C5 (here, it was not possible to study the C8 spinal level; see "Limitations" section). However, combining advanced image processing and better MR imaging pulse sequences is promising to investigate the effect of GM atrophy on muscle-specific deficits in the low thoracic and lumbar cord.[23] The ability to isolate lower motor neuron from upper motor neuron contribution in ALS might provide additional information for understanding the pathogenesis of the disease.

Prediction of Clinical Disability at 1 Year After Baseline

A significant association was found between GMCSA (measured at baseline) and the ALSFRS-R score at 1 year after MR imaging acquisition ($P = .03$). However, it was not possible to perfectly fit a regression model to predict clinical disability at 1 year by using clinical biomarkers and MR imaging measures (CSA), which is challenging regarding the heterogeneity of the present ALS cohort in terms of clinical score and site of onset. The best prediction score was obtained by combining MR imaging measures (GM, WM, and ratio of WM CSA to GMCSA). Therefore, this suggests that the association of MR imaging measures could be helpful to predict the evolution of clinical disability for patients with ALS ($R^2 = 0.54$ without versus $R^2 = 0.74$ with MR imaging measures). Evaluated with a leave-one-out cross-validation, prediction accuracy and generalization were improved by including MR imaging biomarkers in the prediction model (error = 1.63 ± 8.42 with versus 2.05 ± 12.97 without MR imaging measures). More complex models such as deep learning would be a potential alternative to achieve a more specific prediction.[24]

Methodologic Considerations

Classical Bias in ALS Studies. Because patients with ALS with heavy respiratory symptoms could not be recruited for the study, a lack of external validity needs to be pointed out. By recruiting subjects in a less drastic state (from a medical standpoint), a certain selection bias takes place that limits generalization to the whole ALS population and affects the power of the study. Moreover, the recruited population included mostly

Table 5: Results of regression tree predictions to make prediction of total ALSFRS-R score at 1 year after MRI with several clinical and MRI predictors[a]

Predictors	Coefficient of Determination R^2 (Best Value = 1.0)	Mean Squared Error (Best Value = 0.0)
Clinical predictors	0.54	41.87
Clinical predictors + SCCSA	0.72	25.39
Clinical predictors + GMCSA + WMCSA/GMCSA	0.74	23.77

Note:—WMCSA indicates white matter cross-sectional area.

[a] GMCSA, WMCSA, and SCCSA are averaged across the C4–C6 vertebral levels. Clinical predictors include age, body mass index, sex, site of onset, delay between first symptoms and diagnosis, total ALSFRS-R score at baseline, and total ALSFRS-R score progression rate at baseline.

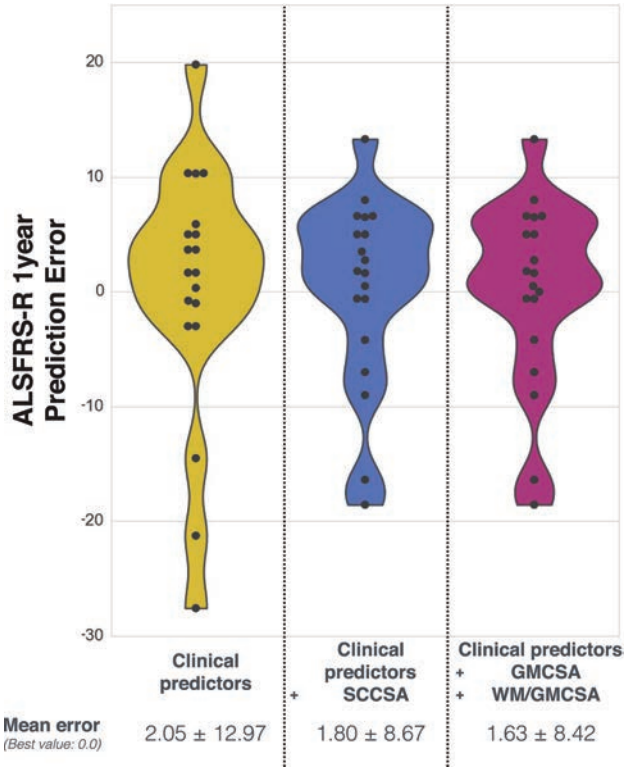

FIG 5. Prediction error on the ALSFRS-R at 1 year, from a leave-one-out cross-validation with regression trees. Results are compared between the regression model including clinical predictors (left distribution plot), clinical predictors + SCCSA (middle distribution plot), and clinical predictors + GMCSA + WM/GMCSA (right distribution plot), where each point represents 1 iteration of the leave-one-out cross-validation. The best value is at 0.

probable patients with ALS ($n = 18$) and only a few definite patients with ALS ($n = 7$), which may have introduced heterogeneity in the tested ALS population and thus impacted the statistical analyses. However, further analysis performed with the 18 probable patients with ALS led to a correlation between GMCSA and ALSFRS-R of $R = 0.61$ and $P = .006$ (versus $R = 0.56$ and $P = .004$ when including all patients with ALS).

Vertebral Levels. Establishing a vertebral region that maximizes atrophy across patients with ALS was not feasible here because of the large interpatient variability. Consequently, statistical analyses were conducted for each vertebral level between C3–C6. The average CSAs across the C4–C6 vertebral levels was also studied to maximize the sensitivity to clinical markers of the brachial plexus.

In comparison with previous works,[3] which included levels C2–T6, the present study only focused on the cervical region from C3–C6 because of the poor quality of the T2*-weighted images below C6 caused by respiratory-related dynamic B0 field variations.[25] Thus, the exclusion of the C7 vertebral level slightly restricted the study of the hand muscle deficit.[7] Moreover, the exclusion of the lumbar and thoracic regions (unavailable in the T2*-weighted images) precluded studying the correlation between GMCSA and the total ALSFRS-R score, which includes a clinical evaluation of the lower limbs. Optimized MR imaging sequences now provide the possibility to image the thoracic and lumbar GM with satisfactory quality[23] and should be investigated in future studies.

Measuring CSA with MR Imaging. Being able to measure spinal GM atrophy has potential applications in other diseases, such as spinal muscular atrophy.[26] Furthermore, an original aspect of the present study is the fully automatic segmentation of the cord and its GM, providing minimum user bias and facilitating the reproducibility of the current technique to other centers (software and processing scripts were made freely available). Previous studies have validated the accuracy of these segmentation methods for the SC[14,27] and the GM,[8,28] including in patients with multiple sclerosis and degenerative cervical myelopathy.[28] In particular, the GM segmentation used in this study resorts to nonlinear deformations to match the shape of atrophic cord exhibited by patients with ALS. The accuracy has been further validated in the present study in 5 randomly selected patients with ALS and showed satisfactory results (Dice coefficient in the GM = 0.708) in comparison with healthy controls from a previous study[8] (Dice coefficient in the GM = 0.711).

Whereas previous studies have reported that the CSA of the SC is associated with morphologic features such as brain volume[29] and total intracranial volume,[30] the correlations were mild, and there is no clear consensus as to what is the best normalization method to use[31]; several published studies have not performed CSA normalization,[3,26,31-33] and neither did we in the present study. Future work could further investigate methods for normalization, and specifically for the GMCSA.

As investigated in a previous study,[30] age and sex could affect both SC and GMCSA. In the present study, the controls and patients were age-matched but not sex-matched (number of women, 6 with ALS versus 11 controls). However, the larger proportion of women in the control group would in fact decrease the sensitivity to detect a CSA difference between controls and patients, given that both SC and GM are smaller in women compared with men.[30]

Although it would have been relevant to measure CSA in the lateral and anterior funiculi, the current MR imaging protocol, which is based on T2*-weighted contrast, made it impossible to distinguish the anterior and lateral fasciculus from the rest of the WM tissue. Therefore, it was not feasible to measure specific CSAs of these tracts from our data. Recent work combining multiparametric MR imaging at an ultra-high field showed promising re-

sults for isolating specific SC tracts, opening the door to such evaluation.[34]

CONCLUSIONS

Gray matter atrophy as measured noninvasively with MR imaging correlates with clinical disability in ALS at baseline and at 1-year follow-up. Although efforts toward the development of sensitive and reliable biomarkers for ALS need to be pursued and confirmed in larger cohorts, the present study offers an encouraging incentive about the relevance of spinal cord gray matter cross-sectional area. This article includes a downloadable link to the MR imaging acquisition and processing protocol to enable other researchers to reproduce the entirety of the analysis performed here. We believe these efforts are critical not only for transparency, but also for standardizing spinal cord imaging biomarkers to help assess their reliability and make them more amenable to clinicians.

ACKNOWLEDGMENTS

We would like to acknowledge all members of the NeuroPoly Lab, especially Benjamin De Leener and Gabriel Mangeat for the useful discussions, and Dominique Eden for the English review. This study was supported by the Association Française contre les Myopathies-Téléthon (AFM-Téléthon) and the Institut pour la Recherche sur la Moelle épinière et l'Encéphale (IRME). The research leading to these results has also received funding from the program "Investissements d'Avenir" ANR-10-IAIHU-06. We thank the neurologists of the Paris ALS center who participated in the recruitment of the patients in the study: Drs. Nadine Le Forestier, Vincent Meininger, Gaelle Bruneteau; François Salachas, Maria del Mar Amador, and Rabab Debs. We thank Sophie Blancho (IRME) for her help in the management and coordination of the study. We deeply thank the subjects who participated in this research.

Disclosures: Marie-Ève Paquin—*RELATED*: *Grant*: Canada Research Chair in Quantitative Magnetic Resonance Imaging (JCA), Canadian Institute of Health Research (CIHR FDN-143263), Canada Foundation for Innovation (32454), Fonds de Recherche du Québec – Santé (28826), Fonds de Recherche du Québec – Nature et Technologies (2015-PR-182754), Natural Sciences and Engineering Research Council of Canada (435897-2013), Quebec BioImaging Network*. Mohamed M. El Mendili—*RELATED: Grant*: Association Française contre les Myopathies-Téléthon (AFM-Téléthon), Institut pour la Recherche sur la Moelle épinière et l'Encéphale (IRME), program "Investissements d'Avenir" ANR-10-IAIHU-06, *Comments*: The funders had no role in study design, data collection and analysis, decision to publish, or preparation of the manuscript*. Charley Gros—*RELATED*: *Grant*: Canada Research Chair in Quantitative Magnetic Resonance Imaging (JCA), Canadian Institute of Health Research (CIHR FDN-143263), Canada Foundation for Innovation (32454), Fonds de Recherche du Québec – Santé (28826), Fonds de Recherche du Québec – Nature et Technologies (2015-PR-182754), Natural Sciences and Engineering Research Council of Canada (435897-2013), Quebec BioImaging Network*. Sara Dupont—*RELATED*: *Grant*: Canada Research Chair in Quantitative Magnetic Resonance Imaging (JCA), Canadian Institute of Health Research, (CIHR FDN-143263), Canada Foundation for Innovation (32454), Fonds de Recherche du Québec – Santé (28826), Fonds de Recherche du Québec – Nature et Technologies (2015-PR-182754), Natural Sciences and Engineering Research Council of Canada (435897-2013), Quebec BioImaging Network*. Julien Cohen-Adad—*RELATED*: *Grant*: Canadian Institutes of Health Research*. *Money paid to the institution.

REFERENCES

1. Chiò A, Logroscino G, Traynor BJ, et al. **Global epidemiology of amyotrophic lateral sclerosis: a systematic review of the published literature.** *Neuroepidemiology* 2013;41:118–30 CrossRef Medline
2. Blumenfeld H. *Neuroanatomy through Clinical Cases.* Sunderland, Massachusetts: Sinauer Associates; 2010
3. El Mendili MM, Cohen-Adad J, Pelegrini-Issac M, et al. **Multi-parametric spinal cord MRI as potential progression marker in amyotrophic lateral sclerosis.** *PLoS One* 2014;9:e95516 CrossRef Medline
4. Turner MR, Benatar M. **Ensuring continued progress in biomarkers for amyotrophic lateral sclerosis.** *Muscle Nerve* 2015;51:14–18 CrossRef Medline
5. Swinnen B, Robberecht W. **The phenotypic variability of amyotrophic lateral sclerosis.** *Nat Rev Neurol* 2014;10:661–70 CrossRef Medline
6. Turner MR, Verstraete E. **What does imaging reveal about the pathology of amyotrophic lateral sclerosis?** *Curr Neurol Neurosci Rep* 2015;15:45 CrossRef Medline
7. Cohen-Adad J, El Mendili MM, Morizot-Koutlidis R, et al. **Involvement of spinal sensory pathway in ALS and specificity of cord atrophy to lower motor neuron degeneration.** *Amyotroph Lateral Scler Frontotemporal Degener* 2013;14:30–38 CrossRef Medline
8. Dupont SM, De Leener B, Taso M, et al. **Fully-integrated framework for the segmentation and registration of the spinal cord white and gray matter.** *Neuroimage* 2017;150:358–72 CrossRef Medline
9. Brooks BR, Miller RG, Swash M, et al. **El Escorial revisited: revised criteria for the diagnosis of amyotrophic lateral sclerosis.** *Amyotroph Lateral Scler Other Motor Neuron Disord* 2000;1:293–99 CrossRef Medline
10. Cedarbaum JM, Stambler N, Malta E, et al. **The ALSFRS-R: a revised ALS functional rating scale that incorporates assessments of respiratory function.** *J Neurol Sci* 1999;169:13–21 CrossRef Medline
11. De Leener B, Lévy S, Dupont SM, et al. **SCT: Spinal Cord Toolbox, an open-source software for processing spinal cord MRI data.** *Neuroimage* 2017;145(Pt A):24–43 CrossRef Medline
12. Fonov VS, Le Troter A, Taso M, et al. **Framework for integrated MRI average of the spinal cord white and gray matter: the MNI–Poly–AMU template.** *Neuroimage* 2014;102 Pt 2:817–27 CrossRef Medline
13. De Leener B, Fonov V, Collins DL, et al. **PAM50: multimodal template of the brainstem and spinal cord compatible with the ICBM152 space.** In: *Proceedings of the International Society for Magnetic Resonance in Medicine 25th Annual Meeting and Exhibition,* Honolulu, Hawaii. April 22–27, 2017
14. De Leener B, Kadoury S, Cohen-Adad J. **Robust, accurate and fast automatic segmentation of the spinal cord.** *Neuroimage* 2014;98:528–36 CrossRef Medline
15. De Leener B, Taso M, Fonov V, et al. **Fully-integrated T1, T2, T2*, white and gray matter atlases of the spinal cord.** In: *Proceedings of the International Society for Magnetic Resonance in Medicine 24th Annual Meeting and Exhibition*, Singapore. May 7–8, 2016
16. Tustison NJ, Avants BB. **Explicit B-spline regularization in diffeomorphic image registration.** *Front Neuroinform* 2013;7:39 CrossRef Medline
17. Avants BB, Epstein CL, Grossman M, et al. **Symmetric diffeomorphic image registration with cross-correlation: evaluating automated labeling of elderly and neurodegenerative brain.** *Med Image Anal* 2008;12:26–41 CrossRef Medline
18. Avants BB, Tustison NJ, Stauffer M, et al. **The Insight ToolKit image registration framework.** *Front Neuroinform* 2014;8:44 CrossRef Medline
19. Cohen-Adad J, Levy S, Avants B. **Slice-by-slice regularized registration for spinal cord MRI: SliceReg.** In: *Proceedings of the International Society for Magnetic Resonance in Medicine 23rd Annual Meeting and Exhibition,* Toronto, Canada. May 30–June 5, 2015
20. Breiman L, Friedman JH, Olshen RA, et al. *Classification and Regression Trees.* Belmont, California: Wadsworth International Group; 1984
21. Kushner PD, Stephenson DT, Wright S. **Reactive astrogliosis is widespread in the subcortical white matter of amyotrophic lateral sclerosis brain.** *J Neuropathol Exp Neurol* 1991;50:263–77 CrossRef Medline
22. Sitte HH, Wanschitz J, Budka H, et al. **Autoradiography with [3 H]**

PK11195 of spinal tract degeneration in amyotrophic lateral sclerosis. *Acta Neuropathol* 2001;101:75–78 Medline
23. Yiannakas MC, Kakar P, Hoy LR, et al. **The use of the lumbosacral enlargement as an intrinsic imaging biomarker: feasibility of grey matter and white matter cross-sectional area measurements using MRI at 3T.** *PLoS One* 2014;9:e105544 CrossRef Medline
24. van der Burgh HK, Schmidt R, Westeneng HJ, et al. **Deep learning predictions of survival based on MRI in amyotrophic lateral sclerosis.** *Neuroimage Clin* 2017;13:361–69 CrossRef Medline
25. Verma T, Cohen-Adad J. **Effect of respiration on the B0 field in the human spinal cord at 3T.** *Magn Reson Med* 2014;72:1629–36 CrossRef Medline
26. El Mendili MM, Lenglet T, Stojkovic T, et al. **Cervical spinal cord atrophy profile in adult SMN1-linked SMA.** *PLoS One* 2016;11: e0152439 CrossRef Medline
27. Yiannakas MC, Mustafa AM, De Leener B, et al. **Fully automated segmentation of the cervical cord from T1-weighted MRI using PropSeg: application to multiple sclerosis.** *Neuroimage Clin* 2016; 10:71–77 CrossRef Medline
28. Dupont SM, Martin AR, Stikov N, et al. **Fully automatic segmentation of spinal cord gray matter on patients with degenerative cervical myelopathy**. In: *Proceedings of the International Society for Magnetic Resonance in Medicine 25th Annual Meeting and Exhibition.* Honolulu, Hawaii; April 22–27, 2017
29. Engl C, Schmidt P, Arsic M, et al. **Brain size and white matter content of cerebrospinal tracts determine the upper cervical cord area: evidence from structural brain MRI.** *Neuroradiology* 2013;55:963–70 CrossRef Medline
30. Papinutto N, Schlaeger R, Panara V, et al. **Age, gender and normalization covariates for spinal cord gray matter and total cross-sectional areas at cervical and thoracic levels: a 2D phase sensitive inversion recovery imaging study.** *PLoS One* 2015;10:e0118576 CrossRef Medline
31. Healy BC, Arora A, Hayden DL, et al. **Approaches to normalization of spinal cord volume: application to multiple sclerosis.** *J Neuroimaging* 2012;22:e12–e19 CrossRef Medline
32. Behmanesh B, Gessler F, Quick-Weller J, et al. **Regional spinal cord atrophy is associated with poor outcome after surgery on intramedullary spinal cord ependymoma: a new aspect of delayed neurological deterioration.** *World Neurosurg* 2017;100:250–55 CrossRef Medline
33. Kearney H, Yiannakas MC, Abdel-Aziz K, et al. **Improved MRI quantification of spinal cord atrophy in multiple sclerosis.** *J Magn Reson Imaging* 2014;39:617–23 CrossRef Medline
34. Taso M, Massire A, Besson P, et al. **Towards in vivo spinal cord cyto- and myelo-architecture deciphering using multi-modal MRI parcellation at 7T.** In: *Proceedings of the International Society for Magnetic Resonance in Medicine 25th Annual Meeting and Exhibition,* Honolulu, Hawaii. April 22–27, 2017

Long-Term Effectiveness of Direct CT-Guided Aspiration and Fenestration of Symptomatic Lumbar Facet Synovial Cysts

V.N. Shah, N.D. von Fischer, C.T. Chin, E.L. Yuh, M.R. Amans, W.P. Dillon, and C.P. Hess

ABSTRACT

BACKGROUND AND PURPOSE: Lumbar facet synovial cysts are commonly seen in facet degenerative arthropathy and may be symptomatic when narrowing the spinal canal or compressing nerve roots. The purpose of this study was to analyze the safety, effectiveness, and long-term outcomes of direct CT-guided lumbar facet synovial cyst aspiration and fenestration for symptom relief and for obviating an operation.

MATERIALS AND METHODS: We retrospectively reviewed the medical records and imaging studies of 64 consecutive patients between 2006 and 2016 who underwent 85 CT-guided lumbar facet synovial cyst fenestration procedures in our department. We recorded patient demographics, lumbar facet synovial cyst imaging characteristics, presenting symptoms, change in symptoms after the procedure, and whether they underwent a subsequent operation. We also assessed long-term outcomes from the medical records and via follow-up telephone surveys with patients.

RESULTS: Direct CT-guided lumbar facet synovial cyst puncture was technically successful in 98% of procedures. At first postprocedural follow-up, 86% of patients had a complete or partial symptomatic response. During a mean follow-up of 49 months, 56% of patients had partial or complete long-term relief without the need for an operation; 44% of patients underwent an operation. Patients with calcified, thick-rimmed, or low T2 signal intensity cysts were less likely to respond to the procedure and more likely to need an operation.

CONCLUSIONS: CT-guided direct lumbar facet synovial cyst aspiration and fenestration procedures are safe, effective, and minimally invasive for symptomatic treatment of lumbar synovial facet cysts. This procedure obviates an operation in a substantial number of patients, even at long-term follow-up, and should be considered before surgical intervention.

ABBREVIATION: LFSC = lumbar facet joint synovial cyst

Lumbar facet joint synovial cysts (LFSCs) are synovial lined outpouchings that arise from the facet joint capsule.[1,2] While LFSCs may occur at any lumbar level, they most commonly occur at the L4–L5 facets in degenerative facet arthropathy.[1,3-5] LFSCs have been reported to be present in 0.7%–2.0% of lumbar cross-sectional imaging studies.[6,7] On imaging, LFSCs are well-circumscribed masses contacting or in immediate proximity to the facet joint. Cysts typically demonstrate a thin or thick hypointense signal rim on MR imaging. The internal cyst signal is most commonly T1 hypointense and T2 hyperintense, though these features can be variable on the basis of intracystic protein content, blood products, calcification, or gas.[5,6]

LFSCs may present with radiculopathy secondary to inflammation or encroachment on nerve roots within the spinal canal or neural foramina or with axial low back pain when arising as a sequela of facet disease. Traditional management consists of laminectomy and surgical resection of the cysts, but in segmental instability or symptomatic spondylolisthesis, facetectomy and posterior spinal fusion are also required.[8,9] Fluoroscopically guided cyst inflation and indirect rupture have been described as a minimally invasive treatment for symptomatic LFSCs with variable outcomes (23%–72% success rates) and follow-up periods (6–44 months).[5,7,10-14] More recently, direct CT-guided LFSC injection and rupture in a small number of patients have also been described for nonsurgical management.[15]

The aim of our study was to evaluate the effectiveness of direct CT-guided aspiration and fenestration of LFSCs by assessing short-term postprocedural symptom relief and whether an operation could be avoided during long-term follow-up. As a second-

Received May 1, 2017; accepted after revision August 19.

From the Department of Radiology and Biomedical Imaging, University of California, San Francisco, San Francisco, California.

Paper previously presented at: American Society of Neuroradiology Annual Meeting and the Foundation of the ASNR Symposium, April 25–30, 2015; Chicago, Illinois.

V.N. Shah and N.D. von Fischer contributed equally to this work.

Please address correspondence to Vinil Shah, MD, 505 Parnassus Ave, L352, San Francisco, CA 94143-0628; e-mail: vinil.shah@ucsf.edu

http://dx.doi.org/10.3174/ajnr.A5428

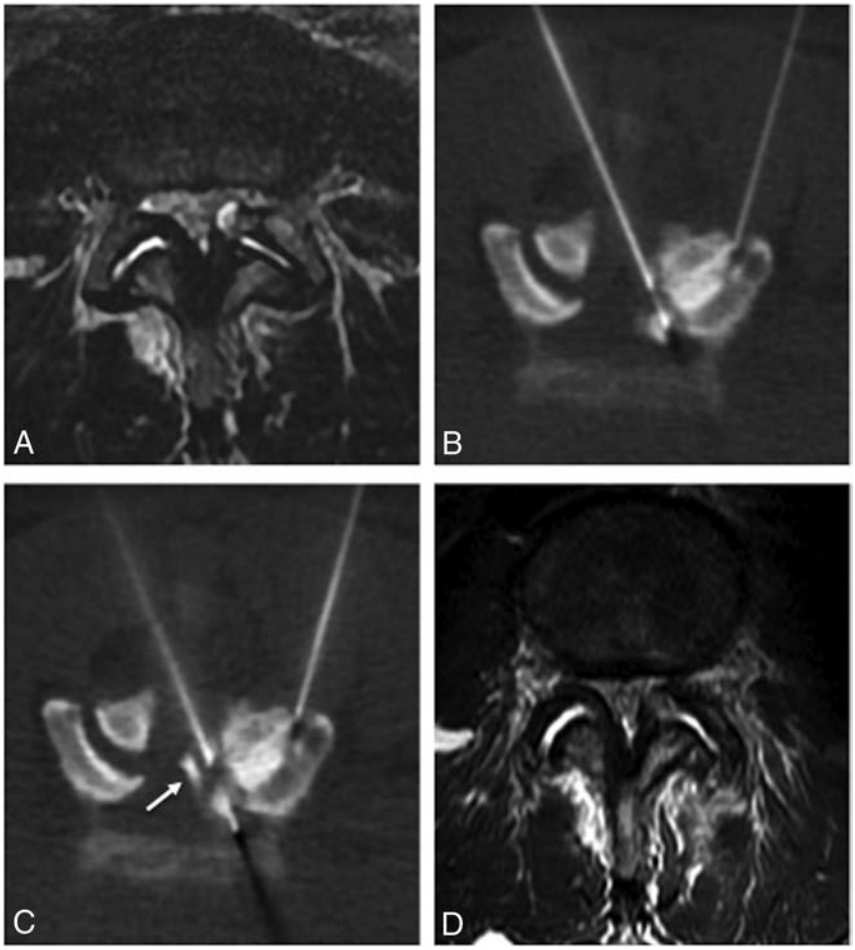

FIG 1. Successful CT-guided cyst puncture, aspiration, and fenestration. *A*, Axial T2-weighted MR image demonstrates bilateral L4–5 facet synovitis and a thin-rimmed T2-hyperintense cyst arising from the left L4–5 facet joint. *B*, Intraprocedural CT image shows contrast opacification of the cyst via injection into a 22-ga spinal needle placed within the left L4–5 facet joint (step 1). A second 22-ga spinal needle has been advanced coaxially into the cyst via a translaminar approach (step 2). *C*, CT image obtained after cyst aspiration and repeat fenestration demonstrates successful cyst perforation with leakage of contrast into the epidural space (*arrow*, step 3). *D*, Follow-up MR imaging shows resolution of the treated cyst.

ary objective, we sought to determine whether the patient's presenting symptoms, LFSC imaging characteristics, or injection technique could be used to predict response.

MATERIALS AND METHODS

Study Design

The institutional review board approved our retrospective review of patients who underwent CT-guided LFSC aspiration and fenestration during a 10-year period from 2006 to 2016. Patients were identified using a search of our radiology information system. We performed a detailed medical record review and recorded patient demographics, presenting symptoms, change in symptoms at initial follow-up, and whether an operation was performed during the 6-month postprocedural interval. Additionally, we reviewed the most recent preprocedural MR imaging to identify the level of the LFSC, determine its size using the largest diameter on either sagittal or axial images, and record its T2-signal characteristics. We also recorded CT characteristics of the cyst from images obtained during the procedure. For those patients in whom a postprocedural MR imaging or CT was available, we also noted whether the cyst persisted or recurred. Finally, we assessed long-term outcomes as documented in the patient's medical record and via a follow-up telephone survey.

Cyst Aspiration and Perforation Technique

All CT-guided LFSC aspiration and fenestration procedures were performed at our outpatient imaging center by 1 of 6 neuroradiologists experienced in spine intervention (range of experience, 3–34 years; mean, 13 years). The patient was placed in the prone position, and limited low-dose CT of the lumbar spine was performed for procedural planning. The overlying skin was marked, prepped, and draped using an aseptic technique. Local anesthesia was achieved with lidocaine 1% buffered with 8.4% sodium bicarbonate. Moderate conscious sedation was provided for most procedures. Intermittent low-dose CT was used for needle guidance. In all except 8 procedures, the parent facet joint was first accessed. One to two milliliters of a mixture of bupivacaine 0.75% and either Celestone 6 mg/mL (betamethasone sodium phosphate) or Kenalog 40 mg/mL (triamcinolone acetonide) combined with a small volume of Omnipaque 240 (iohexol; GE Healthcare, Piscataway, New Jersey) was injected to treat underlying facet arthropathy and to opacify the associated synovial cyst. Then, the LFSC was directly accessed via a contralateral interlaminar or ipsilateral transforaminal approach (depending on whether the cyst was intracanalicular or foraminal) using either a 19-, 20-, 21-, 22-, or 25-ga spinal or Chiba needle (Cook Medical, Bloomington, Indiana). After we confirmed the position of the needle tip within the LFSC, aspiration was first performed followed by repetitive forward-and-back needle motion to fenestrate the cyst wall (Fig 1). CT was then used to confirm successful decrease in the size of the LFSC and/or leakage of previously administered contrast into the epidural space. In all except 10 procedures, a separate transforaminal/interlaminar epidural injection using 1–2 mL of the steroid and anesthetic mixture was also performed at the same level to concurrently treat the patient's radiculopathy.

After the procedure, the patients were observed for at least 1 hour before discharge. The referring physician, most often an orthopedic surgeon, neurosurgeon, or pain management specialist, assessed postprocedural changes in symptoms and the decision to pursue additional therapy during short-interval follow-up.

Table 1: Demographic data

	Responders	Nonresponders	*P* Value
Age (mean) (yr)	61.5 (11.4)	59.3 (8.4)	.65[a]
Sex (No.) (%)			.34[b]
Male	21 (36)	1 (17)	
Female	37 (64)	5 (83)	
Presenting symptoms (No.) (%)			.58[b]
Radiculopathy	27 (47)	2 (33)	
Axial back pain	4 (6)	0 (0)	
Both	27 (47)	4 (67)	

[a] *P* value based on the 2-sample *t* test of the difference between means.
[b] *P* value based on a χ^2 test of the difference in proportions.

Statistical Analysis

For analysis, patients were categorized as responders (those with partial or complete symptom relief) or as nonresponders (those with no change or exacerbation of symptoms based on their first postprocedural visit with referring physicians). We tested for differences between the responders and nonresponders using the *t* test for LFSC size and patient age and the χ^2 test for sex, presenting symptoms, imaging characteristics, and injection technique. Regarding imaging characteristics, we considered cyst level, degree of canal stenosis, T2 signal intensity, and the presence of cyst calcification. *P* values of $<.05$ were considered statistically significant and *P* values of $\geq.05$ and $\leq.1$ indicated a trend toward significance. Statistical analysis was performed by using STATA data analysis and statistical software (StataCorp, College Station, Texas).

RESULTS

Study Population

During the 10-year study period, 64 patients underwent CT-guided LFSC aspiration and fenestration and were included in this investigation. The study population included 22 men and 44 women with an average age of 61 years (range, 36–86 years). Most patients presented with radiculopathy (46%) or radiculopathy with axial low back pain (48%). Three (5%) patients had a prior operation for LFSC resection and presented with recurrent symptomatic cysts. There were no significant associations between a successful outcome and age, sex, or symptoms at presentation ($P > .1$) (Table 1).

Imaging Characteristics

The mean LFSC size was 10 mm (range, 5–21 mm). The most commonly treated level of LFSC was L4–L5 (58%). There was no significant difference in the cyst size, level, or degree of central canal stenosis between the responders and the nonresponders or between those patients who required a subsequent operation and those managed conservatively ($P > .1$) (Tables 2 and 3).

Preprocedural MRIs were available for review in 60 (94%) patients. Most (67%) patients had cysts that were predominantly T2 hyperintense with a thin T2-hypointense rim. The remaining patients had T2-hyperintense cysts with a thick T2-hypointense rim (30%) or cysts that were predominantly T2 hypointense (3%). On CT, 28% of cysts were partially or completely calcified. Patients with thin-rimmed T2-hyperintense or noncalcified cysts were more likely to have a favorable response to the procedure than those patients with thick-rimmed, hypointense, or calcified cysts ($P < .05$) (Table 2). Patients with calcified cysts were more likely to have required an operation at long-term follow-up than patients with noncalcified cysts ($P = .003$, OR = 6.5) (Table 3). There was a trend toward a greater need for surgical management in patients with thick-rimmed or hypointense cysts as opposed to those with thin-rimmed T2-hyperintense cysts ($P = .07$).

Table 2: Differences in imaging characteristics of cysts between responders and nonresponders

	Responders	Nonresponders	*P* Value
LFSC size (mean) (SD) (mm)	10.1 (3.7)	9.3 (2.5)	.62[a]
Cyst level (No.) (%)			.66[b]
L1–L2	1 (2)	0 (0)	
L2–L3	3 (5)	1 (17)	
L3–L4	6 (10)	1 (17)	
L4–L5	35 (60)	2 (33)	
L5–S1	13 (22)	2 (33)	
MRI central canal stenosis (No.) (%)			.70[b]
None	19 (33)	2 (33)	
Mild	9 (15)	0 (0)	
Moderate	11 (19)	1 (17)	
Severe	19 (33)	3 (50)	
MRI signal intensity (No.) (%)			.011[b]
High T2 with a thin rim	39 (72)	1 (17)	
High T2 with a thick rim	13 (24)	5 (83)	
Low T2	2 (4)	0 (0)	
CT characteristics (No.) (%)			.027[b]
Calcified	14 (24)	4 (67)	
Not calcified	44 (76)	2 (33)	

[a] *P* value based on the 2-sample *t* test of the difference between means.
[b] *P* value based on a χ^2 test of the difference in proportions.

Table 3: Differences in imaging characteristics of cysts between patients who required surgery and those who did not at long-term follow-up

	Surgery	No Surgery	*P* Value
LFSC size (mean) (SD) (mm)	10.5 (3.9)	9.5 (3.3)	.32[a]
MRI signal intensity (No.) (%)			.07[b]
High T2 with a thin rim	11 (48)	24 (78)	
High T2 with a thick rim	11 (48)	6 (19)	
Low T2	1 (4)	1 (3)	
CT characteristics (No.) (%)			.003[b]
Calcified	12 (48)	4 (12)	
Not calcified	13 (52)	28 (88)	

[a] *P* value based on the 2-sample t test of the difference between means.
[b] *P* value based on a χ^2 test of the difference in proportions.

Postprocedural MR imaging or CT studies were available in 26 (41%) patients. In most (77%) of these patients, the treated cyst was noted to be smaller or had resolved; in 5 patients (19%) the cyst was unchanged, and in 1 patient (3.9%) the treated cyst was noted to have increased in size.

Injection Technique and CT Fenestration Success

Direct CT-guided LFSC puncture and fenestration were technically successful in 81 (98%) procedures performed with no complications. In 1 patient, the calcified nature of bilateral L5–S1 cysts precluded direct puncture (Fig 2). In another, a foraminal synovial cyst could not be successfully accessed due to overlying bone. Most (94%) calcified cysts, however, were successfully fenestrated. Facet joint injections were performed before direct cyst fenestration in most of these patients. The ipsilateral facet joint was injected in 56 (88%) patients to opacify the LFSC and to treat under-

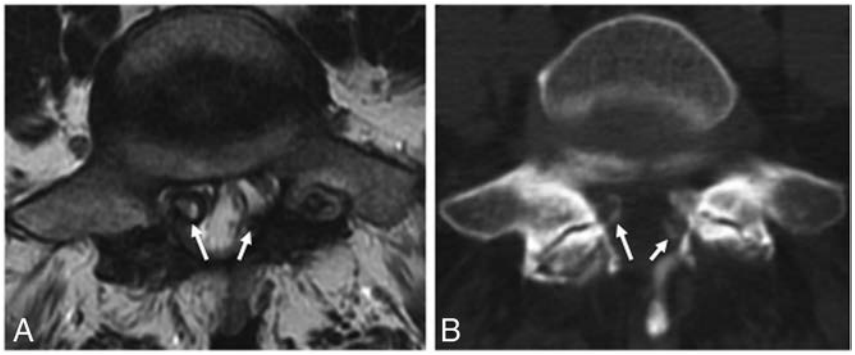

FIG 2. Calcified synovial cysts. *A*, Axial T2-weighted MR image shows severe bilateral L5–S1 facet arthrosis with thick-rimmed facet cysts (*arrows*), which result in severe lateral recess narrowing on the right and indentation of the thecal sac on the left. *B*, Axial CT image shows peripheral calcification of both cysts (*arrows*). Direct cyst puncture and fenestration were not performed in this patient, who instead underwent CT-guided facet injections and nerve blocks and ultimately required an operation.

lying facet arthropathy. The average volume injected in each facet joint was 1.2 ± 0.9 mL. Concurrent, interlaminar, or transforaminal epidural steroid injections were performed in 54 (84%) patients to treat associated radiculopathy. There was no significant association between a successful outcome (or subsequent need for an operation) and concurrent facet or epidural steroid injection or needle gauge used during the procedure ($P > .1$).

Patient Outcomes

Postprocedure outcome data at first clinical follow-up were available in 61 (95%) patients. Long-term follow-up data were available for 57 (89%) treated patients. Mean long-term follow-up was 49 months (range, 2–136 months; median, 44 months). At first postprocedural clinical follow-up, 55 (86%) patients had a partial or complete symptomatic response to CT-guided LFSC aspiration and fenestration. Conversely, 4 (6%) patients had no change in symptoms while 2 (3%) patients reported mild worsening of pain. There were no procedure-related complications. Seventeen (27%) patients underwent repeat procedures for recurrent symptoms, though they were satisfactorily managed by repeat percutaneous fenestration in two-thirds of cases. Most (76%) of the repeat patients underwent 1 additional cyst-fenestration procedure; 4 patients required 2 additional cyst-fenestration procedures. Three patients who required repeat procedures had multiple cysts. Two patients underwent repeat cyst fenestration for cysts that recurred after surgical resection. There were no significant differences in imaging features of cysts in patients who required repeat procedures and those who did not ($P > .1$ for cyst size, calcification, T2 signal, level of stenosis, and follow-up MR imaging findings).

Within 6 months following CT-guided LFSC treatment, 18 (30%) patients underwent an operation for either persistent or recurrent symptoms. At long-term follow-up, 25 (44%) patients underwent an operation for recurrent symptoms. Patients who needed repeat CT procedures for symptomatic relief were more likely to require an operation at long-term follow-up ($P = .007$). Three patients needed repeat surgery for recurrent symptoms that could not be managed conservatively. Most of the patients who required surgical management for symptom relief underwent minimally invasive decompression (laminectomy or laminotomy) and cyst resection (61%), and only 39% of patients had fusion. The 3 patients who had repeat surgery required fusion. No cyst recurrence was noted in fused patients. The mean time between the CT-guided cyst aspiration procedure and the first operation was 11 ± 20 months.

Telephone Follow-Up

Our institutional review board approved patient telephone contact to obtain follow-up data. Patients were contacted by the first author (V.N.S.), and explicit voluntary consent was obtained before administering a brief telephone survey. Patients who agreed to participate were asked to state their pain scores before and after the procedure, comment on the duration of pain relief, report if they had an operation for the cyst, and were asked if they thought the CT-guided procedure was successful. Forty (63%) treated patients were contacted by telephone, and all agreed to participate in the survey, at a mean follow-up of 43 months (range, 2–136 months). Seventy-eight percent thought that the CT-guided cyst aspiration procedure was successful. Eighty-seven percent would recommend the procedure to others. The mean numeric rating score of worst pain before the CT aspiration procedure on a scale of 0–10 was 8.2 ± 1.7. The mean numeric rating score at long-term follow-up was 1.6 ± 2.2. There was no significant difference between preprocedural and long-term follow-up numeric rating scores between patients who underwent an operation and those who only underwent the CT-guided fenestration procedure ($P > .1$).

DISCUSSION

Our study describes a novel CT-guided, minimally invasive technique for managing symptomatic LFSCs as an alternative for surgical resection with a technical success rate of 98% and no procedural complications. Most (86%) patients in our study had at least a partial response at short-term follow-up. More than half (56%) of our patients did not need an operation at long-term follow-up. Most of the patients who were contacted via phone at long-term follow-up thought the procedure was a success.

In the spine, synovial cysts arise as outpouchings of synovial tissue from the facet joint capsule, which may be symptomatic when located within the spinal canal or neural foramina. Facet joint cysts are more common in the lumbar regions and usually arise at the L4–L5 level.[1,3-5] Previous authors have postulated that the relatively increased mobility, propensity for degenerative facet arthropathy, and spondylolisthesis at L4–L5 account for the higher frequency of LFSCs.[4,7,13] On imaging, LFSCs are well-circumscribed masses contacting or in immediate proximity to the facet joint. Cysts typically demonstrate a thin or thick hypointense signal rim on MR imaging. Internal cyst signal is most commonly T1 hypointense and T2 hyperintense, though these features can be variable on the basis of intracystic protein content, blood products, calcification, or gas.[5,6]

Percutaneous Management: Fluoroscopy versus CT Guidance

Minimally invasive, image-guided, management of LFSCs has previously been described. Fluoroscopically guided treatments that have been reported include intra-articular facet injections, cyst aspirations, and predominantly indirect cyst ruptures via parent facet joint access.[12-13,16,17] Parlier-Cuau et al[16] reported 30 patients with LFSCs who were treated with fluoroscopically guided facet joint steroid injections. At 6-month follow-up, only 33% of patients had a favorable response and almost half of the treated patients underwent an operation. In a large study of 101 patients who underwent fluoroscopically guided LFSC rupture (Martha et al[12]), cyst rupture was technically successful in 81% of cases, and 46% of patients were free of pain at a mean follow-up of 3.2 years. In that study, cyst rupture was attempted via intra-articular injection of local anesthetic and/or steroid with contrast into the parent facet joint under increasing pressure until the cyst ruptured. Compared with the results described in our study, a larger proportion of their patients had recurrence of symptoms necessitating surgical resection of the LFSC, which may be attributable to differences in procedural techniques. Most interesting in their study, patients whose cysts were successfully ruptured reported higher levels of pain-related disability 3 years postinjection compared with patients whose cysts were not ruptured. We hypothesize this difference may be partly related to neuronal compression following forceful cyst expansion and ultimately rupture.

More recently, investigators have used CT for image-guided spine procedures, including treating LFSCs using both direct and indirect cyst-rupture techniques.[5,15,18] The indirect technique is similar to that described for fluoroscopically guided cyst inflation and forceful pressurization to achieve cyst rupture. Amoretti et al[18] used CT guidance to directly rupture LFSCs in 120 patients, which was technically successful in 77%. Their technique consisted of direct cyst puncture followed by injection of up to 3 mL of steroid and anesthetic mixture to forcefully rupture the cyst. After ≥1 injection, 75% of patients were free of pain at 12 months. In another CT-guided study, Ortiz and Tekchandani[15] performed ≥1 direct percutaneous CT-guided LFSC rupture in 20 patients and reported a 90% success rate after a mean follow-up of 18 months. Their technique consisted of direct cyst puncture, followed by cyst aspiration, and attempted cyst rupture via injection of 1–3 mL of steroid and anesthetic mixture. These studies demonstrate that the outcome of percutaneous LFSC treatment varies depending on the injection technique, imaging technique used, and follow-up, with good technical success and short-term pain relief and variable longer term outcomes.

The advantages of CT guidance include precise visualization of the cyst, facilitating direct puncture while avoiding critical structures such as thecal sac and exiting nerve. Compared with direct cyst puncture, the indirect cyst rupture technique has limited success in patients in whom it is not possible to access the parent facet joint, in whom the cyst does not communicate with the facet, or in cases in which adequate pressurization of the cyst cannot be achieved. The latter limitation may occur in cases in which the injectate refluxes out of the posterior joint capsule and in patients who may have thick or calcified cyst walls that are resistant to pressure-induced rupture.

Our CT-guided fenestration technique has not been previously described and differs from other CT-guided techniques that have used forceful pressurization of the cyst to induce cyst rupture after direct cyst puncture. Our back-and-forth fenestration technique likely creates multiple sites of cyst wall disruption, which may delay recurrence compared with cyst rupture under pressure (which likely results in a single fenestration). In our experience, the fenestration technique is far less painful than cyst inflation and forceful pressurization to induce rupture, facilitating faster patient recovery and minimizing the amount of procedural sedation. This technique may also be less likely to cause injury to adjacent nerves, which may occur with rapid cyst inflation. As part of our procedure, we injected a small volume of steroid, anesthetic, and contrast to opacify the cyst and treat facet arthropathy. Our average injectate volume of 1.2 mL is the lowest among all published studies and contrasts with reported volumes of 3.5–15 mL[7,13,14] used for indirect cyst rupture.

Surgical Management and Associated Complications

Surgical resection may be considered for patients with persistent intractable pain and neurologic deficits. As part of a systematic review, Bydon et al[19] reviewed 82 studies including 966 patients treated with synovial cyst excision with or without concomitant spinal fusion. During a follow-up of 25 months, 22% of patients had recurrent back pain, 6% required reoperation, and 78% of those required spinal fusion for instability and mechanical back pain. Recurrence of synovial cysts at the same level occurred in 1.8% of patients after decompression alone, but none recurred in patients who underwent decompression with concomitant spinal fusion. The surgical complication rate was 4.8% and included a dural tear, CSF leak, deep venous thrombosis, and 1 death.

Other complications that have been reported after an operation include worsening postoperative instability (especially after laminectomy without fusion), nonunion following fusion, infection, and postoperative hemorrhage.[8] Similar to the previously reported surgical literature, 12% of our patients required re-operation and none of our patients who underwent fusion during the primary operation had cyst recurrence or needed re-operation. The surgical data suggest good overall long-term outcomes after surgical cyst excision with a low recurrence rate, but a non-trivial complication rate. The management of symptomatic lumbar synovial cysts is therefore challenging, regardless of the treatment option.

Imaging Predictors of Success

Twenty-eight percent of the cysts in our study were calcified on CT, comparable with previous descriptions.[20] While we were able to successfully fenestrate even calcified cysts, patients with calcified cysts were less likely to respond to our procedure and more likely to require an operation at long-term follow-up. On MR imaging, those patients with thin-rimmed T2 hyperintense cysts, as opposed to thick-rimmed or low-T2 signal cysts, were more likely to have a successful outcome (statistically significant) and were less likely to require an operation (trend). Reasons for this could be that cysts with calcification, hemorrhage, or elevated protein content or cysts with thick fibrous capsules are less likely

to collapse and more likely to recur, even after successful aspiration and fenestration. These results are consistent with those of Cambron et al[5] and Huang et al.[13] Cambron et al examined the ability of the MR imaging appearance of LFSCs to predict the response to CT-guided indirect cyst rupture. In their study of 110 patients, LFSCs with high or intermediate T2 signal were easier to rupture and were less likely to require an operation. Huang et al reported their experience with percutaneous cyst rupture in 71 patients, 36% of whom had calcified cysts. In their study, calcified cysts were less likely to result in a technically successful procedure, but there was no effect on long-term outcome or the need for an operation.

Long-Term Follow-Up

Our mean follow-up of 49 months is the longest reported for percutaneous treatment of LFSCs. At long-term follow-up, 56% of our patients had sufficient symptomatic relief from the procedure to obviate an operation. This result is similar to or better than those of previous long-term studies[5,12,13] (follow-up range, 34–44 months; 43%–55% of patients requiring an operation). However, our mean time to the first operation at 11 months is longer than that reported by studies[5,12-13] with a similar number of patients, which may be due to the greater technical success achieved by our CT-guided aspiration and fenestration technique.

Study Limitations

The limitations of our study include its retrospective design with variable follow-up intervals and lack of a control group. We had long-term follow-up data available on 89% of patients. Our success rate from the procedure would have been lower if all patients lost to follow-up (11%) had required an operation. Our study design (retrospective observational cohort) without a control group may also have introduced several biases that could have influenced our outcomes. These include, but are not limited to, patient recall bias and placebo effect. Additionally, because an epidural steroid injection was performed concurrently in most patients, it is possible that this may have caused a positive response, rather than the cyst fenestration. We recognize these limitations and think that the results of our study should be further validated with a control group. Study strengths include our large number of patients and long-term follow-up.

CONCLUSIONS

CT-guided direct LFSC aspiration and fenestration are a unique technique associated with high technical success, low complication rates, and resolution of symptoms. In our experience, with careful patient selection, the procedure obviates an operation in a substantial number of patients and should be considered before surgical intervention.

Disclosures: Christopher P. Hess—*UNRELATED*: *Expert Testimony*: various, *Comments*: miscellaneous medicolegal; *Grants/Grants Pending*: Quest Diagnostics, GE Healthcare*; *Travel/Accommodations/Meeting Expenses Unrelated to Activities Listed*: Siemens. *Money paid to the institution.

REFERENCES

1. Kao CC, Winkler SS, Turner JH. **Synovial cyst of spinal facet: case report.** *J Neurosurg* 1974;41:372–76 CrossRef Medline
2. Knox AM, Fon GT. **The appearance of lumbar intraspinal synovial cysts.** *Clin Radiol* 1991;44:397–401 CrossRef Medline
3. Jackson DE, Atlas SW, Mani JR, et al. **Intraspinal synovial cysts: MR imaging.** *Radiology* 1989;170:527–30 CrossRef Medline
4. Hsu KY, Zucherman JF, Shea WJ, et al. **Lumbar intraspinal synovial and ganglion cysts (facet cysts): ten-year experience in evaluation and treatment.** *Spine (Phila Pa 1976)* 1995;20:80–89 CrossRef Medline
5. Cambron SC, McIntyre JJ, Guerin SJ, et al. **Lumbar facet joint synovial cysts: does T2 signal intensity predict outcomes after percutaneous rupture?** *AJNR Am J Neuroradiol* 2013;34:1661–64 CrossRef Medline
6. Apostolaki E, Davies AM, Evans N, et al. **MR imaging of lumbar facet joint synovial cysts.** *Eur Radiol* 2000;10:615–23 CrossRef Medline
7. Allen TL, Tatli Y, Lutz GE. **Fluoroscopic percutaneous lumbar zygapophyseal joint cyst rupture: a clinical outcome study.** *Spine J* 2009;9:387–95 CrossRef Medline
8. Lyons MK, Atkinson JL, Wharen RE, et al. **Surgical evaluation and management of lumbar synovial cysts: the Mayo Clinic experience.** *J Neurosurg* 2000;93(1 suppl):53–57 CrossRef Medline
9. Khan AM, Synnot K, Cammisa FP, et al. **Lumbar synovial cysts of the spine: evaluation of surgical outcome.** *J Spinal Disorder Tech* 2005;18:127–31 CrossRef Medline
10. Lutz GE, Shen TC. **Fluoroscopically guided aspiration of a symptomatic lumbar zygapophyseal joint cyst: a case report.** *Arch Phys Med Rehabil* 2002;83:1789–91 CrossRef Medline
11. Melfi RS, Aprill CN. **Percutaneous puncture of zygapophyseal joint synovial cyst with fluoroscopic guidance.** *Pain Med* 2005;6:122–28 CrossRef Medline
12. Martha JF, Swaim B, Wang DA, et al. **Outcome of percutaneous rupture of lumbar synovial cysts: a case series of 101 patients.** *Spine J* 2009;9:899–904 CrossRef Medline
13. Huang AJ, Bos SA, Torriani M, et al. **Long-term outcomes of percutaneous lumbar facet synovial cyst rupture.** *Skeletal Radiol* 2017;46:75–80 CrossRef Medline
14. Eshraghi Y, Desai V, Cajigal C, et al. **Outcome of percutaneous lumbar synovial cyst rupture in patients with lumbar radiculopathy.** *Pain Physician* 2016;19:E1019–25 Medline
15. Ortiz AO, Tekchandani L. **Improved outcomes with direct percutaneous CT guided lumbar synovial cyst treatment: advanced approaches and techniques.** *J Neurointerv Surg* 2014;6:790–94 CrossRef Medline
16. Parlier-Cuau C, Wybier M, Nizard R, et al. **Symptomatic lumbar facet joint synovial cysts: clinical assessment of facet joint steroid injection after 1 and 6 months and long-term follow-up in 30 patients.** *Radiology* 1999;210:509–13 CrossRef Medline
17. Shah RV, Lutz GE. **Lumbar intraspinal synovial cysts: conservative management and review of the world's literature.** *Spine J* 2003;3:479–88 CrossRef Medline
18. Amoretti N, Huwart L, Foti P, et al. **Symptomatic lumbar facet joint cysts treated by CT-guided intracystic and intra-articular steroid injections.** *Eur Radiol* 2012;22:2836–40 CrossRef Medline
19. Bydon A, Xu R, Parker SL, et al. **Recurrent back and leg pain and cyst reformation after surgical resection of spinal synovial cysts: systematic review of reported postoperative outcomes.** *Spine J* 2010;10:820–26 CrossRef Medline
20. Wang A, Haykal H, Lin J, et al. **Synovial cysts of the lumbar spine: CT evaluation.** *Comput Radiol* 1987;11:253–57 CrossRef Medline

Imaging Appearances and Pathologic Characteristics of Spinal Epidural Meningioma

L.H. Zhang and H.S. Yuan

ABSTRACT

BACKGROUND AND PURPOSE: Spinal epidural meningioma is an uncommon tumor. This study aimed to analyze the imaging and pathologic characteristics of this rare tumor.

MATERIALS AND METHODS: Fourteen confirmed cases of epidural meningioma were retrospectively reviewed, and imaging characteristics and pathologic findings were analyzed to identify the typical features.

RESULTS: The mean age of the patients (4 men, 10 women) was 44.9 years. Twelve tumors were in the cervical spinal canal, and 2, in the thoracic spinal canal. There were 9 en plaque meningiomas, 4 dumbbell-shaped meningiomas, and 1 fusiform/ovoid meningioma. The epidural meningiomas extended over 2–5 spinal segments (mean, 3.2 spinal segments). A soft epidural mass was seen in 12/14 (86%) patients. Dural calcification was seen in 8/14 (57%) tumors. Tumor caused intervertebral foramen enlargement in 10/14 (71%) patients and adhered to the nerve roots in 11/14 (79%) patients. Intradural invasion was seen in 8/14 (57%) patients. The dural tail sign was present in 13/14 (93%) tumors on contrast-enhanced T1WI. Regarding pathologic type, 10 of 14 (71%) were psammomatous, 2 of 14 (14%) were meningothelial, 1 of 14 (7%) was angiomatous, and 1 of 14 (7%) was transitional. During follow-up (mean follow-up, 73.4 months; range, 4–192 months), 7 patients had recurrence. Recurrences were between 4 and 192 months after the operation.

CONCLUSIONS: Epidural meningioma has 3 different growth patterns. Dural thickening, calcification, invasion, and epidural mass formation are characteristic features of epidural meningioma. Regular follow-up imaging is required to detect recurrence.

Meningiomas are the second most common intraspinal tumors after schwannomas and account for approximately 25% of all intraspinal tumors. Meningiomas may be intradural or epidural. Most are intradural, and the most common presentation is an intradural meningioma in the thoracic spinal canal of a middle-aged woman. Epidural meningiomas are rare and account for only 3%–21% of meningiomas.[1,2] Only 39 epidural meningiomas (10 in male patients and 29 in female patients) have been reported in the literature from 1963 to 2013.[3-12] The age of the patients ranged from 13 to 74 years (mean, 41.24 ± 17 years). Of the 39 tumors, 21 were in the cervical spinal canal; 14, in the thoracic spinal canal; 3, in the cervicothoracic spinal canal; and 1, in the lumbar spinal canal. The cases reported until now showed a female predilection and susceptibility of the patients in their fourth decade of life. Epidural meningiomas may be en plaque, dumbbell-shaped, or ovoid.[1,13] There are distinct differences in biologic behavior between epidural and intradural meningiomas. Because of its aggressive behavior, epidural meningioma may easily be mistaken for a malignant spinal tumor on preoperative imaging studies; postoperative recurrence is also not rare. Accurate diagnosis is therefore of great importance. Epidural meningiomas have some distinctive imaging features. The aim of this study was to identify the characteristic imaging findings of epidural meningioma.

MATERIALS AND METHODS

Patients

From 2006 to 2015, fourteen patients were diagnosed with epidural meningioma at our institution. Three patients had postoperative recurrence. All patients underwent CT and MR imaging. The final diagnosis was based on intraoperative confirmation of an extradural tumor and postoperative pathologic diagnosis of meningioma. Intradural meningiomas invading or extending into the epidural space were excluded. Clinical information, including age at presentation, sex, history, duration of signs and symptoms,

Received May 24, 2017; accepted after revision July 29.

From the Department of Radiology, Peking University Third Hospital, Beijing, People's Republic of China.

Please address correspondence to Huishu Yuan, MD, Department of Radiology, Peking University Third Hospital, No. 49, North Garden St, Haidian District, Beijing 100191, People's Republic of China; e-mail: lihuazhang1013@126.com or Huishuyuan69@126.com

http://dx.doi.org/10.3174/ajnr.A5414

imaging findings, and follow-up data were collected from the case records and retrospectively reviewed.

Imaging Protocol

CT examinations were performed with a multidetector CT system (LightSpeed 64; GE Healthcare, Milwaukee, Wisconsin) with intravenous administration of contrast material (80 mL injected at a rate of 3 mL/s). Tube voltage of 120 kV and tube current of 250 mA were used. The acquisition section thickness was 0.625 mm. For image reconstruction, a standard method was selected. All datasets were reconstructed with an effective section thickness of 3 mm. The exposure time was 800 ms.

MR imaging was performed with a 3T scanner (Magnetom Tim Trio; Siemens, Erlangen, Germany) with the patient in a supine position. MR phased array spine coils and related scanning techniques were applied. The standardized protocol included sagittal T1-weighted FSE imaging (TR/TE, 618/11 ms; FOV, 280 × 100 mm) and sagittal (TR/TE, 2852/96 ms; FOV, 190 × 180 mm) and axial (TR/TE, 2720/88 ms; FOV, 190 × 180 mm) T2WI. Sagittal proton-density imaging (TR/TE, 2800 /34 ms; FOV, 250 × 280 mm) was also performed. The same section thickness (3 mm) and section gap (0.3 mm) were used in all procedures. All patients also underwent axial, sagittal, and coronal gadolinium-enhanced (0.2 mmol/kg; injection rate, 2 mL/s) T1-weighted fat-saturated (3D volumetric interpolated breath-hold examination) imaging (TR/TE, 700/11 ms; FOV, 280 × 100 mm; section thickness, 3 mm; section gap, 0.3 mm).

Table 1: Location, shape, and calcification of epidural meningioma

Case	Sex	Age (yr)	Location	Shape	Calcification
1	F	20	C1–2	Dumbbell	−
2	F	43	C1–2	Dumbbell	+
3	F	40	C6–7	Dumbbell	−
4	F	76	C2–3	Dumbbell	+
5	M	46	C2–5	En plaque	+
6	F	48	C2–4	En plaque	+
7	F	43	C4–6	En plaque	+
8	F	46	C2–4	En plaque	+
9	M	36	C1–4	En plaque	+
10	M	30	C2–4	En plaque	−
11	M	38	C3–5	En plaque	−
12	F	47	C2–7	En plaque	−
13	F	50	T9–10	En plaque	+
14	F	59	T4–6	Fusiform	−

Image Analysis

Two radiologists specializing in spinal diseases reviewed all images on a PACS workstation. Abnormalities were identified and characterized by consensus. They assessed the following features: tumor location, morphology, and growth patterns; signal intensity on T1- and T2-weighted images (hypointense, isointense, or hyperintense relative to the normal spinal cord); and pattern and degree of enhancement. Bony erosion and calcification were evaluated on CT.

Pathologic Examination

All 14 patients underwent complete or partial resection of the tumor. Pathologic review was performed on hematoxylin-eosin–stained tissue from all cases.

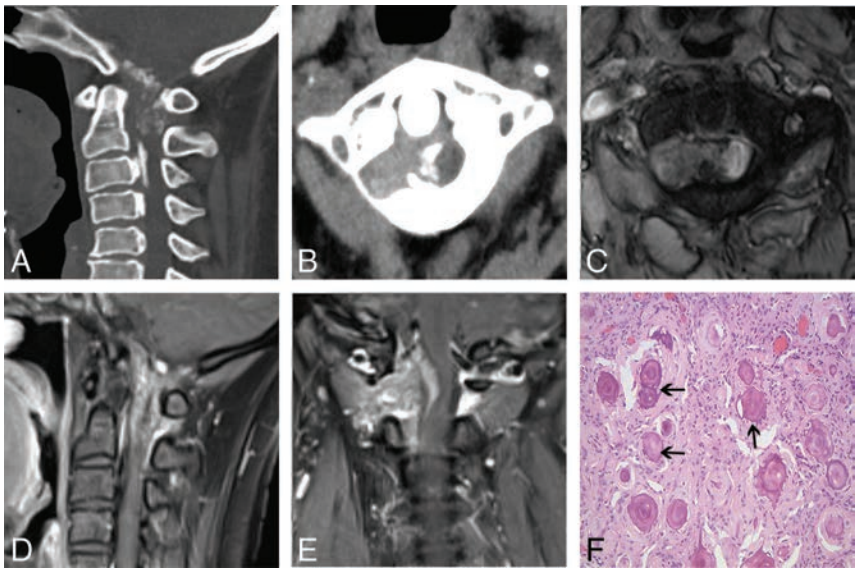

FIG 1. A dumbbell-shaped epidural psammomatous meningioma in 43-year-old woman at C1–2. Sagittal CT image (*A*) reveals the dura from the occiput to C2 thickened with patchy calcification. The ossification of the posterior longitudinal ligament is seen in the C2–3 segment. Axial CT image (*B*) shows a high-intensity epidural mass formed at C1–2 with adjacent bone thinned. Axial T2-weighted image (*C*) shows that the soft mass has low signal intensity compared with that of the spinal cord. Postcontrast T1-weighted sagittal (*D*) image demonstrates a diffusely enhancing dorsal and ventral dura extending over 2 vertebral segments. Postcontrast T1-weighted coronal image (*E*) shows an epidural mass with moderate enhancement and C1–2 intervertebral foramen enlargement. The spinal cord was markedly displaced, and intradural invasion can be seen. *F*, Photomicrograph of the epidural component shows a psammomatous meningioma characterized by the presence of psammoma bodies (*arrows*). H&E, original magnification, ×200.

RESULTS

Clinical Findings

The 14 patients included 4 men and 10 women (mean age, 44.9 years; age range, 20–76 years). The presenting symptoms were bilateral lower limb numbness (6 patients), bilateral lower limb numbness plus upper limb weakness (4 patients), bilateral lower limb numbness plus upper limb pain and numbness (3 patients), and cervical mass (1 patient). Symptom duration ranged from 3 months to 10 years.

CT Findings

Table 1 lists the location, morphology, and growth patterns of the 14 tumors. The tumor was in the cervical spinal canal in 12/14 (86%) patients and in the thoracic spinal canal in 2/14 (14%) patients. Regarding shape, 4/14 (29%) tumors were dumbbell, 9/14 (64%) were en plaque, and 1/14 (7%) was oval/fusiform. Six en plaque and 2 dumbbell-shaped tumors showed flaky dura calcification on CT (Figs 1*A*, -*B* and 2*A*); thus, calcification was present in 57% (8/14) of patients. In 10/14 (71%) pa-

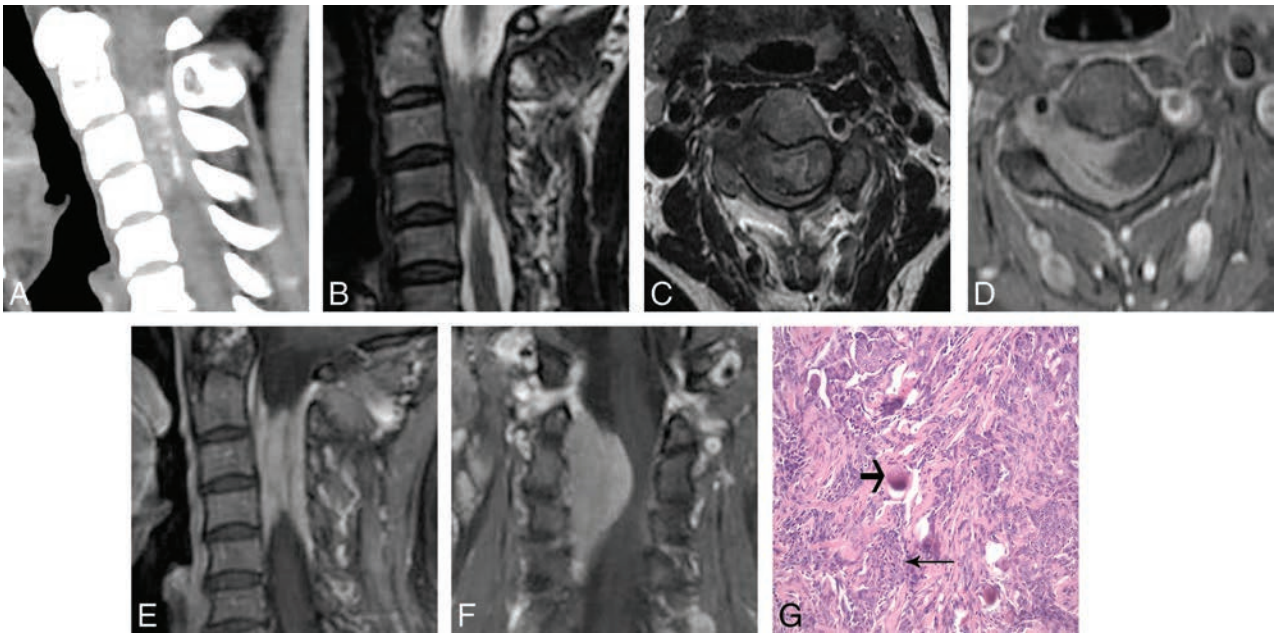

FIG 2. En plaque epidural psammomatous meningioma in a 48-year-old woman at C2–4. Sagittal CT image (*A*) reveals the dural calcification at the C2–4 spinal segments. Sagittal T2-weighted image (*B*) shows that the epidural lesion is isointense. Axial T2WI (*C*) shows that epidural soft mass encircles spinal cord as a half ring. Axial postcontrast T1-weighted image (*D*) shows that the homogeneously enhanced epidural mass encircling the spinal cord from the ventral and dorsal sides. Sagittal postcontrast T1-weighted image (*E*) shows homogeneous enhancement of the ventral and dorsal dura, and the dural tail sign can be seen. Coronal postcontrast image (*F*) shows homogeneous enhancement of the epidural mass that compresses the spinal cord. *G*, Photomicrograph of a psammomatous meningioma is characterized by the presence of psammoma bodies (*arrow*). There are meningothelial cells (*long arrow*) and a small number of fibrous components. H&E, original magnification, ×200.

Table 2: Imaging and pathologic findings

Tumor Type/Imaging Findings	En Plaque	Dumbbell	Fusiform	Total	Percentage
Tumor location					
Cervical spine	8	4	0	12	86%
Thoracic spine	1	0	1	2	14%
Well-defined boundary	0	1	1	2	14%
Dural thickening	8	3	0	11	79%
Dural calcification	6	2	0	8	57%
Adherence to nerve roots	7	4	0	11	79%
Neural foramen enlargement	6	4	0	10	71%
Bone erosion	2	3	0	5	36%
Intradual invasion	4	4	0	8	57%
Epidural mass formation	7	4	1	12	86%
Spinal cord compression	8	3	1	12	86%
T1WI					
Isointensity	6	2	0	8	57%
Hypointensity	3	2	1	6	43%
T2WI					
Isointensity	3	2	0	5	36%
Hypointensity	5	2	0	7	50%
Heterogeneous	1	0	1	2	14%
Dural tail sign	8	4	1	13	93%
Tumor enhancement					
Moderate	2	3	0	5	36%
Marked	7	1	1	9	64%
Pathologic type					
Psammomatous	7	3	0	10	71%
Meningothelial	1	1	0	2	14%
Transitional	1	0	0	1	7%
Angiomatous	0	0	1	1	7%

tients, the tumor extended through the intervertebral foramen to the outer part of the spinal canal, causing enlargement of the foramen. In 5/14 (36%) patients, tumors in the cervical spine compressed adjacent bone, leading to bone erosion; however, there was no bone destruction. Table 2 lists the CT findings.

MR Imaging Findings

Table 2 lists the MR imaging findings. There were 9 en plaque meningiomas with a sheet-like or collar-like appearance on sagittal images. In these cases, the mean thickness of the dura was 4.56 mm, and the mean length of the thickened dura was 54 mm. En plaque epidural meningiomas extended along the dorsal and/or ventral dura, and 7/9 (78%) presented a half-ring appearance on axial MR images (Figs 1*C* and 2*B*, *-C*).

The epidural meningiomas in this study extended over 2–5 spinal segments (mean, 3.2 spinal segments). A soft epidural mass was seen in 12/14 (86%) patients, including 7 patients with en plaque, 4 with dumbbell-shaped, and 1 with fusiform epidural meningiomas (Fig 3*A–C*). Meningiomas caused spinal canal narrowing in 12/14 (86%) patients, with 9 en plaque meningiomas with even narrowing, 4 dumbbell-shaped, and 1 fusiform with lateralized narrowing. Spinal compression was seen in 12/14 (86%) patients. The epidural meningiomas in this study tended to

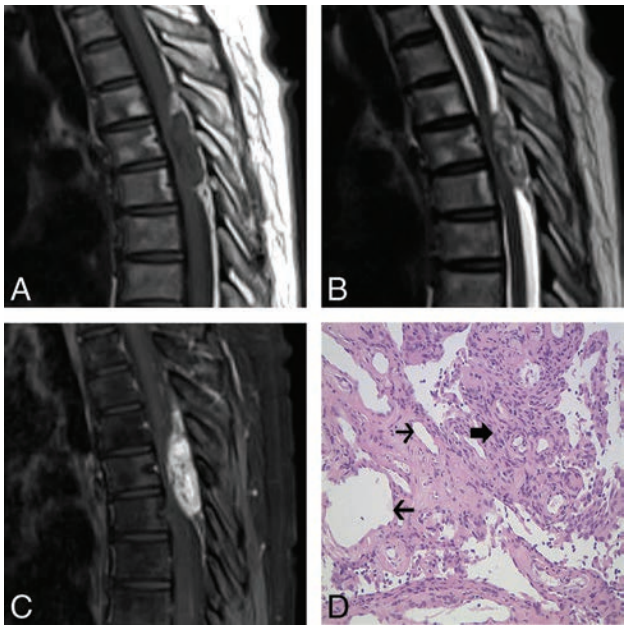

FIG 3. Fusiform epidural angiomatous meningioma in a 59-year-old woman at T4–6. Sagittal T1-weighted MR image (*A*) shows the epidural mass with signal intensity like that of the spinal cord. The subarachnoid space is obliterated at the level of the mass. Sagittal T2-weighted MR image (*B*) shows that the mass has heterogeneous signal intensity and the spinal cord is compressed with edema. Sagittal T1-weighted postcontrast image (*C*) reveals homogeneous enhancement of the extradural meningioma, and the dural tail sign can be seen. Photomicrograph shows that this tumor is composed of islands of meningothelial cells with many vascular vessels (*thin arrows*, *D*). H&E, original magnification, ×200.

adhere to the dura; only 2 tumors did not show that adhesion. In 11/14 (79%) patients, the tumors adhered to the nerve roots, leading to difficulty in separating the nerve from tumor during the operation. Intradural invasion was seen in 8/14 (57%) patients.

On T1WI, epidural meningiomas were isointense (8/14, 57%) or hypointense (6/14, 43%) relative to the normal spinal cord. On T2WI, hypointense signal was seen in 7/14 (50%) patients; isointense signal, in 5/14 (36%) patients; and heterogeneous signal, in 2/14 (14%) patients. The tumors showed moderate (5/14, 36%) or marked (9/14, 64%) enhancement on postcontrast scans (Figs 1*D*, *-E* and 2*D*, *-F*). On contrast-enhanced T1WI, the dural tail sign was present in 13/14 (93%) tumors.

Pathologic Characteristics and CT/MR Imaging Findings

On gross examination, the tumors were red (11 tumors) or gray–white (3 tumors). On pathologic examination, 10/14 (71%) tumors were diagnosed as psammomatous and 2/14 (14%), as meningothelial meningiomas. Under light microscope, the tumor was composed of fibroblast-like cells; calcified psammomatous bodies were visible in 8/14 (57%) tumors (Figs 1*F* and 2*G*). These findings were consistent with their imaging manifestations, namely hypointensity on T1- and T2-weighted images and strip or flaky calcification on CT. One tumor was diagnosed as angiomatous, and one, as a transitional meningioma. The angiomatous meningioma was composed of numerous blood vessels with focal meningioma morphology (Fig 3*D*), while the transitional type was composed of characteristic uniform tumor cells. These findings were consistent with the heterogeneous signal on T2WI. All the above-mentioned tumor types are benign and are classified as World Health Organization grade I meningiomas.

Table 3: Treatment and follow-up results

Case	Treatment	Follow-Up (mo)	Results
1	Subtotal resection	120	Recurrence
2	Subtotal resection	5	Recurrence
3	Complete resection	60	No recurrence
4	Subtotal resection	156	Recurrence
5	Subtotal resection	68	No progress
6	Complete resection	79	No recurrence
7	Subtotal resection	192	Recurrence
8	Subtotal resection	48	No progress
9	Subtotal resection	49	No progress
10	Subtotal resection	36	Recurrence
11	Subtotal resection	No	No MRI follow-up
12	Subtotal resection	7	Recurrence
13	Subtotal resection	180	Recurrence
14	Complete resection	4	No recurrence

Treatment and Follow-Up

Complete and subtotal resection of the tumor was achieved in 3/14 (21%) and 11/14 (79%) patients, respectively. The mean follow-up was 73.4 months (range, 4–192 months). Thirteen cases were followed up with MR imaging. Recurrence was identified in 7 patients, 3 patients did not have recurrence, and 3 patients who had subtotal resection did not show any progression of the tumor during the follow-up period (Table 3).

DISCUSSION

Epidural meningioma is a rare type that may originate from arachnoid cells on the nerve roots outside the dural sac,[14] arachnoid cells located outside the dural sac,[15] or the periosteum of the vertebra.[16] The imaging features, biologic behavior, and prognosis of epidural meningiomas differ from those of intradural meningiomas. This study aimed to identify the characteristic features of epidural meningiomas.

Among the 14 patients with epidural meningiomas in the current study, the male/female ratio was 4:10 and the mean age was 44.9 years; this sex distribution and age are consistent with those in previous reports.[10,17] In terms of tumor location, 12 tumors in this series were in the cervical spinal canal and 2 were in the thoracic spinal canal. This location is contrary to the findings of Frank et al,[18] who reported that the thoracic spine is the typical location of epidural meningioma. However, like us, Wu et al[19] also found the cervical spine to be the most common site of these tumors. In contrast, intradural meningiomas are typically located in the thoracic spinal canal.

Epidural meningiomas may be en plaque, dumbbell-shaped, or fusiform/ovoid. In the current study, 9 epidural meningiomas appeared as en plaque on the sagittal view; the ratio of en plaque to dumbbell-shaped and fusiform tumors was 9:4:1. In en plaque meningiomas, thickened dorsal and ventral dura encircled the spinal cord, forming a C-shape or half ring on the axial MR images. This sign was seen in 78% of our patients and, according to the literature, is common in en plaque meningiomas.[8] Epidural meningioma may extend through the intervertebral foramen to the outer part of the spinal canal. This feature was seen in 10/14

(71%) tumors in the present study. The imaging appearance is like that of a neurogenic tumor. Intervertebral foraminal widening is mainly due to epidural growth pattern, and epidural meningioma is different from its intradural counterpart. Some investigators have suggested that there is proximity to the nerve root or intervertebral foraminal widening, mainly due to presence of arachnoid villi at the nerve root.[20] Enlargement of the intervertebral foramen can be used to differentiate intradural meningioma and schwannoma,[20] but it is difficult to distinguish epidural meningioma from schwannoma with this sign. Another characteristic of epidural meningiomas is calcification, which is uncommon in spinal intradural meningiomas. Radiologically visible calcification has been described in only 1%–4.6% of all spinal meningiomas.[2] In this study, flaky calcification was observed in 8 epidural meningiomas (6 en plaque and 2 dumbbell-shaped). Calcification was mainly due to psammoma bodies, and it was present in 8 of the 10 psammomatous meningiomas. Epidural meningiomas may have different shapes and may be of different pathologic types, but all except 2 epidural meningiomas showed isointensity or hypointensity on T2WI, mainly due to the presence of calcification, psammomatous bodies, and interstitial collagen fibers, which tend to decrease the signal intensity. Epidural meningiomas commonly show moderate or marked enhancement, reflecting the good epidural blood supply.

The dural tail sign is commonly seen in meningiomas. It manifests as linear thickening and contrast enhancement of the meninges adjacent to the meningioma. In the current study, 13 (93%) meningiomas showed the dural tail sign on contrast-enhanced T1-weighted images. Wu et al[19] described the dural tail sign in 75% of extradural en plaque meningiomas in their series of 12 patients. We found the dural tail sign to be common in epidural meningiomas. The dural tail sign is said to be present in 50%–60% of intradural meningiomas.[20] Although this sign favors the diagnosis of extradural meningioma, it is not specific for this tumor and is also seen in other lesions such as metastases and lymphoma.

Epidural spinal meningiomas show more aggressive behavior than intradural meningiomas.[21] Most epidural meningiomas, especially the en plaque type, often adhere to the dura. They show an epidural growth pattern and often display intradural invasion; consequently, the tumor boundary may not be clearly defined as in intradural meningiomas. In this study, only 2/14 (14%) tumors had clear boundaries. Epidural meningiomas can grow through the intervertebral foramen and involve an adjacent nerve root. In this series, 8 tumors showed intradural invasion on MR imaging and 11 tumors demonstrated adhesions to nerve roots during an operation. Tuli et al[22] were the first to report invasion of nerve roots by epidural meningioma in a pathologic specimen. This behavior makes complete tumor removal difficult, and in our series, complete resection was achieved in only 3 of the 14 patients.

Postoperative recurrence of epidural meningioma is not rare. Rutherford et al[23] reported 1 patient who had 2 recurrences. One of the 6 patients reported by Yao et al[3] had a recurrence 6 years after surgery. In the current study, 7 of the 14 patients had postoperative recurrence between 5 and 192 months after the operation. Of these 7 cases, 1 was an infiltrated meningothelial-type meningioma; the risk of recurrence was high because this large-sized tumor had invaded adjacent muscles and complete resection was impossible. In the other 6 patients, the recurrences were due to close adherence of tumor to the dura or nerve roots, which made complete resection difficult to perform. In this study, the longest interval between the operation and recurrence was 192 months, which shows that long-term follow-up is particularly important in these patients. Many investigators have suggested that calcification of meningiomas is associated with tumor recurrence. In the present series, 5 of the 7 patients with recurrences had dural calcification; such calcification adds to the difficulty of complete removal of the tumor.[24]

Depending on the imaging findings and the shape of the epidural meningioma, the differential diagnosis could include spinal lymphoma, neurogenic tumor, angiolipoma, metastatic tumor, and ossification of ligament. En plaque epidural meningioma shows the same growth pattern and signal as a lymphoma. However, lymphomas are mostly observed on the ventral side of the dura and are characterized by formation of a paravertebral soft-tissue mass and infiltration of adjacent bone.[25] Epidural meningiomas rarely destroy adjacent bone; they mostly cause bone compression and erosion.[7] In this study, 5 patients had bone compression and reactive osteosclerosis, features that are more likely to be seen with benign tumors. Dumbbell-shaped epidural meningiomas should be differentiated from neurogenic tumor. Neurogenic tumors rarely show calcification, whereas punctuate calcification is common in epidural meningiomas. In addition, neurogenic tumors show heterogeneous enhancement, whereas meningiomas are characterized by homogeneous contrast enhancement.[20] Fusiform meningioma needs to be differentiated from metastatic tumor and angiolipoma. A metastatic tumor is often accompanied by adjacent bone destruction and paravertebral involvement.[26] An angiolipoma is hyperintense on T2WI, whereas most meningiomas are iso- or hypointense. The dural tail sign is also useful for identification of a meningioma. Ossification of the posterior longitudinal ligaments could be confused with an epidural meningioma; however, the former condition is not accompanied by dura thickening or enhancement.

Our study had several limitations. First, this was a retrospective study without a control group. Second, the number of patients was small; however, epidural meningioma is an uncommon entity, and ours is one of the largest studies to date. Third, T2-weighted gradient-echo images were not acquired; this acquisition would have been useful for differentiating these tumors from schwannomas.[27] Fourth, intradural invasion was not confirmed pathologically. Finally, long-term clinical and MR imaging follow-up was not performed for all patients.

CONCLUSIONS

In this study, epidural meningioma was most common in middle-aged women. The cervical spinal canal was the most common location of the tumor. Tumor shape was en plaque, dumbbell, or ovoid/fusiform. Enlargement of the intervertebral foramen, adhesion to or infiltration of adjacent nerve roots, and intradural extension were common. CT revealed linear or flaky calcification in the dura mater. Epidural meningioma had isointense or hypointense signal on T2WI. The dural tail sign was common on

postcontrast MR imaging. The psammomatous tumor was the most common pathologic type in this sample. Complete removal of tumor can be difficult because of encirclement and infiltration of the dura or an adjacent nerve root. Long-term follow-up is necessary to detect recurrence.

REFERENCES

1. EI Khamary SM, Alorainy IA. **Case 100: spinal epidural meningioma.** *Radiology* 2006;241:614–17 CrossRef Medline
2. Messori A, Rychlicki F, Salvolini U. **Spinal epidural en-plaque meningioma with an unusual pattern of calcification in a 14-year-old girl: case report and review of the literature.** *Neuroradiology* 2002; 44:256–60 CrossRef Medline
3. Yao N, Jun Y, Wang HG, et al. **The clinic study of spinal epidural meningioma (a report of 6 cases).** *Beijing Medicine* 2010;32:795–98
4. Wang SH, Gao X, Peng XP, et al. **MRI diagnosis of extradural spinal meningiomas (report of 3 cases).** *J Med Imaging* 2010; 20:1394–96
5. Yoshiura T, Shrier DA, Pilcher WH, et al. **Cervical spinal meningioma with unusual MR contrast enhancement.** *AJNR Am J Neuroradiol* 1998;19:1040–42 Medline
6. Achari G, Behari S, Mishra A, et al. **Extradural meningioma en-plaque of the cervical cord.** *Neurol Res* 2000;22:351–53 CrossRef Medline
7. Takeuchi H, Kubota T, Sato K, et al. **Cervical extradural meningioma with rapidly progressive myelopathy.** *J Clin Neurosci* 2006;13: 397–400 CrossRef Medline
8. Yamada S, Kawai S, Yonezawa T, et al. **Cervical extradural en-plaque meningioma.** *Neurol Med Chir* 2007;47:36–39 CrossRef
9. Mariniello G, Briganti F, De Caro ML, et al. **Cervical extradural "en-plaque" meningioma.** *J Neurol Surg A Cent Eur Neurosurg* 2012;73: 330–33 CrossRef Medline
10. Gamache FW Jr, Wang JC, Deck M, et al. **Unusual appearance of an en plaque meningioma of the cervical spinal canal: a case report and literature review.** *Spine (Phila Pa 1976)* 2001;26:E878–79 Medline
11. Calogero JA, Moossy J. **Extradural spinal meningioma: report of four cases.** *J Neurosurg* 1972;37:442–47 CrossRef Medline
12. Zhong W, Chen H, Huang S. **Cervical en-plaque epidural meningioma.** *Neurol India* 2011;59:132–34 CrossRef Medline
13. Zevgaridis D, Thomé C. **Purely epidural spinal meningioma mimicking metastatic tumor: case report and review of the literature.** *Spine* 2002;27:E403–05 CrossRef Medline
14. Kumar S, Kaza R, Maitra TK, Chandra M. **Extradural spinal meningioma arising from a nerve root: case report.** *J Neurosurg* 1980;52: 728–29 CrossRef Medline
15. Sato N, Sze G. **Extradural spinal meningioma: MRI.** *Neuroradiology* 1997;39:450–52 CrossRef Medline
16. Kaya U, Ozden B, Turantan MI, et al. **Spinal epidural meningioma in childhood: a case report.** *Neurosurgery* 1982;10:746–47 CrossRef Medline
17. Dehcordi SR, Ricci A, Chiominto A, et al. **Dorsal extradural meningioma: case report and literature review.** *Surg Neurol Int* 2016;7:76 CrossRef Medline
18. Frank BL, Harrop JS, Hanna A, et al. **Cervical extradural meningioma: case report and literature review.** *Spinal Cord Med* 2008;31:302–05 CrossRef
19. Wu L, Yang T, Deng X, et al. **Spinal extradural en plaque meningiomas: clinical features and long-term outcomes of 12 cases.** *J Neurosurg Spine* 2014;21:892–98 CrossRef Medline
20. Liu WC, Choi G, Lee SH, et al. **Radiological findings of spinal schwannomas and meningioma: focus on discrimination of two disease entities.** *Eur Radiol* 2009;19:2707–15 CrossRef Medline
21. Bettaswamy A, Ambesh P, Kanti Das K, et al. **Extradural spinal meningioma: revisiting a rare entity.** *J Craniovertebr Junction Spine* 2016;7:65–68 CrossRef Medline
22. Tuli J, Drzymalski DM, Lidov H, et al. **Extradural en-plaque spinal meningioma with intraneural invasion.** *World Neurosurg* 2012;77: 202.e5–13 CrossRef Medline
23. Rutherford SA, Linton KM, Durnian JM, et al. **Epidural meningioma of the sacral canal: case report.** *J Neurosurg Spine* 2006;4:71–74 CrossRef Medline
24. Lee JW, Lee IS, Choi KU, et al. **CT and MRI findings of calcified spinal meningioma: correlation with pathological findings.** *Skeletal Radiol* 2010;39:345–52 CrossRef Medline
25. Cugati G, Singh M, Pande A, et al. **Primary spinal epidural lymphomas.** *J Craniovertebr Junction Spine* 2011;2:3–11 CrossRef Medline
26. Sako T, Iida Y, Yokoyama Y, et al. **Solitary spinal epidural metastasis from gastric cancer.** *Case Rep Orthop* 2016;2016:1591269 CrossRef Medline
27. Mishra A, Thomas B, Kapilamoorthy TR. **Susceptibility weighted imaging - a problem-solving tool in differentiation of cerebellopontine angle schwannomas and meningiomas.** *Neuroradiol J* 2017; 30:253–58 CrossRef Medline

Celebrating 35 Years of the AJNR

January 1983 edition

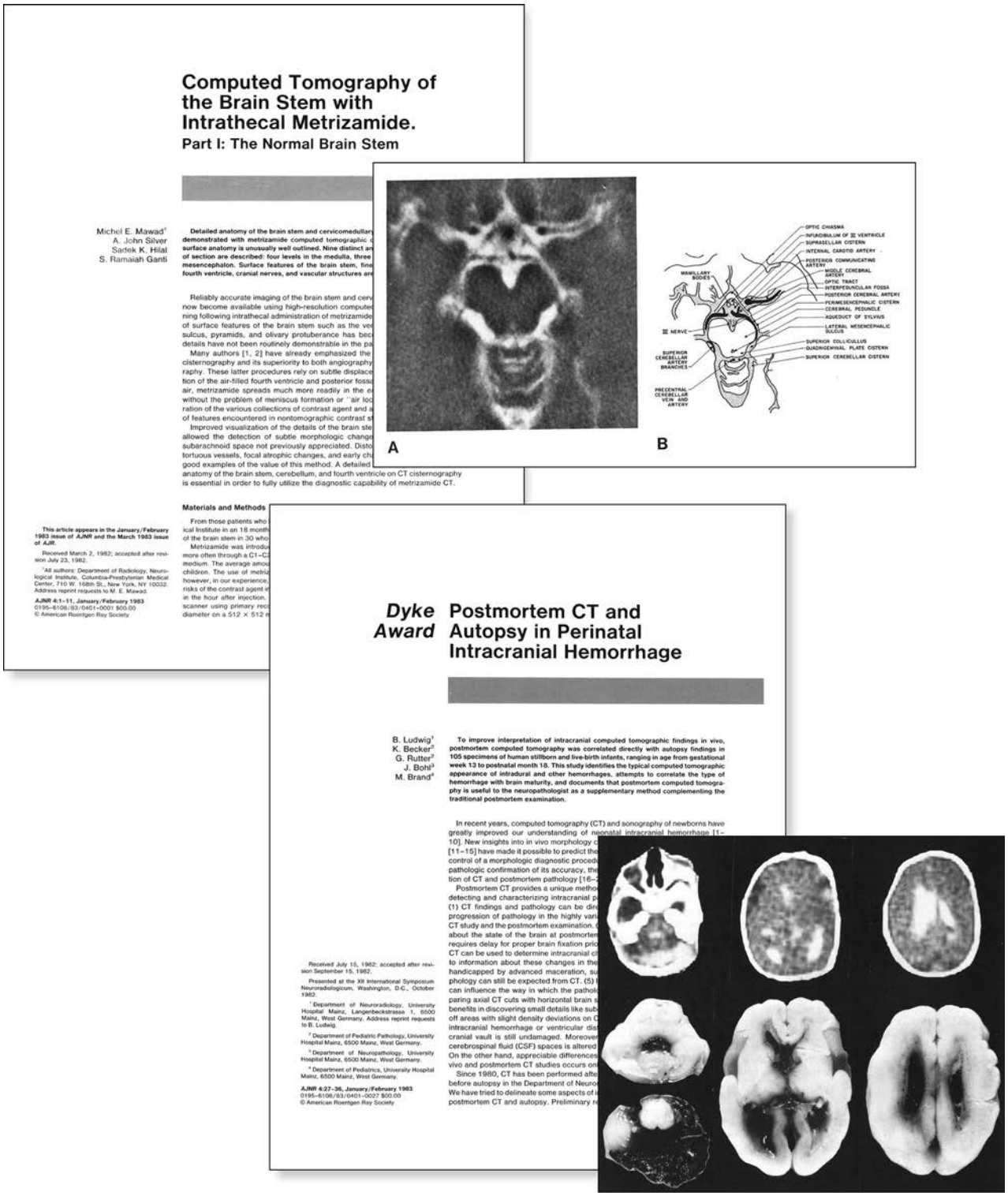

Computed Tomography of the Brain Stem with Intrathecal Metrizamide.
Part I: The Normal Brain Stem

Michel E. Mawad
A. John Silver
Sadek K. Hilal
S. Ramaiah Ganti

A

B

Dyke Award

Postmortem CT and Autopsy in Perinatal Intracranial Hemorrhage

B. Ludwig
K. Becker
G. Rutter
J. Bohl
M. Brand

Bipolar Radiofrequency Ablation of Spinal Tumors: The Effect of the Posterior Vertebral Cortex Defect on Temperature Distribution in the Spinal Canal

We read with interest the article in the June 2017 *American Journal of Neuroradiology* by Wallace et al entitled, "Percutaneous Spinal Ablation in a Sheep Model: Protective Capacity of an Intact Cortex, Correlation of Ablation Parameters with Ablation Zone Size, and Correlation of Postablation MRI and Pathologic Findings."[1] The researchers postulated that an intact cortex appears to protect against radiofrequency ablation-induced spinal cord injury, but not against non-impedance-based modalities. This conclusion is an important consideration in the treatment of spinal metastases with bipolar radiofrequency ablation (RFA).

In agreement with the accompanying commentary by Gemmete,[2] we believe that more animal research with bipolar RFA systems is needed, in contrast to monopolar RFA. The main limitation of the study, as Wallace et al[1] stated, is that the research was performed with normal bone, which is unlike the typical clinical situation. To strengthen the aforementioned conclusion and solve the limitation of the study, we present our preliminarily results as supportive data.

Tumors are known to affect the posterior vertebral cortex (PVC).[3] An insulating effect of the PVC during monopolar RFA has been reported.[4] Others have postulated that RFA should only be performed on patients with an intact PVC and not too far advanced osteolysis.[5] No research regarding the effect of a PVC defect on temperature distribution during bipolar RFA in the spinal canal was found during our literature review. Thus, we performed our ex vivo research.

A preliminarily evaluation of the temperature distribution change during bipolar RFA in the spinal canal in porcine lumbar vertebrae was performed. As shown in Fig 1, lumbar vertebrae from 10 pigs were collected and randomly divided into 2 groups (4 lumbar vertebrae per group). Group 1 was the intact cortex group; and group 2, the cortex defect group. The PVC defect was achieved by removal of the cortex with a rongeur. We used a radiofrequency generator connected to an expandable electrode catheter (1500X; AngioDynamics, Latham, New York) for the ablation. An infrared thermometer system (CTlaser LT; Optris, Berlin, Germany) was used to monitor the temperature. The highest temperature during RFA was recorded. RFA was performed on each sample for 15 minutes at the 75-W setting and 95°C. The temperature (37.43°C ± 4.43°C) in the intact cortex group was noted. A significant increase (49.44°C ± 3.34°C) was seen in the cortex defect group ($P < .01$). Our data suggest that an intact PVC provides thermal isolation during bipolar RFA. For the cases with altered PVC, bipolar RFA is still a potentially safe therapy.

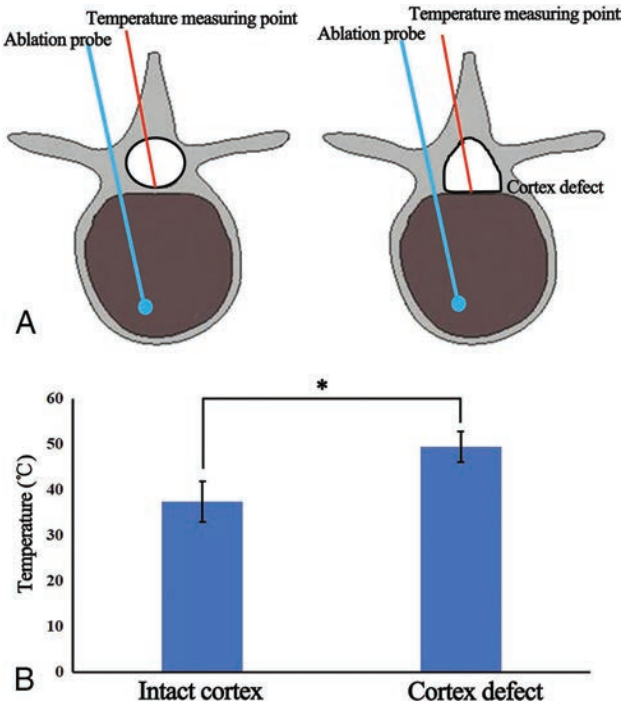

FIG 1. The effect of the posterior vertebral cortex defect on temperature distribution in the spinal canal during bipolar radiofrequency ablation.

We offer these preliminary data suggesting that an intact PVC can potentially protect against RFA-induced spinal cord injury. We show changes in the temperature distribution within the spinal canal of the samples with PVC defects during bipolar RFA.

REFERENCES

1. Wallace AN, Hillen TJ, Friedman MV, et al. **Percutaneous spinal ablation in a sheep model: protective capacity of an intact cortex, correlation of ablation parameters with ablation zone size, and correlation of postablation MRI and pathologic findings.** *AJNR Am J Neuroradiol* 2017;38:1653–59 CrossRef Medline

http://dx.doi.org/10.3174/ajnr.A5393

2. Gemmete JJ. **Is an intact posterior vertebral body cortex protective for percutaneous ablation?** *AJNR Am J Neuroradiol* 2017;38:1660–61 CrossRef Medline
3. Alkalay RN. **Effect of the metastatic defect on the structural response and failure process of human vertebrae: an experimental study.** *Clin Biomech (Bristol, Avon)* 2015;30:121–28 CrossRef Medline
4. Dupuy DE, Hong R, Oliver B, et al. **Radiofrequency ablation of spinal tumors: temperature distribution in the spinal canal.** *AJR Am J Roentgenol* 2000;175:1263–66 CrossRef Medline
5. Bornemann R, Grötz SF, Pennekamp PH, et al. **Radiofrequency ablation: temperature distribution in adjacent tissues.** *Z Orthop Unfall* 2016;154:294–98 CrossRef Medline

C. Zhang
X. Han
Department of Bone and Soft Tissue Tumors
Tianjin Medical University Cancer Institute and Hospital
National Clinical Research Center for Cancer
Key Laboratory of Cancer Prevention and Therapy
Tianjin's Clinical Research Center for Cancer
Tianjin, China
P. Douglas
Tianjin Medical University
Tianjin, China
Y. Dai
Institute of Robotics and Automatic Information System
Tianjin Key Laboratory of Intelligent Robotics
College of Computer and Control Engineering, Nankai University
Tianjin, China
G. Wang
Department of Bone and Soft Tissue Tumors
Tianjin Medical University Cancer Institute and Hospital
National Clinical Research Center for Cancer
Key Laboratory of Cancer Prevention and Therapy
Tianjin's Clinical Research Center for Cancer
Tianjin, China

Heinz First to Routinely Catheterize Carotid and Vertebral Arteries in America

The 1967 article of Amundsen et al, "Cerebral Angiography via the Femoral Artery with Particular Reference to Cerebrovascular Disease,"[1] was chosen by the *American Journal of Neuroradiology* (*AJNR*) as the "Best Paper" in neuroradiology in 2003. Heinz and associates developed the technique and routinely used it at Emory University in the United States in 1964, 3 full years earlier than its publication date.

There is a tendency to take our basic investigative tools in neuroradiology for granted. These include transfemoral cerebral angiography. Remember Egaz Moniz's original experience in which several of his first 9 patients died in 1927![2] Percutaneous direct carotid puncture followed Moniz's original work, and this procedure persisted until 1964. In direct carotid puncture, the tip of the needle frequently created a posterior carotid wall "flap" when the tip was withdrawn to the midstream to obtain the best flow. This antegrade flow could elevate the posterior wall flap and obstruct blood flow to the brain. These flaps were not infrequently the site of local thrombotic deposition or cerebral embolism. We knew when we performed a carotid puncture that we were putting the patient at some small but definite risk. However, this technique was all we had to offer. Attempts at direct vertebral puncture were extremely difficult and the artery, when transfixed by the side-hole Sheldon-Swann needle, would frequently be narrowed by spasm. Failure to visualize the vertebrobasilar system by direct puncture led to the use of the right retrograde brachial arteriogram, but this study usually failed to sufficiently map the complete vertebrobasilar system.

When neuroradiologists attempted direct carotid puncture in infants and children in the early 1960s, we encountered many technical failures, most of which were secondary to the small caliber of the artery and the associated spasm that followed. Some centers had to resort to surgical cut-down for access. However, in 1964, we found a way to access all of the cerebral arteries with 1 puncture, the transfemoral cerebral angiogram (TFCA). We no longer had to puncture each carotid and vertebral artery individually in the neck.

Both Per Amundsen of Oslo, Norway, and the Emory University neuroradiology group in Atlanta, under my direction, began to use TFCA for routine selective carotid and vertebral catheterization for all patients in 1964. However, Amundsen did not publish his TFCA article until 1967.[1] Given neuroradiologists' common failure to image the vertebrobasilar arterial anatomy and, second, the great difficulty in puncturing and cannulating the carotid arteries in infants, it is not surprising that a solution would be found on each of 2 continents at roughly the same time. At the time, I did not think the technical change was sufficient to justify a scientific paper.

In 2001, the *AJNR* named a special panel to select the 10 neuroradiologic articles that would most represent the seminal underpinnings of our current clinical practice. Dr Amundsen's article on TFCA was published in a supplement to the journal *Acta Neurologica Scandinavica* in 1967 and was chosen as the most important of the 10 publications.[3]

Dr Amundsen's fellow Scandinavians, Eric Lindgren and Torgny Greitz, described the development of the Amundsen technique in 1995:

"Amundsen of Norway was the first routinely to catheterize and examine all cerebral vessels, carotid as well as vertebral arteries, a technique he had been using at the Ullevål Hospital in Norway since 1964. Hans Newton learned about the routine use of the femoral approach when he was in Sweden in 1966. He had earlier only occasionally used this method for carotid angiography. Newton was actually the first to perform a catheterization of the carotid artery from the femoral artery at the Karolinska Hospital. That was in 1966 when he came back from a week's visit in Oslo."[3]

For a description of the San Francisco neuroradiology technical procedures for the performance of cerebral angiography, I quote the description of John Mani, a member of the University of California, San Francisco (UCSF) team at the time Dr Newton left San Francisco for his sabbatical in 1965–1966 and who worked with Dr Amundsen[3]:

"After one week, Per told me that he understood the UCSF approach. He was now going to introduce the Amundsen technique that he had been using in Norway for some time. Cerebral angiographic procedures were now to be done by the femoral technique, by using catheters and modified Seldinger technique."

During my training at Columbia, I chafed over the inadequacies of the retrograde brachial angiogram because of our usual failure to map the vertebrobasilar system adequately. Because I

http://dx.doi.org/10.3174/ajnr.A5429

had experience with brachial venous angiography for the heart as a fourth-year medical student at the University of Pennsylvania, I was comfortable with vascular procedures. Later, I had a unique opportunity to learn the Seldinger technique for aortic and renal catheterization as a resident in radiology at the Philadelphia General Hospital. This took place in 1962, a year before my New York fellowship. Because I felt competent with arterial catheterization, I wanted very much to use it at Columbia for femoral-carotid angiography in 1962–1964, but I had to wait until I had my own program before I could put my experience to work. I was appointed as chief of "Special Procedures" at Emory University on July 1, 1964. In the next several months, our group initiated TFCA for all cerebral procedures in infants and adults. This included all vertebral angiograms. At the same time, we started a National Institutes of Health–sponsored neuroradiology fellowship program. Neuroradiology trainees included Dale Cooper MD, James Brylski MD, Peter Sones MD, and James Hoffman MD, as well as others. Dr Hoffman later became director of the program.

TFCA offered a second equally important advance, allowing catheterization of the tiny cerebral arteries in infants. This was as great as the gain in imaging the vertebrobasilar system in adults. Applying the newly developed TFCA approach at Emory using pediatric needles, 0.021-inch guidewires, and Kifa small-caliber catheters, which still had to be imported from Scandinavia, provided the answer. The femoral artery was much larger in caliber and easier to catheterize, farther away from the neck with its redundant soft tissue, and less painful and, finally, allowed easy selective catheterization of each of the cerebral arteries.

Drs Erik Lindgren and Torgny Greitz wrote an article on the evolution of vertebral angiography, "The Stockholm School of Neuroradiology."[4] Radner was reported to be the first to catheterize the vertebral artery from the brachial artery approach.[5] Lindgren was himself the first to catheterize the vertebral artery from the femoral artery in 1954.[4]

"Amundsen of Norway was the first to catheterize and examine routinely all cerebral vessels, carotid as well as vertebral via the femoral route, a technique that he had been using at the Rikshospitalet in Oslo since 1964. Newton learned about this when Amundsen introduced this routine while the former was in Sweden in 1964."[2,4] According to Lindgren and Greitz and according to Rosenbaum et al,[3] the sabbatical dates were 1965–1966, not 1964.

From these references, it appears that UCSF was mainly using existing standard angiographic techniques until Dr Newton returned from his 8-month sabbatical in 1965, after which UCSF began using cerebral catheterization for all cerebral angiography. By contrast, at Emory in 1964, we began to routinely use femoral-cerebral catheterization for all cerebral angiography. Thus, Emory University was the first institution in America to use TFCA routinely for all of its cerebral angiography patients. It appears that Emory University and Amundsen's Rikshospitalet Hospital in Oslo each initiated the use of TFCA for routine cerebral angiography in 1964.

When I arrived at my new position at Emory in 1964, all procedures were performed by neurosurgery. Fortunately, our neurology colleagues realized that we might have something to offer and did refer a few patients. Our big opportunity came in the usual way: by showing our new colleagues that we could bring something new and better to patient diagnosis. It was the TFCA selective studies that gave access to the posterior circulation in adults and carotid and vertebral angiography in infants and children that made the difference. Within 1 year, neuroradiology performed all of the Emory studies. I was able to repeat this same process at Yale (1966), Pittsburgh (1969), and Duke (1978).

Why publish this information now? If the *AJNR* panelists came together and agreed that the Amundsen procedure was the most outstanding on the American list of contributions, then all the pertinent historical information about the presentation should be identified and included. My review of the 2001 *AJNR* report regarding TFCA suggests that there has been a historical omission. This omission could be corrected by adding 3 sentences to the *AJNR* panel report:

"While Amundsen published his classic article describing TFCA in 1967, routine utilization of TFCA for cerebral angiography was already instituted at Emory University in the United States in1964, 3 years earlier. Routine use of TFCA in Atlanta took place in the same year that Amundsen began his routine use of TFCA in Oslo in 1964. While much of the emphasis on TFCA has focused on overcoming our inability to adequately image the vertebrobasilar circulation in adults, we call attention to the equally great additional contribution of TFCA to selective pediatric angiography of the carotid and vertebral arteries in infants and children."

My writing takes nothing away from the brilliant investigators Per Amundsen and Hans Newton (a personal friend). My goal is to simply fill in some of the details for the historical record while those of us who served in the period can accurately record it.

REFERENCES

1. Amundsen P, Dugstad G, Noyes W. **Cerebral angiography via the femoral artery with particular reference to cerebrovascular disease.** *Acta Neurol Scand* 1967;43:Suppl 31:115 Medline
2. Moniz E. **L'encephalographie arterielle, son importance son la localisation des tumors des tumoeurs cerebrals.** *Rev Neurol (Paris)* 1927;2:72–90
3. Rosenbaum AE, Eldevik OP, Mani JR, et al. **In re: Amundsen P. Cerebral angiography via the femoral artery with particular reference to cerebrovascular disease—Acta Neurol Scand 1967; Suppl. 31:115.** *AJNR Am J Neuroradiol* 2001;22:584–89 Medline
4. Lindgren E. Greitz T. **The Stockholm School of Neuroradiology.** *AJNR Am J Neuroradiol* 1995;16:351–60 Medline
5. Radner S. **Vertebral angiography by catheterization; a new method employed in 221 cases.** *Acta Radiol Suppl* 1951;87:1–134 Medline

E.R. Heinz
Department of Radiology
Duke University
Durham, North Carolina

Does the Volume of CSF Removed Affect the Response to a Tap in Normal Pressure Hydrocephalus?

We read with great interest the article by Thakur et al,[1] in which they investigated the association of CSF volume removed by a tap test and the clinical response in patients with normal pressure hydrocephalus (NPH). In the "Conclusions" of their study, they found no evidence to support a higher volume of CSF removal impacting gait testing, and they discussed a high volume of CSF removal possibly not being necessary in a diagnostic lumbar tap test. We appreciate the authors for evaluating the data of such a large group of patients with NPH ($n = 249$) and conducting detailed analyses of these patients. Nonetheless, we think that this is a devastating result and detailed interrogations of the study results should be conducted to avoid misleading conclusions. Hence, we would like to discuss some points for a better understanding of this valuable report, which may also add crucial perspectives for future studies.

First, in the introduction, the authors mention some complications of the lumbar tap test (LTT), such as headache and pain that may compromise gait testing in these patients. However, the potential impact of these complications, which may be more frequent in patients with higher CSF volume removed, was not mentioned in the "Discussion" of the study. On the other hand, the authors suggested that passive flow of CSF from the puncture site, which might have been altered according to the size of the bore needle, could have influenced the study results. In accordance with this hypothesis, they found that patients whose taps involved a larger bore needle showed significantly more improvement in immediate time scores ($P = .04$, in the patient subset showing improvement in time scores immediately after LTT). In contrast, they stated that patients whose taps involved a larger bore needle had a nonsignificant tendency to have a greater improvement in 24-hour times scores ($P = .06$). However, we think that from a mechanistic point of view, the main effect of passive CSF flow is supposed to be more pronounced in the 24-hour evaluations (considering the cumulative effect across time), whereas in the immediate evaluations, CSF volume removal would be more efficient; this outcome was not the case in this study. Moreover, it would be completely irrational to comment about an association between the measured amount of CSF removal and the clinical response if we agreed that the effect of passive flow changes according to the needle size. Of note, an association between the needle gauge and improvement was not found in the overall group ($P = .283$). Therefore, we think that the necessity for further analyses of the needle size effect as well as a related discussion should be considered by the authors.

Second, the authors stated that the study was retrospective and that randomization was not a factor other than that age and sex might have confounded the results. We agree with this thought. Nevertheless, we think that confounding variables might not be eliminated via a method of randomization of patients. Although there are various hypotheses trying to explain the pathophysiology of NPH, the underlying mechanisms as well as responsible agents have not been fully clarified currently. Distortion of periventricular tissue due to altering CSF pressure dynamics, the pressure gradient between the ventricles and periventricular tissues, and the influence of accompanying deep vascular disease constitute some of these hypotheses.[2] Besides, a major consideration regarding the occurrence of NPH is the evolution of the mechanisms involved and changing pressure gradients according to the stage of the disease.[3] Thus, it can be suggested that the combination of functioning mechanisms in the occurrence of NPH may differ among individuals and according to the stage of the disease. Therefore, we think that for a rational evaluation of the association between CSF removal volume and clinical improvement of the patients, the LTT test should be performed in the same patients with NPH in distinct time courses (at an interval sufficient to avoid the influence of the initial LTT) to totally exclude confounding factors. The results of the studies with this method would yield substantial information for clinicians regarding the optimal CSF volume to be removed for determining the appropriate patients for shunt surgery.

REFERENCES

1. Thakur SK, Serulle Y, Miskin NP, et al. **Lumbar puncture test in normal pressure hydrocephalus: does the volume of CSF removed affect the response to tap?** *AJNR Am J Neuroradiol* 2017;38:1456–60 CrossRef Medline
2. Keong NC, Pena A, Price SJ, et al. **Imaging normal pressure hydrocephalus: theories, techniques, and challenges.** *Neurosurg Focus* 2016;41:E11 CrossRef Medline
3. Bradley WG Jr. **Magnetic resonance imaging of normal pressure hy-**

http://dx.doi.org/10.3174/ajnr.A5422

drocephalus. *Semin Ultrasound CT MR* 2016;37:120–28 CrossRef Medline

H. Onder
Department of Neurology
Ministry of Health, Yozgat City Hospital
Ankara, Turkey
S. Hanalioglu
Department of Neurosurgery
University of Health Sciences
Dışkapı Yıldırım Beyazıt Training and Research Hospital
Ankara, Turkey

REPLY:

We thank Onder and Hanalioglu for their comments on our article, "Lumbar Puncture Test in Normal Pressure Hydrocephalus: Does the Volume of CSF Removed Affect the Response to Tap?" Our work, though retrospective, casts doubt on the use of a high-volume spinal tap of >30 mL in the assessment of patients with normal pressure hydrocephalus (NPH). The practice of using a high-volume spinal tap has theoretic but no empiric foundation and, now, some evidence to question its use. Further investigation including Onder and Hanalioglu's suggestion of repeat studies in the same patients, though difficult to perform in an often-frail elder population, could provide important additional evidence.

Onder and Hanalioglu raise a legitimate point that given that headaches may compromise the results of lumbar tap test (LTT), higher volume taps may have more associated headaches and this will explain why higher volume taps perform worse. In response to their point, we reviewed our own cases of LTT and noted that severe headaches were extremely rare, occurring in <1% of patients with NPH. It would be unlikely for headaches to be affecting the results of our study.

We agree that the needle gauge findings were not definitive in our investigation, but results were promising, trending toward significance ($P = .06$) at 24-hour walk time testing and significant ($P = .04$) at 4-hour walk time testing in those subgroups that responded at these end points. We suggest that future research consider how post-lumbar puncture epidural CSF leakage may influence the clinical response beyond that induced by the volume drained during the procedure itself. We plan to continue to investigate needle gauge effects using larger bore needles to explore this relationship.

Nevertheless, ongoing prospective research to define invasive and noninvasive diagnostic end points that predict shunt response in the NPH syndrome is highly desirable.

http://dx.doi.org/10.3174/ajnr.A5525

S.K. Thakur
Department of Medicine
University of California, Los Angeles
Los Angeles, California
Y. Serulle
Department of Radiology
University of Maryland Medical Center
Baltimore, Maryland
N.P. Miskin
Department of Radiology
Brigham and Women's Hospital
Boston, Massachusetts
H. Rusinek
Department of Radiology
J. Golomb
Department of Neurology
A.E. George
Department of Radiology
New York University School of Medicine
New York, New York

The authors of "Validation of an MRI Brain Injury and Growth Scoring System in Very Preterm Infants Scanned at 29- to 35-Week Postmenstrual Age" (*AJNR Am J Neuroradiol* 2017;38:1435–42, https://doi.org/10.3174/ajnr.A5191) wish to clarify for the reader that the image in On-line Fig 2 shows bilateral connatal cysts. The figure, along with its amended legend, is displayed below.

http://dx.doi.org/10.3174/ajnr.A5448

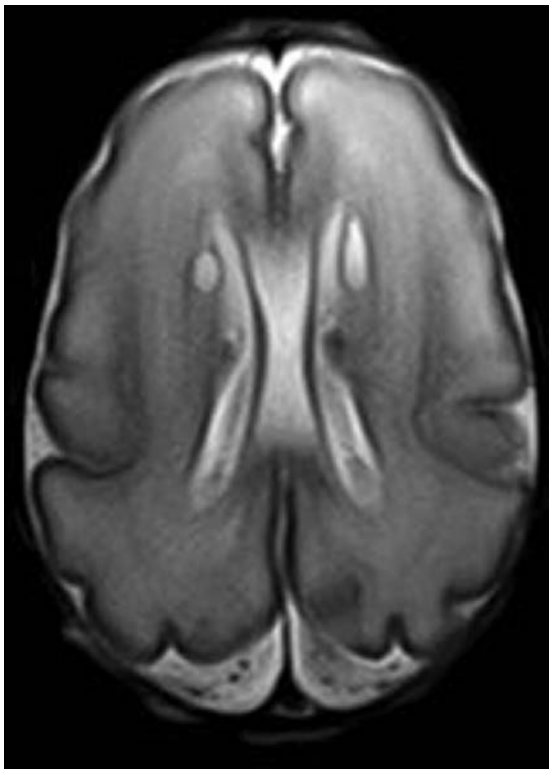

ON-LINE FIG 2. Bilateral connatal cysts, classified as cerebral WM, cystic lesion, focal bilateral, score 2 (axial T2).